Springer Water

Amin Shaban *Editor*

Satellite Monitoring of Water Resources in the Middle East

Springer

Springer Water

The book series Springer Water comprises a broad portfolio of multi- and interdisciplinary scientific books, aiming at researchers, students, and everyone interested in water-related science. The series includes peer-reviewed monographs, edited volumes, textbooks, and conference proceedings. Its volumes combine all kinds of water-related research areas, such as: the movement, distribution and quality of freshwater; water resources; the quality and pollution of water and its influence on health; the water industry including drinking water, wastewater, and desalination services and technologies; water history; as well as water management and the governmental, political, developmental, and ethical aspects of water.

Amin Shaban
Editor

Satellite Monitoring of Water Resources in the Middle East

Springer

Editor
Amin Shaban
National Council for Scientific Research
Beirut, Lebanon

ISSN 2364-6934 ISSN 2364-8198 (electronic)
Springer Water
ISBN 978-3-031-15548-2 ISBN 978-3-031-15549-9 (eBook)
https://doi.org/10.1007/978-3-031-15549-9

This Springer imprint is published by the registered company Springer Nature Switzerland AG
The registered company address is: Gewerbestrasse 11, 6330 Cham, Switzerland

Foreword

Water and environmental scientists should pay attention to the recent book of Professor Amin Shaban, senior experts in the field of water resources management and satellite remote sensing.

I proudly state that this book is a unique international reference in the sense that new information is presented for the first time, for the scientific research community related to remote sensing applicability to water resources management sustainability.

This book represents a comprehensive overview of the hydraulic situation in the MENA region and proposes solutions, direct technologies applications of advanced systems within the scope of Sustainable Development Goals. It also covers various key areas and fields of interest such as the fundamentals of satellite remote sensing, water resources in the Middle East, MODIS Satellite Images, and TRMM Products to Compare Rainfall and Streamflow along the Coastal Rivers of Lebanon, Landsat Satellite Images for Lineaments Detection: a Tool to Identify Groundwater Productivity in Lebanon...among many other areas of expertise.

During the regional complexity, Prof. Shaban's contribution is fundamental since it puts within our reach effective realistic combinations that are necessary to understand the various facets of hydraulic reality in the MENA region.

Moreover, the methodological and scientific depth covered by this book is very enriching since it facilitates the flow of facts and knowledge in the hydraulic field and its related components. It demands great intellectual ability to document and propose more than 20 articles presented by prominent scientists in the field and propose solutions based on extremely sensitive technological tools, helping Water leaders to a better Management of this vulnerable resource.

This publication provides guidance for the researchers around the world while ensuring an easy access to real data, authentic information, documented approaches, and technical procedures that are all required for an adequate integrated water resources management.

In addition to this, the analysis presented in various chapters of this book is specifically written while taking into consideration the decision makers and while highlighting the necessity of improving the global understanding of water resources

around the world. It also describes the numerous studies that were done at the international level to review and face the multiple challenges that are threatening future generations' hydraulic security.

Once again, we discover throughout this publication that strategic alliances, cooperation, and dialogue between water actors are necessary to achieve the sustainable development goals and to guarantee therefore an everlasting water peace.

Readers will clearly sense the complexity of sustainable water management in the MENA region and the constant challenges of water adaptation policies in order to face extreme events phenomenon caused by the global changes impacts.

At the end, I can state that Professor Amin Shaban's efforts in publishing this book were impressive and noteworthy.

It is a striking addition to the already existing knowledge.

It is an asset for water experts, researchers, and policy makers.

Fadi Georges Comair
Director of the EEWRC-CYPRUS INSTITUTE
Chair of UNESCO'S IHP COUNCIL
(2019–2021)

Preface

The Middle East Region with a surface area of more than 7 million km^2 (i.e., 5% of the total area of the Globe) is inhabited by more than 4.4 % of World's people who live in diverse geographic locations including coastal zone, mountains, and deserts. This region is almost situated between three continents and constitutes a significant geographic zone for the entire World. The Middle East Region encompasses 18 countries where 13 of them belong to the Arab Region and comprising 62 % (285.19 million people) of the total population and 66.5% (4848674 km^2) in the surface area. The Middle East Region is mainly an arid to semi-arid zone with some sub-humid mountainous localities; and thus, it is the most water-poor region where the average annual precipitation is less than 200 mm besides a potential evapotranspiration exceeding 2000 mm per year.

Lately with the exacerbated population growth and its relevant increase in human activates, notably in the agricultural sector resulted in abrupt water shortage and water became a valuable commodity; and therefore, the per capita does not exceed 100 m^3/year in many instances in this region. The changing climate is another main reason in water scarcity in the Middle East Region, and all obtained studies confirmed abrupt oscillations in the climatic conditions which have been changed into torrential rain patterns and recurrence of climatic extremes accompanied with considerable increase in temperature. This has been reflected on the socioeconomic aspects of the entire region, while the geo-political conflicts added another challenges on water resources and especially on shared water resources.

The countries of the Middle East Region are addressing the problem of water scarcity with different tools and measures. Therefore, some of these countries, even with minimal water availability, can manage their supply/demand by adopting non-conventional water resources. While, other Middle Eastern countries, even with considerable water availability, are still witnessing water shortage and the supply/demand is still imbalanced and this has been reflected in several shortages of many other vital sector, notably the agriculture and energy sectors.

Beside the existed challenges on water resources in the Middle East Region, the applied measures to conserve the available resources and to adapt to the changing

climatic conditions are inadequate to resolve the problem, plus the mismanagement in many instances plays a negative role in securing pure water with sufficient amounts.

In this regard, the role of the scientific research is significant and it can assist in putting water policies and strategies in the Middle East countries. There are several studies and research projects applied on water resources assessment in this region, including monitoring and exploration approaches. Recently, this studies have been supported by the use of advanced techniques with a special emphasis on the use of space techniques where satellite images with different spatial and temporal resolution. The history of monitoring satellites in the Middle East has been come to light since the beginning of 1970s, at the time when new water resources in the Middle East Region have been explored and it puts the initial step forward to adopt these techniques which proved its creditability to be a useful tool in studying water resources and the relevant themes. This includes: identifying hydrogeological clues for groundwater reservoirs, monitoring water infiltration to subsurface rocks, monitoring the changes in groundwater level, delineating surface water basins, detecting groundwater seeps to the sea, identifying fracture systems and their relationship with groundwater flow/storage, and many other applications.

The authors in this book introduce a number of case studies obtained by outstanding experts. It has been dedicated to be used by a miscellany of audiences including academics, scientific researchers, experts and decision makers, universities and research centres, as well as to the national institutes belonging to water sector.

Beirut, Lebanon Amin Shaban

Contents

Fundamentals of Satellite Remote Sensing 1
Amin Shaban

Water Resources in the Middle East 15
Amin Shaban

The Suitability of Satellite Remote Sensing and GIS Technologies for Mapping, Monitoring and Managing Water Resources in the Middle East 29
Serwan M. J. Baban

Atmospheric Rivers and Precipitation in the Middle East 49
Elias Massoud, Theresa Massoud, Duane Waliser, Bin Guan, and Agniv Sengupta

Inventory of Shared Water Resources in Western Asia: Selected Aquifer Systems in the Arabian Peninsula for the Application of Remote Sensing Techniques 71
Yusuf Al-Mooji

GIS-Based Multi-criteria Approach to Assess Water Resources Vulnerability in a Changing Climate over the Arab Domain 87
Marlene A. Tomaszkiewicz

Unraveling the Spatiotemporal Dynamics of Satellite-Inferred Water Resources in the Arabian Peninsula 99
Youssef Wehbe

A Technical Note on Least Squares Mascon Fitting to GRACE Satellite Data to Estimate Total Water Storage Changes in the Middle East 115
Zohreh Safdari, Gholamreza Joodaki, and Hossein Nahavandchi

Spatial–Temporal Change of a Dam Lake Using Remote Sensing and Meteorological Drought Indices 129
Emre Özelkan

Forecasting Domestic Water Demand Using Meteorological and Satellite Data: Case Study of Greater Beirut Area 149
J. Saade, S. Ghanimeh, M. Atieh, and E. Ibrahim

MODIS Satellite Images and TRMM Products to Compare Rainfall and Streamflow Along the Coastal Rivers of Lebanon 171
Amin Shaban, Cordula Robinson, and Farouk El-Baz

Water Balance and Demand for Different Environmental Changes and Management Scenarios in the Hasbani Basin Using a WEAP Model and Geospatial Data 187
Mohammad Merheb and Chadi Abdallah

Agricultural Water Management in the Nile Delta Using Remote Sensing Techniques 205
Ayat Elnemer

Studying the Water Resources and Hydrological Characteristics of the West Bank and Gaza Strip, Palestine Using GIS and Remote Sensing Data 219
Ahmed Ghodieh

Landsat Satellite Images for Lineaments Detection: A Tool to Identify Groundwater Productivity in Lebanon 251
Amin Shaban and Farouk El-Baz

Using Information from Remote Sensing to Estimate Groundwater: GRACE and Sentinel-1 Satellites 273
Elias Massoud, Amin Shaban, Zhen Liu, and Mhamad El Hage

Volcanic Terrains Reveal Bright Hydrogeological Prospects in Saudi Arabia: A GIS & RSA Linked Research on Harrat Rahat 287
Nayyer A. Zaigham, Omar S. Aburizaiza, Zeeshan A. Nayyar, and Gohar A. Mahar

Regional Mapping of Groundwater Potential Zones in the Saudi Arabia Using Remote Sensing and Machine Learning Algorithms 311
Samy Elmahdy and Mohamed Mohamed

A DRASTIC-Based Fuzzy C-means Clustering Technique for Evaluating Groundwater Vulnerability Under Uncertainty 335
Jahangir Abedi Koupai, Nastaran Zamani, and Farshad Rezaei

Prospect of Retrieving Non-optical Water Quality Properties with Remote Sensing Techniques 365
Hala Abayazid

A Combined Remote Sensing and Modelling Approach to Simulate the Impact of Climate Change on the River Discharge in a Lebanese Snow-Covered Basin 379
Ali Fadel, Ghaleb Faour, Mario Mhawej, Mahmoud Ghazal, and Lionel Jarlan

Remote Sensing of Water Quality for Human Activity Use of Shat Al-Hilla" 393
Suhad M. Al-Hedny, Atheer Saieb Naji Al-Azawey, and Qassim A. Talib Alshujairy

Correction to: Atmospheric Rivers and Precipitation in the Middle East C1
Elias Massoud, Theresa Massoud, Duane Waliser, Bin Guan, and Agniv Sengupta

Index 407

Fundamentals of Satellite Remote Sensing

Amin Shaban

1 General Overview

The term "remote sensing" was first mentioned in the early 1960s to describe tools for observing the Earth from space, when initially the classical capturing of aerial photographs has been found and the camera was the first used sensor. Hence, observing objects on Earth's surface from height requires energy interaction between the object and the sensor. The energy signal emitted from objects on terrain surface is detected by space sensors, and it is either stored in memory on board the satellite system or transmitted to ground receiving stations for further processing.

Normally, the human vision represents a sophisticated remote sensing process within a unified system, providing great spatial and color advantages. Thus, digital (electronic) processing of satellite images extends our capability to integrate combined spatial information from different sources. The first mission that officially incorporated photography for potential geological and meteorological applications from space was the Gemini Titan in 1965 (Chuvieco 2020).

There are numerous types of satellite images retrieved today, and the type of these images is attributed to many digital and physical characteristics, such as spatial resolution, orbiting time, properties of the captured rays from objects, plus many other characteristics. Therefore, remote sensing is considered as geo-spatial data source which can cover large areas wherever they are. It is a significant tool for monitoring and capturing observations with least cost and time saving. Remote sensing, notably by using satellite images, has occupied large applications and it is included in many academic centers, ministries, and many other institutions.

A. Shaban (✉)
National Council for Scientific Research—Lebanon (CNRS-L), CNRS-L, P.O. Box 11-8281, Beirut, Lebanon
e-mail: geoamin@gmail.com

A. Shaban (ed.), *Satellite Monitoring of Water Resources in the Middle East*,
Springer Water, https://doi.org/10.1007/978-3-031-15549-9_1

From remote sensing, maps are usually the target products, because they can be easily read and even understood by non-specialists. They are supplementary documents for decision makers as well who rely mainly of maps to elaborate strategies and plans, notably in the view of the economic development and resources sustainability.

The beginning of topographic maps production has been joined with the use of stereoscopic photographs and lately with satellite images where the latter is able to produce topographic maps with high accuracy. Whereas satellite remote sensing has been used for topographic mapping purposes since the launch of ERTS-1 in 1972 (Dixon-Gough 1994).

The earliest aerial photograph, which was taken from a balloon and entitled "Boston", was taken in 1860. Therefore, photography and photogrammetry sciences have been developed, and then commonly used especially for the military purposes during the World Wars I and II. Therefore, aerial photos represent the beginning of Remote Sensing era when the first recorded photograph was taken from an airplane by Wilbur Wright in 1909. Later on, aerial photos with a miscellany of specifications are interpreted by stereoscopes. This resulted in the development of science of photogrammetry which enables applying analysis and measurements for the Earth's surface.

Recently, the use of satellite images and the relevant and supplementary remote sensing tools (e.g. drones, color aerial photos, geo-information systems, etc.) has become widespread and applied for several applications, including the assessment and exploration of natural resources and monitoring and diagnose of the surficial processes whether the physical/or natural ones.

Satellite remote sensing is a vast topic with applications on terrain analysis, physical oceanography, land/ocean ecosystem, and the science of cryosphere atmospheric and near-earth space. Hence, learning the entire field would require studying perhaps a dozen books on the topic, and lately many researchers with other field than remote sensing have been involved in this field and dedicate their jobs for remote sensing while their background knowledge is totally different. This is also the case with the applications of geo-information systems and the related geo-spatial data extraction and analysis.

The fundamentals of satellite remote sensing requires understanding several basic information, concepts and definitions. Here are some basics definitions and concepts relevant to satellite remote sensing:

- Electromagnetic radiation is energy propagates through space or through any media in the form of electromagnetic waves. The characteristics of electromagnetic radiation vary in the wavelength. The entire range of wavelengths is called the electromagnetic spectrum, which is classified into different regions of the spectrum, depending on their characteristics. Visible light is an example of these spectral bands. Radio waves, infrared rays, and ultraviolet rays are other familiar forms (Fig. 1).
- Satellite Remote Sensing is a recent technology for obtaining geo-spatial information about the features on surface of the Earth with special (and different) sensors mounted on satellites.

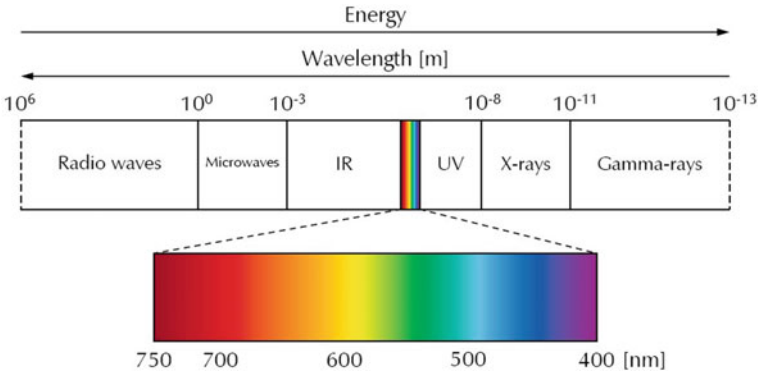

Fig. 1 The electromagnetic spectrum (UoB 2021)

- Each type of these features, absorbs and reflects solar radiation in a characteristic manner.
- Remote sensors on-board satellites do not capture all of the electromagnetic radiation that reaches from their source on Earth to satellites. Mainly due to technological and economic constraints, only some limited regions or bands of the electromagnetic spectrum are selectively detected by remote sensors. Thus, potential applications of a certain remote sensor depend on the number of bands it can be detected and the range these bands are located in the electromagnetic spectrum (Shimizu 2011).

  According to spectral signatures from sources, there are two main Remote Sensing sensors: passive and active (or microwave). Passive sensors detect the electromagnetic radiation naturally emanating from the surface of the Earth. Typically, they are camera and electro-optical sensors. While, active sensors, such as radar and laser, transmit energy for illumination which is directed toward the target object, and then it capture the reflected radiation reflected from that target.
- Images can be as raster or vector ones. Hence, raster image is a pixel-based image, and it is also called "bitmap", which represents a grid of individual pixels that collectively compose an image (Fig. 2). While, vector image refers to vector graphics that are based on mathematical formulas that define geometric primitives such as polygons, lines, curves, circles and rectangles (Fig. 2).

Remote sensing is also attributed to the type of radiation received by sensors and the ranges wavelengths, as follows:

- Visible and Reflective Infrared RS,
- Thermal Infrared RS,
- Microwave (or radar) RS.

Space techniques, as new innovative tools, have several types where numerous aspects of sensors are mounted of shuttles (platforms carrying satellites) to compose satellites travelling in space along define orbits. There are tens thousands of satellites

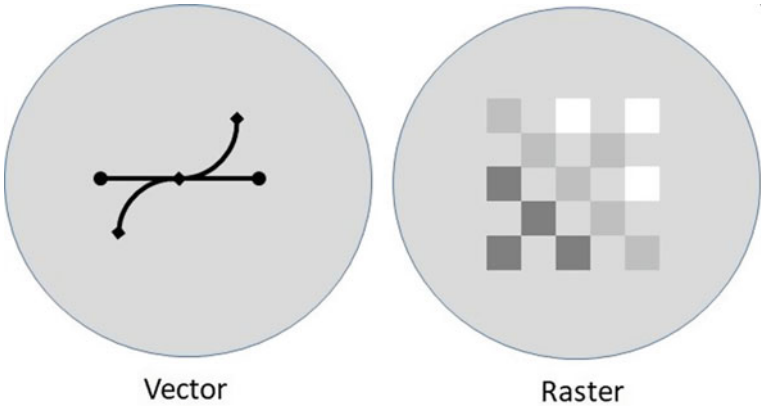

Fig. 2 Simplified illustration for raster and vector images

have been lunched into space moving around the Earth, where the largest part of them is not operating.

Two main types of orbits satellites follow, these are the communication satellites and land (or Earth) observatory satellites. Hence, communication satellites connect between different sources and receives all over the globe (e.g. navigation, TVs, GPS, radios, etc.). Observatory satellites are dedicated to monitor Earth's surface by acquiring observations and images covering the marine and terrestrial environments. Thus, satellites follow two global orbital trends; the geostationary satellites follow WE orbit, and it is mainly used for meteorological and communication purposes; however, land observatory satellites are orbiting in the near-polar orbit (Fig. 3).

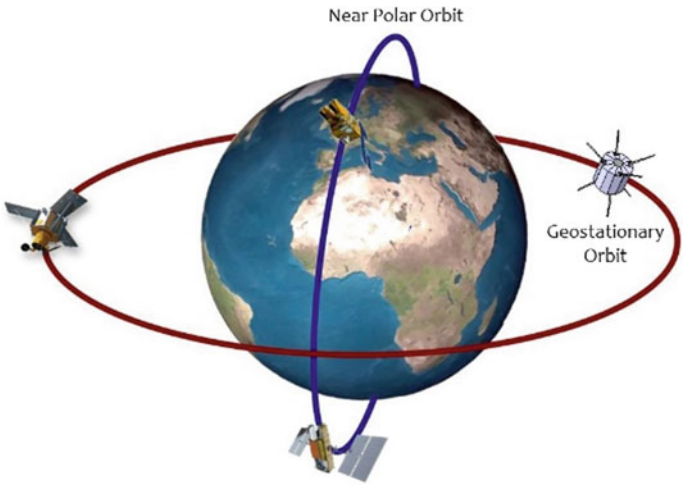

Fig. 3 Polar and geostationary satellite orbits (SEOS 2021)

The flight characteristics of space shuttles are important for the resolution of the acquired geos-spatial data; however, the optical and technical characteristics of the fixed sensors on satellites are most significant in this concern. That is why some satellite images with low-altitude shuttles have less spatial resolution that other satellite images with high-altitude shuttles. The most known flight altitudes of shuttles for inquiring geo-spatial data are: (1) satellites (altitude: 500–900 km), (2) space shuttle (altitude: 185–575 km), (3) high-latitude flying aircraft (altitude: 10–12 km), (4) moderate-latitude flying aircraft (altitude: 1.5–3.5 km) and (5) low-latitude flying aircraft (with altitude below 1 km).

2 Characteristics of Satellite Images

Recently, there are many satellite systems orbiting around the Earth and collecting images for different themes. Each type of satellite data offers specific characteristics that make it more or less appropriate for a particular application (Eastman 2001).

The first lunched remote sensing satellites are: Sputnik in 1957; Explorer in 1958 and Corona in 1960. They were used in many new applications. Later on, these applications were progressed with the advancements of the space techniques. Hence, remote sensing occupies a variety of applications including assessment, monitoring and exploration. This has been extended to (but not limited) water resources, agricultural, natural hazards, marine environment, pollution, change detection, etc.

Usually, determining the specifications of a satellite image is prerequisite step in order to select the type of satellite images that fit with the purpose of any study. It is often happened that satellite images available do not fulfill the requirements of a specific study. Therefore, several specifications characterize satellite images and should be primarily known by the investigator. The most significant ones are:

1. Resolution:
   Resolution of an image refers to the number of pixels displayed per inch of an image; however, this in a broad sense describes the spatial resolution, but there are other types of images resolution which are represented by spatial, temporal, spectral and radiometric resolution.

   - Spatial resolution
     It is the size of a pixel size recorded in a raster images. While, the pixel is the smallest detectable element in the image, and it enables distinguishing features. The pixel in a satellite image is a function of discriminating objects on Earth's surface. Hence, there are supportive tools act in the clarification on the images such as lens antennae, display, exposure, processing and many other specifications. Therefore, low-resolution images occupy large pixel size, and thus small objects will not be able to be clearly observed (Fig. 4). Hence, sensors mounted satellites result diverse spatial resolution.

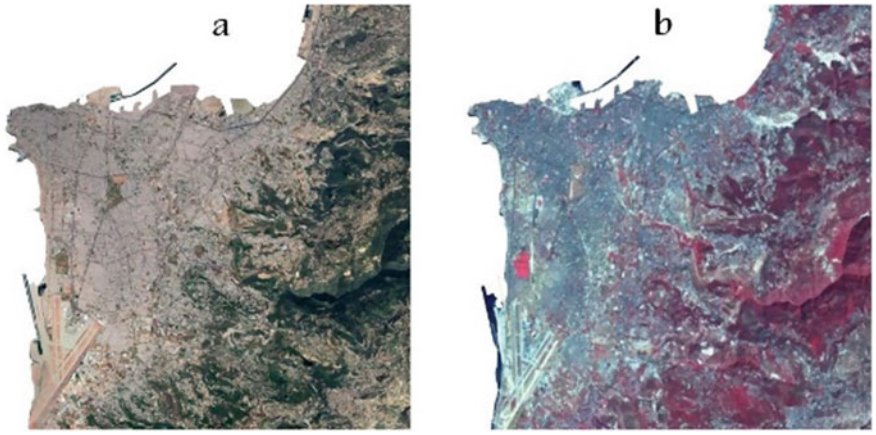

Fig. 4 Two satellite images with different spatial resolution showing Beirut area, Lebanon. **a** Aster 2019 (15 m); **b** Landsat 7, 2018 (30 m)

- Temporal resolution
  This is also described as revisit time, and it is the time needed to revisit and acquire image/s for the exact same location on Earth's surface. However, the amount of time depends on the orbital characteristics of the satellite shuttle as well as the characteristics of sensor fixed on the shuttle. The temporal resolution is high when the revisiting delay is low and vice-versa. Temporal resolution is usually expressed in days for most satellites (Théau 2008).

  The temporal resolution of a satellite image does not affected by the spatial, spectral or radiometric resolution. For example, Landsat images with 30 m spatial resolution and Aster images with 15 m spatial resolution both require 16 days revisit the same location on Earth's surface. While, Spot-6 images with 6 m spatial resolution requires 26 days' revisit time.
- Spectral resolution
  The spectral resolution represents band range or band width that recorded by the sensor. It is also the ability of a sensor to identify fine *wavelength* intervals. Thus, the finer the *spectral resolution,* the narrower the *wavelength* range for a particular channel or band. For example, the satellite image of Landsat sensor has seven bands, where it includes infrared spectrum, with a spectral resolution ranges between 0.7 μm and 2.1 μm. While, the sensor of Aster satellite image has 14 spectral bands where three of them are in the visible band range and 11 in the infrared band range.
- Radiometric resolution
  This is measured in bit, and it is corresponds to the ability of a sensor to distinguish grey-scale within the same *spectral band* of differences in the electromagnetic energy reflected by ground surfaces. Therefore, a sensor with finer radiometric resolution is able to record more significant intensity levels. The more bit an image has, the more grey-scale values can be stored, and,

Fig. 5 The relationship between bit and the grayscale values (American Cinematographer 2005)

thus, more differences in the reflection on the land surfaces can be spotted. Hence, one bit stands for a sensor that knows only black and white. 2 bit equals 4 grey-scale values and 4 bit 16 values (Fig. 5). The convert equation is as follows:

$$2\ to the\ Power of\ Bit\ =\ number of\ Grey - Scale\ Values$$

2. Multi-look imagery:
   Several satellite-based imaging systems have the ability to acquire images at different view angles, where more than one sensor are mounted on the satellite platform to produce stereo satellite imaging (or 3-D imagine). In this process, two pictures of an object are taken from slightly different angles allowing for depth to be perceived when viewing the images. Typical of these satellites are: Spot, Ikonos, Quick-bird and many other satellites. In remote sensing applications photographs of Earth's surface are taken and 3D topographic maps and computer models can be created using the stereo images.

   In this regard, there is a tradeoff between spectral and spatial resolution when designing a system (Galbraith et al. 2005). In multispectral systems, each detector occupies different spectral bands. Hence, the increase of image resolution is designed through a capable sensor system for acquire images at a lower resolution and use the sensor system's pointing capabilities to allow collection of multiple low-resolution images within a short time span as the sensor travels over a target area. Then, image processing methods to fuse the multiple low-resolution images into a single high resolution image may be used (Borman and Stevenson 1998).
3. Swath width:
   Swath width describes the images area that represents the actual surface area on the Earth's surface. It depends on the specifications of the sensor in sizing the imaged observation, which is also named as "image scene". In aerial photographs, swath width is usually a function of flight altitude; but this is not the case for images retrieved by satellites which depend mainly on the specifications of the sensor.

Most satellite images with large size scene (swath width) are found with low spatial resolution. For example, Modis satellite images have swath width of 2030 km

Table 1 Example of commonly used land observatory satellite images (Al Saud 2020)

Satellite	No. of bands	Spatial resolution (m)	Temporal resolution (days)	Swath width(km)
Worldview-4	6	0.31	1.7	13.1 × 13.1
Geo-Eye	5	0.50	2.8	15.2 × 15.2
Kompsat-6	6	0.50	28	30 × 30
Quick-Bird	5	0.61	1–3	16.5 × 16.5
IKONOS	5	0.82	3	11.3 × 11.3
Rapid-Eye	5	5	5.5	77
Sentinel-1A	13	5	6	250
SPOT-7	4	1.5	26	60 × 60
Aster	14	15 VNIR, 30 SWIR, 90 TIR	16	60 × 60
IRS 1D	4	23	5	70 × 142
Landsat 7 ETM +	8	30, 120 thermal,15 pan	16	183 × 183
Landsat 8 OLI-TIRS	14	30, 100 thermal,15 pan	16	183 × 183
MODIS	36	250, 500, 1000, 2000, 4000	Twice/day	2030 × 1354
AVHRR	4	1.1 km	Twice/day	3000

× 1354 km, while they are characterized by low spatial resolution that starts from 250 m; whereas AVHRR has swath width of 3000 km and 1.1 km spatial resolution.

It is obvious that the specifications of an image, notably those retrieved by satellites, must be primarily identified while selecting the type of image to be processed for define purposes as it is shown in Table 1.

3 Processing of Satellite Images

Satellite image processing is a significant field in research and development. It consists of the images of earth and satellites acquired by artificial satellites. Primarily, the photographs are captured in digital form and then they are processed by the computers to extract the geo-spatial information required. Further on, a number of statistical and interpolation approaches are applied to the digital images and after processing the various discrete surfaces are identified by analyzing the pixel values.

The available digital raster images of spectral reflectance data is resulted from the solid state multispectral scanners and other raster input devices. The advantage of having digital raster image data enables elaborating several computer-based analysis. Hence, the efficiency of acquiring clear and comprehensive observations and

data analysis from satellite images is mainly based on the optical and spectral characteristics of these images, and this include identification of terrain features with a comprehensive observation, monitoring and change detection, environmental and coastal assessment, etc.

As a typical example illustrated by Al Saud (2020), in that the tracking Earth's surface by Ikonos satellite images enables distinguishing objects with approximately 0.82 m × 0.82 m size, and this is more likely to watch these objects from approximately 100 m above terrain surface. This virtually means that human can fly over any area and clearly observe all objects exceed 0.67 m^2 (0.82 m × 0.82 m).

There are two main components must be ready in order to start the analysis of the satellite images. These raw data (in digital form) and the suitable software for image processing. For this purpose, there a miscellany of software types used for satellite images processing, with a special focus on:

- *ECognition*: Produced by Trimble Inc. California, USA.
- *ENVI*: Produced by: IBM. Colorado, USA.
- *ERDAS Imagine*: Produced by: Lucia, Georgia, USA.
- *QGIS*: Produced by Wikimedia Foundation. San Francisco, USA.
- *PCI* Geomatics: Developer of Geomatica, Toronto, Canada.
- *ILWIS*: Produced by ITC, Enschede, Netherlands.

Each software occupies different specifications and has miscellany of usage approaches. Therefore, a flow chart of images processing would be carried out in order to reach the best observation on a satellite image and to be able to apply different images classifications and the relevant calculations.

The main procedures applied in satellite image processing can be summarized as follows (Fig. 6):

1. Preprocessing: This step represents the preparation of satellite images, which are produced as raw data, for further processing and classification. Consequently, the available satellite images can be processed after applying the following procedures on the software:

    - Image sub-setting: It is one of the primary steps applied to define and crop the area of interest (AOI) from the entire scene of an image. This is in order reduce the size of the images and focus on the AOI, which assists in faster downloading on computing resources.
    - Atmospheric correction: This is a process done to remove any noise in the images for best purification of surface reflectance where it is done by removing atmospheric effects from satellite images.
    - Geometric correction: This correction is to reduce the noise and the sun-angle which might be resulted as images displacement due to the altitude of platform carrying the sensor. Therefore, registration is applied using "rubber sheet" transformation which warps the image on defined points.

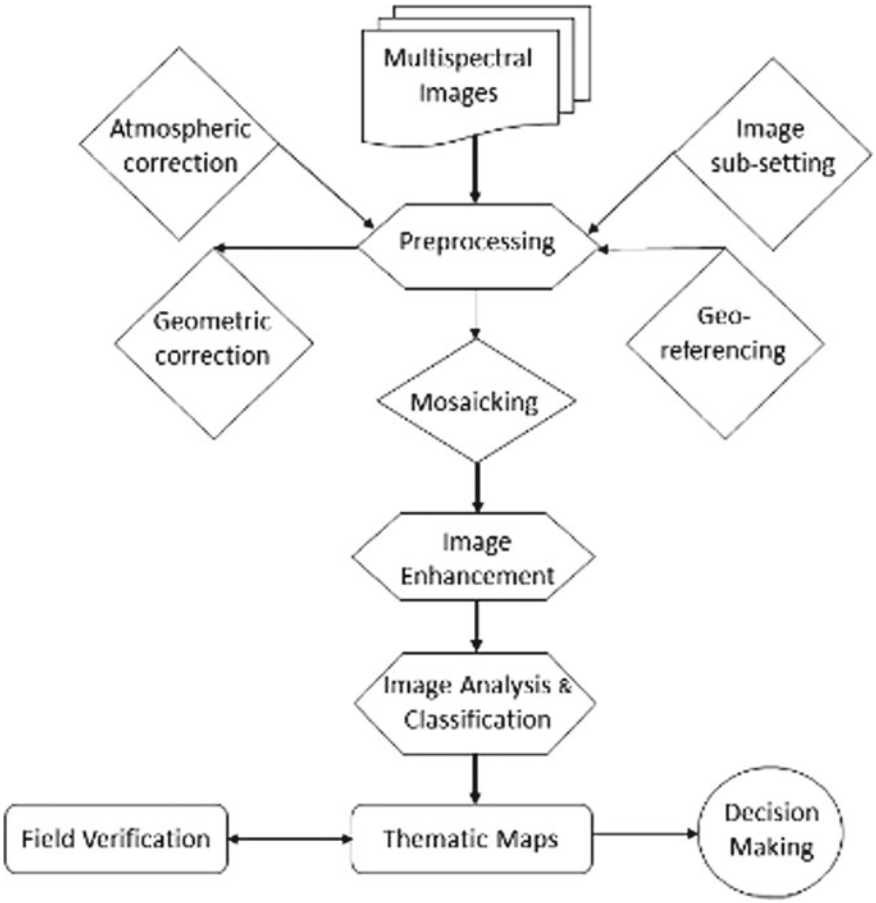

Fig. 6 Major elements of satellite images processing

- Geo-referencing: It is a necessary step for the positioning of the images with respect to the real geographic location, scale, and alignment to a file. Geo-referencing is performed on both the raster and vector data to rectify internal coordinate system with the associate objects.
- Mosaicking: This is a reversible process of image sub-setting, where multiple images from different scenes are associated together in one scene order to have a unified observation for the AOI. This is usually dependent of the purpose of the study and the surface area required.

2. Image enhancement: This is a major step applied while preparing satellite images for classification and analysis. Hence, several digital and spectral applications are applied using image processing software in order to attain the most reliable/distinguishable observation for the objects on Erath's surface. Most of

these digital applications are mostly tentative and their use is dependent on the knowledge of the images analyzer and the purpose of the study.

The most common applications of images enhancement are the: sharpness, contrasting, edge detection, color slicing, directional filtering, enhancements and interactive stretching. There is also "band combination" which is often performed for the single band and multi-band where different bands (diverse wavelengths) are arranged to reach the most suitable favorable observation.

3. Image analysis and classification: When the satellite image has been prepared according to the aforementioned pre-processing steps. Thus, the analysis and classification of a satellite image is a target process applied to recognize and discriminate the existing objects on Earth's surface, calculating their dimensions and land areas of AOI, as well as monitoring changes over time, etc.

   "Classifier", as a digital option on software, is used to group the satellite images into unified units with similar spectral signatures which also includes grouping the image pixels into categories. Image classification follows many approaches; however, the most common ones are: (1) Supervised classification where the analyzer is able to identify representative classes (i.e. training sites); and therefore, the software adopts these sites and then mainstream them to the entire image, (2) Unsupervised classification where pixels are grouped into "clusters" depending on their spectral signatures, and the each cluster can be tentatively attributed to land class, (3) Object-based classification where images pixels are grouped into representative vector shapes with define size and geometry. It is; therefore, different from supervised and unsupervised classification which are pixel-based (GIS Geography 2020).
4. Production of Thematic Maps: When the images becomes clear with defined classes and categories; therefore, the next step can be as the representation of these classes into mappable form where different colors and pattern can be illustrated to each class. Therefore, thematic maps can be produced with their legends. These produced hematic maps are usually used as base maps for filed verification to assure the reliability of the extracted data and information from the processed satellite images.

   The produced thematic maps with appropriate mapping and with readable production enabled decision makers and policy making to easily understand terrain elements and put their visions for planning based on these maps.

4 Geo-Information System

As a supplementary and significant tool for geo-spatial data extraction from satellite images, geo-information system, also called Geographic Information System (GIS) is often used. It is a computer-based system performed when the extracted geo-spatial data requires digital manipulation including digitization of the geo-spatial data, and

then vector and raster data illustration of maps and layouts, storage, display all geo-spatial data as one set display, overlapping, classification and many other necessary application.

The used GIS software is almost similar to those for images processing, but the advantages of GIS technology is mainly utilized for maps production, where it integrates common database operations, such as query and statistical analysis, with maps. Therefore, different geo-spatial categories can be interlinked with attribute tables and the relevant statistics and measurements. Hence, the GIS software enables users to store and manipulate large amounts of data from remotely sensed data, GPS and other sources.

One of the main purposes for using GIS is in data modelling where different factors are integrated to elaborate a map with target results (Shaban 2020). Therefore, these factor, which represent influencers on specific theme, are then they are converted into digital thematic maps (i.e. GIS layers). Modelling of these factors is carried out by the overlapping of the thematic maps in the GIS system, where each map has a define theme, and this enables integration of different themes into a unified figure (example in Fig. 7).

Recently, the techniques of the geo-information system have been involved in the management plans at different levels, and they became a instrumentation in many institutions (e.g. authorities, research centers, universities, etc.), then these techniques became a primary tool for data management.

There are many types software types used for the manipulation of the geo-information systems. Most of the GIS software types have been developed and embedded with images processing tools. Therefore, ESRI (Environmental System Research Institute, Redlands, USA) is the major used software where it utilizes Arc-GIS, as the principal Geo-information system tool extended on ITS computers, and is installed in UNIX and Networked PC devices.

There is specified Arc-GIS terminology, the principal ones are summarized in Table 2.

The principal tools of the Arc-GIS are:

- Arc-Map which enables visualizing spatial data, performing spatial analysis and drawing maps.
- Arc-Catalog is a tool for browsing and exploring spatial data, as well as viewing a creating metadata and managing spatial data
- Arc-Toolbox is an interface for accessing the data conversion and analysis function the come from Arc-GIS.

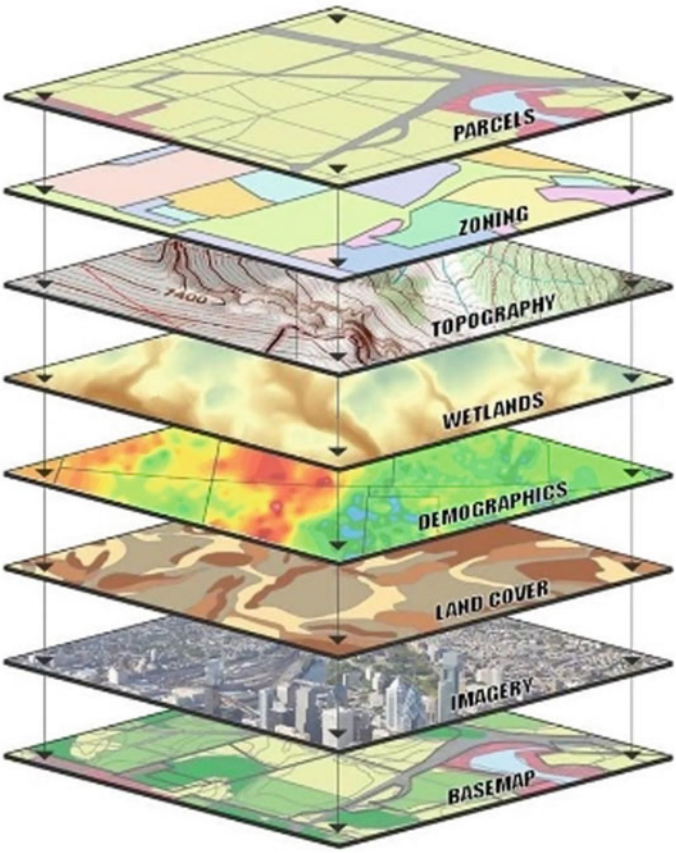

Fig. 7 GIS data layers visualization and overlaying (USGS 2016)

Table 2 Terminology of Arc-GIS (UMD 2012)

Term	Definition	Example
View	A collection of themes	Beirut
Theme	A single layer of data	Urban areas
Value	A specific quality or quantity assigned to an attribute, for a specific instance	125

References

Al Saud M (2020) Sustainable land management for NEOM region. Springer Publisher, 220 pp

American Cinematographer (2005) Bit-depth scales courtesy of Douglas Walker. https://www.theasc.com/magazine/april05/conundrum2/image11.html

Borman S, Stevenson R (1998) Super-resolution from image sequences a review. In: IEEE Midwest symposium on circuits and systems, pp 374–378

Chuvieco E (2020) Fundamentals of remote sensing, 3rd edn. CRC Press, 432 pp. https://doi.org/10.1201/9780429506482
Dixon-Gough RW (1994) Geographical information management: the way forward for remote sensing. Geodet Inf Mag 8(8):68–74
Eastman J (2001) Guide to GIS and image processing, vol l. IDRISI 32 Release 2. Clark University, 172 pp
Galbraith A, Theiler J, Kurtis T, Ziolkowski R (2005) Resolution enhancement of multilook imagery for the multispectral thermal imager. IEEE Trans Geosci Remote Sens 43(9):1964–1977
SEOS (Science Education through Earth Observation) (2021) Satellite orbits. https://www.seos-project.eu/remotesensing/remotesensing-c02-ws01-t.html
Shaban A (2020) Water resources of Lebanon. Springer Science Publisher, ISBN 978-3-030-48716-4, 229 pp
Shimizu E (2011) Satellite remote sensing. encyclopedia of life support systems (EOLSS)
Théau J (2008) Temporal resolution. In: Shekhar, Xiong (eds) Encyclopedia of GIS. https://doi.org/10.1007/978-0-387-35973-1_1376
UoB (University of Bergen) (2021) The electromagnetic spectrum. https://www.uib.no/en/hms-portalen/75292/electromagnetic-spectrum
USGS (2016) GIS data layers visulazation. https://www.usgs.gov/media/images/gis-data-layers-visualization

Water Resources in the Middle East

Amin Shaban

1 General Overview

The World's population is growing rapidly, and estimates show that with current practices, the World will face a 40% water shortfall between forecast demand and available supply by 2030. Furthermore, chronic water shortage, hydrological uncertainty, and the existing climatic extremes (e.g. floods, heat waves, etc.) are perceived as the biggest threats to global prosperity and stability (World Bank 2021).

Today, about 4 billion people (i.e. equivalent to about 2/3 of the global population) experience unlikely water shortage during at least one month of the year, and this may ascend to touch 4.8–5.7 billion in 2050 (Mekonnen and Hoekstra 2016). In this respect, any country drawing more than 25% of its renewable freshwater resources is considered as "water-stressed". Globally, 5 out of 11 regions have water stress values above 25%, including two regions with high water stress and one with extreme water stress. There is 2.3 billion people live in water-stressed countries, of which 733 million live in high and critically water-stressed regions (UN Water 2021).

The agricultural production requires about 60% increase in order to feed more than 9 billion people by 2050, and this will lead to 15% increase in water abstraction from different resources (surface water and groundwater). The increased water demand stands beside increased scarcity in water resources are scarce in many regions, and many estimates indicate that 40% of the World population live in water scarce areas, and approximately one-fourth of World's GDP is exposed to this challenge (World Bank 2021).

In the Middles East Region, water became a scarce resource with uneven distribution between different geographic regions, resulting in geo-environmental problems on the national level and geo-political conflicts between riparian countries on the

A. Shaban (✉)
National Council for Scientific Research—Lebanon (CNRS-L), CNRS-L, P.O. Box 11-8281, Beirut, Lebanon
e-mail: geoamin@gmail.com

A. Shaban (ed.), *Satellite Monitoring of Water Resources in the Middle East*,
Springer Water, https://doi.org/10.1007/978-3-031-15549-9_2

regional level. Today, the sixteen countries in this region are placing unprecedented stress on water supply led to an abrupt increase in water demand, threatening food security and the entire ecosystem. The largest part of the Middle East Region is located within arid and semiarid regions where precipitation is lower than 200 mm and evapotranspiration exceeds 55%. Thus, it is a typical example where water resources are inadequate to cope with human demand for all major sectors.

There are 13 Arab countries within the Middle East Region (Fig. 1), comprising 62% (285.19 million people) of the total population and 66.5% (4,848,674 km^2) in surface area.

The Arab Region is mainly an arid or semi-arid, receiving less than 250 mm of rainfall annually beside a rapid increase in population. Hence, water shortage is widespread and it threatens people and livelihoods, particularly in rural and poor communities, but it also affects urban dwellers in the developing countries. It has been reported from the current projections that by 2025 the water supply in the Arab Region will be only 15% of what it was in 1960 (UNDP 2013). According to FAO (2013), 12 Arab countries have water availability below the World Health Organization threshold for severe scarcity (1000 m^3/capita/year).

Fig. 1 Location maps for the Middle East countries (Alamy 2022)

Likewise, many regions worldwide, the freshwater scarcity in the Middle East is influenced by several factors, including mainly rapid population growth, climate change impacts and extreme climatic events, dependency on transboundary water resources, water pollution, non-revenue water losses from ageing water systems, intermittency in the discharge, inefficient water use.

The surface area and population of the Middle East countries are shown in Table 1. It is clears that the largest area is for the Kingdom of Saudi Arabia (2.15 million km^2), besides the smallest one for Palestine (6020 km^2), while the biggest population is in Egypt (104.26 million people) and the least one is in Cyprus (1.21 million people).

Table 1 also shows that the average surface area is about 455,530 km^2, whereas the average population was estimated at 28.5 million people. Moreover, the density population density in the Middle East Region is extremely diverse and it ranges between 16 and 2285 person per km^2.

Table 1 Area and population of the Middle East in 2021 (UN 2021)

Country	Surface area (km^2)	Population (million people)	Population density (person/km^2)
Bahrain	766	1.75	2285
Cyprus	9251	1.21	132
Egypt	1,002,000	104.26	104
Iran	1,647,000	85.02	52
Iraq	438,317	41.17	94
Jordan	89,342	10.27	115
Kuwait	17,818	4.32	243
Lebanon	10,452	6.76	647
Oman	309,500	5.22	17
Palestine	22,145	14.4	840
Qatar	11,586	2.95	253
Saudi Arabia	2,150,000	35.34	16
Syria	185,180	18.27	99
Turkey	783,562	85.04	109
UAE	83,600	9.99	120
Yemen	527,968	30.49	58
Total	7,288,487	456.46	–
Average	455,530	28.53	324

2 Water Availability/Supply and Demand

Water availability is the biophysical supply of water resources with respect to the demand and access to water. It can be assessed from the diagnose of the water cycle starting from precipitating and becoming available as surface water and groundwater. In other words, the availability of water is the amount of renewable water which is naturally available in an area with respect to the population size in this area, and it is often calculated by m^3/capita/year. Thus, water availability is controlled by the total water volume (i.e. resource) and the population size (i.e. consumers).

Water supply is well known as the volume of water that delivered for different consumers, and this is often implemented by the formal sector (e.g. water authorities, ministries, etc.). Besides, water demand is the water volume required for consumers (for all uses) in order to cope with their requirements for sustainable life.

In this regard, the internationally water-poverty threshold is 1000 m^3/capita/year and this characterizes all arid and semiarid regions where water is naturally scarce. However, calculating water availability often results imprecise figures, especially in relatively vast areas with major water resources (e.g. major rivers), and then these resources can supply water only the nearby areas while remote ones remain scarce.

For example, there are Nile River in Egypt, and Tigris and Euphrates Rivers in Iraq which span for long distances, but almost over dry areas and deserts. Hence, water is available only in the surrounding of these rivers, but this is not the case for the remote areas in these countries. Therefore, the general calculations for water availability in these regions is high, while water scarcity exists in many parts in these countries at the same time. Therefore, water availability does not reflect acceptable water supply.

Except Cyprus, Lebanon, NW part of Syria, Turkey and Iran, the rest Middle East countries are known by low precipitation and frequent drought spells. These five regions are located above 33° latitudes and they are also characterized by elevated topography. Figure 2 shows examples from two diverse regions from the Middle East reflecting water availability.

The Middle East countries occupy a number of large-scale water resources (i.e. rivers and aquifers). However, these resources are shared between the riparian countries even outside the Middle East Region, and then result in geo-political conflicts. Besides, there is an obvious drop in the renewable water resources estimated by 50% over the last few decades (UNESCO 2017). Table 2 shows the list of water availability, supply and demand and the ratio between them for the Middle East countries.

It is obvious that the average renewable water (water availability) in the Middle East Region is about 631m^3/capita/year which can be considered as low to moderate if compared with the global figure on water availability.

Out of the 16 Middle East countries, there are 13 already considered as water-scarce countries (i.e. below water poverty threshold, of 1000 m^3/capita/year), where 9 of them are under 500 m^3/capita/year, and 7 of the latter are even under 100 m^3/capita/year. Based on the existing climatic conditions and the urban development,

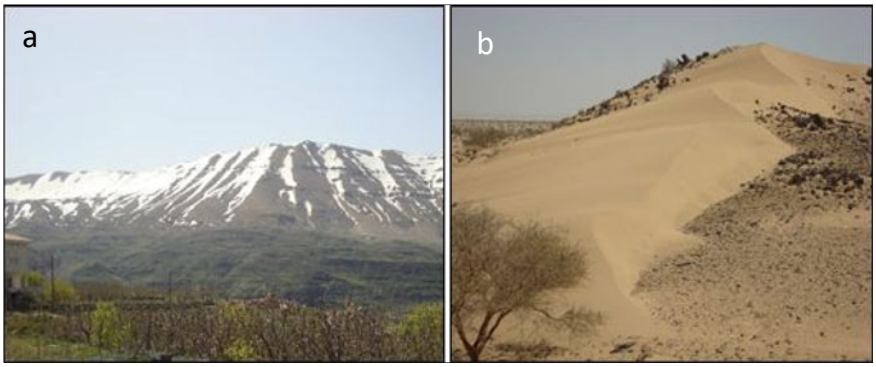

Fig. 2 Diverse landscapes in the Middle East Region reflecting water availability. **a** Jabal Sannine (Lebanon); **b** Rabigh Region (Saudi Arabia). Photos taken by the author

Table 2 Water availability, supply and demand in the Middle East Region

Country	Water availability (m^3/capita/year)	Water supply (m^3/capita/year)	Water demand (m^3/capita/year)	Availability/demand ratio
Bahrain	3	291	305	0.009
Cyprus	656	166	241	2.72
Egypt	596	803	804	0.74
Iran	1571	488	1141	1.33
Iraq	2392	1026	1053	2.27
Jordan	70	107	109	0.64
Kuwait	0	308	427	–
Lebanon	980	180	220	4.45
Oman	300	401	554	0.54
Palestine	171	79	97	1.76
Qatar	21	335	513	0.04
Saudi Arabia	73	705	706	0.10
Syria	417	980	913	0.45
Turkey	2757	330	721	3.82
UAE	16	441	871	0.03
Yemen	75	128	177	0.42
Average	631	423	553	1.20

it can be presumed that by 2030 all the countries in the Middle East Region could be with an average less than 1000 m^3/capita/year, except Iraq and Turkey.

It has been noted that there is a sharp declining trend in water availability per capita in the Middle East Region and more specifically on the coastal zones where

population density is high, and this has been exacerbated in the last three decades. This was also accompanied by increased water demand besides a decrease in water supply. The ratio of decline has been estimated (for example) at: 98%, 58%, 42%, 37% in Bahrain, Oman, Iraq and Egypt; respectively. The current status is due to a number of influencers including principally the oscillations in the climatic conditions which have been well pronounced in the region, increased population size and the newly existed aspects of water use, uncertainty in managing several water resources, especially the non-conventional ones, unmanaged transboundary water resources, as well as the geo-political instability in the region which has been reflected on the displacement of large number of people between different regions, such as the case in Lebanon and Jordan, Yemen and Iraq. For example, in Lebanon water availability has been rapidly decreased from 1350 to 980 m^3/capita/year between 2011 and 2017 (Shaban 2020).

Table 2 shows an abrupt diversity in the ratio between renewable water resources (water availability) and the demand for water for different uses. It reveals that, for example, Lebanon occupies the largest ration where the renewable water equals about 4.45 times water demand, and the least reported ratio is 0 and 0.009 for Kuwait and Bahrain; respectively. While the average water availability/ demand ration is 1.2, which means that the renewable water resources in the Middle East Region is 1.2 times the water required for different purposes (i.e. domestic, agriculture and industrial).

The same comparative concept cans applied between water availability and water supply (as the delivered water from the formal water sector), where Table 2 shows that approximately 2/3 (423/631) of renewable water is supplied for different uses. Besides, the supplied water equals only 0.76 of the water demand for the entire Middle East Region, which is an alarming indicator for the insufficient water supply in the region. It has been estimated that the gap between water supply/demand (in the Arab Region (for example) at more than 43 km^3 in 2009, is expected to reach 127 km^3 a year by 2030 (El-Ashry, Saab, and Zeitoon 2010).

Nevertheless, this ratio sometimes does not reflect the actual status in water supply/demand. For example, the ratio of water availability/supply in Lebanon is 5.4, while it is estimated at 0.65 in Jordan and 0.036 in the United Arab Emirates; however, water supply/demand in Jordan and UAE is more satisfactory than that in Lebanon. The adoption of non-conventional water resources, mainly water harvesting in Jordan and desalination in UAE is the main reason behind.

The ratio between water supply (423 m^3/capita/year), as shown in Table 2 and average water demand (553 m^3/capita/year) is about 76%, and this means that about 3/4 of the required water volume is received in the region, and the rest 1/4 is almost a gap in water supply. However, this is a general assessment for the entire region, but this ratio is almost high in several countries of the Middle East where the supply is sometimes 77% less water demand such as in Iran. While, there are some countries in the region have almost a balanced water supply demand, these are in Bahrain, Egypt, Iraq, Jordan and Saudi Arabia (Table 2), regardless of water availability in these countries, which can be low (Bahrain, Jordan and Saudi Arabia) or high availability (Egypt and Iraq).

3 Challenges on Water Resources

Water is naturally unevenly distributed around the World, with the Middle East Region being one of the most water-challenged. This region, likewise the entire MENA Region, is suffering from severe water scarcity, which is named by many researchers as "drought". The problem has been lately exacerbated and widened temporally and geographically.

A 2015 Report introduced by the World Resources Institute (WRI) found that of the 33 likely most water-stressed countries in 2040, 14 are in the Middle East (IHE 2018). Hence, there are several factors contributing to water scarcity in the Middle East Region. In fact, the largest geographic part experiences arid conditions with low rainfall and high rate of evaporation, leading to limited naturally available water resources. Nevertheless, the unavailability of water resources is not the only reason behind, but the region is also confronted with many other challenges including extreme weather events, mismanaged infrastructure, instable socioeconomic status due geo-political conflicts and transboundary issues, pollution, poor water management and misuse. All these challenges added pressure on water management, and then increased risks and uncertainty associated with water quantity and quality.

With its current water resources, the Middle East has numerous struggles, and the region needs more than one solution to generate an optimistic environmental position for the future. The respond to the existing challenges can be addressed by improving the adaptive approaches for water resources management, empowering the resilience and preparedness, balancing supply/demand and conserve water resources and the related ecosystem and expanding the use of non-conventional water resources.

3.1 Increased Population

Population growth, as a number, is not the only reason behind the increase in water consumption; however, there is additional use of water that has been existed lately and resulted from the developed urbanized aspects and modern lifestyle. According to the World Bank (2019), the average population growth rate in the Middle East Region is approximately 1.9%, which means that there is an average annual increase in the population estimated at about 8.67 million people in the region. If this value is multiplied by the average water demand in the Middle East Region (553 m^3/capita/year); therefore, a water volume of about 4795 million m^3 is expected as an additional amount of water required every year. Table 3 shows the increase in the population until 2030 and water demand for each country in the Middle East, and thus over the next nine years (between 2021 and 2030), there is more than 60 million increase in the population of the Middle East.

In the Middle East Region, the largest portion of water consumption is for irrigation which consumes between 75 to 85%, and then 8–15% and 5–12% for domestic and industrial uses; respectively.

Table 3 Population the increased water demand between 2021 and 2030 in the Middle East region (WB 2019; UNICEF 2019)

Country	Population in 2021 (million people)	Population in 2030 (million people)	Water demand (m^3/capita/year)	Increased volume of water demandbetween 2021 and 2030 (Million m^3)
Bahrain	1.75	2.01	305	79
Cyprus	1.21	1.72	241	123
Egypt	104.26	119.74	804	12,446
Iran	85.02	88.86	1141	4381
Iraq	41.17	52.29	1053	11,709
Jordan	10.27	11.12	109	93
Kuwait	4.32	4.87	427	235
Lebanon	6.76	5.37	220	-
Oman	5.22	5.89	554	371
Palestine	14.4	17.84	97	334
Qatar	2.95	3.23	513	144
Saudi Arabia	35.34	39.48	706	2923
Syria	18.27	26.60	913	7605
Turkey	85.04	91.23	721	4463
UAE	9.99	11.05	871	923
Yemen	30.49	36.81	177	1119
Total	456.46	518.11	8852	46,848
Average	28.53	32.38	553	2934

3.2 Climate change

The Middle East Region as well as North Africa (i.e. MENA Region) is particularly sensitive to climate change-related outcomes. This region emerges globally as one of the hot spots for worsening extreme heat, drought and aridity conditions under the changing climate conditions, notably that it extends almost above the equatorial line and it possess a number of large deserts located in the Arabian Peninsula and in North Africa. Yet, the MENA Region records the heights temperature levels with extreme and oscillating climatic conditions.

- Precipitation: There is an obvious change in precipitation rate and oscillation in rainfall patterns noticed/measured in the Middle East Region. However, there is still contradictory in the general assessment of these changes between different region. The majority of the assessed precipitation implies that there is decrease in the volume of precipitated water in some regions besides and increase in other regions and this has been mostly agreed by IPCC since 2007. Nevertheless, there

are some other studies which declared that the volume of precipitated water is minimally changing (i.e. less than tens of millimetres) but there is a clear oscillation in the patterns of rainfall that represented by the increased spells of torrential rainfall, shifting in seasons timing and an abrupt high change in temperature over short time periods (Shaban and Houhou 2015).

According to Waha et al. (2017), the incoming northward shifts of air moisture associated with a stronger North Atlantic Oscillation (NAO) anomaly are projected to reduce rainfall rate in North Africa and West Asia (i.e. Maghreb and Mashreq). For the Middle East Region, Egypt and Cyprus are projected to receive substantially less rainfall (Figure 3). However, a projected northward shift is anticipated to increase moisture delivery to the southern parts of the MENA Region (which are already under the influence of monsoon systems), and certainly to the southern part of the Arabian Peninsula including mainly Yemen, Oman. Thus, the absolute increase in precipitation rate in the southern regions will be negligible, given this regions the existing hyper-arid climate conditions (with the exception of Yemen). An increase in precipitation in the southern part of the MENA region may be associated with more intense and extreme torrential rain events.

In this respect, the World Bank (2014) elaborated large-scale scenarios for different regions Worldwide. Example is shown in Figure 3 which reveals the percentage change in winter (December–January–February) precipitation for scenario RCP2.6 by 2071–2099 relative to 1951–1980. It shows an obvious increase in the precipitation rate in the Arabian Peninsula beside a stable precipitation rates in the North Africa and Eastern Mediterranean Sea.

- Temperature: Warming of about 0.2 °C per decade has been observed in the MENA Region between1961 and 1990, and at even faster rate since then. The highest warming is projected to take place close to the Mediterranean coast (Fig. 4). While, a regional warming by 3 °C with 2 °C global warming is projected by the end of the century. Along with expected 4 °C global warming, mean summer temperatures are anticipated to be increase up to 8 °C warmer in parts of Saudi

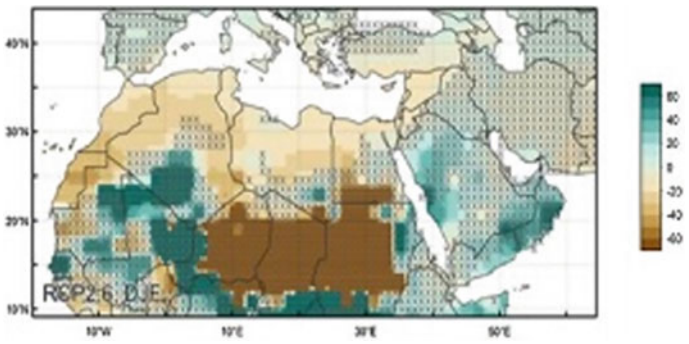

Fig. 3 Scenario RCP2.6 by 2071–2099 relative to 1951–1980 for the winter precipitation (World Bank 2014). Hatched areas indicate uncertain results, with models disagreeing on the direction of change

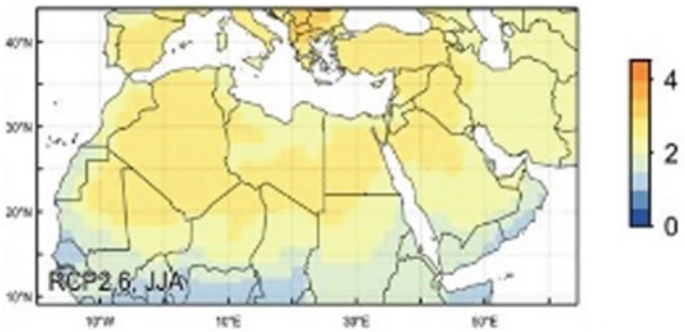

Fig. 4 Temperature projections (in °C) for the scenario RCP2.6 (for months of June–July–August) in 2071–2099 per grid cell (World Bank 2014)

Arabia and Iraq by the end of the century due to a simultaneously drying trend in the region (Fig. 4), and this will result water runoff that could decrease by 75%, and land aridity could increase in many parts of the region by more than 60%. The observational record revealed a robust increase in the number of extreme temperatures (Seneviratne et al. 2012) and in the warm spells duration index which has been recorded since the 1960s.

In general, the Middle East Region is highly vulnerable to negative impacts of climate change. The region is not only affected by increased temperature and changing patterns of precipitation as aforementioned, but there are several changing climatic aspects including mainly heat extremes, increased storms (dust and snow), sea level rise and the increased drought and aridity spells. The impact of climate change has been well pronounced in the region where it affects many vital sectors. According to Waha et al. (2017), the impact of climate change in the Middle East Region can be summarized as follows:

1. Impact on agriculture and water, where the largest part of the region is receiving less than 200 mm of annual rainfall (200–300 mm roughly represents the lower limit of rain fed agriculture). Therefore, the critical situation of water and arable land scarcity, global warming is likely to result in further increased pressures on water resources and ago-culture such as:

    - Cropland where drier climate is projected to shift vegetation and agricultural zones northwards, e.g., by 75 km for 2090–2099 relative to 2000–2009 in a 4 °C world (Evans 2009).
    - The lower rainfalls and higher temperatures will shorten growing periods for wheat in the MENA region by about two weeks by mid-century (2031–2050) (Ferrise et al. 2013).
    - Crop yields are expected to decrease by 30% with 1.5–2 °C warming (Al-Bakri, et al. 2011) and may reach to 60% with 3–4 °C warming (Schilling et al. 2012).

2. Impact on health, where the societies in the region face many aspects of health risks, which are exacerbated mainly due to the dry conditions and water deficit. Therefore, water-related diseases, which is associated with high temperatures, water contamination and dry conditions and poor sanitation, already affect the region (WHO and EMRO 2009; International Trachoma Initiative 2016).
3. Impacts on migration and the related socioeconomic aspects is also common in the Middle East where the changing climate played a major role. As the economies of Middle East countries have changed, migration has become a common solution to improve livelihood security. Hence, migration has always been a human response to climatic and other hazards, and it happens as soon as the physical, economic, social or political security of a population decreases. Some studies therefore consider migration as a last resort (Laczko and Piguet 2014).

3.3 Transboundary Water Resources

Transboundary water resources comprise one of the major challenges in the Middle East Region in general and in the Arab countries in particular. A large volume of renewable water resources in the region is shared between neighbouring countries, and it is well reported that a considerable volume of these resources (surface water and groundwater) is originated from outside the Arab Region, where they are represented by 17 shared aquifer systems and 6 shared rivers (FAO 2013). In addition, there are two major shared rivers added to comprise 7 major rivers I the entire Middle East Region.

There are 8 main transboundary rivers located in the Middle East Region which account for most of the region's surface water. These rivers are: Nile, Tigris, Euphrates, Orontes, Harirud and Helmand (in Iran) Rivers. While, the Yarmouk River and El-Kabir River are shared between Arab countries. In addition, there are 16 shared surface water basins with different catchment dimensions. Moreover, a number of springs occur nearby/or on the boundaries between riparian countries of the Middle East Region.

Yet, the Middle East Region, with its remarkable transboundary freshwater resources, is still lacking to mutual concession on water allocation in shared rivers and aquifers which add a problem to water resources management and potential conflict due to water scarcity situation in the region. Hence, concern is always on surface water, and more certainly the transboundary rivers. All these resources are not well managed and almost all of them have conflicts between the riparian countries, especially in Nile, Jordan, Tigris, Euphrates Rivers.

References

Alamy (2022) Map of Middle East with borders of countries. https://www.alamy.com/map-of-middle-east-with-borders-of-countries-image342339984.html

Al-Bakri J, Suleiman A, Abdulla F, Ayad J (2011) Potential impact of climate change on rainfed agriculture of a semi-arid basin in Jordan. Phys Chem Earth Parts a/b/c 36(5–6):125–134. https://doi.org/10.1016/j.pce.2010.06.001

El-Ashry N Saab, Zeitoon B (2010) Arab water: sustainable management of a scarce resource. Beirut: Arab Forum for Environment and Development. org/en/inner.aspx?contentID=583

Evans J (2009) Twenty-first century climate change in the Middle East. Climate Change 92(3–4):417–432. https://doi.org/10.1007/s10584-008-9438-5

FAO (2013) AQUASTAT database. Rome. http://www.fao.org/nr/water/aquastat/data/query/index.html

Ferrise R, Moriondo M, Trombi G, Miglietta F, Bindi M (2013) Climate change impacts on typical Mediterranean crops and evaluation of adaptation strategies to cope with. In: Navarra A, Tubiana L (eds) Regional assessment of climate change in the Mediterranean. Springer, Berlin, pp 49–70

IHE (2018) Taking on the water crisis in the Middle East. IHE, Delft Report. https://www.un-ihe.org/stories/taking-water-crisis-middle-east

International Trachoma Initiative (2016) Global Atlas of Trachoma. http://www.trachomaatlas.org/

Laczko F, Piguet E (2014) Regional perspectives on migration, the environment and climate change. In: Laczko F, Piguet E (eds) People on the move in a changing climate. the regional impact of environmental change on migration. Global migration issues 2, pp 1–20. Springer Netherlands, Dordrecht

Mekonnen M, Hoekstra A (2016) Four billion people facing severe water scarcity. Sci Adv 2(2):e1500323. https://doi.org/10.1126/sciadv.1500323

Schilling J, Freier K, Hertig E, Scheffran J (2012) Climate change, vulnerability and adaptation in North Africa with focus on Morocco. Agric Ecosyst Environ 156:12–26. https://doi.org/10.1016/j.agee.2012.04.021

Seneviratne S, Nicholls N, Easterling D, Goodess C, Kanae S, Kossin J, Luo Y, Marengo J, McInnes K, Rahimi M, Reichstein M, Sorteberg A, Vera C, Zhang X (2012) Changes in climate extremes and their impacts on the natural physical environment. In: Field CB, Barros et la. (eds) Managing the risks of extreme events and disasters to advance climate change adaptation. A special report of working groups I and II of the intergovernmental panel on climate change (IPCC). Cambridge University Press, Cambridge, pp 109–230

Shaban A (2020) Water resources of Lebanon. Springer Science Publisher, ISBN 978-3-030-48716-4. 229 pp

Shaban A, Houhou R (2015) Drought or humidity oscillations? The case of coastal zone of Lebanon. J Hydrol 529(2015):1768–1775

UN (2021) The Middle East Population 2021. World population review. Department of Economic and Social Affairs Population Dynamics. https://www.worldpopulationreview.com/continents/the-middle-east-population

UNESCO (2017) Arab region faces ever-increasing water challenges. http://www.unesco.org/new/en/syria-crisis-response/regional-response/singleview/news/arab_region_faces_ever_increasing_water_challenges/

UNICEF (2019) MENA generation 2030. https://www.unicef.org/mena/media/4141/file/MENA-Gen2030.pdf

UN-Water (2021) Sustainable development goal 6 on water and sanitation (SDG 6). https://www.sdg6data.org/

Waha K, Krummenauer L, Adamas S, Aich V, Baarsch F, CoumoU D, Fader M, Hoff H, Jobbins G, Marcus R, Mengel M, Otto I, Perrette M, Rocha M Robinson A, Schleussner C (2017) Climate change impacts in the Middle East and Northern Africa (MENA) region and their implications for vulnerable population groups. Regional Environmental Change. https://doi.org/10.1007/s10113-017-1144-2

WHO and EMRO (2009) The work of WHO in the Eastern Mediterranean Region: annual report of the regional director 1 January–31 December 2008. World Health Organization, Geneva, Switzerland

World Bank (2014) Turn down the heat: confronting the new climate normal. A report for the World Bank by the Potsdam Institute for Climate Impact Research and Climate Analytics, p 275. Washington DC

World Bank (2019) Population growth (annual %)—Middle East & North Africa. The International Bank of Reconstruction and Development (IBRD) International Development Association (IDA). https://www.data.worldbank.org/indicator/SP.POP.GROW?locations=ZQ

World Bank (2021) Water resources management. The International Bank of Reconstruction and Development (IBRD) International Development Association (IDA). https://www.worldbank.org/en/topic/waterresourcesmanagement

The Suitability of Satellite Remote Sensing and GIS Technologies for Mapping, Monitoring and Managing Water Resources in the Middle East

Serwan M. J. Baban

1 Introduction: Water Resources in the Middle East

The Middle East is an area of low *precipitation* and high *evapotranspiration*, much of it with less than 200 mm *precipitation* a year and *potential evapotranspiration* of over 2000 mm; this defines it as 'arid'. The Middle East region accounts for almost five percent of the total land area in the world and hosts 4.4% of its population, but the region's 484 km^3 of renewable water only represents 1.1% of the worlds' total renewable water resources. This is defined as the average manual flow of rivers and recharge of aquifers generated from precipitation (NATO 2019). A few large rivers which originate in neighbouring countries present the major source of water in the Middle East (Baban 1997; Baban and AL-Ansari 2001; Al-Ansari 2013). The rivers are given as follows.

1.1 Tigris and Euphrates

These are two of the largest rivers in the region, the total length of the Euphrates is about 2,800 km whilst the Tigris is about 1,900 km (Fig. 1). These two rivers have their sources within 50 miles (80 km) of each other in the northern parts of Turkey and the Caucasus Mountains. They flow southeast across northern parts of Syria and through Iraq. The rivers then join together in *Shatt Al-Arab* which empties out into the Arabian Gulf (Baban and AL-Ansari 2001; Al-Ansari 2013; Rashed 2020).

S. M. J. Baban (✉)
Federal Region of Kurdistan, Erbil, Iraq
e-mail: serwan.baban@presidency.krd

A. Shaban (ed.), *Satellite Monitoring of Water Resources in the Middle East*,
Springer Water, https://doi.org/10.1007/978-3-031-15549-9_3

Fig. 1 Major rivers in the Middle East. *Source* https://www.en.wikipedia.org/wiki/Mesopotamia#/media/File:N-Mesopotamia_and_Syria_english.svg

1.2 Jordan River

The total length of the river is about 360 km and it rises on the slopes of Mount Hermon, on the border between Syria and Lebanon (Fig. 1). Jordan river is fed by rains falling on the neighbouring plateaus; the waters then flow southward through the Sea of Galilee, exiting the sea, it continues south, dividing Israel and the Israeli-occupied West Bank to the west from Jordan to the east before emptying into the Dead Sea (Al-Ansari 2001; Rashed 2020).

The trend and expectations show that water resources in the Middle East will continue to decline whist the demand will continue to increase. Hence, the region and water resources managers in particular will face significant challenges. Furthermore, they will be required to make accurate and judicious management decisions for the distribution and use of the limited available water resources. Hence, they will require accurate and timely information and the more information the managers have, the better they will able to make effective decisions. These is turn will promote political and social stability, sustainable development and environmental safety.

This chapter seeks to illustrate the potential and pitfalls of employing satellite Remote sensing and GIS technologies to collect, handle and analyse the necessary data sets to manage water resources in Middle East. This study is important to the Middle East as the region is experiencing a fast rate of development and the demand for water can outpace supply. Furthermore, it is likely to be faced with a unique

water shortage scenario in the future due to activities in the neighboring countries and climate change impacts.

2 Water Resources Issues and Challenges in the Middle East

Water scarcity poses a global threat, but its effects are more visible in arid or semi-arid regions like the Middle East, which is one of the most water scarce regions in the world. An added difficulty is that some 60% of surface water resources in the region are transboundary, and all countries share at least one aquifer, thus highlighting the importance of cooperation and coordination amongst neighbouring countries. This is most evident by the effects on downstream countries resulting from policy decisions implemented by their upstream neighbors, which has often resulted in increased tensions. Furthermore, the severity of the water scarcity problem in the region is compounded by a number of potential threat multipliers, such as worse case scenarios for climate change or the vicious cycle of conflict and fragility, these will significantly exacerbate water scarcity and provoke security risks such as socio-economic instability and migration (Alqallaf 2003; Baban and AL-Ansari 2001; Al-Ansari 2013; Rashed 2020). More specifically in terms of the main sources of water represented by the major rivers, some particular issues and challenges are present and facing each river as follows.

2.1 Tigris and Euphrates

The Euphrates and Tigris rivers are the cause of a major area of water dispute with Turkey. Turkey, as the upstream country, claims the right to control the water that originates within its border. Iraq claims historical rights to the rivers as its people have depended on them for thousands of years, in what was Mesopotamia, using them for large-scale irrigation. Syria claims both ownership rights and historical user rights. Unfortunately, there is just not enough water for all the counties, leading to conflict and, at times, threats of war. For example, Turkey has reduced flows to Syrian and Iraq substantially in recent years as the first phase of filling a series of dams (Atta Turk dams) was in progress. This unilateral action resulted in the failure of some crops, decline in water quality due to increased salinity, and reduction in groundwater storage. Evidently, further reductions are likely in the future (Clark 1991; Al-Ansari 2013; Rashed 2020).

Moreover, the lack of formal agreements on the use of the Tigris and Euphrates water resources also affected the relationship between Iraq and Syria. In the mid-1970s, the political hostility that existed between the respective Baathist regimes in Baghdad and Damascus encompassed Iraqi criticisms of a Syrian dam project on the

Euphrates. The political disagreements and water resource criticisms developed into a crisis that included the movement of military forces by both Iraq and Syria to their respective border areas. Active intervention by Saudi Arabia and the Arab League eventually resolved the crisis and assured an increased flow of Euphrates water from Syria into Iraq (Alqallaf 2003; Baban and AL-Ansari 2001**;** Al-Ansari 2013; Rashed 2020; Janabi 2013).

Evidently, greater cooperation between the three countries to manage the rivers on a catchment scale, and changes to agricultural practice will be necessary to manage the water resources of these major rivers effectively. However, reaching formal agreements on the control and use of the Tigris and Euphrates water resource has proven to be problematic. This is evident in the numerous meetings and conferences which have already taken place between Iraq, Syria and Turkey regarding this issue. The Iraq-Turkey 1946 Treaty remains the last formal bilateral agreement that addresses this subject. Although Iraq no longer chooses to rely on this Treaty since it believes that it unnecessarily cedes control of the Tigris and Euphrates to Turkey, Iraq has not formally repudiated this Treaty (Alqallaf 2003; Al-Ansari 2013; Janabi 2013).

2.2 Jordan River

After the Arab-Israeli War of 1948, the river marked the frontier between Israel and Jordan from just south of the Sea of Galilee to the point where the Yābis River flows into it from the east. During the six-day war with Israel in 1967, the Israeli forces managed to occupy the West Bank (i.e., the territory on the west bank of the river south of its confluence with the Yābis), Jordan river became the cease-fire line as far south as the Dead Sea (Clark 1991; Rashed 2020). In recent times, the Jordan river water has decreased significantly through use by the local populations who depend on it. Furthermore, its strategic location has made it a source of political discourse on who exactly owns the right to source from it. Jordan, Israel, and Palestine have all disputed ways to manage the sourcing for the river as well as conserving the climate that surrounds it (Rashed 2020).

It is clear the water supply to Middle East is falling and this trend is liable to continue. As a result, water is likely to become an even more precious resource in the future. This is due to several reasons which include (Clark 1991; Alqallaf 2003; Baban and AL-Ansari 2001; Al-Ansari 2013; Rashed 2020);

1. Approximately 60% of the river water resources that are utilized by a number of Arab nations in the Middle East do not originate within their respective national boundaries. Thus, the direct control of these water resources by other nation-states provides them with the means to exert various types of political, social, economic and security influence and pressure on the downstream countries in the Middle East.

2. The interrelated politics of water resources and security issues have historically influenced regional politics and resulting armed conflicts, and will continue to do so in the future.
3. The lack of water-sharing agreements between states in the same river- basin. Hence, the upstream countries have tended to act unilaterally, typically taking the largest share of resources, as they have no incentive to cede their advantageous position. Consequently, the water resources affect fundamental bilateral and multilateral political, economic, social, and security relationships in the Middle East, because both the origin, flow, and use of these water resources transcends existing national boundaries.
4. The negative impact of human intervention in the natural hydrological cycle through building major dams and diversion schemes on the rivers and their tributaries by upstream countries. For example, building dams in Turkey can significantly reduce the water flow and level in Iraq's main rivers. Consequently, Iraq is and will be facing a water shortage which is expected to become worse in the future where the supply is predicted to be 17.61 Billion Cubic Meters (BCM) in 2025 respectively while current demand is estimated to be between 66.8 and 77 BCM. It has been estimated that the Tigris and Euphrates River discharges will continue to decrease with time, and they will be almost dry by 2040 (Al-Ansari 2013).
5. The noticeable impact of global climate change on water resources in the region will worsen the situation (Lelieveld et al. 2012; Janabi 2013). In fact, the IPCC using climate models has developed several potential international scenarios to illustrate the possibilities and projections of future climate changes. For example, based on the A1B Scenario, which presents the resulting projections of changes to the future climate in Iraq, the country is likely to be affected by an overall low rainfall with higher intensity and lower frequency. Furthermore, the predictions of the General Circulation Models (GCMs) used by the IPCC indicates that the precipitation in the highlands of Turkey, the sources for Tigris and Euphrates rivers, is predicted to be reduced by 10–60%, which in turn translates into a similar decline in the flow in the Tigris and Euphrates rivers (Lelieveld et al. 2012; IPCC 2014).

3 Satellite Remote Sensing and Geographic Information System (GIS) Technologies, the Fundamentals

3.1 Remote Sensing (RS) Technology

The principal purpose of Remote Sensing (RS) is to extract environmental and natural resources data needed for a better understanding of various components of our environment (Lo 1986). The fundamental basis of most remote sensing investigation is based on the wavelength-distribution of electromagnetic energy transmitted or reflected by land use/cover types, which provides signatures of the materials involved.

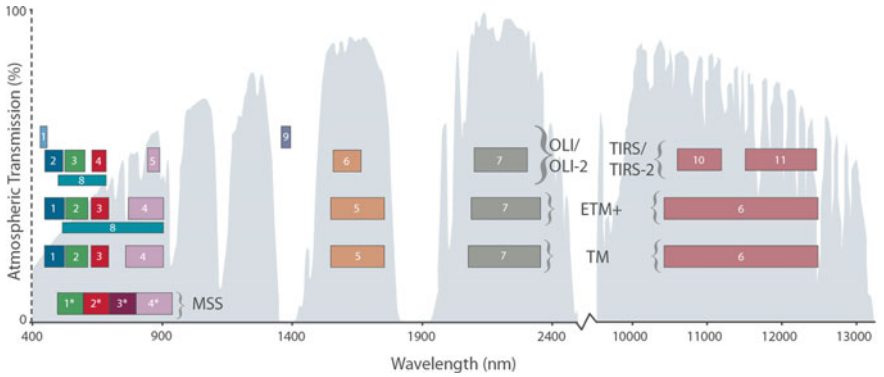

Fig. 2 The spectral bands of the Satellite Multispectral Scanner System (MSS) Landsats 1–5 (four bands); The Thematic Mapper (TM) aboard Landsats 4 & 5 (seven bands); Landsat 7's Enhanced Thematic Mapper Plus (ETM+) (8 bands); and Landsats 8 & 9 (11 bands). *Source* https://www.landsat.gsfc.nasa.gov/sites/landsat/files/2016/10/all_Landsat_bands.png

This information is used to distinguish between different types of vegetation, soil, water and rock (Lilliesand and Kiefer 1994; Baban 2005). The quality of the information depends on the number of spectral bands, their spectral width and their location within the electromagnetic spectrum (Fig. 2). A number of satellites have been designed to take advantage of this phenomena and record information for specific applications; these include the Landsat-TM and the Super- Spectral Satellite Remote Sensing ASTER (Fig. 2). In addition, a number of high-resolution satellite imaging, including IKONOS, Quick-bird and SPOT, are able to provide one band of panchromatic data of about 1 m resolution and four bands of multispectral data of about 4 m resolution. Hence, they assist applications in mapping, vegetation monitoring, land use and land cover, and the impacts of natural disasters.

The analysis of satellite remotely sensed data is primarily concerned with mapping and quantifying such characteristic spectral signatures of all the relevant features to environmental management. However, at first the raw image will need to be adjusted and numerically processed through a number of stages (e.g., correcting the image for any distortions and degradations, increasing the apparent distinction between the features to optimise visual interpretation, and to maximise the contrast between features of interest) producing an optimised image for use. Finally, the image will need to be calibrated with a number of measured relevant parameters on the ground (ground referenced samples) (Baban 1999). In addition, the researcher will need to be familiar with the basic concepts of spatial, spectral, temporal and radiometric Resolutions (Baban 2004).

3.2 Satellite Remote Sensing (RS) Technology Applications in Water Resources

3.2.1 Applications in Surface Water

These applications are based on the fact that water absorption is less than 10% of incoming electromagnetic radiant energy in the visible wavelength (0.4–0.6 μm), while it will increase rapidly above this limit to reach about 60% at 0.7 μm. Satellite sensing wavelength bands are designed to benefit from these characteristics (Barrett and Curtis 1992; Baban 2000). Sensors operating in the wave band 0.6–0.7 μm show good contrast between land features and vegetated and non-vegetated areas (Curran 1985, Baban 1996, 1998a, 1999), while sensors operating in the 0.8–1.1 μm are best suited to reveal most contrast between land and water features.

3.2.2 Applications in Subsurface Water

These applications include mapping both groundwater and soil moisture. Groundwater is mapped indirectly. This is done by mapping a significant number of groundwater-related phenomena such as detecting fractures, and the intersection of linear fractures or lineaments, which correlate with the occurrence of groundwater or, by locating anomalous areas of temperature in streams or coastal regions, which might be due to groundwater outflow (Askew and Nemec 1980; Siegal and Gilespie 1980). Soil moisture is also an important water resource as it is the immediate water supply for crops.

3.2.3 Applications in Developing Water Supplies

The majority of the applications discussed above are concerned with improving the understanding of the hydrology of the Middle East as a basis for an assessment of its surface and groundwater resources. Landsat observations can also be used to aid in the location of potential dam sites, aqueducts and canals and in this way contribute directly to the planning of water resource projects designed to meet the national water demand (Baban 1997; Lo 1986; Barrett and Curtis 1992). This application is particularly important as the fate of reliable continuous water sources in the Middle East are likely to be subject to future reductions. More reservoirs and water storages are likely to be needed in order to fulfill the water needs of the countries in the Middle East.

3.3 Geographical Information Systems (GIS) Technology

GIS has evolved for handling diverse spatial and temporal data sets for specific geographic areas by using co-ordinates as the basis for an information system (Fig. 3). GIS also promotes spatial thinking, which is a method of assessing a situation based on perception of information that includes location, and also promotes a structural approach to problem solving. GIS integrates many types of data. It analyzes spatial location and organizes layers of information into visualizations using maps and 3 dimensional scenes. This capability enables GIS to reveal patterns, relationships, and situations, helping water resources managers to make smarter decisions (Baban 1998a, 2001).

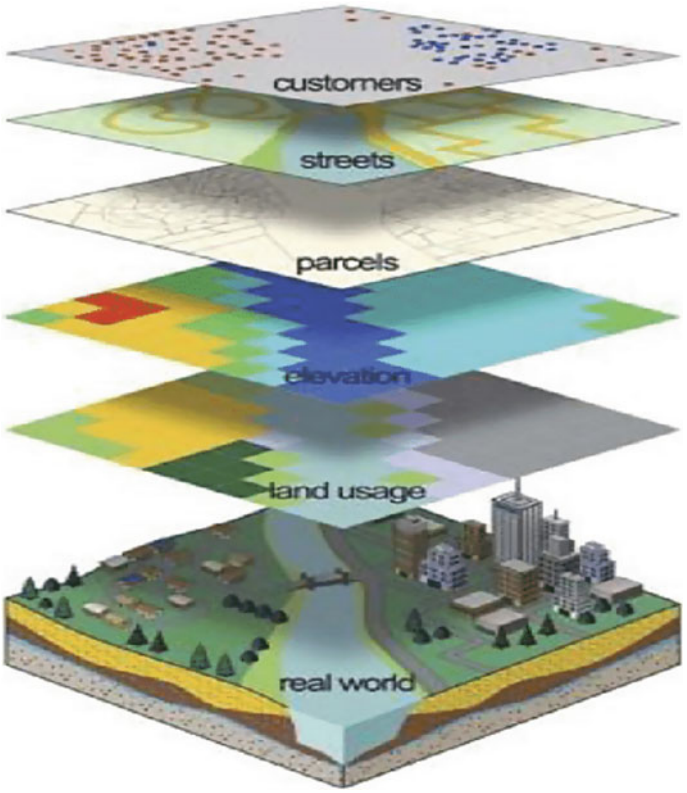

Fig. 3 GIS depiction of the world as data layers. *Source* https://www.researchgate.net/figure/Example-of-GIS-layers-16_fig3_281586364

3.4 GIS Technology Applications in Water Resources

Based on the spatial nature of the acquired data, GIS can be used effectively to: firstly, input, store, organise and analyse the ground referenced data, then to integrate these data with data from satellite imagery and other sources (Jones 1997; Heywood et al. 1998; Baban 2005). Secondly, to employ the spatial analysis, visualisation and query capabilities of GIS to identify hydrological catchment degradation water quantity and quality as well as the geographical distribution of population, industrial locations and agricultural lands (Baban 2001). GIS can also be used at operational, management and strategic planning levels by a variety of water specialists and users in the Middle East including the scientific community, universities (which must be capable of playing a leading role in the process) and decision makers and legislative bodies (Fig. 4) (Baban 2005).

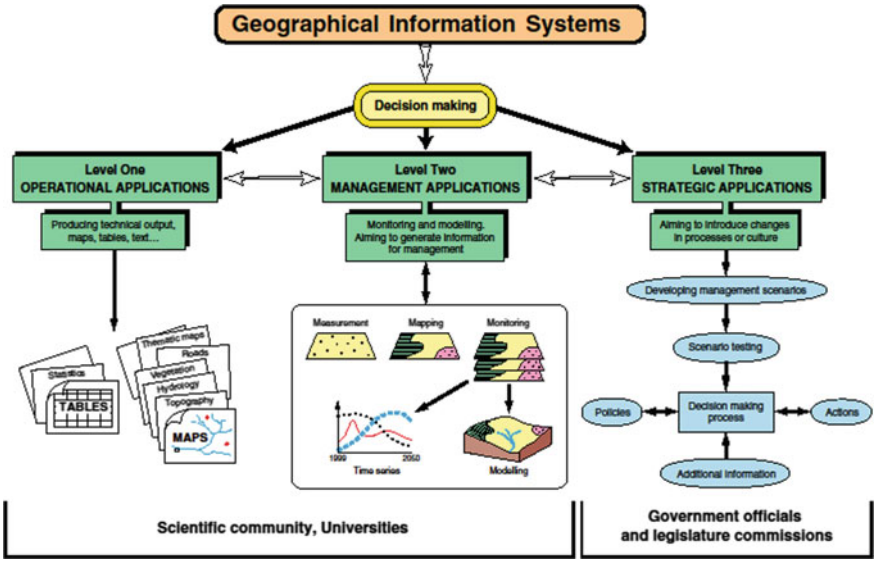

Fig. 4 GIS protocols at various levels of decision making and applications. Adapted from Morain et al. (1996), Baban (1997), Hewwood at al. (1998)

4 The Suitability of Satellite Remote Sensing and GIS Technologies for Mapping, Monitoring and Managing Water Resources in the Middle East

4.1 An Evaluation of the Suitability of Satellite Remote Sensing and GIS in the Middle East

Overall, the water supply to Middle East is falling and this trend is liable to continue. As a result, water is likely to become an even more precious resource in Middle East in the future. Consequently, accurate and judicious management of limited water resources are of great importance. The more information the manager has about water resources in the region, the better he/she is able to make decisions in terms of operations, management and strategic decisions. These include for example effectively allocating available water at specific times for consumption, industrial use, irrigation, power generation and recreation. In times of excess, flood control may become the primary task; in times of shortage, irrigation and power generation may be primary concerns (Baban 1993a, 1997, 2005; Baban and AlAnsari 2001).

In Middle East obtaining accurate and timely information on the availability as well as the quantity and quality of water resources is a problem (Baban 2005, 1998a). Satellite Remote sensing and GIS technologies hold great potential for deriving information in this context as well as contributing practically towards the effective management of water resources in Middle East. This is the case due to;

1. The region, which has little or no cloud cover each summer (June to September). Agricultural systems are simple, pollution is limited and regular ground referenced data can be gathered from the establishments which are in charge of rivers, dams and reservoirs, irrigation and reclamation schemes (Baban 1997). It should be indicated that the potential of satellite remote sensing is sometimes difficult to realise. This is because the current civilian satellites lack the necessary spatial and temporal resolution for some applications, as well as suffering from interface from cloud cover (Barrett and Curtis 1992). The spatial and temporal resolution of these satellites, however, is suited to all the potential applications discussed in this chapter.
2. Remote Sensing as a mapping, monitoring and management tool has a number of advantages, including accessibility, synoptic viewing, uniformity of collected information, repetitive coverage and cost effectiveness. These advantages will provide an opportunity to adopt a holistic approach, enabling water resources to be studied as an integrated system rather than individual entities.
3. The holistic approach, using GIS, will allow managers to observe, study and monitor, for instance, the effects and consequences of a particular decision on water resources within a large geographical area concurrently and over appropriate periods of time (Fig. 5). It will also provide data for areas which have no ground measurements based on the interpolation of area-based information from sampled sites with similar attributes; subject only to the size of the area and the

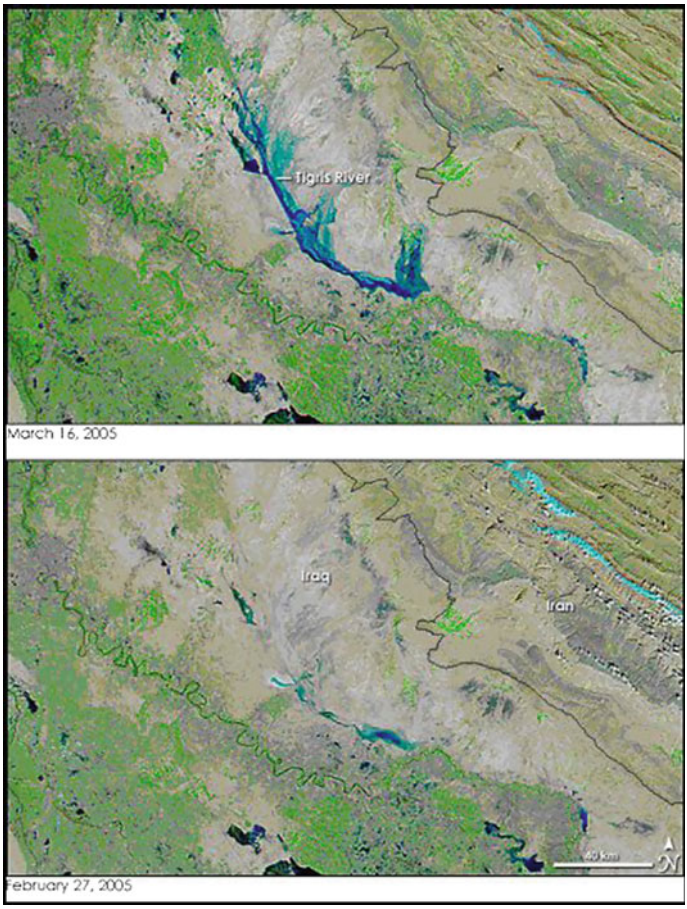

Fig. 5 River Tiger floods during March 16, 2005. *Source* http://www.earthobservatory.nasa.gov/

spatial resolution of the imagery. The GIS could also be used for constructing, simulating and modelling various management scenarios responding to a range of environmental, physical, demographic and socioeconomic conditions and challenges (Baban 1997, 1998a, 1998b).

4.2 Potential Application of Satellite Remote Sensing and GIS in the Middle East

The effective management of water resources in Middle East requires an approach that is regional in scale and holistic in scope. This can be achieved by examining,

monitoring, understanding and modelling water bodies and their catchments, rainfall as well as the social and cultural impacts of local communities. In addition to examining the possible impacts of water development schemes (digging boreholes, digging artificial ponds, harvesting natural ponds, digging canals for river diversion or feeding irrigation schemes) on both the environment and the socio- economic settings of specific sites (Baban 1997).

Planning and management of water resources at a regional scale will increasingly demand an integrated overview of different types of hydrological data gathered from different sources, by variety of means, and often maintained in separate establishments. Therefore, data homogenisation must be introduced by establishing organisational devices, such as a Regional Office for water resources and planning. Furthermore, it will be necessary to categorise the region it into a number of homogeneous areas based on physical and human factors and then focus the research on a number of representative sites. Remote sensing could be used to define the representative sites, guide the field work and generate a series of thematic coverages of the whole area for themes such as vegetation, rainfall and climate, geology and geomorphology, surface hydrology, and human impact (Baban 1998a, 1998b). These properties should be arranged for thematic applications at the later step of information integration and analysis using the GIS. The remote sensing and the GIS through the repetitive coverage and the synoptic view can be used in change detection studies, enabling researchers to observe and quantify trends and to correlate these with local, regional or global changes, which might provide some relevant answers. (Baban 1997, 1998a, 1998b).

In the Middle East region obtaining accurate information on the geographical distribution as well as the condition of water resources is a problem. Remote sensing can assist with the identification and the mapping of these two critical aspects. Remotely sensed data can also provide information for mapping and monitoring change on a regional scale, the topography and relief and data for areas that have no ground measurements (Baban 2000, 2005). Furthermore, it has been used successfully to provide relevant information on catchment characteristics, e.g., mapping and monitoring the spatial extent of various types of land use/cover including; changes in agricultural land (Pattie 1993), mapping parent material type, soils, vegetation type and canopy densities (Lo 1986; Barrett and Curtis 1992) as well as turbidity in rivers, lakes and reservoirs (Baban 1994). Remotely sensed data can also be utilised to provide the necessary area-based land use/cover parameters to run conventional mathematical models used to simulate environmental response to different water resources management scenarios (Baban 1999; Baban 1997). The outcome from these operations will provide information for various interest groups, including the scientific community and legislative bodies in the Middle East feeding information into, and assisting with the decision making process at the following gropus of applications (Morain et al. 1996; Baban 1997; Heywood et al. 1998).

4.2.1 Operational Applications

Producing timely maps at various scales and updating the necessary information for rivers, lakes and reservoirs with the view to facilitate operations.

i. Mapping available water resources. Regular and timely information on the quantity of water available in storage reservoirs and lakes in the Middle East is required for judicious utilisation for irrigation, hydropower development etc. Satellite data can help by estimating the volume of storage either through mapping depths (if possible) and extensions of water or establishing statistically significant relationships between water area and stored water volume (Baban 1994, 1993b, 1993c, 1993d, 1998a). The repetitive coverage will help in the estimation of water availability not only in the beginning of the agricultural season, but also help to monitor its depletion with time so that irrigation targets can be realistically fixed and achieved (Baban 1997, 2000, 1996). This application will become extremely important when upstream countries carry out further developments and the water inflow reduces. Water development and irrigation project calculations should be based on the available water storage within the Middle East. This application is possible, although cloud cover may be the major limiting factor in monitoring efforts during winter and early spring seasons.
ii. Snow cover mapping. The extent of snow cover, which represents the stored amount of water in the mountains, and the state of the snow are both important for river flow forecasting. This information is necessary for water power generation, irrigation, domestic water supply, flood control and planning by water management generally (Lo 1986; Lilliesand and Kiefer 1994). If a multiple purpose reservoir is to maintain a specified storage capacity to leave room for flood control, and at the same time keep a minimum water volume stored in order to improve the low flows, its successful operation depends on short-term and seasonal forecasts of inflow (Baban 1993c, 1999). This application is possible, but the cloud cover might prevent useful application during the winter. Such an application requires scientific coordination between upstream countries and low stream countries within the Middle East.

4.2.2 Management Applications

Generating new information towards managing water resources through measuring, mapping, monitoring, developing time series analysis and modelling processes related to water quality, river networks, flood management and sedimentation in reservoirs.

i. Water quality. Detecting the chemical, physical and biological characteristics of all water bodies in the country, and identifying the source of any possible pollution or contamination which might cause degradation of the water quality, is also possible with SRS (Baban 1993a; 1994). This application will become more important as the effects of eutrophication are speeded up and magnified

due the reduction in water quantity. Industrial discharges to the waterbodies will then represent a real threat to water quality, particularly in the summer season, where the temperature and light, the other two necessary parameters for algae growth, are available. By using satellite imagery and remote sensing techniques all waterbodies can be classified trophically and monitored regularly by updates. Representative individual members for each class could be selected for ground referenced data collection and for calibration purposes (Baban 1996, 2005).

ii. Mapping and Monitoring River networks.

Satellite imagery can provide frequent images of the larger rivers, such as Tigris and Euphrates, configurations. Comparing multi-date images can clearly indicate the vulnerable portions of the embankments and spurs where the rivers are concentrating their erosional attack (Baban 1999; Deutsch and Ruggles 1978; Mamat and Mansor 1999) (Fig. 5). This information will help engineers to plan erosion control works. This application is possible as the increase in inflow takes place in late spring the weather conditions are suitable for obtaining many satellite images (Mamat and Mansor 1999; Baban 2005).

iii. Managing sedimentation problems in reservoirs. Sedimentation in reservoirs is a serious problem with most impoundments in Middle East. Sedimentation reduces their capacity and shortens their productive life (Baban 1998a) (Fig. 4). Remote sensing techniques can map concentrations of suspended solids/turbidity in the surface water (Baban 1993b, 1994,). This may help in eliminating or tracing sediment sources, usually as a result of bank or soil erosion. Cloud cover might be a serious limiting factor in the winter and early spring seasons, particularly in northern Middle East, where most of the tributaries exist.

iv. Flood Management. The rivers in Middle East inundate their floodplains on a regular basis (Fig. 5). Immense areas are regularly flooded and levees often collapse resulting in wide scale damage. Satellite imagery of these rivers and their basins before, during or even few days after the flood can provide good coverage for a vast area (Deutsch and Ruggles 1978). Improved contrast between land and water boundaries can be obtained by rationing and contrast stretching techniques (Lo 1986). This will furnish crucial information concerning the flood, help appraise the spatial extent of flood-prone areas and rapidly estimate the economic consequences of flooding; particularly with respect to infrastructure and agriculture. This information can be used for the planning of flood control and the development of flood protection measures (Baban 1999). The existence of cloud-free skies, and the duration of the flood which usually extends for a week or more, makes this application possible as at least one satellite coverage can be obtained for this purpose.

v. Mapping physical characteristics, mapping of landforms and drainage networks is important in delineating catchment boundaries and the major physical dimensions affecting the occurrence of stream flow. Both automated and visual analyses of satellite data can detect changes in the drainage pattern, land cover/land use (forest, agriculture, barren land, settlement, wetland, waterbody) in river basins accurately (Lo 1986; Lillesand and Kiefer 1994; Baban 1999). The reconnaissance and development of water resources in many developing countries,

including Middle East, is based on simple regression models relating stream flow to catchment characteristics. Near infrared bands (0.7 1.0 μm) in satellite imagery (Fig. 1) are reliable for preparing maps of the Tigris and Euphrates networks, catchment boundaries, catchment areas, drainage density (total length of channel per unit area) and stream frequency (number of junctions per unit area). These are the most important parameters in developing regional (national) hydrologic models and can be involved in many calculations and predictions concerning the development of water resources in rivers. This application is again possible as many coverages could be obtained under suitable conditions.

4.2.3 Strategic Applications

These applications aim towards generation information for inducing change or managing imposed changes due to actions by upstream countries or climate change impacts in processes or cultures. These include managing water supplies, mapping land use and cover as well mapping ground water and soil moisture and developing polices to carry out these actions effectively.

i. Water supply. Landsat observations can be used to aid in the location of potential dam sites, aqueducts and canals and in this way contribute directly to the planning of water resource projects designed to meet the national water demand. This application is particularly important as the fate of reliable continuous water sources (Tigris and Euphrates) are likely to be subject to future reductions. More reservoirs and water storage are likely to be needed in order to fulfil the water needs of the countries in the Middle East (Baban 1993a, 1993b, 1997).
ii. Drainage basin and river characteristics. Mapping of landforms and drainage networks is important in delineating basin boundaries and the major physical dimensions affecting the occurrence of a stream flow. Both automated and visual analyses of satellite data can detect changes in the drainage pattern, land cover/land use (forest, agriculture, barren land, settlement, wetland, waterbody) in river basins accurately. The reconnaissance and development of water resources in many countries in the Middle East, including Iraq, is based on simple regression models relating streamflow to drainage basin characteristics. Near infrared bands (0.7–1.0 μm) are reliable for preparing maps of the Tigris and Euphrates River networks, basin boundaries, drainage basins, drainage density (total length of channel per unit area) and stream frequency (number of junctions per unit area). These are the most important parameters in developing regional (national) hydrologic models which can be involved in many calculations and predictions concerning the development of water resources in rivers. This application is possible as much coverage can be obtained under suitable conditions. (Baban 1997, 2005).
iii. Detecting Groundwater. Satellite data are useful for mapping zones of potential groundwater resources. From satellite imagery a significant number of groundwater-related phenomena can be surveyed qualitatively and, occasionally, quantitatively (Lo 1986; Lilliesand and Kiefer 1994; Askew and Nemec

1980). Examples include landforms, drainage patterns, structural lineaments, geological formations of interest (mostly limestone and conglomerates) vegetation patterns, recharge and discharge areas. This information is of great value in large scale preliminary investigations of available groundwater resources (thus saving time, labour and the expense of ground-search procedures). This would be valuable in many parts of central and western Middle East, where groundwater is the main source of water. Such groundwater resources can be used to supplement the limited sources of surface water for irrigation in most parts of the country. This application is possible as all the necessary conditions are fulfilled for successful ground coverage during the long dry summer season.

iv. Mapping land cover/use. Land cover/use is important for hydrological studies in Middle East, first, because they determine to a large extent the process of runoff generation. Secondly, they are excellent indirect indicators of the hydrologic conditions and the geophysical characteristics, which determine them. Information on land cover/use is also of indirect, but fundamental, importance to the estimation of current and future demands for water. In Middle East the principle use of water is for irrigation. It is very difficult, by conventional means, to accurately survey the areas sown each season to each type of crop, and yet without such information it is impossible to design and operate agricultural water supply schemes in an effective manner (Pattie 1993; Baban 1998b). This application is possible as much successful coverage can be obtained under cloud free conditions.

v. Soil moisture. Soil moisture information is important to the agriculturist. A deficit in moisture may lead to the wilting of plants, and timely remedial action through irrigation can save the crops. Remote sensing has a crucial role to play in this field by ensuring the optimum use of water and the best possible conditions for various crops (Askew and Nemec 1980; Sigal and Gilespie 1980).

vi. Monitoring agricultural resources. Irrigation areas fed by reservoirs are distinctly visible on satellite imagery. Multi-date information could be used to monitor the irrigated cropland through time (Pattie 1993). This information could be used effectively in many applications such as establishing an agricultural base mapping programme, which is necessary to provide information on soils, percent vegetation cover and land use for establishing of new agricultural areas and information on topography which would be of assistance in irrigation planning and watershed management. It can also provide a significant input to water consumption models for large irrigation projects; Forecasting and estimating crop production. One approach is to identify agricultural crop types and estimate the area covered by the crops using classification techniques (Pattie 1993). Another approach is to estimate the vegetation cover by using a vegetation index involving red and near infrared ratios. This will lead to better planning to meet flood and agricultural needs. Using multi-date information will have great potential for improving the recognition of crop species because different stages of growth of the crops will be taken into consideration for estimating crop production. The area is obtained by computer classified images and yield estimates can be obtained from statistical regression analysis relating crop yield to

local meteorological conditions, notably precipitation and temperature; Determining the effectiveness of various irrigation and cropping methods. Different methods have varying levels of water application efficiency and recommendations regarding improved efficiency levels could be made particularly where non-efficient cropping patterns and irrigation methods are used (Baban 2004). These applications will increase in importance as water resources are reduced and better management is needed to make higher production and optimum crop selection possible with less available water. This application is possible through the summer. However, the cloud cover will be the major limiting factor during the winter (Baban 1997).

5 Discussion

The overall water supply to the Middle East is falling and this trend is liable to continue. Whilst the demand for water consumption is increasing to meet the demands for expanding industrialisation, agriculture, population growth and the increase in living standards, the upstream countries have ambitious plans for using larger amounts of the river water, which consequently will reduce the flow into the Middle East. Consequently, water resource managers are required to make operational, management and strategic decisions to cope with and manage the use of this limited and precious resource. However, the shortage of accurate and up-to-date information on water resources presents a real challenge to decision makers in the region.

The economic growth in the Middle East is most likely to be associated with a rapid rate of urbanisation, and population growth leading to a substantial expansion in industrial and agricultural development. These actions are expected to lead to increasing demand on ever decreasing water resources in the region. Consequently, there is a real need to plan and successfully manage future demands for water resources.

The lack of reliable and compatible data sets as well as the deficiency in the scientific knowledge regarding some of the processes involved represents a problem. However, this problem can be managed by adopting a holistic approach and using Remote sensing and GIS technologies to collect, handle and analyse the necessary data sets as well as expanding our knowledge of the processes involved at the appropriate scales. Having established the status and the distribution then the abundance can be monitored efficiently over time. The GIS can be used to understand, evaluate, simulate and manage the impact of various development projects. This information will allow effective sustainable development strategies to be developed, simulated and tested, within a GIS framework, for vulnerable regions.

The examination and analysis above indicate the suitability of Geoinformatics for managing water resources in Middle East. Providing that the following aspects of the Satellite imagery are suited for the application(s) of interest; spatial resolution, spectral resolution, radiometric resolution and temporal resolution as well as having

cloud free skies. Encouraging factors for using Remote Sensing in this region include; the simple systems such as agricultural systems, in place, the limited amount of pollution and the public ownership of water resources.

Adopting the proposed approach will have a number of advantages: it will help managers to adopt an holistic approach and will update them with information concerning the quantity and quality of available water resources within a particular period, and through the GIS various management options can be examined, suggesting the best option to effectively manage these resources to satisfy a priority list (drawn by the managers); indirectly, it will promote objective thinking, planning and decision making.

References

Al-Ansari N (2013) Management of water resources in Iraq: perspectives and prognoses. Engineering 5(8):667–684

Alqallaf A (2003) Water resources and security issues in the Middle East: the next arena of future conflicts Kuwait air force. US Army War College, 30 p. https://www.apps.dtic.mil/dtic/tr/fulltext/u2/a414945.pdf

Askew AJ, Nemec J (1980) Space observations for water resources a potential to be developed. In: Salomonson VV, Bhavsar PD (eds The contribution of space observations to exploration, GB, vol 9, 280pp

Baban SMJ (1993a) Detecting water quality parameters in Norfolk Broads, UK using Landsat imagery. Int J Rem Sens 14(7):1247–1267

Baban SMJ (1993b) The evaluation of different algorithms for bathymetric charting of lakes using Landsat Imagery. Int J Rem Sens 14(12):2263–2273

Baban SMJ (1993c) Detecting and evaluating the influence of water depth, volume and altitude on variations in the surface temperature of lakes using Landsat imagery. Int J Rem Sens 14(15):2747–2758

Baban SMJ (1993d) The evaluation of different algorithms for bathymetric charting of lakes using Landsat Imagery. Int J Rem Sens 14(12):2263–2273

Baban SMJ (1994) Mapping turbidity, surface temperature and water circulation patterns with the aid of satellite imagery. J Inst Wat Environ Manage 8(2):197–204

Baban SMJ (1996) Trophic classification and ecosystem checking of lakes using remotely sensed information. Hydro Sci J 48(6):939–957

Baban SMJ (1997) Potentialapplications of Satellite remote sensing and GIS in maximising the use of water resources in the Middle East: examining Iraq as a case study. In: IAHS International symposium on remote sensing and GIS for design and operation of water resources systems, vol 242. IAHS Publications, pp 23–32

Baban SMJ (1998a) An integrated approach to effectively manage reservoirs in the Maghreb States of North Africa: examining Tunisia as a case study. In: Proceedings of the satellite-based observation: a tool for the study of the Mediterranean Basin, International Conference, the Centre National D'ETUDES SPATIALESR, Tunis, November 1998a, pp 41–49

Baban SMJ (1998b) An integrated approach to minimise natural habitat loss in Tunisia. In: Proceedings of the satellite-based observation: a tool for the study of the Mediterranean Basin, International Conference, the Centre National D'ETUDES SPATIALESB, Tunis, November 1998b, pp 57–64

Baban SMJ (1999) Use of remote sensing and gis in developing lake management strategies. Hydrobiologia 395(396):211–226

Baban SMJ (2000) Developing a holistic plan to manage desertification and water shortages in the Badia region in Jordan using remote sensing and GIS. Desertification Control Bullet United Nations Environmental Programme 36:34–41

Baban SMJ (2001) Managing the environment in the Caribbean Region using remotely sensed data and GIS. In: Proceedings of the Urban and regional information systems association (URISA) 2001 Caribbean GIS conference, September 9–12, Montego Bay, Jamaica, pp 202–213

Baban SMJ (2004) Attaining a balance between environmental protection and sustainable development in the Caribbean using geoinformatics. West Indian J Eng 2:22–34

Baban SMJ (2005) Accomplishing sustainable development in Middle East using geoinformatics: an overview. J Kurdish Sci Med Assoc ZANIN 1(1):31–43

Baban SMJ, AL-Ansari N (eds) (2001) Living with water scarcity, water resources in the Jordan Badia Region, The way forward. AL al-Bayt University Publications, Jordan, 211pp

Barrett EC, Curtis LF (1992) Introduction to environmental remote sensing, 3rd edn. Chapman & Hall, London

Clark R (1991) Water the international crisis. Earthscan publications, London, p 193p

Curran (1985) Principles of remote sensing. 260 Pages. Longman, London, UK

Deutsch M, Ruggles Jr FH (1978) Hydrological applications of Landsat imagery used in The study of the 1973 Indus River flood. Pakistan Water Resour Bullet 14:261–274

Heywood I, Cornelius S, Carver S (1998) An introduction to geographical information systems. Longman, p 279

IPCC (2014) Climate change 2014: synthesis report. Contribution of working groups I, II and III to the fifth assessment report of the intergovernmental panel on climate change IPCC, Geneva, Switzerland, 151 pp

Janabi H (2013) Water security in Iraq. 5 p. http://www.iraqieconomists.net/en/wp-content/uploads/sites/3/2013/01/Water-Security-in-Iraq-HJ-article-1.pdf

Jones C (1997) Geographical information systems and computer cartography. Longman, England, p 319p

Lelieveld J, Hadjinicolaou P, Kostopoulou E, Chenoweth J, El Maayar M, Giannakopoulos C, Hannides C, Lange MA, Tanarhte M, Tyrlis E, Xoplaki E (2012) Climate change and impacts in the Eastern Mediterranean and the Middle East. Clim Change 114:667–687

Lillesand TM, Kiefer RW (1994) Remote sensing and image processing interpretation, 3rd edn. John Wiley & Sons, USA

Lo CP (1986) Applied remote sensing. Longman, London

Mamat R, Mansor SB (1999) Remote sensing and GIS for flood prediction. Asian Association of Remote Sensing

Morain S, Estes J, Foresman T, Joseph S (1996) Image formation and raster characteristics. In: Morian S, Baros SL (eds) Raster imagery in geographic information systems. Onward Press, USA, pp 1–27

NATO Strategic Direction South (2019) Water scarcity in The Middle East. 20 p. https://www.thesouthernhub.org/resources/site1/General/NSD-SHubPublications/Water_scarcity_in_the_Middle_East.pdf

Pattie N (1993) Farmwatch UK. GIS Europe. November 22–24

Rashed Y (2020) Rivers are plentiful in the Middle East. Arab America. https://www.arabamerica.com/rivers-of-the-middle-east/

Siegal BS, Gillespie AR (1980) Remote sensing in geology. J. Wiley and sons, USA

Atmospheric Rivers and Precipitation in the Middle East

Elias Massoud, Theresa Massoud, Duane Waliser, Bin Guan, and Agniv Sengupta

1 Introduction

1.1 Precipitation in the Middle East and North Africa

The Middle East and North Africa (MENA) region is located at the interface of the subtropics and mid-latitudes, and precipitation changes in the future in this region are subject to influences from various factors, such as the Hadley circulation and

The original version of this chapter was revised: The following belated corrections have been incorporated: The author name "Agniv Sengputa" has been changed to "Agniv Sengupta" in the Frontmatter, and in the Chapter. The correction to this chapter is available at https://doi.org/10.1007/978-3-031-15549-9_23

E. Massoud (✉) · D. Waliser · B. Guan
NASA Jet Propulsion Laboratory, California Institute of Technology, 4800 Oak Grove Dr, Pasadena, CA 91109, USA
e-mail: massoudec@ornl.gov

D. Waliser
e-mail: duane.waliser@jpl.nasa.gov

B. Guan
e-mail: bin.guan@jpl.nasa.gov

E. Massoud
University of California, Berkeley. 130 Hilgard Way, Berkeley, CA 94720, USA

Oak Ridge National Laboratory, 1 Bethel Valley Rd, Oak Ridge, TN 37830, USA

T. Massoud
University of Balamand, Green Community Village, Dubai, United Arab Emirates
e-mail: theresa.massoud@fty.uobd.ac.ae

B. Guan
University of California, 607 Charles E. Young Drive East, Los Angeles, CA 90095, USA

A. Sengupta
University of California, San Diego. 8622 Kennel Way, La Jolla, CA 92037, USA
e-mail: agsengupta@ucsd.edu

A. Shaban (ed.), *Satellite Monitoring of Water Resources in the Middle East*,
Springer Water, https://doi.org/10.1007/978-3-031-15549-9_4

winter storms (Hasanean 2004). These storms can emerge as atmospheric rivers (ARs), which are long and narrow filaments of water vapor transport that release precipitation in the form of rain or snow upon making landfall or encountering uplift (AMS 2017). Recent events have shown that ARs in MENA can produce extremely heavy precipitation, and they can provide both significant benefits as well as major costs to water resources management in the region. Given this awareness of the significance of ARs in the MENA region, we investigate here the importance of ARs for precipitation, and we estimate how ARs and precipitation will change in the future in MENA.

Changes in precipitation in a warmer climate are dictated by several factors. A primary physical mechanism for increases in precipitation is the enriched water vapor content in a warmer atmosphere, which reinforces moisture convergence into storms (Wang, et al. 2015). Projecting regional changes in precipitation is difficult because of the chaotic nature of the Earth system (Slingo et al. 2011; Massoud et al. 2018a) which makes it very difficult to accurately predict weather and climate past a few weeks, but also because of uncertainty in projecting changes in the large-scale circulation (Shepherd et al. 2014). For the MENA region, observed changes in precipitation have included a mix of increases, decreases, or little change (Almazroui 2019a; Bucchignani, et al. 2018; Ozturk, et al. 2018) depending on location and season.

Throughout the world, high-latitude regions are generally projected to become wetter, whereas the subtropical regions are projected to become drier (Held et al. 2006). Since the MENA region lies between these two areas, there is a large uncertainty about the sign and magnitude of future changes in precipitation in much of the region. Yet, since atmospheric water vapor will increase with increasing temperatures, there is confidence that precipitation extremes will increase in frequency and intensity in the future throughout MENA and the rest of the globe (Espinoza et al. 2018; Massoud et al. 2019).

1.2 Extreme Precipitation and Atmospheric Rivers

We investigate extreme precipitation in this study by focusing on ARs, which can have an important impact on hydrologic events such as droughts or floods in many regions of the world, including western North America (Dettinger et al. 2004; Guan et al. 2010; Neiman et al. 2011; Ralph et al. 2006, 2013), western South America (Viale et al. 2011), Europe (Lavers et al. 2013; Sodemann et al. 2013), and other regions (Paltan et al. 2017; Nash et al. 2018). ARs play a significant role for regional precipitation, which can include rain or snow (Guan et al. 2010; Dettinger et al. 2011; Huning et al. 2017, 2019), and can cause large flooding events (Neiman et al. 2011; Ralph et al. 2006; Ralph et al. 2013; Leung et al. 2009; Ralph et al. 2011; Lavers et al. 2011) and extreme winds (Waliser and Guan 2017) as well as mitigate droughts (Dettinger et al. 2013).

The importance of AR storms has motivated an increasing number of studies related to climate change impacts on ARs (as reviewed in (Payne et al. 2020), with

many studies focusing on Western North America (Dettinger et al. 2011; Pierce et al. 2013; Payne et al. 2015; Warner et al. 2015; Gao et al. 2015; Radić et al. 2015; Hagos et al. 2016; Shields et al. 2016b; Gershunov et al. 2019; Huang et al. 2020) and Europe (Lavers et al. 2013; Gao et al. 2016; Ramos et al. 2016; Shields et al. 2016a). Espinoza et al. (2018) and Massoud et al. (2019) provided a global view of AR frequency and strength in future climates and reported that increases in both frequency and strength of ARs is expected to occur for many regions of the globe by roughly 25–50%.

Many studies have investigated the MENA region as part of their study domain, such as the International Coordinated Regional Climate Downscaling Experiment (CORDEX-MENA) initiative. This community has published numerous studies about climate in the MENA region, such as temperature and precipitation analyses (Almazroui et al. 2019a; Almazroui et al. 2016; Almazroui et al. 2019b; Bucchignani et al. 2016; Spinoni et al. 2020). As for ARs in the MENA region, studies have just started to appear in the literature. Akbary et al. (2019) explored the historical spatio-temporal changes of ARs and their pathways into the MENA region, and they found a decrease in frequency over the period of 1984–2013. Esfandiari and Lashkari (2020a, b) studied ARs in Iran, and they looked at the effect of ARs on cold-season heavy precipitation events as well as their pathways and landfall locations. Dezfuli (2020) reviewed a rare atmospheric river event named AR Dena that happened in March 2019, which caused record floods across Iran and the Arabian Peninsula. Massoud et al. (2020a) investigated historical and future projected changes in ARs and precipitation in the MENA region. Furthermore, in Guan and Waliser (2019), AR activity in the MENA region is also noted in the context of their global analysis of ARs.

1.3 Uncertainty in Estimates of Future Climates

There is a climate modeling community that provides a suite of model simulations and projections, named the Coupled Model Intercomparison Project, or CMIP (e.g., CMIP5; Taylor et al. 2012). CMIP5 is the fifth generation of CMIP, and is used to characterize uncertainty arising from model differences and greenhouse-gas concentration pathways, as well as to characterize uncertainty inherent in the climate system due to processes like internal climate variability (Kay et al. 2015; Massoud et al. 2018b). These ensembles provide an important tool for estimating the uncertainties in future climate projections, such as those for ARs and precipitation. In our study, the climate model historical simulations (CMIP5) and the future scenario simulations (RCP8.5) are processed through an AR detection algorithm (Guan et al. 2015; Guan et al. 2018) to catalogue AR conditions with various metrics accounted for, such as AR frequency and intensity.

This study is set up in the following manner. First, the study domain is introduced, and we highlight various individual AR events that stand out in the historic record. These include an AR that occurred in January 1994 and is one of the longest regional

ARs on record, and another event named AR Dena which occurred in March 2019, notable for its very heavy precipitation. We then calculate the fraction of precipitation that arises from ARs for this region, and we showcase how ARs can account for nearly half of the total precipitation for some local areas. Then, we show seasonal and annual historical estimates of AR dynamics and mean daily precipitation over the MENA region, along with sea level pressure and mean wind vector fields. Finally, we use the CMIP5 set of models to investigate historical and future changes in ARs and precipitation for the MENA region. Although studies have performed similar analyses on global scales (Espinoza et al. 2018; Massoud et al. 2019), this is one of the first to explore future changes in ARs and precipitation for the MENA region using the CMIP multi-model ensemble (c.f. Massoud et al. 2020a).

2 Materials and Methods

2.1 MENA Domain

Ordinarily, ARs require a type of lifting mechanism for condensation to occur and produce precipitation. In many cases, this mechanism comes in the form of orographic, or mountain, lifting. Within MENA (see Fig. 1), the regions of Turkey and Iran are rich with mountain ranges that absorb the impact of ARs and where local precipitation from ARs is generally high. Climatological mean precipitation is low for most of the MENA region, and the domain includes the Sahara and Arabian deserts, home to the largest stretch of desert in the world.

A topographic map of the MENA region is shown in Fig. 1. This figure uses topographic, bathymetric and shoreline data from NOAA National Geophysical Data Center's ETOPO1 Global Relief Model (Amante et al. 2009). This is a 1 arc-minute model of the Earth's surface, developed from diverse global and regional digital datasets and then shifted to a common horizontal and vertical datum. In general, 1 arc-minute equates to 1/60th of 1 degree. So, depending on the region of the globe, 1 arc-minute is equal to ~2 km. The map in Fig. 1 shows the elevation (m) for the MENA region, and 3 arbitrary lines that intersect the region are shown with red dashed lines and are highlighted in the subpanels on the right. The high elevation in certain locations is highlighted here, such as the mountain areas in Turkey and Iran, which cause orographic lifting of ARs and creates favorable conditions to greatly enhance precipitation.

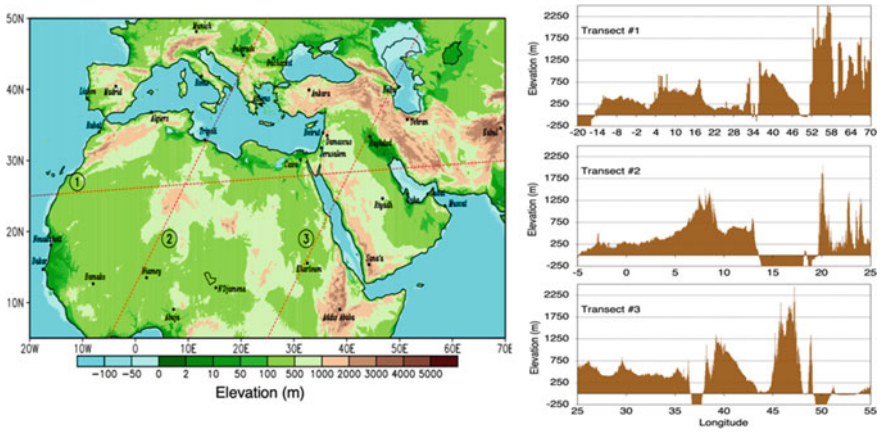

Fig. 1 Topographical map of the Middle East and North Africa (MENA) using the NOAA National Geophysical Data Center's ETOPO1 Global Relief Model. The map shows the elevation (m) for the MENA domain. The three transects that intersect the region are shown with red dashed lines and are highlighted in the subpanels on the right. The high elevation in certain areas is highlighted here, such as the mountain terrains in Turkey and Iran. Figure adopted from Massoud et al. (2020a)

2.2 *Observed Precipitation, Winds, and Mean Sea Level Pressure*

The data for monthly precipitation is obtained from the German Meteorological Service's (Deutscher Wetterdienst, DWD) Global Precipitation Climatology Centre (GPCC; Schneider et al. 2018) version 8 on a 0.5° continental grid (provided by the Physical Sciences Division of the NOAA Earth System Research Laboratory; https://www.esrl.noaa.gov/psd/data/gridded/data.gpcc.html).

This study also uses the National Centers for Environmental Prediction (NCEP) reanalysis (Kalnay et al. 1996) to characterize the circulation field, specifically the 925-hPa winds and the mean sea level pressure (MSLP). This retrospective analysis data of atmospheric fields is available on a 2.5° × 2.5° global grid from January 1949 to the present. On seasonal and annual timescales, Carvalho (2019) shows that MERRA2 and NCEP are very similar.

2.3 *Integrated Water Vapor Transport (IVT)*

This study uses specific humidity and wind fields from National Aeronautics and Space Administration's (NASA) Modern-Era Retrospective Analysis for Research and Applications, Version 2 (MERRA-2; (Gelaro et al. 2017) reanalysis to compute the IVT field. The MERRA-2 reanalysis, available on a 0.5° latitude by 0.625° longitude grid for the period 1980-present, assimilates satellite observations not

available to its predecessor, MERRA, with additional updates to the Goddard Earth Observing System (GEOS) model and its analysis scheme.

2.4 AR Detection Algorithm

Guan and Waliser (2015) developed a global AR detection algorithm, which was updated and validated with in-situ and dropsonde data (Guan et al. 2018). This algorithm is used in our study and is based on a combination of the IVT magnitude, direction, and geometry characteristics, to objectively identify ARs. Continuous regions of enhanced IVT transport are first identified and documented using magnitude thresholding (i.e., grid cells with IVT above the seasonally and regionally dependent 85th percentile) and further filtered using directional and geometry criteria requirements.

The detection algorithm was utilized on both the reanalysis data and the CMIP5 models in their native resolution. For the CMIP5 models, once the AR dynamics are estimated, results are re-gridded using a bi-linear function, as was done in Espinoza et al. (2018) and Massoud et al. (2019). This global algorithm had over ~90% agreement in detected AR landfall dates with other regional algorithms that focused on locations with different climatologies, such as western North America (Neiman et al. 2008), Britain (Lavers et al. 2011), and East Antarctica (Gorodetskaya et al. 2014). This agreement provides us with confidence in using this algorithm for our application in the MENA region. Note, these algorithms are best viewed as complementary to each other, and the agreement rate should not be interpreted in terms of "hits" and "misses". The agreement rate mentioned above for other regions gives us confidence that the results we investigate in our current study would not significantly change if another detection algorithm was to be developed or used. In that regard, it is noted that the Iran-focused studies in Esfandiari and Lashkari (2020a, b) used AR IVT percentile and geometry criteria largely following the global algorithm used in our study. Readers are referred to Guan and Waliser (2015) for more information on the AR detection algorithm used in our study.

2.5 Climate Model Simulations of ARs and Precipitation

The historical simulations and future projections from CMIP5 under the representative concentration pathway RCP8.5 warming scenario (Hibbard et al. 2007; Meehl et al. 2006; Meehl et al. 2009) informing the Fifth Assessment report (AR5) of the Intergovernmental Panel on Climate Change (IPCC) are used in the present analysis. All model simulations are re-gridded on a common grid using bi-linear interpolation when needed to maintain the consistency between the resolution of the different data products. Then, the various metrics investigated in this study are computed (see

below). The coarse resolution of GCMs means that this analysis reflects regional-scale processes rather than finer-resolution ones such as the effects of small topographic variations. Results shown here should be interpreted with this caveat in mind. However, it is not expected that a higher-resolution model would meaningfully affect the broad patterns shown here, such as the latitudinal shifts of ARs due to climate change.

All CMIP5 models used in this study are the 'r1i1p1' version of the model simulations, and the 'precipitation flux (pr)' variable was analyzed for these simulations. As in Espinoza et al. (2018) and Massoud et al. (2019), ARs are defined using Integrated Vapor Transport (IVT) values constructed from daily values of 3-D wind and water vapor model outputs at four pressure levels between 500 and 1000 hPa (data described in Lavers et al. 2015; their Table S1). IVT values are estimated and calculated at native model resolutions ranging from 1.125° to 2.813°. The dates for the climate model (CMIP5) historical simulations range from 1979 to 2002 and the future (RCP8.5) scenario simulations range from 2073 to 2096, following Lavers et al. (2015), Espinoza et al. (2018), and Massoud et al. (2019). These time periods are determined as the periods that contain the maximum number of overlapping years among all models, with 24 years for both the historical and future runs.

The AR frequency is calculated for each period (historical vs future) and in each grid cell as the percentage of time steps where an AR is detected, ranging from 0% (no ARs) to 100% (an AR at every time step). Around the globe, a typical value for AR frequency is roughly 10%, which translates to AR conditions being present 10% of the time steps, or around 36 days per year.

3 Results

3.1 Individual AR Events in MENA

The comprehensive AR dataset in this study is used to survey some of the most notable MENA ARs documented in previous literature. This comparison facilitates a uniform perspective on AR dynamics and extremes in this region. Akbary et al. (2019) highlighted several AR events and showed that on average about 13 ARs occur each year (range of 6–25 ARs per year) in the MENA region. They also showed that most of the ARs occur in the fall and winter seasons. Furthermore, most ARs in the MENA region originate over the North Atlantic Ocean and enter Africa from Mauritania and Senegal, then pass Egypt, Saudi Arabia and Iran before dissipating in Afghanistan and Pakistan (e.g. Fig. 1). Also shown in Akbary et al. (2019), the Red Sea was determined to be a major source of moisture that feeds ARs on their path into this region. In this study, we survey the diversity of ARs in MENA by examining the pathways and intensities of notable observed events (Fig. 2).

Figure 2a shows the longest AR storm documented in the literature for the MENA region which occurred in January 1994, and stretched from western North Africa to

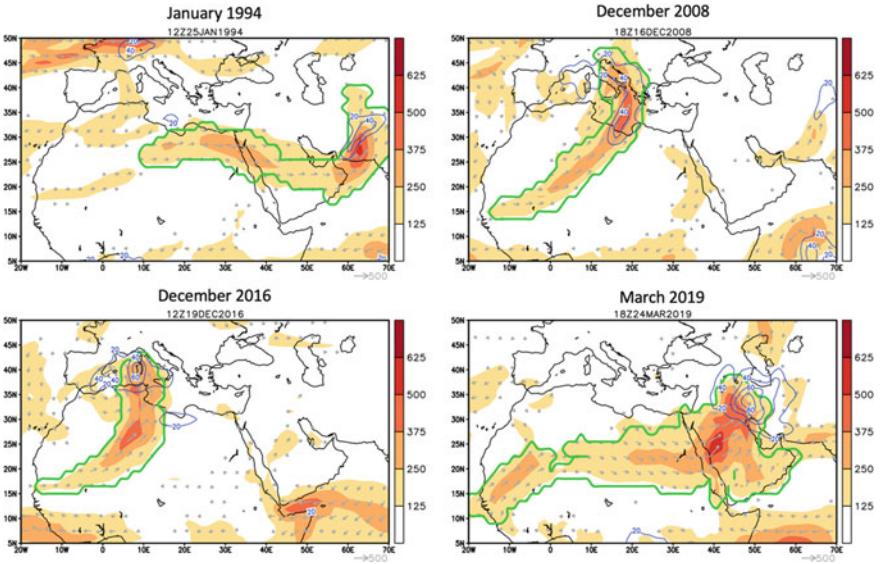

Fig. 2 Individual AR cases: **a** AR event in January 1994. **b** AR event in December 2008. **c** AR event in December 2016. **d** AR event Dena in March 2019. (Legend) Green: AR shape from the AR detection algorithm. Arrows: IVT vectors (not shown if magnitude smaller than 100 kg/m/s). Shading: IVT magnitude (kg/m/s). Blue: 2-day cumulative precipitation (in mm) centered on the time step shown in the panel title. Figure adopted from Massoud et al. (2020a)

the Himalayan Mountains with a length of 12,000 km. This AR event is also reported in Akbary et al. (2019), in their Fig. 3h. Note, this AR event is the longest on record up to 2013, however it is not the longest in the AR database used here.

The next AR event we display here is shown in Fig. 2b, which documents an AR that occurred in December 2008. This AR originated from a similar location in the Atlantic as the one shown in Fig. 2a, however the pathway of this AR led towards Europe and resulted in extreme rainfall over Italy. The AR is also documented in Akbary et al. (2019), in their Fig. 3.

In Fig. 2c, an individual AR event that occurred in December 2016 is shown. Like the AR shown in Fig. 2b, this event originated from the Atlantic and the pathway led towards Europe, with even heavier extreme rainfall than the previous AR. To the best of our knowledge, this AR is not documented in any other study in the literature.

Another impactful AR event that occurred in the MENA region was AR Dena, which happened in March 2019, had a maximum length of 9,000 km, and produced devastating extreme precipitation, as shown in Fig. 2 (bottom right panel). Dezfuli (2020) highlighted this event and showed how record floods across the Middle East during March 2019 were driven largely by moisture transported from the North Atlantic Ocean. Iran was substantially affected by the floods (c.f United Nations 2019), with widespread damage to infrastructure and a death toll of at least 76. The nearly 9,000-km-long AR propagated across the MENA region and was fed by

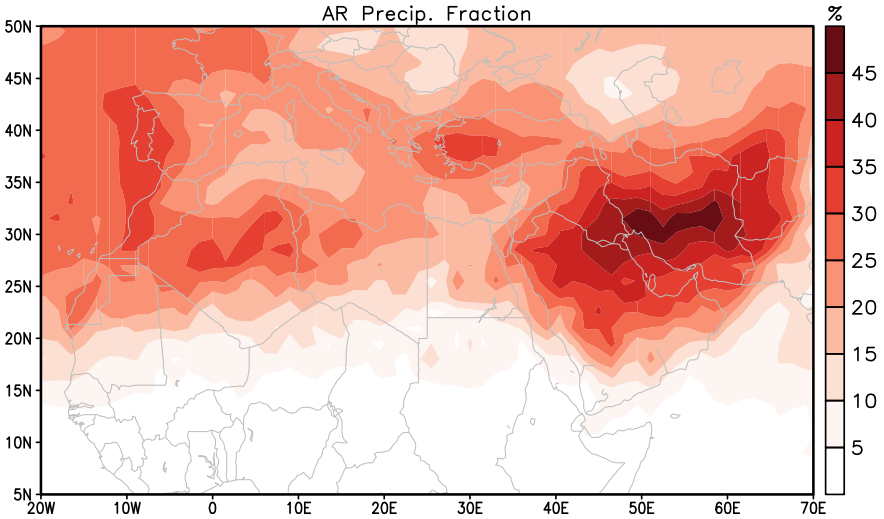

Fig. 3 A representation of the fraction of annual precipitation that is associated with atmospheric rivers. The darker shades of red contours indicate areas where ARs account for more than 30% of the total rainfall, with central Iran having nearly half of its precipitation coming from ARs. Figure adopted from Massoud et al. (2020a)

additional moisture sources from several other locations on its pathway. The simultaneous presence of a midlatitude system and a subtropical jet facilitated the moisture supply and convergence, while the orographic lifting from the Zagros Mountains helped produce record rainfall. AR Dena presented a compelling example of rapid shifts from prolonged drought to frequent floods (Dezfuli 2020) and it reinforced the notion that "extremes become more extreme" in a changing climate (Dettinger et al. 2013; Swain et al. 2018).

3.2 Climatology of ARs and Precipitation in the MENA Region

The Middle East does not typically appear in surveys of previous AR literature (although c.f. Gimeno et al. 2016), highlighting the novel aspects of studying ARs for this region. However, there are a few well-documented examples that are available (Bozkurt et al. 2004; Ziv et al. 2005). In this study, we find that the MENA region is one of the few locations around the globe in which precipitation from ARs can account for a significant portion of the total annual precipitation (see Fig. 3). We show in Fig. 3 the fraction of precipitation associated with ARs for the MENA region. Regions where ARs account for more than 30% of the total rainfall are shown in red to dark red, with some areas having nearly half of their precipitation coming from ARs, especially in Iran. This indicates that ARs are not only very important

for water resource management in the area, but that ARs can help this region escape drought conditions that are caused by a lack of rainfall or depletion of fresh water sources (Massoud et al. 2021). However, this also indicates that ARs can provide enough rainfall to produce deadly floods, which further highlights the importance of studying ARs in this region.

Figure 4 displays the AR IVT (kg/m/s) and frequency (% of time steps) for the MENA region over the analysis period of 1981–2018, shown annually (a) as well as for each season (b–e). ARs in the MENA region are mostly a cool-season phenomenon (Fig. 4a–c, e), with Ars being absent during the summer months due to high-pressure systems induced by the downwelling branches of the Hadley Cell and South Asian summer monsoon (Fig. 4d). An accurate way to represent the possibility of storms (and their precipitation, if they do happen) is mid-tropospheric relative humidity, which is less than 20% over the entire Middle East in the summer (JJA), versus 30–50% in the winter (DJF). For comparison, it is 60–70% in summer over central India (Tyrlis et al. 2013). These low values for the Middle East are due to large-scale descent through most of the free troposphere, induced by the South Asian summer monsoon. The seasonal and annual precipitation and wind dynamics for MENA are shown in Fig. 5. Comparing the AR climatology with the overall mean precipitation and wind climatologies for the region (Figs. 4 and 5) shows similar dynamics, with some minor variants.

3.3 Model Simulations of Historic and Future Climate

CMIP5 simulations for ARs and precipitation for the MENA region are shown in Fig. 6. According to the CMIP5 multi-model ensemble of historical AR frequency (Fig. 6a), some regions of MENA experience up to 8% AR frequency on average. The CMIP5 multi-model ensemble of historical mean daily precipitation (Fig. 6c) demonstrates that although ARs play an active role in the region, much of the area has a desert landscape, with very little to no rainfall. However, there are some regions, such as the north and south parts of the domain, as well as the mountains of Turkey and Iran, do experience higher precipitation rates, with up to 8 mm/day for certain areas. For some of these regions, a large fraction of this rainfall comes from ARs (as shown in Fig. 3). Previous back-trajectory analysis confirms this conclusion (Heydarizad et al. 2019).

To explore future changes in AR and precipitation over MENA, the CMIP5 model ensemble is simulated to 2100, and we investigate the RCP8.5 scenario which represents a high-emissions future. Figure 6b displays the projected future AR frequency for the MENA region, represented as the percent of timesteps that show AR conditions. Additionally, Fig. 6d displays the projected future mean daily precipitation, represented in mm/day. To investigate the values of the projected changes for AR frequency and mean daily precipitation for the MENA region, the historical values in Fig. 6a, c are subtracted from the future values in Fig. 6b, d. This provides the raw

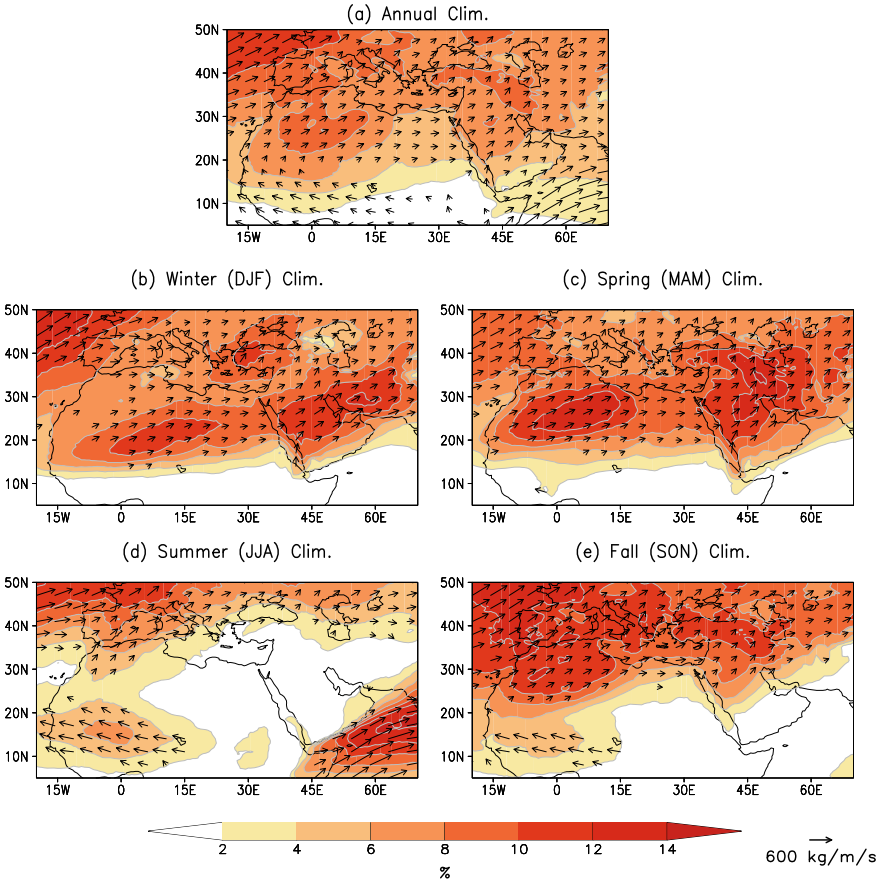

Fig. 4 AR frequency (% of time steps) and IVT (kg/m/s) plots for the MENA region, shown **a** annually and **b**–**e** for each season. Figures show the AR occurrence frequency at 6-hourly time steps over the analysis period of 1981–2018. Figure adopted from Massoud et al. (2020a)

values for projected future changes, which are displayed in Fig. 7 and discussed in the next Section.

3.4 Future Change in AR Frequency and Precipitation in MENA

The projected changes for AR frequency in the MENA region are shown in Fig. 7a. The values in this plot show a large part of the domain, specifically in the northern part (mostly in mid-latitude Eurasia), that is expected to see increases in AR frequency (up to +3% of timesteps). This is seen as far south as the North African coast of the

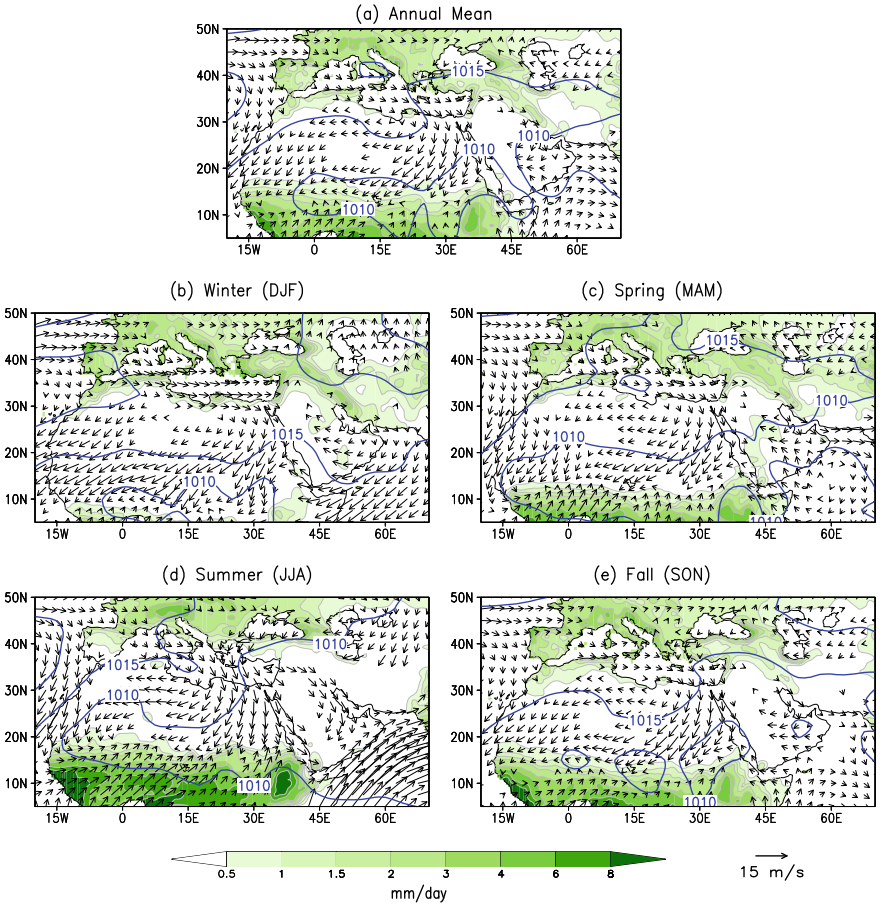

Fig. 5 The climatological precipitation (in green contours, mm/day) from GPCC ver. 8, the mean wind vector field at 925-hPa (black arrows, m/s) and the mean sea level pressure (blue contours, hPa) from NCEP Reanalysis, shown **a** annually, and **b–e** for each individual season. The period of analysis is 1951–2015. Figure adopted from Massoud et al. (2020a)

Mediterranean Sea, as well as in Turkey and Iran. However, the rest of the region is not expected to see any significant change in AR frequency, with some regions in the southern portions of the domain expecting to see a decrease in AR frequency.

For the values of projected future changes in mean daily precipitation, shown in Fig. 7b, different signs of change are expected depending on the location. For example, decreases in precipitation are expected for the Mediterranean Sea and countries that border it (−0.3 mm/day). Yet for the Arabian Peninsula, there is an expected increase in precipitation (+0.3 mm/day), in line with previous studies (Terink et al. 2013; Zappa et al. 2015). In Fig. 7, the significance of these results is highlighted using a paired-sample t-test with $p = 0.05$, and grids where the projected change

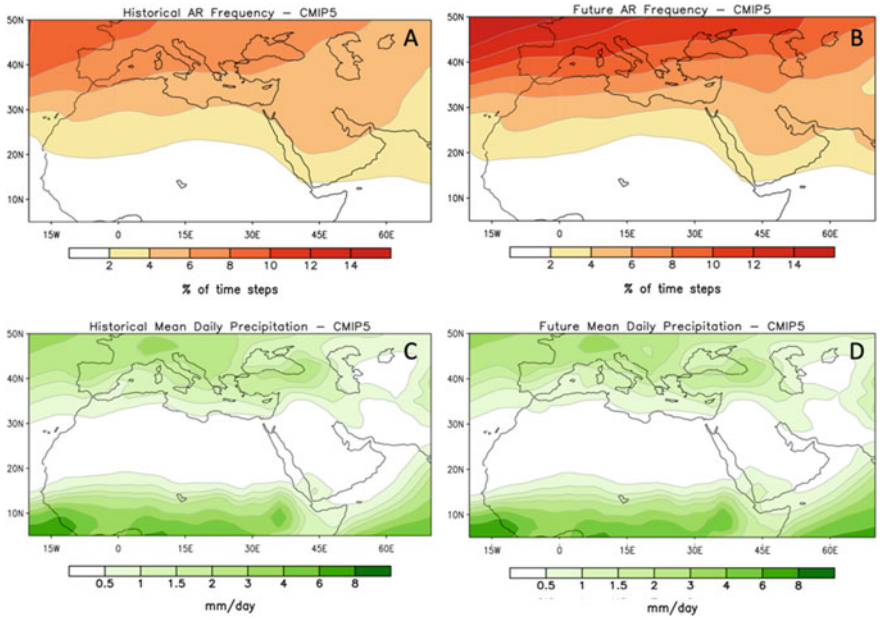

Fig. 6 **a** Historical AR frequency (% of timesteps) for the MENA region as represented by CMIP5 models. Like Fig. 4a, Panel A of this figure represents the annual historical AR frequency but shown here for CMIP5 models. **b** Projected future AR frequency (% of timesteps) for the MENA region obtained from CMIP5 models (RCP85). This figure represents the same process as the AR frequency shown in Panel A, but for the future simulations. **c** Historical mean daily precipitation (mm/day) for the MENA region as represented by CMIP5 models. Like Fig. 5a, Panel C of this figure represents the annual historical mean daily precipitation but shown here for CMIP5 models. **d** Projected future mean daily precipitation (mm/day) for the MENA region obtained from CMIP5 models (RCP85). This figure represents the same process as the mean daily precipitation shown in Panel C, but for the future simulations. The CMIP5 historical simulations range from 1979 to 2002 and the future (RCP8.5) scenario simulations range from 2073 to 2096. Figure adopted from Massoud et al. (2020a)

in AR frequency or precipitation are statistically significant are marked with black dots.

To further elucidate these results, the expected future changes shown in Fig. 7 are normalized to explore 'relative' future changes. This is done by dividing the future change values in each grid cell from Fig. 7 by the historical values in each grid from Fig. 6a, c. This provides a relative sense of how much the change compares to the historical climatology. These relative change values are shown in Fig. 8 as a percentage of historical climatology.

According to the results in Fig. 8a, Eurasia is expected to see increases in AR frequency of up to 50% from historical values. New regions emerge in importance when exploring the relative changes in AR frequency shown in Fig. 8a, such as the Arabian Peninsula (up to +20% from historical values). For the relative values of projected future changes in mean daily precipitation, we see in Fig. 8b different

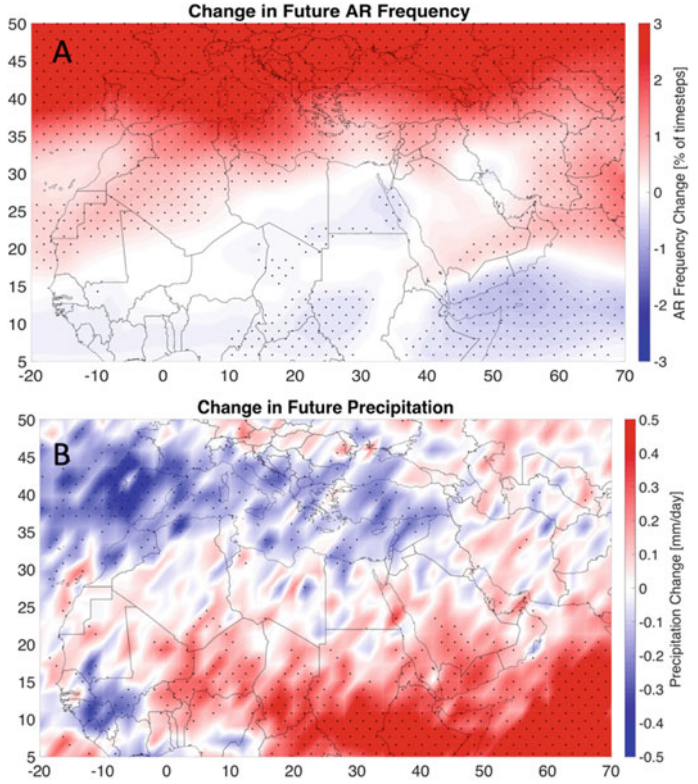

Fig. 7 **a** Raw values for the projected change in future AR frequency (% of timesteps), calculated as the difference between projected future values and historic climatology for the MENA region. **b** Raw values for the projected change in future mean daily precipitation [mm/day] for the MENA region. The CMIP5 historical simulations range from 1979 to 2002 and the future (RCP8.5) scenario simulations range from 2073 to 2096. Grids with a black dot indicate where the projected change in AR frequency or precipitation is statistically significant, based on a paired-sample t-test with $p = 0.05$. Figure adopted from Massoud et al. (2020a)

signs of change depending on the area. Like the raw expected changes from Fig. 7b, the relative changes in Fig. 8b show that the Mediterranean basin should expect decreases in precipitation (down -30% from historical values). Yet, for the Arabian Peninsula, there is an expected increase in precipitation (up + 50% from historical values). Therefore, the stretch of countries from the Horn of Africa to the United Arab Emirates should expect an increase in precipitation, which will have some contributions from ARs as shown in Fig. 8a, but also from other sources of precipitation as indicated in Fig. 8b. The maps showing black dots in Fig. 7 indicate where the future change estimates are statistically significant for the metrics and values shown in Figs. 7 and 8.

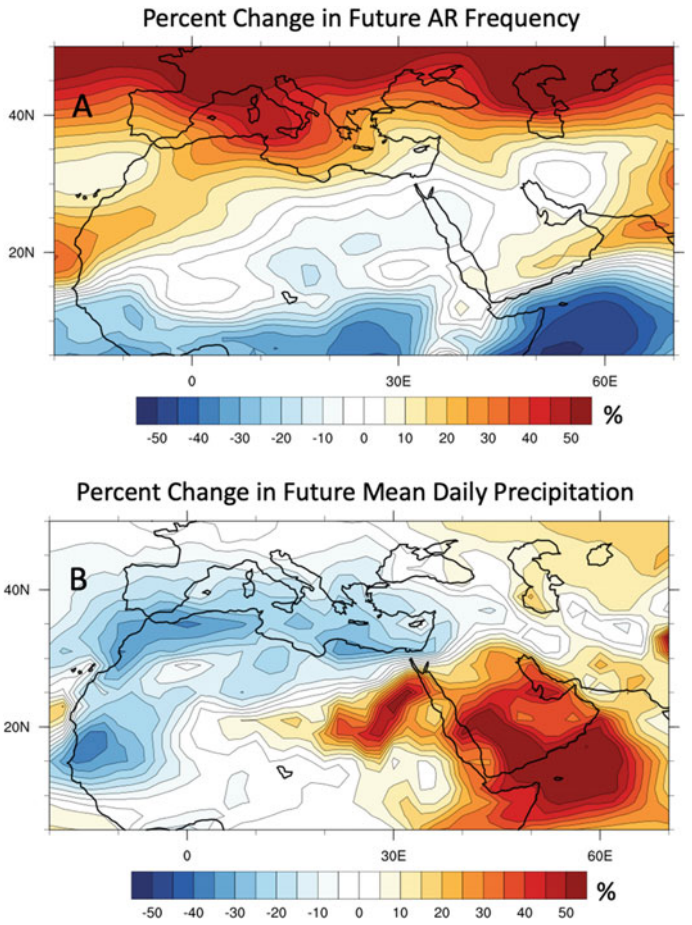

Fig. 8 **a** Relative values for the projected change in future AR frequency, calculated as the percent change in projected future values compared to historic climatology (%) for the MENA region. **b** Relative values for the projected change in future mean daily precipitation (%) for the MENA region. The CMIP5 historical simulations range from 1979 to 2002 and the future (RCP8.5) scenario simulations range from 2073 to 2096. Figure adopted from Massoud et al. (2020a)

3.5 Significance of Expected Changes Based on Latitude

The usefulness of climate simulations for understanding significant future changes depends on a proper accounting of uncertainties (Vrugt and Massoud 2018). For example, when the model spread is too large, the expected change as reported by a multi-model ensemble mean may not be meaningful. Different models can present very different results, and the spread of the multi-model ensemble informs the confidence of the future change results (Lee et al. 2018; Gibson et al. 2019). Shown in Fig. 9 is the spread of the multi-model ensemble for the CMIP5 simulations of AR

frequency and mean daily precipitation for the historical (blue), RCP8.5 (red), and the projected differences (green), presented as latitudinal averages throughout MENA. The green bars on the green difference curves indicate 95% significance, which is determined by using 2 times the standard deviation of the multi-model ensemble spread.

In this study, the investigation of statistical significance of future changes in AR frequency is initially shown using the black dots in Fig. 7a, which indicate where the future change estimates are statistically significant at the $p = 0.05$ level based on a paired-sample t-test. For additional investigation of statistical significance, Fig. 9a shows that areas with higher latitude than 35 N are expected to see significant increases in AR frequency in the future. These latitudes are marked with black x's on the 0-change line in Fig. 9a. Comparing the values in the future change curves of Fig. 9a (red, RCP8.5) with the historical values (blue, historical), we see that projected changes (green, difference) in AR frequency are significant for regions at higher latitudes than 35 N. Massoud et al. (2019) showed the natural variability of AR frequency around the globe (c.f. their Fig. 9), and reported that for the MENA region the natural variability can range from 1 to 2 (% of time steps). Therefore, the

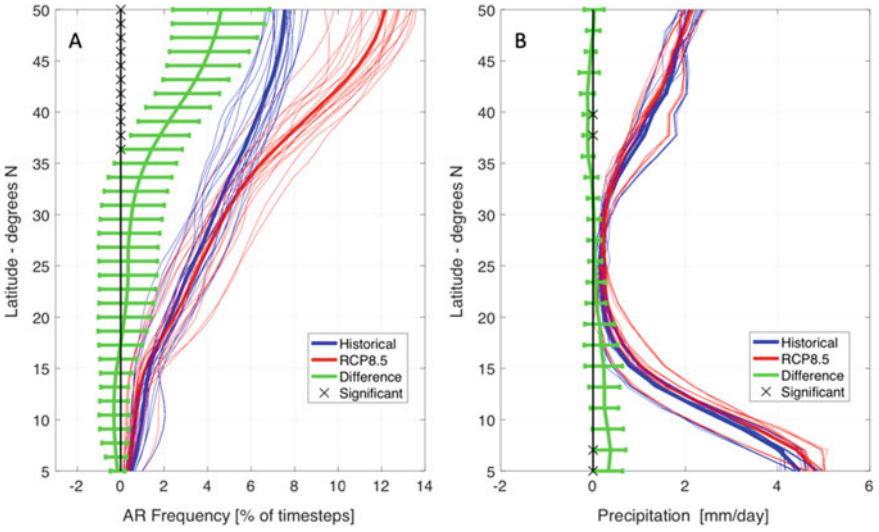

Fig. 9 Multi-model ensemble for the CMIP5 historical simulations (blue), the RCP85 simulations (red), and the difference bars showing 95% significance range for the projected differences (green), and latitudes with statistical significance marked with a black 'x'. The 95% bounds are determined using 2 times the standard deviation of the multi-model ensemble spread. These plots are shown as latitudinal averages. (Left) This panel shows the AR frequency plots, and areas with higher latitudes than 35 N are expected to see significant increases in AR frequency in the future. (Right) This panel shows the precipitation plots, showing an expected increase in precipitation from 5 to 20 N, and slight decrease in precipitation around 40 N. These results coincide with the regions highlighted in Figs. 7 and 8. The CMIP5 historical simulations range from 1979 to 2002 and the future (RCP8.5) scenario simulations range from 2073 to 2096. Figure adopted from Massoud et al. (2020a)

variability in AR frequency in the MENA region is lower than the expected future changes reported here for areas higher than 35 N, which show an increase of +3 (% of time steps).

In this study, the investigation of statistical significance of future changes in precipitation is initially shown using the black dots in Fig. 7b, which indicate where the future change estimates are statistically significant at the $p = 0.05$ level based on a paired-sample t-test. For additional investigation of statistical significance, Fig. 9b shows the spread of precipitation simulations based on latitudinal averages. This plot shows an expected increase in precipitation from 5 to 20 N, and a projected decrease in precipitation around 40 N (black 'x' marks indicate latitudes with statistical significance). These results show similar regions of interest as in Figs. 7 and 8, which depict how the Mediterranean basin and Europe should expect a decrease in precipitation, and the Arabian Peninsula to expect an increase in precipitation. The results are shown to be statistically significant for much of the region from 5 to 20 N (e.g. as seen with black dots in Fig. 7b and the black x's in Fig. 9b), however for much of the rest of the region, it is difficult to distinguish changes in future precipitation around MENA. Figures 7, 8 and 9 show that there is little to no projected changes in precipitation for most of the area. This is not surprising for a variable like precipitation, whose projections of future changes are usually uncertain compared to the multi-model ensemble spread or the natural variability of precipitation for many regions of the globe, especially for arid and semi-arid locations (Swain et al. 2018; Massoud et al. 2020b; Neelin et al. 2013). This makes it difficult to confidently project the sign of change for future precipitation.

4 Summary and Discussion

This study investigates the historical climatology and future projected change of atmospheric rivers (ARs) and precipitation in the Middle East and North Africa (MENA) region using a suite of models from the Coupled Model Intercomparison Project Phase 5 (CMIP5 historical and RCP8.5). To signify the importance of studying ARs in this region, we displayed (Fig. 3) the subregions where ARs account for more than 30% of the total rainfall, with some areas having nearly half of their rain coming from ARs. We reported on various individual AR events (Fig. 2), showing one of the longest AR events in recorded history for the MENA region, which occurred on January 1994, and highlighting AR Dena which happened in March 2019 and caused widespread damage. These events presented a compelling example of shifts from prolonged drought to frequent floods and showed how "extremes can become more extreme" in a changing climate (Dettinger et al. 2013; Dezfuli et al. 2020; Swain et al. 2018). In essence, the reduction of ARs in these regions can cause droughts over a multi-year period, however, the emergence of extreme AR activity following a drought can be beneficial for water resource management. Yet, this increased activity in ARs can also cause widespread destruction through extreme winds and flooding.

We found (Figs. 7 and 8) that increases in AR frequency are projected for much of the region (~+50% from historical values). For changes in mean precipitation, we found that much of the region surrounding the Mediterranean Sea showed an expected decrease (down −30% from historical values), however for the Arabian Peninsula, there is an expected increase in precipitation (up +50% from historical values). The stretch of countries from the Horn of Africa to the United Arab Emirates should expect an increase in precipitation, which will have some contributions from ARs, but also from non-AR sources of precipitation.

We showed the regions that have statistical significance in the future change estimates (Fig. 7), based on a paired-sample t-test with $p = 0.05$. For mid-latitude regions with higher latitude than 35 N (Fig. 9a), we found that projected changes in AR frequency are statistically significant, with the mean projected change being several times larger than the standard deviation of the model ensemble spread. For precipitation, there is little to no projected changes for much of the region, and the projected changes are significant only for certain areas (Fig. 9b).

For most areas within the MENA region, our results indicate that the projected change in AR frequency is opposite in sign to the projected change of mean precipitation. This finding, along with the fact that a large fraction of precipitation in the MENA region is associated with ARs, underscores the importance of ARs to the MENA region and thus of understanding the thermodynamic and dynamic drivers of the changes we describe here. This enhanced understanding can be benefit makers and water resources managers in the region. This paper presented one of the first case studies to use CMIP model simulations to investigate historical and future changes in ARs and precipitation for the MENA region.

References

Akbary M, Salimi S, Hosseini SA, Hosseini M (2019) Spatio-temporal changes of atmospheric rivers in the Middle East and North Africa region. Int J Climatol 39(10):3976–3986

Almazroui M (2016) RegCM4 in climate simulation over CORDEX-MENA/Arab domain: selection of suitable domain, convection and land-surface schemes. Int J Climatol 36(1):236–251

Almazroui. (2019a) Climate extremes over the arabian peninsula using RegCM4 for present conditions forced by several CMIP5 models. Atmosphere 10(11):675

Almazroui M (2019b) Temperature changes over the CORDEX-MENA domain in the 21st century using CMIP5 data downscaled with RegCM4: a focus on the Arabian Peninsula. Adv Meteorol

Amante C, Eakins BW (2009) ETOPO1 1 Arc-minute global relief model: procedures, data sources and analysis. NOAA Technical Memorandum NESDIS NGDC-24. National Geophysical Data Center, NOAA

AMS Glossary of Meteorology (2017) Atmospheric river. http://www.glossary.ametsoc.org/wiki/Atmospheric_river. Accessed 12 Aug 2020

Bozkurt D, Ezber Y, Sen OL (2019) Role of the East Asian trough on the eastern Mediterranean temperature variability in early spring and the extreme case of 2004 warm spell. Clim Dyn 53(3–4):2309–2326

Bucchignani E, Mercogliano P, Rianna G, Panitz HJ (2016) Analysis of ERA-Interim-driven COSMO-CLM simulations over Middle East–North Africa domain at different spatial resolutions. Int J Climatol 36(9):3346–3369

Bucchignani E, Mercogliano P, Panitz HJ, Montesarchio M (2018) Climate change projections for the Middle East-North Africa domain with COSMO-CLM at different spatial resolutions. Adv Clim Chang Res 9(1):66–80

Carvalho D (2019) An assessment of NASA's GMAO MERRA-2 reanalysis surface winds. J Clim 32(23):8261–8281

Dettinger MD (2013) Atmospheric rivers as drought busters on the US West Coast. J Hydrometeorol 14(6):1721–1732

Dettinger MD, Cayan DR, Meyer MK, Jeton AE (2004) Simulated hydrologic responses to climate variations and change in the Merced, Carson, and American River basins, Sierra Nevada, California, 1900–2099. Clim Change 62(1–3):283–317

Dettinger MD, Ralph FM, Das T, Neiman PJ, Cayan DR (2011) Atmospheric rivers, floods and the water resources of California. Water 3(2):445–478

Dezfuli A (2020) Rare atmospheric river caused record floods across the Middle East. Bull Am Meteor Soc 101(4):E394–E400. https://doi.org/10.1175/BAMS-D-19-0247.1

Esfandiari N, Lashkari H (2020a) Identifying atmospheric river events and their paths into Iran. Theoret Appl Climatol 1–13

Esfandiari N, Lashkari H (2020b) The effect of atmospheric rivers on cold-season heavy precipitation events in Iran. J Water Clim Change

Espinoza V, Waliser DE, Guan B, Lavers DA, Martin Ralph F (2018) Global analysis of climate change projection effects on atmospheric rivers. Geophys Res Lett 45(9):4299–4308

Gao Y, Lu J, Ruby Leung L, Yang Q, Hagos S, Qian Y (2015) Dynamical and thermodynamical modulations on future changes of landfalling atmospheric rivers over western North America. Geophys Res Lett 42(17):7179–7186

Gao Y, Lu J, Ruby Leung L (2016) Uncertainties in projecting future changes in atmospheric rivers and their impacts on heavy precipitation over Europe. J Clim 29(18):6711–6726

Gelaro R, McCarty W, Suárez MJ, Todling R, Molod A, Takacs L, Randles CA et al (2017) The modern-era retrospective analysis for research and applications, version 2 (MERRA-2). J Clim 30(14):5419–5454

Gershunov A, Shulgina T, Clemesha RES, Guirguis K, Pierce DW, Dettinger MD, Lavers DA et al (2019) Precipitation regime change in Western North America: the role of atmospheric rivers. Sci Rep 9(1):1–11

Gibson PB, Waliser DE, Lee H, Tian B, Massoud E (2019) Climate model evaluation in the presence of observational uncertainty: precipitation indices over the contiguous United States. J Hydrometeorol 20(7):1339–1357

Gimeno L, Dominguez F, Nieto R, Trigo R, Drumond A, Reason CJC, Taschetto AS, Ramos AM, Kumar R, Marengo J (2016) Major mechanisms of atmospheric moisture transport and their role in extreme precipitation

Gorodetskaya IV, Tsukernik M, Claes K, Ralph MF, Neff WD, Van Lipzig NPM (2014) The role of atmospheric rivers in anomalous snow accumulation in East Antarctica. Geophys Res Lett 41(17):6199–6206

Guan B, Waliser DE (2015) Detection of atmospheric rivers: evaluation and application of an algorithm for global studies. J Geophys Res Atmos 120(24):12514–12535

Guan B, Waliser DE (2019) Tracking atmospheric rivers globally: spatial distributions and temporal evolution of life cycle characteristics. J Geophys Res Atmos 124:12523–12552

Guan B, Waliser DE, Ralph FM (2018) An intercomparison between reanalysis and dropsonde observations of the total water vapor transport in individual atmospheric rivers. J Hydrometeor 19:321–337

Guan B, Molotch NP, Waliser DE, Fetzer EJ, Neiman PJ (2010) Extreme snowfall events linked to atmospheric rivers and surface air temperature via satellite measurements. Geophys Res Lett 37(20)

Hagos SM, Ruby Leung L, Yoon J-H, Lu J, Gao Y (2016) A projection of changes in landfalling atmospheric river frequency and extreme precipitation over western North America from the Large Ensemble CESM simulations. Geophys Res Lett 43(3):1357–1363

Hasanean HM (2004) Middle east meteorology. http://www.eolss.net/. Accessed 7 Aug 2015
Held IM, Soden BJ (2006) Robust responses of the hydrological cycle to global warming. J Clim 19:5686–5699
Heydarizad M, Raeisi E, Sorí R, Gimeno L (2019) Developing meteoric water lines for Iran based on air masses and moisture sources. Water 11:2359
Hibbard KA, Meehl GA, Cox PM, Friedlingstein P (2007) A strategy for climate change stabilization experiments. EOS Trans Am Geophys Union 88(20):217–221
Huang X, Swain DL, Hall AD (2020) Future precipitation increase from very high resolution ensemble downscaling of extreme atmospheric river storms in California. Sci Adv 6:eaba1323
Huning LS, Margulis SA, Guan B, Waliser DE, Neiman PJ (2017) Implications of detection methods on characterizing atmospheric river contribution to seasonal snowfall across Sierra Nevada, USA. Geophys Res Lett 44:10445–10453
Huning LS, Guan B, Waliser DE, Lettenmaier DP (2019) Sensitivity of seasonal snowfall attribution to atmospheric rivers and their reanalysis-based detection. Geophys Res Lett 46:794–803
Kalnay E, Kanamitsu M, Kistler R, Collins W, Deaven D, Gandin L, Iredell M et al (1996) The NCEP/NCAR 40-year reanalysis project. Bull Am Meteorol Soc 77(3):437–472
Kay JE, Deser C, Phillips A, Mai A, Hannay C, Strand G, Arblaster JM et al (2015) The community earth system model (CESM) large ensemble project: a community resource for studying climate change in the presence of internal climate variability. Bull Am Meteor Soc 96(8):1333–1349
Lavers DA, Allan RP, Villarini G, Lloyd-Hughes B, Brayshaw DJ, Wade AJ (2013) Future changes in atmospheric rivers and their implications for winter flooding in Britain. Environ Res Lett 8(3):034010
Lavers DA, Allan RP, Wood EF, Villarini G, Brayshaw DJ, Wade AJ (2011) Winter floods in Britain are connected to atmospheric rivers. Geophys Res Lett 38(23)
Lavers DA, Martin Ralph F, Waliser DE, Gershunov A, Dettinger MD (2015) Climate change intensification of horizontal water vapor transport in CMIP5. Geophys Res Lett 42(13):5617–5625
Lee H, Goodman A, McGibbney L, Waliser DE, Kim J, Loikith PC, Gibson PB, Massoud EC (2018) Regional climate model evaluation system powered by Apache open climate workbench v1.3.0: an enabling tool for facilitating regional climate studies. Geosci Model Dev 11:4435–4449
Leung Ruby L, Qian Y (2009) Atmospheric rivers induced heavy precipitation and flooding in the western US simulated by the WRF regional climate model. Geophys Res Lett 36(3)
Massoud EC, Huisman J, Benincà E, Dietze MC, Bouten W, Vrugt JA (2018a) Probing the limits of predictability: data assimilation of chaotic dynamics in complex food webs. Ecol Lett 21(1):93–103
Massoud EC, Purdy AJ, Miro ME, Famiglietti JS (2018b) Projecting groundwater storage changes in California's Central Valley. Sci Rep 8(1):1–9
Massoud EC, Espinoza V, Guan B, Waliser D (2019) Global climate model ensemble approaches for future projections of atmospheric rivers. Earth's Fut https://doi.org/10.1029/2019EF001249
Massoud E, Massoud T, Guan B, Sengupta A, Espinoza V, De Luna M, Raymond C, Waliser D (2020a) Atmospheric rivers and precipitation in the Middle East and North Africa (Mena). Water 12(10):2863
Massoud EC, Lee H, Gibson P, Loikith P, Waliser D (2020b) Bayesian model averaging of climate model projections constrained by precipitation observations over the contiguous United States. J Hydrometeorol
Massoud EC, Liu Z, Shaban A, El Hage M (2021) Groundwater depletion signals in the Beqaa plain. Lebanon: evidence from GRACE and Sentinel-1 Data. Rem Sens 13(5):915
Meehl GA, Hibbard K (2007) Summary report: a strategy for climate change stabilization experiments with AOGCMs and ESMs: Aspen global change institute 2006 session, Earth System models: the next generation (Aspen, Colorado, July 30-August 5, 2006). World Climate Research Programme
Meehl GA, Goddard L, Murphy J, Stouffer RJ, Boer G, Danabasoglu G, Dixon K et al (2009) Decadal prediction: can it be skillful? Bull Am Meteorol Soc 90(10):1467–1486

Nash D, Waliser D, Guan B, Ye H, Ralph M (2018) The role of atmospheric rivers in extratropical and polar hydroclimate. J Geophys Res Atmos 123:6804–6821

Neelin David J, Langenbrunner B, Meyerson JE, Hall A, Berg N (2013) California winter precipitation change under global warming in the coupled model intercomparison project phase 5 ensemble. J Clim 26(17):6238–6256

Neiman PJ, Martin Ralph F, Wick GA, Lundquist JD, Dettinger MD (2008) Meteorological characteristics and overland precipitation impacts of atmospheric rivers affecting the West Coast of North America based on eight years of SSM/I satellite observations. J Hydrometeorol 9(1):22–47

Neiman PJ, Schick LJ, Ralph FM, Hughes M, Wick GA (2011) Flooding in western Washington: the connection to atmospheric rivers. J Hydrometeorol 12(6):1337–1358

Ozturk T, Turp MT, Türkeş M, Kurnaz ML (2018) Future projections of temperature and precipitation climatology for CORDEX-MENA domain using RegCM4.4. Atmos Res 206:87–107

Paltan H, Waliser D, Lim WH, Guan B, Yamazaki D, Pant R, Dadson S (2017) Global floods and water availability driven by atmospheric rivers. Geophys Res Lett 44:10,387–10,395

Payne AE, Magnusdottir G (2015) An evaluation of atmospheric rivers over the North Pacific in CMIP5 and their response to warming under RCP 8.5. J Geophys Res Atmos 120(21):11–173

Payne AE, Demory M, Leung LR et al (2020) Responses and impacts of atmospheric rivers to climate change. Nat Rev Earth Environ 1:143–157

Pierce DW, Cayan DR, Das T, Maurer EP, Miller NL, Bao Y, Kanamitsu M et al (2013) The key role of heavy precipitation events in climate model disagreements of future annual precipitation changes in California. J Clim 26(16):5879–5896

Radić V, Cannon AJ, Menounos B, Gi N (2015) Future changes in autumn atmospheric river events in British Columbia, Canada, as projected by CMIP5 global climate models. J Geophys Res Atmos 120(18):9279–9302

Ralph FM, Dettinger MD (2011) Storms, floods, and the science of atmospheric rivers. EOS Trans Am Geophys Union 92(32):265–266

Ralph FM, Coleman T, Neiman PJ, Zamora RJ, Dettinger MD (2013) Observed impacts of duration and seasonality of atmospheric-river landfalls on soil moisture and runoff in coastal northern California. J Hydrometeorol 14(2):443–459

Ralph FM, Neiman PJ, Wick GA, Gutman SI, Dettinger MD, Cayan DR, White AB (2006) Flooding on California's Russian river: role of atmospheric rivers. Geophys Res Lett 33(13)

Ramos AM, Tomé R, Trigo RM, Liberato MLR, Pinto JG (2016) Projected changes in atmospheric rivers affecting Europe in CMIP5 models. Geophys Res Lett 43(17):9315–9323

Schneider U, Becker A, Finger P, Meyer-Christoffer A, Ziese M (2018) GPCC full data monthly product version 2018 at 0.25: Monthly land-surface precipitation from rain-gauges built on GTS-based and historical data. GPCC: Offenbach, Germany

Shepherd TG (2014) Atmospheric circulation as a source of uncertainty in climate change projections. Nat Geosci 7(10):703

Shields CA, Kiehl JT (2016a) Atmospheric river landfall-latitude changes in future climate simulations. Geophys Res Lett 43(16):8775–8782

Shields CA, Kiehl JT (2016b) Simulating the pineapple express in the half degree community climate system model, CCSM4. Geophys Res Lett 43(14):7767–7773

Slingo J, Palmer T (2011) Uncertainty in weather and climate prediction. Philos Trans R Soc A Math Phys Eng Sci 369(1956):4751–4767

Sodemann H, Stohl A (2013) Moisture origin and meridional transport in atmospheric rivers and their association with multiple cyclones. Mon Weather Rev 141(8):2850–2868

Spinoni J, Barbosa P, Bucchignani E, Cassano J, Cavazos T, Christensen JH, Christensen OB, Coppola E, Evans J, Geyer B, Giorgi F, Hadjinicolaou P, Jacob D, Katzfey J, Koenigk T, Laprise R, Lennard CJ, Kurnaz ML, Nikulin G, Ozturk T, Panitz H-J, Zittis G, Dosio A (2020) Future global meteorological drought hot spots: a study based on CORDEX data. J Clim 33(9):3635–3661

Swain DL, Langenbrunner B, Neelin JD, Hall A (2018) Increasing precipitation volatility in twenty-first-century California. Nat Clim Change 8(5):427–433

Taylor KE, Stouffer RJ, Meehl GA (2012) An overview of CMIP5 and the experiment design. Bull Am Meteor Soc 93(4):485–498

Terink W, Immerzeel WW, Droogers P (2013) Climate change projections of precipitation and reference evapotranspiration for the Middle East and Northern Africa until 2050. Int J Clim 33:3055–3072

Tyrlis E, Lelieveld J, Steil B (2013) The summer circulation over the eastern Mediterranean and the Middle East: influence of the South Asian monsoon. Clim Dyn 40(5–6):1103–1123

United Nations Office for the Coordination of Humanitarian Affairs (2019) Disasters. Iran: floods—Mar 2019. Ann Rev Environ Resour 41:117–141. https://www.reliefweb.int/disaster/fl-2019-000022-irn

Viale M, Nuñez MN (2011) Climatology of winter orographic precipitation over the subtropical central Andes and associated synoptic and regional characteristics. J Hydrometeorol 12(4):481–507

Vrugt JA, Massoud EC (2018) Uncertainty quantification of complex system models: Bayesian analysis. In: Duan Q, Pappenberger F, Thielen J, Wood A, Cloke HL, Schaake JC (eds) Handbook of hydrometeorological ensemble forecasting

Waliser D, Guan B (2017) Extreme winds and precipitation during landfall of atmospheric rivers. Nat Geosci 10(3):179

Wang C-C, Lin B-X, Chen C-T, Lo S-H (2015) Quantifying the effects of long-term climate change on tropical cyclone rainfall using a cloud-resolving model: examples of two landfall typhoons in Taiwan. J Clim 28(1):66–85

Warner MD, Mass CF, Salathé EP Jr (2015) Changes in winter atmospheric rivers along the North American west coast in CMIP5 climate models. J Hydrometeorol 16(1):118–128

Zappa G, Hawcroft MK, Shaffrey L, Black E, Brayshaw DJ (2015) Extratropical cyclones and the projected decline of winter Mediterranean precipitation in the CMIP5 models. Clim Dyn 45:1727–1738

Ziv B, Dayan U, Sharon D (2005) A mid-winter, tropical extreme flood-producing storm in southern Israel: synoptic scale analysis. Meteorol Atmos Phys 88(1–2):53–63

Inventory of Shared Water Resources in Western Asia: Selected Aquifer Systems in the Arabian Peninsula for the Application of Remote Sensing Techniques

Yusuf Al-Mooji

1 Introduction

For millennia, sharing of water resources has been an influential feature affecting life, society and development in this mostly arid and semi-arid region. Water management and irrigation schemes, such as the underground aqueducts networks ('*qanat*' or '*falaj*' in Arabic) built centuries ago in Bahrain, Oman, Saudi Arabia and Yemen, stand as evidence for the sharing of water by different societies in the past to sustain communal needs. The concept of sharing water as a 'common resource' began to somehow dissolve with the creation of modern states in the region by political borders during the first half of the twentieth century. Most of the region's major rivers and many aquifer systems were found to extend beyond political borders and became sources of conflict as each country across the border claimed ownership of the resources.

In a region inflicted with political conflicts, severe water shortage and rapidly growing population, it is understandable why countries continued to compete rather than cooperate over the existing aquifer systems. Management of these transboundary resources became a real challenge in particular because they are non-renewable and at an increasingly high risk of being exhausted. Sustaining these "fossil" aquifer systems for future generations and for the continuation of life in this harsh environment requires a sound knowledge and cooperation among riparian countries towards joint development and management of the available resources. With this objective in mind, the preparation of the *Inventory of Shared Water Resources in Western*

Y. Al-Mooji (✉)
Economic and Social Commission for Western Asia (ESCWA), C/O Naeem Almutawakel, P.O. Box 11-8575, Beirut, Lebanon
e-mail: mooji46@yahoo.com

A. Shaban (ed.), *Satellite Monitoring of Water Resources in the Middle East*,
Springer Water, https://doi.org/10.1007/978-3-031-15549-9_5

Asia[1] was jointly undertaken by the United Nations Economic and Social Commission for Western Asia (ESCWA) and the German Federal Institute for Geosciences and Natural Resources (BGR). This inventory is the first systematic effort to characterize all transboundary surface water and groundwater resources throughout the Western Asia Region. It constitutes a comprehensive reference document that encompasses water resources crossing the political borders of Arab and non-Arab states in the region. The inventory has shown the existence of several large aquifers in the Western Asia region extending across political borders. Due to the paucity of data/information, delineation of the aquifer system boundaries was based on information that was mostly outdated, obsolete, contradictory or of different nature and scale. Recent data on the majority of the aquifer systems were classified in national databases and unpublished reports to which the study team did not have access. Hence, the description and findings contained in the Inventory were meant to provide a starting point towards a more comprehensive analysis for an absolute delineation of the aquifer boundaries. This can be achieved through the application of remote sensing techniques (RS), in combination with the GIS data already available from the Inventory.

This chapter is prepared for the purpose of advocating this objective. Section 1 of this chapter is a brief description of the methodology and information sources for the Inventory. Section 2 describes the process of identifying shared aquifer systems, highlighting the main limitations to the delineation of different aquifer systems. Section 3 gives an overview of the aquifer systems identified. Finally, Sect. 4 provides a detailed information on two aquifer systems (*Saq-Ram* and *Wasia-Biyadh-Aruma -South*) selected as pilot projects for the applications of RS techniques.

2 Methodology and Information Sources

Information on shared groundwater resources was initially collected and summarized from data/information available in the literature (scientific publications, country papers, national and regional maps and datasets, satellite imagery, media reports) including ESCWA reports. Groundwater resources had not been previously catalogued across borders and there was no common methodology for achieving this purpose while taking into consideration the specific conditions of the region. Hence the Inventory started with the screening of all available geological/hydro(geo)logical information and its interpretation in view of identifying potentially shared aquifers/aquifer systems. The findings were discussed internally and with a panel of regional and international experts via regional expert consultations. The experts were also involved in a peer review of data sets and chapter drafts with a focus on the overall coherence and integrity, and possible shortcomings and gaps. Information packages were compiled and circulated among relevant riparian countries for any modifications and/or addition of data/information needed for completing

[1] http://www.waterinventory.org

the chapters. Any relevant information subsequently received from the countries was incorporated into the chapter drafts to finalize them.

3 Shared Aquifer Systems Identification Process

Shared aquifer systems were identified through the following five steps:

Step One: Identifying Shared Aquifers in the Literature

Based on the results of initial screening of *known* aquifers in the region, additional research was carried out on shared or potentially shared aquifers, using regional/national geological hydro(geo)logical maps, geological cross-sections, stratigraphy tables, journal articles and studies.

Step Two: Verifying Shared Aquifers Versus Shared Aquifer Systems

The aim of this step was to verify whether water-bearing geological formations extending across specific political borders constitute shared aquifers or shared aquifer systems.[2] A good understanding of hydrogeological units in the area was achieved through examination of the vertical and lateral hydraulic linkages between shared aquifers and aquifer layers. Single or multiple layers of interconnected aquifers were combined into aquifer systems if the vertical and lateral hydraulic conditions allowed water flow between and across formations. Given the complexity of the region's hydrogeology and the general lack of data and information, this step was based to some extent on logical reasoning.

Step Three: Dealing with Issues of Scale

The region covered by the inventory is predominantly a vast desert underlain by thick and widespread geological formations (Arabian Peninsula) with two chains of faulted and folded mountains in the northeast (Taurus-Zagros) and northwest (Anti Lebanon). The hydraulic setting and groundwater dynamics at the extremities of the large aquifer systems under the Arabian Peninsula may vary significantly since structural features or groundwater divides are likely to create different hydrogeological sections in the aquifer system. Hence extensive aquifer systems were geographically divided into sub-units, or sections, such that different sections would represent shared aquifer systems only for countries affected by groundwater flow in relevant section(s). By contrast, the aquifer systems in Anti-Lebanon and the Taurus-Zagros consist of small units that cross political borders in several places and generally discharge through springs such that it is difficult to determine their hydraulic relationship and/or delineate their geographical extent across political borders. These units

[2] A series of two or more aquifers that are hydraulically connected. Aquifer systems are defined by continuity and characteristics rather than by the origin of the aquifer material. They may therefore be made up of several lithologies and stratigraphic units. An aquifer system may include aquitards and confining beds (UNESCO 1978).

are grouped together in separate chapters that give a description of the overall hydrogeological framework conditions and the main aquifer formations without specifying whether or not they constitute single aquifers or aquifer systems.

Step Four: Approximating Aquifer System Boundaries

This step aimed to refine the delineation of each section of the shared aquifers and aquifer systems where found necessary. Since groundwater divides were not available in many cases, groundwater flow information was used to approximate aquifer system boundaries, taking into consideration boundaries of hydrological basins that had been delineated in previous studies on the basis of surface water drainage. However, the Inventory went beyond these boundaries for the purpose of describing the aquifer system(s), which normally extend outside the basin. Structural features (faults, graben structures, anticlines or synclines) that usually control groundwater flow were then used to approximate groundwater boundaries where possible.

Step Five: Description of Shared Aquifer Systems

In this final step, each of the shared aquifer systems, sections, or basins was characterized with respect to hydrogeology, groundwater use, agreements and cooperation. Each of these aspects was described within a standardized chapter template containing the following information (Table 1).

Suitability for groundwater development, referred to as "exploitability" in the Inventory, was also analyzed. Exploitability, based on water quality, technical feasibility and economic viability, was determined by the following three parameters:

Table 1 Standard template of information on each aquifer system

Heading	Content
Summary	Executive summary, basin facts
Introduction	Location, area, climate, population, other aquifers in the area, information sources
Hydrogeology—aquifer characteristics	Aquifer configuration (geometry, depth, outcrop areas, subsurface extent), Stratigraphy, Aquifer thickness, Aquifer type (confined/unconfined), Aquifer parameters (transmissivity, storativity)
Hydrogeology—groundwater	Recharge, flow regime (water levels, gradients, flow direction), Storage, Discharge (springs, vertical leakage), Water quality, Exploitability
Groundwater use	Groundwater abstraction and use (timeline of development, areas and sector use, abstraction volumes), Groundwater quality issues (return flows, salinization, pollution), Sustainability issues (trends, over-abstraction)
Agreements, cooperation and outlook	Agreements (treaties, Memorandum of Understanding, negotiations), cooperation (timeline, form, mechanism, issues of conflict), outlook (main management issues, opportunities)

- *Depth to top of aquifer*: The Inventory has adopted a depth of 2,000 m that was applied by other researchers in the region.
- *Depth to water level*: A maximum depth to water level of 250–300 m was applied in some regional studies and hence a limit of 250 m was set for the Inventory, while using the most recent data available from official sources, wherever possible,
- *Water quality*: While a salinity level of <2,000 mg/L TDS is usually desirable for "exploitability", groundwater with this quality is rare in large parts of the region, particularly in the extensive aquifer systems of the Arabian Peninsula. Moreover, brackish groundwater in this arid and hyper-arid region is also considered an exploitable resource since it is used in combination with desalination or to grow highly salt-tolerant crops such as date palms. Therefore, a salinity level of 10,000 mg/L TDS was applied in the Inventory as a limiting factor for the exploitability of aquifer systems.

4 Overview of the Aquifer Systems

Geologically, the study area extends across the Arabian Plate, which has been moving incrementally from the African Plate to the north and north-east since the Miocene time, where it collides with the Turkish and Eurasian Plates along its northern boundaries. This has led to the development of different tectonic zones and geological structures that created significant differences in the hydrogeological features of the main part of the plate (*Arabian Peninsula*) and its northern areas (*Mashrek, Mesopotamian Plain*, and *Taurus-Zagros*). Based on tectonics and geological structure/history, the Region can be divided into four distinct main sub-regions:

- The ***Arabian Peninsula*** has been tectonically reasonably stable throughout different geological era such that its eastern half provided a depositional basin for thick (up to 7,500 m) and extensive sedimentary strata that form large regional aquifer systems. The largest part of the Peninsula is covered by the Kingdom of Saudi Arabia (KSA), which has political borders with 8 countries: Jordan and Iraq in the north; Bahrain, Kuwait, Qatar, and United Arab Emirates (UAE) in the east; and Oman and Yemen in the south. Aquifer systems identified across the border of KSA and neighboring countries are listed in Table 2.
- The ***Mashrek*** extends along the eastern Mediterranean incorporating the political borders of Israel, Lebanon, Palestine, Egypt (Sinai Peninsula) and Syria. It is characterized by high mountains in the western areas near the coast and wide plateaus further inland. The plateaus are covered by a sequence of basalt complex while the mountains consist of well exposed and highly fissured/karstified carbonate rocks, which form complex aquifers. Five transboundary aquifer systems have been identified in this sub-region, one of them extending along the Anti-Lebanon Mountain range with 3 separate catchments that discharge springs inside Syria (Table 3).

Table 2 Aquifer systems identified across the Arabian Peninsula

Shared aquifer system	Area (km^2)	Thickness (m)	Riparian countries
Saq-Ram (West)	308 000	250–700	KSA, Jordan
Tawil-Quaternary (Wadi Sirhan)	44 000	Up to 1 300	KSA, Jordan
Wasia-Biyadh-Aruma (North)—Sakak-Rutba	112 000	250–400	KSA-Iraq
Wasia-Biyadh-Aruma (South)—Tawila-Mahra-Cretaceous Sands	157 000	100–200	KSA-Yemen
Neogene (Southeast)-Dibdiba	153 000	Up to 550	KSA-Kuwait-Iraq
Umm er Radhuma-Dammam (North)	246 000	270–680	KSA-Kuwait-Iraq
Umm er Radhuma-Dammam (Centre)	281 000	265–680	KSA-Bahrain-Qatar
Umm er Radhuma-Dammam (South)	680 000	110–1040	KSA-Oman-UAE-Yemen
Wajid	455 000	100–900	KSA-Yemen

Table 3 Aquifer systems identified across the Mashrek

Shared aquifer system	Area (km^2)	Thickness (m)	Riparian countries
Anti-Lebanon (3 catchments)	248 (Anjar-Chamsine), 149 (Barada), 658 (Figeh)	900 (Anjar-Chamsine), 2 000–2 200 (Barada), 480–680 (Figeh	Lebanon-Syria
Western Basin	9 000–14 167	600–1 000	Egypt-Israel-Palestine
Coastal Basin	18 370	60–140	Egypt-Israel-Palestine
Basalt (West)—Yarmouk Basin	7 000	100–300	Jordan-Syria
Basalt (South)—Azraq-Dhuleil Basin	8 500	100–500	Jordan-Syria

The ***Mesopotamian Plain*** is bounded by two major faults and has formed a depositional basin since the Neogene time. The basin extends across Iraq into Syria and Turkey and is characterized by clastic sedimentary aquifer systems. Two shared aquifer systems have been identified in this sub-region as indicated in Table 4.

The ***Taurus-Zagros*** extends from the northwestern border of Iran with Iraq into Turkey. This highly folded and faulted region features elevated areas made up of karstified carbonate rocks with many springs discharging good-quality water, and younger clastics that form isolated to semi-isolated aquifer systems. A single aquifer

Table 4 Aquifer systems identified across the Mesopotamia Plain

Shared aquifer system	Area (km^2)	Thickness (m)	Riparian countries
Jezira Tertiary Limestone	14 000	200–700	Syria-Turkey
Neogene (Northwest)—Jezira Basin	65 000	500–550	Iraq-Syria

Table 5 Aquifer systems identified across the Taurus-Zagros

Shared aquifer system	Area (km^2)	Thickness (m)	Riparian countries
Taurus-Zagros	11 760 (*Central Diyala*), 566 (*Halabja-Khurmal*), 1 960 (*Zakho*)	1 000–2 500	Iran-Iraq (*Central Diyala, Halabja-Khurmal*) and Iraq-Turkey (*Zakho*)

system with 3 different catchments (*Central Diyala, Halabja-Khurmal*, and *Zakho*) is identified across political borders in this zone (Table 5).

5 Selected Aquifer Systems for the Applications of RS Techniques

Saq-Ram (West)

The Cambro-Ordovician Sandstones extending from the Tabuk-Tayma region of Saudi Arabia to the the Dead Sea area in western Jordan (Fig. 1) is known as *Saq* and *Ram* or *Rum* in the two countries, respectively. In this inventory, it is referred to as *Saq-Ram (West)* Aquifer System. The system is heavily exploited in the Tabuk-Mudawwara-Disi area, which extends from the Tabuk Plain in Saudi Arabia to Wadi Rum in Jordan as delineated in the overview map below. In Jordan, the aquifer system is widely exposed in the southern desert and is present in the subsurface throughout most of the country.

In Saudi Arabia, the *Saq* formation lies directly on the crystalline Basement and dips gradually towards the north and north-east under less permeable formations as shown in Fig. 2b. Further east and south, the *Saq* is separated from the overlying sandstones by the *Hanadir* Shale. Figure 2a shows the continuation of the *Saq* northward to Jordan where the sandstones of the *Ram* rest on the Basement. The sandstones are widely exposed in the southern desert and are present at depth throughout Jordan except for the outcrop areas of the Basement in the extreme south-west. In Jordan, the average thickness of the sequence is about 1,000 m, but increases to over 2,250 m in the southern part of *Wadi Sirhan* and more than 2,500 m in the *Risha* area near the Iraqi border. In the *Tabuk* area of Saudi Arabia, the thickness of a typical profile of the *Saq* is 800 m and reaches more than 1,000 m in some places, but thicknesses of 250–500 m are also common. The aquifer system is generally unconfined in the outcrop areas and their surroundings and becomes a confined or leaky aquifer towards the north and north-east where the sandstones dip below shales and other aquitards. A

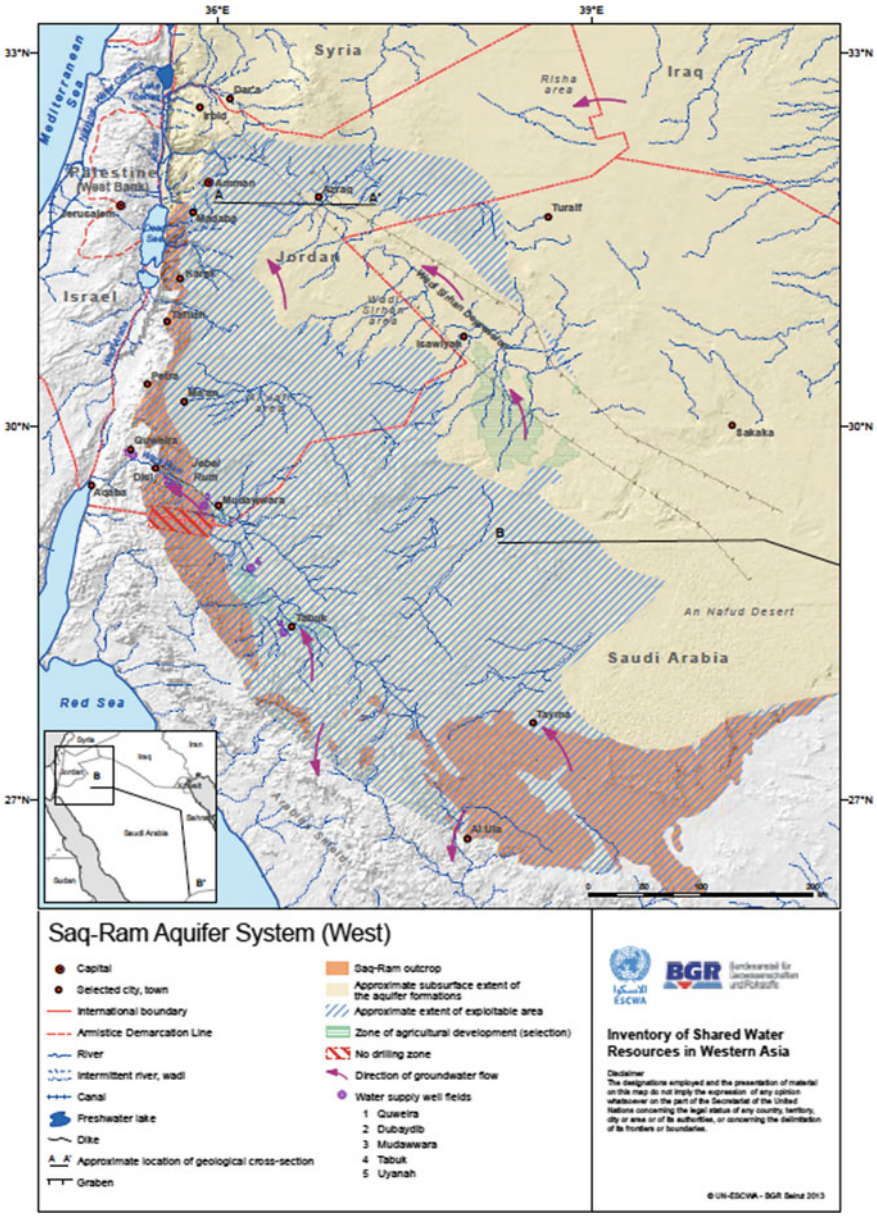

Fig. 1 Overview map of *Saq-Ram* (*West*). *Source* Inventory of Shared Water Resources in Western Asia. Beirut. UN-ESCWA and BGR (2013)

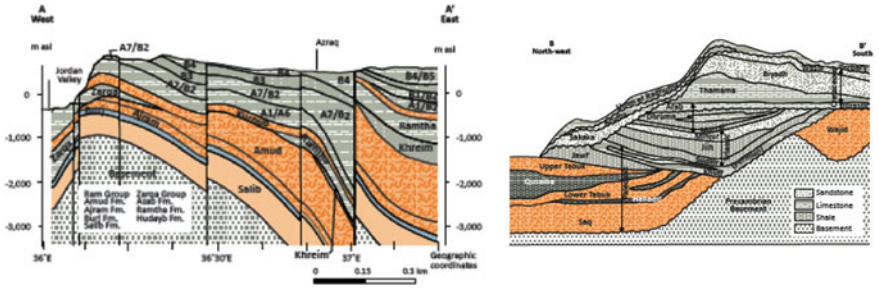

(a) Ram System **(b)** Saq System

Fig. 2 Geological cross section of subsurface stratigraphy of the Saq-Ram Aquifer System**a** Ram system. **b** Saq system. *Source* Inventory of Shared Water Resources in Western Asia. Beirut. UN-ESCWA and BGR (2013)

large variation in hydraulic parameters was observed in a number of studies between confined and unconfined areas and towards the northern and northeastern areas where the base of the aquifer system reaches great depths. Transmissivity values vary over a wide range for the entire system with higher values for the confined/leaky part as compared with the unconfined, while storativity/storage coefficient values show relatively less variation.

The Resource

Isotopic data indicate that recharge to the *Saq-Ram* Sandstones occurred between 10,000 and 30,000 years ago, as evidenced by the oldest waters now emerging from deep wells in the Jordan Valley. Modern recharge is negligible (0.03 mm/year.) in areas with no outcrops and where rainfall is less than 75 mm/year. However, in escarpment areas such as the Wadi Araba in Jordan, recharge has been shown to increase with elevation from 3 to 11 mm/year. In KSA, an average annual recharge of 2.5 mm was estimated for the *Saq* outcrops.

Until the 1980s, natural groundwater flow was directed northwards, starting from the Tayma-Tabuk area in Saudi Arabia, and across the southern desert in Jordan, towards the low-lying Dead Sea natural discharge zone. Since then, however, increased abstraction has changed the general pattern of groundwater flow, with a significant effect in the Tabuk area, where substantial volumes of water are abstracted for agriculture purposes as shown below. This has resulted in the occurrence of a very large and deep cone of depression, locally diverting the natural north-easterly groundwater flow direction and reducing the assumed natural flow across the border to Jordan of around 140 MCM/year. to negligible amounts. Near the border, there is basaltic dike (*Kharawi*) *that* forms a natural hydraulic barrier impounding the groundwater such that the flow is deflected in a south-easterly direction towards Saudi Arabia or north-westerly direction towards the Wadi Araba. Some 100 km south of Tabuk and as far as Al Ula, the groundwater flow is directed outward to the Arabian Shield (see overview map).

In the Tabuk area, available groundwater reserves in the *Saq* were estimated at 43 BCM, of which about 20 BCM is in the unconfined part. However, it was estimated that with continued pumping at the current rate of pumping, the exploitable reserve will drop from currently 75% to 38% between 2005 and 2055. In Jordan, it is estimated that available water reserve commonly ranges between 4 and 10 BCM though a maximum of 40 BCM has also been reported.

The low-lying Dead Sea area is the main discharge zone for the aquifer system is the where natural discharge occurs in the form of springs and base flow in the deeply incised wadis that discharge into the Dead Sea. The springs occur mainly in areas along the eastern side of the Jordan Rift Valley, where average rainfall is around 150–200 mm/year, and feed the wadis along the central and southern part of the Dead Sea (mainly Wadi Ibn Hammad, Wadi Karak, Wadi Feifa). Base flow in these wadis was estimated at around 25 MCM though it fluctuates widely from year to year. Groundwater discharge also occurs in the Wadi Sirhan Depression and its northern extension into the Azraq Graben, as well as in the Shield. Further discharge emanates from springs in valleys draining towards the Red Sea has also been reported.

The quality of water in the aquifer system is generally good with total dissolved solids (TDS) levels of around 1,000–1,200 mg/L dominated by calcium (Ca^{2+}) and bicarbonate (HCO_3^-). However, a significant increase in TDS from 200 to 400 mg/L the Mudawwara-Disi area to 1,000–3,000 mg/L at the Dead Sea, where thermal springs are common, has been observed. This salinity increase has been attributed to downward leakage from the overlying formations, which contain highly saline waters (up to 35,000 mg/L TDS), and the dissolution of evaporites contained in the aquifer.

In Saudi Arabia where most abstraction takes place, elevated concentrations of boron, selenium and nitrate have been detected, mostly in wells that tap the unconfined part at a depth of less than 150 m. The occurrence of natural radionuclides is common in Cambro-Ordovician Sandstones, and their presence in groundwater within both countries has been reported. Possible sources of radioactive elements include the Basement rocks, shale layers, phosphate-bearing formations and cementing material in the sandstones such as iron and manganese oxides with other trace metal oxides, including those of uranium. A decrease in pH enhanced the dissolution of uranium and radium from the matrix and thermal springs in the Dead Sea area discharging waters with elevated concentrations of carbon dioxide, hydrogen sulfide, and radon gases. Elevation in radioactivity appears to be related to water level declines, most probably due to an increase in vertical leakage from less permeable layers that contain higher concentrations of radioactive minerals. The concentrations of radium isotopes is highest in groundwater discharging from confined areas, which can be explained by the fact that the isotopes are most mobile under reducing conditions.

The Exploitation

Current abstraction in the Mudawwara-Disi area (Jordan) is 60 MCM/year. although higher values of 70–80 MCM/year. were reported in 2008. Groundwater abstraction in the Tabuk area (KSA) has increased drastically from about 29 MCM/year. in 1983

to between 1,050 and 1,700 MCM/year. in 2004, mostly in the agricultural sector, while recharge remains at 3–11 MCM/year. There are indications that the exploitable part of the resource may be exhausted within 30–40 years, unless abstraction can be controlled on both sides of the border.

The water level continues to decline steadily with rising groundwater abstraction. Boreholes in the Tabuk area indicate significant declines, with total water level drops of 100 m to 160 m from 1983 to 1988, resulting in a reversal of the horizontal and vertical hydraulic gradient in some areas. Currently water level is mostly in the range of 50–150 m bgl. In the Tabuk area and continued abstraction from this area could result in further head level decline in south-western Jordan, as the pressure changes in the confined system may be transferred over more than 100 km.

There are also indications that groundwater quality deterioration may arise in the future. In particular natural sources of radioactivity may affect the entire aquifer system in the long term and limit its use, while other potential sources that may affect water quality could develop locally as a result of heavy pumping. Potential sources include leakage of saline from overlying shale formations, nitrate concentration from irrigation return flows, upconing of saline and hypersaline, and formation waters in faulted and geothermal areas.

The Wasia-Biyadh-Aruma-South

In the southern areas of Saudi Arabia, the Wasia-Biyadh Sandstones merge with the Aruma to constitute the so-called Cretaceous Sands, which extend across the Rub' al Khali Depression into Yemen where stratigraphically correlatable sandstones exist (the so-called Tawila-Mahra Group), forming a transboundary aquifer system denoted in the inventory as the Wasia-Biyadh-Aruma Aquifer System (South) and delineated as shown in the overview map (Fig. 3).

The aquifer system

The area of the Wasia-Biyadh-Aruma Aquifer System (South) is around 157,000 km^2, of which 52,000 km^2 lies in Yemen, and 105,000 km^2 in Saudi Arabia. The system occurs in a largely inaccessible, arid and hyper-arid region, where the only sign of human settlement is in the Sharurah/Al Abr area. In Saudi Arabia, the sandstones lie in extensive dune areas. On the Yemeni side, the aquifer system is located in the north-eastern plateau zone, which descends gradually from the north of the Rub' al Khali Desert at an elevation of approximately 900 m.

The aquifer system is part of the Rub' al Khali structural depression that formed a depositional basin for Paleozoic and Mesozoic Formations. The main outcrops of the sandstones are found along a fault extending across the political border. They also occur on the surface at the foot of Jibal al Wajid near the western margin of the Rub' al Khali. The sandstones are overlain by superficial deposits of Quaternary age in the northern part of the study area.

During the Cretaceous period, the sea advanced into the region from the east with a series of short transgressions followed by regressions, but marine conditions never covered the western areas where terrestrial, fluvial and fluvio-deltaic conditions prevailed. Figure 4 shows that in Yemen the zone of the main lateral interdigitation of the individual formations occurs roughly between longitudes 49°30′ and 50°30′. West

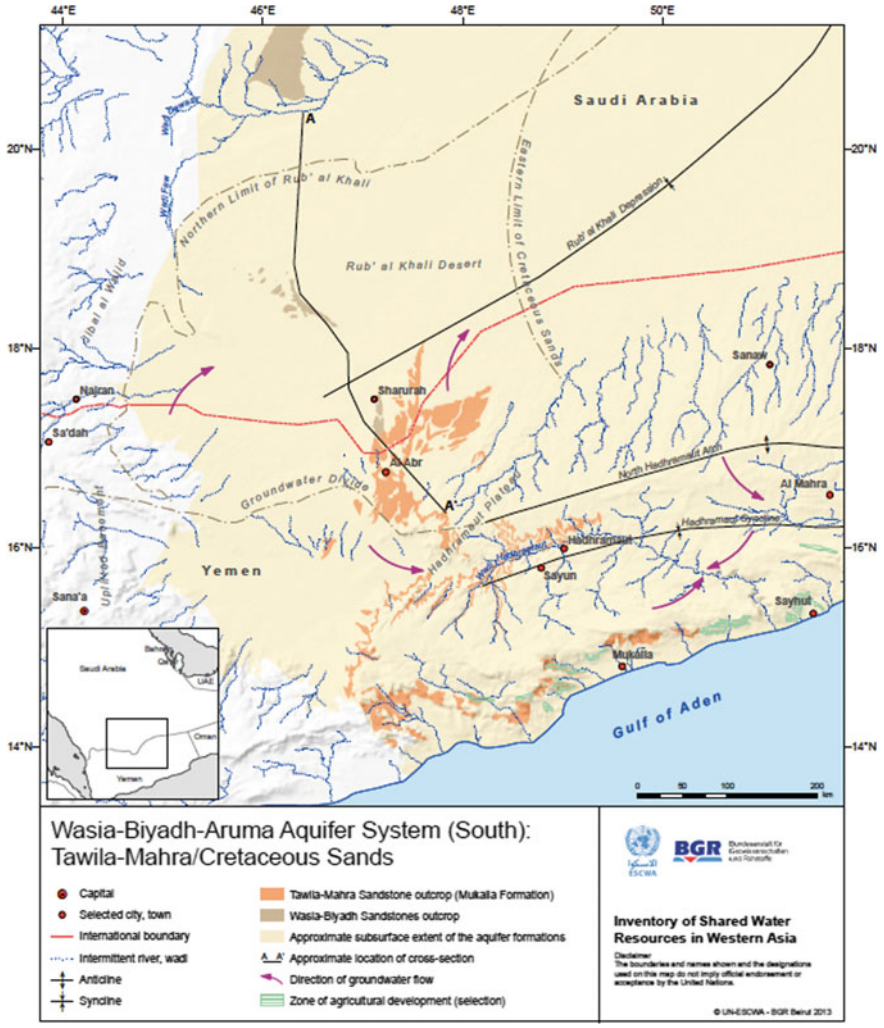

Fig. 3 Overview map of Wasia-Biyadh-Aruma Aquifer System (South). *Source* Inventory of Shared Water Resources in Western Asia. Beirut. UN-ESCWA and BGR (2013)

of longitude 47°, the entire Tawila Group is made up of undifferentiated clastics that constitute the major aquifer in north-western Yemen. East of this longitude, however, the Mukalla Formation constitutes the main aquifer within the Mahra Group. Similarly, in the eastern areas Saudi Arabia only the lowest unit of the Wasia-Biyadh Formations (Khafji-Safaniyah) is water-bearing whereas in the central part the sandstone deposition was much thicker and continued until the Late Cretaceous epoch (sandstone unit of the Aruma Formation not shown in Fig. 4).

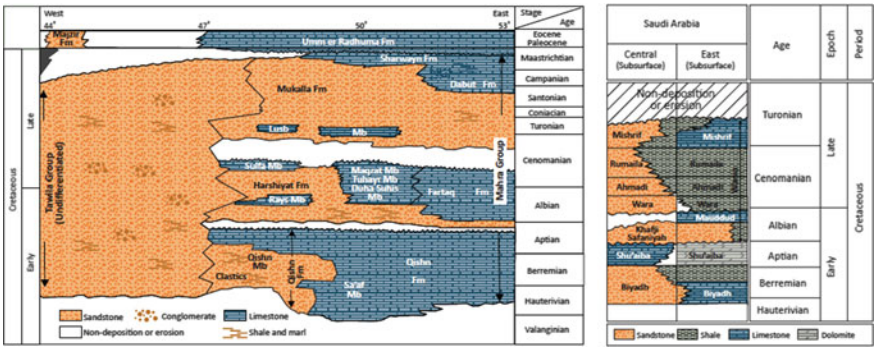

Fig. 4 Lithostratigraphy of the Wasia-Biyadh-Aruma Aquifer System (South) in Yemen (left) and Saudi Arabia (right). *Source* Inventory of Shared Water Resources in Western Asia. Beirut. UN-ESCWA and BGR (2013)

Within Saudi Arabia, the Wasia Sandstone reaches a maximum thickness of 600 m in the Rub' al Khali whereas a thickness of 1,000 m is not uncommon for the Cretaceous Sands east of Wadi Dawasir. The Mukalla Sandstone in Yemen also reaches a thickness of 1,000 m south of the North Hadhramaut Arch whereas in the North Hadhramaut Arch and its Rub' al Khali Depression flank, the thickness of the sandstone in the subsurface varies between 100 and 200 m. This would mean that the Cretaceous Sands are less thick in the border areas than they are further to the north in Saudi Arabia, or to the south in Yemen. Water table conditions are common in the aquifer system whereas some perched water is found in localized areas where it is held above the clay layers. In the eastern part of the basin, the system may be mostly confined as the sandstones are overlain by a thick sequence of Paleogene carbonate rocks in these areas.

The Resource

Despite the very low rainfall, present-day recharge to the Mukalla Sandstone reportedly occurs across the area through 3 possible ways: (1) Infrequent but intense rain is quickly absorbed by aeolian and alluvial sands near the outcrop areas where the alluvial cover is thin; (2) There is a strong potential for structurally-facilitated recharge in the western and central areas where the Mukalla Sandstone and the Umm er Radhuma Formation are exposed, because of the intensive structural dislocation and faulting within these rocks; and (3) The eastern part of the plateau that is covered by a practically impervious formation (Jeza Formation), which generates considerable runoff. This runoff infiltrates into the permeable Umm er Radhuma and Mukalla Formations underneath exposed in the deeply incised valleys, and into the Quaternary alluvial valley fill further north. Available data suggest a direct recharge of 8.8 mm/year. to 1.5 mm/year. for the outcrop areas in Saudi Arabia and Yemen, respectively. Indirect recharge is also likely to occur via runoff, particularly through the wadis descending from the uplifted basement areas where precipitation is higher though no estimates of this additional recharge were available.

Recharge of the aquifer system has also taken place in the past. Carbon-14 dating determined the age of deep water in the Mukalla Sandstone at 8,000 years, which is relatively young compared to the deep water in the Umm er Radhuma Aquifer System (20,000 years). This young age, together with the stable ^{18}O isotopic composition of -2.0 to $-3.5‰$ suggest that recent recharge water must be reaching the sandstones. Similar situation has been reported for the Umm er Radhuma -Dammam Aquifer System to the north where it was found that groundwater at the main outcrop near Al Kharj is 8,000 years old as compared with water down-dip in the Khurais area, which is 16,000.

No visible signs of discharge are seen on the surface but downward flow discharge into the Upper Wajid Sandstone could occur on the Yemeni side of the border where the Khuff Formation, which separates the two aquifer systems in Saudi Arabia, seems to disappear though there is no data to confirm or negate this.

The dip of the Mukalla Sandstone in an easterly to north-easterly direction suggest that groundwater flows towards the Rub' al Khali and south-eastern Saudi Arabia. Further north, groundwater in the Wasia-Biyadh Formations flows towards the Persian Gulf under the influence of consistent hydraulic head despite being small. A comprehensive study undertaken by the Ministry of Agriculture and Water in Saudi Arabia in 1980, in which both depth and water quality limitations were taken into consideration, estimated that the total volume of water in this aquifer system with acceptable quality (TDS = 2,000 ppm) that could be extracted from a depth of 300 m (the maximum depth currently possible with pumping technology existing at the time) is in the order of 500 BCM. Groundwater from boreholes drilled into the Mukalla Sandstone south of the North Hadhramaut Arch was found to be of excellent quality, with TDS values in the range of 406–833 mg/L.

The Exploitation

Information on depth to groundwater (100–200 m bgl.) and water quality (TDS of <1,000 mg/L), available for the Yemeni part of the study area, are within the limits of the criteria selected for exploitation (see above) and the top of the Cretaceous has an approximate maximum depth of 600 m bgl. across the whole area delineated in the Overview Map. Hence the entire delineated area can be considered exploitable, subject to accessibility and drilling/well stability in areas of thick sand dunes. It is expected however that groundwater exploitation would probably present logistical and access issues at such depth, thus significantly increasing unit cost per volume of groundwater extracted. If depth to water and TDS were not considered limiting factors, the area of exploitation could even extend beyond the mapped area. However, recent available data suggests that one or both parameters may be limiting factors, since practically no exploitable area is shown beyond the eastern limit of the Cretaceous Sands. At the present, the use of groundwater from the aquifer system is limited to insignificant shallow quantities available in wadi bed areas for the needs of small groups of nomadic populations.

6 Conclusions

Sparsely populated remote areas of the Arabian Peninsula are underlain by extensive aquifer system with abundant supplies of fresh groundwater that is hardly tapped. With the advancement of technology and scientific innovations, these freshwater resources can be extracted and transported to the growing human settlements in these areas and expanding urban centers across the Peninsula as well as made available for future generations. The application of remote sensing techniques is advocated as one of the most important tools to fine-tune the mapping of these aquifer systems and assess their potential for exploitation.

Bibliography

Abunayyan Trading Corporation and BRGM (Bureau de Recherches Géologiques et Minières) (2008)

Investigations for Updating the Groundwater Mathematical Model(s) of the Saq Overlying Aquifers (Main Report) and (Geology). Published by the Ministry of Water and Electricity in Saudi Arabia (2008). http://www.scribd.com/doc/16845648/Saq-Aquifer-Saudi-Arabia-2008; http://www.scribd.com/doc/16769693/FR-Vol-13-Geology. Accessed 17 Mar 2012

Al Alawi J, Abdulrazzak M (1993) Water in the Arab world: problems and perspectives. In: Water in the Arab world: perspectives and prognoses, 1st edn. Harvard University Division of Applied Sciences, Harvard

Barthelemy Y, Buscarlet E, Gomez E, Janjou D et al (2010) Jordan aquifers modelling project-final report

Beydoun ZR, As-Saruri MAL, El-Nakhal H, Al-Ganad IN et al (1998) International Lexicon of stratigraphy. Ministry of Oil and Mineral Resources in Yemen, Sana'a

BGR, SGD and UN-ESCWA (Bundesanstalt fur Geowissenschanften und Rohstoffe; Staatliche Geologische Dienste; United Nations Economic and Social Commission for Western Asia) (1999) Application of environmental isotope methods for groundwater studies in the ESCWA region, Berlin

BRGM and CNABRL (Bureau de Recherches Géologiques et Minières; Compagnie Nationale d'Aménagement de la Région du Bas-Rhône et du Languedoc) (1985) Water, agriculture and soil studies of Saq and overlying aquifers. In: Water studies—main report. Ministry of Agriculture and Water in Saudi Arabia, Riyadh

Christian L (2000) Middle East geological map series (MEG-maps). Gulf PetroLink, Manama

Ferragina E, Greco F (2008) The Disi project: an internal/external analysis. Water Int 33(4):451–463

Haiste Kirkpatrick International and Scott Wilson Kirkpatrick (1995) Long term management of aquifer resources: study of the rum aquifer of South Jordan. In: Qa Disi aquifer study. Water Authority of Jordan, Amman

Hobler M, Bender H, Rashdan J, Schmidt G (1991) Groundwater resources of Southern Jordan. Water Authority of Jordan and BGR (Bundesanstalt für Geowissenschaften und Rohstoffe), Hannover

Komex International Inc (1997) Groundwater resources assessment in Hadramout—Masila region: report prepared for the ministry of oil and mineral resources. Canadian Occidental Petroleum Yemen. Sana'a, Republic of Yemen

Ministry of Agriculture and Water in Saudi Arabia (1984) Water Atlas of Saudi Arabia, Riyadh

Rybakov VS, Tkachenko RI, Mikhailin NN, Gamal N et al (1995) Groundwater resources available for development; explanatory note to the potential exploitational groundwater resources map.

International Academy of Sciences on Nature and Society in Russia and the Ministry of Oil and Mineral Resources in Yemen, Sana'a/Moscow

Salameh E, Rimawi O (1987) Natural radioactivity and hydrochemistry of some Jordanian groundwater resources, vol 9. University of Jordan, Amman

UN-ESCWA and BGR (United Nations Economic and Social Commission for Western Asia; Bundesanstalt für Geowissenschaften und Rohstoffe) (2013) Inventory of Shared Water Resources in Western Asia, Beirut

UN-ESCWA, UNEP and IDB (United Nations Economic and Social Commission for Western Asia; United Nations Environment Programme et al) (1996) Water resources assessment in the ESCWA region using remote sensing and GIS techniques. New York

Van der Gun JAM, Ahmed AA (1995) The water resources of Yemen: a summary and digest of available information. In: Water resources assessment Yemen. Ministry of Oil and Mineral Resources in Yemen and the Ministry of Foreign Affairs in The Netherlands, Sana'a/Delft

Water Watch (2006) Historic groundwater abstractions at national scale in the Kingdom of Saudi Arabia. Ministry of Water and Electricity in Saudi Arabia, the World Bank and UNDP (United Nations Development Programme), Wageningen

GIS-Based Multi-criteria Approach to Assess Water Resources Vulnerability in a Changing Climate over the Arab Domain

Marlene A. Tomaszkiewicz

1 Introduction

Water resources availability across the Arab region face increasing obstacles stemming from a growing population, urbanization, environmental degradation, climate change, and other factors. However, intervention prioritization can pose challenges for decision makers. Often, local governments and communities have differing views of vulnerability (Preston et al. 2008) due to diverging interests and personal experiences. Vulnerability assessments can help bridge the gap between science and public perceptions by identifying those areas at greatest risk by aggregating certain geospatial indicators and visualizing the result on a map. The map can be used to set management and planning priorities, inform and develop adaption strategies, and facilitate effective resource allocation (Füssel and Klein 2006; Glick et al. 2011).

Vulnerability is a nebulous concept. A current popular definition has been proposed by Adger (2006): vulnerability is the susceptibility of a system from exposure to stresses due to socio-environmental change and the ability to cope with said stressors. In the context of climate change, the idea has been formulated into a vulnerability assessment framework proposed by the Intergovernmental Panel on Climate Change (IPCC) in the Fourth Assessment Report (IPCC 2007). Vulnerability is composed of three primary elements: exposure, sensitivity, and adaptive capacity. Exposure entails the climate change catalysts that affect a given system. The social and environmental susceptibility of a system is reflected in sensitivity. Combining these two facets reveals potential impact. In turn, potential impact is countered by adaptive capacity, which is characterized by a system's ability to cope, mitigate, and adapt (Fig. 1).

M. A. Tomaszkiewicz (✉)
Climate Change and Natural Resources Sustainability Cluster, Arab Centre for Climate Change Policies, Economic & Social Commission for Western Asia (ESCWA), United Nations House, Beirut, Lebanon
e-mail: tomaszkiewiczm@un.org

A. Shaban (ed.), *Satellite Monitoring of Water Resources in the Middle East*,
Springer Water, https://doi.org/10.1007/978-3-031-15549-9_6

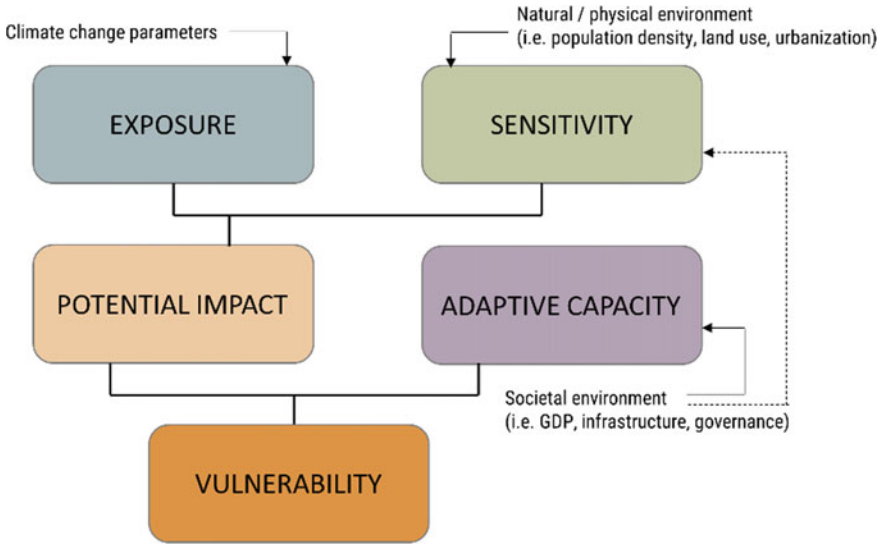

Fig. 1 Vulnerability assessment framework. Adapted from ESCWA et al. (2017a)

Despite a solidified vulnerability assessment framework, transferring the theoretic concept into a measurable outcome is not easy. This process is simplified through the use of selected geospatial indicators which best portray exposure, sensitivity, and adaptive capacity. Each of these indicators can be quantified. Thus, when aggregated together, the resultant vulnerability is tallied. Areas with high resultant vulnerability are identified by the highest aggregated values.

Here, we take a closer look at the first Arab region-wide vulnerability assessment on water availability, presented for the Regional Initiative for the Assessment of Climate Change Impacts on Water Resources and Socio-Economic Vulnerability in the Arab Region (RICCAR; ESCWA et al. 2017b). Current threats to water availability include access in least developed countries and in areas of conflict, deteriorating quality, variable precipitation, lack of reliable data to ascertain water use efficiency, transboundary water resources, and adverse ecosystem impacts. These threats will exacerbate due to population growth, migration, shifting agricultural policies, the water-food-energy nexus, land degradation, governance, and climate change (Borgomeo et al. 2020). The vulnerability assessment case study will highlight strengths and weaknesses in terms of indicator selection, weighting and aggregation, and evaluation of results.

2 Vulnerability Assessment Methodology

Vulnerability assessments depend on multi-step iterative methodology. The approach entails the use of vetted geospatial datasets that fit within the assessment framework. These datasets are weighted and aggregated together to eventually be presented on a map.

2.1 Determine Objectives and Scope

Determining a clear purpose and area of study will help streamline the vulnerability assessment. For RICCAR, five sectors and nine subsectors related to water were proposed, including general water availability (ESCWA et al. 2017b). Other studies have evaluated certain water resources subtopics including agriculture (Bär et al. 2015; ACSAD et al. 2019), urban ecosystems (Shen et al. 2016; Gober and Kirkwood 2010), water quality (Kim et al. 2019), groundwater (Kaur and Rosi 2011), shared surface water (Hamouda et al. 2009), and water supply (Goharian et al. 2017; Zohra et al. 2012). Other researchers have focused on other sectors including animal species (Foden et al. 2019; Gardali et al. 2012), forests (Thorne et al. 2018; Preston et al. 2008), and coastal zones (Yoo et al. 2011; Moreno and Becken 2009). Vulnerability assessments are intended to inform and support policymaking and should therefore be designed for the end user (Glick et al. 2011).

Vulnerability assessments can be conducted using different scales from sub-national or basin level to region-wide analysis. However, the resultant map will be only relative to the selected study area. Areas characterized by high or low vulnerability in a given study may differ when compared to other studies that may be different in areal scope. Often, climate change vulnerability assessments necessitate evaluation at a larger scale even when end-users may be solely concerned at a localized level due to far-reaching impacts (Glick et al. 2011).

2.2 Impact Chain Development

Impact chains are effective planning tools which help visualize cause-effect relationships between indicators and the final assessment. A given impact chain is the metaphorical bridge between the science and the end-user. Drawing from scientific knowledge, indicators are suggested which typify the three vulnerability components (exposure, sensitivity, and adaptive capacity). A simplified water availability impact chain from RICCAR is presented (Fig. 2).

Shareholder engagement can help identify which indicators potentially are best suited to typify exposure, sensitivity, and adaptive capacity. Moreover, decision

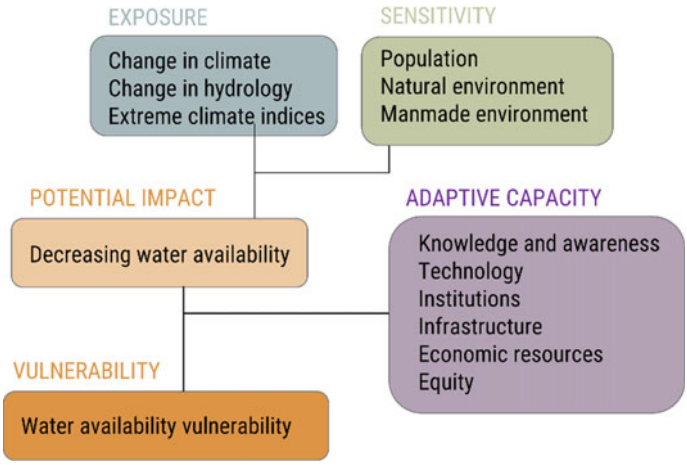

Fig. 2 Sample impact chain. Adapted from ESCWA et al. (2017b)

maker involvement from the onset can help support end-user buy-in. Lastly, a participatory approach can help pare down a broad number of indicators to those that have most significance. However, no indicator should be discarded in case more preferred indicators are ultimately unsuitable due to lack of data availability or other factors (Zebisch et al. 2021).

2.3 Indicator Selection

From the impact chain, proposed indicators face further scrutiny to deem their suitability. Key considerations include relevance, data availability, measurability, homogeneity, and reliability (ESCWA et al. 2017a). Although indicator relevance was evaluated during impact chain development, it is often worth revisiting based on knowledge gained during subsequent vulnerability assessment steps.

Because the vulnerability assessment result is presented on a map, indicators should be available in geospatial format for the entire study area. Example open-source geospatial datasets are summarized in Table 1. Indicators may also be available from stakeholders, crowdsourcing, household survey, remote sensing, statistical data, or map digitization. Indicators should ultimately be in raster format to facilitate aggregation and maintain the same spatial resolution. This may require conversion from shapefile to raster and raster data may need to be resampled to a common spatial resolution.

Each indicator must be measurable. Although many indicators are derived from quantified values, such as °C, other indicators may be descriptive, such as land use. Nevertheless, these descriptive indicators can be assigned an ordinal value based on its relationship to sensitivity (and thus vulnerability) for the given system.

Table 1 Examples of indicators and open source geospatial datasets

Vulnerability component	Indicator	Source
Exposure	Change in temperature; change in precipitation	RICCAR Data Portal (2019)
Sensitivity	Land cover	FAO Map Catalog (2013)
Sensitivity	Population density	Frye et al. (2018)
Sensitivity	Urban expansion	Seto et al. (2016)
Adaptive capacity	Transportation infrastructure	USGS (2019)

Homogeneity suggests that each indicator should be derived from a single source, from the same time period, and using the same methodology. This may not be possible in all cases; it is best to discard such indicators in favor of an alternate or proxy indicator. However, as a last resort, indicators can be derived from multiple sources, but care should be taken to maintain indicator homogeneity to the best extent possible.

In addition, some indicators may not be represented geospatially across the entire study area. Some indicators, such as groundwater well data, may only be represented as points. In such cases, spatial interpolation methods such as kriging should be utilized to estimate values at unmeasured locations. Statistical datasets may include one value per governorate or country. Values can be joined with the appropriate administrative boundary and thus converted to a geospatial dataset. However, this not preferred because values are assumed to be equal within the entire administrative area and may skew the vulnerability assessment.

Lastly, indicators should be reliable. Selecting data from widely recognized sources will help build end-user confidence. Although it may be desirable to use projected datasets for sensitivity and adaptive capacity indicators, careful review is necessary to assure credibility. It may be better to use static indicators using current data. Exposure indicators based on climate modelling outputs will likely be projected data, however.

There is no ideal number of indicators. The RICCAR vulnerability assessments used approximately 60 indicators in coordination with shareholders. The number of indicators was effectively reduced by grouping them into dimensions within each vulnerability component (ESCWA et al. 2017a). Even so, using many indicators will often result in a duplicative effect due to strong correlation with other indicators. In addition, using too many indicators has a dilution effect. Upon review of several vulnerability assessments, approximately 10 to 12 geospatial indicators are the norm.

2.4 Indicator Normalization and Classification

Because indicators have widely varying units of measurement and magnitude, they must be transformed to a common unitless value scheme. This step is both mathematical, but also entails careful decision making because of its significant impact

upon the vulnerability assessment (Zebisch et al. 2021). Indicator values are reclassified based on a common scale, such as 1 to 10. This can be done using min–max normalization or one of the methods embedded in GIS software: natural breaks, equal interval, quantile, or standard deviation. Natural breaks, also known as Jenks optimization method, classifies values by the best group of similar values that maximize differences between classes. Equal interval simply divides the data values into equal-sized classes. Quantile divides each class based on an equal number of features. Lastly, standard deviation determines classes using an equal value range that are a proportion of the standard deviation of the dataset. Determination of the best classification method is subjective but should be best representative of the indicator dataset and employs the full range of the 1 to 10 scale.

In some instances, datasets may contain outliers or be skewed. In such instances, removal of outliers should be considered as well as data transformation prior to reclassification. Differing transformation methods include log method, square roots method, square method, cubic root method, and quadratic root method. No transformation method is preferred over the other and should be selected based on the best means to reduce skewness for each geospatial dataset.

2.5 Indicator Weighting

Indicator weighting is the most sensitive step during the vulnerability assessment process. Its purpose is to assess relative importance compared to other datasets (Papathoma-Köhle et al. 2019). The most common method is to apply equal weights to each indicator. This approach is acceptable, particularly for normalized indicators, but should not be used arbitrarily. The use of equal weighting should not be construed as the absence of weighting; usage is justified by evaluation of alternative weighting methods.

Unequal weighting methods are derived from statistical or participatory approaches. Statistical assessments are typically based on principal component analysis (PCA). Alternate techniques include data envelopment analysis, linear regressions, and multi-criteria decision analysis. Statistical methods can counteract the influence of subjective decision-making conducted during other assessment steps. However, the resultant weighting may counter logic resulting in unbalanced relationships among indicators.

Common participatory approaches include analytic hierarchy process (AHP) or budget allocation process (BAP). The former is based on a decision matrix to estimate the relative importance of indicators through pair-wise comparisons and is employed in over half of the vulnerability assessments in literature. This methodology results in a coherent and robust weighting system but is complex and time-consuming. A simpler participatory method is represented by BAP, whereby experts are asked to allocate a fixed amount of points among the varying indicators.

Regardless of the selected weighting method, a sensitivity analysis should be conducted to the maximum extent possible to justify the final weighting. To ensure

balance, verify for each aggregation level, the weights sum 1.0 (or 100%). For example, all indicator weights represented in the exposure component should equal 1.0 and the components (exposure, sensitivity, adaptive capacity) themselves should also have summed weights equal to 1.0 to aggregate for vulnerability.

2.6 Indicator Aggregation

Individual indicators are aggregated together to formulate each of the three vulnerability components and in the end, the completed vulnerability assessment itself (Fig. 3). There are two primary methods to aggregate data: arithmetic and geometric. The arithmetic mean is more commonly used, particularly when indicators are weighted equally, due to its simplicity. However, the method is described as compensatory; geographical areas that score poorly for one or more indicators can still obtain a high aggregated index value counterbalanced by other high scoring indicators. Conversely, the geometric mean is only partially compensatory and is considered a better representation to measure vulnerability (Sironen et al. 2015; Zebisch et al. 2021).

Using raster datasets with a common spatial resolution help facilitate aggregation in GIS. An aggregated composite indicator, *CI*, can be calculated based on *n* number of indicators and their respective weights, *w*. Both arithmetic (Eq. 1) and geometric aggregation (Eq. 2) can be performed a tool like the raster calculator in ArcMap. Each level of aggregation should be performed separately.

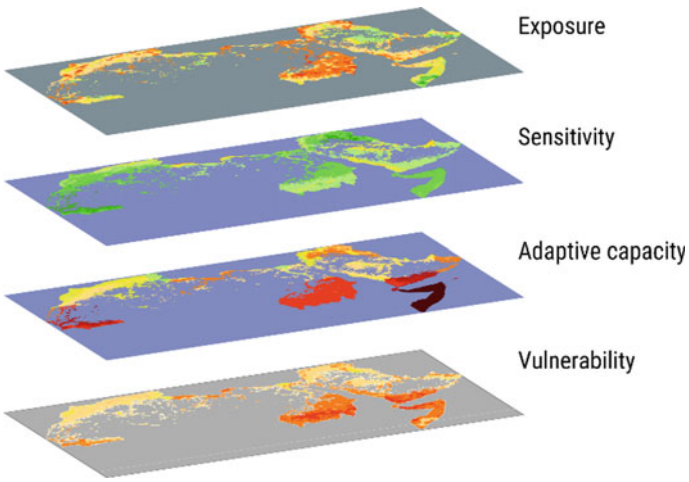

Fig. 3 Aggregation schematic

$$CI = indicator_1 \mathrm{x} w_1 + indicator_2 \mathrm{x} w_2 + \ldots + indicator_3 \mathrm{x} w_3 \quad (1)$$

$$CI = indicator_1^{w1} \times indicator_2^{w2} \times + indicator_n^{wn} \quad (2)$$

Note that it is common to represent high exposure and high sensitivity, both signaling unfavorable conditions, with high indicator classified values. Similarly, high adaptive capacity is also assigned a high value, but in this case designates a favorable condition. Such that low aggregated values indicate low vulnerability, and high aggregated values stipulate high vulnerability, adaptive capacity values may need to be inverted to maintain consistency.

2.7 Presentation of Results

Once indicator and component aggregation are complete, the composite vulnerability will result and be presented on a map. Commonly, a stoplight color scheme is utilized such that green designates low vulnerability and red represents high vulnerability. The final map is an effective communication tool that can highlight vulnerability hotspots. The map can also be compared to other geospatial datasets for planning and implementation of adaptation measures.

It is important to clearly present the methodology steps in addition to the map to decision makers. Otherwise misunderstandings may result. For example, it is important to communicate that the map is relative to the study area alone; areas perceived as most vulnerable may actually be only moderately vulnerable comparatively. In addition, many shareholders do not distinguish potential impact from vulnerability and disregard adaptive capacity. Areas that may be subjected to significant climate change impacts may have moderate vulnerability due to high adaptive capacity. Likewise, area with little or no adaptive capacity may reveal high vulnerability, despite few climate change impacts.

3 Results from RICCAR

For RICCAR (ESCWA et al. 2017b), five sectors and nine subsectors were studied. Each evaluated sector and subsector result included five vulnerability assessment maps. Four of the maps signified future conditions and stemmed from the exposure indicators. Two climate scenarios were evaluated, RCP4.5 and RCP8.5, for two future periods: (a) mid-century, representing 2046–2065, and (b) end-century, representing 2081–2100. In addition, a baseline vulnerability map was presented using the historical reference period (1986–2005). Here, one of the resultant maps is presented, water availability for RCP8.5, mid-century (Fig. 4).

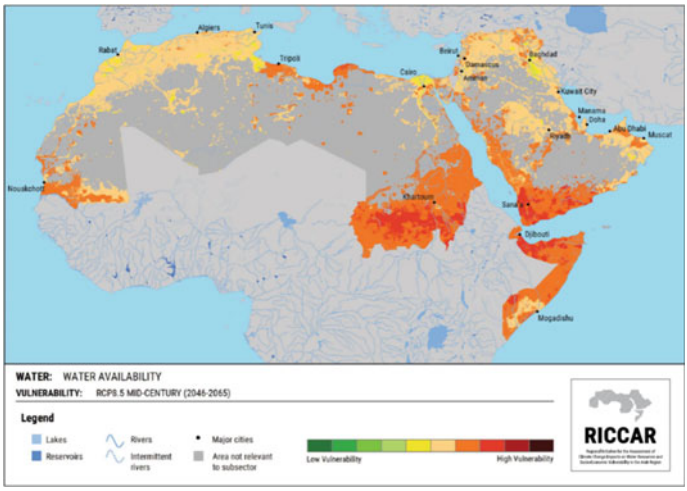

Fig. 4 Water availability vulnerability map for mid-century, RCP8.5 (ESCWA et al. 2017b)

For this study, experts agreed to solely exhibit results for a specific study area. The study area for the water availability subsector was defined by relevant shapefiles: forested areas, wetland areas, rainfed areas, irrigated areas, livestock population, and human population (ESCWA et al. 2017a). Masking a study area served two purposes. Because the assessment entailed a large geographical region, highlighting a relevant study area brings attention solely to impacted locales. For example, water availability is not necessarily a concern in unpopulated desert landscapes. In addition, because many of the adaptive capacity indicators selected were based on national statistical data, administrative borders were apparent in the final map. Use of a study area helped remove any implied borders.

Indicator weighting used a participatory approach. Surveys were sent to an expert panel assessing the importance of proposed indicators relative to water availability. However, most panel members were reluctant to evaluate any of the indicators at either extreme, instead generally assessing moderate importance for all indicators, thus rendering the resultant weighing effectively equal. As a result, expert opinion was solicited to finalize the weighting. The most significant indicator in each component was determined by consensus and assigned a value of 0.5; remaining indicators were weighted in accordance with survey results (ESCWA et al. 2017a). Use of budget allocation process instead may have produced a better outcome; most vulnerability assessment studies in literature employed an analytic hierarchy process.

Among the four evaluated future scenarios, 43% (RCP4.5) to 52% (RCP8.5) of the study area predicts high vulnerability (ESCWA et al. 2017b). Results show that areas of high vulnerability relative to water availability include the upper Nile Valley, the south-western Arabian Peninsula and the north Horn of Africa. This is largely due

to the low adaptive capacity in these areas as potential impact is considered low-to-moderate. Conversely, areas suggesting low vulnerability, relative to the study area, include the Tigris-Euphrates basin and the lower Nile Valley (ESCWA et al. 2017b).

Trend analysis reveals the largest increases in vulnerability include the Libyan coastal region, partly due to a significant projected increase in the maximum length of dry spell. On the other hand, the largest decreases are revealed in the Horn of Africa due to increasing precipitation and runoff. The most vulnerable water users include pastoralists and livestock due to the requisite large quantities for water to produce feed, facilitate grazing, and permit drinking. Human populations are comparatively less vulnerable but still are subjected to adverse factors not considered as part of the vulnerability assessment including environmental degradation and population growth (ESCWA et al. 2017b).

Although vulnerability assessment maps were produced for both the reference period (1986–2005) and two future periods (2046–2065 and 2081–2100), comparisons present a challenge. This is primarily because exposure indicator classification was conducted differently for the reference period and the future periods. The reference period exposure indicators were classified based on the absolute value of the selected climate parameters (i.e. temperature and precipitation). However, future periods were based on the net change in climate parameters. For temperature, low exposure (class 1) was defined as any increase < 1 °C; high exposure (class 10) was specified by increases > 5 °C. Because changes in precipitation can be increasing or decreasing, < -8 mm/month was designed as low exposure and >+ 8 mm/month was high exposure. This approach was intended to highlight the differences due to climate change and match the individual climate parameter maps. However, in terms of vulnerability mapping, this approach poses challenges when comparing the reference period to the future periods due to indicator classification. A better method would be to classify both time periods using the absolute values.

4 Concluding Remarks

GIS-based vulnerability assessments are effective communication tools that clearly identify the most vulnerable geographic regions for a given sector due to climate change. Decision makers can use the maps to plan and implement adaptive measures. However, they are only as effective as the indicators selected, the classification scheme, and the indicator weighting. Shareholder involvement during the process as well as conducting a sensitivity analysis of the resultant map helps to instill confidence in the vulnerability assessment.

It is noted that the concept of vulnerability slightly evolved for the Fifth Assessment Report (AR5; IPCC, 2014). The AR5 approach is intended more for disaster risk reduction, a paradigm shift from climate change policymaking. The notion of hazard is introduced as a physical event, trend, or impact that causes adverse quantifiable harm, such as financial loss. Vulnerability is redefined, encompassing multidimensional sensitivity and susceptibility to disaster harm, and is a component of risk. The

role of adaptive capacity is greatly diminished. This concept is more reactive than proactive and for this reason, the AR4 methodology and results described in the text is preferred for climate change adaptation planning.

References

Adger WN (2006) Vulnerability. Global Environ Change 16(3):268–281

Arab Center for the Studies of Arid Zones and Dry Lands (ACSAD), Ministry of Agriculture in Lebanon (MoAg), National Council for Scientific Research (CNRS) and United Nations Economic and Social Commission for Western Asia (ESCWA) (2019) Integrated Vulnerability Assessment Application on the Lebanese Agricultural Sector. RICCAR Technical Report, Beirut, E/ESCWA/SDPD/2019/RICCAR/TechnicalReport.6

Bär R, Rouholahnejad E, Rahman K, Abbaspour KC, Lehmann A (2015) Climate change and agricultural water resources: a vulnerability assessment of the Black Sea catchment. Environ Sci Policy 46:57–69

Borgomeo E, Fawzi NA, Hall JW, Jägerskog A, Nicol A, Sadoff CW, Salman M, Santos N, Talhami M (2020) Tackling the trickle: ensuring sustainable water management in the Arab region. Earth's Future 8(5):e2020EF001495

Foden WB, Young BE, Akçakaya HR, Garcia RA, Hoffmann AA, Stein BA, Huntley B (2019) Climate change vulnerability assessment of species. Wiley Interdiscip Rev Clim Change 10(1):e551

Food and Agriculture Organization of the United Nations (FAO) Map Catalog (2013) Global land cover share database. data.apps.fao.org/map/catalog

Frye C et al (2018) Using classified and unclassified land cover data to estimate the footprint of human settlement. Data Sci J 17:20. https://doi.org/10.5334/dsj-2018-020

Füssel HM, Klein RJ (2006) Climate change vulnerability assessments: an evolution of conceptual thinking. Clim Change 75(3):301–329

Gardali T, Seavy NE, DiGaudio RT, Comrack LA (2012) A climate change vulnerability assessment of California's at-risk birds. PLoS ONE 7(3):e29507

Glick P, Stein BA, Edelson NA (2011) Scanning the conservation horizon: a guide to climate change vulnerability assessment. National Wildlife Federation, Washington, DC, p 168

Gober P, Kirkwood CW (2010) Vulnerability assessment of climate-induced water shortage in Phoenix. Proc Natl Acad Sci 107(50):21295–21299

Goharian E, Burian SJ, Lillywhite J, Hile R (2017) Vulnerability assessment to support integrated water resources management of metropolitan water supply systems. J Water Resour Plan Manag 143(3):04016080

Hamouda MA, El-Din MMN, Moursy FI (2009) Vulnerability assessment of water resources systems in the Eastern Nile Basin. Water Resour Manage 23(13):2697–2725

Intergovernmental Panel on Climate Change (IPCC) (2007) Climate Change 2007: Impacts, Adaptation and Vulnerability. Contribution of Working Group II to the Fourth Assessment Report of the Intergovernmental Panel on Climate Change, M.L. Parry, O.F. Canziani, J.P. Palutikof, P.J. van der Linden and C.E. Hanson, Eds., Cambridge University Press, Cambridge, United Kingdom

Intergovernmental Panel on Climate Change (IPCC) (2014) Climate Change 2014: Impacts, Adaptation, and Vulnerability. Part A: Global and Sectoral Aspects. Contribution of Working Group II to the Fifth Assessment Report of the Intergovernmental Panel on Climate Change. Field CB, Barros VR, Dokken DJ, Mach KJ, Mastrandrea MD, Bilir TE, Chatterjee M, Ebi KL, Estrada YO, Genova RC, Girma B, Kissel ES, Levy AN, MacCracken S, Mastrandrea PR, White LL (eds) Cambridge University Press, Cambridge, United Kingdom

Kaur R, Rosi KG (2011) Ground water vulnerability assessment–challenges and opportunities. Division of Environmental Sciences, Indian Agricultural Research Institute

Kim JS, Jain S, Lee JH, Chen H, Park SY (2019) Quantitative vulnerability assessment of water quality to extreme drought in a changing climate. Ecol Ind 103:688–697

Moreno A, Becken S (2009) A climate change vulnerability assessment methodology for coastal tourism. J Sustain Tour 17(4):473–488

Papathoma-Köhle M, Cristofari G, Wenk M, Fuchs S (2019) The importance of indicator weights for vulnerability indices and implications for decision making in disaster management. Int J Disaster Risk Reduct 36:101103

Preston BL, Brooke C, Measham TG, Smith TF, Gorddard R (2008) Igniting change in local government: lessons learned from a bushfire vulnerability assessment. Mitig Adapt Strat Glob Change 14(3):251–283

Regional Initiative for the Assessment of Climate Change Impacts on Water Resources and Socio-Economic Vulnerability in the Arab Region (RICCAR) Data Portal (2019) www.riccar.org

Seto K, Güneralp B, Hutyra LR (2016) Global Grid of Probabilities of Urban Expansion to 2030. Palisades, NY: NASA Socioeconomic Data and Applications Center (SEDAC). https://doi.org/10.7927/H4Z899CG

Sironen S, Seppälä J, Leskinen P (2015) Towards more non-compensatory sustainable society index. Environ Dev Sustain 17(3):587–621

Shen J, Lu H, Zhang Y, Song X, He L (2016) Vulnerability assessment of urban ecosystems driven by water resources, human health and atmospheric environment. J Hydrol 536:457–470

Thorne JH, Choe H, Stine PA, Chambers JC, Holguin A, Kerr AC, Schwartz MW (2018) Climate change vulnerability assessment of forests in the Southwest USA. Clim Change 148(3):387–402

United Nations Economic and Social Commission for Western Asia (ESCWA), Arab Center for the Studies of Arid Zones and Dry Lands (ACSAD) and GIZ (Deutsche Gesellschaft für Internationale Zusammenarbeit) (2017a) Integrated Vulnerability Assessment: Arab Regional Application. RICCAR Technical Note, Beirut, E/ESCWA/SDPD/2017/RICCAR/TechnicalNote.2

United Nations Economic and Social Commission for Western Asia (ESCWA) et al. (2017b). Arab Climate Change Assessment Report – Main Report. Beirut, E/ESCWA/SDPD/2017b/RICCAR/Report.

United States Geological Survey (USGS) (2019) Earth explorer. earthexplorer.usgs.gov/

Yoo G, Hwang JH, Choi C (2011) Development and application of a methodology for vulnerability assessment of climate change in coastal cities. Ocean Coast Manag 54(7):524–534

Zebisch M, Schneiderbauer S, Fritzsche K, Bubeck P, Kienberger S, Kahlenborn W, Schwan S, Below T (2021) The vulnerability sourcebook and climate impact chains–a standardised framework for a climate vulnerability and risk assessment. Int J Clim Change Strateg Manag

Zohra HF, Mahmouda B, Luc D (2012) Vulnerability assessment of water supply network. Energy Procedia 18:772–783

Unraveling the Spatiotemporal Dynamics of Satellite-Inferred Water Resources in the Arabian Peninsula

Youssef Wehbe

1 Introduction

The Arabian Peninsula (AP) has been experiencing a significant increase in water demand as a result of population growth, urbanization, and an overall increase in living standards. The stress on the region's already scarce water resources is further exacerbated by the increasing reliance on groundwater, especially in deep inland locations where water supply from seawater desalination is not economically feasible. Even in coastal areas, the frequent deterioration of seawater quality due to harmful algal blooms or oil spills (Zhao et al. 2015, 2014) hinders the operation of desalinations plants. In such context, the monitoring of renewable water resources is essential, yet also challenging, due to the sporadic nature of rainfall events that are extremely unevenly distributed in space and time over the AP (Wehbe et al. 2018, 2020; El Kenawy and McCabe 2016; Almazroui et al. 2012; Fekete et al. 2004). Sources of precipitation estimates can be broadly grouped into three classes, namely: (i) ground-based rain gauge and radar observations, (ii) satellite precipitation retrievals, and (iii) model reanalysis products.

While global climate models (GCMs) and earth system models (ESMs) provide worldwide coverage of water cycle components, their relatively coarse spatiotemporal resolution limits their value for local and basin-scale analyses. To address this, both statistical and dynamical downscaling of GCMs and/or ESMs have evolved over the past decade to enable more reliable local- and catchment-scale monitoring (Tapiador et al. 2020). For example, the most recent release of the European Centre for Medium Range Weather Forecasts Reanalysis product (ERA-5) provides a 30-km global coverage with 137 atmospheric pressure levels capped at 80 km with uncertainty ranges reported at each level (Hersbach and Dee 2016). However, despite the

Y. Wehbe (✉)
National Center of Meteorology, P.O. Box 4815, Abu Dhabi, UAE
e-mail: ywehbe@ncms.ae

Climate and Water Program, Middle East Institute, 1763 N St. NW, Washington DC 20036, USA

A. Shaban (ed.), *Satellite Monitoring of Water Resources in the Middle East*,
Springer Water, https://doi.org/10.1007/978-3-031-15549-9_7

exponential growth in computing power, many fundamental and precursory physical processes for precipitation generation like radiative transfer, convection initiation, hydrometeor phase change, and other cloud microphysical interactions occur at the sub-kilometer scale down to the microscale—nine orders of magnitude less than current model resolutions.

Remotely sensed precipitation retrievals from satellite platforms offer an attractive alternative to reanalysis products due to their higher spatiotemporal resolutions and continuous coverage. These include products from the Tropical Rainfall Measurement Mission (TRMM) (Huffman et al. 2007) and its successor the Global Precipitation Measurement (GPM) mission (Huffman et al. 2015), the Global Precipitation Climate Center (GPCC) (Becker et al. 2011), the Climate Research Unit (CRU) (Mitchell and Jones 2005), the Climate Prediction Center morphing (CMORPH) technique (Joyce et al. 2004), and the Willmott–Matsuura (WM) dataset (Willmott and Robeson 1995; Willmott et al. 2001), among others. Despite their widespread applications, their uncertainties remain high, especially over arid regions with absolute and relative biases reaching 100 mm and 300%, respectively (Fekete et al. 2004; El Kenawy et al. 2019). The sparse distribution of rain gauges and inhomogeneity of observations hamper the calibration of such products over AP (Wehbe et al. 2017). Figure 1 shows the spatial distribution of rain gauges included in the Global Historical Climatology Network (GHCN) during (a) 1992 and (b) 2013. Although most regions show an expansion in the number of rain gauge networks, the lowest density persists across the MENA region. However, the GHCN archive may not reflect the existing rain gauge networks deployed by local agencies across the MENA region. In fact, the UAE's advanced meteorological monitoring infrastructure presents a unique area to improve the accuracy of global satellite products to fall within acceptable global error margins.

Whilst increasing the availability of ground-truth from rain gauges is a crucial step for improving continuous precipitation monitoring, this is only the tip of the iceberg. In contrast to the top-down estimation and evaluation approaches outlined in Sects. 2 and 3, a bottom-up approach, termed "reverse hydrology", has been recently proposed (Ciabatta et al. 2020). A physically-based selection of surface explanatory variables (e.g. soil moisture and topography) is expected to preserve land–atmosphere dynamics and their interlinkages within datasets, which remain unresolved in conventional statistical downscaling or bias-correction methods (Wehbe et al. 2020). Hence, a three-way fusion of remote sensing, model reanalysis and ground-based measurements is widely acknowledged as the current best practice, particularly by leveraging machine learning tools with large input datasets as outlined in Sect. 4 (Alizadeh and Nikoo 2018; Li et al. 2018; Ma et al. 2019).

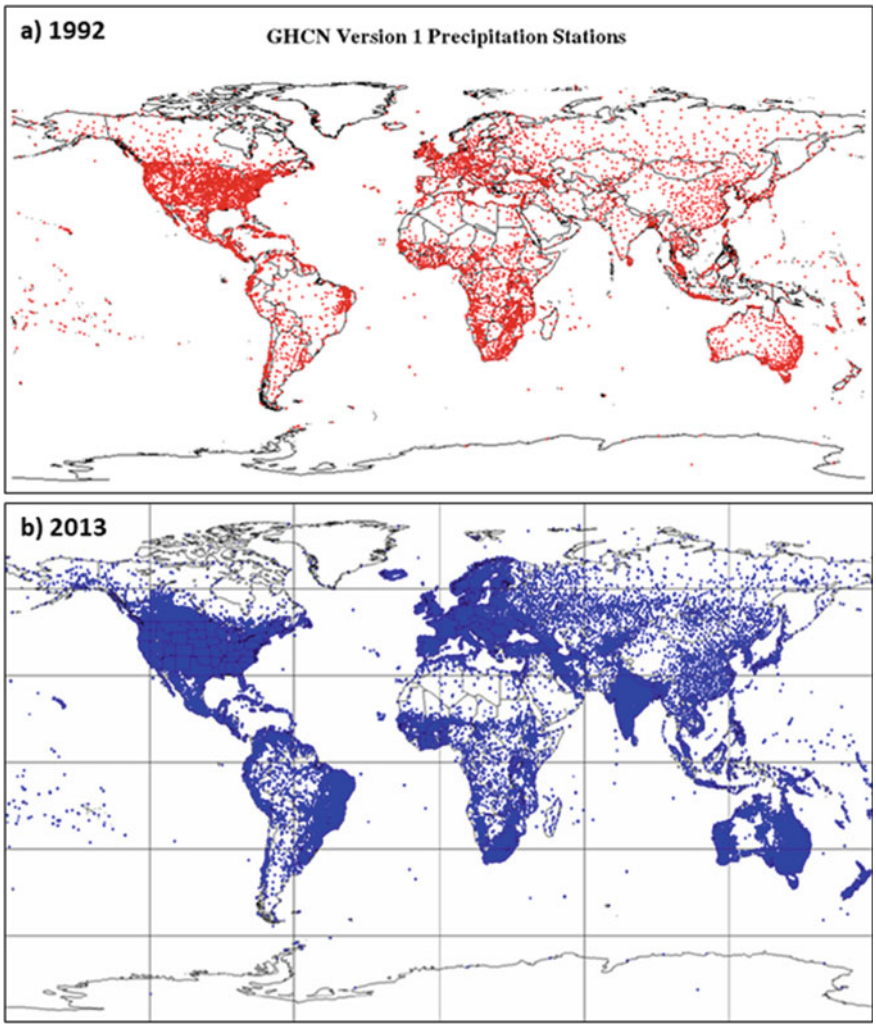

Fig. 1 Spatial distribution of rain gauges included in the Global Historical Climatology Network during **a)** 1992 and **b)** 2013, adapted from Vose et al. (2016) and Schneider et al. (2016), respectively

2 Inter-comparison of Precipitation Products and their Interactions with Water Budget Components over the AP

The development of accurate and reliable precipitation products has received much attention over the past years, particularly multi-input derived products from ground observations, satellite remote sensing, and climate model simulations (Rafieeinasab et al. 2015; Wen 2015; Wang and Lin 2015; Stocker et al. 2015). The global long-term spatial patterns of annual precipitation were found to be in good agreement

between numerous products, but they often reveal marked differences regionally (Fekete et al. 2004; Adler et al. 2001; Costa and Foley 1998). The agreement among distinct precipitation products has not been thoroughly studied for the MENA region, and particularly for arid regions like the AP (Milewski et al. 2015). This is attributed mainly to the scarcity of dense and reliable observation networks and the absence of large urban developments in arid and hyper arid regions (Wehbe et al. 2017).

The assessment of precipitation products can be conducted at global or regional scales. The comparison of global overland precipitation estimates from the TRMM, GPCC, and WM showed climatology agreement in terms of spatial distribution, zonal means as well as seasonal variations, but large discrepancies were found for light rain (Liu 2015). The analysis of precipitation products globally tends to depict overall changes in variability of precipitation estimates with no specific focus on the link with prevailing local conditions which could be achieved by regional analyses.

A limited number of studies exist over the AP region. Almazroui (2011) conducted a ground-based calibration of the TRMM product with rain gauge measurements over Saudi Arabia for the period 1998–2009. The correction resulted in approximately a 0.9 correlation coefficient with a 99% significance level on a monthly scale, indicating the reliability of TRMM usage in water-related studies in the region. Also, El Kenawy and McCabe (2015) studied rainfall climatology, anomalies, and trends over Saudi Arabia using gauge based products. Their work suggested that the monthly GPCC product showed the most accurate rainfall estimates over the regional scale of Saudi Arabia.

The lack of a dense network for rainfall observation across the AP is the major factor that hampers the verification of the available global products. The regional response of the surface and groundwater storage, as terrestrial water components, to rainfall, as a climate input, can reveal important spatiotemporal dynamics of the water cycle. Therefore, in the absence of in situ rainfall observations, other components of the water cycle namely, soil moisture and water storage may be used as proxies for station data to assess the reliability of different precipitation products.

Several studies on the surrounding areas of the AP have involved remote sensing data coupled with models to perform large-scale monitoring. Ahmed et al. (2011) showed that the observed Total Water Storage (TWS) anomaly variations from the Gravity Recovery and Climate Experiment (GRACE) platforms are largely controlled by elements of the hydrologic cycle, namely, runoff, infiltration, and groundwater flow and have not been obscured by noise, as previously thought. Ghebreyesus et al. (2016) stated that accounting for soil moisture is essential for the closure of the water balance in arid watersheds. Also, Yan et al. (2010) applied an integrated, remote sensing-based approach to improve estimations of renewable water resources in the arid to semiarid areas of the Sinai Peninsula and the Eastern Desert of Egypt. Their approach successfully incorporated the Special Sensor Microwave Imager (SSM/I), Landsat Thematic Mapper (TM), Advanced Very High Resolution Radiometer (AVHRR), Advanced Microwave Scanning Radiometer (AMSR-E), Advanced Spaceborne Thermal Emission and Reflection Radiometer (ASTER), and TRMM datasets to determine precipitation, soil moisture, reservoir volume and stages, and flows in large river channels with the application of a hydrologic model.

For the same study area, Milewski et al. (2009) developed an integrated remote sensing data extraction model (RESDEM) for analysis of an ensemble of remote sensing data sets, including TRMM, SSM/I, AVHRR, MODIS, QuikSCAT, and AMSR-E. Milewski et al. (2015) also assessed the four TRMM 3B42 products: V6, V7temp, V7, RTV7 using a rain gauge network in Northern Morocco. The 3B42 V7 was found to be the most consistent with the gauge observations based on their spatial correlation analyses, while overestimations were recorded across all four products.

The first attempt to assess the consistency of different precipitation products specifically over the AP is outlined in Wehbe et al. (2018). They employed geographically-temporally weighted regression (GTWR) to infer water storage variations from inputs of soil moisture, terrain elevation and four different precipitation datasets. The TRMM V7 product showed the best predictive performance with a goodness-of-fit coefficient (R^2) of 0.84. They also reported results from an ensemble of pairwise t-tests to assess the significant of the difference in means across multiple products. The TRMM-GPCC comparison showed the most spatially dominant equality of means for over 95% of the AP extent. The inclusion of additional explanatory variables, namely, soil type, evapotranspiration, and vegetation cover in the GTWR setup was recommended for future work to support both basin-scale hydrological modeling and regionally integrated water resource planning.

3 Climatological Time Series Analysis and Statistical Change Point Detection

This section presents a 10-year record of remote sensing data applied on the regional scale of the AP to study the climatology and macro processes of TWS, precipitation, and soil moisture determined by observations from GRACE, TRMM, and AMSR-E, respectively. As concluded in Sect. 2, the TRMM V7 product showed the highest consistency with other hydrological variables, which corroborates its use in the current analysis. The focus is placed on the examination of trend statistical significance and detectable change points. The spatial distribution of the selected key hydrological variables is also investigated and the temporal consistency of the detected changes in their variability is analyzed. In the absence of large-scale and dense observation networks, the trend of GRACE estimates was verified locally using observations from wells in the UAE. The inferred agreement between GRACE and local well observations in the UAE is assumed to be reflective of the performance of the retrieval of TWS anomalies over the entire study area. Moreover, this section assesses the feasibility of inferring relationships between hydrological variables and macroscale processes by exclusively using remote sensing data. This makes the proposed analyses expandable to other ungauged watersheds where in situ observations are scarce or not available (Wehbe and Temimi 2021).

3.1 Study Area and Datasets

Figure 2 shows the topography of the AP varying from the lowest points along the coast of the Arabian Gulf to over 3500 m at the highest southern peaks in Yemen. The Hajar Mountain range on the border between Oman and the UAE is also depicted with peaks reaching 3000 m. Recharge mechanisms are highly dependent on both the existing topography and soil textures. Figure 2b shows widespread shallow and poorly developed soils, enriched with lime, gypsum, or salts, which are strongly coupled to the arid desert climate. Sand dunes and sheets of transported materials cover the majority of the region. Alternatively, shallow and stony soils cover the southern highlands in Yemen and the Hajar Mountain range, which may favor lateral flow rather than recharge of the deep aquifer. Ephemeral rivers (wadis) are fed by runoff from these highlands, which frequently trigger flashfloods downstream (Abdouli et al. 2019; Alsumaiti et al. 2020; Harrower 2010).

The dry (June, July, August, and September—JJAS) and wet (December, January, February, and March – DJFM) seasons for much of the AP are consistent with the region and typical hydrological regimes. However, accurate details on the seasonal rainfall distribution for the AP using long-term observations are generally not available in the literature (Almazroui et al. 2012). Large rainfall amounts are observed over the northern AP during the wet season associated with pressure troughs from the eastern Mediterranean, while the southern portion records peak rainfall amounts during the dry season with the advancement of moist air masses from the Indian Monsoon Trough (Yousef et al. 2020; Breed et al. 2005; Sherif et al. 2014). Consequently, two transitional periods (April–May and October–November) separate these dry and wet regimes, which dictate the region's climatology. For the sake of the intercomparison, the products are analyzed for the overlapping period of June 2002 to September 2011. Table 1 includes a summary of the used datasets.

3.2 Time Series and Change Point Analyses

The methodology incorporated trend analysis using the modified Mann–Kendall test 1 (Hamed and Rao 1998) and change point detection based on the Cumulative Sum (CUSUM) method (Page 1954). GRACE TWS anomalies vary between −6.2 to 3.2 cm/month and −6.8 to −0.3 cm/month during the winter and summer periods, respectively. Trend analysis shows decreasing precipitation trends (-2.3×10^{-4} mm/day) spatially aligned with decreasing soil moisture trends (-1.5×10^{-4} g/cm^3/month) over the southern part of the AP, whereas the highest decreasing TWS trends (-8.6×10^{-2} cm/month) are recorded over areas of excessive groundwater extraction in the northern AP. Interestingly, change point detection reveals increasing precipitation trends pre- and post-change point breaks over the entire AP region. Significant spatial dependencies are observed between TRMM and GRACE

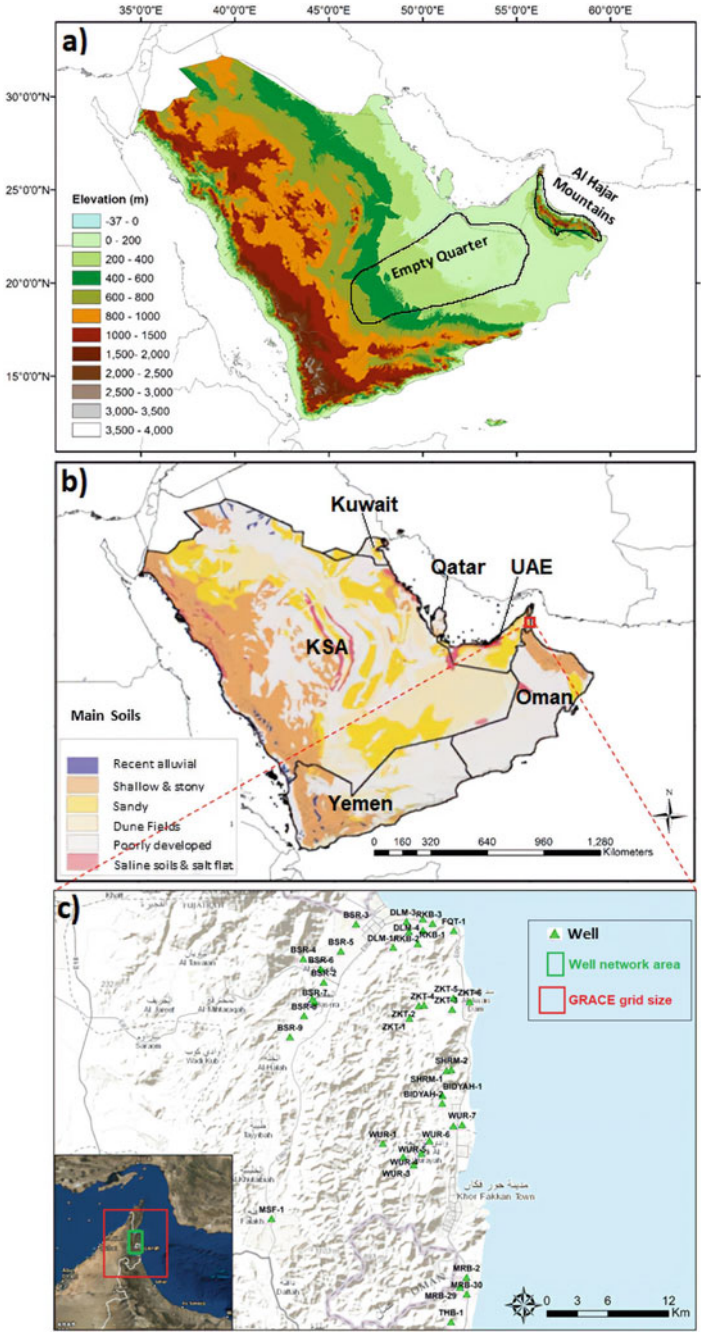

Fig. 2 Terrain elevations (**a**) soil types (**b**) and (**c**) the spatial distribution of the observational well network in the northern UAE—adapted from Wehbe et al. (2021)

Table 1 Temporal coverages and resolutions of the Gravity Recovery and Climate Experiment (GRACE), Tropical Rainfall Measuring Mission (TRMM), and Advanced Microwave Scanning Radiometer for Earth Observing System (AMSR-E) datasets

Variable	Product	Temporal coverage	Spatiotemporal resolution
Water storage	GRACE	April 2002–October 2017	1°; Monthly
Precipitation	TRMM	January 1999–July 2015	0.25°; Daily
Soil moisture	AMSR-E	June 2002–September 2011	0.25°; Daily

change points, particularly over Yemen during 2010, revealing the dominant impact of climatic changes on TWS depletion.

The GRACE TWS depletion rates are found to be the highest (-6.9×10^{-2} to -8.6×10^{-2} cm/month) over northern Saudi Arabia and Kuwait, mainly over agricultural areas that are subject to excessive groundwater extraction. These depletion rates override the co-located increasing trends of rainfall and soil moisture in line with the findings of Sultan et al. (2014). In fact, large areas of desert lands around central Saudi Arabia have been developed into highly productive farms with an agricultural water demand of 29.82 billion m^3 or 94% of the total water consumption in 1994 (Dabbagh and Abderrahman 1997). The decrease of TWS anomalies in the southern part—reaching -2×10^{-2} to -0.5×10^{-2} cm/month over Yemen and Oman was not as significant as in the case of the northern part of the AP, despite the southern decreasing trends of rainfall and soil moisture. The milder climatology and lower evapotranspiration rates over this region permit more recharge and, consequently, less groundwater depletion rates.

Considering the entire time series for assessing the trend direction and magnitude may be erroneous, particularly in the presence of change points in the time series marking a significant change in trend. For instance, the TRMM data showed both increasing post- and pre-change point trends, while the overall time series showed a decreasing trend. Based on the similarity in spatial distribution between change points of TRMM and GRACE, water storage variability at the macroscale is highly susceptible to changes in precipitation, and not solely controlled by anthropogenic extraction.

In terms of soil moisture, the difference in overpass time with AMSR-E is augmented by the high potential evapotranspiration in the region, which causes most of the rain to evaporate from the skin soil layer following a rain event. Additionally, ASMR-E uses high frequency (not L-band) which dictates low penetration depth and more sensitivity to the top skin soil layer subject to the high evaporation at the monthly scales considered above. Soil moisture is an instantaneous short-lasting response because of rapid drainage and evaporation. Nonetheless, soil moisture at daily or sub-daily scales is expected to provide key information for bias correction of precipitation products in dryland environments as outlined in Sect. 4.

4 Soil Moisture–Precipitation Interactions and Reverse Hydrology

Sections 2 and 3 outlined the systematic attempts for spatiotemporal consistency assessments and inter-comparisons of historical records across hydro-meteorological datasets. Here, we explore recent attempts targeting precipitation correction and multisource estimation accounting for the specific conditions of the AP's hydro-meteorological regime.

We distinguish between (1) the conventional approach of exclusively relying on rain gauge observations (Moghim and Bras 2017; Alharbi et al. 2018; Almazroui 2011) and (2) the more recent approach of incorporating additional explanatory variables to correct precipitation estimates (Bellerby et al. 2000; Tao et al. 2016; Fereidoon and Koch 2018; Brocca et al. 2019). In the latter approach, a physically-based selection of explanatory variables is expected to preserve process dynamics and interlinkages within datasets, which remain unresolved in conventional statistical correction methods. For example, water content in the uppermost soil layer exhibits an instantaneous response to co-located precipitation and is widely used as a proxy for precipitation occurrence. In fact, most currently used soil moisture retrieval algorithms are corrected by precipitation flags (rain/no rain) from available precipitation sources (Jackson et al. 2011; Chan et al. 2013; Brocca et al. 2014). This soil moisture–precipitation dependency is particularly relevant for arid regions and desert environments, where background/residual soil moisture prior to a rain event is relatively uniform due to negligible surface flow. Therefore, any soil moisture perturbations are controlled by the spatiotemporal distribution of rainfall events and provide a sustained surface signature beyond the satellite overpass time.

Using the Weather Research and Forecasting (WRF) model, Weston et al. (2019) studied the sensitivity of the heat exchange coefficient to surface conditions, including soil moisture, and demonstrated a strong impact on heat fluxes and local meteorological conditions within the UAE. Elevation is another explanatory variable that has been widely used for precipitation correction (Staub et al. 2014; Ninyerola et al. 2007; Brunsdon et al. 2001; Li et al. 2019). Topography is especially relevant to the AP due to the high frequency of local orographic summertime convective events over the northeastern UAE (Wehbe et al. 2019, 2021; Chaouch et al. 2017; Yousef et al. 2019). Additional surface and atmospheric variable inputs, such as slope, air temperature, vegetation indices, surface energy fluxes and cloud characteristics have been investigated (Chao et al. 2018). The significance of the selected inputs varies based on the geographic and climatic attributes of each study domain and, more importantly, based on the methodology followed.

Blending explanatory variables to enhance precipitation estimates has been increasingly applied using Artificial Neural Networks (ANNs), a subset of machine learning (ML) techniques, which perform adaptive, efficient, and holistic mappings of nonlinearities between large datasets (Hsu et al. 1997; Hsu et al. 1995). Maier et al. (2010) and Gopal (2016) give a detailed overview on the development and application of ANNs and their most compatible configurations for geospatial analyses. While

several types of ANNs have been developed for different applications, the feedforward multilayer perceptron (MLP) architecture remains the most commonly used framework for modeling precipitation (Esteves et al. 2019; Bolandakhtar and Golian 2019; Nasrollahi et al. 2013; Di Piazza et al. 2011; Coulibaly and Evora 2007). In addition to model- and satellite-based precipitation correction attempts, ANNs have also been successfully applied to improve weather radar rainfall estimates (Liu et al. 2001; Xiao and Chandrasekar 1995, 1997; Tsintikidis et al. 1997; Teschl et al. 2007). Moghim and Bras (2017) applied a three-layer feedforward neural network to correct precipitation and temperature model outputs over northern South America. For precipitation correction, they obtained consistent improvements of 8%, 8.5%, and 15.7% in mean square error, bias, and correlation metrics, respectively, from the ANN configuration compared to linear regression. On the other hand, without incorporating precipitation inputs, Fereidoon and Koch (2018) trained an ANN with daily inputs from the AMSR-E soil moisture product and air temperature measurements against rainfall records at five weather stations. Nevertheless, the ANN performed reasonably well with R^2 values reaching 0.65 during testing. Importantly, despite using separate time periods, they locally tested their model at the same stations used for training without attempting to verify the generalized spatial performance of the ANN-based estimates. They also highlighted the need for further case studies to be conducted over other regions with different soil moisture products.

4.1 Feedforward ANN-MLP Architecture: UAE Case Study

The first attempt of multivariate nonlinear precipitation estimation over the UAE by correcting the GPM mission's latest daily product release (IMERG V06B) overland using ancillary data and explanatory variables is given in Wehbe et al. (2020). Figure 3 illustrates the proposed configuration of the feedforward MLP with an input layer consisting of 4 neurons, a hidden layer of 16 neurons, and an output layer of 1 neuron, as well as the selected activation functions. In addition to the IMERG V06B product, daily 9-km soil moisture retrievals from the Soil Moisture Active Passive (SMAP) mission (Entekhabi et al. 2010, 2014), terrain elevations from the Advanced Spaceborne Thermal Emission and Reflection digital elevation model (ASTER DEM, 30 m), and 0.5-km precipitation estimates from a local weather radar network are incorporated as explanatory variables in the model, while rain gauges are used as ground truth. Model testing showed Nash–Sutcliffe efficiency (NSE) coefficients improvements of 56% (and 25%) for GPM estimates and 34% (and 53%) for radar estimates during summer (and winter) periods. Details on the proposed model architecture, calibration, and the training/testing can be found in Wehbe et al. (2020).

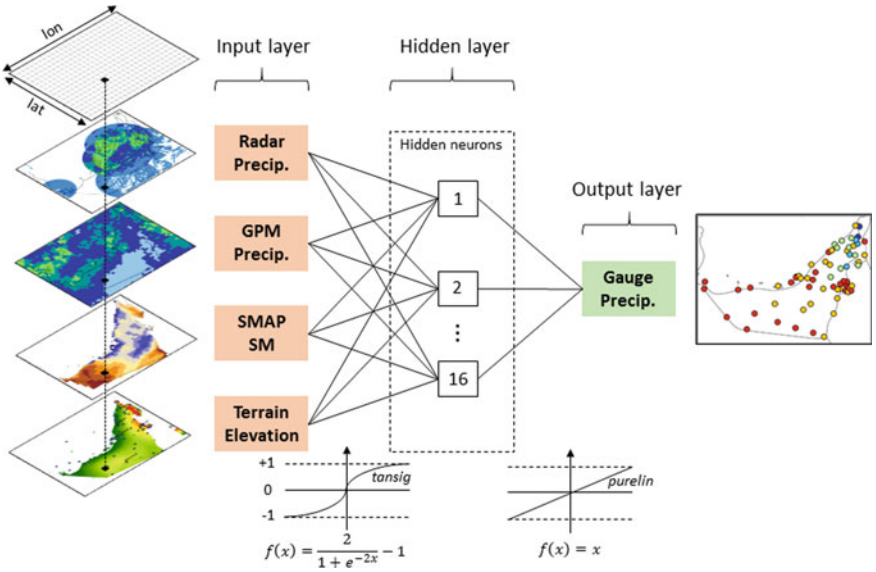

Fig. 3 Architecture of the proposed feedforward MLP with input (4 neurons), hidden (16 neurons), and output (1 neuron) layers—adapted from Wehbe et al. (2020)

5 Conclusion

The AP is known to be under severe water stress with only 200 m^3/cp/year of renewable water, which is alarmingly below the conventional water stress threshold of 500 m^3/cp/year (Alkolibi 2002). Hence, understanding the macro processes by large-scale monitoring of key hydrological variables, namely, rainfall, water storage, and soil moisture is essential. In this chapter, we present an overview on the spatiotemporal dynamics of water resources in the AP in terms of the consistency of global remote sensing hydro-meteorological products, their trends and change points, as well as their local-scale validation and fusion with ground observations.

The TRMM product (and its GPM successor) show the most reliable precipitation estimates relative to three other globally gridded precipitation products (GPCC, CMORPH, and WM). A 10-year time series analysis reveals an overall depletion of GRACE TWS over the entire AP, especially, the northern part while rainfall and soil moisture trends were decreasing over the southern part. Alternatively, an overall increasing rainfall trend was observed after change point division of the TRMM time series. Change point detection revealed significant spatial dependencies between the TRMM and GRACE products indicating hotspots of climate change impacts on TWS variations, which must be accounted for alongside anthropogenic factors.

The ANN-based correction framework presented in Sect. 4 can be used to generate more reliable inputs for hydrological studies over ungauged areas across the UAE.

These include hydrological assessments from the catchment-scale to the regional-scale. While the developed ANN configuration is derived locally for the UAE, the methodology followed is applicable to other arid and hyper-arid regions requiring improved precipitation monitoring. Future work with additional surface variables, particularly soil texture and land cover, is suggested to account for soil moisture drawdown and its spatial variation to further improve the physically-based ANN representation.

References

Abdouli KA, Hussein K, Ghebreyesus D, Sharif HO (2019) Coastal runoff in the United Arab Emirates—The hazard and opportunity. Sustainability 11(19):5406

Adler RF, Kidd C, Petty G, Morissey M, Goodman HM (2001) Intercomparison of global precipitation products: the third Precipitation Intercomparison Project (PIP-3). Bull Am Meteor Soc 82(7):1377

Ahmed M, Sultan M, Wahr J, Yan E, Milewski A, Sauck W, Becker R, Welton B (2011) Integration of GRACE (Gravity Recovery and Climate Experiment) data with traditional data sets for a better understanding of the time-dependent water partitioning in African watersheds. Geology 39(5):479–482

Alharbi R, Hsu K, Sorooshian S (2018) Bias adjustment of satellite-based precipitation estimation using artificial neural networks-cloud classification system over Saudi Arabia. Arab J Geosci 11(17):508

Alizadeh MR, Nikoo MR (2018) A fusion-based methodology for meteorological drought estimation using remote sensing data. Remote Sens Environ 211:229–247

Alkolibi FM (2002) Possible effects of global warming on agriculture and water resources in Saudi Arabia: impacts and responses. Clim Change 54(1–2):225–245

Almazroui M (2011) Calibration of TRMM rainfall climatology over Saudi Arabia during 1998–2009. Atmos Res 99(3–4):400–414

Almazroui M, Islam MN, Jones P, Athar H, Rahman MA (2012) Recent climate change in the Arabian Peninsula: seasonal rainfall and temperature climatology of Saudi Arabia for 1979–2009. Atmos Res 111:29–45

Alsumaiti TS, Hussein K, Ghebreyesus DT, Sharif HO (2020) Performance of the CMORPH and GPM IMERG products over the United Arab Emirates. Remote Sens 12(9):1426

Becker A, Finger P, Meyer-Christoffer A, Rudolf B, Ziese M (2011) GPCC full data reanalysis version 6.0 at 1.0: monthly land-surface precipitation from rain-gauges built on GTS-based and historic data. Global Precipitation Climatology Centre (GPCC): Berlin, Germany

Bellerby T, Todd M, Kniveton D, Kidd C (2000) Rainfall estimation from a combination of TRMM precipitation radar and GOES multispectral satellite imagery through the use of an artificial neural network. J Appl Meteorol 39(12):2115–2128

Bolandakhtar MK, Golian S (2019) Determining the best combination of MODIS data as input to ANN models for simulation of rainfall. Theor Appl Climatol:1–10

Breed D, Jensen T, Bruintjes R, Piketh S, Al Mangoosh A, Al Mandoos A Precipitation development in convective clouds over the eastern Arabian Peninsula. In: 16th Conference on Planned and Inadvertent Weather Modification (85th AMS Annual), San Diego, CA, USA, January, 2005. pp 9–13

Brocca L, Ciabatta L, Massari C, Moramarco T, Hahn S, Hasenauer S, Kidd R, Dorigo W, Wagner W, Levizzani V (2014) Soil as a natural rain gauge: estimating global rainfall from satellite soil moisture data. J Geophys Res Atmos 119(9):5128–5141

Brocca L, Filippucci P, Hahn S, Ciabatta L, Massari C, Camici S, Schüller L, Bojkov B, Wagner W (2019) SM2RAIN-ASCAT (2007–2018): global daily satellite rainfall from ASCAT soil moisture. Earth Syst Sci Data Discuss:1–31

Brunsdon C, McClatchey J, Unwin D (2001) Spatial variations in the average rainfall–altitude relationship in Great Britain: an approach using geographically weighted regression. Int J Climatol A J Royal Meteorol Soc 21(4):455–466

Chan S, Bindlish R, Hunt R, Jackson T, Kimball J (2013) Soil moisture active passive (SMAP) ancillary data report: vegetation water content. Pasadena, California

Chao L, Zhang K, Li Z, Zhu Y, Wang J, Yu Z (2018) Geographically weighted regression based methods for merging satellite and gauge precipitation. J Hydrol 558:275–289

Chaouch N, Temimi M, Weston M, Ghedira H (2017) Sensitivity of the meteorological model WRF-ARW to planetary boundary layer schemes during fog conditions in a coastal arid region. Atmos Res 187:106–127

Ciabatta L, Camici S, Massari C, Filippucci P, Hahn S, Wagner W, Brocca L (2020) Soil moisture and precipitation: the SM2RAIN algorithm for rainfall retrieval from satellite soil moisture. In: Satellite Precipitation Measurement. Springer, pp 1013–1027

Costa MH, Foley JA (1998) A comparison of precipitation datasets for the Amazon basin. Geophys Res Lett 25(2):155–158

Coulibaly P, Evora N (2007) Comparison of neural network methods for infilling missing daily weather records. J Hydrol 341(1–2):27–41

Dabbagh AE, Abderrahman WA (1997) Management of groundwater resources under various irrigation water use scenarios in Saudi Arabia. Arab J Sci Eng 22(1):47–64

Di Piazza A, Conti FL, Noto LV, Viola F, La Loggia G (2011) Comparative analysis of different techniques for spatial interpolation of rainfall data to create a serially complete monthly time series of precipitation for Sicily, Italy. Int J Appl Earth Obs Geoinf 13(3):396–408

El Kenawy AM, McCabe MF (2015) A multi-decadal assessment of the performance of gauge- and model-based rainfall products over Saudi Arabia: climatology, anomalies and trends. Int J Climatol

El Kenawy AM, McCabe MF (2016) A multi-decadal assessment of the performance of gauge- and model-based rainfall products over Saudi Arabia: climatology, anomalies and trends. Int J Climatol 36(2):656–674

El Kenawy AM, McCabe MF, Lopez-Moreno JI, Hathal Y, Robaa S, Al Budeiri AL, Jadoon KZ, Abouelmagd A, Eddenjal A, Domínguez-Castro F (2019) Spatial assessment of the performance of multiple high-resolution satellite-based precipitation data sets over the Middle East. Int J Climatol 39(5):2522–2543

Entekhabi D, Njoku EG, O'Neill PE, Kellogg KH, Crow WT, Edelstein WN, Entin JK, Goodman SD, Jackson TJ, Johnson J (2010) The soil moisture active passive (SMAP) mission. Proc IEEE 98(5):704–716

Entekhabi D, Yueh S, O'Neill P, Kellogg K, Allen A, Bindlish R, Brown M, Chan S, Colliander A, Crow W (2014) SMAP Handbook, JPL Publication JPL 400–1567. Jet Propulsion Laboratory, Pasadena, California 182

Esteves JT, de Souza RG, Ferraudo AS (2019) Rainfall prediction methodology with binary multilayer perceptron neural networks. Clim Dyn 52(3–4):2319–2331

Fekete BM, Vörösmarty CJ, Roads JO, Willmott CJ (2004) Uncertainties in precipitation and their impacts on runoff estimates. J Clim 17(2):294–304

Fereidoon M, Koch M (2018) Rainfall Prediction with AMSR–E Soil Moisture Products Using SM2RAIN and Nonlinear Autoregressive Networks with Exogenous Input (NARX) for Poorly Gauged Basins: Application to the Karkheh River Basin. Iran. Water 10(7):964

Ghebreyesus DT, Temimi M, Fares A, Bayabil K. H (2016) Remote sensing applications for monitoring water resources in the UAE using Lake Zakher as a water storage gauge. Book Chapter in the series "Water Security": Emerging Issues in Groundwater

Gopal S (2016) Artificial neural networks in geospatial analysis. International Encyclopedia of Geography: People, the Earth, Environment and Technology: People, the Earth, Environment and Technology:1–7

Hamed KH, Rao AR (1998) A modified Mann-Kendall trend test for autocorrelated data. J Hydrol 204(1–4):182–196

Harrower MJ (2010) Geographic Information Systems (GIS) hydrological modeling in archaeology: an example from the origins of irrigation in Southwest Arabia (Yemen). J Archaeol Sci 37(7):1447–1452

Hersbach H, Dee D (2016) ERA5 reanalysis is in production. ECMWF Newsletter 147(7):5–6

Hsu K-l, Gao X, Sorooshian S, Gupta HV (1997) Precipitation estimation from remotely sensed information using artificial neural networks. J Appl Meteorol 36(9):1176–1190

Kl H, Gupta HV, Sorooshian S (1995) Artificial neural network modeling of the rainfall-runoff process. Water Resour Res 31(10):2517–2530

Huffman GJ, Bolvin DT, Braithwaite D, Hsu K, Joyce R, Xie P, Yoo S-H (2015) NASA global precipitation measurement (GPM) integrated multi-satellite retrievals for GPM (IMERG). Algorithm Theoretical Basis Document (ATBD) Version 4:26

Huffman GJ, Bolvin DT, Nelkin EJ, Wolff DB, Adler RF, Gu G, Hong Y, Bowman KP, Stocker EF (2007) The TRMM multisatellite precipitation analysis (TMPA): Quasi-global, multiyear, combined-sensor precipitation estimates at fine scales. J Hydrometeorol 8(1):38–55

Jackson TJ, Bindlish R, Cosh MH, Zhao T, Starks PJ, Bosch DD, Seyfried M, Moran MS, Goodrich DC, Kerr YH (2011) Validation of Soil Moisture and Ocean Salinity (SMOS) soil moisture over watershed networks in the US. IEEE Trans Geosci Remote Sens 50(5):1530–1543

Joyce RJ, Janowiak JE, Arkin PA, Xie P (2004) CMORPH: A method that produces global precipitation estimates from passive microwave and infrared data at high spatial and temporal resolution. J Hydrometeorol 5(3):487–503

Li C, Tang G, Hong Y (2018) Cross-evaluation of ground-based, multi-satellite and reanalysis precipitation products: Applicability of the Triple Collocation method across Mainland China. J Hydrol 562:71–83

Li Y, Zhang Y, He D, Luo X, Ji X (2019) Spatial Downscaling of the Tropical Rainfall Measuring Mission Precipitation Using Geographically Weighted Regression Kriging over the Lancang River Basin. China. Chinese Geogr Sci 29(3):446–462

Liu H, Chandrasekar V, Xu G (2001) An adaptive neural network scheme for radar rainfall estimation from WSR-88D observations. J Appl Meteorol 40(11):2038–2050

Liu Z (2015) Evaluation of precipitation climatology derived from TRMM Multi-Satellite Precipitation Analysis (TMPA) monthly product over land with two gauge-based products. Climate 3(4):964–982

Ma H, Zeng J, Chen N, Zhang X, Cosh MH, Wang W (2019) Satellite surface soil moisture from SMAP, SMOS, AMSR2 and ESA CCI: a comprehensive assessment using global ground-based observations. Remote Sens Environ 231:111215

Maier HR, Jain A, Dandy GC, Sudheer KP (2010) Methods used for the development of neural networks for the prediction of water resource variables in river systems: current status and future directions. Environ Model Softw 25(8):891–909

Milewski A, Elkadiri R, Durham M (2015) Assessment and comparison of TMPA satellite precipitation products in varying climatic and topographic regimes in Morocco. Remote Sensing 7(5):5697–5717

Milewski A, Sultan M, Jayaprakash SM, Balekai R, Becker R (2009) RESDEM, a tool for integrating temporal remote sensing data for use in hydrogeologic investigations. Comput Geosci 35(10):2001–2010

Mitchell TD, Jones PD (2005) An improved method of constructing a database of monthly climate observations and associated high-resolution grids. Int J Climatol J Royal Meteorol Soc 25(6):693–712

Moghim S, Bras RL (2017) Bias correction of climate modeled temperature and precipitation using artificial neural networks. J Hydrometeorol 18(7):1867–1884

Nasrollahi N, Hsu K, Sorooshian S (2013) An artificial neural network model to reduce false alarms in satellite precipitation products using MODIS and CloudSat observations. J Hydrometeorol 14(6):1872–1883

Ninyerola M, Pons X, Roure JM (2007) Monthly precipitation mapping of the Iberian Peninsula using spatial interpolation tools implemented in a Geographic Information System. Theoret Appl Climatol 89(3–4):195–209

Page E (1954) Continuous inspection schemes. Biometrika 41(1/2):100–115

Rafieeinasab A, Norouzi A, Seo D-J, Nelson B (2015) Improving high-resolution quantitative precipitation estimation via fusion of multiple radar-based precipitation products. J Hydrol 531:320–336

Schneider U, Finger P, Meyer-Christoffer A, Rustemeier E, Ziese M, Becker A (2016) Evaluating the Hydrological Cycle over Land Using the Newly-Corrected Precipitation Climatology from the Global Precipitation Climatology Centre (GPCC). Atmosphere 8(3):52

Sherif M, Almulla M, Shetty A, Chowdhury RK (2014) Analysis of rainfall, PMP and drought in the United Arab Emirates. Int J Climatol 34(4):1318–1328

Staub CG, Stevens FR, Waylen PR (2014) The geography of rainfall in Mauritius: modelling the relationship between annual and monthly rainfall and landscape characteristics on a small volcanic island. Appl Geogr 54:222–234

Stocker EF, Kelley O, Kummerow C, Huffman G, Olson W, Kwiatkowski J (2015) Global Precipitation Measurement (GPM) Mission: Precipitation Processing System (PPS) GPM Mission Gridded Text Products Provide Surface Precipitation Retrievals

Sultan M, Ahmed M, Wahr J, Yan E, Emil MK (2014) Monitoring aquifer depletion from space: Case studies from the saharan and arabian aquifers. Remote Sensing of the Terrestrial Water Cycle 206:349

Tao Y, Gao X, Hsu K, Sorooshian S, Ihler A (2016) A deep neural network modeling framework to reduce bias in satellite precipitation products. J Hydrometeorol 17(3):931–945

Tapiador FJ, Navarro A, Moreno R, Sánchez JL, García-Ortega E (2020) Regional climate models: 30 years of dynamical downscaling. Atmos Res 235:104785

Teschl R, Randeu WL, Teschl F (2007) Improving weather radar estimates of rainfall using feed-forward neural networks. Neural Netw 20(4):519–527

Tsintikidis D, Haferman JL, Anagnostou EN, Krajewski WF, Smith TF (1997) A neural network approach to estimating rainfall from spaceborne microwave data. IEEE Trans Geosci Remote Sens 35(5):1079–1093

Vose, RS, Schmoyer RL, Steurer PM, Peterson TC, Heim R, Karl TR, and Eischeid JK (2016). Global Historical Climatology Network, ORNL DAAC, Oak Ridge, Tennessee, USA 1753–1990.

Wang XL, Lin A (2015) An algorithm for integrating satellite precipitation estimates with in situ precipitation data on a pentad time scale. Journal of Geophysical Research: Atmospheres 120(9):3728–3744

Wehbe Y, Ghebreyesus D, Temimi M, Milewski A, Al Mandous A (2017) Assessment of the consistency among global precipitation products over the United Arab Emirates. Journal of Hydrology: Regional Studies 12:122–135

Wehbe Y, Temimi M (2021) A Remote Sensing-Based Assessment of Water Resources in the Arabian Peninsula. Remote Sensing 13(2):247

Wehbe Y, Temimi M, Adler RF (2020) Enhancing Precipitation Estimates Through the Fusion of Weather Radar, Satellite Retrievals, and Surface Parameters. Remote Sensing 12(8):1342

Wehbe Y, Temimi M, Ghebreyesus DT, Milewski A, Norouzi H, Ibrahim E (2018) Consistency of precipitation products over the Arabian Peninsula and interactions with soil moisture and water storage. Hydrol Sci J 63(3):408–425

Wehbe Y, Temimi M, Weston M, Chaouch N, Branch O, Schwitalla T, Wulfmeyer V, Zhan X, Liu J, Mandous AA (2019) Analysis of an extreme weather event in a hyper-arid region using WRF-Hydro coupling, station, and satellite data. Nat Hazard 19(6):1129–1149

Wehbe Y, Tessendorf SA, Weeks C, Bruintjes R, Xue L, Rasmussen RM, Lawson P, Woods S, Temimi M (2021) Analysis of aerosol-cloud interactions and their implications for precipitation

formation using aircraft observations over the United Arab Emirates. Atmospheric Chemistry and Physics Discussions:1–28
Wen Y (2015) Towards Improved QPE by Capitalizing Ground-and Space-based Precipitation Measurements
Weston M, Chaouch N, Valappil V, Temimi M, Ek M, Zheng W (2019) Assessment of the sensitivity to the thermal roughness length in Noah and Noah-MP land surface model using WRF in an arid region. Pure Appl Geophys 176(5):2121–2137
Willmott CJ, Matsuura K, Legates D (2001) Terrestrial air temperature and precipitation: Monthly and annual time series (1950–1999). Center for climate research version 1
Willmott CJ, Robeson SM (1995) Climatologically aided interpolation (CAI) of terrestrial air temperature. Int J Climatol 15(2):221–229
Xiao R, Chandrasekar V Multiparameter radar rainfall estimation using neural network techniques. In: Conference on Radar Meteorology, 27 th, Vail, CO, 1995. pp 199–201
Xiao R, Chandrasekar V (1997) Development of a neural network based algorithm for rainfall estimation from radar observations. IEEE Trans Geosci Remote Sens 35(1):160–171
Yan E, Milewski A, Sultan M, Abdeldayem A, Soliman F, Abdel Gelil K Remote sensing based approach to improve regional estimation of renewable water resources for sustainable development. In: Proceedings of US-Egypt workshop on space technology and geo-information for sustainable development, Cairo, Egypt, 2010. pp 14–17
Yousef LA, Temimi M, Molini A, Weston M, Wehbe Y, Al Mandous A (2020) Cloud Cover over the Arabian Peninsula from Global Remote Sensing and Reanalysis Products. Atmos Res 238:104866
Yousef LA, Temimi M, Wehbe Y, Al Mandous A (2019) Total cloud cover climatology over the United Arab Emirates. Atmos Sci Lett:e883
Zhao J, Temimi M, Ghedira H (2015) Characterization of harmful algal blooms (HABs) in the Arabian Gulf and the Sea of Oman using MERIS fluorescence data. ISPRS J Photogram Remote Sens 101:125–136
Zhao J, Temimi M, Ghedira H, Hu C (2014) Exploring the potential of optical remote sensing for oil spill detection in shallow coastal waters-a case study in the Arabian Gulf. Opt Expr 22(11):13755–13772

A Technical Note on Least Squares Mascon Fitting to GRACE Satellite Data to Estimate Total Water Storage Changes in the Middle East

Zohreh Safdari, Gholamreza Joodaki, and Hossein Nahavandchi

1 Introduction

The concept "mascon" stands for "mass concentration" and is a user-defined region of the Earth's surface. It originates from Muller and Sjogren (1968), who have used mascons to model the gravity field of the moon. There are three classes of GRACE mascon solutions that are used to study time-variable gravity. The first class of mascon solution is one in which an analytic expression for the mass concentration function is provided, and explicit partial derivatives relating the inter-satellite range-rate measurements to the analytic mascon formulation are used to directly estimate mass variations. An example of this first type of mascon solution is found in Ivins et al. (2011), where spherical cap mascons are estimated directly from range accelerations to interpret the regional ice mass loss and Glacial Isostasy Adjustment (GIA) processes. The second class of mascon solution comes from the group at NASA Goddard Space Flight Center (Luthcke et al. 2006, 2013; Rowlands et al. 2010; Sabaka et al. 2010). This type of mascon solution shares commonality with the first type of mascon solution in the sense that the mascon basis functions are directly related to the inter-satellite range-rate measurements through explicit partial derivatives, which are used in the gravity estimation. The difference is that each mascon basis function is represented by a finite truncated spherical harmonic expansion, rather than an analytical expression, such that the functional representation of each mascon has signal power outside of the mascon boundary. Finally, the third class of so-called "mascon" solution or "Least Squares Mascon Fitting (LSMF)" are when users fit mass elements to spherical harmonic coefficients (Stokes coefficients from GRACE level 2 solutions) to reduce satellite measurement error, leakage error, and

Z. Safdari · H. Nahavandchi
Norwegian University of Science and Technology (NTNU), Trondheim, Norway

G. Joodaki (✉)
Norwegian University of Life Sciences (NMBU), Ås, Norway
e-mail: gholamreza.joodaki@nmbu.no

A. Shaban (ed.), *Satellite Monitoring of Water Resources in the Middle East*,
Springer Water, https://doi.org/10.1007/978-3-031-15549-9_8

correlated error (striping error). These are not true mascon solutions in the sense that there is no direct relation between the formulation of the mass elements and the inter-satellite range-rate measurements (i.e., there are no explicit partial derivatives relating the observations to the state). Examples of this type of mascon solution include (Tiwari et al. 2009; Jacob et al. 2012; Schrama et al. 2014; Velicogna et al. 2014; Joodaki et al. 2014). In this chapter, we explain the third class of mascon solution in details and how it can be used to estimate TWS changes in a regional and a basin scale.

2 GRACE Data

The GRACE satellite mission was launched in March 2002 by NASA and the German Aerospace Center (DLR) (Tapley et al. 2004). It ended in October 2017, but the GRACE project has been continued by lunching GRACE Follow-On mission in May 2018. The GRACE project consists of two satellites, flying at an altitude of 450–500 km in identical near-polar orbits (89.5° inclination), with a separation distance of about 250 km. Continuous microwave measurements of the range between the two satellites, combined with data from on-board accelerometers and Global Positioning System (GPS) receivers, are used by the GRACE Project to determine global, monthly solutions for the Earth's gravity field at scales of a few hundred kilometers and greater. Those fields are derived as monthly sets of spherical harmonic ("Stokes") coefficients, and are made publicly available by the GRACE Project. These coefficients can be used to estimate month-to-month changes in mass stored on or near the Earth's surface, integrated over regions of a few hundred km or larger in scale (e.g., Wahr et al. 1998). The ability to observe an entire regional mass change without the need of spatial interpolation is a major strength of GRACE. But the lower bound on its resolution means that GRACE cannot determine precisely where the mass change within the region is coming from. In addition, GRACE can only deliver variations in water storage, not the total water storage itself.

2.1 Low Degree Stokes Coefficients (n = 0, 1, 2)

Because of the degree-0 Stokes coefficient is proportional to the total mass of the Earth and atmosphere, it is assumed constant, and it is not used in the computations of the time series of TWS changes. The geocenter motion is showed by the changes in degree-1 Stokes coefficients which cannot be derived from GRACE data. The absence of the geocenter motion might introduce an error in the TWS changes estimates (Chambers et al. 2004; Chen et al. 2005). Degree-1 Stokes coefficients can be computed as described by Swenson et al. (2008). The lowest-degree zonal harmonics, C_{20} Stoke coefficient is related to the Earth's oblateness. Because of the

relative short separation length between the two GRACE Spacecrafts, the C_{20} coefficient cannot be well determined by GRACE. The C_{20} values provided in the level-2 data also show anomalous variability (e.g., Chen et al. 2005). Therefore, the monthly Satellite Laser Ranging (SLR) values for C_{20} coefficients derived from five SLR satellites (LAGEOS-1 and 2, Starlette, Stella and Ajisai) (Cheng et al. 2013) are used to replace the estimates from GRACE. This method is a well-established technique for determining independent degree-2 coefficients. The degree-1 coefficients, and SLR C_{20} coefficients and their associated standard deviations are continuously provided in the GRACE project Technical Notes (ftp://podaac.jpl.nasa.gov/pub/grace/doc).

2.2 Ocean's Gravity Contributions on Lakes and Water Reservoirs

The GRACE Project uses a global ocean model to remove the ocean's gravity contributions from the raw GRACE data before solving for the Stokes coefficients. But in that model, signals from large lakes and water reservoirs are not included, so there are nonnegligible signals in those areas which should be removed. The signal for each lake/water reservoir can be removed by computing the Stokes coefficients caused by a uniform 1 m rise of lake/water reservoir, and then scaling those coefficients using monthly altimeter estimates (Birkett et al. 2009) (http://www.pecad.fas.usda.gov/cropexplorer/global_reservoir/) of the lake/water reservoir surface height (see Swenson and Wahr 2007).

3 Least Squares Mascon Fitting (LSMF) Solution

Mascon is a user-defined area of Earth's surface and more than one mascon is necessary for this solution. In this solution, mascon amplitudes are fitted to the GRACE Stokes coefficients to obtain estimates of the monthly mass variability of each mascon. For each mascon, the set of Stokes coefficients are found such that they would be resulted by a unit mass distributed uniformly over that mascon. Let the degree n and order m Stokes coefficients for mascon i be (C^{i}_{nm}, S^{i}_{nm}). Let the actual, but unknown, mass of mascon i be M_i. The M_is for all mascons are estimated by fitting them simultaneously to the GRACE monthly Stokes coefficients.

Let $(\Delta C_{nm}, \Delta S_n m)$ be the GRACE Stokes coefficients at time t, after removing the mean of all monthly solutions. The mean must be removed because otherwise contributions from the Earth's interior, which dominate the mean signal, would be misinterpreted as surface mass signals. As a result, GRACE can be used to determine change of total water storage, but not total water storage. Before fitting, the GRACE Stokes coefficients and the Stokes coefficients for each mascon are multiplied by $W_n(2n + 1)/(1 + k_n)$, where W_n are the coefficients of the Gaussian smoothing

function, and the k_n are load Love numbers to transform these geoid coefficients into smoothed spherical harmonic coefficients of mass (Wahr et al. 1998). A Gaussian smoothing function is applied to the Stokes coefficients to reduce the noise in the monthly M_i time series. These modified Stokes coefficients are denoted with asterisks (i.e. $\Delta C^{*}_{nm}(t)$, $C^{*,i}_{nm}$ etc.) and the $\{M_i(t)\}$ are found such that they minimize the standard least squares merit function:

$$E = \sum_{n,m} [\left(\Delta C^{*}_{nm}(t) - \sum_{i} C^{*,i}_{nm} M_i(t) \right)^2 + \left(\Delta S^{*}_{nm}(t) - \sum_{i} S^{*,i}_{nm} M_i(t) \right)^2 \quad (1)$$

For each monthly time step, t, the $\{M_i(t)\}$ that minimize (1) solve

$$Y_j(t) = \sum_{i} B_{ji} M_i(t) \quad (2)$$

where

$$Y_j(t) = \sum_{nm} \Delta C^{*}_{nm}(t) C^{*,j}_{nm} + \Delta S^{*}_{nm}(t) S^{*,j}_{nm} \quad (3)$$

$$B_{ji} = \sum_{nm} C^{*,j}_{nm} C^{*,i}_{nm} + S^{*,j}_{nm} S^{*,i}_{nm} \quad (4)$$

The solution to (2) is

$$M_i(t) = \sum_{j} B^{-1}_{ij} Y_j(t) \quad (5)$$

Ideally, the solution for $M_i(t)$ would recover the true spatial average of mascon i's mass: It means a spatial average that samples every point inside the mascon with a sensitivity of 1, and every point outside with a sensitivity of 0. Unfortunately, because of the finite number of harmonic degrees in the GRACE solution (for example, $n_{max} = 60$ for CSR solutions), this is not the case. It is possible to determine the sensitivity kernel of each mascon solution, which not only provides insight into possible biases in those solutions but also can help when deciding how to choose mascon sizes, shapes, and locations.

Let $\Delta\sigma(\vartheta\lambda, t)$ be the surface mass at co-latitude ϑ, longitude λ, and time t. Because the inverted mascon masses, M_i, , are linearly related to the GRACE coefficients (through (5)), and those coefficients are linearly related to t (through Newton's Law of Gravity), there must be a linear relation between each M_i and t. The most general linear relation has the form

$$M_i(t) = \sum_{nm} \left[A^{C,i}_{nm} \Delta C_{nm}(t) + A^{S,i}_{nm} \Delta S_{nm}(t) \right] \quad (6)$$

where $A_i(\vartheta, \lambda)$ is the sensitivity kernel for mascon i, and would ideally equal 1 for points inside the mascon and 0 outside, and a is the mean radius of the Earth. In order to explain about $A_i(\vartheta, \lambda)$, note that Eqs. (2)–(4) imply a linear relation between M_i and the GRACE Stokes coefficients:

$$M_i(t) = \sum_{nm} \left[A_{nm}^{C,i} C_{nm}(t) + A_{nm}^{S,i} \Delta S_{nm}(t) \right] \tag{7}$$

where the factors $A_{nm}^{C,i}, A_{nm}^{S,i}$ can be determined as described below. The relation between the Stokes coefficients and $\Delta\sigma(\vartheta, \lambda, t)$, implied by Newton's Law of Gravity, is (Wahr et al. 1998)

$$\begin{pmatrix} \Delta C_{nm}(t) \\ \Delta S_{nm}(t) \end{pmatrix} = \frac{3(k_n+1)}{4\pi\rho_{ave} a^3 (2n+1)} \int \Delta\sigma(\vartheta, \lambda, t) P_{nm}(cos\vartheta) \begin{pmatrix} cos(m\lambda) \\ sin(m\lambda) \end{pmatrix} a^2 sin\vartheta \, d\vartheta \, d\lambda \tag{8}$$

where the $P_{nm}(cos\vartheta)$ are Associated Legendre functions, and ρ_{ave} is the Earth's mean density. Putting (8) into (7) gives

$$M_i(t) = \int \Delta\sigma(\vartheta, \lambda, t) a^2 sin\vartheta \, d\vartheta \, d\varphi \sum_{nm} \frac{3(k_n+1)}{4\pi\rho_{ave} a^3 (2n+1)} P_{nm}(cos\vartheta)(A_{nm}^{c,i}(t) cos(m\lambda) + A_{nm}^{s,i} sin(m\lambda)) \tag{9}$$

Comparing (9) with (6), the sensitivity Kernel is:

$$A_i(\vartheta, \lambda) = \sum_{nm} P_{nm}(cos\vartheta) \left(A_{nm}^{C,i} cos(m\lambda) + A_{nm}^{S,i} sin(m\lambda) \right) \frac{3(k_n+1)}{4\pi\rho_{ave} a^3 (2n+1)} \tag{10}$$

Consequently, the sensitivity kernel can be determined from knowledge of $A_{nm}^{C,i}$ and $A_{nm}^{S,i}$. We can determine these terms numerically, as follows.

Define a synthetic set of Stokes coefficients, where $\Delta C_{n'm'}(t) = 1$ for a single (n', m'), and all other Stokes coefficients are 0. Apply the fitting procedure described in (3)– (5) to this simple set of Stokes coefficients. From (7) we know the result for $M_i(t)$ equals $A_{n'm'}^{c,i}$. Repeating this for each (n', m'), and then for the $\Delta S_{n'm'}$'s as well, yields every $A_{n'm'}^{c,i}$, and $A_{n'm'}^{s,i}$, one at a time, which can then be put into (10) to obtain the sensitivity kernel. These steps can be repeated for every mascon i. It can be shown that the mascon sensitivity kernels have the following useful property. Let i and j represent any two mascons used in a simultaneous mascon fit, and let $A_i(\vartheta, \varphi)$ be the sensitivity kernel for mascon i. Then

$$\frac{1}{S_j} \int_{S_j} A_i(\vartheta, \pi) sin\vartheta \, d\vartheta \, d\varphi = \sigma_{i,j}$$

where S_j is the surface area of mascon j: it means that the area-averaged sensitivity kernel of a mascon is 1 over itself and 0 over any other mascon used in the simultaneous inversion. This implies that if a mass anomaly is distributed uniformly across a mascon, the solution for that mascon will deliver the true mascon average, and that this mass anomaly will not contaminate the solution for any other mascon.

4 Results

4.1 Time Series Estimates in the Middle East

By using LSMF solution, as described in Sect. 3, to 114 months, from February 2003 to December 2012, of GRACE Release 05 Stokes coefficients, from the Center for Space Research (CSR) at the University of Texas (data available at http://podaac.jpl.nasa.gov), we construct time series of GRACE TWS changes for specific regions of the Middle East, chosen largely to coincide with political boundaries. The entire region is subdivided into seven mascons: Iran, Iraq, Syria, eastern Turkey (east of 35° longitude), northern and southern Saudi Arabia (north and south of 25° latitude), and the region immediately west of the Caspian Sea (Fig. 1).

As mentioned in Sect. 2, the GRACE data is modified with replacing the low degree coefficients and removing the signal from the Caspian Sea and from two large lakes in the region: Lake Tharthar in Iraq and Lake Urmieh in Iran. The Stokes coefficients are contaminated with short-wavelength noises that have striping pattern (Kusche et al. 2009). In this case study, de-striping of the coefficients is done by using a 100 km Gaussian smoothing function. The use of a smaller Gaussian radius instead of a decorrelation filter results in noisier monthly time series but improves the characteristics of sensitivity kernels (Eq. 10). Figure 2, for example, shows the sensitivity kernel for the Iran mascon, when fitting all seven mascons to the Stokes

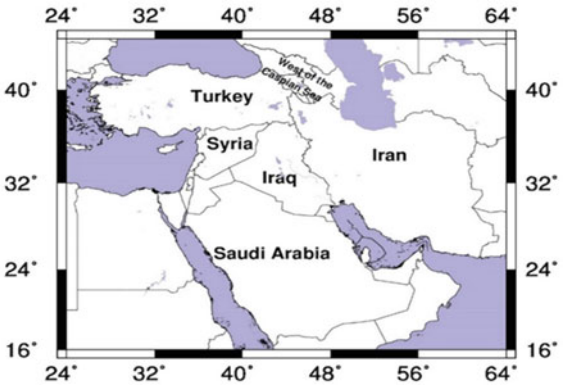

Fig. 1 The mascons which have been used to estimate time series of TWS changes in the Middle East

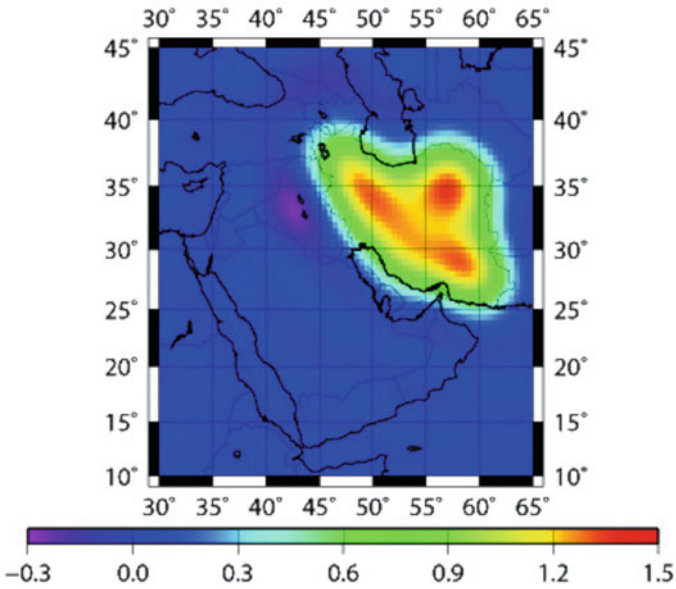

Fig. 2 The sensitivity kernel for Iran

coefficients. The kernel's value is small outside Iran and is close to unity inside Iran, but it does depart somewhat from those ideal values.

Figure 3 compares the GRACE estimate of total water storage variability for Iran, with a land surface model such as version 4.5 of the Community Land Model (CLM4.5) (Oleson et al. 2013). To extract a seasonally varying time series from the GRACE TWS and the total CLM4.5 water storage output, 12-month and 6-month periodic terms are fitted to both data sets across a 13-month sliding window. The black and red curves show result that have been smoothed to reduce sub-seasonal noise; the blue and green curves show the long-period (i.e. interannual and secular) components of the black and red curves. Note that the GRACE and model results agree well at seasonal periods, and they both show a sharp decrease in water storage that started with the onset of the drought, in 2007. The model results seem to have leveled off, and even recovered some, by 2009. The GRACE results, however, show a continuing water loss. Since CLM4.5 does not include an anthropogenic component, we interpret the increasing difference between GRACE and CLM4.5 as evidence of post-2007 anthropogenic groundwater loss.

The GRACE results for the other mascons such as Iraq, eastern Turkey, northern and southern Saudi Arabia all agree well with the CLM4.5 results at seasonal periods and their long-period components show a similar abrupt decrease in 2007 (Fig. 4). In eastern Turkey the GRACE results subsequently recover, though not as rapidly as the CLM4.5 results.

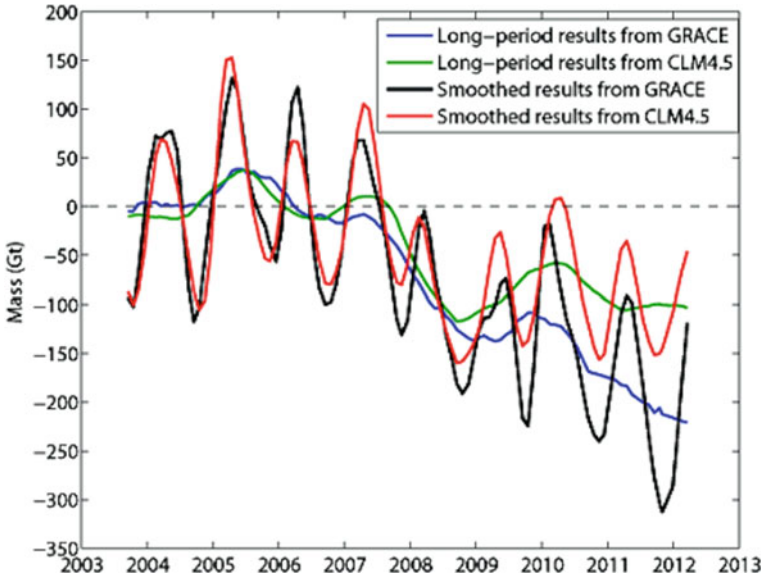

Fig. 3 Changes in TWS, in gton, for Iran

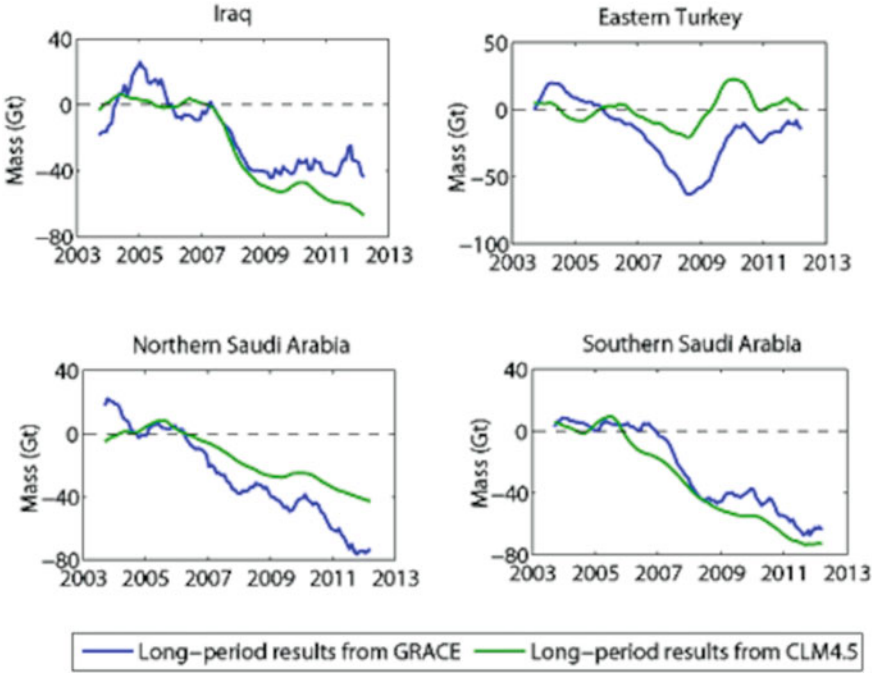

Fig. 4 Changes in TWS, in gton, for Iraq, Eastern Turkey, Northern and Southern Saudi Arabia

4.2 Time Series Estimates in Iran's Water Main Basins

Figure 5 shows six main water basins in Iran including: Caspian Sea basin (175,051 km^2), Urmieh lake basin (52,000 km^2), Persian Gulf and Oman sea basin (424,029 km^2), Central Plateau basin (825,000 km^2), Eastern Boundary basin (106,000 km^2), and Gharaghom basin (44,295 km^2). We estimate time series of GRACE TWS for each basin by using LSMF solution. We assume each basin as a mascon and fit mass amplitudes for each of these mascons, simultaneously, to the GRACE monthly data as described in Sect. 3. We thereby obtain monthly times series of mass variability for each of those basins during 2002–2017. Modifying the GRACE Stokes coefficients and the other necessary modifications such as removing the lake signal and smoothing radius are done as described in Sect. 4.1.

Because GRACE data have finite resolution, it is impossible to obtain a perfect unweighted average of mass variability within a basin, no matter what technique is used for the GRACE analysis or what basin is considered. Results from a mascon fitting method are no exception. For example, a GRACE estimate for the mass change in the central plateau basin will include contamination from mass variations outside it and will not weight every point inside it equally. Effects of mass variations outside the central plateau basin can be reduced by using a sensitivity kernel (Eq. 10) for the central plateau basin, when fitting all six mascons to the Stokes coefficients (Fig. 6).

Figure 7 compares changes in the GRACE TWS for the six main water basins of Iran, with variation of groundwater level data from observation wells. There are 17,865 active observation wells in the whole of Iran. To obtain time series of groundwater level changes in the six main water basins, each main water basin is divided into several sub-basins, and each sub-basin is divided into several study areas. The

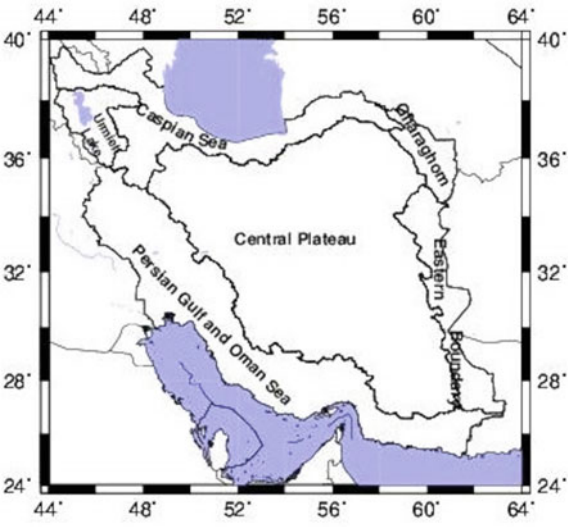

Fig. 5 Iran's main water basins

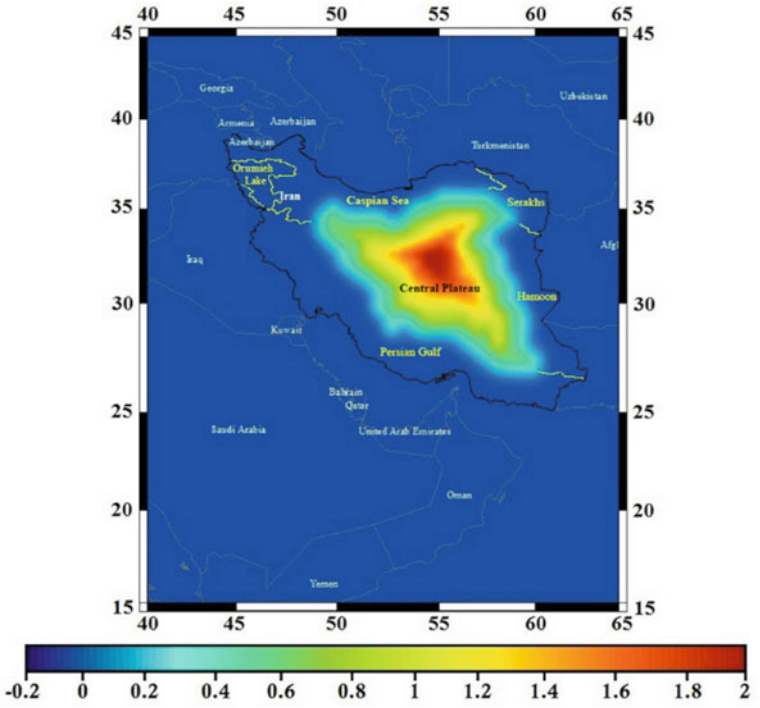

Fig. 6 The sensitivity kernel for the central plateau

Thiessen polygon method has been used to make a time series of the groundwater level changes across each study area. Then we scale up it for each study area by multiplying it by the ratio: $(\frac{\text{area of the study area}}{\text{area of the Thiessen polygon}})$.

The total change in groundwater storage across each sub-basin is computed by adding together the scaled change in groundwater storage of all its study areas. The same procedure is carried out for each main water basin. Note that the GRACE and well results both show a sharp decrease in water storage that started with the onset of the drought, in 2007 and most of the GRACE long-term water loss is due to a decline in groundwater storage. Using a smaller Gaussian radius results in noisier monthly time series and some fluctuation in the GRACE long-term variability.

4.3 Time Series Estimates of TWS from GRACE and GRACE FO in Iran's Main Water Basins

Figure 8 shows time series of water storage variability, in Million cubic meter (Mm^3), from GRACE and GRACE FO during 2002 to 2020 for six main water basins of Iran. As described in Sect. 4.2, mascons are chosen largely to coincide with boundaries

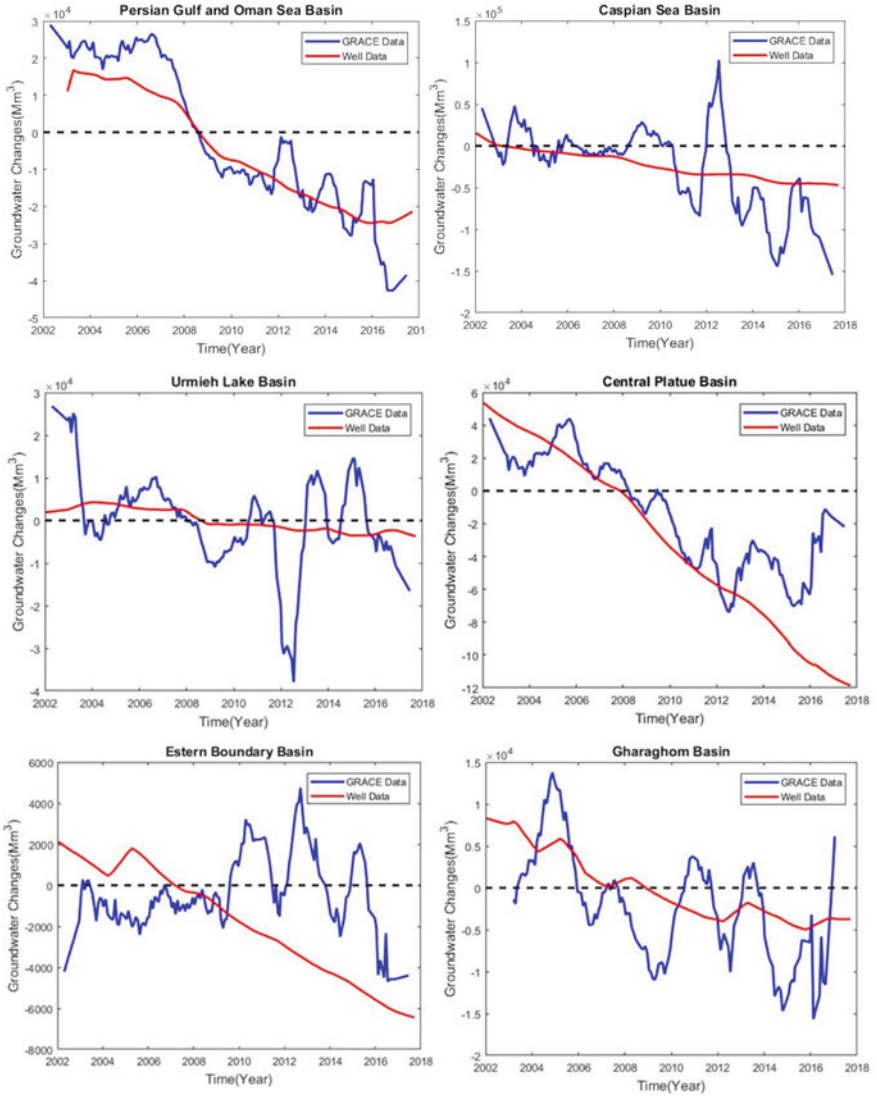

Fig. 7 Changes in GRACE TWS, in Million cubic meter (Mm^3), compared with monthly values inferred from the well data, across the Persian Gulf and Oman Sea basin, the Caspian Sea basin, Urmieh Lake, Central Plateau, Eastern Boundary, and Gharaghom basin respectively

of six main water basins of Iran (see Fig. 5). By using LSMF solution, as described in Sect. 3, to 163 months, from April 2002 to August 2017, of GRACE Release 06 Stokes coefficients, and to 15 months from May 2018 to October 2019, of GRACE FO Release 06 Stokes coefficients, both of the Center for Space Research (CSR) at the

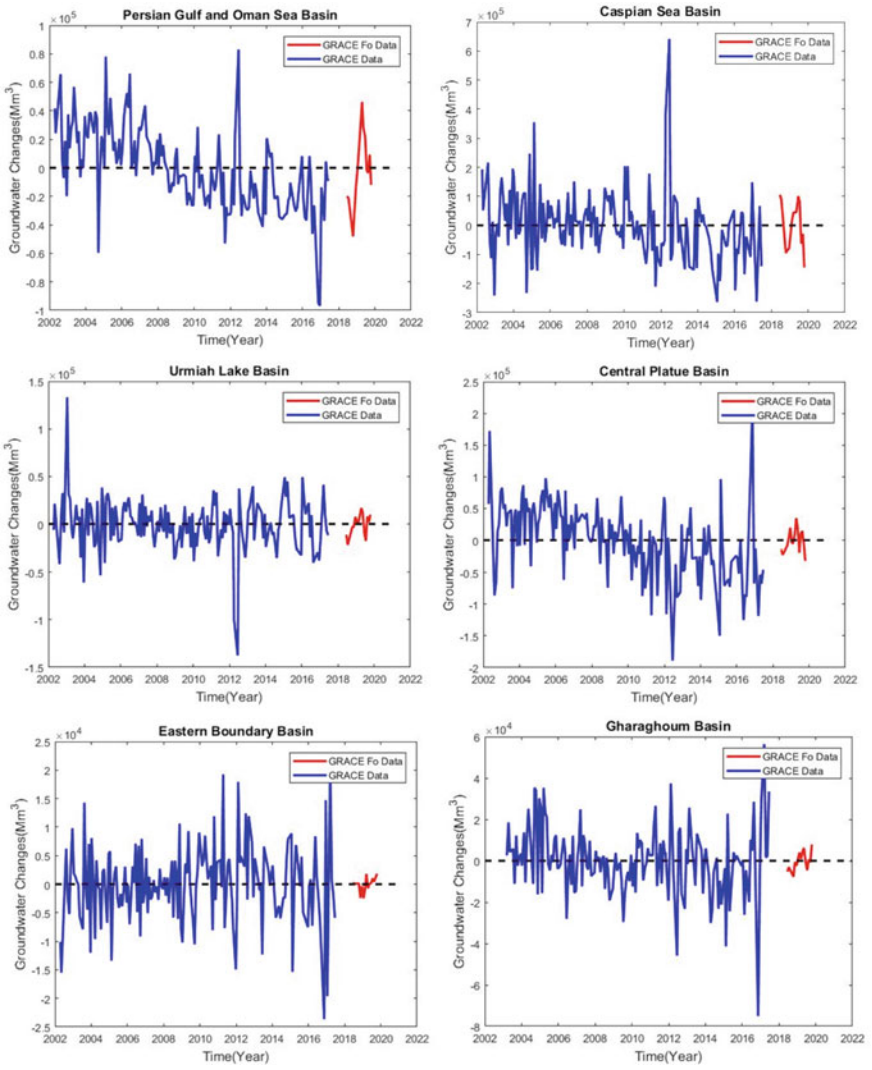

Fig. 8 Changes in GRACE/GRACE FO TWS, in Million cubic meter (Mm^3), across the Persian Gulf and Oman Sea basin, the Caspian Sea basin, Urmieh Lake, Central Plateau, Eastern Boundary, and Gharaghom basin respectively

University of Texas (data available at https://podaac-tools.jpl.nasa.gov/drive/files/allData), we construct time series of GRACE/GRACE FO TWS changes for the six main water basins. In order to include the degree-1 geocenter terms, we follow the methodology of Swenson et al. (2008). The degree-1 coefficients are recalculated consistently for each GRACE/GRACE-FO solution. We replace the GRACE/GRACE FO results for the lowest-degree zonal harmonic coefficient, $C_{20,}$ with those obtained

from Satellite Laser Ranging (Cheng et al. 2013). All harmonics are smoothed with a 100 km radius Gaussian smoothing function (Wahr et al. 1998). In all of the water basins, time series of water storage variability from GRACE/GRACE FO line up well across the data gap from mid-2017 to mid-2018. The GRACE/GRACE FO results consist mainly of short-period, seemingly random fluctuations, superimposed on long-period variability. The short period fluctuations represent the effects of GRACE/GRACE FO measurement errors and month-to-month errors in the modeled water storage quantities. The long-period variability, which stands out more clearly after smoothing the GRACE/GRACE FO results, represents changes in total water storage. The most obvious characteristic of that variability is a steady groundwater loss during this 18-year period.

5 Summary and Conclusions

Total Water Storage (TWS) is a basic element of the hydrological cycle and a key state variable for land surface-atmosphere interaction. However, measuring TWS in a comprehensive way for different storage compartments and beyond the point scale is a challenge. Gravity measurements are influenced by water storage due to the Newtonian attraction of masses. Observations of temporal gravity changes provide a direct and depth-integrated measure of water storage change. GRACE and GRACE Follow On (GRACE FO) missions are two valuable satellite missions for measuring of temporal gravity changes. A standard method to compute time series of TWS changes using temporal satellite gravity data, named spherical harmonics solution, has been described in Wahr et al. (1998). In this chapter, we have demonstrated the Least Squares Mascon Fitting (LSMF) solution to GRACE and GRACE FO data to estimate time series of TWS changes in two spatial scales: at a regional scale in the Middle East and at a basin scale in the six main water basins of Iran. The results show that the LSMF technique is a useful method to estimate time series of TWS changes using the satellite gravity data in both basin and regional scales. The GRACE and GRACE FO data line up across the data gap at a basin scale.

References

Birkett CM, Reynolds C, Beckley B, Doorn B (2009) From research to operations: The USDA global reservoir and lake monitor. Springer Verlag, In Coastal altimetry, Heidelberg

Chambers D, Wahr J, Nerem R (2004) Preliminary observations of global ocean mass variations with GRACE. Geophys Res Lett 31:L13310. https://doi.org/10.1029/2004GL020461

Chen J, Wilson C, Famiglietti JS, Rodell M (2005) Spatial sensitivity of the gravity recovery and climate experiment (GRACE) time-variable gravity observations J Geophys Res 110 B08408, doi:https://doi.org/10.1029/2004JB003536

Cheng MK, Tapley BD, Ries JC (2013) Deceleration in the Earth's oblateness. J Geophys Res 118:1–8. https://doi.org/10.1002/jgrb.50058

Ivins ER, Watkins MM, Yuan DN, Dietrich R, Casassa G, Rülke A (2011) On-land ice loss and glacial isostatic adjustment at the Drake Passage: 2003–2009. J Geophys Res 116:B02403. https://doi.org/10.1029/2010JB007607

Jacob T, Wahr J, Pfeffer WT, Swenson S (2012) Recent contributions of glaciers and ice caps to sea level rise. Nature 482:514–518. https://doi.org/10.1038/nature10847

Joodaki G, Wahr J, Swenson S (2014) Estimating the human contribution to groundwater depletion in the middle east, from GRACE data, land surface models, and well observations. Water Resour Res 50(3):2679–2692

Kusche J, Schmidt R, Petrovic S, Rietbroek R (2009) Decorrelated GRACE time-variable gravity solutions by GFZ, and their validation using a hydrological model. J Geodesy 83(10):903–913

Luthcke SB, Zwally HJ, Abdalati W, Rowlands DD, Ray RD, Nerem RS, Lemoine FG, Mccarthy JJ,Chinn DS (2006) Recent greenland ice mass loss by drainage system fromsSatellite gravity observations Science 1286–1289

Luthcke SB, Sabaka TJ, Loomis BD, Arendt AA, McCarthy JJ, Camp J (2013) Antarctica, Greenland and gulf of Alaska land-ice evolution from an iterated GRACE global mascon solution. J Glaciol 59(216):613–631

Muller PM, Sjogren WL (1968) Mascons: lunar mass concentrations. Science 161(3842):680–684. https://doi.org/10.1126/science.161.3842.680 PMID: 17801458

Oleson KW, Lawrence DM, Bonan GB, Drewniak B, Huang M, Koven CD, Levis S, Li F, Riley WJ, Subin ZM, Swenson SC, Thornton PE, Bozbiyik A, Fisher R, Heald CL, Kluzek E, Lamarque J-F, Lawrence PJ, Leung LR, Lipscomb W, Muszala S, Ricciuto DM, Sacks W, Sun Y, Tang J, and Yang ZL (2013) Technical description of version 4.5 of the Community Land Model (CLM), NCAR Technical Note NCAR/TN-503+STR, 434 pp

Rowlands DD, Luthcke SB, McCarthy JJ, Klosko SM, Chinn DS, Lemoine FG, Boy JP, Sabaka TJ (2010) Global mass flux solutions from GRACE: a comparison of parameter estimation strategies—Mass concentrations versus Stokes coefficients. J Geophys Res 115:B01403. https://doi.org/10.1029/2009JB006546

Sabaka TJ, Rowlands DD, Luthcke SB,Boy JP (2010) Improving global mass flux solutions from gravity recovery and climate experiment (GRACE) through forward modeling and continuous time correlation. J Geophys Res 115 (B11): B11403 [https://doi.org/10.1029/2010JB007533]

Schrama EJO, Wouters B, Rietbroek R (2014) A mascon approach to assess ice sheet and glacier mass balances and their uncertainties from GRACE data. J Geophys Res Solid Earth 119:6048–6066. https://doi.org/10.1002/2013JB010923

Swenson S, Wahr J (2007) Multi-sensor analysis of water storage variations of the Caspian Sea. Geophys Res Letter 34:L16401. https://doi.org/10.1029/2007GL030733

Swenson S, Chambers D, Wahr J (2008) Estimating geocenter variations from a combination of GRACE and ocean model output. J Geophys Res 113(B08410):2008. https://doi.org/10.1029/2007JB005338

Safdari Z (2021) Groundwater level monitoring across Iran's main water basins using temporal satellite gravity solutions and well data, PhD Thesis, NTNU, Norway.

Tapley BD, Bettadpur S, Watkins M, Reigber C (2004) The gravity recovery and climate experiment: mission overview and early results. Geophys Res Lett 31:L09607. https://doi.org/10.1029/2004GL019920

Tiwari VM, Wahr J, Swenson S (2009) Dwindling groundwater resources in northern India, from satellite gravity observations. Geophys Res Lett 36:L18401. https://doi.org/10.1029/2009GL039401

Velicogna I, Sutterley TC, Van Den Broeke MR (2014) Regional acceleration in icemass loss from Greenland and Antarctica using GRACE time-variable gravity data. J Geophys Res Space Physics 41:8130–8137. https://doi.org/10.1002/2014GL061052

Wahr J, Molenaar M, Bryan F (1998) Time variability of the Earth's gravity field: hydrological and oceanic effects and their possible detection using GRACE. J Geophys Res 103 30 205–230,229

Spatial–Temporal Change of a Dam Lake Using Remote Sensing and Meteorological Drought Indices

Emre Özelkan

1 Introduction

Drought, defined as lack of water in a certain period, is a natural disaster of meteorological origin that affects our lives dramatically in ecological, sociological, economic and many other areas (Özelkan 2016; Özelkan 2019a). Drought progresses slowly, its beginning and end are very difficult to predict, and its effects continue for a long time (Wilhite 2020). Drought first affects natural resources such as water, agricultural area and forest. An increasing population, the increased need for natural resources and excessive consumption have made combating drought more important than ever, especially in arid and semi-arid climatic regions (Genc et al. 2011; Çamoğlu et al. 2018; Çakaroz et al. 2020).

Drought is a four-stage process that begins with a lack of precipitation, and its first stage is called meteorological drought (Mishra et al. 2010; Özelkan 2019a). The second stage is hydrological drought, expressed as a shortage of water resources (Mishra et al. 2010; Kapluhan 2013; Özelkan 2019a). The third stage is agricultural drought, which refers to the adverse conditions in agricultural production such as loss of product and yield (Mishra et al. 2010; Kapluhan 2013; Özelkan 2019a). The last stage of drought is the impact of meteorological, hydrological and agricultural drought on social and economic life (unemployment, migration, economic depression, unrest, poverty, etc.) and this is referred to as socio-economic drought (Mishra et al. 2010; Kapluhan 2013; Özelkan 2019a). Considering the destructive effects, every stage of drought should be carefully examined, modeled and necessary precautions should be taken. In this context, the present research examined the effect of meteorological drought on water resources.

E. Özelkan (✉)
Faculty of Architecture and Design, Department of Urban and Regional Planning, School of Graduate Studies, Risk Management of Natural Disasters Program, Çanakkale Onsekiz Mart University, 17020 Çanakkale, Turkey
e-mail: emreozelkan@comu.edu.tr

A. Shaban (ed.), *Satellite Monitoring of Water Resources in the Middle East*,
Springer Water, https://doi.org/10.1007/978-3-031-15549-9_9

The most common methods used to determine meteorological drought are meteorological drought indices, which are calculated according to equations that include meteorological parameters such as temperature, precipitation and humidity (Mohammed and Scholz 2017). Some of the major meteorological drought indices can be listed as Standard Precipitation Index (SPI) (McKee et al. 1993), Standard Precipitation Evapotranspiration Index (SPEI) (Vicente-Serrano et al. 2010), Percent of Normal Index (PNI) (Willeke 1994), Reconnaissance Drought Index (RDI) (Tsakiris 2005) and Palmer Drought Severity Index (Palmer 1965). The cumulative deviation curve is a frequently preferred method to determine the change and behavior of drought from past to present and to make predictions for the future (Liu et al. 2019; Özelkan 2019a, b). In addition to meteorological drought, excessive evapotranspiration and human activities (daily consumption, irrigation, energy production, etc.) that occur in water resources such as lakes and streams may also cause hydrological drought (Li et al. 2017; Veijalainen et al. 2019). Losses that occur in water resources can be determined by many methods such as water level measurements (Yıldız and Deniz 2005), hydrometeorological calculations (Penman–Monteith, Thornthwaite, etc.) (Lang et al. 2017), empirical open water surface evaporation calculations (Dalton, Meyer, etc.) (Gorjizade et al. 2014), water balance and budget calculations (Yaykiran et al. 2019), heat and mass transport (Zannouni et al. 2017), and energy balance (Duan and Bastiaanssen 2017).

In the monitoring and management of water resources, satellite remote sensing is frequently and successfully used (McFeeters 1996; Xu 2006; Özelkan 2019b; Karaman 2021). Satellite remote sensing, which can view wide areas at once and conveniently provide the rapid and detailed examination of large water bodies (Karaman et al. 2015; Kale and Acarlı 2019a, b; Karaman 2022). Therefore, remote sensing has become a very useful tool in determining and modeling hydrological drought (Özelkan and Karaman 2018a; Schultz and Engman 2019). Water indices produced from spectral bands of remote sensing data, with their simple algorithms, have become one of the most preferred methods for determining water bodies (Ji et al. 2015; Özelkan 2020). The normalized difference water index (NDWI), created by considering the difference between the high reflectance of water in the green region and the low reflection in the near infrared (NIR) region, is one of the most frequently used water body detection and analysis indices for satellite remote sensing (McFeeters 1996; Karaman and Özelkan 2022). Following these, many different water indices have been presented to determine water bodies, such as the modified NDWI (MNDWI) generated using the short-wave infrared (SWIR) instead of the NIR in the NDWI (Xu 2006), and the automated water extraction index (AWEI) that additionally considers reflection in the blue region (Feyisa et al. 2014). However, correlation and verification of the remote sensing findings with meteorological and hydrological drought indicators calculated by in-situ measurement values make remote sensing studies more meaningful (Özelkan and Karaman 2018a).

In this study, the spatial–temporal change of a dam lake area was monitored by satellite remote sensing and the influence of meteorological drought on this areal change was examined. The Atikhisar Dam Lake, which is near the city of Çanakkale and the only water source that feeds the region, was preferred as the study area. The

areal change of the dam lake was determined by using NDWI derived from multi-spectral Landsat satellite images. The temporal change of the drought is presented by the cumulative deviation curve. To determine meteorological drought, SPI and SPEI drought indices were utilised comparatively. The study covers the period between 1984 and 2020 and all calculations were made according to the 12-month water year calendar, which begins on the first day of October and ends at the end of September. In conclusion, this study reveals how successfully the areal change of a dam lake influenced also by anthropogenic effects such as daily consumption, irrigation and energy production, can be modeled by considering only the meteorological drought.

2 Materials and Methods

This section explains the general characteristics of the study area, meteorological and remote sensing data used, processing of these data, meteorological and remote sensing indices produced and how the analysis was carried out.

2.1 Study Area

Atikhisar Dam Lake is located between 26°31′2.22"–26°33′10.30"E eastern meridians and 40°3′49.67"–40°7′36.31" northern parallels and within Çanakkale province in the west of Turkey (Fig. 1). Atikhisar Dam Lake is the only water source of Çanakkale city and used for several purposes such as for drinking water, irrigation and flood protection (Akbulak et al., 2008; Koca, 2005). The dam was built between 1971 and 1975 as a body of earth fill on Sarıçay Creek, which is within the boundaries of the Sarıçay Basin (Akbulut et al. 2009). Saricay Basin covers an area of approximately 473 km^2 with a maximum height of 908 m and a slope of 45.7°. Saricay Creek is the longest stream in the basin and is approximately 43 km long and 8.5 km of it within the dam's limits. Saricay Creek then passes through the middle of the city and flows into the Çanakkale Strait (Dardanelles) (Özelkan 2020). Atikhisar Dam Lake is situated 11 km from Çanakkale city center, 60 m above sea level, has an area of more than 3 km^2 at normal water elevation, and an average volume of 40 hm^3 (Koca 2005). It has been recorded that the water availability in the dam lake has decreased to 10% of its normal level due to severe droughts experienced in the past (Koca 2005).

The study area is under the influence of the subtropical Mediterranean climate zone (Altan and Türkeş 2015). More particularly, the regional mild Marmara climate, a transition zone from the Black Sea to the Mediterranean, is experienced in the invetigated region (Şensoy et al. 2018). According to the long-term data of the Turkish State Meteorological Service, the most rainy month is December with an average monthly total of 106.8 mm, and the driest period is August with 6.4 mm. July is the hottest month with an average of 25 °C and the coldest month is January with 6.1 °C.

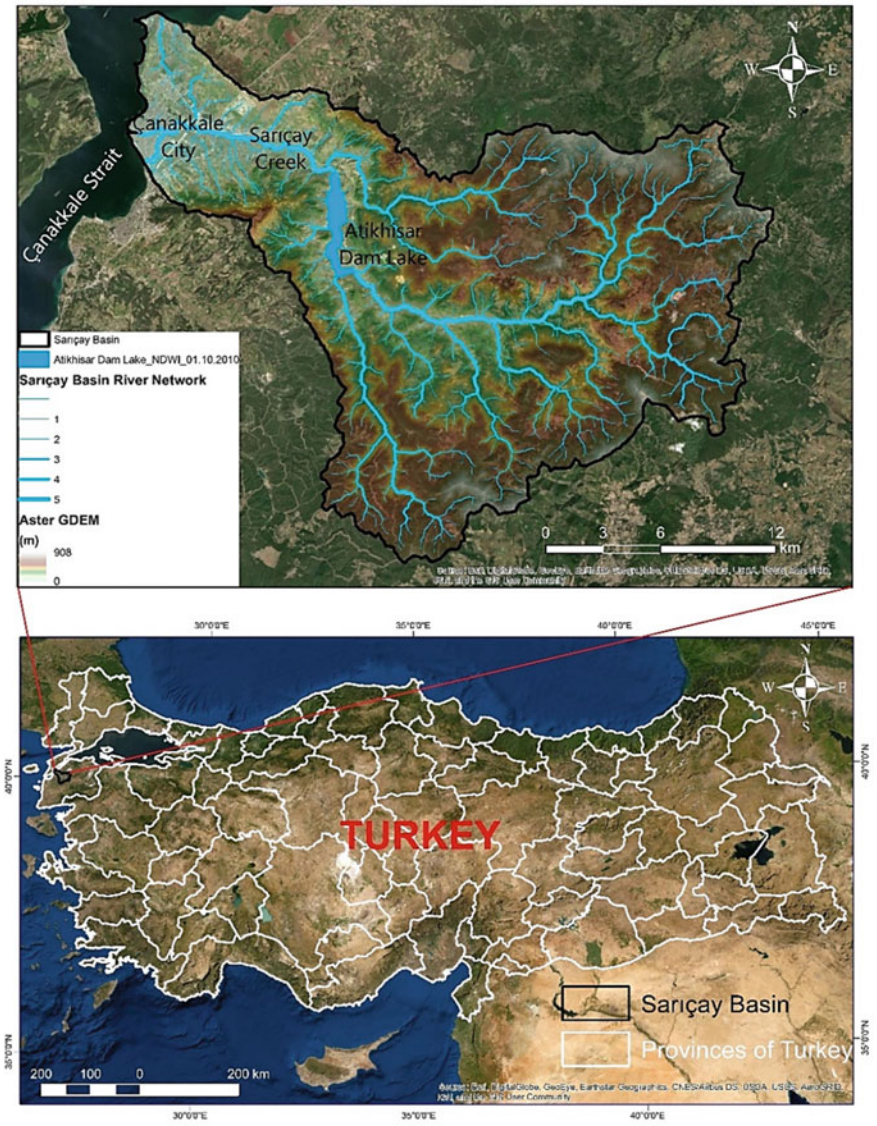

Fig. 1 Location of study area

Winds from the north cause low temperatures in winter while winds from the south bring precipitation to the region (Ilgar 2010). Around the dam lake vicinity are found the flora olea oleaster, laurus nobilis, guercus coccifera, rhus coriaria, pinus brutia and pinus nigra growing, which are maquis elements belonging to Mediterranean vegetation. In the northern slopes of the dam lake are the species guercus, fagus

orientalis and castanea sativaunder which thrive under the influence of humid mild forests (Koca 2005).

2.2 Meteorological Data and Pre-processing

The precipitation and temperature data measured between 1984 and 2020 at the meteorological station of the Turkish State Meteorological Service located in the center of Çanakkale city were used to determine the drought in the study area. All investigations were performed according to the 12-month water year calendar, starting at the beginning of October (i.e., beginning of rainy season) and ending at the end of September (i.e., end of dry season). For example, the 12-month period between October 1983 and September 1984 was included in the 1984 water year data.

The temporal change (length, frequency, trend, etc.) of the drought experienced in the region was firstly examined using the cumulative deviation curve. The cumulative deviation is calculated as the sum of deviations of the total precipitation for each period (water year in this study) from the long-term average of the investigated time interval (1984–2020 in this study) and reveals the dry and rainy periods in the time interval investigated (Sener et al. 2010; Özelkan and Karaman 2018b; Özelkan 2019a). The cumulative deviations are calculated using the Eq. 1 and graphically drawn as a function of t, with t = 1, 2, …, n (Karabulut 2015).

$$S_t = \sum_1^t (X_i - X_m) \tag{1}$$

where S_t is the sum of deviations, X_i is the total precipitation of each period, and X_m is the long-term average of the investigated time interval. The lower and upper safety limits of the precipitation and coefficient of variation (Cv), in which small values indicate regions with regular and enough precipitation, are used in the interpretation of the cumulative deviation, and are calculated by using X_m and standard deviation (σ) of the long-term data, as follows (Türkeş 2010; Yetmen 2013; Yolcubal 2019).

$$\text{Lower safety limit} = X_m - \sigma \tag{2}$$

$$\text{Upper safety limit} = X_m + \sigma \tag{3}$$

$$Cv = \sigma / X_m \tag{4}$$

The meteorological drought was determined by using the Standard Precipitation Index (SPI) and Standard Precipitation Evapotranspiration Index (SPEI). SPI

is computed by dividing the difference of the corresponding period's (water year in this study) (X_i) precipitation total from the long-term average (X_m) of totals by the standard deviation value (σ) calculated from the long-term data (McKee et al. 1993; Dhakar et al. 2013; Özelkan et al. 2016).

$$SPI = (X_i - X_m)/\sigma \tag{5}$$

SPEI takes into account both precipitation and temperature variability to predict drought conditions (Vicente-Serrano et al. 2010). The first step in calculating the SPEI proposed by Vicente-Serrano is to estimate the monthly potential evapotranspiration (PET) using the simple and useful Thornthwaite method (Vicente-Serrano et al. 2010; Danandeh and Vaheddoost 2020). Afterwards, the water surplus or deficit (D_i) of the corresponding month (i) is computed using the water balance equation that calculates the difference between precipitation (P_i) and PET_i (Vicente-Serrano et al. 2010; Danandeh and Vaheddoost 2020).

$$D_i = P_i - PET_i \tag{6}$$

Then, the evolved water deficit values (D_i) are standardized, and finally fitted to a log-logistic distribution (Vicente-Serrano et al. 2010; Danandeh and Vaheddoost 2020). The SPEI value of the corresponding month (i) is the standardized value of the exceeding probability (p) of a given D_i (Danandeh and Vaheddoost 2020).

$$SPEI = W_i - \frac{2.515517 + 0.802853W_i + 0.010328{W_i}^2}{1 + 1.432788W_i + 0.189269{W_i}^2 + 0.001308{W_i}^3} \tag{7}$$

If $p \leq 0.5$, $W_i = \sqrt{-2\ln(p)}$, and if $p > 0.5$, $W_i = \sqrt{-2\ln(1-p)}$, the sign of the resultant SPEI is reversed where p is the probability of exceeding a designated D value, and $p = 1 - F(x)$. SPI and SPEI can be used to study meteorological drought for 1, 3, 6, 9, 12 and 24-month periods (McKee 1993; Vicente-Serrano et al. 2010; Arslan et al. 2016; Osuch et al. 2016). In this study, 12-month SPI and SPEI values covering the water year were calculated. The positive values of the SPI and SPEI represent the rainy periods without drought, while the negative values represent the drought periods with less precipitation. The drought classes (i.e., climatic moisture categories) and values are shown in Table 1.

2.3 Remote Sensing Data and Pre-processing

A total of 33 multispectral Landsat satellite images (path/row: 173/34) with 16 bit radiometric and 30 m spatial resolution were obtained between 1984 and 2018 over the study area from the United States Geological Survey (USGS) data portal (Table 2). Note that all images are provided at the end of the water year to be consistent with

Table 1 Meteorological drought classes and values of SPI and SPEI (Liu et al. 2021)

Drought class	Drought values
Extremely wet	≥ 2
Severely wet	$1.5 \leq \text{SPI} \leq 1.99$
Moderately wet	$1.0 \leq \text{SPI} \leq 1.49$
Normal	$-0.99 \leq \text{SPI} \leq 0.99$
Moderate drought	$-1.49 \leq \text{SPI} \leq -1.00$
Severe drought	$-1.99 \leq \text{SPI} \leq -1.5$
Extreme drought	≤ -2.00

Table 2 List of Landsat satellite images used in study

No	Acquisition date	Satellite	Path/Row
1	07.09.1984	Landsat 5 TM	181/032
2	26.09.1985	Landsat 5 TM	181/032
3	13.09.1986	Landsat 5 TM	181/032
4	23.09.1987	Landsat 5 TM	182/032
5	25.09.1988	Landsat 5 TM	182/032
6	07.10.1989	Landsat 5 TM	181/032
7	01.10.1990	Landsat 5 TM	182/032
8	27.09.1991	Landsat 5 TM	181/032
9	29.09.1992	Landsat 5 TM	181/032
10	23.09.1993	Landsat 5 TM	182/032
11	19.09.1994	Landsat 5 TM	181/032
12	24.09.1996	Landsat 5 TM	181/032
13	04.10.1997	Landsat 5 TM	182/032
14	30.09.1998	Landsat 5 TM	181/032
15	17.09.1999	Landsat 5 TM	181/032
16	19.09.2000	Landsat 5 TM	181/032
17	30.09.2001	Landsat 7 ETM +	181/032
18	24.09.2002	Landsat 7 ETM +	182/032
19	05.10.2003	Landsat 5 TM	182/032
20	30.09.2004	Landsat 5 TM	181/032
21	03.10.2005	Landsat 5 TM	181/032
22	04.09.2006	Landsat 5 TM	181/032
23	30.09.2007	Landsat 5 TM	182/032
24	05.10.2009	Landsat 5 TM	182/032
25	01.10.2010	Landsat 5 TM	181/032
26	04.10.2011	Landsat 5 TM	181/032
27	30.09.2013	Landsat 8 OLI	182/032

(continued)

Table 2 (continued)

No	Acquisition date	Satellite	Path/Row
28	19.10.2014	Landsat 8 OLI	182/032
29	20.09.2015	Landsat 8 OLI	182/032
30	01.10.2016	Landsat 8 OLI	181/032
31	18.09.2017	Landsat 8 OLI	181/032
32	01.10.2019	Landsat 8 OLI	182/032
33	03.10.2020	Landsat 8 OLI	182/032

the drought index results. In 1995, 2008, 2012 and 2018, cloudless images could not be obtained at the end of the water year. However, 33 images were obtained consisting of 24 Landsat-5 Thematic Mapper (TM), 2 Landsat-7 Enhanced Thematic Mapper (ETM +) and 7 Landsat-8 Operational Land Imager (OLI) images. Furthermore, atmospheric and geometric corrections of all images representing surface reflectance were made by the vendor.

The NDWI of McFeeters (1996), which takes into account the high reflectance in the visible region and low reflectance in the infrared of the water, was preferred to determine the lake area, since NDWI gives better results in natural areas (i.e., water, vegetation, mud and soil) compared to MNDWI indices that work with SWIR (Özelkan 2020). NDWI ranges from −1 to 1 and values above 0 indicate water (McFeeters 1996). The NDWI index was first proposed for Landsat 5 TM (McFeeters 1996), then numerous water body determination studies were performed using Landsat 7 ETM + (Zhou et al. 2017; Özelkan 2019a) and Landsat 8 OLI (Özelkan 2019b; Yang et al. 2015). NDWI images are generated by replacing the second and fourth bands of Landsat 5 TM and Landsat 7 ETM + and the third and fifth bands of Landsat 8 OLI satellite images in Eq. 8, in which R means reflectance. The NDWI index is expressed in Eqs. 9, 10 and 11 with the center wavelengths in micrometers of green and NIR bands for each satellite as follows:

$$NDWI = \frac{(R_{Green} - R_{NIR})}{(R_{Green} + R_{NIR})} \tag{8}$$

$$NDWI_{Landsat5TM} = \frac{(R_{0.5690} - R_{0.8400})}{(R_{0.5690} + R_{0.8400})} \tag{9}$$

$$NDWI_{Landsat7ETM+} = \frac{(R_{0.5600} - R_{0.8350})}{(R_{0.5600} + R_{0.8350})} \tag{10}$$

$$NDWI_{Landsat8OLI} = \frac{(R_{0.5613} - R_{0.8646})}{(R_{0.5613} + R_{0.8646})} \tag{11}$$

2.4 Data Analysis

Between 1984 and 2018, at the end of the water year (i.e., at the end of the dry period), 33 lake area values extracted from NDWI created from Landsat satellite images were associated with 33 SPI and SPEI meteorological drought indices values respectively for the same period by correlation-regression analysis. In this context, Pearson's correlation coefficient (r) and significance probability (p) values of ANOVA (Analysis of Variance) (i.e., significance F (SF)) were calculated among the data sets. Additionally, root mean square error (RMSE) was used to determine the accuracy of the water body areas derived from NDWI compared to areas measured by the Turkish State Hydraulic Works.

3 Results and Discussion

In this section, the spatial–temporal change of meteorological drought and dam lake area will be examined, and the findings will be discussed by considering the field data and previous studies.

3.1 Meteorological Drought Analysis

The trend and frequency of the meteorological drought in the study area is presented by the cumulative deviation curve analysis (Fig. 2). The average precipitation in the study area, which is under the influence of the subtropical Mediterranean climate zone, is 581 mm and its standard deviation is 136 mm. The lower and upper safety limits of the precipitation are 718 mm and 445 mm, respectively. The 1985, 1990, 1992, 2007, 2008 and 2020 values are under the lower safety limit, and the minimum precipitation was experienced in 2008 with 333 mm. The precipitations of 1995, 1998, 2002, 2013 and 2018 were over the upper safety limits, and the maximum was experienced in 2013 with 844 mm. Between 1984 and 2020, 70.27% of the precipitation of 37 water years was found to be within the safety limits. The coefficient of variation (Cv) was found as 0.23, indicating that the region receives regular and sufficient precipitation. On the other hand, in the last two decades it has been observed that the difference between minimum and maximum precipitation has increased (i.e., the σ tends to grow) and the precipitation regime has begun to deteriorate, although there is a small increase in the average annual precipitation totals covering the long term. Change in precipitation patterns is an obvious indicator of climate change (Dore 2005; Kale and Acarlı 2019b). Moreover, small Cv value 0.23 indicates that changes in groundwater levels are also more regular in water wells located in such regions (Yolcubal 2019).

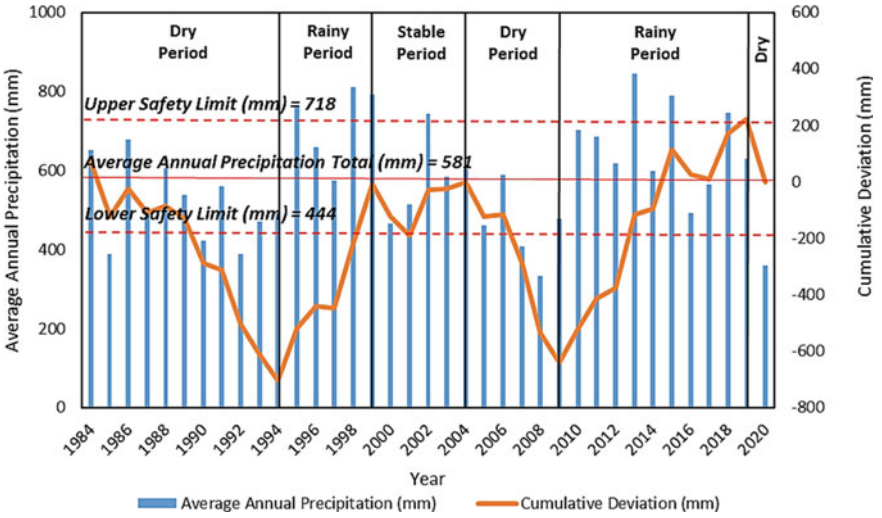

Fig. 2 Cumulative deviation curve from water year precipitation data between 1984 and 2020

According to the cumulative deviation curve graph created from the total water year precipitation data between 1984 and 2020 (Fig. 2), a long dry period occurred between 1984 and 1994, followed by a rainy period until 1999, then a partially stable period until 2004, a dry period between 2004 and 2010, then a long rainy period between 2010 and 2019 were experienced in the study area. It should be noted that the dry period until 1994 begins in 1982. Since before 1984 was not included in the period investigated, it has been excluded from the analysis. Finally, the past (1984–2019) behavior and current trend of the curve indicate that a dry period was entered as of 2019. In the analyzed period, the least precipitation after 2008 was 360 mm in 2020, just after 2019 with 630 mm. This sharp decrease in precipitation from 2019 to 2020 may indicate that the dry period we are in currently may be extremely severe in the coming years.

The temporal variation of drought was examined according to the 12-months SPI (SPI-12) and SPEI (SPEI-12) drought values calculated from the total precipitation of the water year and shown together with the dry and rainy periods according to the cumulative deviation curve (Fig. 3). SPI and SPEI values generally exhibit similar behavior as the cumulative deviation curve in the long term and are naturally more correlated with the precipitation. The average of differences between SPI and SPEI values is 0.18 and the biggest difference is 0.51. Pearson's correlation coefficient (r) between SPI and SPEI is 0.97. It was observed that SPI and SPEI values differ more in arid conditions below zero, while this difference is less in rainy periods, which are expressed with values above zero. Compared to SPEI, SPI generally gives more extreme values due to lack of precipitation in arid conditions. According to SPI and SPEI, the most severe drought years were determined as 2008 and 2020, respectively. As mentioned, a dry period was entered after 2019 and the severe drought in 2020

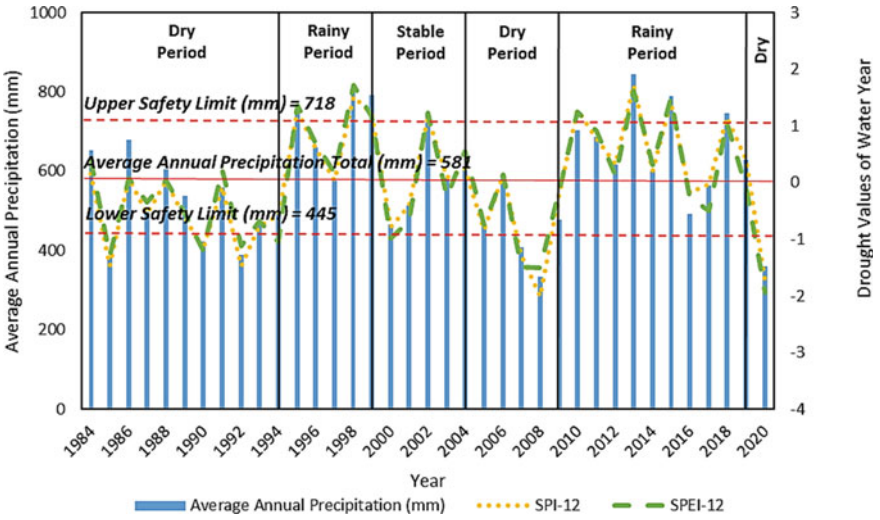

Fig. 3 SPI and SPEI drought values from water year precipitation data between 1984 and 2020

(SPI $= -1.74$ and SPEI $= -1.94$) at the beginning of the dry period is a worrying precursor for coming years.

3.2 Determination of Lake Area Using Remote Sensing and Its Correlation with Drought

The spatial–temporal changes of the water body area in the dam lake were examined with NDWI generated from the Landsat satellite images obtained at the end of the water years between 1984 and 2020 (Fig. 4). Since cloudless images are not available for 1995, 2008, 2012 and 2018, these four years were excluded from the analysis in determining the correlation of the lake area with drought. Within the analyzed NDWI data set, the average of the lake water area is 2.02 km^2 and the standard deviation is 0.61 km^2. The lake area reached its widest limits in 2010 with 2.98 km^2. According to the water body area values determined from local measurements by the Turkish State Hydraulic Works, the lake area was determined by NDWI to have an average of 5.78 km^2 RMSE, with 82.68% accuracy. The driest year hydrologically (i.e., the year with the smallest lake area) was determined as 1990 with a lake water area of 1.09 km^2, even though the driest years meteorologically were 2008 (not included in analysis) and 2020 (Fig. 5). Despite the severe meteorological drought in 2020, the reason why the water area is larger than in 1990 is the improvement and modernization of agricultural irrigation systems (i.e., preferring drip and sprinkler irrigation instead of wild flooding systems) over the years and the decrease in water consumption.

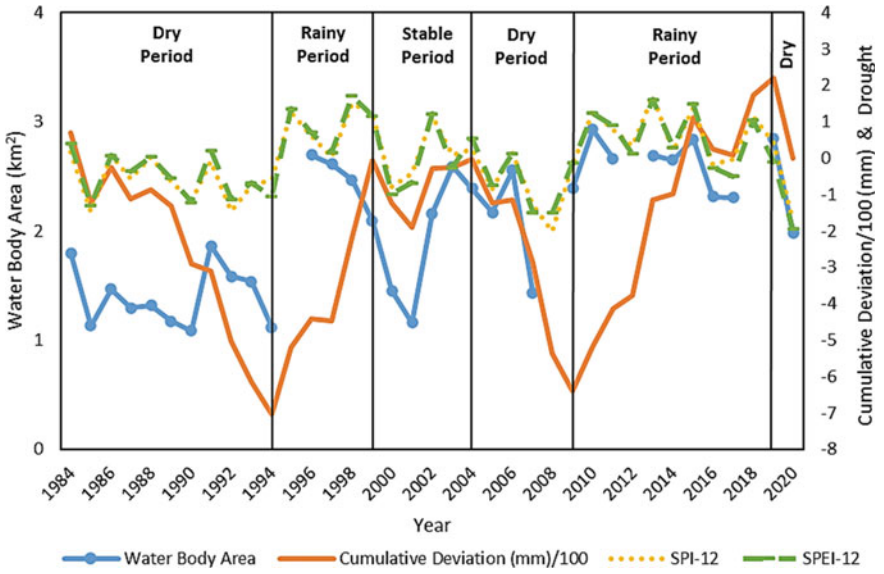

Fig. 4 The spatial–temporal change of water body area of Atikhisar Dam Lake, cumulative deviation, SPI and SPEI values. (Note: Cumulative deviation values were divided by 100 to display together with water body area, SPI and SPEI values.)

Similar to meteorological drought, hydrologically, the driest period was between 1984 and 1994 with an average of 1.4 km^2, and the rainy period was between 2010 and 2019 with an average of 2.62 km^2. Especially at the end of the water year, there was a 26% increase in the average precipitation in September between 2010 and 2019 compared to the 1980s, and this precipitation increase is a major factor in the increase of the lake area (Fig. 5). At the end of the water years since 2009, the lake area decreased below 2 km^2 for the first time in 2020. The 30.5% decrease from 2.85 km^2 in 2019 to 1.98 km^2 in 2020 at the beginning of the dry period creates concern regarding the coming years (Fig. 5). The lake area determined by NDWI at the transition dates to rainy or dry periods according to the cumulative deviation curve, and the minimum and maximum water body area of the lake within the data set for the examined dates, are shown in Fig. 5.

When the temporal variation of the data was examined, it was seen that the change in the lake area is related to meteorological drought (Fig. 4). However, since the cumulative deviations are computed as the sum of the differences of precipitation from the mean and are not suitable for short-term interpretation (annually, in this study), they were found to be uncorrelated with the lake areas determined by remote sensing (Fig. 6a). However, in the long-term analysis, there is a significant relationship in the trend between cumulative deviation and the area values (Fig. 4). Compared to cumulative deviation values, the change in the SPI and SPEI drought values were found to be significantly more correlated with the change in the water body area (Fig. 6b, c). According to ANOVA, the SF values between the water body area and drought

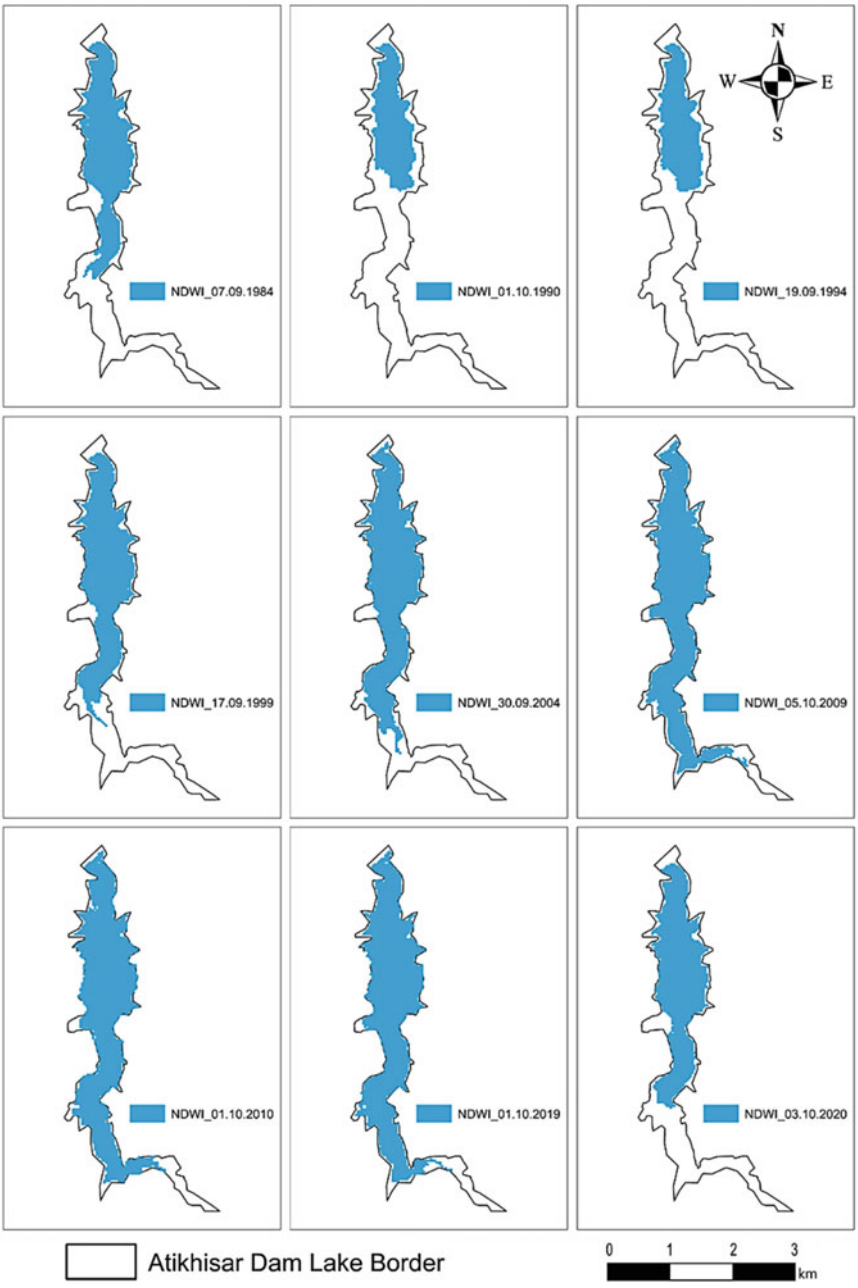

Fig. 5 Areas of lake determined by NDWI on transition date to a rainy or dry period, according to cumulative deviation curve. (Note: 1990 and 2010 represent minimum and maximum areas of lake, respectively, within data set examined.)

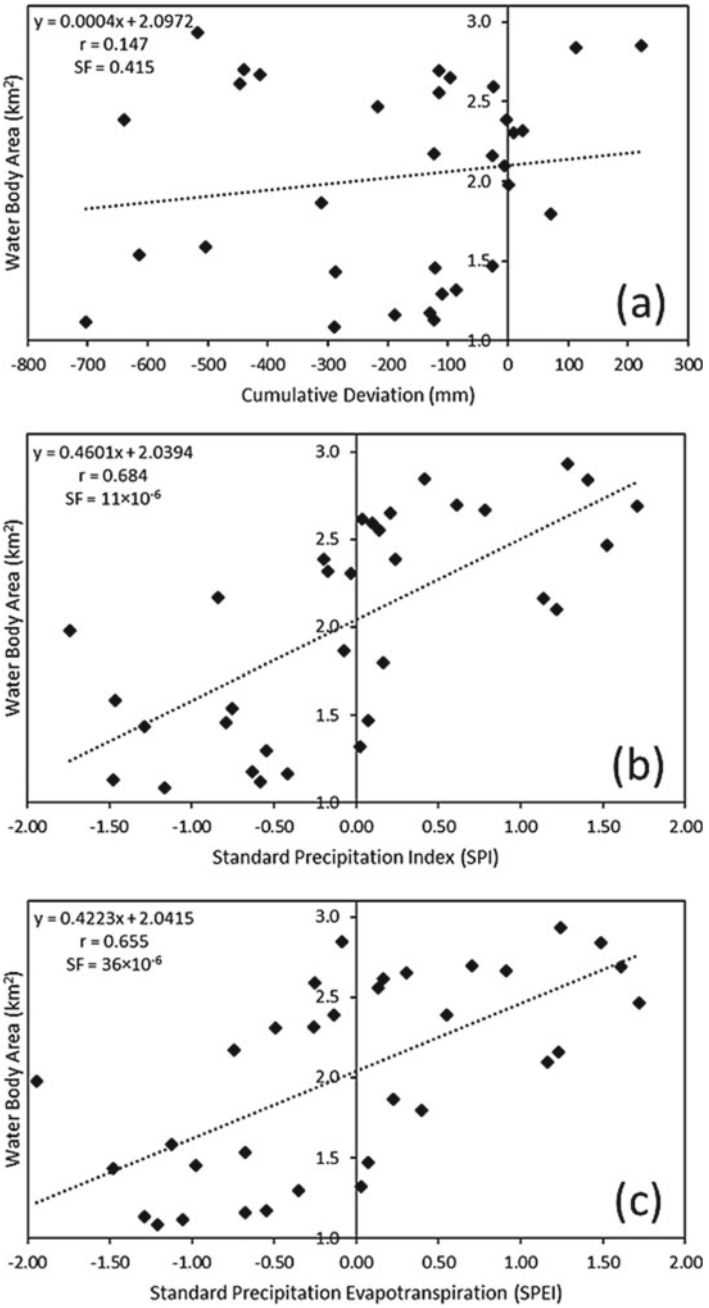

Fig. 6 Correlation between water body area from NDWI and **a** cumulative deviation, **b** SPI, and **c** SPEI values

indices (i.e., SPI and SPEI) were found to be almost 0, and all correlations shown in Fig. 6b, c have almost 100% confidence level. SPI values with 0.68 correlation were found to be slightly more correlated with the water body area values from NDWI than SPEI with 0.65. SPI may have generated better results because the valley where the dam is located is narrow, far from the sea, and richly forested in vegetation. Therefore, the wind triggering evapotranspiration is not high in the region and as a result rainfall is more dominant in the water budget.

The imperfect correlations show that the dam lake area not only changes due to meteorological drought. Atikhisar Dam Lake is multi-purpose and was built to provide drinking water, agricultural irrigation and flood protection (Koca 2005; Akbulak et al. 2008; Kale and Acarlı 2019b). On the other hand, the population of Çanakkale city has increased approximately 120 times since the initial construction of the dam and more than 30% in just the last 10 years (TÜİK 2020; Özelkan et al. 2018). While this population growth has caused an increase in anthropogenic demand (i.e., water consumption) from the dam lake, it may result in a decrease in the correlation between the water body area of the lake and meteorological drought. Preventing floods that may threaten the city of Çanakkale and agricultural areas, and leaving excess water accumulated in the lake due to precipitation, are other important tasks of the Atikhisar Dam (Koca 2005; Kale and Acarlı 2019b) that may also cause a decrease in the correlations. In addition, when examined in terms of flora, the vegetation density around the dam prevents erosion and prolongs the life of the dam. Conversely, dense vegetation slows down surface flow in the Sarıçay Basin, where the dam is located, and increases the groundwater level, which causes a decrease in the water reaching the dam lake (Koca 2005). The findings listed so far strongly suggest that the presence of water in the lake area may not be solely due to meteorological drought.

Finally, since the change of drought over the long term was examined in this study, 30 m was preferred as the common spatial resolution used in NDWI data produced from different Landsat satellites. However, with 15 m resolution the lake area can be determined more successfully (Özelkan, 2020), and this may increase the correlation between the lake area and drought in this study. Additionally, since the water area values created from the NDWI images are associated with SPI and SPEI calculated based on water year meteorological data, the time difference between the image acquisition dates and the end of the water year may affect the correlations.

4 Conclusions

The ever-increasing population worldwide together with severe drought puts tremendous pressure on water resources. Particularly in arid and semi-arid regions, the influence of drought on water resources should be carefully monitored and examined in all aspects. In other words, water resources management should be the most important issue in drought-prone regions; implementing urgent precautions such as education of the public on water management, a preference for technologies that consume less

water in our lives and industry, strict control of agricultural irrigation and usage of sensitive methods, and preference of agricultural plants that do not consume excessive water according to climatic characteristics. Otherwise, it is inevitable that we will experience a lack of drinking water and food. Misguided water management causes meteorological drought to evolve into hydrological, agricultural and eventually socio-economic drought. In this study, the correlation between spatial–temporal change in a dam lake and meteorological drought was investigated. While the cumulative deviation curve, SPI and SPEI were used to determine the meteorological drought, NDWI was used to determine the water change in the lake area. The main findings of this study are as follows.

- The cumulative deviation curve was very convenient in the interpretation of meteorological drought over a long period.
- SPI and SPEI gave precise results in the interpretation of meteorological drought in short periods.
- The drought values generated by SPI and SPEI were significantly correlated with the water area values of the lake determined by NDWI. Since the valley where the dam is located may have made evaporation slightly less important than precipitation, SPI gave a slightly better result than SPEI.
- Since the investigated reservoir is not a natural lake but a dam lake, meteorological drought cannot be said to be the only determinant factor in changes in the water body area.

This study shows that in order to create more successful models, the water budget of the dam lake (water consumption, irrigation, discharged water, etc.) as well as hydrogeological and environmental factors should be considered. The results of this study proved that the ability to ensure continuous monitoring, view large areas at once, and construct digital data easily associated with different sources of data make remote sensing a very successful tool to monitor and examine the impact of drought on water resources.

Acknowledgements The author would like to thank the USGS for the Landsat data, the Turkish State Hydraulic Works for the hydrological data, the Turkish State Meteorological Service for the meteorological data.

References

Akbulak C, Erginal A, Gönüz A, Öztürk B, Çavuş C (2008) Investigation of land use and coastline changes on the Kepez delta using remote sensing. J Black Sea/Mediterranean Environ 14(2):95–106

Akbulut M, Odabaşı DA, Kaya H, Çelik ES, Yıldırım MZ, Odabaşı S, Selvi K (2009) Changing of Mollusca fauna in comparison with water quality: Saricay Creek and Atikhisar reservoir models (Canakkale-Turkey). J Anim Vet Adv 8(12):2699–2707

Altan G, Türkeş M (2015) Hydroclimatologic characteristics of the forest fires occurred at the Çanakkale district and relationship with climate variations. Aegean Geograph J 20(2):1

Arslan O, Bilgil A, Veske O (2016) Meteorological drought analysis in Kizilirmak basin using standardized precipitation index method. Nigde Omer Halisdemir Univ J Eng Sci 5(2):188–194
Çakaroz D, Özelkan E, Karaman M (2020) Investigation of the effect of drought on temporal change in wetlands determined by remote sensing: the case study in Umurbey Delta (Çanakkale). Eur J Sci Technol 20:898–916. https://doi.org/10.31590/ejosat.799717
Çamoğlu G, Demirel K, Genc L (2018) Use of infrared thermography and hyperspectral data to detect effects of water stress on pepper. Quant InfraRed Thermograph J 15(1):81–94
Danandeh Mehr A, Vaheddoost B (2020) Identification of the trends associated with the SPI and SPEI indices across Ankara, Turkey. Theor Appl Climatol 139:1531–1542. https://doi.org/10.1007/s00704-019-03071-9
Dhakar R, Sehgal VK, Pradhan S (2013) Study on inter-seasonal and intra-seasonal relationships of meteorological and agricultural drought indices in the Rajasthan State of India. J Arid Environ 97:108–119
Dore MH (2005) Climate change and changes in global precipitation patterns: what do we know? Environ Int 31(8). ISSN 1167–1181:0160–4120. https://doi.org/10.1016/j.envint.2005.03.004
Duan Z, Bastiaanssen WGM (2017) Evaluation of three energy balance-based evaporation models for estimating monthly evaporation for five lakes using derived heat storage changes from a hysteresis model. Environ Res Lett 12(024005):1–13
Feyisa GL, Meilby H, Fensholt R, Proud SR (2014) Automated water extraction index: a new technique for surface water mapping using Landsat imagery. Remote Sens Environ 140:23–35
Genc L, Demirel K, Çamoglu G, Asik S, Smith S (2011) Determination of plant water stress using spectral reflectance measurements in watermelon (Citrullus vulgaris). Am Eurasian J Agric Environ Sci 11(2):296–304
Gorjizade A, Akhondali AM, Zarei H, Seyyed Kaboli H (2014) Evaluation of eight evaporation estimation methods in a semi-arid region (Dez reservoir, Iran). Int J Adv Biol Biomed Res 2(5):1823–1836
Ilgar R (2010) Drought status and trends in the Dardanelles and the standardized precipitation index determination. Marmara Geograph Rev 0 (22), 183
Ji L, Geng X, Sun K, Zhao Y, Gong P (2015) Target detection method for water mapping using Landsat 8 OLI/TIRS imagery. Water 7(2):794–817
Kale S, Acarlı D (2019a) Shoreline change monitoring in Atikhisar reservoir by using remote sensing and geographic information system (GIS). Fresenius Environ Bull 28(5):4329–4339
Kale S, Acarlı D (2019b) Spatial and temporal change monitoring in water surface area of Atikhisar Reservoir (Çanakkale, Turkey) by using remote sensing and geographic information system techniques. Alinteri J Agric Sci 34(1):47–56
Kapluhan E (2013) Drought and drought in turkey effect of agriculture. Int J Geogr Geogr Educat 27:487–510
Karabulut M (2015) Drought analysis in Antakya-Kahramanmaraş Graben. Turkey J Arid Land 7:741–754. https://doi.org/10.1007/s40333-015-0011-6
Karaman M, Budakoglu M, Uca Avci ZD, Özelkan E, Bülbül A, Civas M, Tasdelen S (2015) Determination of seasonal changes in wetlands using CHRIS/Proba hyperspectral satellite images: a case study from Acigöl (Denizli), Turkey. J Environ Biol 36:73–83
Karaman M (2021) Comparison of thresholding methods for shoreline extraction from Sentinel-2 and Landsat-8 imagery: Extreme Lake Salda, track of Mars on Earth. J Environ Manage 298:113481. https://doi.org/10.1016/J.JENVMAN.2021.113481
Karaman M, Özelkan E (2022) Comparative assessment of remote sensing–based water dynamic in a dam lake using a combination of Sentinel-2 data and digital elevation model. Environ Monitor Assessment 194:92. https://doi.org/10.1007/s10661-021-09703-w
Karaman M (2022) High cadence monitoring of reservoir volume fluctuations using planetScope imagery. J Hydrol 606(2022):127456. https://doi.org/10.1016/j.jhydrol.2022.127456
Koca N (2005) Environmental and economic effects of Atikhisar Dam. Eastern Geographical Review 10(14):209–233

Lang D, Zheng J, Shi J, Liao F, Ma X, Wang W, Chen X, Zhang M (2017) A comparative study of potential evapotranspiration estimation by eight methods with FAO Penman-Monteith method in Southwestern China. Water, 9(10)734: 1–18.

Li Z, Chen Y, Fang G, Li Y (2017) Multivariate assessment and attribution of droughts in Central Asia. Sci Rep 7(1316):1–12

Liu M, Liu P, Guo Y, Wang Y, Geng X, Nie Z, Yu Y (2019) Change-point analysis of precipitation and drought extremes in China over the past 50 years. Atmosphere 11(1):11. https://doi.org/10.3390/atmos11010011

Liu C, Yang C, Yang Q, Wang J (2021) Spatiotemporal drought analysis by the standardized precipitation index (SPI) and standardized precipitation evapotranspiration index (SPEI) in Sichuan Province. China. Sci Rep 11:1280. https://doi.org/10.1038/s41598-020-80527-3

McFeeters SK (1996) The use of normalized difference water index (NDWI) in the delineation of open water features. Int J Remote Sens 17(7):1425–1432

McKee TB, Doesken NJ, Kleist J (1993). The relationship of drought frequency and duration to time scales. In: Proceedings of the 8th Conference on Applied Climatology: American Meteorological Society: 17–22 January 1993, Boston, MA, USA

Mishra AK, Singh VP (2010) A review of drought concepts. J Hydrol 391(1–2):204–216

Mohammed R, Scholz M (2017) The reconnaissance drought index: a method for detecting regional arid climatic variability and potential drought risk. J Arid Environ. https://doi.org/10.1016/j.jaridenv.2017.03.014

Osuch M, Romanowicz RJ, Lawrence D, Wong WK (2016) Trends in projections of standardized precipitation indices in a future climate in Poland. Hydrol Earth Syst Sci 20:1947–1969

Özelkan E, Chen G, Üstündağ BB (2016) Multiscale object-based drought monitoring and comparison in rainfed and irrigated agriculture from Landsat 8 OLI imagery. Int J Appl Earth Observat Geoformat 44:159–170

Özelkan E, Karaman M (2018a) The Analysis of the effect of meteorological and hydrological drought on dam lake via multitemporal satellite images: a case study in Atikhisar Dam Lake (Çanakkale). Omer Halisdemir Univ J Eng Sci 7(2):1023–1037

Özelkan E, Karaman M (2018b) Hydrometeorological evaluation of urban areas in GIS platform. Sağlık A (eds), Changing and developing Laspeki urban infrastructure, Çanakkale Onsekiz Mart University, Çanakkale, s. 97–109

Özelkan E, Sağlık A, Sümer S, Bedir M, Kelkit A (2018) Examination of the effect of urbanization on agricultural areas using remote sensing – a case study in Çanakkale. COMU J Agriculture Faculty 6(1):123–135

Özelkan E (2019a) Evaluation of temporal change of dam lake area determined by remote sensing with meteorological drought: a case study in Atikhisar Dam (Çanakkale). Turkish J Agric Nat Sci 6(4):904–916. https://doi.org/10.30910/turkjans.633634

Özelkan E (2019b) Comparison of remote sensing classification techniques for water body detection: a case study in Atikhisar Dam Lake (Çanakkale). Cumhuriyet Sci J 40(3):650–661. https://doi.org/10.17776/csj.556440

Özelkan E (2020) Water body detection analysis using NDWI indices derived from Landsat-8 OLI. Polish J Environ Stud 29(2), 1759–1769. https://doi.org/10.15244/pjoes/110447

Palmer WC (1965) Meteorological drought. Office of Climatology Research Paper 45, Weather Bureau, Washington, D.C., 58 pp

Pradhan RK, Sharma D, Panda SK, Dubey SK, Sharma A (2019) Changes of precipitation regime and its indices over Rajasthan state of India: impact of climate change scenarios experiments. Clim Dyn 52:3405–3420. https://doi.org/10.1007/s00382-018-4334-9

Schultz GA, Engman ET (2012) Remote sensing in hydrology and water management. Springer, Berlin Heidelberg, Berlin, Almanya, p 483

Sener E, Davraz A, Sener S (2010) Investigation of Aksehir and Eber Lakes (SW Turkey) coastline change with multitemporal satellite images. Water Resour Manage 24(4):727–745

Şensoy S, Demircan M, Ulupınar U, Balta I (2008). Climate of Turkey. Turkish State Meteorological Service Report. https://www.mgm.gov. tr/FILES/genel/makale/13_turkiye_iklimi.pdf. Accessed 01 May 2021

TÜİK (2020) Turkish Statistical Institute Data Base. http://tuik.gov.tr/PreTabloArama.do?metod=search&araType=vt. Accessed 07 May 2021

Türkeş M (2010) Climatology and Meteorology. First Edition, Kriter Publisher – Publication No. 63, Physical Geography Series No. 1, ISBN: 978–605–5863–39–6, 650 + XXII pp., Istanbul

Tsakiris G, Vangelis H (2005) Establishing a drought index incorporation evapotranspiration Eur. Water 9(10):3–11

Veijalainen N, Ahopelto L, Marttunen M, Jääskeläinen J, Britschgi R, Orvomaa M, Belinskij A, Keskinen M (2019) Severe drought in Finland: modeling effects on water resources and assessing climate change impacts. Sustainability 11(8) 2450: 1–26

Vicente-Serrano SM, Beguería S, López-Moreno JI (2010) A multi-scalar drought index sensitive to global warming: the standardized precipitation evapotranspiration index – SPEI. J Clim 23:1696–1718

Wilhite DA (2000) Drought: a global assessment, Vol. I, edited by Donald A. Wilhite, Chap. 1, pp 3–18 (London: Routledge, 2000). http://digitalcommons.unl.edu/droughtfacpub/69

Willeke G, Hosking JRM, Wallis JR, et al (1994) The national drought atlas. In: Institute for Water Resources Report 94-NDS-4. U.S Army Corp of Engineers, CD-ROM. Norfolk, VA

Xu H (2006) Modification of normalized difference water index (NDWI) to enhance open water features in remotely sensed imagery. Int J Remote Sens 27(14):3025–3033

Yang Y, Liu Y, Zhou M, Zhang S, Zhan W, Sun C, Duan Y (2015) Landsat 8 OLI image based terrestrial water extraction from heterogeneous backgrounds using a reflectance homogenization approach. Remote Sens Environ 171:14–32

Yaykiran S, Cuceloglu G, Ekdal A (2019) Estimation of water budget components of the Sakarya River Basin by using the WEAP-PGM Model. Water, 11(2) 271: 1–17

Yetmen H (2013) Van lake basin drought analysis. Education and the Society in the 21st Century, 2(5): 184–198

Yıldız MZ, Deniz O (2005) The impacts of the level changes in closed basin lakes on the coastal settlements: the lake Van example. Fırat Univ J Soc Sci 15(1):15–31

Yolcubal I (2019) Hydrogeology Lecture Notes, Kocaeli University, Geology Department, http://jeoloji.kocaeli.edu.tr/dosyalar/dersNotlari/hidrojeoloji_ders%20notlari_prof_dr_irfan_yolcubal.pdf. Accessed 05 May 2021

Zannouni K, El Abrach H, Dhahri H, Mhimid A (2017) Study of heat and mass transfer of water evaporation in a gypsum board subjected to natural convection. Heat Mass Transfer 53(6):1911–1921

Zhou Y, Dong J, Xiao X, Xiao T, Yang Z, Zhao G, Zou Z, Qin Y (2017) Open surface water mapping algorithms: a comparison of water-related spectral indices and sensors. Water 9(4): 256, 1–16

Forecasting Domestic Water Demand Using Meteorological and Satellite Data: Case Study of Greater Beirut Area

J. Saade, S. Ghanimeh, M. Atieh, and E. Ibrahim

1 Introduction

Acknowledging the dire need for water security, the United Nations established Goal 6 of the Sustainable Development Goals (SDGs), for year 2030, on Clean Water and Sanitation. Nonetheless, the target is still behind as by 2019 around 785 million people still lack basic drinking water service (UN Statistical Commission 2019). The SDGs also acknowledge, through Goal 13: the impacts of climate change on the hydrological cycle, on various ecosystems, and eventually on the existence of humanity. In fact, temperatures in the Middle East and North Africa (MENA) region are expected to become more extreme (Atlantic Council 2019; El-Samra et al. 2017; Lange 2019; Waha et al. 2017) with a 4 °C projected increase in average temperatures by 2050 (WEF 2019). The MENA region is expected to experience hotter summers with more frequent heatwaves (ArabNews 2019; Bucchignani et al. 2018). Consequently, Lebanon's national communications revealed the pronounced impacts of the changing climate in terms of reduction in water supply and increase in water demand.

J. Saade · M. Atieh
Department of Civil and Environmental Engineering, Notre Dame University—Louaize (NDU), P.O. Box 72, Zouk Mikael, Keserwan, Lebanon
e-mail: jesaade@ndu.edu.lb

M. Atieh
e-mail: maya.atieh@ndu.edu.lb

S. Ghanimeh (✉)
Environmental Science Center (ESC), Qatar University, P.O. Box 2713, Doha, Qatar
e-mail: s.ghanimeh@qu.edu.qa

E. Ibrahim
Urban and Environmental Engineering (UEE), University of Liege, Quartier Polytech1, Allee de la Decouverte, 9 Bat. B52—Sart Tilman 4000, Liege, Belgium

A. Shaban (ed.), *Satellite Monitoring of Water Resources in the Middle East*,
Springer Water, https://doi.org/10.1007/978-3-031-15549-9_10

From the water supply perspective, the anticipated cost of climate-induced drop in agricultural, domestic, and industrial water supply in Lebanon is estimated at $ 21 Million, $ 320 Million, and $ 1,200 Million by 2020, 2040, and 2080, respectively—noting that the country's gross domestic product (GDP) is about 60 billion USD (MoF 2019). Similarly, the cost of climate-caused reduction in water availability for generation of hydroelectricity is estimated at $ 3 Million, $ 31 Million, and $ 110 Million by 2020, 2040, and 2080 respectively (MoE 2016). A negative water balance of -518 million cubic meters (MCM) was projected for year 2030 (World Bank 2003).

Likewise, water demand is expected to change with the climate and weather conditions. At the global level, water demand is categorized as: agricultural (69%), industrial (19%), and domestic (12%). The latter has increased substantially from 50 km^3/year in 1950 to more than 500 km^3/year in 2010 (FAO & AQUASTAT 2015). In developing countries like Lebanon, domestic water demand (30%) comes second after agricultural water demand (61%); while industrial demand constitutes the smallest share (9%) (Hamdar et al. 2015; MoEW 2012). In fact, studies of highly congested regions of the country revealed a remarkably high domestic demand, reaching 54% in Beirut and Mount Lebanon and projected to reach up to 46% in Greater Beirut Area (GBA) in 2030 (Comair 2011; Yamout and El-Fadel 2005). In this context, the World Bank projected an increase in annual water demand from 1,257 MCM in 2003 to 2,818 MCM by 2030. This is paralleled with a shift in relative shares of sectors from 9%, 27%, and 64% to 15%, 45%, and 40% for the industrial, domestic, and agricultural demands respectively—showing the anticipated dominance of domestic water demand in the future.

Furthermore, Middle Eastern countries, including Lebanon, have specific challenges attributed to internal and cross-boundary migration. Specifically, in the context of Lebanon, the country hosts 173 refugees per 1,000 citizens, the largest number of refugees per capita worldwide (Hussein et al. 2020). This has exacerbated the already negative water balance, which is expected to peak in 2030 (Hussein et al. 2020), especially with the limited governmental strategies (Shaban 2020).

While worldwide efforts have been made to project the effects of climate change on domestic water demand (Table 1), such studies remain limited in Mediterranean countries—despite the already visible water deficit. In Lebanon, the 2010 National Water Sector Strategy (NWSS), amended in 2015 and adopted by the Ministry of Energy and Water (MoEW), projected a 30% domestic water demand by 2030 with an urban water consumption of 185 lpcd (MoEW 2010, 2012).

The NWSS tackles the water deficit problem by increasing water supply, with marginal attention to optimizing water demand. It aims at providing an additional 935 MCM of water by spring capture (65 MCM), artificial recharge of groundwater aquifers (200 MCM), and surface storage though the construction of 18 dams and 23 hill lakes (670 MCM to reach a water storage of 14.9%) (MoEW 2012).

The anticipated population growth in GBA calls for a better focus on the demand side of the water budget, taking climate change into consideration. Yet, local studies that back up this hypothesis remain limited, especially with data scarcity and lack of access to water records. This study aims at investigating the link between domestic

Table 1 Impact of weather on domestic water consumption

References	Study area	Weather parameters	Findings
Rasifaghihi et al. (2020)	Montreal, Canada	Daily minimum temperature, daily maximum temperature, daily precipitation	Definition of a temperature threshold above which the effect of weather parameters on water demand becomes considerable
Uthayakumaran et al. (2019)	Sydney, Australia	Average daily precipitation, number of days in a month when precipitation exceeds 2 mm, average daily maximum temperature, number of days in a month when temperature exceeds 300 °C, and average daily pan evaporation	Increase in water demand of 2.3% and 4.4% in short-term (up to 2040) and long-term (2060–2080) based on the A2 Scenario
Wang et al. (2017)	Yellow river basin, China	Average temperature	Under RCP 4.5, average water demand will increase by 20.2% by end of the century
Al-Zahrani et al. (2015)	Al Khobar, KSA	Minimum, average, and maximum temperature and humidity, rainfall frequency, total intensity, and wind speed (all at a daily time-step)	Temperature is the most relevant weather parameter in projecting water demand, followed by humidity, wind speed, and rainfall frequency
Chang et al. (2014)	Portland, USA	Maximum temperature and precipitation (daily and monthly), and day of the week	Maximum temperature and precipitation, combined, explain 48% of the variation in seasonal monthly water use in June and July (summer months). Including the day of the week explained 87% of the daily variation in seasonal water use
Al-ahmady (2011)	Mosul, Iraq	Season, water supply continuity, and family size	Yearly average water demand was found to be 180 ± 64 L per capita per day (lpcd), with diurnal variation between 125 ± 65 lpcd and 235 ± 64 lpcd in winter and summer

(continued)

Table 1 (continued)

References	Study area	Weather parameters	Findings
Neale et al. (2007)	British Columbia, Canada	Daily maximum temperature	Annual residential per capita outdoor water demand would increase by 6367 L for every 1 °C increase in monthly mean daily maximum temperature

Source Own elaboration

water demand and meteorological variables and targets future changes in water demand in GBA, under climate Representative Concentration Pathways (RCP) 4.5 and RCP 8.5 through utilizing water demand patterns, meteorological data, and remote sensing data. GBA is one of the most congested areas of the country and is fed by one major watershed (El Kalb river watershed) that is currently under severe stress—and is expected to suffer greatly with the future climatic changes. As such, the findings of this work are crucial to support informed decisions at the level of governmental planning and sound demand-side management of water resources in Lebanon

2 Methods and Materials

2.1 Study Area

Providing home to 2.4 million inhabitants, GBA covers an area of 253 km^2, including Lebanon's capital, Beirut city, that covers an area of 67 km^2 (Fig. 1). About 11% of the Lebanese population lives in Beirut city and another 27% of the population lives in its suburbs (CDR 2017). GBA is located east central Lebanon at an altitude ranging between 0 and 400 m above sea level and is characterized to be with a Mediterranean climate (Faour and Mhawej 2014; OCHA 2016; UN 2020; Yamout and El-Fadel 2005). GBA is heavily populated with an average population density of 6,200 inhabitants/km^2. About 70% of the water demand in GBA is supplied by one main treatment station in Dbaye (Faour and Mhawej 2014).

Dbaye station is fed by two springs; Jeita (172 MCM/year) and Kachkouch (70 MCM/year) (Badran 2016) (CDR/DAR 2014). When the discharge from the springs is low, groundwater is pumped from 26 wells in Jeita watershed and 13 wells in Beirut southern suburbs to overcome the shortage (Badran 2016; Margane and Schuler 2013). Water is conveyed through four main pipelines from Dbaye station to two stations at the north of GBA, one in central Beirut, and another one at the south of Beirut.

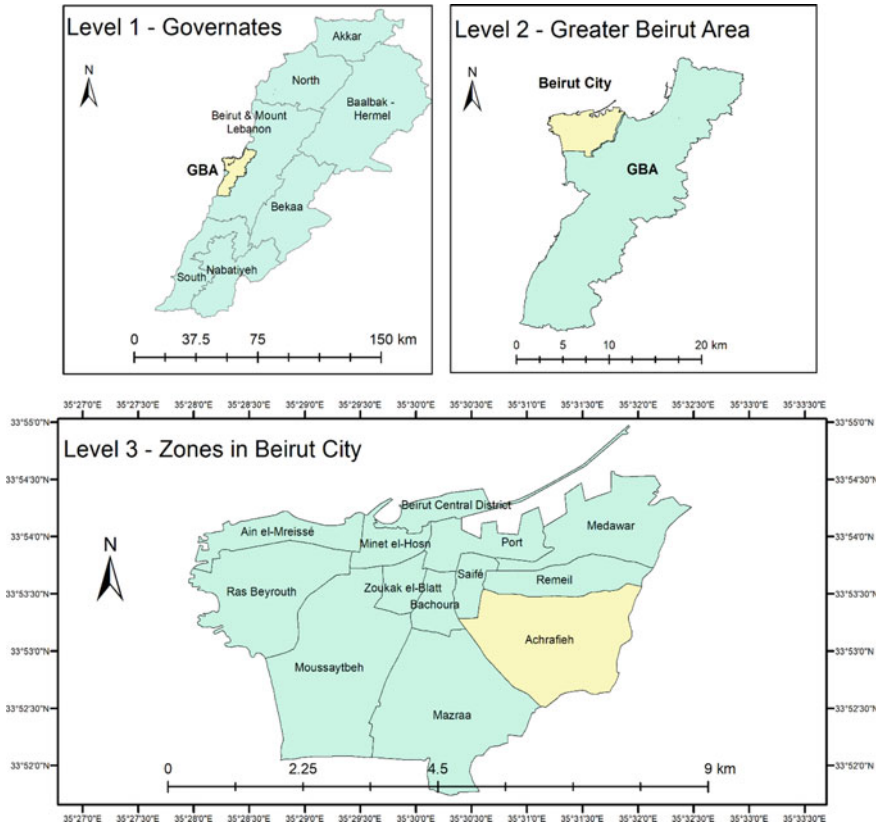

Fig. 1 Map of the study area: location of GBA in Lebanon's map (Level 1), location of Beirut city in GBA's map (Level 2), the zones of Beirut city (Level 3)

2.2 Water Demand Data

Given the absence of records for the GBA water demand pattern, the latter was estimated by applying the GBA local average water demand of 185 L/day/capita (CAS 2008; Jaafar et al. 2020) to the demand time pattern of Syracuse (Fig. 2). Syracuse is an urban coastal city in Italy, characterized by a Mediterranean climate with warm to hot dry summers and mild wet winters, like Beirut. Using WorldClim data, (Hijmans et al. 2005; O'Donnell and Ignizio 2012), a global gridded historical dataset (1960 to 1991), the similarity between the two cities with respect to climatic conditions can be illustrated. The data was accessed through Google Earth Engine (GEE) (Google Earth Engine 2021) with 30 arc-second spatial resolution. The mean annual temperature of the two cities are comparable where in Syracuse it is about 16 °C while in Beirut it is 20 °C (Fig. 3). The annual mean diurnal range capturing temperature fluctuation (Fig. 4) shows consistent fluctuation of 8 °C for the two cities.

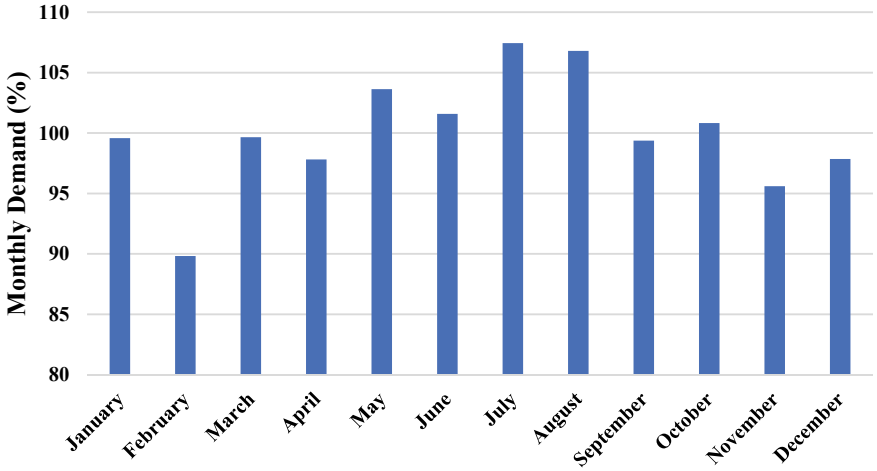

Fig. 2 Monthly demand as compared to average demand (%) in Syracuse, Italy (Campisi-Pinto et al. 2012)

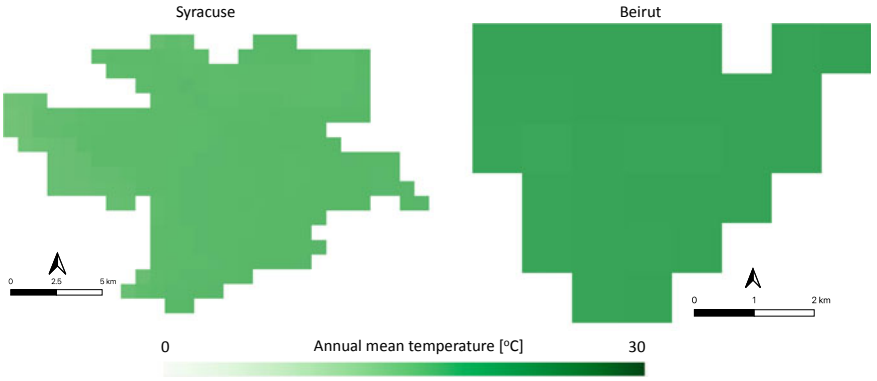

Fig. 3 The annual mean temperature of the two cities using the WorldClim dataset

Regarding precipitation seasonality, both cities exceed 80% variability (expressed as coefficient of variation) (Fig. 5) throughout the year, highlighting the Mediterranean seasons of wet winters and dry summers. Considering the similarities in weather and overall socio-economic aspects, it is assumed that similar water demand patterns would prevail in Syracuse and GBA (Campisi-Pinto et al. 2012). The demand pattern of Syracuse was averaged for the years 2002 to 2008 (Campisi-Pinto et al. 2012).

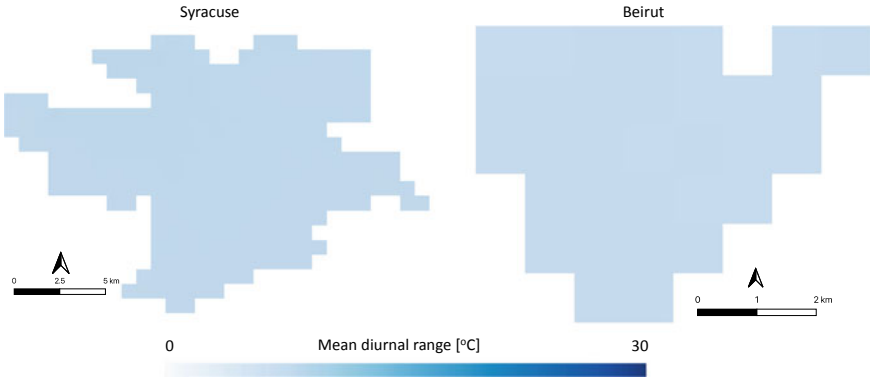

Fig. 4 The mean diurnal range of the two cities using the WorldClim dataset

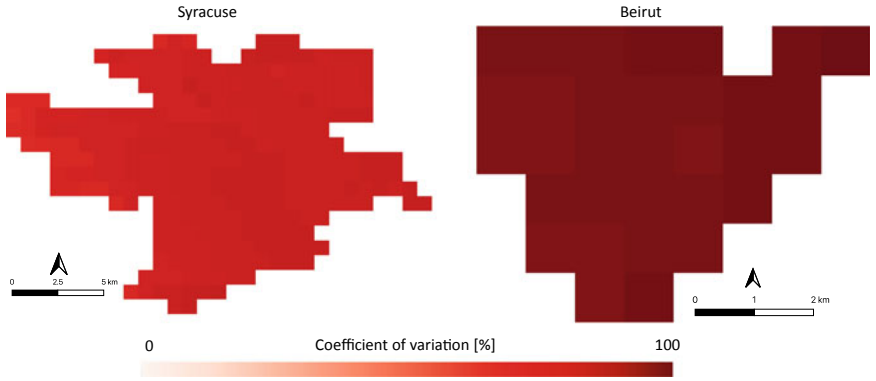

Fig. 5 The precipitation seasonality of the two cities using the WorldClim dataset

2.3 Weather Data Acquired by Ground Stations

Weather data was obtained from Achrafieh (Fig. 1) weather station in GBA for the period ranging from June 2017 to March 2019—considered to be the reference period (Litani River Authority data). The weather parameters used in this study include monthly temperature data, relative humidity, wind speed, and atmospheric pressure (Fig. 6). In addition, solar radiation (R_S), in MJ/m^2/day, was computed using Eq. (1) (Bou-Fakhreddine et al. 2019; Valiantzas 2013).

$$R_S \approx k_{R_S} R_A \sqrt{T_{max} - D} \tag{1}$$

where T_{max} is the maximum monthly temperature k_{Rs} is the radiation adjustment coefficient ranging between 0.12 and 0.25 (default value 0.17), R_A is the extraterrestrial radiation obtained according to the latitude position (FAO 2020). D is the

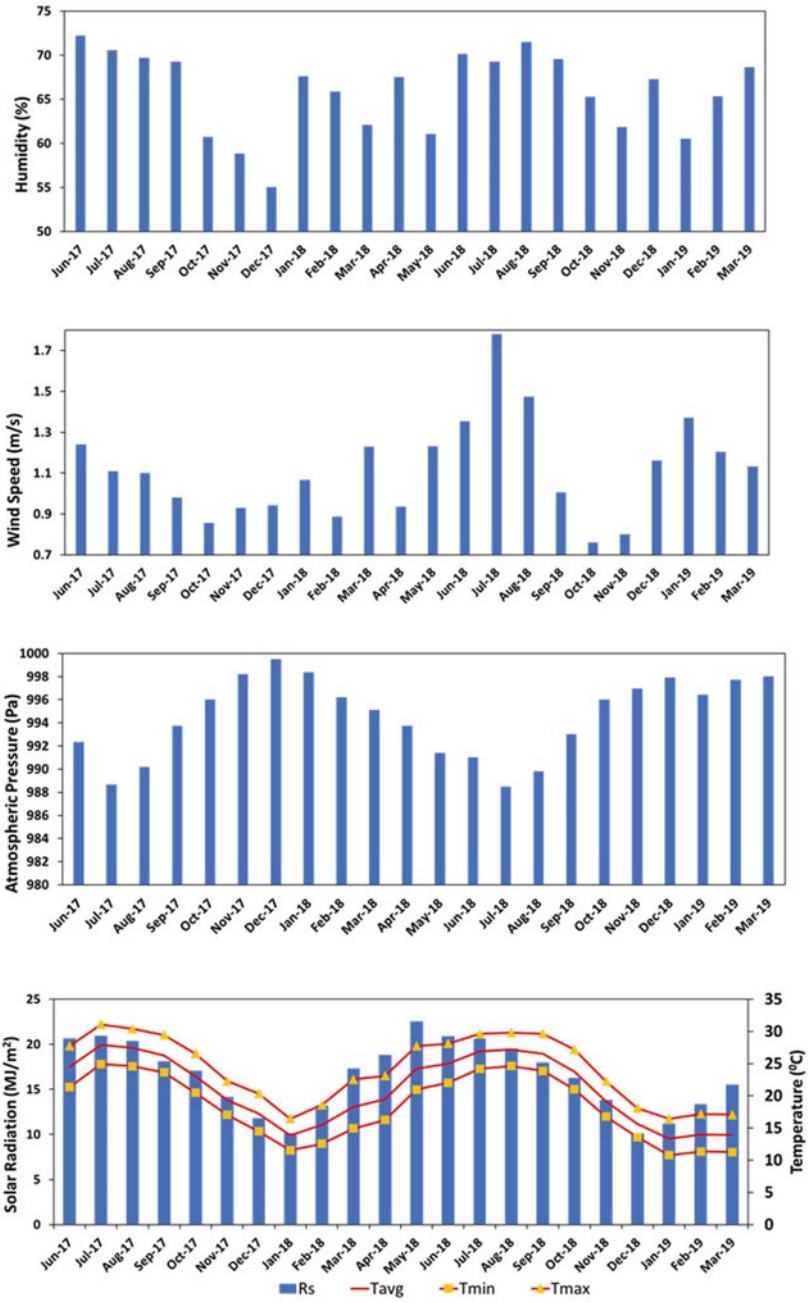

Fig. 6 GBA weather data, Achrafieh station

dew point (°C, temperature at which relative humidity reaches 100% saturation)—calculated using Eq. (2) adopted by the American Meteorological Society (Lawrence 2005), where T_{avg} is the average monthly temperature:

$$D = T_{avg} - \frac{100 - RH}{5} \tag{2}$$

2.4 Land-Surface Temperature Acquired Using Satellite Data

An essential variable in water balance analysis and land-surface processing is Land Surface Temperature (LST) that can be acquired through various approaches including in-situ measurements along with satellite observations. As data is generally scare in Lebanon, in-situ LST data are not available, and thus, Moderate Resolution Imaging Spectroradiometer (MODIS) can provide a great opportunity in this regard. MODIS spaceborne data is the most commonly used remote sensing LST data (Phan and Kappas 2018). It is freely available, has a spatial resolution of 1 km, and continuously covers the study area as cloud cover permits (Mo et al. 2021). MODIS TERRA provides daily coverage with overpass at local times 10:30 a.m. and 10:30 p.m.

For this work, monthly mean (averaged day and night) MODIS LST values were derived for Beirut from daily MODIS data accessed through Google Earth Engine platform where a full day and night data dataset is provided (Fig. 7). The data product is MYD11A1 retrieved using the generalized split-window and day/night algorithms (Phan and Kappas 2018; Wan 2013).

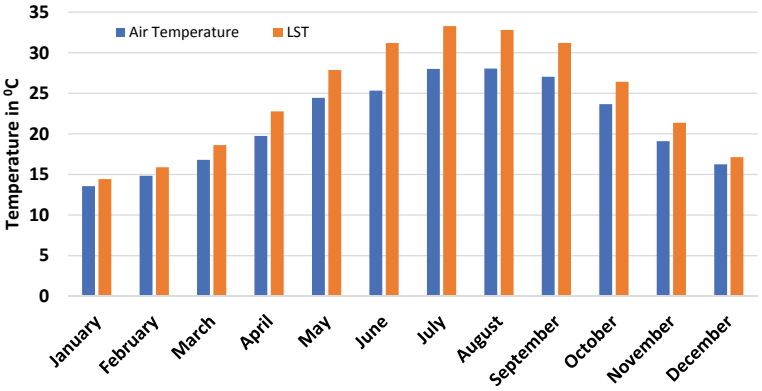

Fig. 7 Average monthly LST and air temperature for Beirut city for the period 2017–2019

2.5 Model Structure and Performance

Linear regression analysis is adopted in this study as it has been proven satisfactory to explain water demand variation in function of weather variables (Al-Zahrani and Abo-Monasar 2015; Chang and Praskievicz 2014; Gato et al. 2007) and MODIS LST (Alavipanah et al. 2016; Enriquez et al. 2019). A linear regression model is developed, of the form provided in Eq. (3). The weather parameters considered for modeling are minimum temperature (T_{min}), average temperature (T_{avg}), maximum temperature (T_{max}), solar radiation (R_S), wind speed (W) and relative humidity (H), and atmospheric pressure (P_{atm}), and Land Surface Temperature (LST).

$$q = \sum_{i=1}^{m} \beta_0 + \alpha_i \beta_i + \in \tag{3}$$

where q is the specific demand flowrate (lpcd), β_0 is the regression intercept, α_i is the is the ith predictor's regression slope, β_i is the ith variable, where the number of selected variable is $i \in [0, m]$, and ε is an error term representing random noise for effect of variables not included in the model equation, referred to as a Gaussian error term (Aitken et al. 1991; Koegst et al. 2008; Rasifaghihi et al. 2020).

The performance of the model was evaluated using: (1) the p-value test of independent variables (weather parameters), with a statistical significance level of 0.05; and (2) the coefficient of determination (R^2) to assess the goodness-of-fit of the model—having a minimum of 0 (indicating that the model does not explain any of the variation in water demand) and a maximum of 1 (indicating that the water demand can be fully predicted by the model) (Eq. 4).

$$R^2 = 1 - \frac{\frac{1}{n}\sum_i^n \left(y_i - \hat{y}\right)^2}{\frac{1}{n}\sum_i^n \left(y_i - \overline{y}\right)^2} \tag{4}$$

where $\hat{y}$ is the forecasted water demand, y_i is the actual water demand, $\overline{y}$ is the mean actual water demand, and n is the number of observations.

The analysis considered simple linear regression (i.e., $m = 1$) and assessed the correlation of demand with each variable. On the other hand, a multivariate linear regression was also carried out, and the selection of the number of independent variables aimed at reducing multicollinearity. The Variation Inflation Factor (VIF) (Eq. 5) was used to select the suitable variables, where (Akinwande et al. 2015),

$$VIF = \frac{1}{1 - R^2} \tag{5}$$

VIF thus iterated among the variable and excluded one variable causing multicollinearity at a time. The multivariate regression was implemented using the Classification and Regression Training (CARET) package in R (Kuhn 2008).

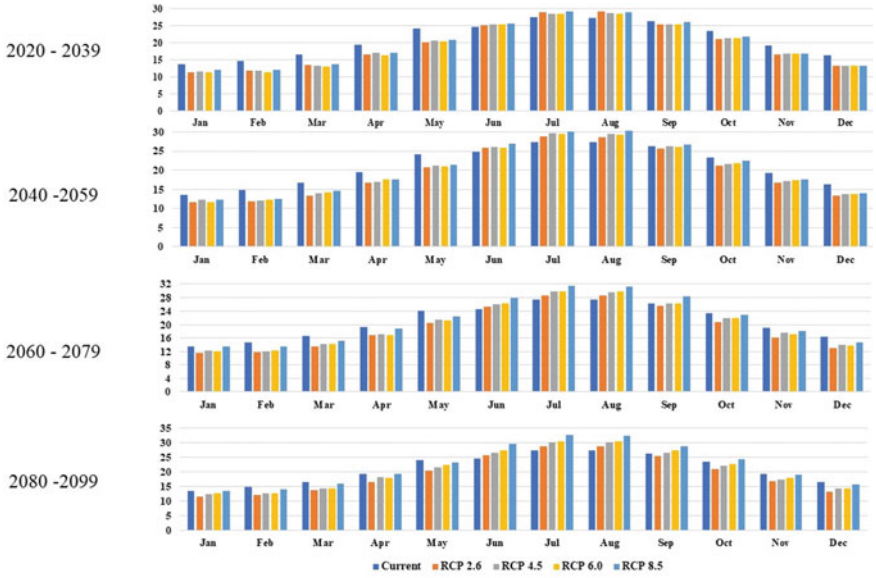

Fig. 8 Current versus future monthly average temperature (T_{avg}) under RCP 2.6, RCP 4.5, RCP 6.0, and RCP 8.5 during 2020–2039, 2040–2059, 2060–2079, 2080–2099 (World Bank 2020)

2.6 Climate Change Projections

Climate change projections for minimum, average, and maximum temperatures were obtained from the Climate Change Knowledge Portal for four 20-year periods: 2020–2039, 2040–2059, 2060–2079 and 2080–2099 (World Bank 2020) (Fig. 8). Those were simulated using the Beijing Climate Center Climate System Model (BCC—CSM 1), adopted in several scholar articles (Wang et al. 2018; Jun Wang et al. 2017).

3 Results and Discussion

3.1 Water Demand Models

The independent variables, including weather and LST datasets, were mostly correlated (Fig. 9). Wind speed and humidity showed the lowest correlation with other variables, yet correlations were still significant. The four-seasoned Mediterranean climate where rainfall is highest in the cold winters is apparent in the high negative correlations between precipitation and each of air temperature and LST.

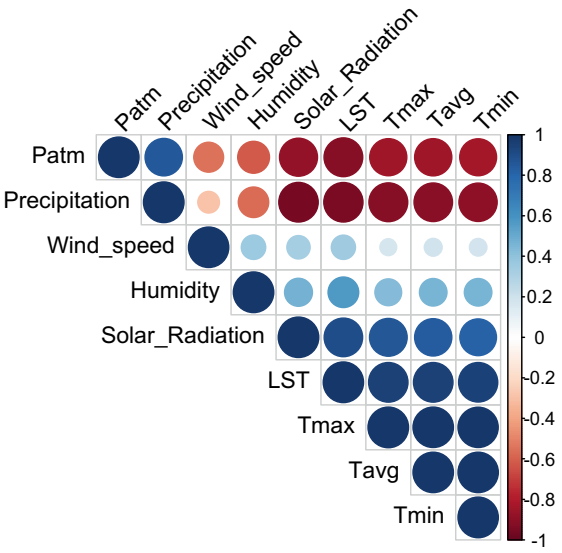

Fig. 9 Pairwise correlation matrix plot of the independent variables indicating Spearman's correlation as per the color legend. All correlations were statistically significant (p-value < 0.05)

Linear regression relationships were established between individual weather parameters (independent variables) and water demand (the dependent variable) (Fig. 10). The analysis of the resulting models revealed that all weather parameters were statistically significant (p-value < 0.05) at the exception of relative humidity (p-value = 0.065) (Table 2). The negative correlation between atmospheric pressure and water demand showed the best fit with R^2 value of 0.58, resulting in a linear regression model with the least error (i.e. minimum difference between predicted and observed water demand). The next best fit regression models were those based on temperature (T_{avg}, T_{min}, T_{max}) as independent variable. They showed positive correlations with R^2 values of 0.52, 0.52, and 0.50, respectively. Similar levels of accuracy were reported: 0.57 to 0.70 for calibration and from 0.56 to 0.68 for validation (Al-Zahrani and Abo-Monasar 2015) and 0.33 to 0.38 (Chang and Praskievicz 2014). Wind speed showed low correlation with water demand ($R^2 = 0.25$), thus proven inadequate to explain the variation in water demand.

For the multi-variable regression analysis, the VIF iterative test with a threshold for excluding variables of VIF > 10, recommended only preserving solar radiation, T_{min}, humidity, and wind speed, where their VIF's in this final subset of variables were 3.37, 3.22, 1.43, and 1.24 respectively. The data were then partitioned 70% and 30% for training and validation, respectively, and the following equation (Eq. 6) was achieved, with an R^2 exceeding 0.7 and high significance of all variables, except for solar radiation where p-value > 0.1 (Table 3).

$$\boldsymbol{Demand} = 176.3 + 0.5\boldsymbol{R_S} + 1.5\boldsymbol{T_{min}} - 0.68\boldsymbol{H} + 13.4\boldsymbol{W} \quad (6)$$

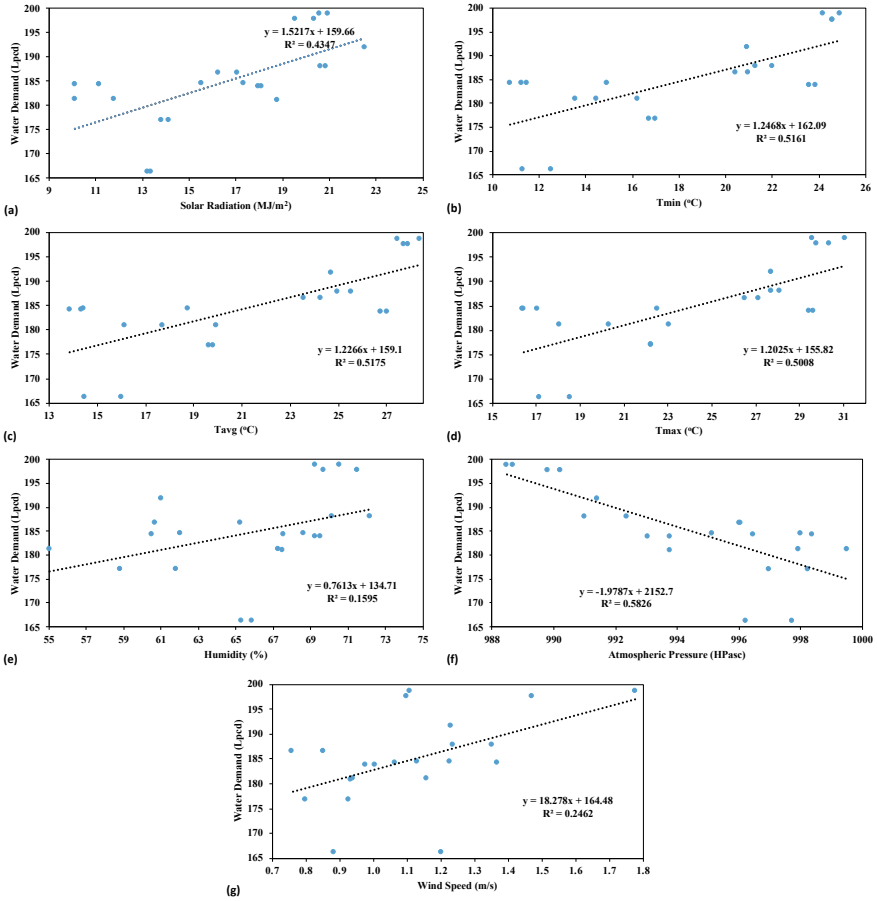

Fig. 10 Linear regression relationships between water demand and weather variables: **a** solar radiation, **b** minimum temperature, **c** average temperature, **d** maximum temperature, **e** humidity, **f** atmospheric pressure and **g** wind speed

Table 2 Model performance and statistical significance of weather variables

Statistical measures	Rs	T_{avg}	T_{min}	T_{max}	H	P_{atm}	W
R^2	0.4340	0.5170	0.5160	0.5000	0.1590	0.5825	0.2460
p-value	0.0008	0.0002	0.0002	0.0002	0.0655	0.00001	0.0188

where RS is the average monthly solar radiation in MJ/m^2, T_{min} is the minimum air temperature in °C averaged monthly, H is the average monthly relative humidity in %, and W is the average monthly wind speed in m/s. Figure 11 shows the partial regression plots detailing the relationship between the demand and each predictor

Table 3 Multivariable regression results

Residuals				
Min	1Q	Median	3Q	Max
−6.09	−3.38	−0.04	3.33	9.40
Coefficients				
Variable	Estimate	Std. error	t-value	Pr (> |t|)
Intercept	176.33	18.43	9.57	~0***
Solar radiation (MJ/m^2)	0.50	0.70	0.72	0.48
T_{min} (^{0} C)	1.53	0.48	3.19	0.07**
Humidity (%)	−0.68	0.35	−1.96	0.07
Wind speed (W)	13.41	5.75	2.33	0.04*

Signif. Codes: 0 '***' 0.001 '**' 0.01 '*' 0.05 '.' 0.1 ' ' 1
Residual standard error: 5.142 on 12 degrees of freedom
Multiple R-squared: 0.7757, Adjusted R-squared: 0.701, F-statistic: 10.38 on 4 and 12 degrees of freedom, p-value: 0.0007197

variable, while controlling for the presence of the other variables in the model. These plots were produced using the "car" package in R (Fox and Weisberg 2019).

3.2 Forecasted Water Demand

Considering that forecasts of future solar radiation wind speed, and humidity levels in Lebanon are lacking, water demand in GBA was projected using the linear regression models for minimum, average and maximum temperature (T_{min}, T_{avg} and T_{max}) (Table 3). These parameters were also adopted in other studies for forecasting the impact of the climate change on residential water demand (Al-Zahrani and Abo-Monasar 2015; Rasifaghihi et al. 2020).

Four periods (2020–2039, 2040–2059, 2060–2079, 2080–2099) were simulated. Climate forecasts revealed higher temperatures during summer months (June, July, August) and lower temperatures during winter months (December, January, February), compared to the reference period (2017–2019). As expected, RCP 8.5 showed the highest increase in temperature (Fig. 8). Consequently, the simulation results, using T_{min}, T_{avg} and T_{max} models, showed an increase of per capita water demand during summer and a decrease during winter. All three models showed very similar trends and the forecasted water demand values were close. For comparison purposes, the benchmark period (2017–2019) was also simulated, and the values are compared to the forecasted demand for all four future periods; the subsequent analysis considers the range of water demand predicted by the three temperature-based models.

On average, the *yearly demand* is forecasted (by the three temperature models) to increase under all scenarios, except RCP 2.6 (Fig. 12). Furthermore, a temporal

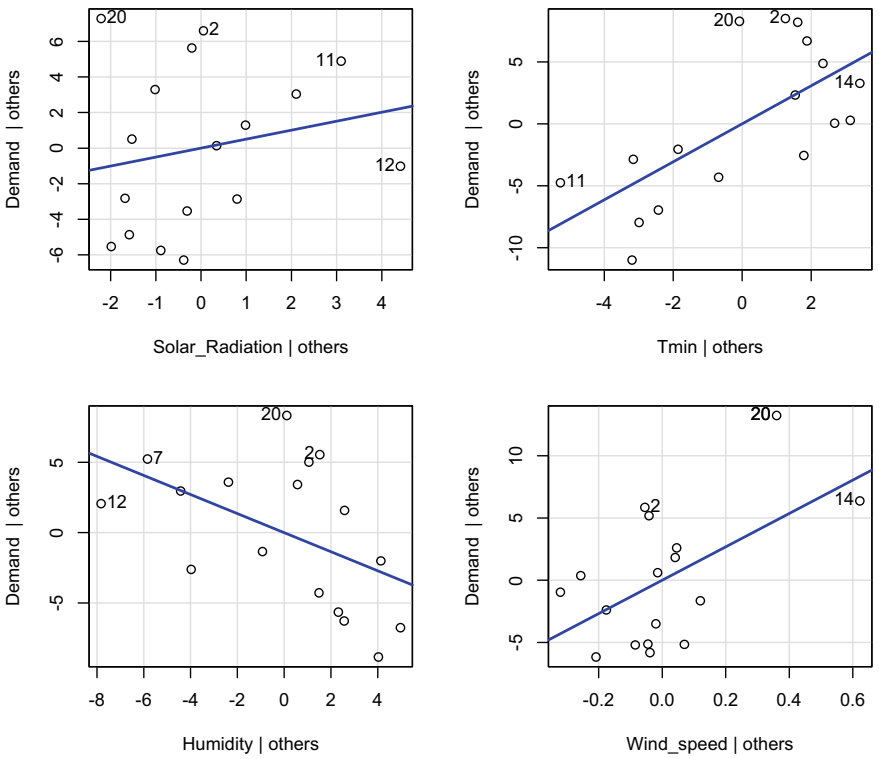

Fig. 11 Partial regression plots showing the effect of adding a new variable to a model by controlling the effect of the predictors in use

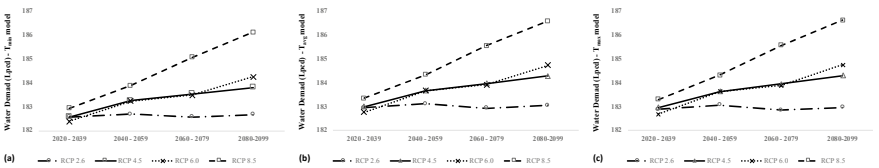

Fig. 12 Average yearly water demand (lpcd) under RCP 2.6, 4.5, 6.0, and 8.5 for the three models: **a** T_{min}, **b** T_{avg} and **c** T_{max}

shift in extreme demands, i.e., minimum and maximum monthly average demand, is expected. The former is expected to gradually shift backward, from February to January; while the latter is anticipated to gradually move forward from July to August—similarly to previously reported observations (Ghimire et al. 2016). This can be attributed to the anticipated climatic changes in terms of (1) shift in seasons, (2) longer dry periods, and (3) more intense yet shorter wet periods (Giorgi and Lionello 2008; Schilling et al. 2012).

The *maximum water demand*, occurring during the dry season, is anticipated to increase by 1 to 2 Lpcd on the short term (2020–2039) and 2 to 6 Lpcd on the long term (2080–2099) (Fig. 13b). Similarly, the *minimum water demand*, occurring during the wet season, is expected to decrease by about 3 Lpcd on the short term (2020–2039). But it will rise again and the difference with respect to current values will gradually drop to 2, 1 and 0 Lpcd, under RCP 4.5, 6 and 8.5, respectively, by the end of the century (Fig. 13a). To note that, under RCP 2.6, minimum and maximum temperatures remain fairly constant throughout the century.

3.3 Impacts on Total Demand

The total population size of GBA was forecasted by the Greater Beirut Water Supply Augmentation project (CDR 2017). It is expected to reach 3.5 million by 2035, compared to a current population of 2.0 million. Thus, about 46% increase in domestic water demand is expected due to population growth alone, leading to a yearly deficit of 227.7 MCM (CDR 2017).

On top of that, this study showed that climate change would cause an additional increase in domestic demand (*during the dry period*) of 45–90 thousand cubic meter per month on the short term (2020–2039) and 90–270 thousand cubic meter per month on the long term (2080–2099), as a best-case scenario as without considering population growth. Despite the fact that these figures do not seem substantial compared to the total yearly deficit, they are expected to occur at the most sensitive time of the year. In fact, the dry period is the most water stressed time of the year. Commonly, the water supply is not sufficient and most citizens buy tanked water at high prices and without any quality control measures. Thus, the expected monthly increase in water demand would result in an acute deficit during summer, accompanied by economic impacts and a possible surge in water-borne diseases. The latter was already proved to be substantial in Beirut due to the anticipated temperature increase alone (Yamout and El-Fadel 2005).

4 Conclusions and Recommendations

This study addresses one component of the anticipated socio-economic impacts of climate change on GBA, that is the increase in water demand. When combining all effects, including those of rising temperatures, reduced water availability, increased heat waves and heat island effect, among others, the anticipated additional burden looks disastrous—considering the already high vulnerability of GBA. In response, the Lebanese national and regional water authorities often advocate measures to ensure additional supply. Examples of planned projects for increased supply to GBA include: Awali river conveyor, Bisri dam, Janneh dam and Damour dam.

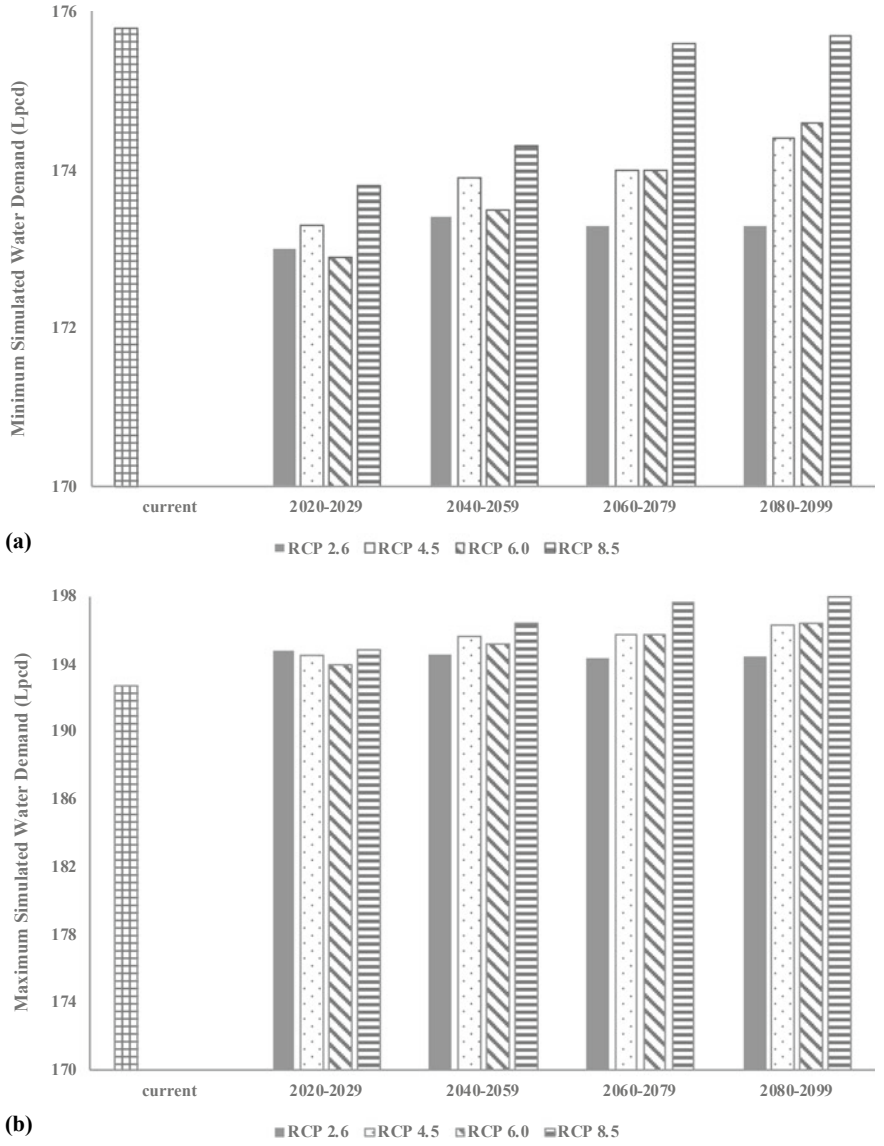

Fig. 13 Simulated water demand (lpcd) under RCP 2.6, 4.5, 6.0, and 8.5 for the three models: **a** minimum monthly average, **b** maximum monthly average

In such a data-scarce environment, Lebanon lacks detailed analysis of its water demand and influencing factors. This work investigated the link between domestic water demand patterns with monthly meteorological data and remotely sensed land surface temperature. The water demand pattern was found to be well described through minimum air temperature, humidity, wind and solar radiation, providing R^2 exceeding 0.7. Temperature was found to be highly correlated to water demand, and as it is the only dataset providing forecasts in the context of scenarios of climate change, it was used to forecast domestic water demand. Without considering an increase in population, an increase of 45–90 thousand cubic meter per month on the short term (2020–2039) and 90–270 thousand cubic meter per month on the long term (2080–2099) is expected for Beirut.

With domestic demand making up 76.9% of the total demand (Hamdar et al. 2015; MoEW 2012), assuming no agricultural water demand in GBA, attention should be drawn to the *reduction of domestic water demand*. This is especially true in the case of GBA where network losses are high (average of 47.5% in Lebanon compared to 35% global average) (MoEW 2012). In fact, a smart metering pilot test performed over a Achrafieh zone, as part of the Greater Beirut Water Supply Project, showed network losses of 52.4% (Bambos 2018). The average deficit between actual supply and demand, at the study zone, was found to be 53.5 Lcpd, equivalent to 28.95% of the demand.

Yet, efficient planning for reduced water demand calls for *improved availability of accurate and systematic data.* The whole country, including GBA, lacks actual demand figures due to (1) incomplete metering infrastructure and (2) absence of governmental monitoring and control of private water distribution businesses. Similarly, losses and actual water supply (reaching the consumer end) are not tracked by water authorities.

Acknowledgements We would like to thank Eng. Mary Saade, Eng. Antoine Zoghbi and Eng. Habib El Asmar from Beirut and Mount Lebanon Water Establishment (EBML) for helping in the provision of the water supply data. We would also like to thank Dr. Ziad Rached from the faculty of applied sciences at NDU for his insight on time series analysis.

References

Aitken CK, Duncan H, McMahon TA (1991) A cross-sectional regression analysis of residential water demand in Melbourne Australia. Appl Geogr 11(2):157–165. https://doi.org/10.1016/0143-6228(91)90041-7

Akinwande MO, Dikko HG, Samson A (2015) Variance inflation factor: as a condition for the inclusion of suppressor variable(s) in regression analysis. Open J Stat 05(07):754–767. https://doi.org/10.4236/ojs.2015.57075

Al-ahmady KK (2011) Calculating and modeling of an indoor water consumption factor in mosul city, Iraq. J Environ Stud 39–52. https://www.researchgate.net/profile/Kossay-Alahmady/publication/324115649_Calculating_and_Modeling_of_an_Indoor_Water_Consumption_Factor_in_Mosul_City_Iraq/links/5abeb4f9aca27222c757780b/Calculating-and-Modeling-of-an-Indoor-Water-Consumption-Factor-in-M

Al-Zahrani MA, Abo-Monasar A (2015) Urban residential water demand prediction based on artificial neural networks and time series models. Water Resour Manage 29(10):3651–3662. https://doi.org/10.1007/s11269-015-1021-z

Alavipanah SK, Haashemi S, Kazemzadeh-zow A, Bloorani AD, Asadolah S (2016) Remotely sensed survey of Land surface temperature (LST) for evaluation of monthly changes of water consumption. Uppd 66–76. https://doi.org/10.5176/2425-0112_uppd16.27

ArabNews (2019) Why such rainy, cold weather in the Middle East this spring?

Atlantic Council (2019) Why the MENA region needs to better prepare for climate change

Badran AF (2016) Securing the future of water resources for beirut : a sustainability assessment of water governance

Bambos C (2018) PBC for NRW reduction—the case of Beirut Lebanon

Bou-Fakhreddine B, Mougharbel I, Faye A, Pollet Y (2019) Estimating daily evaporation from poorly-monitored lakes using limited meteorological data: a case study within Qaraoun dam—Lebanon. J Environ Manage 241(July):502–513. https://doi.org/10.1016/j.jenvman.2018.07.032

Bucchignani E, Mercogliano P, Panitz HJ, Montesarchio M (2018) Climate change projections for the Middle East-North Africa domain with COSMO-CLM at different spatial resolutions. Adv Clim Chang Res 9(1):66–80. https://doi.org/10.1016/j.accre.2018.01.004

Campisi-Pinto S, Adamowski J, Oron G (2012) Forecasting urban water demand via wavelet-denoising and neural network models. Case study: city of Syracuse, Italy. Water Resour Manage 26(12):3539–3558. https://doi.org/10.1007/s11269-012-0089-y

CAS (2008) Water consumption maps

CDR (2017) Lebanon—Greater Beirut urban transport project : environmental assessment : environmental and social impact assessment (ESIA) for the bus rapid transit (BRT) system between Tabarja and Beirut and feeders buses services (English)

Chang H, Praskievicz S (2014) Sensitivity of urban water consumption to weather and climate variability at multiple temporal scales : the case of Portland, Oregon sensitivity of urban water consumption to weather and climate. Int J Geospat Environ 1(1), Article 7

Comair F (2011) L'efficience d'utilisation de l'eau et approche économique. Plan BLeu, Centre d'Activités Régionales PNUE/PAM, 64

Council for Development and Reconstruction (CDR) (2014) Greater Beirut water supply augmentation project—environmental and social impact assessment, vol 1. https://doi.org/10.1017/CBO9781107415324.004

El-Samra R, Bou-Zeid E, Bangalath HK, Stenchikov G, El-Fadel M (2017) Future intensification of hydro-meteorological extremes: downscaling using the weather research and forecasting model. Clim Dyn 49(11–12):3765–3785. https://doi.org/10.1007/s00382-017-3542-z

Enriquez R, Rodriguez M, Blanco AC, Estacio I, Depositario LR (2019) Spatial and temporal analysis of monthly water consumption and land surface temperature (LST) derived using landsat 8 and modis data. International Archives of the Photogrammetry, Remote Sensing and Spatial Information Sciences—ISPRS Archives 42(4/W19):193–198. https://doi.org/10.5194/isprs-archives-XLII-4-W19-193-2019

FAO (2020) Meteorological data

FAO & AQUASTAT (2015) FAO—world water demand distribution

Faour G, Mhawej M (2014) Mapping urban transitions in the Greater Beirut Area using different space platforms. Land 3(3):941–956. https://doi.org/10.3390/land3030941

Fox J, Weisberg S (2019) An R comparison to applied regression (Third)

Gato S, Jayasuriya N, Roberts P (2007) Forecasting residential water demand: case study. J Water Resour Plan Manage 133(4):309–319. https://doi.org/10.1061/(ASCE)0733-9496(2007)133:4(309)

Ghimire M, Boyer TA, Chung C, Moss JQ (2016) Estimation of residential water demand under uniform volumetric water pricing. J Water Resour Plan Manage 142(2):1–6. https://doi.org/10.1061/(ASCE)WR.1943-5452.0000580

Giorgi F, Lionello P (2008) Climate change projections for the Mediterranean region. Global Planet Change 63(2–3):90–104. https://doi.org/10.1016/j.gloplacha.2007.09.005

Google Earth Engine (2021) WorldClim BIO variables V1. https://www.developers.google.com/earth-engine/datasets/catalog/WORLDCLIM_V1_BIO
Hamdar B, Hejaze H, Boulos J (2015) Managerial efficiency modeling of water use in the Republic of Lebanon. J Soc Sci 4(1):649–663. https://doi.org/10.25255/jss.2015.4.1.726.744
Hijmans RJ, Cameron SE, Parra JL, Jones PG, Jarvis A (2005) Very high resolution interpolated climate surfaces for global land areas. Int J Climatol 25(15):1965–1978. https://doi.org/10.1002/joc.1276
Hussein H, Natta A, Yehya AAK, Hamadna B (2020) Syrian refugees, water scarcity, and dynamic policies: how do the new refugee discourses impact water governance debates in Lebanon and Jordan? Water (Switzerland), 12(2). https://doi.org/10.3390/w12020325
Jaafar H, Ahmad F, Holtmeier L, King-Okumu C (2020) Refugees, water balance, and water stress: lessons learned from Lebanon. Ambio 49(6):1179–1193. https://doi.org/10.1007/s13280-019-01272-0
Koegst T, Tranckner J, Krebs P (2008) Multi-Regression analysis in forecasting water demand based on population age structure. December 2015, 1–10
Kuhn M (2008) Building predictive models in R using the caret package. J Statist Softw 28(5):1–26. https://doi.org/10.18637/jss.v028.i05
Lange MA (2019) Impacts of climate change on the Eastern Mediterranean and the Middle East and North Africa region and the water-energy nexus. Atmosphere 10(8):455. https://doi.org/10.3390/atmos10080455
Lawrence MG (2005) The relationship between relative humidity and the dewpoint temperature in moist air: a simple conversion and applications. Bull Am Meteor Soc 86(2):225–233. https://doi.org/10.1175/BAMS-86-2-225
Margane A, Schuler P (2013) Groundwater vulnerability in the groundwater cathchment of jeita spring and delineation of groundwate protection zones using the COP method. February, 133
Mo Y, Xu Y, Chen H, Zhu S (2021) A review of reconstructing remotely sensed land surface temperature under cloudy conditions. Remote Sensing 13(14):2838. https://doi.org/10.3390/rs13142838
MoE (2016) Lebanon's third national communication to the UNFCCC
MoEW (2010) The state and trends of the lebanese environment. file:///C:/Users/Drake Group/Downloads/SOER_en.pdf
MoEW (2012) National water sector strategy (Issue August). http://www.extwprlegs1.fao.org/docs/pdf/leb166572E.pdf
MoF (2019) Citizen budget
Neale T, Carmichael J, Cohen S (2007) Urban water futures: a multivariate analysis of population growth and climate change impacts on urban water demand in the Okanagan basin BC. Can Water Resour J 32(4):315–330. https://doi.org/10.4296/cwrj3204315
O'Donnell MS, Ignizio DA (2012) Bioclimatic predictors for supporting ecological applications in the conterminous United States. US Geol Surv Data Ser 691:10
OCHA (2016) Population in Beirut and Mount Lebanon (Issue March)
Phan TN, Kappas M (2018) Application of MODIS land surface temperature data: a systematic literature review and analysis. J Appl Remote Sens 12(04):1. https://doi.org/10.1117/1.jrs.12.041501
Rasifaghihi N, Li SS, Haghighat F (2020) Forecast of urban water consumption under the impact of climate change. Sustain Cities Soc 52(September 2019). https://doi.org/10.1016/j.scs.2019.101848
Schilling J, Freier KP, Hertig E, Scheffran J (2012) Climate change, vulnerability and adaptation in North Africa with focus on Morocco. Agr Ecosyst Environ 156:12–26. https://doi.org/10.1016/j.agee.2012.04.021
Shaban A (2020) Water resources of Lebanon (Issue July). https://doi.org/10.1007/978-3-030-48717-1.pdf
UN (2020) Beirut population 2020

UN Statistical Commission (2019) Sustainable development goal 6 Ensure availability and sustainable management of water and sanitation for all

Uthayakumaran L, Spaninks F, Barker A, Pitman A, Evans JP (2019) Impact of climate change on water demand. Water E J 4(2):1–7. https://doi.org/10.21139/wej.2019.012

Valiantzas JD (2013) Simplified forms for the standardized FAO-56 Penman-Monteith reference evapotranspiration using limited weather data. J Hydrol 505:13–23. https://doi.org/10.1016/j.jhydrol.2013.09.005

Waha K, Krummenauer L, Adams S, Aich V, Baarsch F, Coumou D, Fader M, Hoff H, Jobbins G, Marcus R, Mengel M, Otto IM, Perrette M, Rocha M, Robinson A, Schleussner CF (2017) Climate change impacts in the Middle East and Northern Africa (MENA) region and their implications for vulnerable population groups. Reg Environ Change 17(6):1623–1638. https://doi.org/10.1007/s10113-017-1144-2

Wan Z (2013) Collection-6 MODIS land surface temperature products users' guide Zhengming. Indian J Chem Technol. https://www.lpdaac.usgs.gov/documents/118/MOD11_User_Guide_V6.pdf

Wang XJ, Zhang JY, Shahid S, Xie W, Du CY, Shang XC, Zhang X (2018) Modeling domestic water demand in Huaihe River Basin of China under climate change and population dynamics. Environ Dev Sustain 20(2):911–924. https://doi.org/10.1007/s10668-017-9919-7

Wang X, jun, Zhang, J. yun, Shamsuddin, S., Oyang, R. lin, Guan, T. sheng, Xue, J. guo, & Zhang, X. (2017) Impacts of climate variability and changes on domestic water use in the Yellow River Basin of China. Mitig Adapt Strat Glob Change 22(4):595–608. https://doi.org/10.1007/s11027-015-9689-1

WEF (2019) How the Middle East is suffering on the front lines of climate change. World Economic Forum

World Bank (2003) Republic of Lebanon policy note on irrigation sector sustainability. 28766. Note on Irrigation Sector Sustainability.pdf. http://www.databank.com.lb/docs/Policy

World Bank (2020) Climate change knowledge portal

Yamout G, El-Fadel M (2005) An optimization approach for multi-sectoral water supply management in the Greater Beirut Area. Water Resour Manage 19(6):791–812. https://doi.org/10.1007/s11269-005-3280-6

MODIS Satellite Images and TRMM Products to Compare Rainfall and Streamflow Along the Coastal Rivers of Lebanon

Amin Shaban, Cordula Robinson, and Farouk El-Baz

1 Introduction

Streamflow of rivers into the sea is a common hydrologic phenomenon of water flow into the sea has received substantial attention in several coastal zones of the World, as many of these regions are witnessing severe water deficit. This is well pronounced applicable in arid and semi-arid regions of the world; such as in the Middle East. Studies carried out in this regard include the Levantine region of Spain, Lebanon and the Arabian Gulf (El-Qareh 1967; FAO 1973; Gomis 1996; Travaglia and Ammar 1998; Brink et al. 1998; Fielding and El-Baz 2001; Fielding et al. 2001; Robinson et al. 2005; Shaban et al. 2005a, b). River water flow to the sea may occurs as direct surface water runoff (i.e., along rivers and streams), or as groundwater discharges that are commonly referred to as "submarine springs".

The relatively high precipitation rate (i.e., 900–1000 mm) in Lebanon results huge amounts of surface water and runoff. Yet, the largest volume of water is rapidly flows to the sea before being utilized. This is attributed mainly to the rugged topography that represented mainly by the steep sloping terrain. The same is true for the groundwater seeps from coastal aquifers in Lebanon, which are controlled by the acute inclination of rock stratum dipping to the west, as well as dense fracture systems. The coastal zone of Lebanon (situated between the geographic coordinates: 33° 03′

A. Shaban (✉)
National Council for Scientific Research-Lebanon, CNRS-L, P.O. Box 11-8281, Beirut, Lebanon
e-mail: geoamin@gmail.com

C. Robinson
Kostas Research Institute at Northeastern University, 141 South Bedford Street, Burlington, MA 01803, USA
e-mail: c.robinson@northeastern.edu

F. El-Baz
Center for Remote Sensing, Boston University, 685 Commonwealth Ave, Boston, MA, USA
e-mail: farouk@bu.edu

A. Shaban (ed.), *Satellite Monitoring of Water Resources in the Middle East*,
Springer Water, https://doi.org/10.1007/978-3-031-15549-9_11

17″; 34° 40′ 00″ N, and 35° 06′ 11″; 36° 19′ 16″ E) is a typical example that illustrates both types of water loss including surface and subsurface water flow into the sea. This loss exacerbated the extreme water shortage found in the area of study. Besides, researchers on hydrology research is largely focused on inland groundwater resources and groundwater seeps in the marine environment. Several studies have been performed to locate these sources, such as those by El-Qareh (1967), FAO (1973), Hakim (1974, 1985), NCRS (1999), Khawlie et al. (2000), and Shaban et al. (2005b). The studies on water conservation for water of the Lebanese rivers are still few due to the insufficient data required.

In Lebanon, there are 14 perennial rivers and about 45 major intermittent streams. Three of these rivers are inner ones and they originate from the Bekaa Plain. One of these inner rivers (i.e. Litani River) flows southward, and then it diverted to the west and outlets in the sea (Fig. 1). There are eleven coastal rivers where they flow directly from the Western Lebanese Mountains (i.e. Mount-Lebanon) into the Mediterranean. The coastal rivers in Lebanon can belong to a unique regional drainage system, because they own almost similar hydrologic behaviour, especially the slopping to the west. One of the coastal rivers (i.e. El-Kabir River) is shared with Syria in the north.

According to Shaban (2020), there is unique hydrologic feature that characterizes the Lebanese rivers where all of them are almost controlled by the rugged topography, and then span within the three geomorphological units of Lebanon (i.e. Mount-Lebanon, Bekaa Plain and the Anti-Lebanon). Lebanon, with its small area (10,452 km^2) represents as a regional hydrologic junction where water flows into three regional directions. These are: (1) northward to comprise a tributary of the Orates River Flow System, (2) southward forming a major tributary for Jordan River Flow System and (3) westward where the Lebanese Coastal Rivers System flow to the Mediterranean Sea (Shaban 2021).

The maximum reported average annual discharge from the Lebanese coastal rivers is approximately 408 million m^3/year flows from Ibrahim River, whereas the least discharge is 55 million m^3/year in the Siniq River (LRA 2001). The largest catchment area is 480 km^2 for Abou Ali River (Shaban 2003), which has an average discharge of about 269 million m^3/year. In addition, the hydrologic characteristics of the coastal rivers of Lebanon are different, remarkably in their drainage density, relief gradient, meandering ratio and width/length ratio (Shaban et al. 2005a). This is attributed to the presence of different rock lithologies and the dominant geologic structures (e.g. faults and fractures). There is a clear difference in discharge between these rivers, in spite of similar hydrologic dimensions (e.g. catchment area, river's length, etc.). The differences should also be considered in the context of rainfall rates (Shaban and Robinson 2006).

There is a direct relationship between the rainfall rate (and patterns) and the streamflow along rivers including the areal extent of freshwater into the sea as turbid water plumes (Fig. 2). This is well noticed from field observations and from the available measurements, whilst the mechanism and dynamics of streamflow are still undetermined. In Lebanon, most instruments for measuring rivers' discharge (i.e. hydrographs and flow-meters), which were located along these rivers, have been

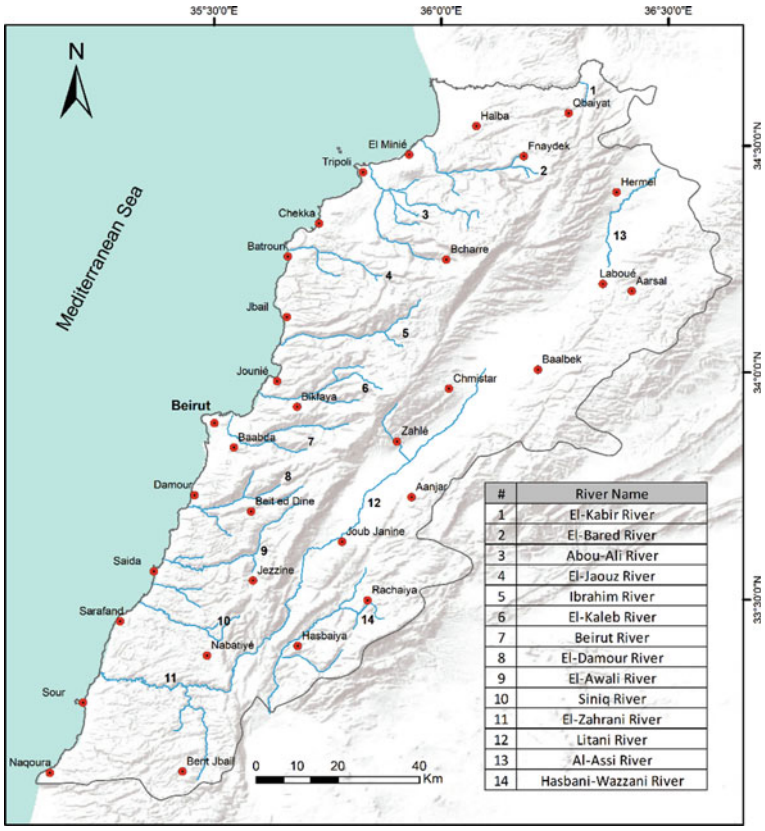

Fig. 1 Rivers of Lebanon (Shaban 2020)

destroyed or non-functional. Therefore, the limited datasets which are retrieved from these instruments are inadequate to elaborate optimal management approaches on water resources. Therefore, new techniques and approaches need to be sought and adopted. In this regards, remote sensing techniques, combined with field studies, can constitute an optimal tool since they enable generating accurate geo-spatial data and maps as well as they are capable to apply periodical monitoring for water flows to the sea.

Two remotely sensed datasets were utilized in this study, and they were compared with field data. The first is the TRMM which provides rainfall data; and the second is the MODIS-Terra satellite which provides data either on the visual extent of water plumes into the sea or by measuring the sea surface temperature which indicates the freshwater plumes into the sea. The objective of this research is to show the capability of using remotely sensing data, notably by comparing it with instrumental measurements; in addition, it aims to use the remotely sensed data for monitoring in order to assess the responses of water output (freshwater plumes into the sea) water input (precipitation) with respect to water output (freshwater plumes).

Fig. 2 Plumes (turbid water) along the Lebanese coast (Step Feed 2017)

The assessment of streamflow along the Lebanese coastal rivers is significant, and it interprets the low water discharge in some rivers besides high precipitated rate. It also reflects the hydrologic characteristics of rivers' catchments including mainly rock lithology and the structural features for understanding groundwater flow paths. In a distributed groundwater flow and transport model, the role of the structures as preferential flow and transport paths, could be accounted for by choosing appropriate hydraulic and transport parameters.

2 Tools and Methods

The main concept behind monitoring water flow from rivers versus rain fall peaks lies in correlating the two datasets (Fig. 3). Water flow is monitored using thermal data from MODIS-Terra satellite images, which are acquired on a daily basis. Sequential time-series rainfall data are available from the TRMM as images and graphs. In this study, data correlations were carried out for the year 2002 to include the whole coastal zone of Lebanon (~225 km) described above.

The selection of this year is based on the availability of records at the time research began, especially with respect to the availability of field data from meteorological and gauging station records. Using these data, the input from rainfall was compared with the output of water flow from rivers to the sea. All rainfall peaks were considered and checked against the areal extent of flow into the sea for each closed hydrologic system, that is, the catchment area or drainage basin. With this premise, the time period between the date of the rainfall peak and the appearance of the thermal plume in the sea (i.e. lag time) was recorded, as well as the residence time of the plume in the

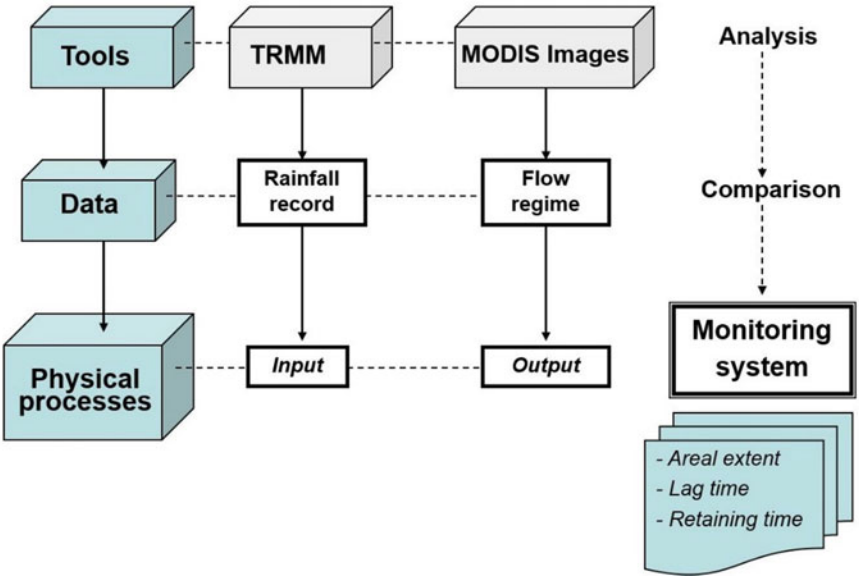

Fig. 3 Major elements of data used in the study

sea (Fig. 3). This allows appraisal of the hydrologic dynamics of the flowing water and the characteristics of the terrain in each drainage basin that captured precipitated water and diverted it seaward.

2.1 TRMM

The number of operational climatic stations in Lebanon are insufficient to build a comprehensive picture of the rainfall regime and intensity or to produce a realistic contour map of precipitation in the area. Existing stations are not distributed evenly and are not closely spaced. Thus, in order to obtain a continuous precipitation record, TRMM rainfall data were used. TRMM is a joint mission between NASA and the Japan Aerospace Exploration Agency (JAXA) and was primarily designed to study and monitor tropical rainfall. These data are acquired on a daily basis globally, and are free of charge. They can be retrieved either as graphs illustrating rainfall amounts over time (Fig. 4) or as contour maps for a specific day.

The accuracy of the TRMM data for the study area was verified by tabular and graphical comparisons between these data and ground data from gauging stations in coastal Lebanon. An obvious correlation was observed for the timing of events, although there was some variance in the amount of precipitation recorded, presumably arising from varying geographic coverage and accuracy of measurement. The

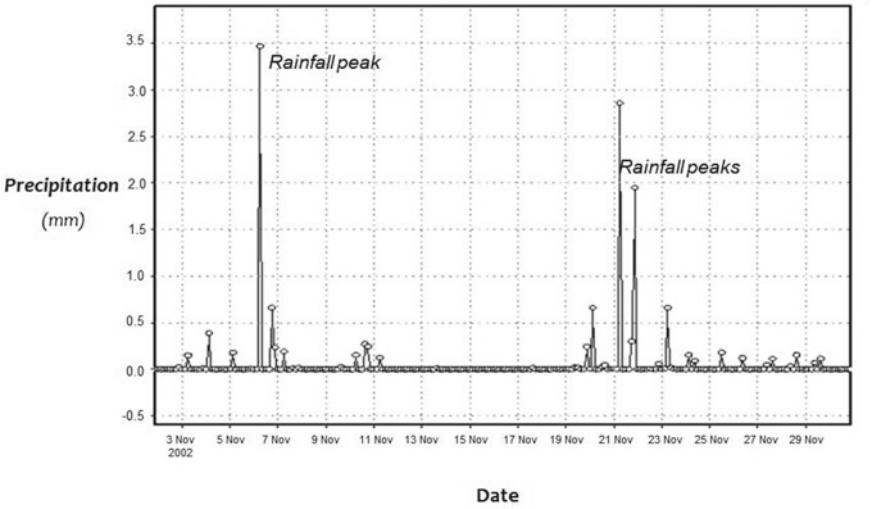

Fig. 4 Example of TRMM data illustration showing rainfall peaks

rainfall record from TRMM data was obtained daily for the purpose of monitoring each drainage basin-related river of the coastal area of Lebanon.

2.2 MODIS-Terra Images

Thermal satellite images were used in this study in order to monitor the timing of occurrence and geographic distribution of freshwater plumes in the sea. The concept of plume identification depends on measuring sea surface temperature (SST) using thermal bands in MODIS images where freshwater is often cooler than saltwater, and this enables applying thermal differentiation between them.

The selection of the processed images was based on their time coincidence with the record of rainfall peaks observed in the TRMM data. Moderate-resolution images such as MODIS, Advanced Very High Resolution Radiometer (AVHRR) or Sea-viewing Wide Field-of-view Sensor (SeaWiFS) are useful in this regard since they have high temporal resolution (they are collected daily), with a 2-day repeat cycle. In this study, day and night time Level 2 11 μm MODIS-Terra images were retrieved from the Goddard Space Flight Center "DISC" website and prepared for analysis. The spatial resolution is 250 m, which is adequate for the purpose of this study.

Images were downloaded for the period January 2002 to February 2003, that is, a one-year time interval. Not all images retrieved were suitable for analysis, however, because of clouds, missing data, or other irregularities. All images selected for processing required a prerequisite geo-referencing. This was performed using PCI's Geomatica GCPworks software, applying the UTM coordinate system and

WGS84 datum. Geo-referencing is needed to co-register the images; store them in a GIS database; and enable the geo-location of satellite observations in the sea and on land. The images were then digitally enhanced using ENVI (Environment for Visualization Images) software.

Band math option was used to apply scaling/conversion algorithm, which enables mapping the "real" temperature in degrees Celsius. The scaling conversion equation is:

$$\begin{aligned}
&\text{Scale type (Y)} = \text{Slope} * X + \text{Intercept} \\
&\text{Slope} = 0.0099999998 \\
&\text{Intercept} = -300\,f; \\
&Y\,(\text{in Deg C}) = 0.01 \text{ times } X - 300
\end{aligned}$$

The natural spread of Digital Number (DN) values were used for anomalous thermal feature detection in seawater—in this case, cool freshwater plumes relative to the ambient temperature of seawater. Thus, images do not need to be contrast stretched. To further emphasize the presence of a thermal anomaly, density slices were applied (Fig. 5).

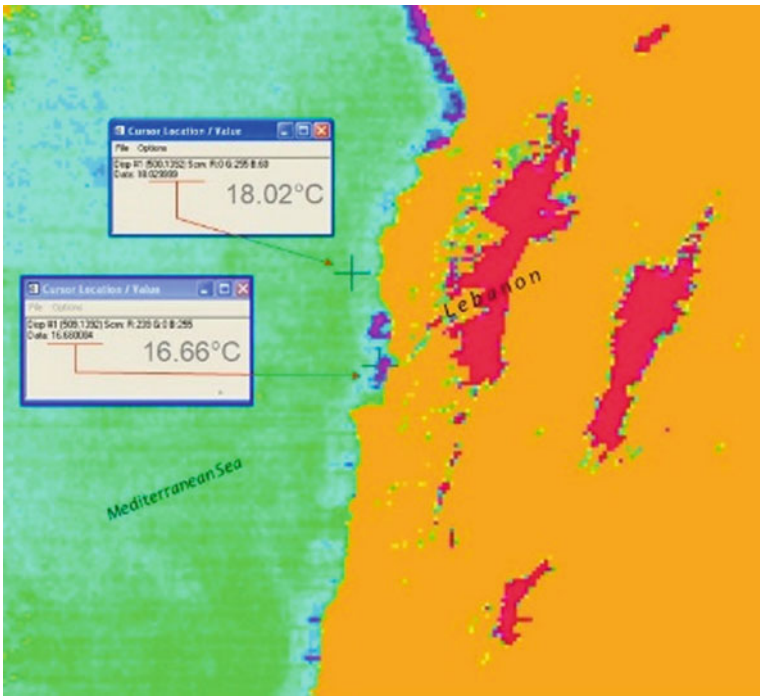

Fig. 5 Density sliced MODIS images showing different temperature levels and cool freshwater plumes

Differentiation in temperature was calculated to reach up to 4 °C. This strong contrast indicates high-energy water flow from the rivers and streams into the sea. Selectively, the temperature differentiation is observed in the satellite data were confirmed in the field using a submersible probe (*YSI*—600XLM) with built-in programming and data logging.

Since the Lebanese coastal zone encompasses a number of groundwater discharges or submarine springs (Shaban et al. 2005b), it was necessary to distinguish them from water flowing into the sea from known rivers. This was applied by the Geographical Information System (GIS) techniques. In this case, processed satellite images were overlain on topographic maps to show the exact geographic location of the river's outlets into the sea. The thermal plumes were only identified where at rivers' outlet.

2.3 Rainfall Peaks Versus Plume Area

When all data retrieved from TRMM and MODIS-Terra has been prepared; therefore, numeric values for each of them were resulted and then put in tables for the year 2002. This is in order to apply the comparison and to assess the rainfall/water flow relationship for the ten coastal rivers of Lebanon. The studies catchments were calculated in particular they represent the amount of water captured from precipitation. From these two variable (i.e. volume of rainfall and plumes area in the sea), the input/output amounts of water can be evaluated.

Measuring the volume of water from rainfall was the first step where it was calculated form TRMM, and it was measured in millimeters (mm). To convert this the mm of rainfall to a volume in million m^3 per day, it was multiplied by the area of the catchment (i.e. km^2). The extent of water plumes into the sea was also measured in km^2. Units were standardized for all calculations. This was applied to the ten rivers for the one-year period.

There are five key measurement were considered for the quantitative analysis. These are:

1. Values of rainfall peaks (R_P),
2. The coincidence between the plume area (P_A) and river within known discharges from gauging stations (D_g),
3. Lag time (τ) between rainfall peak and the existence of water plumes into the sea,
4. The spatial extent (area) of plumes into the sea (P_A) after each rainfall peak,
5. The ratio (R_{pd}) between the spatial extent of plumes with respect to the recorded discharge from rivers.

3 Results

Rivers discharge in the coastal zone of Lebanon varies due to their drainage systems including their physical characteristics as well as the human activities in these catchment. In particular, the hydrologic and geologic characteristics and land cover/use. For example, the catchment area El-Bared River (202 km^2) is almost twice that of the Zahrani River (140 km^2), yet the discharge from the Zahrani River (225 Mm^3) is about 1.5 times that of El-Bared River (155 Mm^3).

The degree of variance changes periodically depending on rainfall intensity and patterns as well as the land-use change, where pumping of groundwater is utmost significant. Therefore, monitoring the balance between water captured by the catchments and water discharged from the belonging rivers allows the hydrologic and anthropic behavior inside the catchment to be appraised. With the availability of remotely sensed data, it is now possible to do this, where TRMM data provide daily information on rainfall and MODIS-Terra data provide daily images of plume size.

The use of TRMM and MODIS-Terra data enables the assessment of various relationships can be established between the different hydrologic elements identified (R_P, P_A, D_g, τ and R_{pd}). Standardization of the units is necessary in all calculations.

Abou Ali River, flows in North Lebanon (Fig. 1) was utilized as a typical example, and the results were illustrated in Table 1. It shows that plumes appear in the Mediterranean Sea 3–4 days after a rainfall event and that these plumes were only visible for one day at a 250 m spatial resolution. This timing of events varies for the other 9 rivers analyzed (Table 2), where lag times range between 1 and 4 days, and residence times between 3 and 8 days.

3.1 Rainfall from Gauges (R_g) and TRMM Data (R_{TR})

Rainfall amounts from available gauging stations were compared with TRMM data as an accuracy assessment for all ten rivers analyzed in this research (Table 2). The results show that the pattern of rainfall (whether it is increasing or decreasing) is represented in the same way by both datasets, although the recorded amounts of rainfall are consistently greater at the gauging stations. This latter effect is further emphasized in Fig. 6 and in Table 2 with respect to the average rainfall ratio for all the rivers, which averages 1.35 (Table 2).

Numerous studies used TRMM products as a reliable source of rainfall data (e.g. Ohsaki 2000; Scott et al. 2007). In this study, rainfall records from gauging stations were compared with TRMM data (Table 2). Therefore, both measuring tools reveal nearly results in a clear coincidence in the trend of rainfall amounts (i.e., ascending and descending), though the recorded amounts of rainfall from gauging station were found to be a little bit exceeded (example in Fig. 6).

The lesser rainfall amounts recorded in TRMM data are possibly a consequence of different areal coverage of the measuring instruments (point source compared with

Table 1 Selected datasets for the Abou Ali River as recorded from gauges, TRMM and MODIS-Terra data

Abou Ali River—2002									
Date	R_{TR}	R_g	$R_g + R_{TR/2}$	R_g/R_{TR}	P_A	Q_m	Q_m/P_A	τ	T_r
	(mm)	(mm)	(mm)	Ratio	(km^2)	(Mm^3/day)	Ratio	(days)	(days)
Feb. 9	0.2	0	0.1	–	0.172	0.618	3.59		
Feb. 10	1	1.6	1.3	1.60	0.169	0.625	3.69		
Feb. 11	8	11.4	➡9.7	1.42	0.168	0.641	3.81		
Feb. 12	0.5	1.43	0.96	2.86	0.166	0.623	3.75		
Feb. 13	0	0	0	–	0.179	0.785	4.38		
Feb. 14	0.9	0	0.45	–	0.488	0.853	1.74	➥4	*
Feb. 15	0.4	0.7	0.65	1.75	1.217	1.034	0.89		*
Feb. 16	0.3	0.7	0.5	2.33	1.531	1.132	0.74		*
Feb. 17	0	0	0	–	1.552	1.214	0.78		*
Feb. 18	0	0	0	–	1.435	1.201	0.84		
Feb. 19	0.8	0	0.4	–	1.462	1.179	0.80		
Feb. 20	0	0.4	0.2	–	1.368	1.094	0.79		
Feb. 21	4	6.3	5.15	1.57	1.325	0.972	0.73		
Feb. 22	0.4	0.9	0.65	2.25	1.226	0.946	0.77		
Feb. 23	6.8	10.54	➡8.67	1.55	1.046	0.901	0.86		
Feb. 24	0.7	2.1	1.4	3.00	1.033	0.894	0.78		
Feb. 25	2.1	4.3	3.2	2.04	1.152	0.937	0.81	➥3	*
Feb. 26	2.7	4.8	3.75	1.77	1.167	0.942	0.80		*
Feb. 27	0.4	1.05	0.725	2.62	1.175	0.857	0.77		*
Feb. 28	0.6	0.4	0.5	0.66	1.181	0.832	0.87		*
March 1	0.1	0.2	0.15	2.00	1.164	0.794	0.68		
March 2	0.1	0.3	0.2	3.00	1.169	0.758	0.65		

➡ Rainfall peak, ➥ lag time, * residence time

synoptic view), the resolution of the TRMM data, and possibly interference effects in more torrential rain events. However, the use of the TRMM data is still encouraging and can fulfill continuous data collection needs to emphasize essential trends and patterns that are needed for this type of research. It may also be that TRMM data are more reliable than field gauging station data simply because gauging stations only represent a point source measurement compared with the synoptic view that satellite data allow (Nirala and Cracknell 2002; Shaban and Robinson 2006). For these reasons, the average value was calculated using both data sources to illustrate average peaks in rainfall (Table 1, column 3).

Table 2 Hydrologic variables for selected coastal Lebanese rivers obtained from TRMM, MODIS-Terra and from field measurements

Coastal Lebanese rivers—2002									
Rivers watershed	R_{TR}	R_g	R_g/R_{TR}	P_A	$Q \gg P_A$	Q_m	Q_m/P_A	Average τ	Average T_r
	(Mm^3/year)		Ratio	km^2	(Mm^3/year)		Ratio	(days)	
Al-Bared	134	233	1.74	2.25	1.74	147	135	0.92	4
Abou-Ali	453	482	1.06	4.10	1.06	246	269	1.09	3
El-Jauz	111	120	1.08	1.75	1.08	101	85	0.84	4
Ibrahim	342	381	1.11	7.75	1.11	572	408	0.71	1
El-Kalb	226	348	1.54	3.55	1.54	258	191	0.74	2
Beirut	219	248	1.13	2.40	1.13	146	111	0.76	2
Damour	289	337	1.67	5.60	1.67	167	217	1.30	1
El-Awali	267	312	1.17	6.15	1.17	203	261	1.28	1
Siniq	58	101	1.74	1.55	1.74	61	55	0.90	3
Zahrani	103	137	1.33	1.95	1.33	254	225	0.88	3
Average	220.2	269.9	1.35	3.70	1.35	215.5	195.7	0.942	2.4
Total	2202	2699			2155	1957			

$Q \gg P_A$ River discharge as indicated by the plumes dimensions

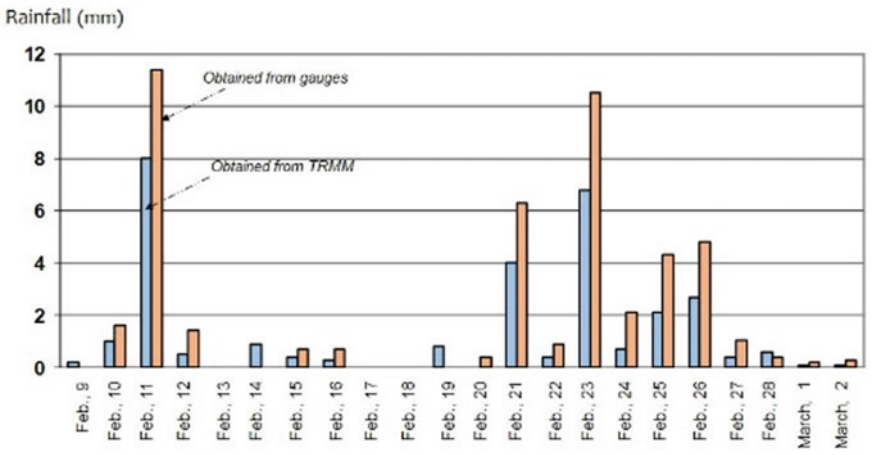

Fig. 6 Comparative analysis between rainfall data from TRMM from field gauges for Abou Ali River

3.2 *Plumes Area (P_A) and Rivers Discharge (Q_m)*

During dry seasons, no significant freshwater plumes can be depicted in the MODIS images. This is because few amount of water is discharged, and it cannot be observed in the 250 m spatial resolution images. This is in contrast to the freshwater plumes that are obvious after a rainfall events which may cover an area exceeding few tens of square kilometers in the sea. Example has been illustrated for Ibrahim River in the middle part of the coast of Lebanon (Table 1).

The extent of a plume, as well as the lag time, differs from one river to another (Tables 1 and 2). The ratio of plume area to river discharge has a variance between 0.71 and 1.30 for the ten rivers in coastal Lebanon (Table 2). The variance is greatest for the rivers located in the middle part of the region—that is, from Ibrahim to El-Awali (Fig. 1). This is likely a consequence of the higher altitudes in these drainage basins (>2500 m), which bring about higher precipitation rates. Rain in these parts may be almost torrential and the transit time to the sea is short since slopes are acute, which contributes to the lower ratio observed. A condition that contributes to the higher ratio occurs when rainfall is especially heavy, as is clearly illustrated for the Abou Ali River (Fig. 7 and Table 2). In this case, the average ratio between the area of a plume and a river's discharge is about 2:1, that is, 2 km^2 of water plume area in the sea corresponds with approximately 1 million m^3 of water discharged from the river.

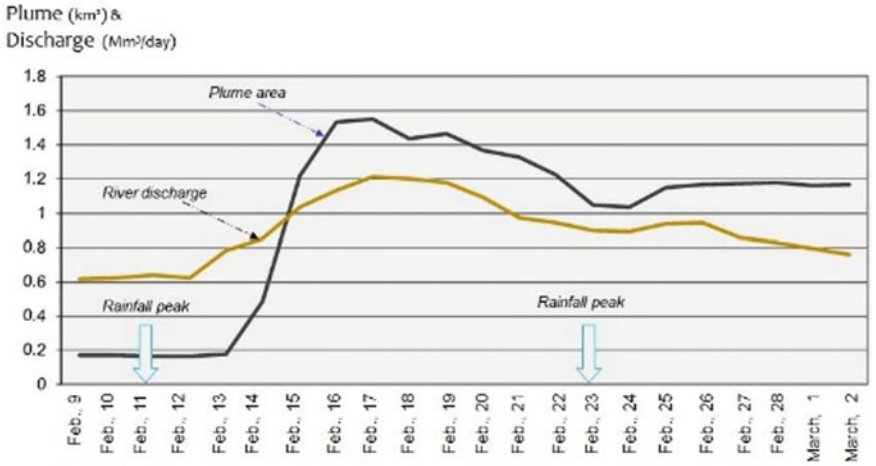

Fig. 7 Comparison between plume area and water discharge for Abou Ali River

3.3 Lag Time (τ) and Residence Time (T_r)

After each torrential rain event a rainfall peak is resulted, and the time needed for a plume to appear in the sea, i.e., the lag time (τ), is estimated from TRMM and MODIS data it was represented graphically (Fig. 8).

Lag time (or *flushing time* as described by Sheldon and Alber 2002) is a function of the hydrologic characteristics of the catchment and river and also the rainfall intensity. The lag time depends on such factors as the amount of time over which the rain falls and the amount of infiltration and interception that takes place along the path to the sea (Nelson 2004). In other words, lag time has diverse aspects as follows:

- If the amount of rain is high over a short time period then the lag time is short;
- If the amount of rain is high over a long time period then the lag time is longer; and
- A lack of infiltration and interception reduces the lag time.

In the study area, the lag time varies significantly between the different rivers (Table 2), reflecting the diversity in their catchments and hydrologic characteristics. The lag time ranges between 1 and 4 days, with an average time of about 2.5 days. This is slightly less than the average lag times of 4 days that were observed in an earlier study in the Sultanate of Oman (Robinson et al. 2005). The lower average is likely reflective of the relatively small area of the drainage basins (<500 km^2). Those rivers located in the middle part of the region (Fig. 1) have the shortest lag time as a result of the locally acute slope gradients (75–100 m/km). This is applicable only when rainfall occurs after a dry spell. If two rainfall peaks follow each other, then the second plume appears to blend in with the first (Fig. 8).

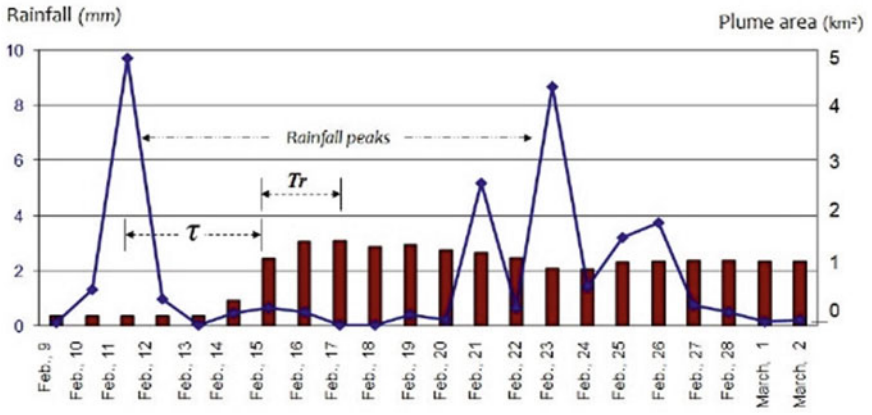

Fig. 8 Example showing the lag (τ) and the residence time (T_r) of plumes and rainfall peaks for Abou Ali River

The residence time (T_r) is another hydrologic component that can be extracted from the remote sensing data. It represents the time that the plume retains its maximum areal extent (Tables 1 and 2), that is, its residence time. The residence time has been defined as the average time for water parcels to reside in a system before they are flushed out (Chi-Fang et al. 2004). It indicates the continuity and regularity of water flow in a stream, as well as a uniform drainage density within the catchment area (Shaban et al. 2005a). Figure 8 clearly illustrates the residence time for Abou Ali River.

For the Lebanese coastal rivers, the residence time of water into the sea ranges between 3 and 8 days, and with an average of 4.6 days for the year 2002 (Table 2). The variation is likely attributable to the influence of several factors, most notably the physical contact between the land/ocean (Washington 2003). In this scenario, the wideness of the continental shelf, the depth of submarine canyons next to the river mouths, the sea current direction and energy all affect the stability of a plume.

4 Conclusion

Space techniques, and more certainly the satellite remote sensing applications, have been utilized in many scientific disciplines. The availability of different types of data governs the selection of the subject and approaches of any study using remotely sensed information. In this study, the MODIS-Terra and TRMM data, with their short retrieve time (daily) permitted establishing a monitoring approach for two major elements of the hydrologic cycle, i.e., precipitation and river discharge. Such an approach, if much improved, can replace instrumental techniques in addition to being low cost and can be achieved in a short time. This was applied to the coastal Lebanon, a typical area for such application, because it encompasses a number of issuing rivers and a variety of climatic conditions, where gauging stations and hydrographs are lacking/or insufficient.

As a result, from this study area, the obtained data indicated that the amount of rainfall is characterized by high frequency of peaks. The presence of steep sloping terrain (75–100 m/km), as well as the short distance between the threshold of rivers and their outlets (<50 km), create a rapid discharge of water into the sea, and this in turn results in a short lag time. But the intensive fracture system of the area hinders this flow regime and results in a moderate lag time, which averages about 2.5 days. This would explain the urgent need for surface water harvesting in this region, as the only solution for a strategic water management system. In addition, this study proved the reliability of the used remotely sensed instruments where several hydrologic elements could be derived, such the river discharge and the plume area on the sea surface.

Based on the used method and the resulted measurements, it is recommended to apply such an approach to each river separately. This results in building a monitoring system for both precipitation and discharge of water among different anthropic changes. This enables an assessment of the impact of human interference in the water cycle in each watershed.

Acknowledgements Funding for this research was made possible through the Fulbright Scholarship awarded to Dr. Amin Shaban (Lebanese National Council for Scientific Research and the Remote Sensing Center, Boston University). The authors would like to thank James Acker from NASA's GSFC for his help related to the MODIS ocean data.

References

Brink K, Arnon R, Coble P, Flagg C, Johnes B, Lee C, Phinney D, Wood M, Yentsch C, Young D (1998) Monsoons boost biological productivity in Arabian Sea. EOS 79(13):233–253

Chi-Fang W, Ming-His H, Albert K (2004) Residence time of the Danshuei River Estuary, Taiwan. Estuar, Coast Shelf Sci 60(3):381–393

El-Qareh R (1967) The submarine springs of Chekka: exploitation of a confined aquifer discharging in the sea. Unpublished MSc thesis, Geology Department, American University of Beirut, p 80

FAO (1973) Projet de développement hydro-agricole du Sud du Liban: Thermométrie aéroportée par Infra-Rouge. In: Programme des Nations Unies pour le développement, HG, vol 110, p 15

Fielding LW, El-Baz F (2001) Linear thermal anomaly offshore from Wadi Dayqah: a probable ground water seep along fracture zones. In: International conference on the geology of Oman, Sultan Qaboos University, Muscat, Oman, 12–16 Jan 2001, abstract vol 1, p 33

Fielding LW, Ozdogan M, Al-Malki A, El-Baz F, Kusky T (2001) Remote sensing of groundwater upwelling off the north-eastern coast of Oman by Landsat thermal data. In: Geological Society of America abstracts with programs, 1–10 Nov, p A-346

Gomis S (1996) Evaluating the potential of locating submarine springs in the Gulf of Oman using Landsat thematic mapper data. Master's thesis, Boston University, p 47

Hakim B (1974) Contribution à la détection des sources sous-marines et littorales de la côte libanaise par thermogravimétrie infrarouge (secteur Beyrouth-Enfé). DESS, Faculté des sciences, Montpellier, p 30

Hakim B (1985) Recherches hydrologiques et hydrochimiques sur quelques karsts méditerranéens: Liban, Syrie et Maroc. Publications de l'Université Libanaise, Section des études géographiques, tome II, p 701

Khawlie M, Shaban A, Abdallah C (2000) Evaluation of potentials of submarine springs: an unconventional groundwater source for the coastal area-Lebanon. In: Expert group meeting on groundwater rehabilitation for water resources protection and conservation, ESCWA, UNEP/ROWA, BGR, MOWE, Beirut, 14–17 Nov 2000

LRA (Litani River Authority) (2001) Unpublished technical report, p 29

NCRS (National Center for Remote Sensing) (1999) TIR survey for freshwater sources in the marine environment. National Center for Remote Sensing, final report, LNCSR, NCRS, p 103

Nelson N (2004) River flooding. Natural disaster course, Tulane University, EENS 204. http://www.tulane.edu/~sanelson/geol204/riverflooding.htm

Nirala M, Cracknell A (2002) The determination of the three-dimensional distribution of rain from the tropical rainfall measuring mission (TRMM) precipitation radar. Int J Remote Sens 23(20):4263–4304

Ohsaki Y, Numata A, Higashinwaatoko T (2000) Validation of rain/no-rain discrimination in the standard TRMM data products 1B21 and 1C21. IEEE 2:875–877

Robinson C, Buynevich A, El-Baz F, Shaban A (2005) Integrative remote sensing techniques to detect coastal fresh-water seeps. In: Annual meeting, Salt Lake City, Utah, 16–19 Oct 2005. Geological Society of America

Scott C, Thomas C, Scott L (2007) A comparison of TRMM to other basin-scale estimates of rainfall during the 1999 Hurricane Floyd flood. Nat Hazards 43:187–198

Shaban A (2003) Etude de l'hydroélogie au Liban Occidental: Utilisation de la télédéctection. PhD dissertation, Bordeaux 1 Université, p 202

Shaban A (2020) Water resources of Lebanon. Springer Science Publisher, Switzerland, p 229. https://doi.org/10.1007/978-3-030-48717-1
Shaban A (2021) Rivers of Lebanon: significant water resources under threats. In: Hydrology: the science of water. IntechOpen Publishing, Oxford. https://doi.org/10.5772/intechopen.94152
Shaban A, Robinson C (2006) A systematic approach using MODIS and TRMM data to monitor rainfall peaks versus water flow from rivers. In: Regional workshop on monitoring of coastal zones, Batroun, Lebanon, 24–25 May 2006. CNRS
Shaban A, Khawlie M, Abdallah C, Awad M (2005a) Hydrological and watershed characteristics of the El-Kabir River, North Lebanon. Lakes Reserv: Res Manag 10(2):93–101
Shaban A, Khawlie M, Abdallah C, Faour G (2005b) Geologic controls of submarine groundwater discharge: application of remote sensing to north Lebanon. Environ Geol 47(4):512–522
Sheldon J, Alber M (2002) A comparison of residence time calculations using simple compartment models of the Altamaha River Estuary, Georgia. Estuaries 25(6):1304–1317
Step Feed (2017) Lebanon dumps trash '100 times more toxic than raw sewage' into the sea. https://stepfeed.com/lebanon-dumps-trash-100-times-more-toxic-than-raw-sewage-into-the-sea-5247
Travaglia C, Ammar O (1998) Groundwater exploration by satellite remote sensing in the Syrian Arab Republic. Technical report FAO.TCP/SYR/6611, p 33
Washington M (2003) The community climate system model (CCSM) to simulate climate change on Earth. In: ISC 2003 conference, Heidelberg, 25 June 2003. The National Center for Atmospheric Research (NCAR)

Water Balance and Demand for Different Environmental Changes and Management Scenarios in the Hasbani Basin Using a WEAP Model and Geospatial Data

Mohammad Merheb and Chadi Abdallah

1 Introduction

Many countries around the globe are facing water shortage problems (UN 2017). This is particularly true in a water stressed environment such as the Mediterranean region that is already under increasing pressure from global changes (García-Ruiz et al. 2011; Balzan et al. 2020). Moreover, this region is characterized by high temporal and spatial variability of rainfall which places further constraints on water availability both in time and space especially since the dry season coincide with the warm season that is also the agricultural activity period of the year. This will certainly increase water demand especially for agriculture and will stresses out renewable water resources such as groundwater and surface waters (Leduc et al. 2017). Indeed, with the current extraction rate, many countries around the Mediterranean will face water shortage problems by the end of the century (Tramblay et al. 2020).

Lebanon is a mountainous country on the eastern shore of the Mediterranean with typical Mediterranean climate and with high population density that is even more exacerbated by the flux of refugees from near-by countries which in turn put more stress on the Lebanese water resources. Hydrological studies, especially in the term of hydrological modeling for management purposes are quite rare and even more so in our study area, the Hasbani basin.

M. Merheb
Faculty of Sciences, Lebanese University, Campus Mont Michel, 1352 Ras Maska, El Koura, Lebanon
e-mail: mohammad.merheb@agrocampus-ouest.fr

Institut Agro, INRAE, SAS, 35000 Rennes, France

C. Abdallah (✉)
National Council for Scientific Research, 59, Zahia Salmane Street, Jnah, P.O. Box 11-8281, Beirut, Lebanon
e-mail: chadi@cnrs.edu.lb

A. Shaban (ed.), *Satellite Monitoring of Water Resources in the Middle East*,
Springer Water, https://doi.org/10.1007/978-3-031-15549-9_12

The Hasbani basin is located in the south-eastern part of Lebanon. It is a rural catchment that is drained by a permanent water course, the Hasbani River which is one of the tributaries of the Jordan River. This work aims to establish a detailed water balance and to quantify water demands in the region taking into account the current situation but also various management and environmental changes scenarios.

2 Study Area Description

2.1 General Settings

The study area is a watershed located in the south eastern part of Lebanon about 120 km south east of the capital Beirut. It has an elongated oval shape of NE-SW direction (Fig. 1). It lies at the Lebanese international boundaries, with the Syrian territories to the east and the Israel to the south. With an area of 670 km^2, it forms about 6% of the total area of the country. It has a permanent watercourse called the Hasbani River.

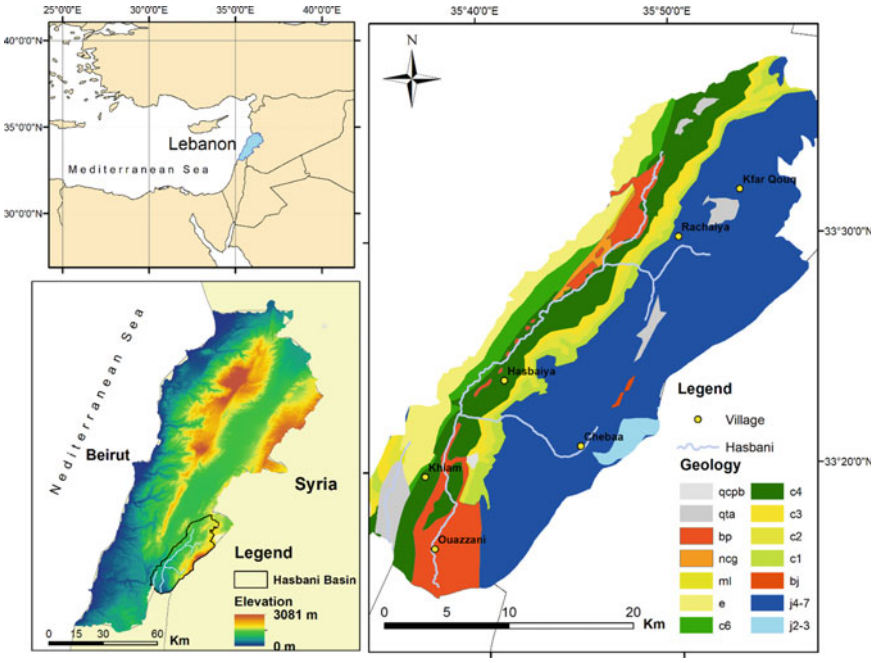

Fig. 1 The location of the Hasbani basin with its geological outcrops. *Source* Dubertret (1955)

2.2 Climate

The area is characterized by a typical Mediterranean climate with wet winters and hot and dry summers. The wet period extends from October to April with more than 80% of the total amount of precipitation recorded within this season. This result in a very high intra-annual variability of rainfall that leaves a long period of drought that coincide with the season of high agricultural activity in late spring and summer. Moreover, the wet season is the cold season, while the dry season coincide with the hot summer. This fact results in high values of reference evapotranspiration in summer, however, actual evapotranspiration tends to be much lower due to opposition of phase between rainfall and temperature. In addition to the high seasonal variability of rainfall, the spatial distribution of rainfall is also variable. The amount of precipitation varies across the catchment; from 600 mm/year in the lower parts to 1100 mm/year over the elevated areas including snowfall (Merheb 2010).

2.3 Land Cover/Use

The land cover/use map of the study area is presented in Fig. 2. The Hasbani basin is an agricultural catchment with around 25% of the area occupied by various agricultural activities. The main crop cultivated in the basin is olives which cover more than 11% of the total basin area. Field crops occupy around 10% of the study area, while the remaining agricultural land are divided between vineyards and various types of fruit trees. The basin is rural in nature, no major city exist within the border of the study area. Urban areas constitute 4.5% of the total basin area and is made of 56 villages with population ranging from less than 500 to a maximum of 14,000 in the most populated village. Natural vegetation covers 34% of the basin and are divided between forests (17%), Grassland (8%) and shrubs (9%). Finally, a large part of the basin is made of bare lands. This is mostly the higher elevation parts of Mount Hermon.

2.4 Geology and Hydrogeology

The main geological formations and their respective lithologies are described in Fig. 1. The major geological outcrop in the basin belongs to the Jurassic, it covers 51.5% of the basin area. The oldest rocks observed in the basin area are the lower Jurassic (J2-3) found as small patches in Mount Hermon area. Middle to upper Jurassic (J4-7) forms the major part of the elevated areas. It is an excellent aquifer and it is the first groundwater reservoir of the region.

Rocks from the Cretaceous form 29.8% of the basin area. The lower Cretaceous (C1, C2 and C3) represents a small part of the basin especially visible in the gentle

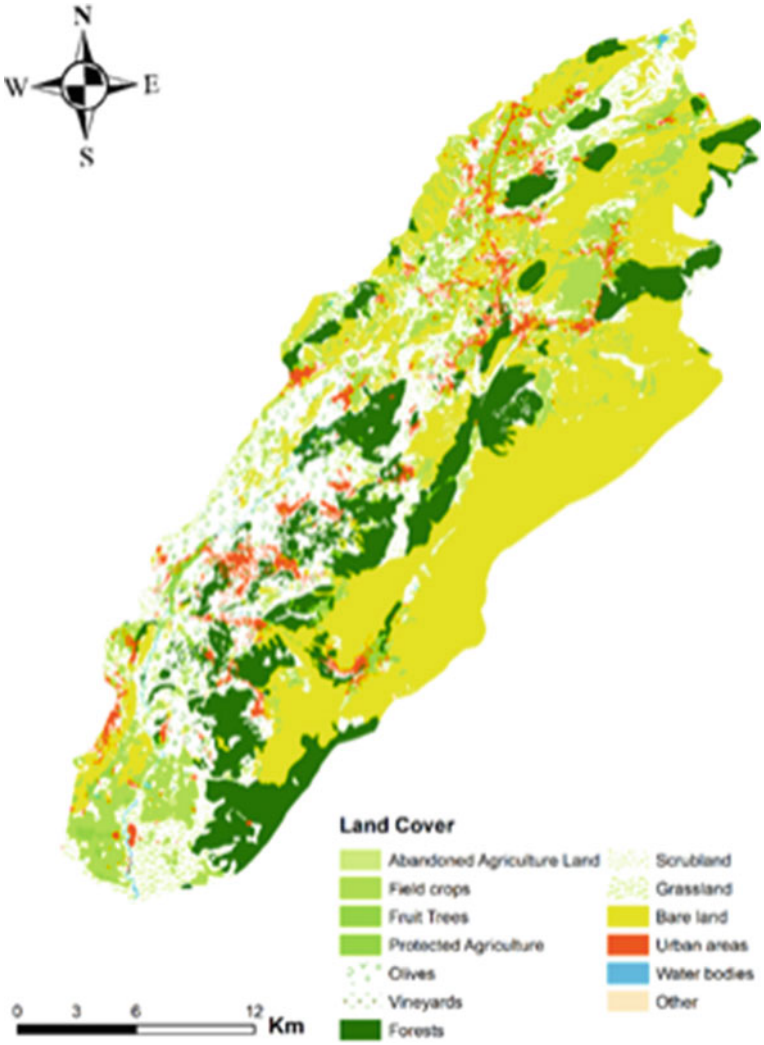

Fig. 2 Land cover use map of the study area. *Source* Faour and Abdallah (2018)

slopes and a small portion of the northern part of the elevated crest, they cut the region from the basaltic plateau to the northern border of the basin in a SSW-NNE direction as three almost parallel thin belts. The Late Cretaceous is represented in the study area by the Cenomanian (C4) and the Senonian (C6), the Turonian (C5) is missing. The Cenomanian represents a relatively thick belt that cut the basin from the southern to the northern border of the basin in a SSW-NNE direction. It forms a good part of both the gentle slopes and the plateau. It is the second major aquifer in the basin. The Senonian is present in a discontinuous manner at the western border

of the Cenomanian formation; it forms a small portion of the gentle slopes and the plateau.

The tertiary is represented in the basin area by the Eocene and the Pliocene, and with some small patches from the Miocene and the Mio-Pliocene. The Eocene represents the western border of the basin as a part of the gentle slopes and a very small part of the plateau. It is the third groundwater reservoir of the study area. The Pliocene rocks are mainly basalts, which outcrop in the southern part of the basin and as small patches in the Northwestern part of the area. The Miocene is found as a small patch in the WNW part of the basin along with the basaltic Pliocene.

Quaternary deposits in the basin area are largely made up of colluviums and arable soils. It is found in the plateau, at the Southwestern part of the region, and in some small scaled plain in the elevated areas.

The Jurassic, Cenomanian, and Eocene constitutes the major 3 aquifers forming geological outcrops on the study area. The Jurassic is by far the most important aquifer in the basin both in term of area and rock thickness, however the Cenomanian is also very important since the main course of the Hasbani river flows through this aquifer and is also fed by two springs that discharges from this same geological formation.

2.5 Water Resources

The main surface water source in the basin is the Hasbani River. It is one of the tributaries of the Upper Jordan River and has an average discharge of 4.7 m^3/s (calculated for the period 2002–2012). However, surface water is not the main water resource of the area. Indeed, groundwater in the basin is the major water source and the population is heavily dependent on it. This is reflected by the very high numbers of springs and both public and private wells. Indeed, the basin features a high number of springs reaching around 188 along with 37 public wells and 166 private wells. Here it should be noted that the number of private wells is very conservative given that many are illegal and thus are not on record.

3 Materials and Methods

3.1 Data Collection

The data for the model were collected from various sources. Climatic data were available from the Meteorological department of the General directorate of Civil Aviation in the Beirut International Airport (General Directorate of Civil Aviation 2011). This data consists of monthly rainfall depth in mm, mean monthly temperature in °C, monthly average humidity in % and monthly average wind speed in m/s. Climatic data were available for the years 2009–2010 and 2010–2011. Discharge

data for the Hasbani River after Wazzani spring is available for the period 2009–2011 from the Litany River Authority (LRA 2011) at a monthly time scale. Land cover use data at a scale of 1:5000 were available for the year 2017 from the Lebanese National Council for Scientific Research (Faour and Abdallah 2018). In addition, a 1:200,000 soil map with information on soil texture, depth and organic matter content was also available from the NSCR. Furthermore, the geological map of the basin is available as a 1:50,000 map digitized from the paper maps developed by Dubertret in 1955. This map was used to retrieve the hydrogeological information of the basin. Moreover, information on the agricultural activities in the basin in term of crop types and irrigation practices are available from the Ministry of Agriculture 2010 Agricultural survey. Finally, information on crop growth stages and their respective crop coefficient were retrieved from the FAO Irrigation and Drainage papers.

3.2 Model Setup

The catchment was modeled using the Water Evaluation and Planning (WEAP) software developed by the Stockholm Environmental Institute (SEI 2011). The catchment was divided into 5 sub-catchments, each one represented by a sub-catchment node. Each one of these fives include agricultural areas. Moreover, in each sub-catchment the urban areas are represented as a single urban demand node. In addition, in each sub-basin a demand node for cattle was also included. Furthermore, the 3 aquifers (Jurassic, Cenomanian, and Eocene) are divided by sub-catchment so in each sub-catchment the groundwater aquifer existing is presented with a groundwater node. Finally, the model includes 3 rivers, the main Hasbani River with its 2 tributaries. Figure 3 shows the schematic view of the model.

The model was set to have a monthly time-step with the water year set to begin in September. The year 2009–2010 was chosen as the base year (Current Account Year in the WEAP terminology). The last year of simulation is the year 2040.

3.3 Model Parameters

The model parameters include land use areas, crop coefficient, soil water capacity, root zone conductivity, runoff resistance factor, preferred flow direction and initial z1.

Land use areas were entered for each sub-catchment based on the 2017 LUC map and was further divided by crop type and irrigated areas for each crop based on the ministry of agriculture 2010 survey. For each land use and crop type a crop coefficient was entered. Crop coefficient each crop was deduced from the FAO irrigation and drainage paper at a monthly time step based on the crop growth stages. Soil water capacity refers to the effective water holding capacity of the top soil layer. This parameter was set to be equivalent to the Field capacity and was extracted using

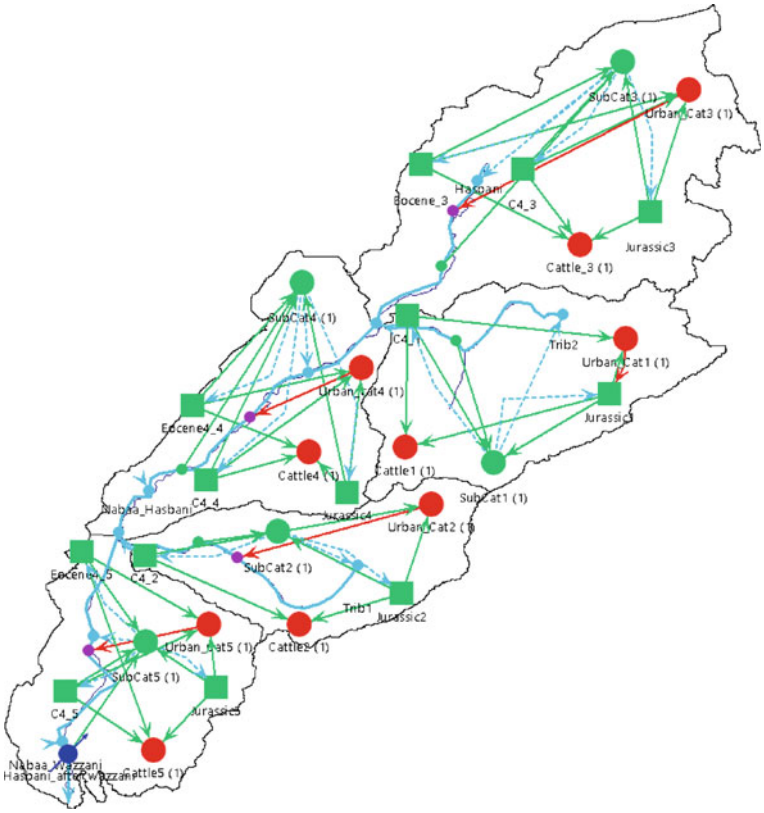

Fig. 3 The schematic view of the model

the soil textural characteristics, organic matter content, and depth retrieved from the soil map and using the Soil Water Characteristics software of the USDA Agriculture Research Service (Saxton and Rawls 2006). Soil water capacity was averaged for each land use type.

Root zone conductivity represent the saturated hydraulic conductivity in the top soil layer, runoff resistance factor is a parameter that control surface runoff with values ranging from 0 to 1000. Higher values mean lower runoff. Moreover, preferred flow direction partition the flow between horizontal (1 = 100% horizontal flow) and vertical flow (0 = 100% vertical flow), and finally initial z1 is the relative storage given as a percentage of the total effective storage of the root zone water capacity at the beginning of the simulation. All four parameters were adjusted manually during the calibration year in order to optimize the model results.

3.4 Soil Moisture Method

This method is initially a one dimensional, two bucket soil moisture accounting scheme that is based on empirical functions that describe evapotranspiration, surface runoff, sub-surface runoff (interflow), and deep percolation for a watershed unit. The top layer is the root zone layer, while the bottom layer represents the aquifer. In the WEAP model, the bottom layer is ignored when the catchment is linked to a groundwater node which is the case here.

A watershed unit can be divided into N fractional areas representing different land uses/soil types, and a water balance is computed for each fractional area, j of N. Climate is assumed uniform over each sub-catchment, and the water balance is given as (SEI 2011):

$$Rd_j \frac{dz_{1,j}}{dt} = P_e(t) - PET(t)k_{c,j}(t)\left(\frac{5z_{1,j} - 2z_{1,j}^2}{3}\right) - P_e(t)z_{1,j}^{RRF_j} - f_j k_{z,j} z_{1,j}^2 - (1 - f_j)k_{z,j} z_{1,j}^2$$

where $Z_{1,j}$ is the relative water storage given as a fraction of the total effective storage of the root zone (mm) for a land cover fraction, j. P_e is the effective precipitation while PET is the reference potential evapotranspiration calculated using a modified Penman–Monteith equation. $K_{c,j}$ is the crop coefficient for each fractional land cover and RRF_j is the runoff resistance factor of the land cover. $K_{z,j}$ is an estimate of the root zone saturated conductivity (mm/time) and f_j is the preferred flow direction; a coefficient used to partition the flow out of the first bucket into interflow and deep percolation (Fig. 4).

3.5 Optimization

The model was calibrated on using the streamflow record of the year 2009–2010 and validated on the year 2010–2011 using the flow record at the gauging station located after the Wazzani spring. The Nash Sutcliffe efficiency index was used to assess the model performance during both the calibration and validation periods.

$$NSE = 1 - \frac{\sum_{i=1}^{n}(Q_i^{sim} - Q_i^{obs})^2}{\sum_{i=1}^{n}(Q_i^{obs} - \overline{Q}^{obs})^2}$$

where Q_i^{obs} is the observed flow at *i*th time-step; Q_i^{sim} is the simulated flow at *i*th time-step and $\overline{Q}^{obs}$ is the mean observed flow discharge of n total time-steps.

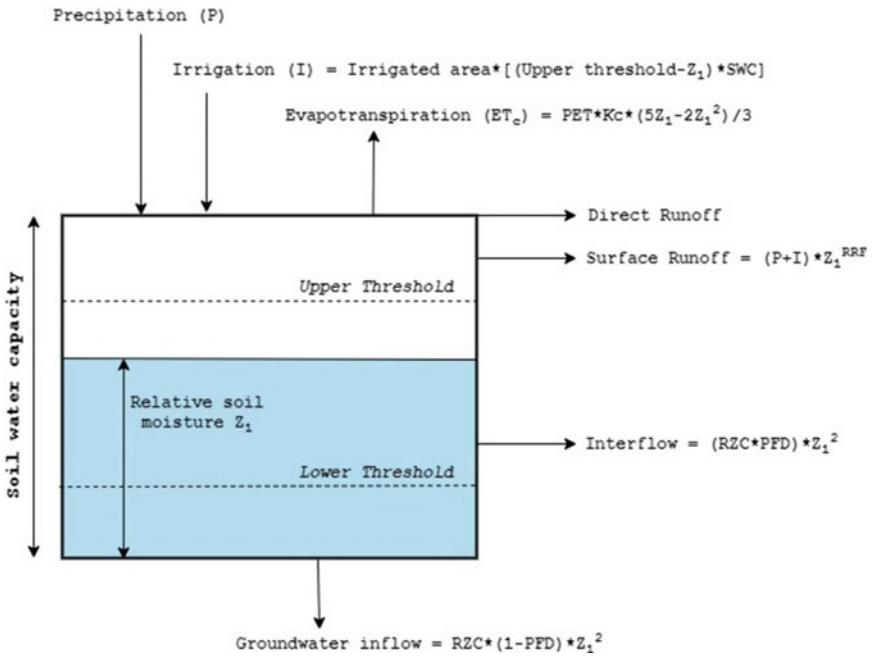

Fig. 4 Conceptual diagram of the one-bucket soil moisture method (adapted from SEI 2011)

3.6 Scenarios

The model was set to run using 5 different scenarios. A business as usual scenario that only take into account population growth. The population growth rate in Lebanon was estimated at 0.1% for the entire simulation period.

Two Climate change scenarios were developed. The assumptions for these scenarios were made based on the "Lebanon's Second National Communication to the UNFCC" Report (Ministry of Environment 2011). The first one, labeled Climate Change 1, assumes a 10% decrease in rainfall and a 1 °C increase in Temperature over the whole simulation period. The second one, labeled Climate Change 2, assumes a 20% decrease in rainfall and a 2 °C increase in Temperature over the whole simulation period. Furthermore, two agricultural intensification scenarios, both assuming a 5% annual increase in agricultural areas. The first one, labeled Agricultural Intensification 1, is based on the scenario Climate change 1. The second one, labeled Agricultural Intensification 2, is based on the scenario Climate Change 2.

4 Results and Discussions

4.1 Model Efficiency

The model was calibrated against the monthly discharge record of the year 2009–2010 of the streamflow gauge located after the Wazzani spring and validated using the monthly record of 2010–2011 at the same gauge. The NS was used to assess the model performance during the calibration and validation period. Figure 5a, b shows the observed versus simulated streamflow for the calibration and validation. The NS index values were 0.71 and 0.6 for the calibration and validation years respectively. The main problem behind the lower NS in the validation year is the fact that the model does not accurately account for water that comes from snow melt and which may represent about 10% of the total water of the Hasbani River (Gil'ad and Bonne 1990).

4.2 Annual Water Balance

The primary result of the WEAP model is the catchment water balance. Figure 6 shows the intra-annual variation of the various water balance components. The main inflows to the system are precipitation, decrease in soil moisture, and irrigation. The high intra-annual variability of rainfall input is clear in Fig. 6. The maximum rainfall is recorded in December with a rainfall volume of 134.8 MCM, followed by January with 141.5 MCM and February with 62.9 MCM. Total precipitation volume is 531.3 MCM for the year 2009–2010. Irrigation is almost null during the rainy season; it starts to rise from March with a volume of 1.62 MCM and reach its peak in June with 10 MCM. The months of May, July and August show high irrigation volumes with 9.52, 9.27, and 8.14 MCM respectively. Total irrigation volume consumed in the current account year is 46.83 MCM. Finally, decrease in soil moisture starts in February and decreases gradually from March to August. The total volume of this last inflow is 115.6 MCM.

The outflows form the system are Actual Evapotranspiration, increase in soil moisture, interflow, flow to groundwater and surface runoff. All outflows show high intra-annual variability which certainly reflect the high seasonal variability of rainfall. The highest monthly actual evapotranspiration is estimated in March with a value of 20.6 MCM, followed by April and May with a value of 19.06 MCM for each Month. The high values of evapotranspiration in spring are understandable given the fact that this is the season of vegetation growth and it coincides with increasing irrigation. The lowest values of evapotranspiration are recorded in August. This might seem counter-intuitive since August features the highest temperature and reference Evapotranspiration, however, in the Mediterranean catchment, precipitation and ET0 are in opposite phase which result in high ET0 but low actual evapotranspiration because when ET0 there is now water to evaporate (Latron et al. 2009). The total

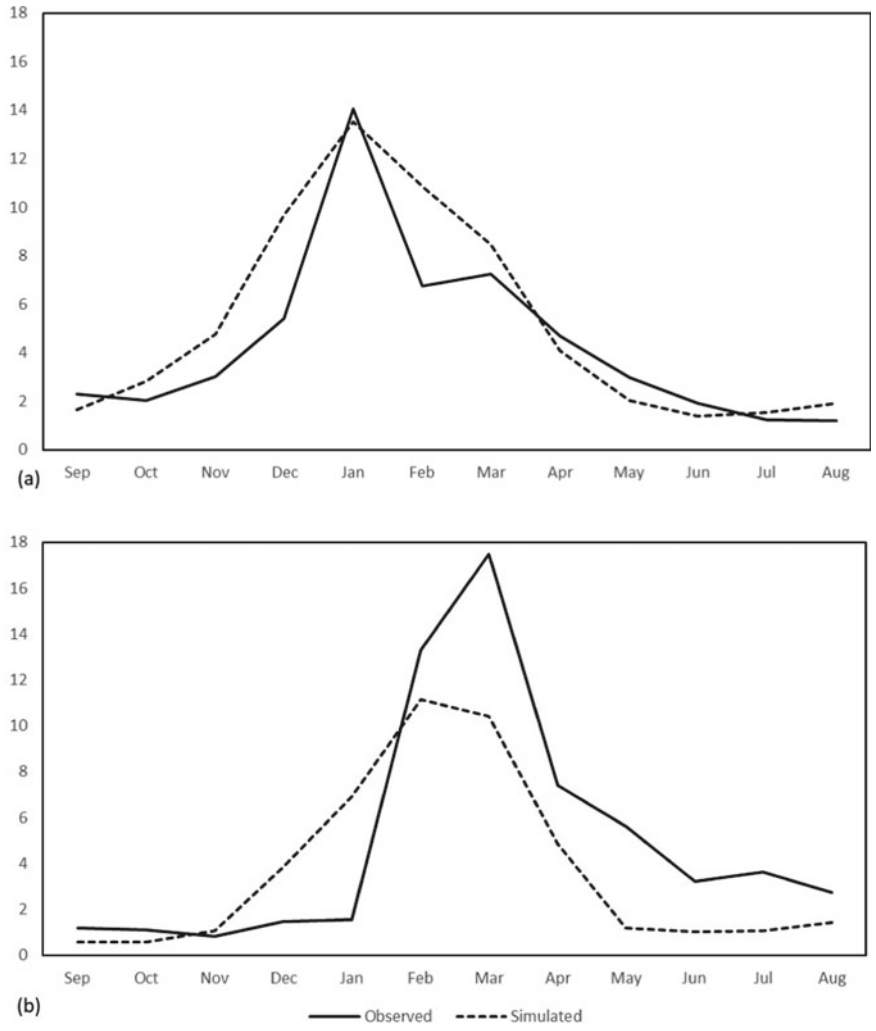

Fig. 5 Simulated versus observed values for the **a** calibration period (2009–2010) and the **b** validation period (2010–2011)

amount of Evapotranspiration for the year 2009–2010 is 173 MCM which represent 32% of total precipitation. Similar and even lower values (12–20% of total rainfall) of real evapotranspiration were estimated for the entire Lebanese territory in the UNDP 2014 Groundwater Assessment Report for Lebanon. The most important outflow is flow to groundwater. It amounts to 346 MCM with the highest monthly values recorded in the winter season with a maximum of 95.4 MCM in January, 86 in December and 62 in February. Flow to groundwater represent 50% of the total outflows and more than 60% of total rainfall. Surface runoff amount to 68 MCM for

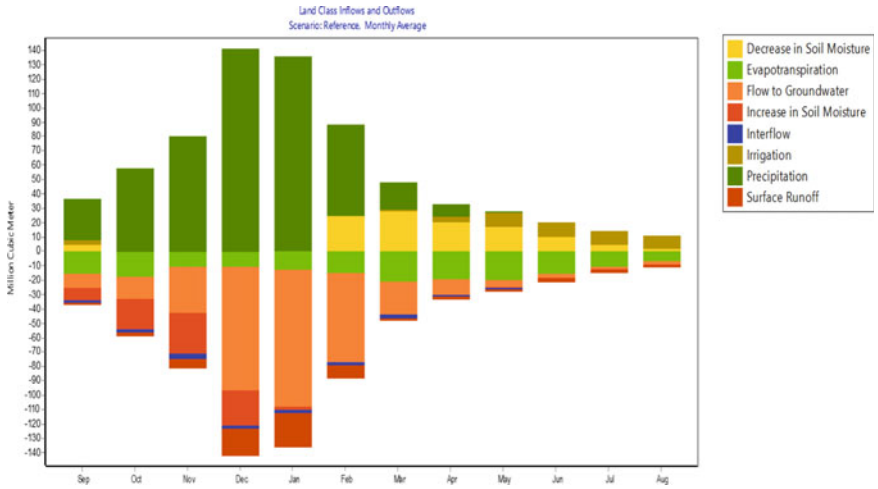

Fig. 6 Monthly variation of the water balance component during the current account year

the year 2009–2010 which represents 13% of total rainfall. The low surface runoff ratio along with a high flow to groundwater corroborates with the fact that baseflow in the basin is a major input to the streamflow while direct runoff represents a smaller fraction of the total river discharge. Indeed, the main sources of the Hasbani River flow are the discharges of the Hasbani and Wazzani springs located on the main river course. Finally, increase in soil moisture and interflow amount to 87 and 18.6 MCM per annum.

Table 1 presents a comparison between the annual depth in mm of the various water balance components at the beginning of the simulation (Current Account Year 2010) and at the end of the simulation for all scenarios (year 2040).

The BAU scenario does not show any measurable differences between the year 2010 and 2040. In fact, this scenario only takes into account the population growth rate which has a rather small impact on the water balance especially in a rural catchment with relatively low population density.

For the climate changes scenarios, precipitation decreases from 848 mm in 2010 to 775 mm and 693 mm at the end of the simulation for climate change 1 and 2 respectively. Evapotranspiration represented 32% of annual rainfall depth in 2010, it will increase to 33% and 35% for climate change scenarios 1 and 2 respectively at the end of the simulation. Surface Runoff will also decrease from 13% of total rainfall depth in 2010 to 11.5% and 10.8% for CC1 and 2 respectively in 2040. In addition, flow to groundwater will also decrease from 65% of total rainfall depth to 62% and 60% in 2040 for CC1 and CC2 respectively. Irrigation does not show a sensitivity to climate change scenarios.

As for the Agricultural intensification scenarios, the changes in the water balance components between the years 2010 and 2040 are quite similar to the climate change

Table 1 Detailed Annual water balance of the study area for the current account, and at the 2040 and at the end of each scenario in mm

		2010	2040				
	Water balance components	Current account year	BAU scenario	Climate change 1	Agricultural intensification 1	Climate change 2	Agricultural intensification 2
Inflows	Precipitation	848	848	775	775	693	693
	Irrigation	75	73	75	82	75	84
	Decrease in soil moisture	184.6	176.5	169.5	170.7	160.9	162
Outflows	Evapotranspiration	−277	−257	−250	−258	−241	−249
	Increase in soil moisture	−139	−176.5	−169.5	−170.6	− 161	−162.2
	Flow to groundwater	−553	−531.8	−483	−474	−429	−421
	Interflow	−29.7	−27	−25	−25.7	−22.5	−23
	Surface runoff	−109	−105	−90.4	−99.5	−75.2	−83

scenarios since they are based on them with the addition of an increase in the irrigation input from 75 to 82 mm and 84 mm for Agricultural Intensification 1 and 2 respectively. This increase in irrigation will also cause a slight increase in surface runoff as compared to the climate change scenarios due to the increasing irrigation return flow.

4.3 Water Demand

4.3.1 Annual Water Demand

Figure 7 shows the variations of water demands during the entire simulation period for all scenarios. Water demand in the basin for the first year of simulation was 54.7 MCM. For the BAU scenario, the variation in water demand from 2010 to 2040 is very small and amount to only 0.26 MCM. This is due to the fact that this scenario only account for population growth.

For both climate change scenarios 1 and 2, water demand increases gradually from 54.7 MCM at the beginning of the simulation to 55.19 and 55.54 MCM and to 55.62 and 56.26 MCM in 2030 and 2040 for climate change scenarios 1 and 2 respectively.

The most important increase in water demand is seen in the Agricultural Intensification scenarios with water demand increasing to 59.91 and 62.84 MCM in 2030 and 2040 for Agricultural Intensification 1 scenario and to 60.69 and 64.17 MCM in 2030 and 2040 respectively for the Agricultural intensification 2 scenario.

Table 2 presents the annual water demand by sector for all scenarios for the current account year and for the years 2030 and 2040. The agricultural sector is the most important economic activity in the region and it accounts for around 84% of the entire water demand in the basin. It includes irrigation and cattle raising and amount

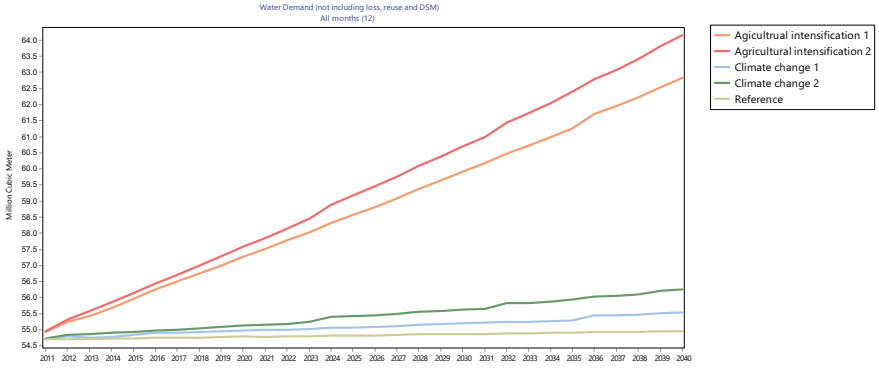

Fig. 7 Variation of annual water demand for the entire basin for the entire period of simulation and for each scenario

Table 2 Water demand for different sectors and scenarios in MCM/year

	Scenarios	2010	2030	2040
Agricultural demand	Climate change 1	46.25	46.3	46.6
	Agricultural intensification 1		51.04	53.88
	Climate change 2		46.75	47.3
	Agricultural intensification 1		51.82	55.2
Urban water demand	BAU scenario	8.71	8.87	8.96

of 46.25 MCM. Urban water demand accounts for the remaining water use in the study area and amounts to 8.71 MCM.

Urban water demand increases slightly (by 0.26 MCM) from the current account year till the end of the simulation period due to population growth in the study area. Moreover, agricultural water demand increase for all scenarios but especially for the agricultural intensification scenarios with an annual increase of 0.08% and 0.09% for Agricultural intensification scenarios 1 and 2 respectively.

4.3.2 Intra-Annual Variation of Water Demand

Water demand in the study area shows a high intra-annual variation. Indeed, water demand is at its lowest at the height of the wet season that extends from November to February. It starts to rise from March and reach its peak in June and remains high in July, August and to a lesser extent in September. Indeed, the water demand in the dry season account for around 93% of the total annual water demand. This period of the year is characterized by not only lower precipitation that becomes practically null from June to August, but also with the period of agricultural activity which increases irrigation water demand. Figure 8 shows the intra-annual variation of water demand for the current account year and at the end of the simulation for all scenarios.

It is noticed in Fig. 8 that the intra-annual distribution of water demand does not vary between the start and the end of the simulation period. Moreover, for the BAU scenario, the increase in demand at the intra-annual level is very small. This is also the case for climate change scenarios 1 and 2, the increase in demand is the most pronounced in the Agricultural intensification scenarios 1 and 2. The highest increase in water demand is recorded, for all scenarios, for the month of June which is also the month with the highest demand at the current account year.

Water demand in June is 10.97 MCM in the current account year, followed by May with 10.29 MCM, then July and August with 10.04 and 8.91 MCM per month respectively. The monthly water demand increases to 10.99, 11.04, 11.07, 12.66, and 12.81 MCM in June at the end of the simulation for the BAU, Climate change 1 and 2, and Agricultural Intensification 1 and 2 scenarios respectively. On the other hand, water demand for the wet period is at 1.01 MCM per month at the beginning of the simulation and witness a very small increase at the end of the simulation.

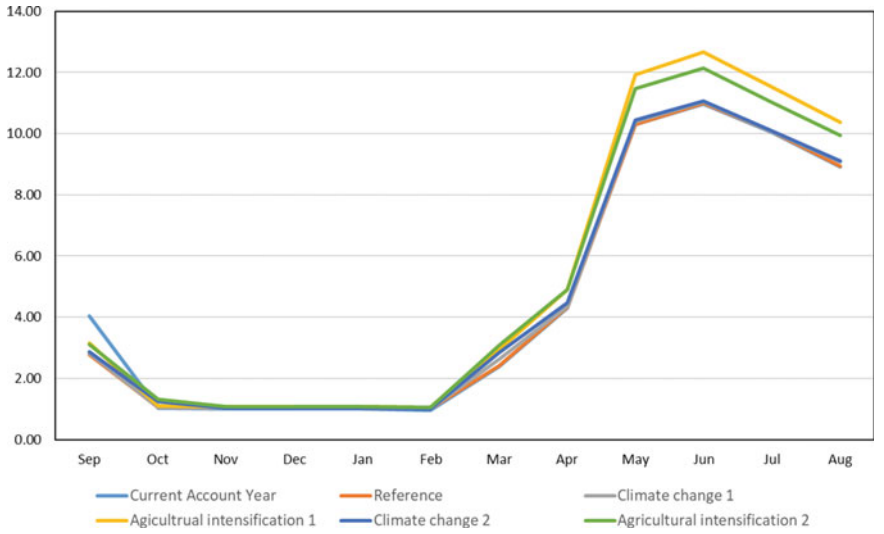

Fig. 8 Monthly variation of water demand in the current account compared to each scenario

5 Conclusions

This work aimed at estimating the annual water balance of the Hasbani basin along with the water demand for various economic sector for the period 2010–2040 using various climatic and management scenarios. The work was done using the soil moisture method of the WEAP model. The model was set at a monthly time step with the year 2010 chosen as the current account year and for a 30 years' simulation period that ends in 2040. Model parameters were extracted from various land use data, agricultural data, soil maps, climatic data and water resources data in term of both groundwater and surface water sources. The model was calibrated and validated using observed streamflow record for the years 2009–2010 and 2010–2011 respectively. The model was run using 5 different scenarios. A reference scenario that assumes business as usual with only population growth rate taken into account. Two climate change scenarios that assumes a 1–2 °C increase in temperature and 10–20% decrease in rainfall respectively. A 2 agricultural intensification scenarios based on the two aforementioned climate change scenarios that assumes a 5% annual increase in agricultural areas. The model showed a NS efficiency of 0.7 and 0.6 for the calibration and validation years respectively.

The water balance in the basin at the start of the simulation showed that precipitation, irrigation and decrease in soil moisture are the main inflows to the catchment with annual depth of 848, 75, and 184.6 mm respectively. The outflows are evapotranspiration, flow to groundwater, surface runoff, increase in soil moisture and interflow with annual depth values of 277, 553, 109, 139, and 29.7 mm respectively. The main outflow is by far the flow to groundwater which highlights the importance

of this water resource as a major source of renewable water in the basin. At the end of the simulation precipitation decreased to 775 and 694 mm for the climate change scenarios 1 and 2 respectively. Evapotranspiration which represented 32% of rainfall in 2010 increased to 33% and 35% at the end of the simulation for the aforementioned climate change scenarios. Flow to groundwater and surface runoff decreased with both climate change scenarios. The agricultural intensification scenarios show similar results with the addition of an increase in irrigation inflows to the increase of agricultural areas.

The main water demand sector in the catchment is agriculture. It accounts for around 93% of the total annual water demand. Moreover, water demand shows a high intra-annual variability with the highest demand estimated for the dry period which coincide with the season of agricultural activities. Total annual water demand in the basin was 54.7 MCM for the year 2010. It increases to reach 54.96, 55.54, 56.26, 62.8, and 64.2 MCM for the BAU, Climate Change 1 and 2, Agricultural Intensification 1 and scenarios respectively. At the intra-annual level, the month with the highest water demand is June, while the period from November to February show a very low monthly water demand.

Finally, the demand coverage in the basin is 100% for all scenarios and during the entire simulation period. The fact that all demand in the basin is met even with the climate change scenarios and agricultural intensification scenarios stems from the fact that groundwater is the main water source in the basin and is available in 3 large and thick well fractured and karstified aquifers that have a large storage and are fed annually by more than 50% of the total rainfall due to the nature of the basin geology that favors infiltration.

References

Balzan M, Hassoun A et al (2020) Ecosystems. In: Cramer W, Guiot J, Marini K (eds.) Climate and environmental change in the mediterranean basin—current situation and risks for the future. First Mediterranean Assessment Report, pp 323–468. Union for the Mediterranean, Plan Bleu, UNEP/MAP

Dubertret L (1955) Geological maps of Lebanon scale 1:50,000. Lebanese Republic, Ministry of Public Works, Beirut, Lebanon

Faour G, Abdallah C (2018) Land use land cover map of Lebanon. 1:20 000. [Vector map]. CNRS Remote Sensing Center, Beirut, Lebanon. Darwish T, Khawlie M, Jomaa I, Abou Daher M, Awad M, Masri T, Shaban A, Faour G, Bou Kheir R, Abdallah C, Haddad T (2006) Soil map of Lebanon: 1:50 000, Monograph edn. CNRS, Remote Sensing Center, Beirut, Lebanon

García-Ruiz JM, López-Moreno JI, Vicente-Serrano SM, Lasanta–Martínez T, Beguería S (2011) Mediterranean water resources in a global change scenario. Earth-Sci Rev 105(3–4):121–139. ISSN 0012-8252. https://doi.org/10.1016/j.earscirev.2011.01.006

Gil'ad D, Bonne J (1990) The snowmelt of Mt. Hermon and its contribution to the sources of the Jordan River. J Hydrol 114:1–15

Latron J, Lorens P, Gallart F (2009) The hydrology of Mediterranean mountain areas. Geogr Compass 3(6):2045–2064

Leduc C, Pulido-Bosch A, Remini B (2017) Anthropization of groundwater resources in the Mediterranean region: processes and challenges. Hydrogeol J 25(6):1529–1547

LRA (2011) Lebanese River Authority
Merheb M (2010) Watershed management of the Hasbani-Wazani. MS thesis, Lebanese University
Ministry of Environment (2011) Lebanon's second national communication to the UNFCC
Ministry of Transport and Public Work, Directory of Civil Aviation, Department of Meteorological Services (2011)
Saxton KE, Rawls WJ (2006) Soil water characteristic estimates by texture and organic matter for hydrologic solutions. Soil Sci Soc Am J 70(5):1569–1578
SEI (2011) WEAP water evaluation and planning system: user guide for WEAP21. Stockholm Environment Institute, Boston
Tramblay Y, Llasat MC, Randin C et al (2020) Climate change impacts on water resources in the Mediterranean. Reg Environ Change 20:83
United Nations Economic and Social Commission for Western Asia (ESCWA) et al (2017) Arab climate change assessment report—main report. E/ESCWA/SDPD/2017/RICCAR/Report

Agricultural Water Management in the Nile Delta Using Remote Sensing Techniques

Ayat Elnemer

1 Introduction

Arid regions like Nile delta, Egypt face great challenges in their development future due to the limited water resources. Additionally, the rapid escalation in the growth of Egyptian population pressures on these limited resources. The agricultural sector in Egypt consumes 85% of its water resources (Khadr et al. 2016). Hence, assessing and improving the irrigation system in Egypt is considered a key for its developing future (Elnmer et al. 2018a, b).

1.1 Irrigation Water Performance Assessment (IWPA)

The irrigation water performance assessment (IWPA) consists of two types; external IWPA and internal IWPA (Bos et al. 2005). The external IWPA concerns of the whole state of the irrigation system such as the overall irrigation efficiency and the irrigation water productivity (Bos et al. 1993). However, this type cannot provide a detailed information about the reginal state of the irrigation system. Additionally, it does not provide the decision maker with the troubles causes and locations (Akhtar et al. 2018). Nevertheless, the internal IWPA is defined as the ratio between the delivered water to an irrigation system and the required water from this system (Akhtar et al. 2018). It is an effective tool to spatial temporal assess the internal irrigation processes to efficiently reallocate the irrigation water (Elnmer et al. 2018a, b). It uses four indicators; adequacy, equity, dependability and efficiency indicators to assess the irrigation system (Bos et al. 1993). The spatial assessment uses the adequacy and

A. Elnemer (✉)
Irrigation and Hydraulic Engineering Department, Faculty of Engineering, Tanta University, Tanta 31734, Egypt
e-mail: Ayat_elnemr@f-eng.tanta.edu.eg

A. Shaban (ed.), *Satellite Monitoring of Water Resources in the Middle East*,
Springer Water, https://doi.org/10.1007/978-3-031-15549-9_13

equity indicators, while the temporal assessment uses the adequacy and dependability indicators (Elnmer et al. 2018a, b). The adequacy indicator measures the ability of the system to deliver the required irrigation water. While the dependability measures also the ability of the system to deliver the irrigation water but in the right time. Nevertheless, the equity indicator measures the fair distribution of the irrigation water between water users according to their water demands (Bos et al. 1993).

1.2 Remote Sensing Techniques in the IWPA

The IWPA requires an accurate estimation for the water demands in the irrigation system at field, catchment, basin and global levels (Senay et al. 2016). The agricultural water demands can be represented by the actual evapotranspiration (ETc) (Elnmer et al. 2019). Hence, the skillful IWPA requires regional information of the ETc. The ETc can be estimated by traditional approaches (Thornthwaite 1948; Blaney 1952) and energy balance methods (Allen et al. 1998). The tradition approaches can be used for the ETc estimation at point scale. Additionally, these approaches have limitation in time and cost for daily estimates (Elhag et al. 2011).

The energy balance methods depend on the residual concept (Calcagno et al. 2007). This concept was implemented in many algorithms. These algorithms are; Surface Energy Balance Algorithm for Land (SEBAL), Two-Source Energy Balance (TSEB), Mapping Evapotranspiration at High Resolution with Internal Calibration (METRIC), Surface Energy Balance Index (SEBI), and Simplified Surface Energy Balance System (SSEBSop) (Elnmer et al. 2019). TheETc estimates using SEBAL, and METRIC algorithms are derived using metrological data which provide many uncertainties in these estimates (Liou and Kar 2014). The SEBI and TSEB require many ground measurements which can be considered a limitation for using them in the ETc estimates (Menenti 1993). The SSEPop estimate the ETc using the temperature scaler (Su 2002).

Recently, remote sensing techniques proved their ability to provide an accurate regional information about agriculture, water and land conditions at time (Elnmer et al. 2018a, b). In 2006, the first to use SEBAL algorithm to assess the irrigation efficiency of the Gediz basin in Turkey based on remotely sensed ETc were derived (Ramos et al. 2006; Karatas et al. 2009). The results indicated that remote sensing techniques could be efficiently used in the IWPA. Moreover, many studies used the remotely sensed ETc in the IWPA around the world (Ahmad et al. 2009; Karatas et al. 2009; Zwart and Leclert 2010; El-Agha et al. 2011; Elnmer et al. 2018a, b).

1.3 IWPA in the Nile Delta

Both external and internal IWPA are essential to assess and improve the irrigation systems. Each IWPA has many indicators to describe the irrigation processes. Many

studies assessed the external and internal IWPA around the world. Despite the several studies that assessed the external IWPA in the Nile delta, few studies assessed the internal IWPA and both internal and external IWPA based on regional data of the Nile delta. Most of these carried assessments in the Nile delta were derived based on tradition approaches in assessing the water demands.

The external IWPA in the Nile delta was assessed in 2008 using remote sensing techniques with MODIS images (250 m resolution) (El-Agha et al. 2011). This assessment indicated a "poor" performance of the irrigation water in the Nile delta where 53% of irrigation water supplies were depleted in groundwater recharge and drainage system (El-Agha et al. 2011). Furthermore, the internal IWPA was assessed in 2008 during winter (from May to October) and summer (from October to May) seasons (Akhtar et al. 2018). A "fair" performance was reported in summer 2008 in the Nile delta where the adequacy and dependability indicators were <0.89 and >0.11 respectively. Nevertheless, the IWPA was "good" in winter 2008 with adequacy < 0.89, equity > 0.11 and dependability > 0.11 indicators (Akhtar et al. 2018). A comprehensive framework of both internal and external IWPA were derived to the Nile delta during winter 2015–2016 using SEBAL algorithm and Landsat 8 images (30 m resolution) (Elnmer et al. 2018a, b). The results indicated that the external IWPA was "poor" during winter 2015–2016 due to the oversupplies of irrigation water to the center of the Nile delta. The internal IWPA showed a non-uniform distribution of irrigation water between water users during different seasons.

Hence, there is an urgent need to provide regional estimation for the water demands in the Nile delta and assess the internal IWPA during summer season. The decision makers could use these estimates to improve the irrigation network of the Nile delta. This chapter aims to assess the internal IWPA in the center of Nile delta during summer 2016 using remotely sensed ETc derived by SSEBop and Landsat 8 images with resolution 30 m.

2 Materials and Methods

2.1 Study Area

The study area is an irrigation scheme with 216 km^2 area and is in the central of the Nile Delta, Egypt as shown in Fig. 1 (Elnmer et al. 2018a, b). This area is irrigated by two main canals called "Al-Qased canal" and "Qanat tanta Al-melahiya" (Elnmer et al. 2015). The annual discharge of fresh water to the study scheme is approximately 190 Mm^3 (MWRI 2010). Then, the scheme was irrigated with the flooding system through a network of secondary, distribution, marwas and mesqas canals (Khadr et al. 2016). The irrigation water is distributed between fields according to the crop water requirements. The monthly crop water requirements are estimated according to the crop pattern. The Egyptian crop pattern consists of two crop patterns: summer from May to October and winter crop pattern from October to May. Each crop pattern

consists of three sub-seasons: beginning, growing, and harvesting seasons (MWRI 2010). The main summer crops are rice and maize, while the main winter crops are wheat and clover (MWRI 2010).

The internal IWPA was derived using three branch canals. Branch 1, 2 and 3 are located at the beginning, middle and tail of the main canal and the study area respectively, as shown in Fig. 1.

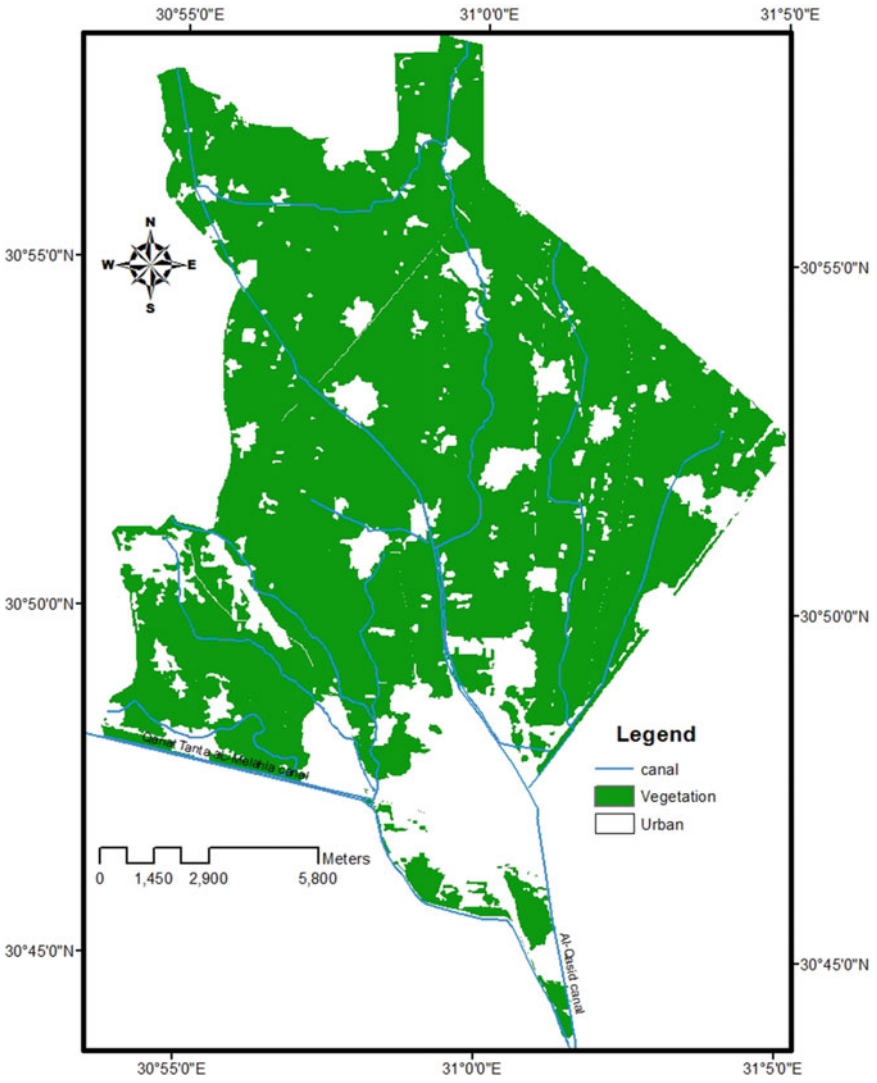

Fig. 1 Location of the study area (adopted from Elnmer et al. 2018a, b)

Table 1 Landsat 8 images for the study area

Acquired date	Path/row	Pixel size (m)
15th June 2016	39/177	30
8th August 2016	39/177	30
10th October 2016	39/177	30

2.2 Data Description

In this study two data sources were used: satellite data and ground metrological data. A total of three cloud free Landsat 8 images with ground resolution of 30 m were used to run SSEBop algorithm. These Landsat images were acquired on Jun. 15th, Aug. 08th, and Oct. 10th, 2016 to cover the beginning, growing and harvesting summer season as shown in Table 1. Nevertheless, the metrological datasets were the temperature, rainfall, humidity, wind speed and solar radiation for summer 2016. These data were measured hourly in a weather station located in the study area. The water supplies to the study area and the three branch canals were obtained from the ministry of water resources and irrigation-Egypt (MWRI). The water demands of the command areas of these three branch canals were derived using the SSEBop algorithm and Landsat 8 images.

2.3 Methodology

2.3.1 The Land Surface Temperature and Reference Evapotranspiration

The thermal bands of Landsat 8 images were used to efficiently estimate the land surface temperature (*Ts*) using split window algorithm with Eq. 1 as follows (Ulivieri et al. 1994),

$$\begin{aligned} Ts = {} & \mathrm{TB}_{10} + \mathrm{C}_1(\mathrm{TB}_{10} - \mathrm{TB}_{11}) + \mathrm{C}_2(\mathrm{TB}_{10} - \mathrm{TB}_{11})^2 \\ & + \mathrm{C}_0 + (\mathrm{C}_3 + \mathrm{C}_4\mathrm{W})(1 - \mathrm{m}) + (\mathrm{C}_5 + \mathrm{C}_6\mathrm{W})\Delta\mathrm{m} \end{aligned} \tag{1}$$

where, TB_{10}–TB_{11} represents the brightness temperature of 10 and 11 Bands respectively, c_1–c_6 are the coefficients of split-window, m is the mean emissivity of the land surface, the atmospheric water-vapour content is W and Δm is the difference of the land surface emissivity (Ulivieri et al. 1994).

Reference evapotranspiration (ET_o) is the evapotranspiration from a reference crop which fully covered the irrigated area with well water conditions. It could be estimated by FAO-Penman Monteith formula using meteorological data; temperature, humidity, wind speed, and vapor pressure (Allen et al. 1989).

2.3.2 SSEBop Algorithm

SSEBop is a modification of SEBAL algorithm which estimates the actual evapotranspiration (ETc) based on variation of the land surface temperature (Senay et al. 2011). Hence, SSEBop uses two anchor values in the calculation: hot and cold temperatures. The hot temperature could be represented by bare soil which has little or no latent heat flux. Nevertheless, the cold temperature could be presented by water areas which has maximum ETc with little or no sensible heat flux. Hence, the SSEBop could be estimated as follows (Eqs. 2 and 3) (Senay et al. 2011);

$$ET_f = \left(\mathrm{T_{hot}} - \mathrm{T_{pixel}}\right)/(\mathrm{T_{hot}} - \mathrm{T_{cold}}). \tag{2}$$

$$ETc_{daily} = ET_o * ET_f \tag{3}$$

where, ET_f is the evapotranspiration fraction, T_{hot} and T_{cold} are the anchor Hot and Cold temperatures respectively, T_{pixel} is the land surface temperature of each pixel and ET_o and ETc_{daily} are the daily reference and actual evapotranspiration (mm/day) respectively (Senay et al. 2011).

2.3.3 Assessment of the Irrigation Water Performance

The spatial–temporal assessment of the irrigation water performance in the study area was derived using three indicators: the adequacy (P_A), dependability (P_D) and equity (P_E) indicators. The temporal assessment was derived using P_A and P_D. Nevertheless, the spatial assessment was derived using P_A and P_E. The results of these indicators were compared to the standard classes of these three indicators as shown in Table 2 (Molden and Gates 1990).

The Adequacy Indicator (P_A)

The P_A indicates the ability of the irrigation system to deliver the irrigation water (Khater et al. 2015). The P_A can be defined as the ratio of the delivered irrigation water for an area (R) to the required irrigation water for this area in a time (T) as follows (Eq. 4) (Khater et al. 2015);

Table 2 Standards for the IWPA (Molden and Gates 1990)

Internal indicator	Classes of the IWPA		
	Good	Fair	Poor
Adequacy (P_A)	0.90–1.0	0.8–0.89	<0.80
Dependability (P_D)	0.0–0.1	0.11–0.2	>0.2
Equity (P_E)	0.0–0.1	0.11–0.2	>0.2

$$P_A = \frac{1}{T}\sum_{T}\left(\frac{1}{R}\sum_{R}\frac{Q_D}{Q_R}\right) \quad (4)$$

In the case of $Q_D \geq Q_R$, the P_A will be equal to 1.0 which indicates that the irrigation system is adequate and delivers the required irrigation water.

The Equity Indicator (P_E)

The P_E is the spatial indicator which expresses the fairness and uniformity of irrigation water distribution over an area (R) during time (T). The P_E uses the coefficient of variation (CV_R) for the (Q_D/Q_R) as follows (Eq. 5) (Fan et al. 2018);

$$P_E = \frac{1}{T}\sum_{T} CV_R\left(\frac{Q_D}{Q_R}\right) \quad (5)$$

If the P_E is about zero, then the water users received the irrigation water in equity values according to their irrigation water requirements (Khater et al. 2015).

The Dependability Indicator (P_D)

The P_D is the temporal indicator which expresses the ability of the irrigation system to deliver the required irrigation water to water users in the required time to avoid crop water stresses (Fan et al. 2018). The P_D uses the coefficient of variation (CV_T) for the (Q_D/Q_R) over time (T) over an area (R) as follows (Eq. 6) (Khater et al. 2015);

$$\mathrm{P_D} = \frac{1}{R}\sum_{R} CV_T\left(\frac{Q_D}{Q_R}\right) \quad (6)$$

If the P_D is about zero, then the water users received their irrigation water from the irrigation system at the right time (Khater et al. 2015).

3 Results and Discussion

3.1 Land Surface Temperature and Reference Evapotranspiration

The *Ts* was assessed over the study area using the thermal bands of the Landsat 8 and the Normalized Difference Vegetation Index (NDVI) which uses the optical bands of Landsat 8 images. The *Ts* was assessed in the beginning, growing and harvesting seasons as shown in Fig. 2a–c. In the beginning season, the *Ts* was ranged from 307

to 314 K in June 2016 with mean 310.3 K and 3.29 standard deviation as shown in Fig. 2a. Nevertheless, in Fig. 2b, the *Ts* increased in the growing season to range from 303 to 316 K in August 2016 with mean and standard deviation 312 K and 4.05 SD, respectively. However, the *Ts* decreased in the harvesting season and ranged from 302 to 314.05 K with mean and standard deviation 309.46 K and 3.75 SD, respectively in October 2016 as shown in Fig. 2c.

The ET_o was derived in the center of the Nile delta using the average temperature, wind speed and humidity in the same dates of the used Landsat 8 images. The average ET_o were 6.8, 8.0 and 6.2 mm/day in the study area in June, August and October 2016, respectively.

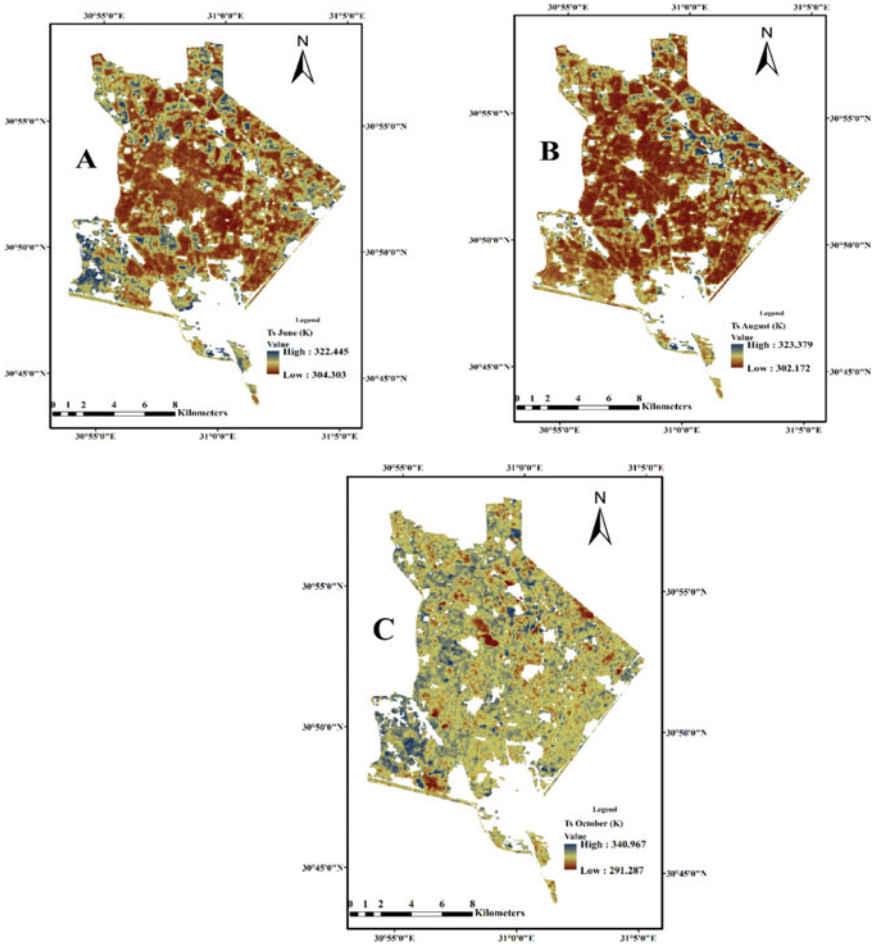

Fig. 2 **a** Land surface temperature on 15 June 2016 over the study area. **b** Land surface temperature on 8 August 2016 over the study area. **c** Land surface temperature on 10 October 2016 over the study area

3.2 SSEBop Algorithm

The actual evapotranspiration was estimated by SSEBop and Landsat 8 images at regional scale as shown in Fig. 3a–c (Elnmer et al. 2018a, b). The ETc was ranged from 0 to 1.8 mm/day in June 2016 due to the absence of vegetation cover as shown in Fig. 3a. In August 2016, the ETc increased to reach its maximum from 4.0 to 9.466 mm/day due to the high temperature (Fig. 2b) and the growth of crops as shown in Fig. 3b. However, in Fig. 3c, the ETc dropped in October 2016 and ranged from 0 to 2.3 mm/day due to the harvesting season, in addition, the temperature also dropped (Elnmer et al. 2018a, b). Elnmer et al., validated the simulated ETc with ground measurements of ETc. The results showed a high ability of SSEBop and Landsat 8 to estimate the ETc with high accuracy $R^2 = 87\%$ (Elnmer et al. 2018a, b).

3.3 Assessment of the Irrigation Water Performance

3.3.1 Temporal Assessment

The temporal assessment was derived using P_A and P_D for the branch canals in the study area as shown in Table 3. For branch 1, the P_A was classified as "Good". There was oversupply in the delivered irrigation water in branch 1 as it is located at the head of the main canal "Al-Qased". The farmers at the beginning canals, get their demands and waste additional amounts of the irrigation water. The P_A was "Poor" and "Fair" in branch 2 and 3 where the plants did not receive enough irrigation water to grow.

The P_D was "good" in branch 1 due to the oversupplies of irrigation water to fields at the head of the main canals. However, the P_D was "Poor" in branch 2 and 3 where the delivered water amounts were less than the required irrigation water.

Khater et al., reported similar results, where the P_D was "fair" and "Poor" at the branch canals located at the tail of the main canal in the Nile delta during summer 2008 (Khater et al. 2015).

3.3.2 Spatial Assessment

The spatial IWPA was derived using the adequacy (P_A) and equity (P_E) indicators the three branch canals during different seasons as shown in Table 3. The P_A was "good" during the beginning season. This could be attributed to the low irrigation water demands in the beginning seasons. However, during the growing and harvesting seasons, the P_A was "poor" due to the high irrigation water demands in the growing seasons. The P_A was "poor" in the harvesting seasons, owing to the low irrigation water supplies to the study area.

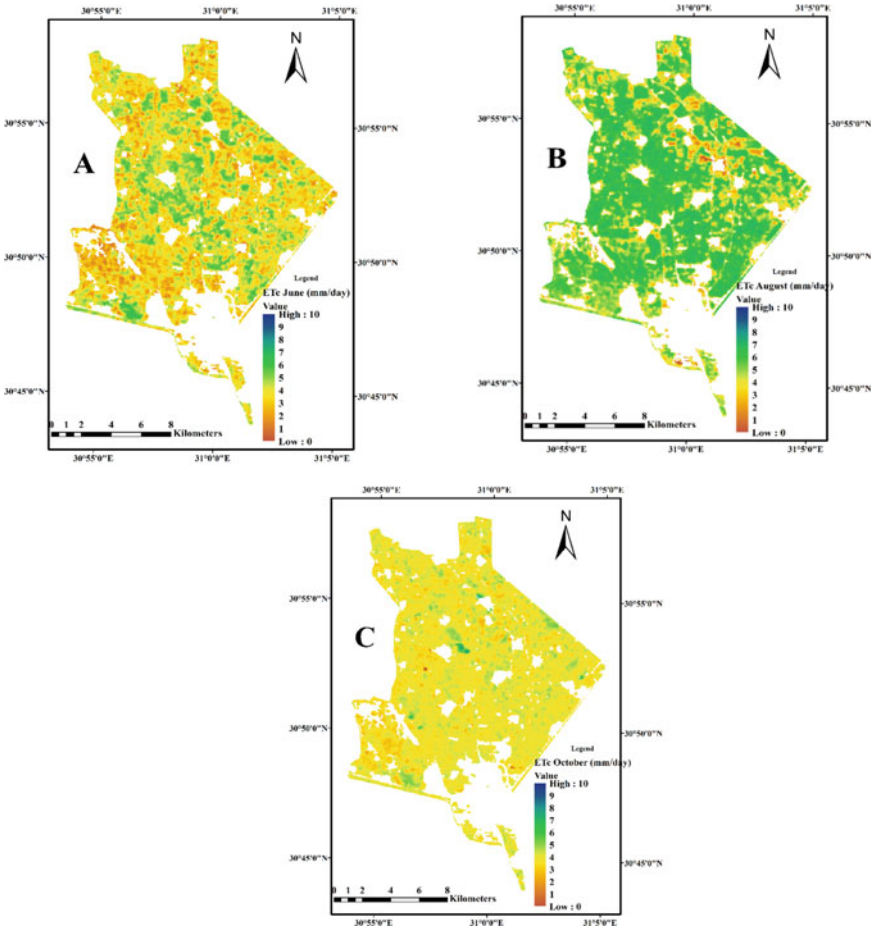

Fig. 3 **a** Actual evapotranspiration on 15 June 2016 over the study area (adopted from Elnmer et al. 2018a, b). **b** Actual evapotranspiration on 8 August 2016 over the study area (adopted from Elnmer et al. 2018a, b). **c** Actual evapotranspiration on 10 October 2016 over the study area (adopted from Elnmer et al. 2018a, b)

The P_E was "Good" in the beginning seasons which refers to a uniform irrigation water distribution between the farmers. However, during the growing seasons, the distribution of the irrigation water was non-uniform as the P_E was "poor". Additionally, there was not equity in the irrigation water distribution between farmers according to their demands.

Table 3 The adequacy, dependability, and equity indicators for the three branch canals in the study area during summer 2016

Month	June 2016	August 2016	October 2016	Temporal P_A	P_D (CV_T)
Branch canal	Branch 1				
Q_D	2.55	2.47	1.22		
Q_R	1.80	2.67	1.39		
$P_A(Q_D/Q_R)$	1.00	0.93	0.88	0.94	0.05
Level	Good	Good	Fair	Good	Good
	Branch 2				
Q_D	5.55	5.38	2.67		
Q_R	6.24	9.23	4.52		
$P_A(Q_D/Q_R)$	0.89	0.58	0.59	0.69	0.21
Level	Fair	Poor	Poor	Poor	Poor
	Branch 3				
Q_D	8.31	8.06	4.00		
Q_R	6.69	9.92	5.09		
$P_A(Q_D/Q_R)$	1.00	0.81	0.78	0.86	0.11
Level	Good	Poor	Poor	Fair	Poor
Spatial P_A	0.96	0.77	0.75		
Level	Good	Poor	Poor		
P_E (CV_R)	0.05	0.18	0.16		
Level	Good	Poor	Fair		

4 Conclusions and Recommendations

The internal irrigation water performance assessment in the center of the Nile delta was derived using remote sensing techniques during summer 2016. These techniques were SSEPop algorithm with Landsat 8 images to derive the actual evapotranspiration. The actual evapotranspiration represents the agricultural water demands in the study area. The internal IWPA consist of temporal and spatial assessments. The temporal assessment was derived adequacy and dependability indicators. This assessment indicated that the farmers at the middle and tail branch canals did not receive their irrigation water demands in the right time. However, the farmers in the beginning branch canals received their demands in time due to their excess usage of the irrigation water. The spatial IWPA was derived using adequacy and equity indicators. The assessment showed a non-uniform distribution of the irrigation water between the beginning, middle and tail branch canals during different seasons. Hence, enhancing the IWPA and monitoring the irrigation water distribution between water users require an accurate information about the irrigation water demands at regional scale. Therefore, remote sensing techniques could provide the managers with the locations and amounts of irrigation water demands in the right time.

References

Ahmad M-u-D (2009) Diagnosing irrigation performance and water productivity through satellite remote sensing and secondary data in a large irrigation system of Pakistan. Agric Water Manag 96(4):551–564

Akhtar F (2018) Assessment of irrigation performance in large river basins under data scarce environment—a case of Kabul river basin, Afghanistan. Remote Sens 10(6):972

Allen RG (1989) Operational estimates of reference evapotranspiration. Agron J 81(4):650–662

Allen RG et al (1998) Crop evapotranspiration: guidelines for computing crop requirements, FAO irrigation and drainage paper no. 56. FAO, Rome, Italy, p 300

Blaney HF (1952) Determining water requirements in irrigated areas from climatological and irrigation data

Bos MG (1993) Methodologies for assessing performance of irrigation and drainage management. Irrig Drain Syst 7(4):231–261

Bos MG, Burton MA, Molden DJ (2005) Irrigation and drainage performance assessment. CABI Publishing, British Library, London

Calcagno G et al (2007) Distributed estimation of actual evapotranspiration through remote sensing techniques. In: Methods and tools for drought analysis and management. Springer, pp 125–147

El-Agha DE (2011) Performance assessment of irrigation water management in old lands of the Nile delta of Egypt. Irrig Drain Syst 25(4):215–236

Elhag M (2011) Application of the SEBS water balance model in estimating daily evapotranspiration and evaporative fraction from remote sensing data over the Nile delta. Water Resour Manage 25(11):2731–2742

Elnmer A et al (2015) Optimal water productivity of crop pattern in central Nile delta, Egypt. In: Eighteenth international water technology conference, IWTC18, Sharm ElSheikh, Egypt, 12–14 Mar 2015

A Elnmer 2018a Assessment of irrigation water performance in the Nile delta using remotely sensed data Water 10 10 1375

Elnmer A et al (2018b) Using remote sensing techniques for estimating water stress index for central of Nile delta. IOP Conf Ser: Earth Environ Sci 151(1):012026

Elnmer A (2019) Mapping daily and seasonally evapotranspiration using remote sensing techniques over the Nile delta. Agric Water Manag 213:682–692

Fan Y (2018) Evaluation of the water allocation and delivery performance of Jiamakou Irrigation Scheme, Shanxi, China. Water 10(5):654

Karatas BS (2009) Using satellite remote sensing to assess irrigation performance in Water User Associations in the Lower Gediz Basin, Turkey. Agric Water Manag 96(6):982–990

Khadr M et al (2016) On-farm water management in the Nile delta. In: The Nile delta. Springer, Cham, pp 325–344

Khater A (2015) Quantitative analysis of reusing agricultural water to compensate for water supply deficiencies in the Nile delta irrigation network. Paddy Water Environ 13(4):367–378

Liou Y-A, Kar SK (2014) Evapotranspiration estimation with remote sensing and various surface energy balance algorithms—a review. Energies 7(5):2821–2849

Menenti M (1993) Parameteraization of land surface evaporation by means of location dependent potential evaporation and surface temperature range. In: Bolle, Feddes, Kalma (eds) Exchange processes at the land surface for a range of space and time scales

Molden DJ, Gates TK (1990) Performance measures for evaluation of irrigation-water-delivery systems. J Irrig Drain Eng 116(6):804–823

MWRI (2010) Water strategy of the Ministry of Water Resources and Irrigation. Ministry of Water Resources and Irrigation, Egypt

Ramos JG et al (2006) Crop management in a district within the Ebro River Basin using remote sensing techniques to estimate and map irrigation volumes. WIT Trans Ecol Environ 96

Senay GB (2011) Enhancing the simplified surface energy balance (SSEB) approach for estimating landscape ET: validation with the METRIC model. Agric Water Manag 98(4):606–618

Senay GB (2016) Evaluating Landsat 8 evapotranspiration for water use mapping in the Colorado River Basin. Remote Sens Environ 185:171–185
Su Z (2002) The surface energy balance system (SEBS) for estimation of turbulent heat fluxes. Hydrol Earth Syst Sci 6(1):85–100
Thornthwaite CW (1948) An approach toward a rational classification of climate. Geogr Rev 38(1):55–94
Ulivieri C (1994) A split window algorithm for estimating land surface temperature from satellites. Adv Space Res 14(3):59–65
Zwart SJ, Leclert LM (2010) A remote sensing-based irrigation performance assessment: a case study of the Office du Niger in Mali. Irrig Sci 28(5):371–385

Studying the Water Resources and Hydrological Characteristics of the West Bank and Gaza Strip, Palestine Using GIS and Remote Sensing Data

Ahmed Ghodieh

1 Introduction

Palestine, a country in the Middle East, remains under Israeli occupation since 1967 (Fig. 1). In 1993, the Palestine Liberation Organization (PLO) and Israel signed the Oslo Interim Agreement. Following this agreement, a Palestinian authority led by the PLO was created in the West Bank and Gaza Strip. The West Bank and Gaza Strip have been divided into three geopolitical areas, namely, A, B, and C. In 2005, Israel withdrew its forces from the Gaza Strip, but the region has remained besieged by Israel from all sides. Areas A and B, which represent 38% of the West Bank, have been placed under the civil control by the Palestinian Authorities. Area C, which represents 62% of the region, has been placed under full control of the Israeli occupation forces (Fig. 2).

In regard to Oslo agreement, negotiations on water issues between the PLO and Israel has been postponed as finalized decision has yet to be made, due to failure in achieving an agreement between the two parties.

2 Study Area

The study area includes the Palestinian lands that have been occupied by Israel since 1967 (the West Bank including East Jerusalem and Gaza Strip) (Fig. 1). The surface area of the West Bank land is approximately 5650 km^2, in addition to the 220 km^2 of the Dead Sea water area, while the surface area of Gaza Strip is around 365 km^2.

The Occupied West Bank is located in the Mediterranean region between the latitudes 31.34 and 32.55° N, and the longitudes 34.96 and 35.56°. It is bounded on

A. Ghodieh (✉)
An-Najah National University, P.O. Box 7, Nablus, West Bank, Palestine
e-mail: ahmed@najah.edu

A. Shaban (ed.), *Satellite Monitoring of Water Resources in the Middle East*,
Springer Water, https://doi.org/10.1007/978-3-031-15549-9_14

Fig. 1 West Bank and Gaza Strip (Wikipedia 2008)

the west, north, and south by Israel, and by Jordan on the east (Hamada and Ghodieh 2021). It includes 4 topographic regions (Ghodieh 2020) namely, The Semi-coastal, the Mountains, the Eastern Slopes, and the Jordan Valley (Fig. 3).

1. The Semi-coastal region: This region is close to the Mediterranean Sea (14 km to the east of the shoreline). Its elevations range from less than 100 to 500 m above the mean sea level. The annual mean temperature in the region is around 20 °C, while the mean annual rainfall is around 500 mm (www.pmd.ps).
2. The Mountains region: This region lies to the east of the Semi-coastal region. Its elevations range from 500 to around 1000 m above the mean sea level. The mean annual temperature of the region is around 17 °C, and the mean annual rainfall is around 650 mm.
3. The Eastern Slopes region: This region lies in the rain shadow away from marine area. Its elevations range from 500 m in the upper slopes to 0 m in the lower slopes. The mean annual temperature is around 22 °C, and the mean annual rainfall is between 200 mm in the lower slopes and 400 mm in the upper slopes.
4. The Jordan Valley region: This region extends from the lower eastern slopes at 0 m elevation to the Jordan River course at around 400 m below the mean sea

Fig. 2 Map of areas A, B, and C after Oslo II (Kersel 2015)

level. The mean annual temperature is around 24 °C, and the mean annual rainfall ranges from 100 mm near the Dead Sea in the south to 300 mm in the north of the region.

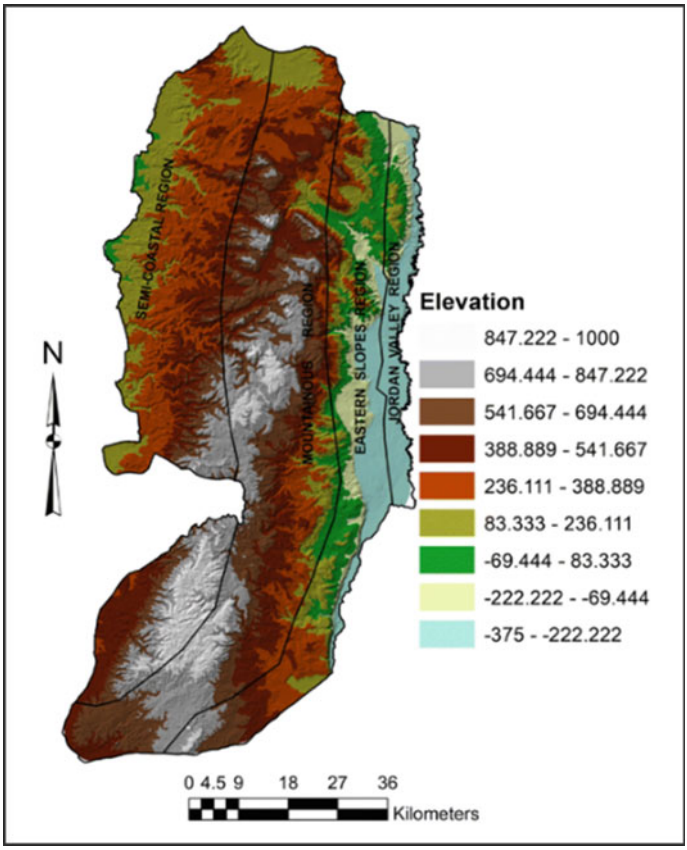

Fig. 3 **a** West Bank topographic map (Ghodieh 2020). **b** Topography of Gaza Strip (derived from SRTM data)

Gaza Strip lies on the shoreline of the Mediterranean Sea between 31.2 and 31.6° N, and between 34.2 and 34.6° E (google earth pro). It is bounded on the north and east by Israel, on the south by Egypt, and on the west by the Mediterranean Sea (Fig. 1). Its topography is relatively flat, and its elevations range from 10 m below the mean sea level near the shoreline to around 110 m above the mean sea level in the east and south of the Gaza Strip (Fig. 3b). The mean annual temperature is around 21 °C, and the mean annual rainfall is around 400 mm (www.weather-atlas.com).

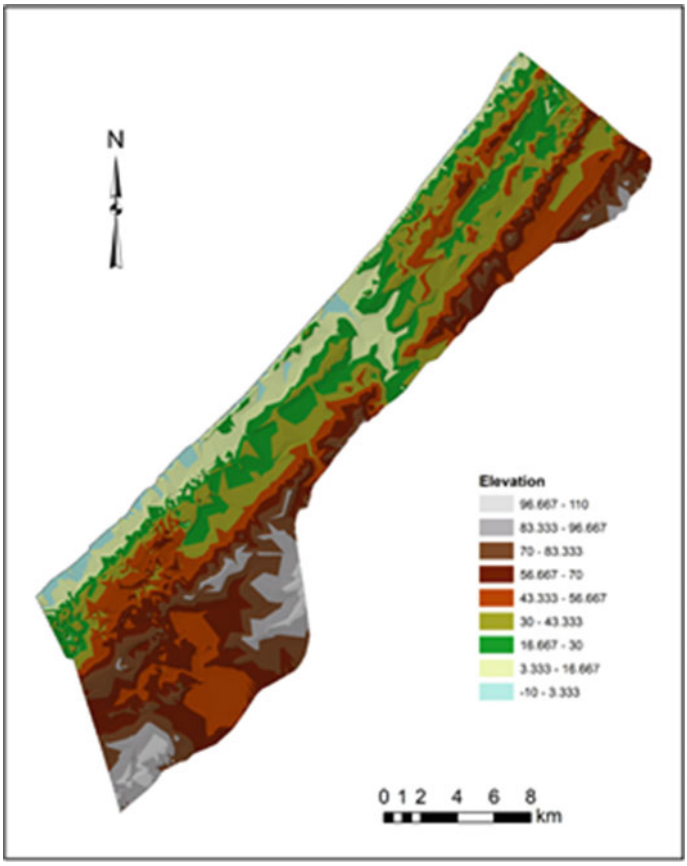

Fig. 3 (continued)

3 Water Resources of the West Bank and Gaza Strip

Water resources in the West Bank and Gaza Strip mainly includes rainfall, surface runoff, groundwater, and springs.

Rainfall: Rainfall is the main source of water in the West Bank and Gaza Strip. It is used for irrigating agricultural lands, mainly the rain-fed crops such as olive trees. Rain in Palestine falls in autumn, winter, and spring seasons. It usually starts in September and ends in April. The highest rainfall is recorded in December, January, and February. The average rainfall varies from one topographical region to another. It is in range of 100–300 mm in the Palestinian part of the Jordan Valley, 100–450 mm in the eastern slopes of the Palestinian central mountains, 500–700 mm in the Palestinian mountains region (the Nablus, Jerusalem, and Hebron mountains), and 400–600 mm in the coastal and semi-coastal region (Fig. 4).

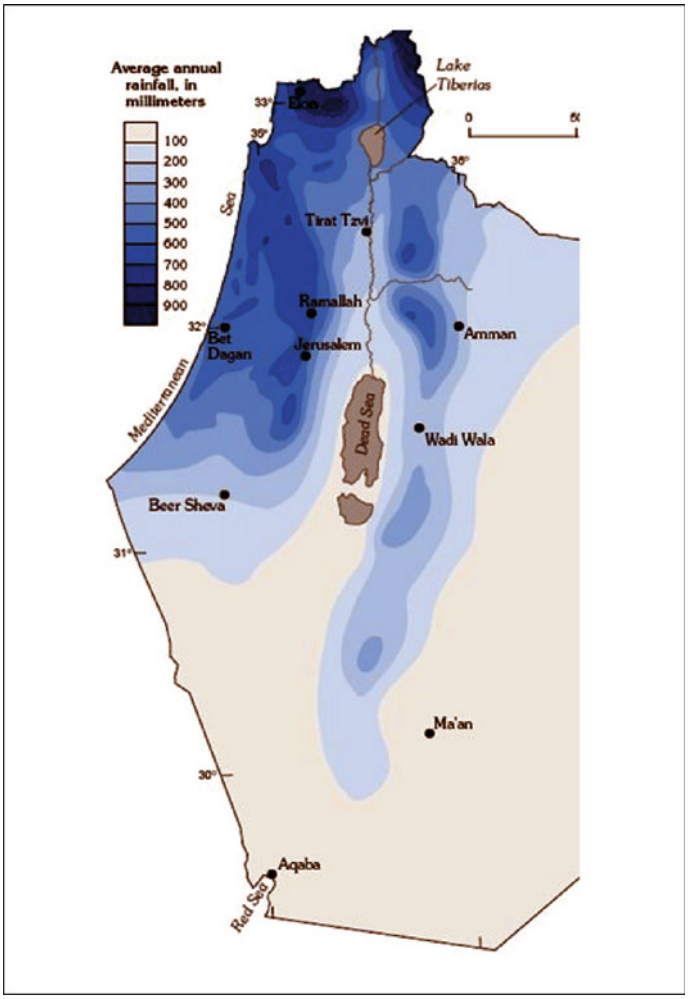

Fig. 4 Rainfall in the West Bank and Gaza Strip. *Source* www.pwa.ps

Surface water in Palestine are mainly drained toward the Mediterranean Sea in the west, and toward the Jordan valley and the Dead Sea in the east. These resources include the Jordan River with its tributaries, Tiberias Lake, and the Dead Sea.

Jordan River: The river originates from the high lands in Lebanon, Syria, Jordan, and Palestine. Length of the river is about 350 km, and the area of its basin is about 43,500 km^2, of which 12,000 km^2 constitutes the Palestine. The main tributaries namely Dan, Hasbani, and Banias meet in the Palestinian lands to form the Jordan River, which flows toward Tiberias Lake, and ends at the Dead Sea (Fig. 5).

Historically, the amount of water drained from the Jordan River to the Dead Sea was about 1400 mcm/year. Nowadays, the amount has reduced to only 30 mcm/year

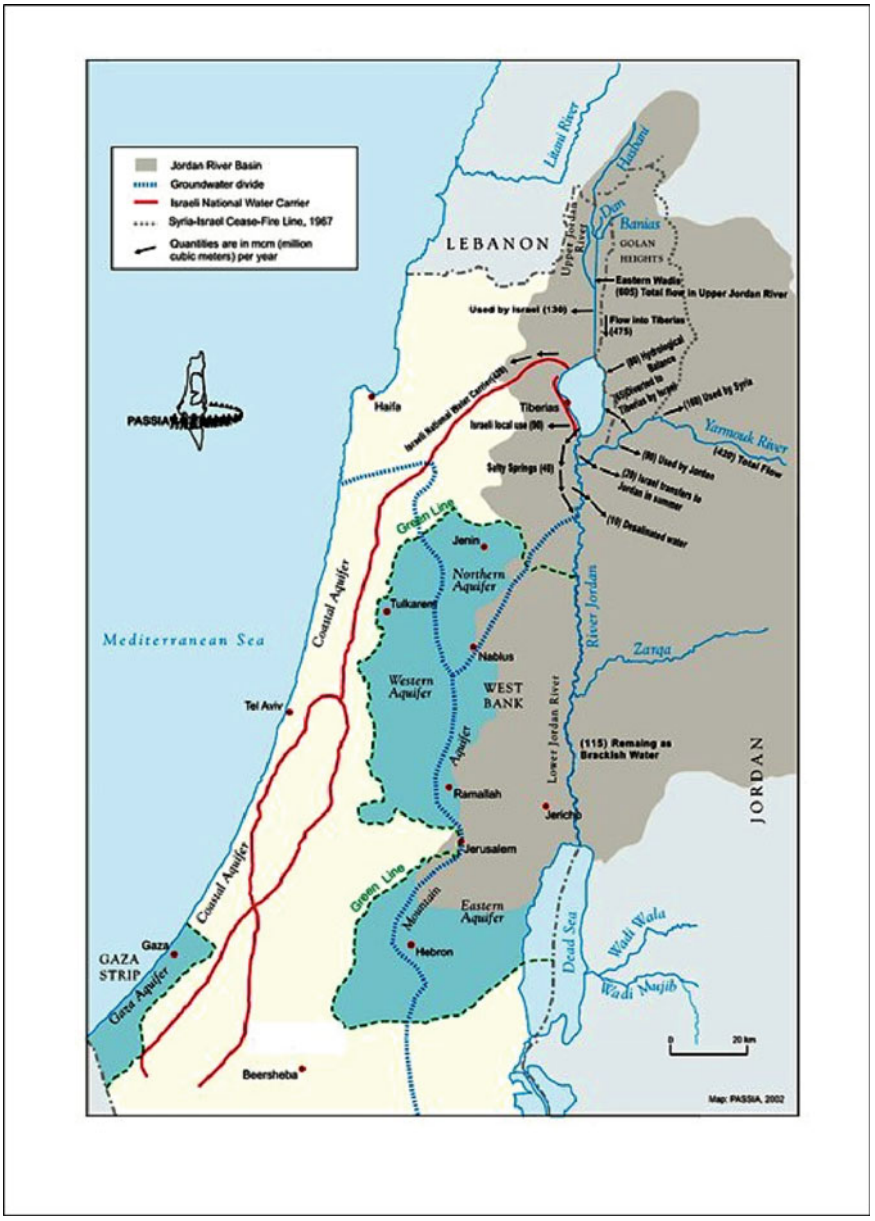

Fig. 5 The Jordan River Basin. *Source* www.pwa.ps

because Israel withdraws about 500 mcm/year from Tiberias Lake to Negev desert through what is called the Israeli National Carrier (Fig. 5), in addition to building dams on the river.

The Palestinian historic allocation is around 300 mcm/year, but the huge reduction in river flow due to Israeli projects in the upper stream, in addition to the Israeli occupation of the West Bank in 1967, has deprived the Palestinians from their water rights in the Jordan River.

Flood water: Flood water in wadis is another source of surface water in Palestine. The flow of flood water is about 165 mcm/year in the West Bank, and 20 mcm/year in Gaza Strip.

The Palestinians are unable to harvest flood water in the West Bank because Israeli occupation forces refuse to give them permits, in addition to the high cost of investment.

The Dead Sea: The Dead Sea is another source of surface water in Palestine. The length of the shoreline in the West Bank is 35 km, but the Palestinians have no access to it due to Israeli occupation.

Groundwater: Groundwater in Palestine is the main source of water. It is used for agricultural, domestic, and industrial purposes. Distribution of groundwater in Palestine depends on the geological formations. In the West Bank, groundwater mainly exists between limestone and dolomite layers, while in Gaza Strip it exists between sandstone layers along the Mediterranean shoreline. Depth and thickness of groundwater aquifers vary from tens of meters in the coastal and semi-coastal regions to hundreds of meters in the mountainous region. All these aquifers of the West Bank and Gaza Strip are renewed by rainfall every year. There are three main groundwater aquifers in the West Bank and each aquifer consists of a number of watersheds (Fig. 9). In Gaza Strip, there is only one groundwater aquifer which consists of a number of watersheds and belongs to the coastal plain aquifer.

These catchments were categorized using ArcGIS 10.8 software into three categories based on the flow direction (west, east, and north) (Fig. 10).

1. The Northern aquifer: It is a commonly known aquifer situated between the Palestinians of the West Bank and Israelis. This aquifer is from the Eocene and Cenomanian geological epoch. According to Oslo Interim Agreement between the PLO and Israel, the Palestinians can use 42 mcm/year of this aquifer, in actual however, the Palestinians are only allowed to use around 20 mcm/year, as opposed to Israelis, who can use around 110 mcm/year (Alyaqoubi and Abdelghafoor 2011).
2. The Easter Aquifer: This aquifer is wholly situated in the West Bank of Palestine. After the Israeli occupation of the West Bank in 1967, the Palestinians have been unable to fully utilize the water from this aquifer. Israelis utilize around 150 mcm/year of water from the area, while the Palestinians are only allowed to utilize around 65 mcm/year. Geologically, this aquifer is from the Pleistocene, Eocene, and Cenomanian epoch.
3. The Western aquifer: This aquifer is the most important groundwater aquifer in Palestine. It occupies the western slopes, the coastal and semi-coastal regions, and

shared by the Palestinians and Israelis. The Palestinians of the West Bank utilize around 38 mcm/year of the water, while Israelis utilize more than 400 mcm/year. On the other hand, Palestinians of the Gaza Strip utilize only 177 mcm/year of the coastal groundwater, while Israelis utilize more than 400 mcm/year.

In total, Israelis utilize around 664 mcm/year, which is equivalent to around 84% of the West Bank groundwater, while the Palestinians are only allowed to utilize around 124 mcm/year, or 16% of their groundwater resources from the West Bank aquifers. It is worth mentioning that the Palestinians of the West Bank buy an additional 52 mcm/year of water from the Israeli water company (Mekorot) (Israel Water Authority 2012). It is also important to highlight that the available renewable groundwater in Gaza Strip is around 120 mcm/year, of which 177 mcm/year is pumped out by the Palestinians in the area. This over pumping in Gaza has seriously affected the water quality. More than 50% of the samples collected from the wells contain high level of Sodium (Na), which is greater than 200 mg/L, a standard set by the World Health Organization (WHO) (Abbas et al. 2013).

4 Hydrological Characteristics of the West Bank and the Gaza Strip Watersheds

This section focuses on the West Bank watershed because it represents the majority of lands occupied by Israel in 1967 (approximately 5650 km^2). Concerning the Gaza Strip, a brief description of its watershed is provided in this section because it represents a small surface area (365 km^2).

Understanding the morphometric characteristics of watersheds is a basic aspect of understanding the hydrological processes of a region (Asmar et al. 2020). Morphology of watersheds can be studied in one, two, or three dimensions (linear, areal, or relief) (Radwan et al. 2017). Horton (1945) was the first to study some of the morphometric parameters of the drainage basin (Kant et al. 2015).

Remote sensing data and Geographical Information Systems (GIS) are used to conduct this study because these techniques proved to be effective tools in analyzing accurately the morphometric characteristics of drainage watersheds (Wani et al. 2018). Availability of free satellite data with adequate spatial resolution has enabled researchers to conduct data analysis at a low cost for various purposes including analysis of drainage watersheds (Jafarzadegan and Merwade 2017). Using these techniques, morphometric analyses have been extensively conducted to interpret various drainage parameters for water resource management and sustainable development (Banerjee et al. 2017).

Although the surface area of Palestine is small, there are four different climate regions identified: the humid climate of the coastal and the semi-coastal areas; the semi-humid climate of the western slopes of the mountainous areas; the semi-arid climate of the eastern slopes of the mountainous areas; and the arid climate of the Jordan valley. These significant variations in climate conditions are due to the tectonic

processes occurred in the region, particularly the formation of the Great Rift Valley. Other types of variations include topographic variations which are observable in the difference in elevation, slope, and aspect of topography, and variations in geographic location in terms of distance and proximity to the Mediterranean Sea. These factors, in singular or in combination, have affected the geomorphology of the land, and the morphometric and hydrologic characteristics of watersheds of the study area.

In this study, thousands of small drainage watersheds were derived from the Digital Elevation Model (DEM) of the West Bank and the Gaza Strip. This large number of watersheds were generalized into 43 watersheds in the West Bank and a few watersheds in Gaza Strip (Fig. 9).

4.1 Material and Methodology

This study mainly used satellite remote sensing data and the Geographical Information System software 10.8 (GIS). The Shuttle Radar Topography Mission (SRTM) data, version 3 (2013) known as SRTM Plus at 30 m resolution was obtained from the United States Geological Survey (USGS) at no cost. Data was collected from the NASA's SIR-C instrument.

The study area was constructed in 4 scenes (Fig. 6). Each scene consists of 3601 $\times$ 3601 pixels at a spatial resolution of 28.627 m. The size of each scene was around 103.085 $\times$ 103.085 km or 10626.69 km^2. The spatial reference of the data was assigned using the Geographic Coordinate System GCS_WGS_1984, with a pixel depth of 16.

The 4 scenes were mosaicked and merged into one image, then projected to the Palestine 1923-Palestine Grid coordinate system. The projected mosaic was clipped to the borders of the West Bank and the Gaza Strip (Fig. 7).

The spatial analyst extension namely ArcGIS 10.8 was used to extract the hydrologic parameters from the DEM. Fill processing tool was used to remove imperfections in the DEM data; Flow Direction tool was used to produce a map of flow direction for each cell of the DEM; and Flow Accumulation tool was used to calculate the accumulated flow of all cells flowing into each downslope cell in the output raster (ESRI 2021). Definition of a threshold is an important step. With the high-resolution DEM, the use of a relatively small threshold can provide a detailed description of drainage networks (Liu and Zhang 2010). In this study, the threshold areas with 1.25 and 0.04 km^2 were used for the delineation of drainage networks in the study area; threshold area with 1.25 km^2 was used for the whole area of the West Bank and Gaza Strip developed in DEM to delineate the main drainage networks; and the threshold of 0.04 km^2 was used for the two selected watersheds of the West Bank. One of the two watersheds flows toward the west, with a pour point in the Mediterranean Sea (Dair Balout watershed), while the other flows toward the east, with the pour points in the Jordan River and the Dead Sea (Faria watershed). These two watersheds were selected to represent the detailed hydrological characteristics of the West BankFig. 8.

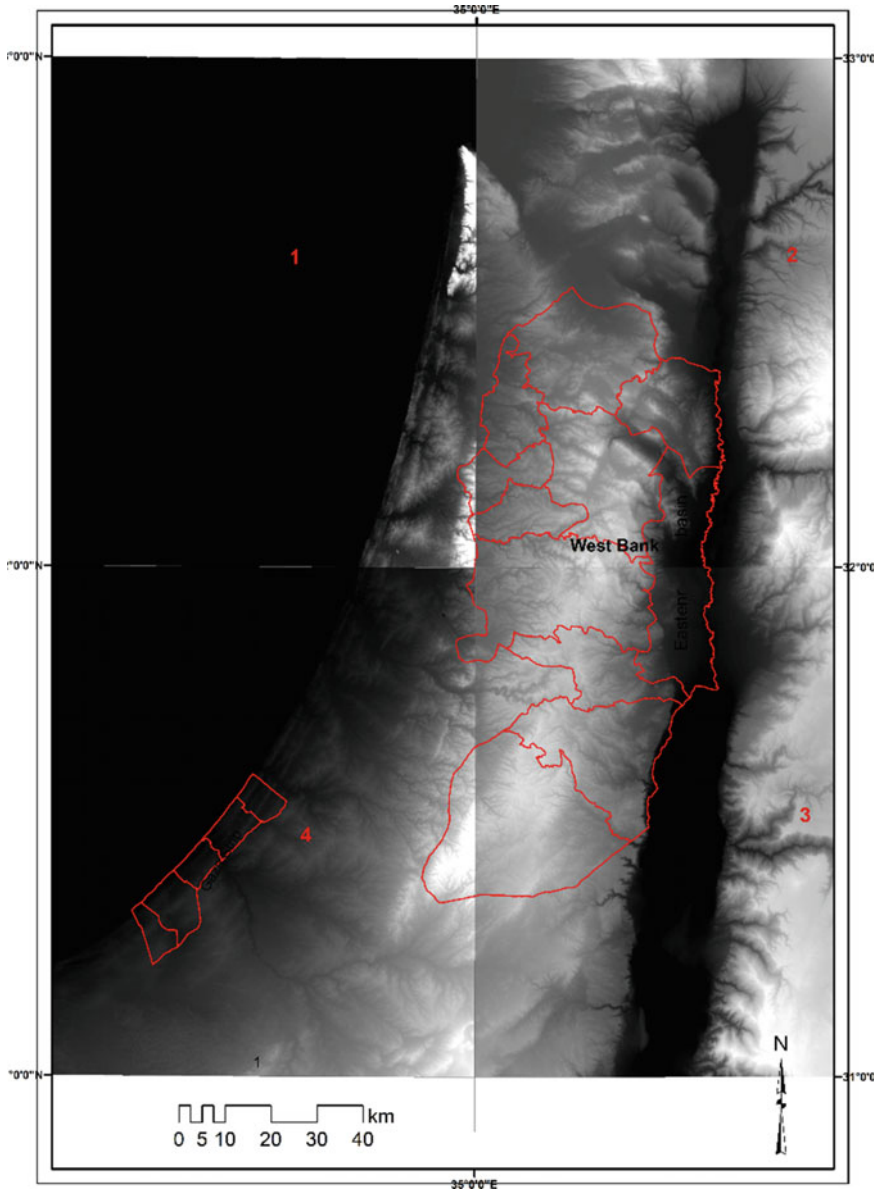

Fig. 6 Location of the study area on the SRTM data

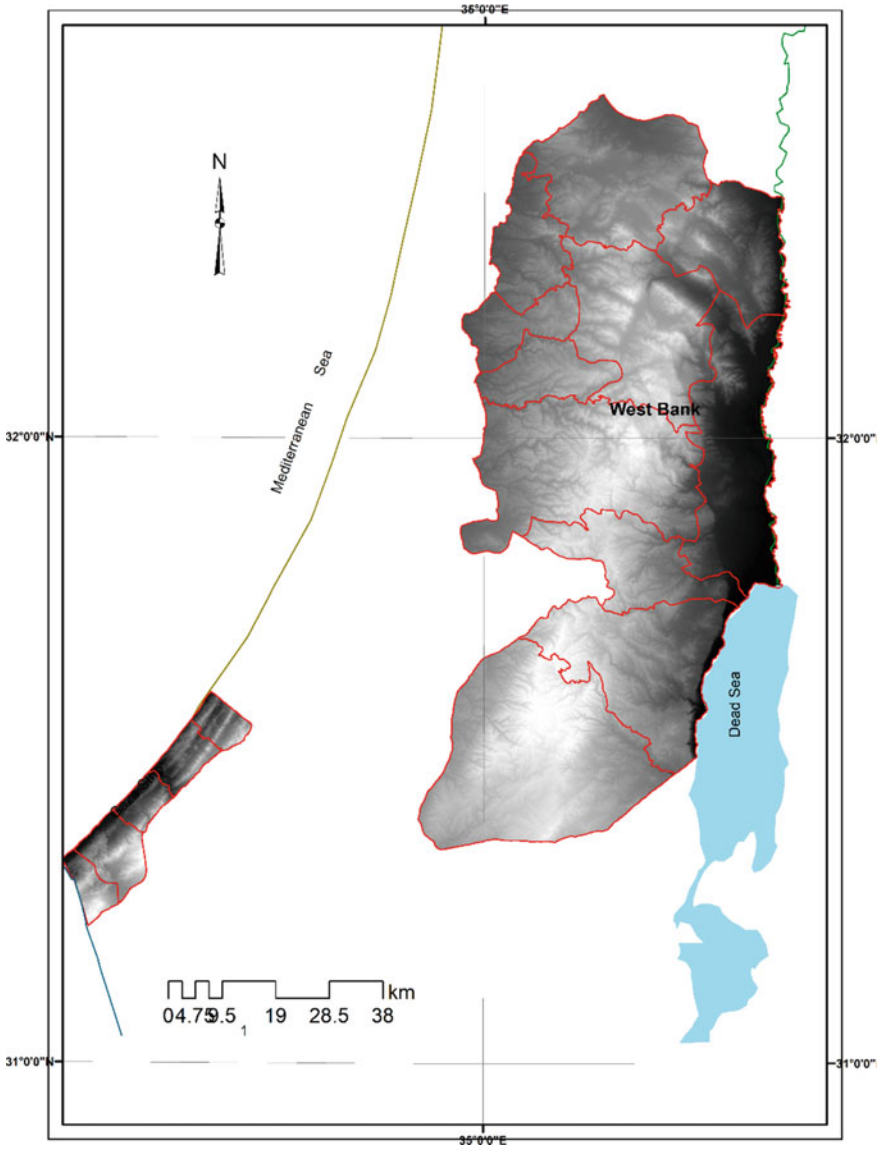

Fig. 7 The mosaicked DEM and clipped data at the borders of study area

Drainage networks can be described quantitatively in terms of some attributes such as stream order, stream lengths, and drainage density (Horton 1945). In 1952, Strahler developed the stream order system of Horton. According to Strahler system, stream order increases when streams of the same order intersect. For example, the junction

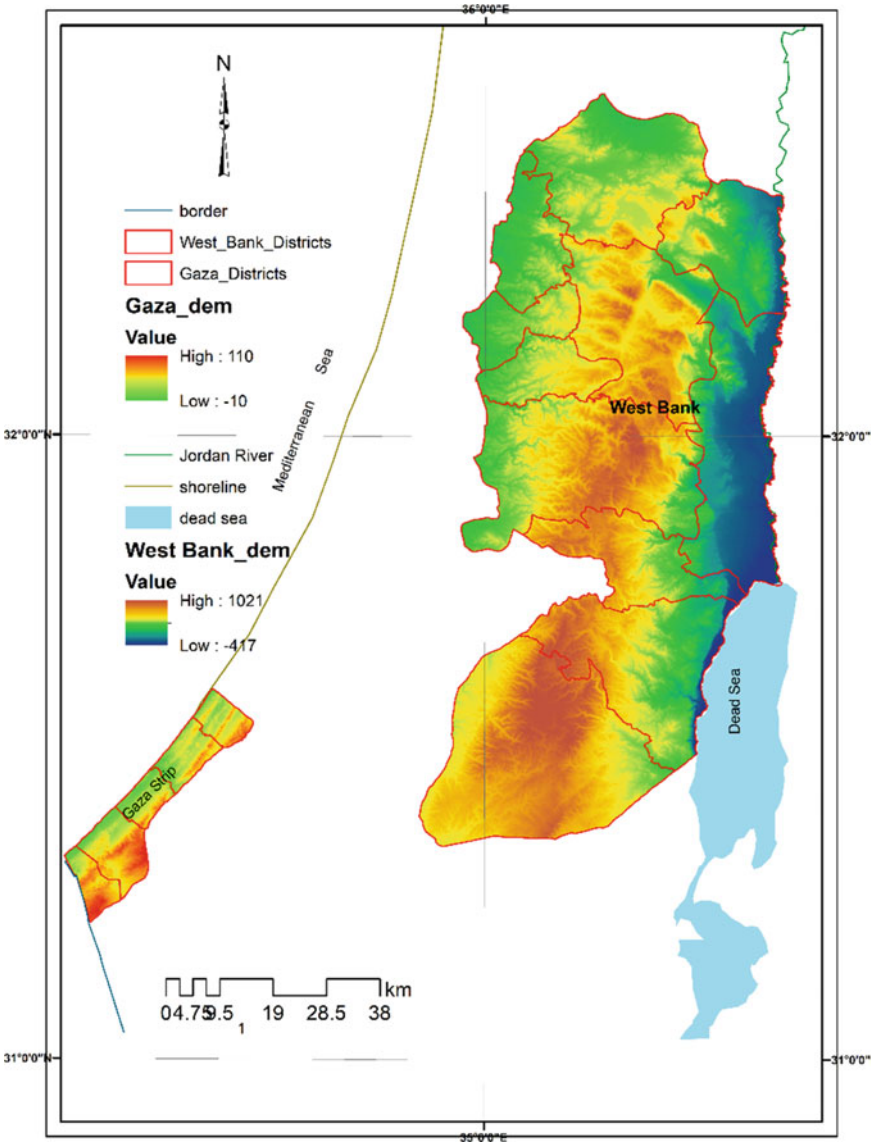

Fig. 8 DEM of the study area with 28.6-m resolution

of any of two first-order streams forms a second-order stream, but the intersection of two streams of different orders will not increase the stream order (Strahler 1952).

This study focused on the West Bank because it represents around 94% of the study area, while brief focus was given on Gaza Strip which represents only around 6% of the study area.

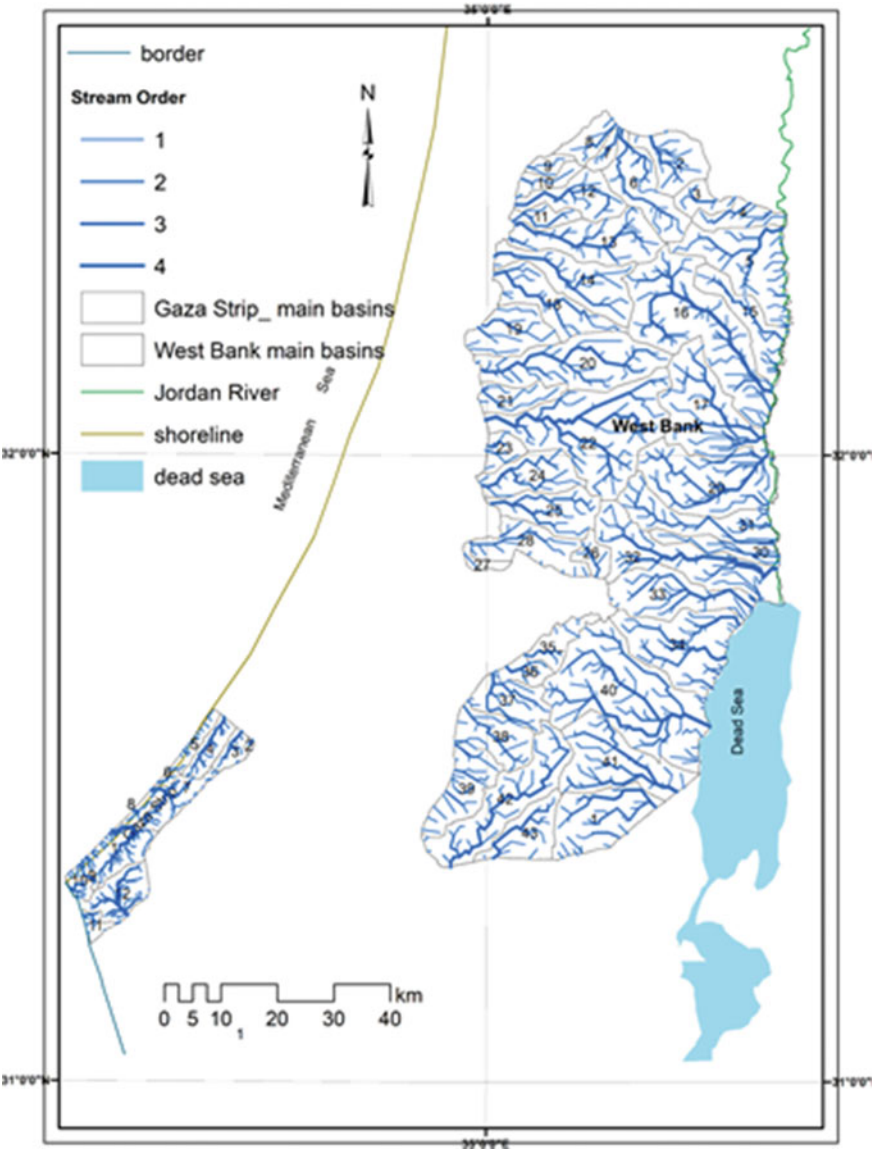

Fig. 9 Main watersheds in the West Bank and Gaza Strip derived from the SRTM

Figure 9 shows that the number of the main watersheds in the West Bank is 43, and that of the Gaza Strip is 12. The original number of watersheds derived from the SRTM is more than 7000 watersheds, but most of them are very small and situated on the boundaries of the study area. The author merged the small watersheds into larger ones after converting them into vector polygons.

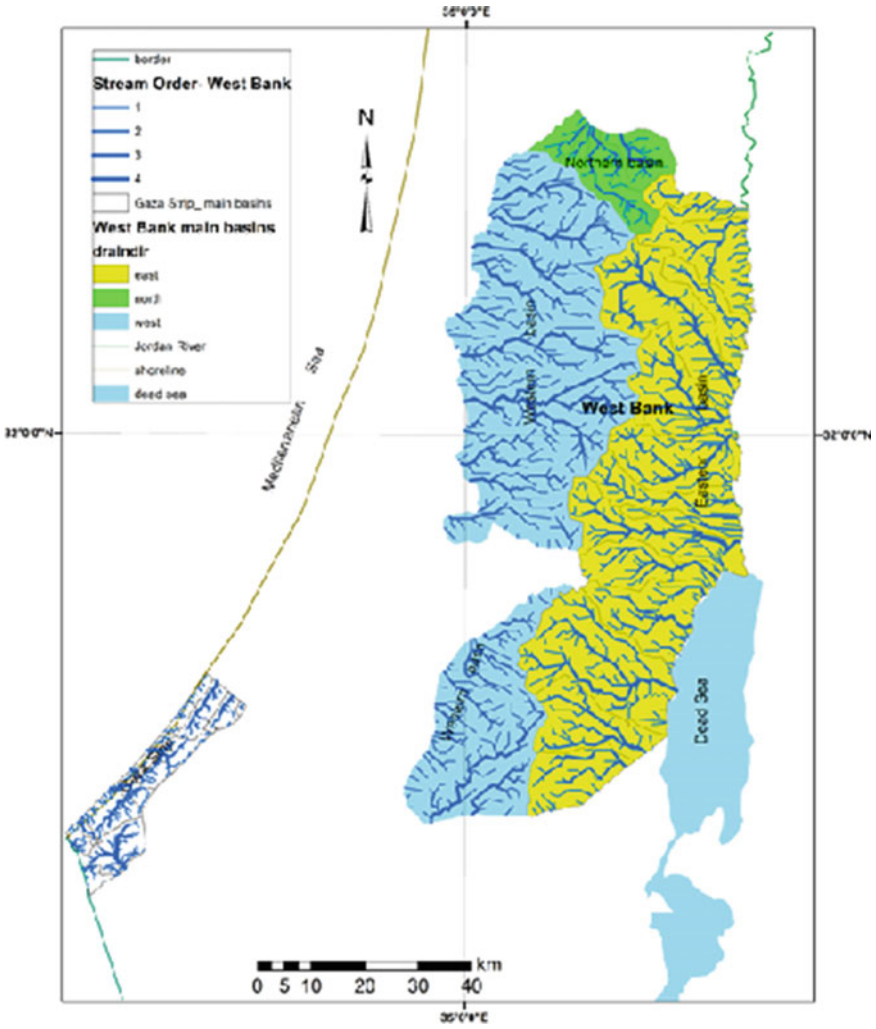

Fig. 10 The main watersheds in the West Bank (developed from Fig. 9)

24 watersheds out of 43 belong to the western basin that ends at a pour point in the Mediterranean Sea; 15 watersheds belong to the eastern basin that ends at the pour points in the Jordan River and the Dead Sea; and the remaining 4 watersheds belong to the northern secondary basin. In the Gaza Strip, all watersheds belong to the coastal basin with a pour point in the Mediterranean Sea. In the West Bank, the average watershed area was 131.25 km^2, with the smallest and largest watershed area of 16.56 km^2 and 412.64 km^2, respectively (Table 1). In the Gaza Strip, the average watershed area was 30.97 km^2, with the smallest and largest watershed area of 3.17 km^2 and 76.2 km^2, respectively. In regard to watersheds perimeters, the smallest in

Table 1 Drainage direction, area, and perimeter of West Bank watersheds

Watershed number	Drainage direction	Area (km^2)	Perimeter (km)
1	East	164.041	56.683
2	North	96.0451	44.5619
3	East	40.7289	31.0244
4	East	54.8043	42.2107
5	East	199.16	79.4428
6	North	129.453	58.7197
7	North	20.9216	21.7935
8	North	45.5894	33.4828
9	West	21.6559	22.3236
10	West	33.0552	32.8021
11	West	35.9112	31.4244
12	West	95.6328	52.0484
13	West	171.767	69.7138
14	West	155.91	74.9038
15	East	106.928	73.9214
16	East	363.311	112.739
17	East	226.366	80.3961
18	West	127.294	65.6468
19	West	108.191	45.0595
20	West	241.04	84.0695
21	West	62.4948	41.2046
22	West	367.469	101.277
23	West	36.3124	25.0173
24	West	107.263	49.4376
25	West	115.034	53.7429
26	West	33.4891	27.3944
27	West	16.5612	24.7129
28	West	112.979	62.8854
29	East	242.8	74.6274
30	East	59.3507	56.6299
31	East	140.914	74.5768
32	East	224.565	98.0441
33	East	156.241	66.3525
34	East	215.348	69.7097
35	West	51.3098	41.1025
36	West	34.8574	28.8173

(continued)

Table 1 (continued)

Watershed number	Drainage direction	Area (km^2)	Perimeter (km)
37	West	89.2781	44.6653
38	West	100.216	44.8501
39	West	113.044	52.5095
40	East	412.636	103.411
41	East	200.769	73.9941
42	West	216.121	88.4883
43	West	97.0374	50.7377
		Total = 5643.9 km^2	Total = 2467.16 km

the West Bank was 21.79 km^2, while the largest was 112.74 km^2, with an average of 57.38 km^2. In Gaza Strip, the smallest watershed perimeter was 7.33 km^2, while the largest was 44.31 km^2, with an average of 26.51 km^2 (Fig. 10).

Three groups of morphometric parameters were included in this study:

– Linear parameters: The parameters include the stream order (Su) which was developed by Strahler in 1964, whereby the smallest and the first segments represent the first order, i.e., two joined streams of the first order form the second order, and so on. Stream length ratio (Rl) is defined as the ratio of the mean length of the streams for a certain order, to the mean length of the streams over the next lower order (Horton 1945). Bifurcation Ratio (Rb) is the ratio of the stream number of any order to the stream number of the next highest order (Strahler 1957). Infiltration Number (If) is defined as the product of stream frequency and drainage density (Pareta and Pareta 2012) that has a positive relationship with direct runoff (Rai et al. 2017). Sinuosity ratio (Si) is defined as the ratio of the longest flow path of the watershed to the maximum length of the watershed (Schumm 1963).
– Areal parameters: Calculations of areal parameters are based on the watershed area and specific perimeter (Table 2). Drainage density (Dd) is one of the parameters which is calculated as the total length of all streams divided by watershed area (km/km^2). Drainage frequency (Df) is calculated by dividing the total number of streams on the watershed area (Nu/A). Drainage texture reflects the smoothness and roughness of the watershed surface, and is calculated by dividing the number of streams by the watershed perimeter (Nu/km). Constant channel maintenance (C) is the inverse value of drainage density (1/Dd) (Horton 1945). Form factor (Ff) is the ratio of the watershed area to the square of the watershed's maximum length. Shape index (Sw) is the inverse value of form factor (1/Ff) (Horton 1932). Elongation ratio (Re) is the ratio of the diameter of a circle, which has the same area as that of a given watershed, to the maximum length of the same watershed (Schumm 1956). Drainage intensity (Di) is defined as the relation of drainage frequency to the drainage density (Fs/Dd) (Faniran 1968). Circularity ratio (Rc) is the ratio of the watershed area to the area of a circle, which has the same

Table 2 Calculation methods for morphometric parameters

Parameters	Formula/definition/methods	Reference
Linear parameters		
Stream order (Su)	Hierarchical order	Strahler (1964)
Stream number (Nu)	–	Horton (1945)
Stream length (Nl)	Length of the stream (km)	
Stream length ratio (Rl)	Rl = Nl/Nl − 1; where, Nl − 1 = stream length of next lower order	
Bifurcation ratio (Rb)	Rb = Nu/Nu + 1 where, Nu + 1 = number of segments of the next higher order	Schumm (1956)
Infiltration number (If)	If = Fs × Dd where, Fs = stream frequency, Dd = drainage density	Faniran (1968)
Length of over land flow (Lof)	Lof = 1/2Dd	Horton (1945)
Areal parameters		
Drainage density (Dd)	Dd = L/A where, L = total length of stream, A = area of the watershed (km/km^2)	Horton (1945)
Drainage texture (Dt)	Dt = Nu/P where Nu = total number of stream, p = perimeter of the watershed	
Stream frequency (Fs)	Fs = Nu/A where, Nu = total number of stream	
Drainage intensity (Di)	Di = Fs/Dd	Faniran (1968)
Texture ratio (T)	T = N1/P where, N1 = total number of first order stream	Horton (1945)
Form factor (Ff)	Ff = A/Lb^2 where, Lb = maximum basin length	Horton (1932)
Circularity ratio (Rc)	Rc = 4ðA/P^2 where, ð = 3.14	Miller (1953)
Elongation ratio (Re)	Re = $\frac{2\sqrt{A/\eth}}{Lb}$	Schumm (1956)
Constant channel maintenance (C)	1/Dd	Horton (1945)
Shape index (Sw)	1/Ff	Horton (1932)
Relief parameters		
Basin relief (Bh)	Vertical distance between the lowest and highest point in watershed in meters (elevation max. − elevation min.)	Schumm (1956)
Relief ratio (Rhl)	Rhl = Bh/Lb; where, Lb = basin length in km	

(continued)

Table 2 (continued)

Parameters	Formula/definition/methods	Reference
Dissection index (Dis)	Dis = Bh/Ra, where, Ra = absolute relief	Singh and Dubey (1994)
Ruggedness number (Rn)	Rn = Bh × Dd	Schumm (1956)
Hypsometric integrals (Hi)	HI = (E mean − E min)/(E max − E min); where E = elevation	Strahler (1952)

Source Asmar et al. (2020)

perimeter as that of the watershed, and used to outline the watershed form (Miller 1953).

– Relief parameters: These parameters describe elevations of the watershed, and the associated impact on the watershed geomorphology. Basin relief (Bh) is the vertical difference between the highest and the lowest point of the watershed in meters (Schumm 1956). Relief ratio (Rhl) is the ratio of basin relief (Bh) to the maximum length of the basin (Lb) that is parallel to the main channel (Schumm 1956). Dissection index (Dis) is the ratio of basin relief to the absolute relief (Singh and Dubey 1994), which explains the stages in landscape development, as well as the morphometric and physiographic attributes of the landscape. Ruggedness number (Rn) is a product of vertical basin relief and drainage density (Strahler 1957). Hypsographic or hypsometric curves (Hs) and hypsometric integrals (Hi) provide valuable information on the watershed geomorphological stage and surface water erosion activity, respectively. The hypsographic curve represents the relationship between elevations of watershed and the respective surface areas, whereby the shape of the curve reflects the geomorphological life stage of the watershed (young, mature, and old). On the other hand, hypsometric integral (Hi) provides an understanding of erosion cycle of the watershed. Based on (Hi) value, Strahler (1952) classified the life cycle of the watershed into three categories: a value less than 0.30 indicates an old stage; a value in the range of 0.30–0.60 indicates a mature or equilibrium stage; and a value above 0.60 indicates a young stage.

5 Results and Discussion

The Hi of the Mediterranean Sea represented by Dair Balout watershed, and the Dead Sea represented by Faria watershed indicate that the watersheds are at mature stage with a Hi value of 0.54 and 0.44, respectively (Fig. 11a, b). The calculated Hi of the Dead Sea (Faria watershed) was lower than that of the Mediterranean Sea (Dair Balout watershed), which indicates that erosion activity in the eastern slopes is higher than that of the western slopes. This is because the western slopes are characterized by dense vegetation cover, while the eastern slopes have sparse vegetation cover despite the latter recording heavier rainfall than the former.

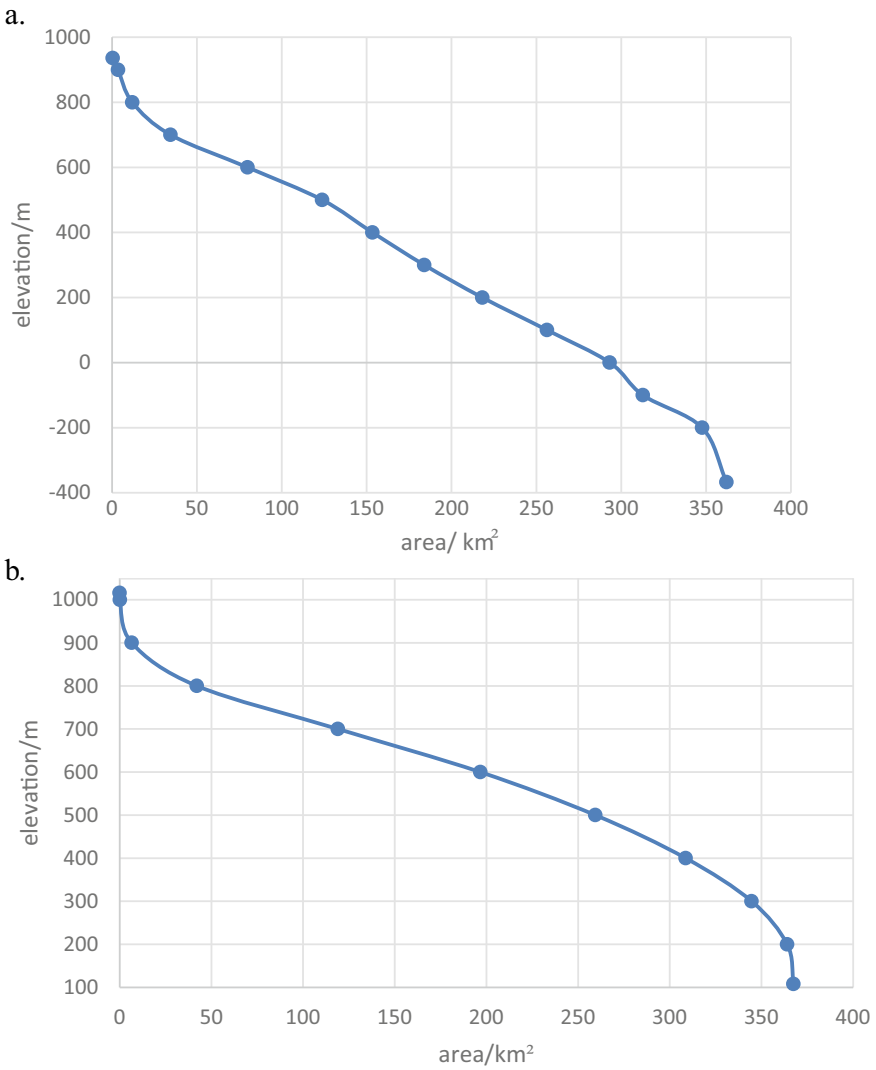

Fig. 11 **a** Hypsography of Faria watershed. **b** Hypsography of Dair Balout watershed

The western watershed also has lower drainage density and lower infiltration number than the eastern watershed. The findings indicate that the western watershed slopes are gentler (Fig. 12) than the slopes in the eastern watershed. The elevation interval in the eastern watershed (Faria) was 1301 m from the upstream point to the outlet point, while that of the western watershed (Dair Balout) was 908 m (Table 4).

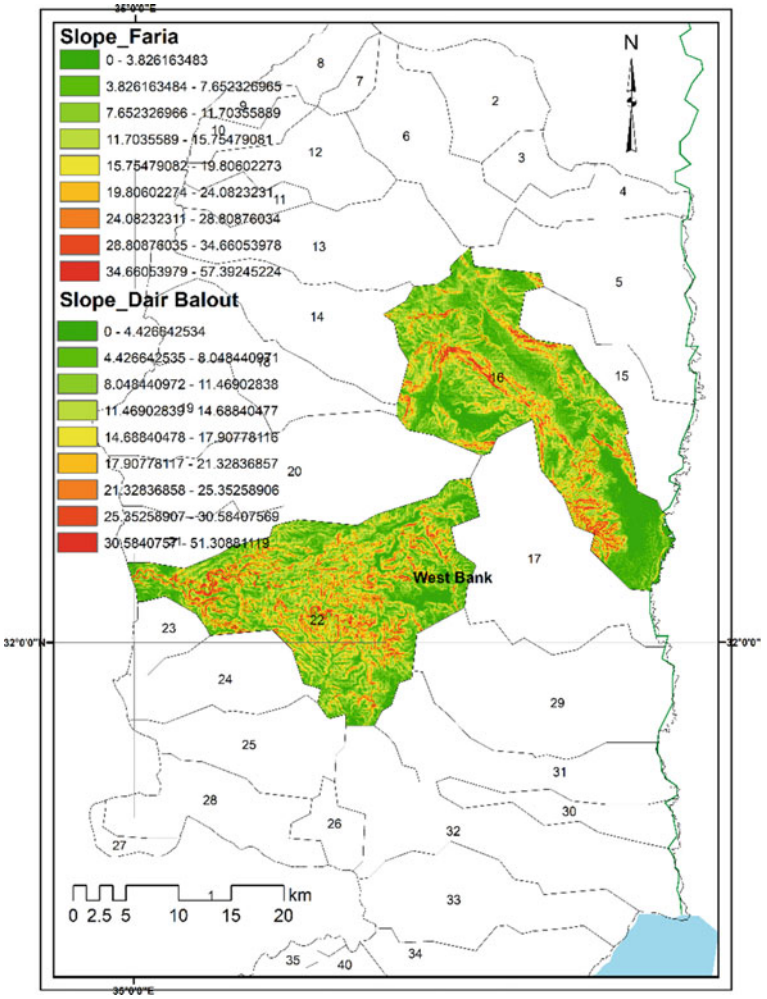

Fig. 12 Map of slopes in Dair Balout (Mediterranean Sea) and Faria watersheds (Dead Sea)

5.1 Linear Morphometric Parameters

The calculated Su reflects the geological structures and topographic landforms of a region. The use of threshold area of 1.25 km^2 for delineation of drainage networks in the West Bank and Gaza Strip resulted in four stream orders of watersheds (Fig. 13). On the other hand, a threshold area of 0.04 km^2 used for Faria and Dair Balout watersheds resulted in six and seven stream orders, respectively (Fig. 14).

The Nu value (Fig. 15) is the total number of stream segments for each stream order. For both western and eastern watersheds, the first-order number constituted 52% of the total streams in the study area, while the second- and the third-order

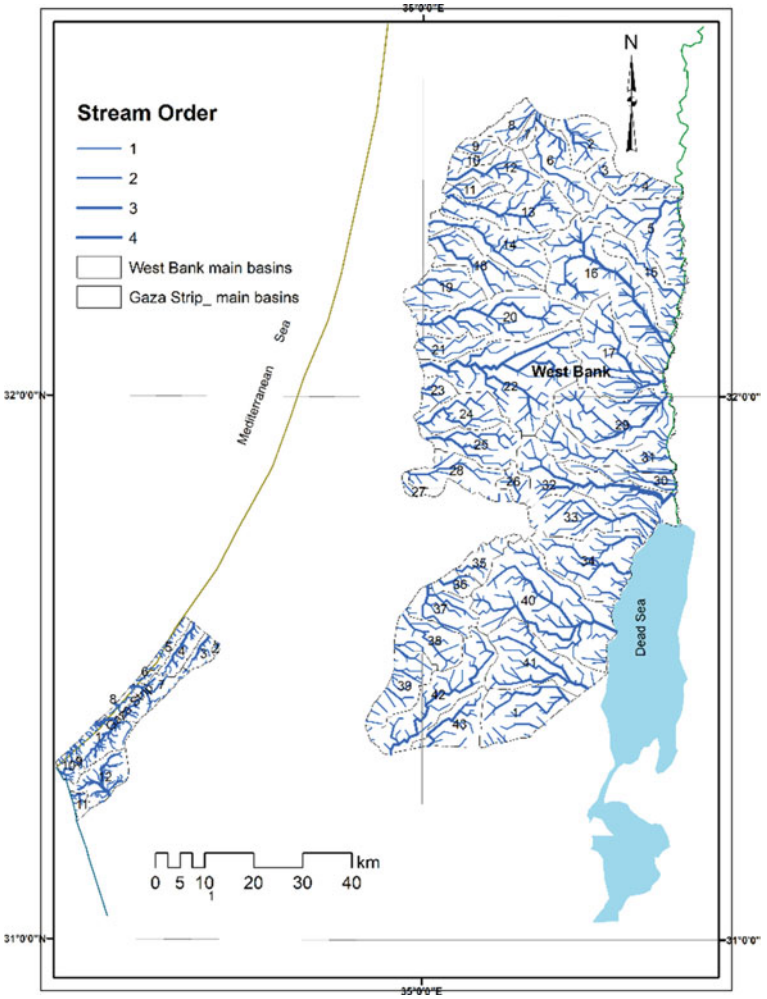

Fig. 13 Stream order of the West Bank and Gaza Strip with a threshold area of 1.25 km^2

constituted 23% and 12% of the area, respectively. It is clear that the Nu has an inverse linear relationship with the Su, except for the fifth- and sixth-order streams of Faria watershed (Dead Sea), whereby the number in the latter was double the former. This may be due to the effects of variations in geologic structures and topography of high relief and steep slopes (Rai et al. 2017).

The calculated Nl denotes the number of stream and the shape of watershed. The length of the first-order stream for both watersheds constituted 51% of the total stream length, which is in parallel with the percentage of stream number; the length of the second- and third-order streams constituted 25% and 12% of the total stream length, respectively. It is also clear that the stream length has an inverse linear relationship

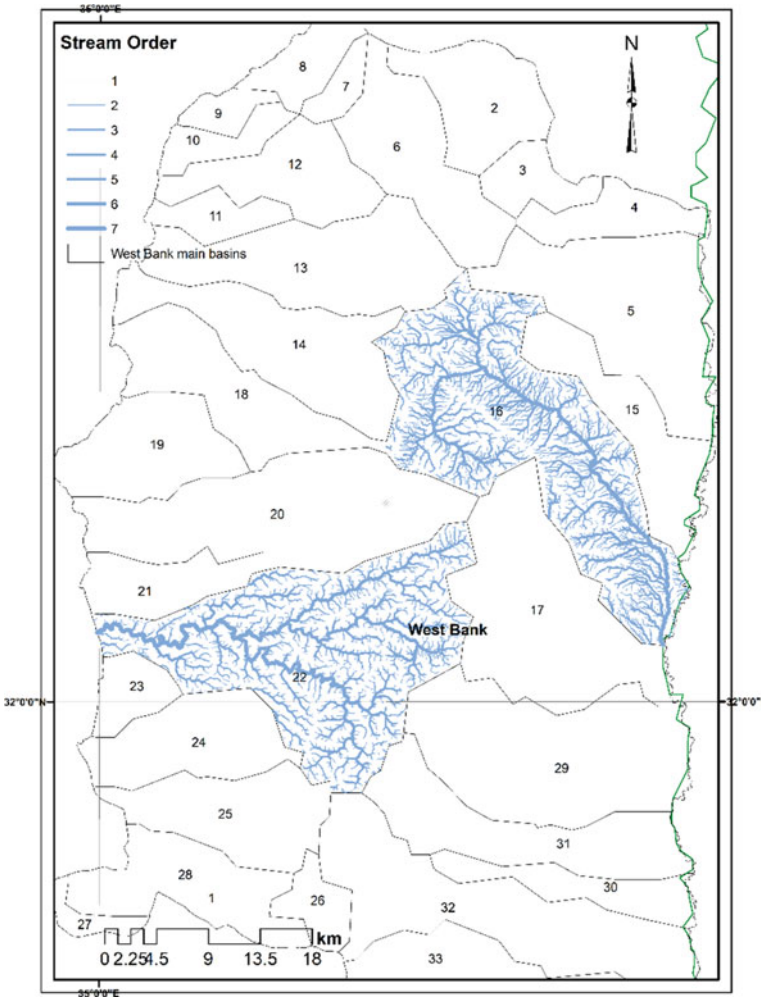

Fig. 14 Stream order of Faria and Dair Balout watersheds with a threshold area of 0.04 km^2

with the stream order, except for the fifth- and sixth-order streams of Faria watershed (Dead Sea), whereby the length of the latter was double the former. This may be due to the effect of the elongated shape of the watershed (Fig. 16).

The mean stream length ratio of Dair Balout watershed was 1.0, with the lowest (0.84) and highest (1.04) ratio recorded for the fifth- and sixth-order stream, respectively. The mean calculated for Faria watershed was, with the lowest (0.92) and highest (1.49) ratio recorded for the first- and fourth-order stream, respectively. The low values of stream length ratio indicate the late mature stage of geomorphic development of the watersheds in the study area (Pareta and Pareta 2012).

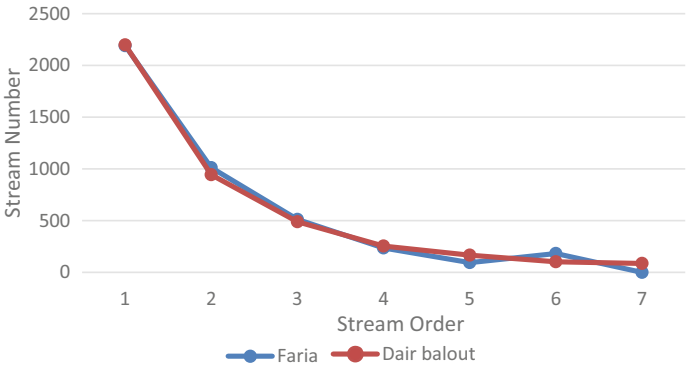

Fig. 15 Stream number of each stream order in the two watersheds

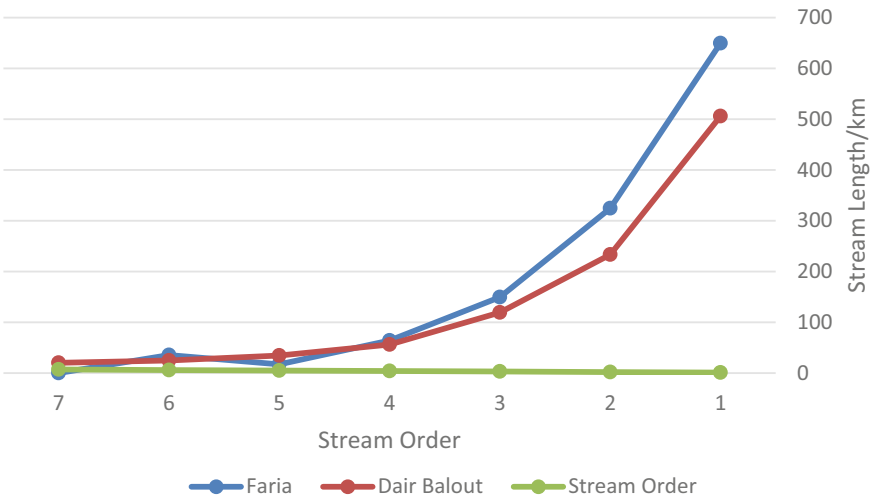

Fig. 16 Stream length of each stream order in both watersheds

The Rb value corresponds to the shape of watershed (Morisawa 1985), whereby low values indicate an elongated shape of watershed, while high values indicate the circular shape of watershed. In this study, Faria watershed recorded a higher mean of Rb than that of Dair Balout, with a valued of 1.87 and 1.71, respectively. Observation made demonstrated that the higher Rb recorded for the eastern watershed (Faria) is probably due to steep slopes and low vegetation cover as compared to that of western watershed (Dair Balout).

The calculated If denotes the infiltration characteristics of the watersheds—the higher the If, the lower the infiltration capacity, and the higher the runoff. Table 3 shows that the eastern watershed (Faria) has higher If, with a value of 39.6, than that of the western watershed (Dair Balout), with a value of 31.1; the results signify the

Table 3 Elevation areas of the western or Mediterranean Sea drainage system (Dair Balout watershed) and the eastern or the Dead Sea drainage system (Faria watershed)

Elevation (m)	Western or Mediterranean watershed (Dair Balout watershed) %	Eastern or Dead Sea watershed (Faria watershed)
−367–300	0.00	3.96
−300–200	0.00	9.61
−200–100	0.00	5.37
−100–0	0.00	10.17
0–100	0.00	10.50
100–200	0.94	9.41
200–300	5.28	8.41
300–400	9.86	8.14
400–500	13.41	12.11
500–600	17.06	12.49
600–700	21.13	6.21
700–800	20.93	2.31
800–900	9.67	0.98
900–1000	1.77	0.12
>1000	0.02	0.00

higher direct runoff and lower infiltration capacity in the former as compared to that of the latter.

The Si value is the ratio of stream length from the source point to the mouth point, to the length of the straight line between the two points. The Si is influenced by factors namely the watershed slope, geological structure, and rock type (Ezlashi 1999). Drainage watershed with a Si value of less than 1.5 is regarded as a sinuous watershed; a Si value of more than 1.5 denotes a meandering watershed (Ezeh and Mozie 2019). The Si value recorded for Faria and Dair Balout watersheds in the study area was 1.25 and 1.30, respectively. The results demonstrate that both are identified as sinuous (Table 4).

5.2 Areal Morphometric Parameters

The calculated Dd is an important areal watershed morphometric parameter. A high Dd value is usually associated with high surface runoff (Omolabi and Fagbohun 2019). In this study, the Dd value of the Faria watershed (eastern watershed) was higher than that of the Dair Balout watershed (western watershed) (Table 4).

The parameter C is defined as the area of basin surface needed to sustain a unit length of the stream channel (Schumms 1956). The value is influenced by factors namely topography of watershed, land cover, slope, and geological structure. A low

Table 4 Morphometric parameters of the western and eastern basins

Stream order (Su)	Dair Balout watershed (Mediterranean Sea drainage system)		Faria watershed (Dead Sea drainage system)	
	Stream number (Nu)	Stream length (Nl) (km)	Stream number (Nu)	Stream length (Nl) (km)
1	2198	506.4	2189	649.6
2	944	233.4	1012	324.5
3	489	119.2	512	149.5
4	255	56.2	236	64.0
5	166	34.4	94	17.1
6	102	24.9	183	35.5
7	86	20.1	–	–
Total	4240	994.6	4226	1240.3
Mean stream length ratio (Rl)	1		1.1	
Mean bifurcation ratio (Rb)	1.71		1.87	
Length of over land flow (Lof)	0.18		0.14	
Infiltration number (If)	31.1		39.4	
Sinuosity ratio (Rs)	1.3		1.25	
Area (km^2)	367.5		363.5	
Perimeter (km)	101.3		112.7	
Stream frequency (Fs)	11.5		11.6	
Circularity ratio (Rc)	0.46		0.36	
Drainage density (Dd)	2.7		3.4	
Drainage texture (Dt)	41.9		37.5	
Texture ratio (T)	21.7		19.4	
Form factor (Ff)	0.34		0.23	
Constant channel maintenance (C)	0.37		0.29	
Elongation ratio (Re)	0.66		0.59	
Shape index (Sw)	2.9		4.3	
Watershed relif				

(continued)

Table 4 (continued)

Stream order (Su)	Dair Balout watershed (Mediterranean Sea drainage system)		Faria watershed (Dead Sea drainage system)	
	Stream number (Nu)	Stream length (Nl) (km)	Stream number (Nu)	Stream length (Nl) (km)
Max. elevation (m)	1016		936	
Min. elevation (m)	108		−367	
Relief ratio (Rh)	29.3		32.5	
Dissection index (Dis)	0.89		0.94	
Ruggedness number (Rn)	2.45		4.94	
Hypsometric integral (Hi)	0.54		0.44	

C indicate low permeability, high surface runoff, and steep slopes. In this study, the C calculated for the Faria watershed (eastern slopes) was lower than that of Dair Balout watershed (western slopes), with a value of 0.29 and 0.37, respectively.

The value of Lof is described as half of the reciprocal of drainage density. The value corresponds to the length of the flow over the ground before the flow converge into the main stream, which affects the hydrologic and physiographic development of drainage basin (Horton 1945). The lower the Lof, the shorter the flow paths, the steeper the ground slopes, the higher the runoff, and the lesser the infiltration. In this study, Lof of the eastern slopes (Faria watershed) is lower than that of the western slopes (Dair Balout watershed), with a value of 0.14 and 0.18, respectively.

The Rc value denotes the shape of the watershed. The values range from 0 to 1, whereby 0 indicates a perfect line and 1 indicates a perfect circle. In this study, the calculated Rc of the eastern slopes (Faria watershed) was lower than that of the western slopes (Dair Balout watershed), with a value of 0.36 and 0.46, respectively. The values suggests that both watersheds are in the mature stage of development.

The Re is another parameter reflecting the shape of watershed. A low Re indicates steep slopes and high relief, and vice versa (Farhan 2017). The calculated Re of the eastern slopes (Faria watershed) was lower than that of the western slopes (Dair Balout watershed), with a value of 0.59 and 0.66, respectively, denoting that the former is more elongated than the latter. In general, both watersheds are identified as moderately elongated (Pareta and Pareta 2012).

The parameter Ff is defined as the ratio of the watershed area to the square of watershed length, which is always less than 1. For a perfectly circular (fan shape) watershed, the Ff would be 0.786, while a value smaller than 0.786 indicates a fern shaped. The smaller the value of Ff, the more elongated the watershed is. In this study, the recorded Ff of the eastern slopes (Faria watershed) was lower than that of the western slopes (Dair Balout watershed), with a value of 0.23 and 0.34, respectively. These values indicate that both watersheds are moderately elongated.

The value of Sw is the inverse value of the Ff. The value is used to identify watersheds with high vulnerability to erosion and flood (Rather et al. 2017). The lower the values of the Sw, the shorter the lag time, and therefore the higher the risk of erosion and flash floods (Al-Saady et al. 2016). In this study, the Sw of the western slopes or the Mediterranean Sea (Dair Balout watershed) was lower than that of the eastern slopes or the Dead Sea (Faria watershed), with a value of 2.9 and 4.3, respectively.

The T value is the ratio between the numbers of streams of the first order to the perimeter of the watershed (Horton 1945). The T calculated for the western and the eastern watersheds were considered high, with a value of 21.7 and 19.4, respectively. The high values indicate that both watersheds are characterized by rough surface and complex topography.

5.3 Relief Morphometric Parameters

The basin relief of the study area was determined as 1,016 m above the mean sea level. The reliefs in the western watershed (Dair Balout watershed) range between 108 and 1016 m, while that of the eastern watershed (Faria watershed) range between −367 m below the mean sea level and 936 m above the mean sea level.

The Rh value is the ratio between the watershed relief and the longest dimension of the watershed that is parallel to the main flow path. High value of relief ratio indicates a steep slope and vice versa. In this study area, the eastern watershed (Faria watershed) has a higher Rh than the western watershed (Dair Balout), with a value of 32.5 and 29.3, respectively. The results indicate that the eastern watershed is steeper than the western.

The calculated Rn is used to delineate landform components and infer process information to derive geomorphological units. The value is a product of the watershed relief (km) and drainage density, whereby it reveals surface unevenness (Selvan et al. 2011). In this study, the calculated Rn of the eastern watershed (Faria watershed) was higher than that of western watershed (Dair Balout), with a value of 4.94 and 2.45, respectively. The results suggest that the eastern watershed surface is more rugged and fragmented than that of western counterpart.

Determination of Dis is used to characterize the surface roughness of watershed. The calculated Dis of the eastern watershed (Faria watershed) was higher than that of the western watershed (Dair Balout watershed), with a value of 0.94 and 0.89, respectively. The values indicate that both watersheds are highly dissected.

The Hs and Hi values reflect the geomorphological stage of the watershed. Figures show that both the western watershed (Dair Balout watershed) and the eastern watershed (Faria watershed) were identified as mature with the Hi values of 0.44 and 0.54, respectively. Both watersheds are considered vulnerable to erosion.

6 Conclusion

In this study, the water resources in the West Bank and the Gaza Strip were investigated, with more focus given to the West Bank. This study revealed that the Palestinians have been unable to fully access their water resources due to the Israeli Occupation. The Palestinians can only use around 15% of their water resources, while the huge remaining amount is controlled by Israeli occupation authorities and settlements. Furthermore, a detailed quantitative analysis was carried out on the characteristics of the eastern (Dead Sea) and western (Mediterranean Sea) watersheds. The Dead Sea was represented by Faria watershed, while the Mediterranean Sea was represented by Dair Balout watershed. Remote sensing data (DEM) was used to conduct the study. ArcGIS 10.8 software was used for analyzing and extracting the necessary spatial and attribute data.

Linear, areal, and relief parameters were extracted and analyzed hydrologically. Analysis of these parameters showed that there are significant differences between the western watershed and the eastern counterpart. The western watershed is characterized by relatively gentle and long slopes, with dense vegetation cover and high precipitation. On the other hand, the eastern watershed is characterized by sparse vegetation cover, relatively steep and short slopes, with low precipitation. The findings demonstrate that both watersheds are vulnerable to more soil erosion and floods.

The findings suggest that the urgent need for decision makers to take actions and measures to reduce the risks of soil erosion and rain floods in both watersheds. In order to do so political intervention between the Palestinians and Israelis must be pushed forward to end Israeli occupation of the West Bank and Gaza Strip.

References

Abbas M et al (2013) Water quality in the Gaza Strip: the present scenario. J Water Resour Prot 5(01):54–63

Al-Saady YI, Al-Suhail QA, Al-Tawash BS, Othman AA (2016) Drainage network extraction and morphometric analysis using remote sensing and GIS mapping techniques (Lesser Zab River Basin, Iraq and Iran). Environ Earth Sci 75:1243

Alyaqoubi A, Abdelghafoor D (2011) Brief on water resources in Palestine. The Palestinian Water Authority, Ralallah, Palestine

Applied Research Institute_Jerusalem (1996) The water conflicts in the Middle East from a Palestinian perspective. Bethlehem, West Bank, Palestine

Asmar NF, Sim JOL, Ghodieh A, Fauzi R (2020) Geospatial analysis of the hydrological characteristics of Nablus Mountain watersheds in Palestine. Malays J Trop Geogr 46(1 and 2)

Banerjee A, Singh P, Pratap K (2017) Morphometric evaluation of Swarnrekha watershed, Madhya Pradesh, India: an integrated GIS-based approach. Appl Water Sci 7:1807–1815

ESRI (2021) ArcGIS desktop help 10.3 flow accumulation

Ezeh CU, Mozie AT (2019) Morphometric analysis of the Idemili Basin using geospatial techniques. Arab J Geosci 12:208

Ezlashi AC (1999) An appraisal of the existing descriptive measures of river channel patterns. J Environ Sci 3(2):253–257

Faniran A (1968) The index of drainage intensity—a provisional new drainage factor. Aust J Sci 31:328–330
Farhan Y (2017) Morphometric assessment of wadi wala watershed, southern Jordan using ASTER (DEM) and GIS. J Geogr Inf Syst 9:158
Ghodieh A (2020) Urban built-up area estimation and change detection of the occupied West Bank, Palestine, using multi-temporal aerial photographs and satellite images. J Indian Soc Remote Sens 48:235–247. https://doi.org/10.1007/s12524-019-01073-8
Hamada S, Ghodieh A (2021) Mapping of solar energy potential in the West Bank, Palestine using geographic information systems. Pap Appl Geogr. 10.1080/23754931.2020.1870540
Horton RE (1932) Drainage-basin characteristics. Eos, Trans Am Geophys Union 13:350–361
Horton RE (1945) Erosional development of stream and their drainage basins; hydrological approach to quantitative morphology. Geol Soc Am Bull 56(3):275–370
http://www.pmd.ps/loadNewsEng.do?pSecId=6
https://en.wikipedia.org/wiki/File:West_Bank_and_Gaza_Strip_location_map.svg
https://www.gov.il/BlobFolder/reports/water-authority-data-english/he/21-Water-Issues-between-Israel-and-Palestinians-Main-Facts.pdf
https://www.weather-atlas.com/en/west-bank/gaza-climate#temperature
Israel Water Authority (2012) The water issues between Israel and the Palestinians
Jafarzadegan K, Merwade V (2017) A DEM-based approach for large-scale floodplain mapping in ungauged watersheds. J Hydrol 550:650–662
Kant S, Meshram S, Dohare R, Singh S (2015) Morphometric analysis of Sonar sub-basin using SRTM data and geographical information system (GIS). Afr J Agric Res 10:1401–1406
Kersel MM (2015) Fractured overnight: the ABCs of cultural heritage in Palestine after the Oslo Accords. J Soc Archaeol 15(1):24–44
Liu X, Zhang Z (2010) Extracting drainage network from high resolution DEM in Toowoomba, Queensland. In: SSSI Queensland 2010 conference, 1–3 Sept
Miller VC (1953) Quantitative geomorphic study of drainage basin characteristics in the Clinch Mountain area, Virginia and Tennessee. Technical report no 3, Department of Geology, Columbia University
Morisawa M (1985) Rivers: form and process. Geomorphology texts
Omolabi PO, Fagbohun BJ (2019) Mapping suitable sites for water storage structure in the Sokoto-Rima Basin of Northwest Nigeria. Remote Sens Appl: Soc Environ 13:12–30
Palestine Water Authority (2013) Status report of water resources in the occupied state of Palestine. Ramallah, Palestine. http://www.pwa.ps/page.aspx?id=ydn3Y0a2545939275aydn3Y0
Palestinian Water Authority (2011) Brief about water resources in Palestine. Ramallah, West Bank, Palestine
Pareta K, Pareta U (2012) Quantitative geomorphological analysis of a watershed of Ravi River Basin, HP India. Int J Remote Sens GIS 1:41–56
Radwan F, Alazba A, Mossad A (2017) Watershed morphometric analysis of Wadi Baish Dam catchment area using integrated GIS-based approach. Arab J Geosci 10:256
Rai PK, Mohan K, Mishra S, Ahmad A, Mishra VN (2017) A GIS-based approach in drainage morphometric analysis of Kanhar River Basin, India. Appl Water Sci 7:1–16
Rather MA, Satish Kumar J, Farooq M, Rashid H (2017) Assessing the influence of watershed characteristics on soil erosion susceptibility of Jhelum basin in Kashmir Himalayas. Arab J Geosciences 10(3):1–25
Schumm SA (1956) Evolution of drainage systems and slopes in badlands at Perth Amboy, New Jersey. Geol Soc Am Bull 67:597–646
Schumm SA (1963) Sinuosity of alluvial rivers on the Great Plains. Geol Soc Am Bull 74:1089–1100
Selvan MT, Ahmad S, Rashid S (2011) Analysis of the geomorphometric parameters in high altitude glacierised terrain using SRTM DEM data in Central Himalaya, India. ARPN J Sci Technol 1:22–27
Singh S, Dubey A (1994) Geoenvironmental planning of watersheds in Indian. Chugh Publications, Allahabad, pp 28–69

Strahler AN (1952) Hypsometric (area-altitude) analysis of erosional topography. Geol Soc Am Bull 63(11):1117–1142
Strahler AN (1957) Quantitative analysis of watershed geomorphology. Eos, Trans Am Geophys Union 38:913–920
Strahler AN (1964) Quantitative geomorphology of drainage basin and channel networks. In: Handbook of applied hydrology
Wani MB, Ali SA, Ali U (2018) Flood assessment of Lolab valley from watershed characterization using remote sensing and GIS techniques. In: Hydrologic modeling. Springer, pp 367–390
www.QSSC.com.AU

Landsat Satellite Images for Lineaments Detection: A Tool to Identify Groundwater Productivity in Lebanon

Amin Shaban and Farouk El-Baz

1 Introduction

The number of water wells in Lebanon has lately been exacerbated, and they are found to be dug in different regions in Lebanon with the largest number located in the coastal zone where more than 70% of people live. In addition, there are also large number of well dug in the agricultural areas such as in the Bekaa Plain. Thus, most of these wells are private and they can be as much as 20 times the number of public ones (Shaban 2020). This in turn results unfavourable status on groundwater reservoirs that is represented by abrupt depletion in water table and decreases in the discharge rate. This has been also affected the discharge from the surrounding springs as well as the intrusion of seawater into the coastal aquifers.

There are numerous illegal boreholes (i.e. the largest number of private wells) which have been dramatically increased in the last few years, in spite of the adopted regulations by the Ministry of Energy and Water (MoEW) in Lebanon. In this regards, the density of boreholes in the suburbs of the capital Beirut has been increased from 500 to 1450 wells/km^2. While, for example water wells dug in Hermel Region (a rural area in Northern of the Bekkaa Plain) was increased from 8000 to 27,000 wells over the last three decades (i.e. an estimated density of 200 wells/km^2). In this regards, it was estimated that in Lebanon the number of illegal (private) wells is 25 times equals wells dug by the formal water sector (Shaban 2020).

There is chaotic pumping of groundwater in Lebanon. The total groundwater abstraction from wells was estimated at 0.70 billion m^3 per year if considering the normal climatic conditions, while a yearly deficit of 0.2 billion m^3 in groundwater

A. Shaban (✉)
National Council for Scientific Research-Lebanon, CNRS-L, P.O. Box 11-8281, Beirut, Lebanon
e-mail: geoamin@gmail.com

F. El-Baz
Center for Remote Sensing, Boston University, 685 Commonwealth Ave, Boston, MA, USA
e-mail: farouk@bu.edu

A. Shaban (ed.), *Satellite Monitoring of Water Resources in the Middle East*,
Springer Water, https://doi.org/10.1007/978-3-031-15549-9_15

has been estimated (IWMI and USAID 2017). While, MoEW and UNDP (2014) put higher estimation of groundwater volume where it was approximately 3.57 billion m^3 in a dry year and 6.1 billion m^3 in a wet year (averaging 4.84 billion m^3). Besides, FAO (2008) illustrated that groundwater recharge in Lebanon is estimated at 3.2 billion m^3.

The selection of wells' location in Lebanon is almost controlled by land ownership and the relevant activities where groundwater is demanded. Nevertheless, not all dug wells produce water and empty boreholes are often resulted. In this regard, hydrogeologists in Lebanon depend mainly on fracture systems to select the most suitable locations for groundwater storage. This is because the hydro-structure of Lebanon is a major groundwater-storage control notably that this hydrologic element is usually accompanied with large karstic voids (e.g. galleries, conduits, cavities, etc.). Based on this hydrogeologic concept; however, the relationship between fracture systems and the successful selection of water wells must be determined, and if it reveals any interlinkage; therefore, it can be adopted as a rule to be followed in groundwater exploration.

In this respect, the development of space techniques, with a special emphasis to satellite remote sensing, allows detecting hidden geological features that might assist in identifying the hydrogeological processes including water flow and storage. In particular, the geologic linear features on terrain surface are often considered, and they called "lineaments". These linear features, as observed on satellite images, are extracted by numerous digital processes on the satellite images by following a number of processing techniques. These geologic features draw the attention of hydrogeologists who believe them reliable indicators of geologic structure.

This study aims at identifying the relationship between these geologic features, which are characterized by linear alignments, and the potentiality of successful water wells in Lebanon. In other words, this study investigates the relationship between the existence of lineaments and the productivity of water wells.

2 Lineaments

The tectonic setting of Lebanon is characterized by active tectonic movements, and it is well defined by its numerous rock deformations and folding systems as a result of its position along the Red Sea Rift System which spans through Lebanon along the Yammounah Fault (i.e. regional fault alignment). This tectonic setting produced a number of secondary rock deformations that are represented mainly by faults and other aspects of fracture systems. This is well pronounced by the geologic maps of Lebanon (Dubertret 1953).

Nevertheless, field surveys showed that there are number of major fault systems that are not clear on these maps which have been produced from black and white aerial photographs since early 1950s. Therefore, the development of advanced space techniques, certainly satellite images and the processing software, enabled detecting

a number of hidden rock structures including faults, which appear on these images with also linear traces.

The relationship between geologic linear features observed on satellite images and rock deformations has been investigated by many studies (Mohammad et al. 1999; Degnan and Clark 2002; Al Saud 2008). These studies proved that these features have significant hydrogeological relationship with fractures systems and other types of rock deformations, notably they play a major role in groundwater recharge (Shaban et al. 2005; Al Saud 2010).

There are many researchers presumed that lineaments, as fracture traces, represent vertical zones of fracture concentration. For example, Berger (1984) suggested that lineaments may be related to the subsurface manifestation of buried structures. Nonetheless, Waters et al. (1990) considered that lineaments must not be a reflection of any subsurface structures. However, field verification of linear features confirmed their genetic relation with fracture systems (Shaban et al. 2005).

The role of linear features has been recognized in many hydrogeological studies, notably in areas where fracture systems are well developed (Ahmed et al. 1984; Edet et al. 1998; Gustafsson 1994; Shaban et al. 2005; Masoud and Koike 2006; Al Saud 2010) where Lebanon is a typical example. The identification of fracture systems sometimes difficult to be conducted directly in the field, especially where remote areas are required to be investigated as well as in the flat areas that are covered by sediments. Therefore, satellite images are useful in this regard. However, it is always a matter of question the relationship between the location of identified lineaments and groundwater flow/storage. It is also unclear what type of relationship between them must be considered. In other word, what is the most reliable criteria (e.g. length of lineament, number of lineaments, etc.) that must be accounted for groundwater exploration?

In order to answer these questions, the objective of this study, the identification of lineaments should be primarily determined, and then mapped lineaments can be used to investigate the relationship with the existing water wells. This would facilitate and support groundwater exploration in an area like Lebanon.

O'Leary et al. (1976) defined a "lineament" as a mappable, simple or composite linear feature of a surface, whose parts are aligned in a rectilinear or slightly curvilinear relationship. While, Woodruff et al. (1982) considered lineaments as a figure which is (1) perceived in an image of a solid planetary body, (2) linear and continuous, (3) characterized by definable end points and lateral boundaries, (4) with relatively high length-to-width ratio, and (5) shown or presumed to be correlative related to stratigraphy or geologic structure.

Whereas, a false lineaments could be cultural manifestations that do not coincide with linear topography, such as roads, fences, pipelines, railroads, and animal trails, etc. Lineaments are ambiguous because they cannot always be field-verified, nor are they precisely reproducible (Garza and Slade 1986). According to Shaban (2003), a lineament also could be (1) almost straight stream and valley segments, (2) aligned surface sags and depressions, (3) soil tonal changes due to variations in soil moisture, (4) agricultural lands' boundary, and (5) abrupt topographic changes. However, all these terrain features might result from geologic structures such as faults.

3 Groundwater and Fracture Systems

Yet, the relationship between the occurrence of groundwater in wells and fracture systems is still a matter of discussion. This has been investigated for the carbonate rock aquifers as well as in the basalt aquifers where lineaments are underlain by zones of localized weathering and increased permeability and porosity. A good example has been illustrated by Rauch and LaRiccia (1978) who investigated a limestone aquifer in Frederick Valley, Maryland, and then they came up with the fact that lineaments are usually associated with higher transmissivity rate, and thus with greater water-well productivities. There are similar works made on following this assumption (El-Shazly et al. 1983; Buckly and Zeil 1984; Teeuw 1995; Travaglia and Ammar 2000; Shaban et al. 2007). Thus, a noticeable relationship has been found between lineaments' location and highly productive water wells. Nevertheless, sometimes erroneous results exist and the identified lineaments found in poorly relationship with the productivity of water wells. This can be attributed to the incorrect identification of lineaments or the failure of the applied methods.

An example of the erroneous selection of water well sites in shown in Fig. 1, where a terrain surface with lineaments (fractured terrain) does not show positive results. Thus, well no. 2 is located on a fractured zone, but drilling for water in this zone is not favourable, because of the groundwater flow is controlled by the inclination of rock layers. While, drilling wells (i.e., wells no. 1 and 3) in low fractured zones might find groundwater storage.

Other than lineaments, there are many factors were added to support the positioning of successful groundwater wells (e.g. El-Shazly et al. 1983; El-Baz and Himida 1995; Per Sandra et al. 1996; Das 2000; Al Saud 2010). These factors can be the: lithology, drainage, soil type, topography, etc.

4 Tools of Analysis

In order to adopt a creditable methodology used for groundwater exploration from the point of view between lineament characteristics and water productivity in wells, four major steps are considered in this study. These are:

1. Mapping sets of dug water wells with different product levels (including mainly the discharge).
2. Using satellite images to detect lineaments where these lineaments are plotted on a map.
3. Analyzing the dimensional characteristics (e.g. lineaments density, etc.) of the detected lineaments.
4. Elaborate an empirical comparison approach to appraise the relation between wells' productivity and lineament location and their lineament dimensional characteristics.

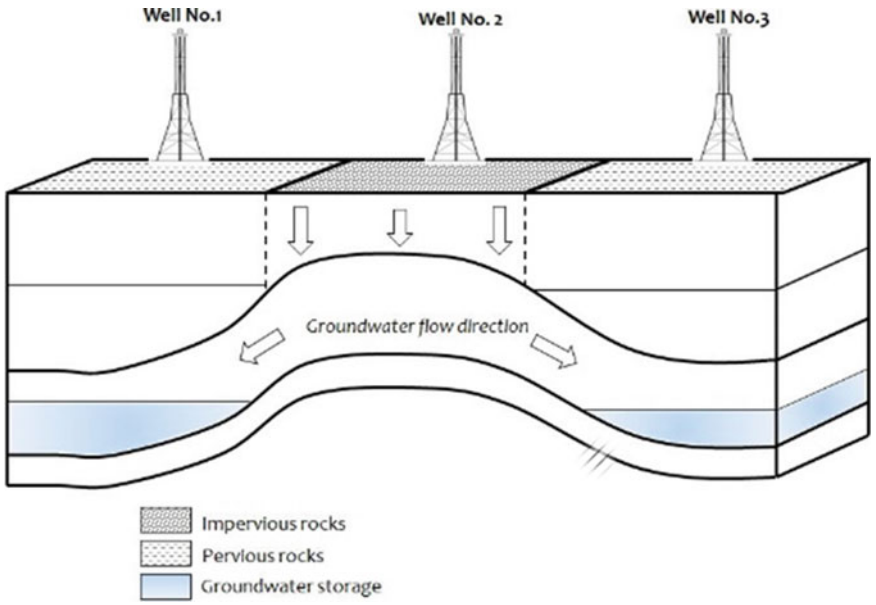

Fig. 1 Example showing the erroneous positioning of water well depending only on the location of lineaments (i.e. fractured zone) regardless of rocks inclination (Shaban et al. 2007)

Four zones were selected from Lebanon for the comparison between lineaments and groundwater productivity (Fig. 2). This was based on data availability from well which are dug in the carbonate rocks. The selected zones comprise different lithological and physiographic characteristics, and they constitute a surface area of about 1600 km^2 (i.e., 15% of Lebanon's area).

4.1 Water Wells Productivity

The majority of aquiferous rock formations in Lebanon is attributed to their secondary porosity (i.e. fractures and joints). This is the case for the carbonate rocks where the thick and widespread sequences of fractured and karistified limestone and dolomite exist. In Lebanon, there are four major aquifers and six semi-aquifers that intervene with a miscellany of Aquiclude and Aquitard rock formations. Thus, the classification of aquiferous rocks properties (from bottom to top) can be summarized in Table 1.

The main aquiferous formations are attributed to (from bottom to top) the: Callovian (dolomite limestone), Kimmeridjian (dolomite and dolomitic limestone), Neocomian-Barremian (sandstone and argillaceous materials), Upper Aptian (dolomite), Cenomanian (dolomitic limestone), Eocene (chalky limestone) and Neogene (conglomeritic limestone).

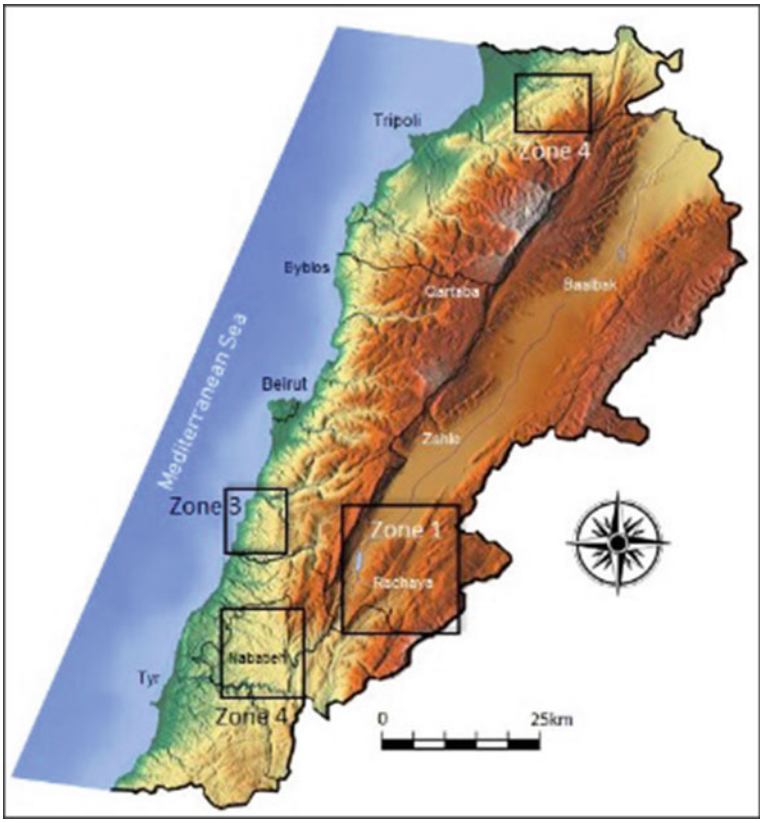

Fig. 2 Studied areas from Lebanon to investigate the relationship between lineaments and groundwater productivity (Shaban 2020)

However, these aquifers have different discharge, depth and discharge. While, the main aquifers in Lebanon are attributed to the Kimmeridjian, Cenomanian and Eocene rocks. According to Shaban (2020), groundwater level and discharge are controlled by the following factors:

1. Positioning of aquiferous rock units within the same rock formations (e.g. upper, middle, etc.),
2. Existing geologic structures (e.g. faults, anticline, etc.),
3. Permeability and porosity of the existing rock masses and the interbedding aspects of these rocks,
4. Altitude and the accompanied geomorphological features,
5. Water feeding rate including precipitation and other water sources located in the proximity,
6. Pumping rate regime of groundwater abstraction.

Table 1 Aquiferous rock formations in Lebanon

Period	Rock formation	Lithological characteristics	Aquiferous property	Thickness (m)
Quaternary	Holocene	Alluviums and mixture of marine deposits and river terraces	Semi-aquifer	Variable
	Pleistocene	Alluvial, colluvial and thick soil deposits mixed with conglomerates		
Neogene	Pliocene	Marly limestone, and basalt with tuffs. Joints are tremendous, notably in marly units	Aquitard	360
	Vindobanian	Conglomeratic limestone, and massive marly limestone and sometime with siltstone	Aquifer	320
	Burdigalian	Marly limestone and marl, sometimes exist as variable facies	Aquiclude	80
Paleogene	Lutetian	Limestone, chalky and marly limestone. Karistified and fractured	Aquifer	800
	Ypresian	Chalky limestone, marly limestone	Aquiclude	370
Cretaceous	Senonian	Marl and marly limestone with joints	Aquiclude	400
	Turonian	Marly limestone and marl. Joints are predominant	Aquitard	200
	Cenomanian	Limestone, dolomitic limestone and marl. Highly karistified and fractured	Excellent aquifer	700

(continued)

Table 1 (continued)

Period	Rock formation	Lithological characteristics	Aquiferous property	Thickness (m)
	Albian	Marly limestone, marl and compacted shale	Aquiclude	200
	Upper Aptian	Dolomite and dolomitic limestone. Highly jointed and fractured	Aquifer	50
	Lower Aptian	Argillaceous sandstone, marl, limestone and clastic limestone	Aquitard	250
	Neocomian-Barremian	Quartzite sandstone, mixed with clayey and argillaceous materials. Highly jointed and sometimes variable and loose	Semi-aquifer	Variable
Jurassic	Portlandian	Oolitic limestone, with marly limestone	Aquitard	180
	Kimmeridjian	Dolomite, dolomitic limestone and limestone. Well karistified and fractured	Excellent aquifer	200
	Oxfordian	Mixed volcanics and tuff with marly limestone	Aquiclude	Variable
	Callovian	Dolomitic limestone and limestone. Karistified rocks	Aquifer	Undefined

Among the selected zones of study, field survey was carried out to determine the productivity (discharge) from water wells, well location and aquifer type. This conducted survey included 90 water wells were dug in different lithologies and regions. The investigated well are distributed as:

- 60.0% Cenomanian
- 15.5% Quaternary
- 8.8% Jurassic (Kimmeridjian)
- 6.6% Eocene

– 3.3% Upper Aptian
– 3.3% tuffaceous rocks
– 2.2% Lower Aptian.

4.2 Extraction of Lineaments from Satellite Images

There are numerous types of satellite images which enable detecting lineaments on terrain surface. However, some of them have advantages than others depending on the band characteristics of these images. In this study, Landsat 7 ETM$^+$ satellite images, with 30 m spatial resolution, were processed using ERDAS-Imagine software. The selection of these images was dependent, in addition to their availability, on their digital advantages such as: edge detection, color slicing, directional filtering, sharpness and enhancement, etc. These advantage assist in visual and automated detection of lineaments.

For the visual detection, all clear/unsuspicious linear features can be directly traced from the image. While the automated detection was achieved by applying a special feature in the software. In this respect, a number of digital applications were elaborated, with emphasis the illustration of single band and multi-band arrangement of the three bands as one set. Thus, band combination was also followed where it was found that the arrangement of bands 2, 5, and 3 gives most linear features on Landsat 7 ETM$^+$.

The use of thermal differentiation is also one of the most significant tool for lineaments detection. In Landsat 7 ETM$^+$ images, the thermal detection is done on band 6 (i.e. thermal band). Using this band, with 120 m spatial resolution provides useful evidences on wet horizons between rocks' fractures which are often filled with moist soil.

All linear features have been then traced, while the un-sure lineaments where verified through a field survey in order to assure if they are geologic-related linear features or man-made ones. For this purpose, the geologic map of Lebanon (scale 1:50,000; done by Dubertret 1953) were used and faults on these maps were superimposed with the resulted lineaments map. This enables the following:

– All faults on the geological maps were obvious on satellite images, but much more number of faults were also detected from satellite images.
– Uncertain faults on geological maps (traced as dashed lines) were correctly delineated by satellite images processing.
– Small-scale faults, which were not plotted on the geologic maps, were detected by images processing.

Therefore, the lineaments maps was produced (example in Fig. 3), for the selected pilot areas in Lebanon, following the integration of the aforementioned approaches on the ERDAS Imagine software and the supplementary tools (e.g. geologic maps and field surveys).

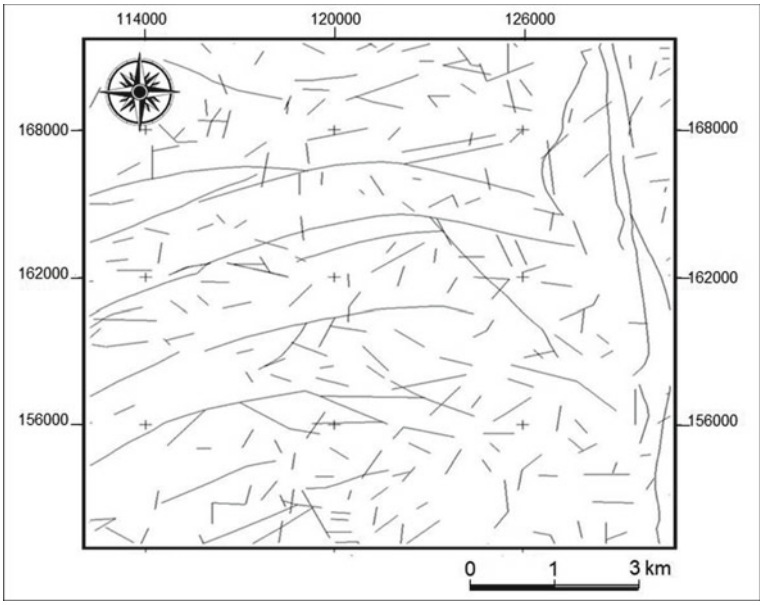

Fig. 3 Example showing a lineament maps as it was produced by the processing of Landsat 7 ETM^{+} images, 2005 (Keserwan area, Lebanon)

4.3 Dimensional Analysis of Lineaments

For the next step of this study, which aims at comparing lineaments alignment and the location of water wells; therefore, dimensional analysis for lineaments was elaborated for all linear features plotted on the produced lineaments map, and this includes their number/or length within a define area, as well as the length of each single lineament. In this regard, there is usually "lineament density" calculated by some researchers (e.g. Teeuw 1995; Edet et al. 1996; Casas et al. 2000), and "lineament frequency" is also calculated by others (e.g. El-Baz and Himida 1995; Shaban 2003; Al Saud 2010; Ekneligoda and Henkel 2010). In addition to these two dimensional aspects of lineaments analysis, length of the recognized lineaments was considered and then named as "fault-lineaments".

1. Lineaments density:

Lineaments density (L_d) represents the sum of total lengths of lineaments within a specific area (Greenbaum 1985). Therefore, it can expressed by the following formula:

$$Ld = \frac{\Sigma \mathrm{L}tl}{\mathrm{A}}$$

where Σ L*tl* is the total length of lineaments, and *A* is the area in km^2. Therefore, the lineaments maps was classified into grids where frames with define areas were resulted, and each frame has an area of 3 km × 3 km (9 km^2). However, the selected area of a frame is dependent on the entire surface area of study and the density of the existing linear features.

When the study area has been classified into define frames; the next step will be the counting of the total length of all linear features in ach frame and the resulted number will be put in the mid-point for each frame. Consequently, having all these values (for the total length of lineaments in each frame), enables applying the "Sliding Windows" method (Shaban 2003). This method can be elaborated by connecting the mid-point between different frames in order to create new frames; and therefore, the average number of the lineaments included into the new frames will be also put in the mid-point (Fig. 4). Therefore, the values of these new points will be used for delineate contour lines in order to end up with a contour line maps showing different lineament density zones (example in Fig. 4).

2. Lineament frequency:

It might be a sort of innovative approach for the lineaments density, lineaments frequency is another way to manipulate the existing linear features into mappable figure. Lineament frequency (L_f) is the visible number of lineaments per unit area (Shaban 2003; Shaban et al. 2007) and it is represented by the following formula:

$$Lf = \frac{\Sigma \mathrm{L}tn}{\mathrm{A}}$$

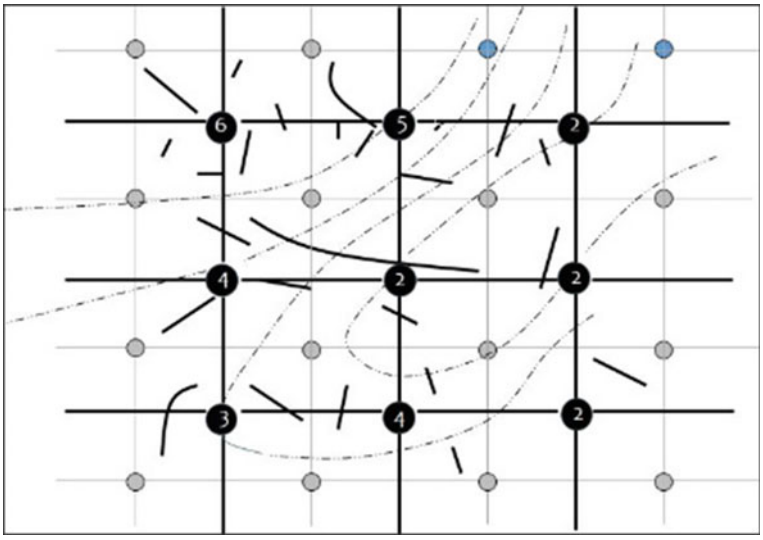

Fig. 4 Example showing the plot of lineaments density into a map using sliding windows method

Table 2 Discrimination between lineaments according to their dimensional properties and their relationship to the hydrogeological processes

Dimensional property	Fault-lineament (*Fl*)	Fracture system
Tonal variation	Sharp shadow and acute tone	No tonal variation can be identified
Length	Long distances (>few kilometers)	Short distances (<few kilometers and almost few hundreds of meters)
Lithological crossing	Can span more than one lithological units	Spans only within one lithological unit
Orientation	Follows in specific orientation and sets (e.g., same direction and parallelism)	Following chaotic orientation (e.g. it can be in different, unspecified directions)
Hydrogeological role	Acts in groundwater flow and storage (vertically and laterally)	Enhanced the vertical surface water flow into substratum (i.e. increases infiltration rate)

where Σ L*tn* is the total number of lineaments within a define area, and *A* is the area in km^2. Therefore, the similar approach for lineaments density (i.e. Sliding Windows) was applied for lineaments frequency contour line map resulted.

3. Fault-lineaments:

As mentioned in the literature of this study, yet there is a contradictory about the dimensional aspects of a lineament. In other words, even though the length of a lineament might be relatively short (i.e. approximately less than few hundreds of meters); however, some researchers considered such a lineament as a fault structure with a role in groundwater flow and storage regime (e.g. Buckly and Zeil 1984; Garza and Slade 1986; Briere and Scanlon 2001). Nevertheless, in the hydrogeological processes, the large-scale lineaments have given much attention, in spite that the smaller one can play a limited role. In this regards, Shaban et al. (2007) discriminated lineaments according to their length; and therefore, the longer lineaments were considered as fault-lineaments which can play a major role in the hydrogeological processes, while shorter ones represent fracture systems with local impact of these processes.

Therefore, the discrimination between lineaments whether as faults or fractures from satellite images was achieved as in Table 2 (Shaban et al. 2007), which show their impact on the hydrogeological processes.

4.4 Lineaments and Groundwater

Depending on the three analyzed dimensional aspects of lineaments (*Ld*, *Lf*, *Fl*), an empirical correlation has been elaborated in order to deduce the relationship between these aspects of lineaments and the productivity of groundwater in the dug

well located in the pilot zones (Fig. 1). Therefore, each of the required components for this correlation (*Ld*, *Lf*, *Fl* and water productivity) was expressed in a separate map. For this purpose, Geographic Information System (GIS) was the main tools for geo-spatial data manipulation and superposition. Thus, the *Arc-Info* software was used.

Examples of the superposition between the dimensional aspects of lineaments and water wells are shown in Fig. 5a–c. In this respects, each of the four components were classified into five classes, and each class expresses a range of values as follows:

1. Lineaments density and frequency were classified into five classes. The intervals between each of the five classes were selected depending on the observed maximum and minimum values of *Ld* and *Lf*. Hence, the intervals of lineaments density ranges between <3 and >12 km per 9 km^2, while the intervals of the lineaments frequency range from <6 to >15 lineaments per 9 km^2 (Fig. 5). These classes were described according to the lineament density or frequency as: very high, high, moderate, low and very low (Table 3).

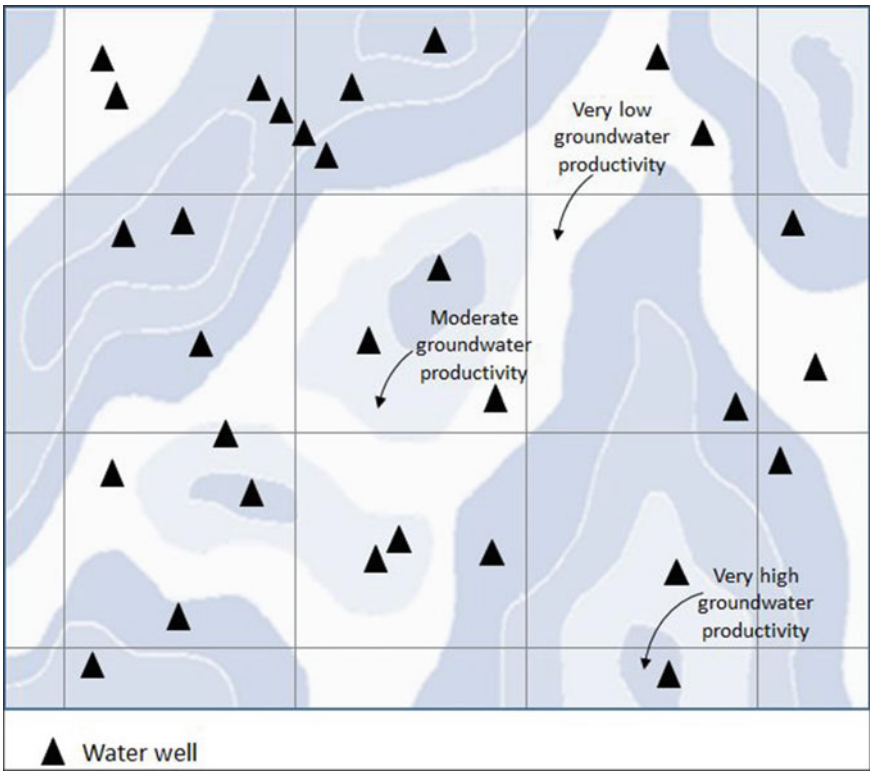

Fig. 5 Examples showing the superposition between the dimensional aspects of lineaments and water wells

Table 3 Lineaments density and frequency categories

Lineament length density (*Ld*) (km/9 km^2)	Lineament frequency density (*Lf*) (Lineaments/9 km^2)	Description
>12	>15	Very high
12–9	15–12	High
9–6	12–9	Moderate
6–3	9–6	Low
<3	<6	Very low

Table 4 Buffer distance between fault-lineaments and of water wells

The buffer distance (m) (*Fl* and wells)	Description
<100	Very close
100–200	Close
200–400	Moderate
400–600	Far
>600	Very far

2. The existence of fault-lineaments (exceeding several kilometers length) was taken into consideration through their proximity to water wells with different productivity (i.e. discharge rate). Therefore, a classification has been adopted considering five buffer distances between fault-lineaments and the location of water wells (Table 4).
3. The productivity of water wells was also classified into five classes, as shown in Table 5. The reported groundwater productivity (i.e. discharge rate) was calculated in all surveyed wells in the identified four zones of lineament, and this might be the most significant criteria to deduce the relationship between lineaments and groundwater.

Table 5 Classification of productivity rate from water wells

Productivity rate (L/s)	Description
≥20	Very high productivity
19–15	High productivity
14–10	Moderately productive
9–5	Low productivity
<5	Very low productivity

5 Results and Conclusion

The inventor of datasets (location, discharge and geologic formation) for the surveyed 90 water wells is listed in Table 6 where these the location of these wells was plotted on a map (in a digital form). Besides these datasets; however, the lineaments characteristics (*Ld*, *Lf* and *Fl*) were also plotted for each well (Table 6).

The obtained and measured datasets were extrapolated by two approaches as follows:

1. Since the lineaments density and frequency (*Ld* and *Lf*) were produced in mappable form with range values; therefore, each of them was manipulated into a matrix that compares between their lineaments and the productivity of the surveyed wells. This followed Congalton (1991) method where different values and descriptions in the matrix is usually applied for evaluate the precision of results.

   Therefore, in the elaborate matrices, water productivity classes were compared with the estimated ranges of lineament density and frequency separately (Tables 7 and 8).

   For lineaments density, Table 7 shows the number of coincided values (in Oblique column with shading) between lineaments density and wells' productivity. The total of coincided for lineaments density (*Tcld*) is 18 out of 90 water wells, therefore, the ratio of reliable measures is:

$$\boldsymbol{Tcld} = \frac{18 \times 100}{90} = 20\%$$

   While for the lineament frequency (Table 8), the total of coincidence (*Tclf*) will be:

$$\boldsymbol{Tclf} = \frac{24 \times 100}{90} = 26.6\%$$

2. For the fault-lineaments, where numerical datasets are available, they were represented graphically according to datasets in Table 6. Hence, Fig. 6 shows the graphic relation between wells' productivity and their proximity to fault-lineaments. Therefore, a proportionality between both variables can be well noticed. It is also clear that most wells, with a distance of less than 350 m from fault-lineaments, are characterized with a water productivity exceeding 15 L/s, while wells located between 350 and 650 m from fault-lineaments have productivity of around 10 L/s.

   In particular, Fig. 6 shows that there is more than 97% of dug wells located at a distance of less than 650 m from fault-lineaments are characterized by considerable productivity (i.e. >10 L/s). Besides, it is obvious that low groundwater productivity exists as the distance from the fault-lineaments increases, regardless to the presence of fracturing system.

Table 6 Datasets on the surveyed wells and their lineaments characteristics

Well no/zone	Rock formation	Discharge (L/s)	Descriptive productivity*	Lineaments properties		
				(*Ld*)	(*Lf*)	(*Fl*)
1*I*	Eocene	15	HP	M	H	210
2*I*	Ditto	21	VHP	M	H	75
3*I*	Ditto	4	VLP	H	H	1350
4*I*	Lower Aptian	15	HP	L	L	250
5*I*	Cenomanian	20	VHP	M	M	50
6*I*	Lower Aptian	4	VLP	M	L	775
7*I*	Jurassic	10	MP	H	M	650
8*I*	Ditto	23	VHP	M	H	150
9*I*	Ditto	21	VHP	H	VH	105
10*I*	Ditto	5	LP	H	M	340
11*I*	Ditto	4	VLP	M	M	850
12*I*	Ditto	20	VHP	H	M	125
13*I*	Ditto	16	HP	M	H	305
14*I*	Upper Aptian	8	LP	L	L	840
15*II*	Cenomanian	12	MP	VL	L	1200
16*II*	Ditto	20	VHP	H	H	50
17*II*	Ditto	11	MP	M	H	100
18*II*	Eocene	0	VLP	VH	H	1500
19*II*	Cenomanian	16	HP	H	M	20
20*II*	Ditto	17	HP	M	H	500
21*II*	Ditto	20	VHP	L	L	50
22*II*	Ditto	18	HP	L	M	70
23*II*	Ditto	22	VHP	H	H	110
24*II*	Ditto	11	MP	L	L	220
25*II*	Ditto	17	HP	M	M	10
26*II*	Eocene	2	VLP	H	M	2500
27*II*	Cenomanian	0	VLP	VL	VL	1200
28*II*	Ditto	12	MP	H	M	650
29*II*	Ditto	16	HP	M	M	20
30*II*	Ditto	9	LP	M	M	1425
31*II*	Ditto	7	LP	M	L	420
32*II*	Ditto	22	VHP	M	M	10
33*II*	Eocene	25	VHP	H	H	15
34*II*	Cenomanian	21	VHP	H	M	5
35*II*	Ditto	20	VHP	M	H	200

(continued)

Table 6 (continued)

Well no/zone	Rock formation	Discharge (L/s)	Descriptive productivity*	Lineaments properties		
				(*Ld*)	(*Lf*)	(*Fl*)
36*II*	Ditto	0	VLP	M	H	1600
37*II*	Ditto	22	VHP	H	M	15
38*III*	Ditto	8	LP	H	M	370
39*III*	Ditto	10	MP	H	L	465
40*III*	Ditto	17	HP	M	L	270
41*III*	Ditto	21	VHP	L	H	130
42*III*	Ditto	10	MP	VL	M	365
43*III*	Ditto	12	MP	L	M	780
44*III*	Ditto	9	LP	L	M	955
45*III*	Ditto	15	HP	H	VH	245
46*III*	Ditto	11	MP	H	M	660
47*III*	Ditto	10	MP	M	L	735
48*III*	Ditto	7	LP	M	L	1835
49*III*	Ditto	5	VLP	L	L	1645
50*III*	Ditto	6	LP	L	L	1210
51*III*	Ditto	6	LP	VL	M	1405
52*III*	Ditto	6	LP	H	L	1350
53*III*	Ditto	12	MP	M	L	620
54*III*	Ditto	10	MP	L	VL	410
55*III*	Ditto	6	LP	L	VL	525
56*III*	Ditto	7	LP	M	H	565
57*III*	Ditto	6	LP	M	M	505
58*III*	Ditto	10	MP	H	M	515
59*III*	Quaternary	11	MP	VH	H	550
60*III*	Cenomanian	10	MP	VH	VH	405
61*III*	Quaternary	6	LP	M	L	175
62*III*	Ditto	5	VLP	L	H	1815
63*III*	Ditto	7	LP	M	H	2075
64*III*	Cenomanian	11	MP	H	VH	215
65*III*	Ditto	15	HP	M	H	135
66*III*	Ditto	16	HP	L	M	140
67*III*	Ditto	15	HP	VL	L	50
68*IV*	Ditto	20	VHP	H	VH	80
69*IV*	Ditto	35	VHP	M	M	20

(continued)

Table 6 (continued)

Well no/zone	Rock formation	Discharge (L/s)	Descriptive productivity*	Lineaments properties		
				(*Ld*)	(*Lf*)	(*Fl*)
70*IV*	Ditto	35	VHP	H	L	10
71*IV*	Ditto	22	VHP	M	L	55
72*IV*	Ditto	16	HP	L	VL	95
73*IV*	Ditto	10	MP	M	M	305
74*IV*	Ditto	16	HP	H	M	225
75*IV*	Tuff	17	HP	M	H	125
76*IV*	Ditto	11	MP	H	H	195
77*IV*	Ditto	12	MP	L	H	385
78*IV*	Upper Aptian	12	MP	L	M	360
79*IV*	Ditto	12	MP	L	L	275
80*IV*	Jurassic	15	HP	VL	L	200
81*IV*	Quaternary	0.5	VLP	VL	L	1655
82*IV*	Ditto	0.5	VLP	L	VL	1675
83*IV*	Ditto	0.5	VLP	M	VL	990
84*IV*	Ditto	0.5	VLP	M	L	1098
85*IV*	Ditto	1	VLP	M	M	1955
86*IV*	Ditto	0.5	VLP	H	M	1123
87*IV*	Ditto	0.5	VLP	H	H	1345
88*IV*	Ditto	0	VLP	L	M	2790
89*IV*	Ditto	0.25	VLP	VL	L	1825
90*IV*	Ditto	0.25	VLP	VL	M	1635

*VHP = very high productivity; HP = high productivity; MP = moderately productive; LP = low productivity; VLP = very low productivity

Table 7 The total coincidence between wells' productivity and lineaments density

	Qualitative estimates of lineaments density						
Qualitative estimates of wells' productivity	Category	Very high	High	Moderate	Low	Very low	Total
	Very high	1	9	6	2	0	18
	High	1	3	8	4	1	17
	Moderate	2	8	5	8	2	25
	Low	0	3	6	4	0	13
	Very low	1	3	6	2	5	17
	Total	5	26	31	20	8	18

Table 8 The total coincidence between wells' productivity and lineaments frequency

	Qualitative estimates of lineaments frequency						
Qualitative estimates of wells' productivity	Category	Very high	High	Moderate	Low	Very low	Total
	Very high	2	7	5	4	0	18
	High	1	5	7	4	1	18
	Moderate	2	4	10	8	1	25
	Low	0	4	4	4	1	13
	Very low	0	3	6	4	3	16
	Total	5	23	32	24	6	24

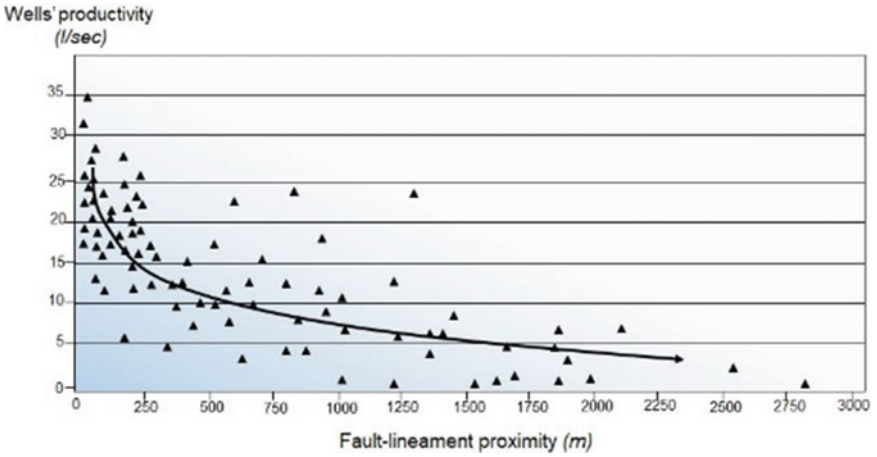

Fig. 6 The relationship between fault-lineaments proximity and groundwater productivity in wells (adapted after Shaban et al. 2007; Shaban 2020)

In conclusion, lineaments correspond to faults have hydrogeological influence, whereas those attributed to fracture systems play a role only in water infiltration into rock stratum (Shaban et al. 2007). This can be attributed to the fact that faults act as groundwater-transmission routes, hydraulic barrier or as groundwater storage zones (Shaban 2020). While fracture systems mainly serve in enhancing the groundwater recharging rates, and this would be a prerequisite in groundwater exploration (Shaban et al. 2005).

The resulted relationship between fault-lineaments and groundwater productivity can be adopted while positioning the suitable locations for water wells in Lebanon. Of course, this needs to consider other hydrogeological parameters with a special focus on the lithological characteristics. In addition, the significance of satellite remote sensing (e.g. Landsat 7 ETM$^+$) is well pronounced in this study where from several hydrogeological elements can be recognized to assist in the issue of groundwater delineation and storage.

References

Ahmed F, Andrawis A, Hagaz Y (1984) Landsat model for groundwater exploration in the Nuba Mountains, Sudan. Adv Space Res 4(11):123–131

Al Saud M (2008) Using ASTER images to analyze geologic linear features in Wadi Aurnah Basin, Western Saudis Arabia. Open Remote Sens J 1:7–16

Al Saud M (2010) Mapping potential areas for groundwater storage in Wadi Aurnah Basin, western Arabian Peninsula, using remote sensing and geographic information system techniques. Hydrogeol J 18:1481–1495

Berger Z (1984) Structural analysis of low-relief basins. In: Proceedings of the international symposium on remote sensing of environment. 3rd thematic conference remote sensing for geology, vol 1, pp 251–271

Briere P, Scanlon K (2001) Lineaments and lithology derived from a side-looking airborne radar image of Puerto Rico. http://pubs.usgs.gov/of/of00-006/htm/lineamen.htm

Buckly D, Zeil P (1984) Fractured rock aquifers in eastern Botswana. Challenges in African hydrology and water resources. In: Proceedings of Harare symposium, July 1984. IAHS Pub. No. 144, pp 26–33

Casas A, Cortés A, Maestro A, Soriano M, Riaguas A, Bernal J (2000) LINDENS: a program for lineament length and density analysis. Comput Geosci 26(9):1011–1022

Congalton RG (1991) A review of assessing the accuracy of classifications of remotely sensed data. Remote Sens Environ 37:35–46

Das D (2000) GIS application in hydrogeological studies. www.gisdevelopment.net

Degnan P, Clark H (2002) Fractured-correlated lineaments at Great Bay, Southeastern New Hampshire. Open-file report 02-13. http://water.usgs.gov/pubs/of/ofr02-013/html/fractured.html

Dubertret L (1953) Carte géologique de la Syrie et du Liban au 1/50000me. 21 feuilles avec notices explicatrices. Ministère des Travaux Publics. L'imprimerie Catholique, p 66

Edet AE, Okereke CS, Teme SC, Esu EO (1996) Application of remote sensing data to groundwater exploration: a case study of the Cross River State, southeastern Nigeria. Hydrogeol J 6(3):394–404

Edet A, Okereke CS, Teme S, Esu E (1998) Application of remote sensing data to groundwater exploration: a case study of the Cross River State, southeastern Nigeria. Hydrogeol J 6(3):394–404

Ekneligoda T, Henkel H (2010) Interactive spatial analysis of lineaments. J Comput Geosci 36(8):1081–1090

El-Baz F, Himida I (1995) Groundwater potential of the Sinai Peninsula, Egypt. Project summary. AID, Cairo, p 18

El-Shazly EM, El Raikaiby NM, El Kassas IA (1983) Groundwater investigation of Wadi Araba area, Eastern Desert of Egypt, using Landsat imagery. In: Proceedings of 17th symposium on remote sensing of the environment, Ann Arbor, Michigan, 9–13 May 1983, pp 1003–1113

FAO (2008) Information system on water and agriculture—Aquastat Lebanon. http://www.fao.org/nr/water/aquastat/countries/lebanon/index.stm

Garza L, Slade R (1986) Relations between areas of high transmissivity and lineaments: the Edwards aquifer, Barto springs segment, Travis and Hays counties. http://www.lib.utexas.edu/geo/BalconesEscarpment/BalconesEscarpment.html

Greenbaum D (1985) Review of remote sensing applications to groundwater exploration in basement and regolith. Br Geol Surv Rep. OD 85(8):36

Gustafsson P (1994) SPOT satellite data for exploration of fractured aquifers in a semi-arid area in Botswana. Hydrogeol J 2(2):9–18

IWMI and USAID (2017) Groundwater governance in Lebanon: the case of Central Beqaa. Groundwater governance in the Arab World. A policy white paper, p 36

Masoud A, Koike K (2006) Tectonic architecture through Landsat-7 ETM+/SRTM DEM-derived lineaments and relationship to the hydrgeologic setting in Siwa region, NW Egypt. J Afr Earth Sci 45:467–477

MoEW and UNDP (2014) Assessment of groundwater resources of Lebanon, p 88

Mohammad M, Sediek K, El-Sobky, El-Raey M (1999) Structural analysis and groundwater potentialities use and field investigation, case study: Siwa region, western Egypt. In: 2nd international symposium on RS, 16–20 Aug 1999

O'Leary DW, Friedman JD, Poh HA (1976) Lineaments, linear, lineation: some standards for old terms. Geol Soc Am Bull 87:1463–1469

Rauch H, LaRiccia M (1978) Water well productivity related to lineaments in carbonates and shale of Hagerstown Valley, Maryland. In: ESO (Am. Geophys. Union Trans.). Annual meeting, Miami Beach, Fla., 17–21 Apr 1978, p 59

Sandra P, Chesley M, Minor T (1996) Groundwater assessment using remote sensing and GIS in a rural groundwater project in Ghana: lessons learned. Hydrogeol J 4(3):78–93

Shaban A (2003) Etude de l'hydroélogie au Liban Occidental: Utilisation de la télédétection. PhD dissertation, Bordeaux 1 Université, p 202

Shaban A (2020) Water resources of Lebanon. Springer Science Publisher, Switzerland, p 229. https://doi.org/10.1007/978-3-030-48717-1

Shaban A, El-Baz F, Khawlie M (2007) The relation between water-wells productivity and lineaments morphometry: selected zones from Lebanon. Nord Hydrol 38(2):178–201

Shaban A, Khawlie M, Abdallah C (2005) Use of remote sensing and GIS to determine recharge potential zones: the case of occidental Lebanon. Hydrogeol J (Accepted)

Teeuw RM (1995) Groundwater exploration using remote sensing and a low-cost geographic information system. Hydrogeol J 3(3):21–30

Travaglia C, Ammar O (2000) Groundwater exploration by satellite remote sensing in the Syrain Arab Republic. Technical report FAO.TCP/SYR/6611, p 33

Waters P, Greenbaum D, Smart P, Osmaston H (1990) Application of remote sensing to groundwater hydrology. Remote Sens Rev 4(2):223–264

Woodruff K, Talley J, Miller J (1982) Selection of sites for high-productivity well. In: Abstracts with programs. N.E. Geol. Soc. Amer., Baltimore, Maryland, USA, pp 87–88

Using Information from Remote Sensing to Estimate Groundwater: GRACE and Sentinel-1 Satellites

Elias Massoud, Amin Shaban, Zhen Liu, and Mhamad El Hage

1 Introduction

1.1 Background

During the past few decades, the demanding needs for freshwater resources in various locations of the globe have exceeded the supply that is renewed naturally, and this has impacted agricultural industries, urban areas, and the environment (McCallum et al. 2013; Huang et al. 2016; Molle et al. 2017). This is especially the case for semi-arid regions such as the Beqaa Plain in Lebanon. Until now, there has been a large gap between water supplies that are available on the surface and water demands that are growing annually, and this has caused immense stress on freshwater systems around the globe.

E. Massoud (✉) · Z. Liu
NASA Jet Propulsion Laboratory, California Institute of Technology, 4800 Oak Grove Dr, Pasadena, CA 91109, USA
e-mail: massoudec@ornl.gov

Z. Liu
e-mail: zhen.liu@jpl.nasa.gov

E. Massoud
University of California, Berkeley. 130 Hilgard Way, Berkeley, CA 94720, USA

Oak Ridge National Laboratory, 1 Bethel Valley Rd, Oak Ridge, TN 37830, USA

A. Shaban
National Council for Scientific Research-Lebanon (CNRS-L), Beirut, Lebanon
e-mail: geoamin@gmail.com

M. E. Hage
Geospatial Studies Laboratory, Lebanese University, Tripoli CVP3+9GW, Lebanon
e-mail: mhamad.elhage@ul.edu.lb

A. Shaban (ed.), *Satellite Monitoring of Water Resources in the Middle East*,
Springer Water, https://doi.org/10.1007/978-3-031-15549-9_16

To fulfill the gap in demand for freshwater, a large dependence on groundwater, a convenient fossil resource stored in shallow aquifers below the ground, has occurred in various regions of the world. This is unsustainable, because groundwater recharge that replenishes the system is a slow process compared to the increasing rates of groundwater pumping. This has created a loss rate that is greater than the replenishing rate of groundwater, resulting in depletion of subsurface aquifers around the world (Woodhouse et al. 2010; Famiglietti et al. 2011; Famiglietti 2014; Massoud et al. 2021).

Changing climates are further exacerbating this problem. With precipitation becoming more variable and droughts more frequent, groundwater pumping is becoming an increasingly relied upon resource, and the recharge needed to replenish the system is becoming more inadequate. Additionally, other variables in the hydrologic cycle are also impacted by a changing climate, such as soil moisture or snowpacks, which are affected by increasing temperatures and precipitation variability (Massoud et al. 2019, 2020a; Wootten et al. 2020). The effects of unsustainable use of groundwater resources and resultant groundwater depletion have been observed through satellite measurements and/or model simulations in many systems of the world (Famiglietti 2014; Massoud et al. 2018, 2020b; Liu et al. 2019), but consistent monitoring of groundwater is still lacking.

1.2 Measuring Groundwater

Despite the critical need for freshwater supplies, the monitoring of water resource availability has often been inadequate. For instance, networks for monitoring groundwater are not set up at the broad scale of surface water observations (Scanlon et al. 2012). Typically, groundwater data is collected at in-situ wells, yet these observations are expensive, spatially and temporally sparse, discontinuous, and often difficult to obtain.

To deal with these issues, methods for interpolating model simulations of the hydrologic cycle are now used to calculate availability of fresh water sources (Harbaugh et al. 2000; Margulis et al. 2016). Although hydrologic and land surface models can estimate the availability of water at high resolution, various commonly used models, such as the Global Land Data Assimilation System (GLDAS) (Rodell et al. 2004; Yang et al. 2011), do not include anthropogenic processes like groundwater pumping. Without this proper representation of human interaction within the climate system, simulations can create a significant bias by underestimating groundwater pumping rates and the degree of groundwater depletion in a region (He et al. 2017). Furthermore, information on other hydrologic variables is rarely available, such as accurate information on soil moisture or snow water equivalent.

Even though there are ways to obtain details on these hydrologic variables of interest, for example using remote sensing, field measurements, and the assimilation of data in model simulations (Zaitchik et al. 2008; Xia et al. 2012; Margulis et al. 2016), accurate knowledge on these processes is still not available.

1.3 Loss of Freshwater Storage

Recently around the globe, various productive agricultural regions have seen declines in levels of total water storage. Depletion of groundwater storage in these regions has been suggested to be a major factor contributing to freshwater losses in these regions (Lo and Famiglietti 2013; Massoud et al. 2018). In the Beqaa Plain, Lebanon, a significant percentage of the annual freshwater usage comes from groundwater, and a large part of it is for use in agriculture (Molle et al. 2017). Data from the United States Agency for International Development (USAID) show that since 1970 groundwater over-use in the region has caused the depletion of groundwater levels at various pumping wells. This is an anthropogenic effect on the system, where extensive groundwater pumping surpasses the natural rates of recharge, and this causes drops in the aquifer levels (Faunt et al. 2009; Massoud et al. 2018).

Furthermore, the freshwater that is stored in the snowpack in the local mountain areas can benefit the region during the spring and summer seasons, which are generally drier. Yet, increasing temperatures paired with decreasing, and sometimes major oscillations, in rainfall due to climate change has caused snowpacks to be generally lower, such as in the mountain regions of the Middle East. Also, during droughts, large surface water reservoirs in the region, such as the Qaraaoun reservoir, can have depleted supplies of surface water. This further exacerbates the reliance on groundwater during droughts in this region. In this study, we aim to quantify the changes in groundwater storage for the Beqaa Plain, by utilizing information on hydrologic cycle variables from remote sensing, model simulations, and in-situ data.

In recent years, satellite data has emerged as a great tool to observe the Earth, including certain variables in the hydrologic cycle (Alley 2002; Famiglietti et al. 2011; Purdy et al. 2019; Massoud et al. 2018, 2020b; Liu et al. 2019). For example, NASA's Gravity Recovery and Climate Experiment (GRACE) satellites (Tapley et al. 2004) have been established as extremely valuable instruments for regional to global scale water cycle studies (Famiglietti 2014; Reager et al. 2015). To obtain information on groundwater dynamics, gravimetric observations from GRACE are obtained and the signal is translated into a mass change signal, which can then be directly related to changes in freshwater sources. To estimate groundwater storage changes, information on other hydrological variables, obtained from in-situ data or model simulations, can be combined with information from the GRACE signal (e.g., Famiglietti et al. 2011; Scanlon et al. 2012; Xiao et al. 2017; Massoud et al. 2018; Liu et al. 2019).

1.4 Using Satellites to Estimate Groundwater

Typically, the hydrologic variables that are needed for this problem include snow water equivalent and freshwater stored in soil moisture, and this information can be acquired from model simulations. Additionally, information on water that is stored in surface reservoirs is needed, and this type of data can be acquired from water

resource managers in the region. Overall, combining these data sets provides the needed evidence to calculate GRACE-derived groundwater storage changes.

Total Water Storage (TWS) from GRACE is combined with data sets that represent hydrologic variables in order to estimate groundwater, or other water sources, in a region. In this study, information for many of these hydrologic variables are obtained from the GLDAS model (Rodell et al. 2004), and this includes the soil moisture storage, snow water equivalent, and canopy water storage. For surface water, we utilize data from the Qaraaoun reservoir, which is the single largest body of water in the region. Ultimately, the groundwater variable is the only missing component needed to complete the water balance. Therefore, all the information for the other hydrologic variables is fused, and we can quantify groundwater storage from the signal of the GRACE satellite data. By utilizing the different data sources available through remote sensing, model simulations, and in-situ observations, we estimate and make quantitative assessments of the evolution of groundwater in the Beqaa Plain.

The motivation for this study is based on recent reports that have brought attention to the fact that groundwater aquifers are depleting in the Beqaa Plain (Molle et al. 2017), and our hypotheses for this study are comprised of the following two points. (1) Groundwater is indeed depleting through much of the Beqaa Plain due to unsustainable groundwater pumping, and GRACE data can be effectively used to provide evidence of this on the basin scale. (2) Other data sources, such as Sentinel-1 interferometric synthetic aperture radar (InSAR) data and in-situ monitoring wells can confirm the GRACE results and provide additional details on high spatial resolution that can pinpoint exact locations where groundwater depletion is most evident. The utilization of the techniques presented in this study provide a country like Lebanon, or similarly other regions with a lack of observational data, a framework to assess groundwater storage on the basin scale, where consistent data on water wells is mostly missing and during a time that chaotic, unchecked, and unsustainable groundwater pumping is being exacerbated in the region.

2 Freshwater Data for Beqaa Plain, Lebanon

The Beqaa Plain (8–15 km wide), in the east part of Lebanon, is a fertile valley that is home to a flourishing industry related to agriculture and is Lebanon's most important farming region. The region is roughly 30 km (19 mi) to the east of the capitol city, Beirut, and is located in between Mount Lebanon (to the west) and the Anti-Lebanon mountains (to the east). The size of the valley is roughly 120 km (75 mi) from north to south and 11 km (9.9 mi) from west to east.

The Beqaa has a Mediterranean climate, with winters that are wet and snowy and summers that are dry and warm. Due to the high peaks of Mount Lebanon to the west, a rain shadow is created that blocks precipitation from the sea, causing limited rainfall to occur in this region compared to other parts of the country. There is

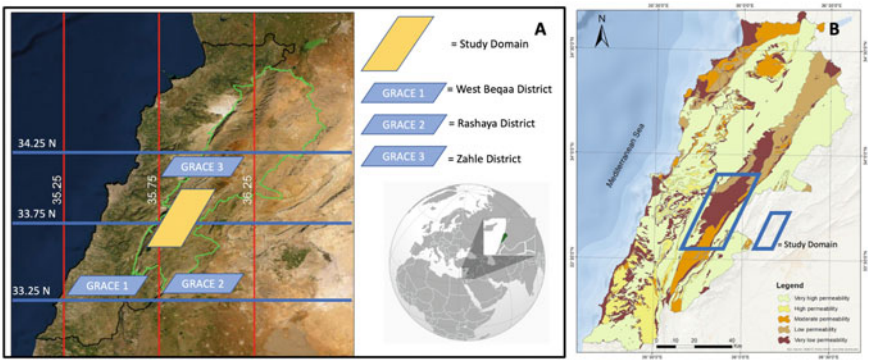

Fig. 1 **A** Study domain, shown in yellow. There are three GRACE grid cells that cover this area, defined as the West Beqaa, Rashaya, and Zahle Districts. Also, the map of Lebanon is shown in relation to the rest of the globe on the bottom right. **B** Permeability maps which indicate the potential recharge for Lebanon. Our study domain is a mixture of high to very high recharge (yellow) in the West Beqaa, moderate recharge (orange) in the Rashaya District, and low to very low recharge (purple) in the Zahle District. Figure adopted from Massoud et al. (2021)

generally lower precipitation in the northern section of the Beqaa Plain with 230 mm (9.1 in), compared to 610 mm (24 in) in the southern portion.

Most of the lithological characteristics in the region implies that the Neogene and Quaternary rocks are mainly composed of rock mixture conglomerates, alluvial deposits and other detrital rocks. Figure 1A shows our study area within the context of greater Lebanon, and the location of the three GRACE grid cells that are examined in this study, defined as the West Beqaa, the Rashaya District, and Zahle District regions. Also, the map of Lebanon is shown in relation to the rest of the globe on the bottom right of this panel. Figure 1B shows the potential recharge map for the whole Lebanese territory, and in our study area there is a mixture of high to very high recharge (yellow) in the West Beqaa, moderate recharge (orange) in the Rashaya District, and low to very low recharge (purple) in the Zahle District (Shaban 2020; El Hage et al. 2020).

2.1 GRACE Data

NASA and the DLR's (German Aerospace Center) satellite mission, GRACE, offered a new way to monitor water storage from the vantage point of space (Tapley et al. 2004; Rodell et al. 2009; Famiglietti et al. 2011). For nearly 15 years, GRACE provided estimates of global mass change at monthly resolution, which have been heavily utilized in applications for water resources management and hydrologic studies.

Recent literature has made evident the benefits that can be obtained with GRACE. These studies include applications to various regions around the globe, including the

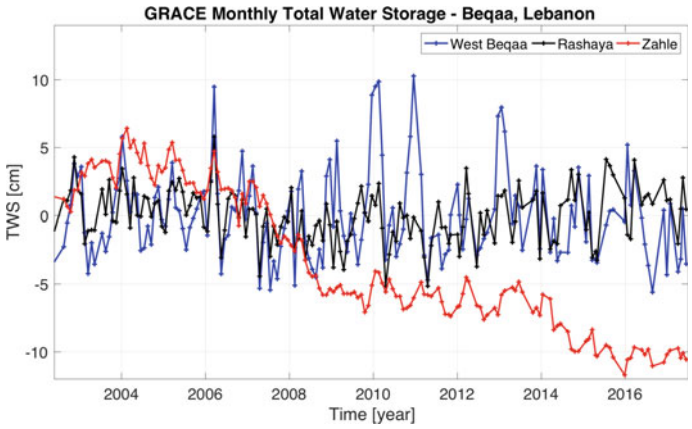

Fig. 2 Total Water Storage (TWS) from the GRACE satellite data record. Three separate regions are shown, and the Zahle District is an area that is experiencing significant loss of water storage. Figure adopted from Massoud et al. (2021)

Middle East (Voss et al. 2013; Forootan et al. 2014), California (Famiglietti et al. 2011; Scanlon et al. 2012; Xiao et al. 2017; Massoud et al. 2018, 2020b), Northern India (Rodell et al. 2009; Tiwari et al. 2009), and Northern China (Moiwo et al. 2009; Feng et al. 2013), to list a few. For our study, we utilize the GRACE mascon product from JPL RL05M.1 Version 2, from April 2003 through June 2017, which can be downloaded at no cost at https://grace.jpl.nasa.gov/data/get-data/ (Watkins et al. 2015; Wiese et al. 2018). We use the data to investigate the changes in TWS in the Beqaa Plain (Fig. 2). The GRACE data product we use in this study has a spatial resolution of 0.5 degrees and a monthly temporal resolution. Please refer to Watkins et al., (2015) for details on the mascons and the scale factors used for the processing of the GRACE data.

For clarity, we briefly describe here how the GRACE data is utilized to measure changes in water mass. GRACE measures change in water mass (in kg), which can be converted to units of (m^3) (volume of water) if we divide by the density of water. Then from this, we can divide by the total area of the GRACE grid cell, and that would give us a unit of (cm of water). This tells you how much cm of water is increased/decreased from the last time step over the whole region on average. So, it is not exactly measuring water change at any specific level below or above the surface but is instead measuring the overall volume/mass of water change for that basin.

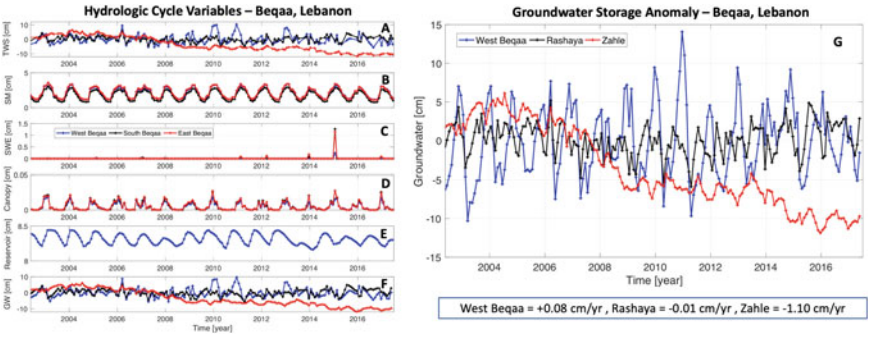

Fig. 3 **A**–**E** Hydrologic variable anomalies for the three regions in this study. All units are converted to cm in order to calculate groundwater anomalies from the GRACE signal. **F** Groundwater storage anomalies, calculated for the three regions in this study. The rate of loss (cm/yr) for each region is noted on the bottom of the figure. Figure adopted from Massoud et al. (2021)

2.2 GLDAS data

The GLDAS system (Rodell et al. 2004) provides details and simulation outputs from various land surface models that simulate the globe based on incorporation of other data products. The system is forced with observed radiation, precipitation, temperature, humidity, and wind, to simulate the earth's land surface and estimate the storage and movement of energy and water, globally.

The system provides estimates of soil moisture storage in the top 2 m, but we only utilize the soil moisture storage in the top 10 cmfor our study (SM). GLDAS also includes snow water equivalent (SWE) and water stored in vegetation (Canopy). Note, we represent the soil moisture storage in the top 10 cm as the entirety of the water storage in soils, and the remaining water storage in the soil is counted as part of the groundwater storage component.

We use monthly outputs from GLDAS to facilitate the combination with the GRACE data, and these outputs are shown in Fig. 3. The units of the GLDAS outputs are in (kg m^{-2}) of fresh water. In order to match the units of the GRACE data in (cm), we perform a unit change on the outputs, which involves dividing by the density of water (1000 kg m^{-3}) and converting from (m) to (cm). Water storage that is on the surface of the land, such as lakes, reservoirs, and rivers, is not explicitly simulated in the GLDAS model. Therefore, we utilize information on the Qaraaoun reservoir height to fulfill this requirement.

2.3 Qaraaoun Reservoir Data

The Qaraaoun Reservoir, or Lake Qaraaoun, is a manmade reservoir or lake situated in the south part of the Beqaa Plain. It was built in 1959 close to the Qaraaoun village,

by erecting a concrete dam that is 61 m (200 ft) high. It is the largest dam in Lebanon and is located in the middle reaches of the Litani River, which is the longest river in Lebanon. The reservoir provides numerous benefits, such as hydropower, water supply to the local population, and for the irrigation of 27,500 hectares (68,000 acres) of agricultural fields.

Every year, the amount of water received at the Qaraaoun Reservoir by the Litani River is 420 million m^3 (15 billion ft^3). To satisfy the freshwater demand of the Kassmieh irrigation project during the dry summer months, 30 million m^3 (1.1 billion ft^3) of water is diverted from Markaba power station annually. In our study, we use timeline data of the Qaraaoun reservoir as information for surface water storage in the Beqaa region, in units of (meters above sea level). To match units of the GRACE data (cm), we perform a unit change on the data, which involves converting from (m) to (cm), and then scaling by the ratio of the area of the reservoir (11.9 km^2) to the area of the GRACE grid cell ($55 \times 55 = 3025$ km^2).

3 Calculating Groundwater Storage in the Beqaa Plain, Lebanon

As indicated previously, the contributions of mass changes from each individual process of the hydrologic cycle must be disentangled from the GRACE signal in order to infer groundwater storage changes (Famiglietti et al. 2011; Purdy et al. 2019; Massoud et al. 2020b). Here, we list the steps needed to derive groundwater estimates for this study. First, all data must be recalculated in order to have units of cm, to match the signal in the GRACE data (TWS(t)). The GLDAS outputs in our study have a resolution of 0.25 degrees, whereas the GRACE grid cell has resolution of 0.5 degrees. Before we process the data spatially, we make sure the units are all in volume of water. Once we combine the data that are in the same units of volume, we then combine all the information in each grid cell and convert the units to (cm) by dividing by the area of the respective grid cell. We convert all values to match the size of the GRACE grid cell of 0.5 degrees. Then, to process the temporal side of the data, we apply interpolation on the temporal data to make sure that we have a data point for each month (some monthly values are missing in the raw GRACE data).

We use information for water stored in the land as soil moisture storage in the top 10 cm (SM(t)), water stored in the snowpack as snow water equivalent (SWE(t)), water stored in vegetation as canopy water (Canopy(t)), and water stored on the land surface as surface water (SW(t)). We then subtract the combined value of all these variables from the TWS data (TWS(t)) obtained from GRACE. Here, t represents the month in which the estimate is being calculated. Therefore, groundwater (GW(t)) storage change estimates at each month for each location defined in this study in the Beqaa Plain is given by the following equation:

$$\mathrm{GW(t)} = \mathrm{TWS(t)} - [\mathrm{SM(t)} + \mathrm{SWE(t)} + \mathrm{Canopy(t)} + \mathrm{SW(t)}] \quad (1)$$

After propagating the effect of all the hydrologic variables from the GRACE signal, we can estimate the temporal groundwater dynamics for the Beqaa Plain (Fig. 3). Note, this equation is valid when assuming all components to be error-free. For our case study, this is assumed to be acceptable. Generally, to achieve this uncertainty assessment, some recent studies have applied Kalman Filters (Khaki et al. 2017, 2018), while others propagated the sources of uncertainty in a Monte Carlo framework (Massoud et al. 2020b).

4 Sentinel-1 InSAR and In-Situ Wells Data

4.1 Sentinel-1 InSAR Signals of Land Subsidence

Land subsidence due to groundwater withdrawal provides independent information to cross-validate the groundwater loss signals as measured by GRACE. Figure 4A shows the Sentinel-1 InSAR estimates of land deformation since October 2014. There is a clear signal of land subsidence, especially in areas with higher density of groundwater pumping wells. Despite short overlap period between GRACE and S-1, the ground subsidence as imaged by Sentinel-1 shows temporal variation that is consistent with GRACE estimates of groundwater depletion.

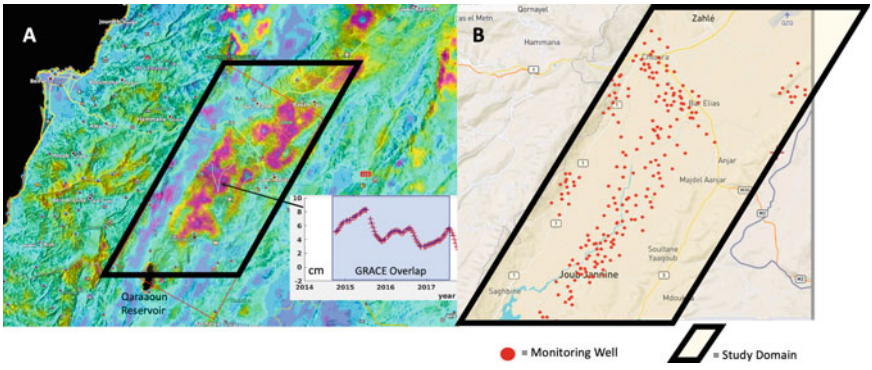

Fig. 4 **A** InSAR LOS velocity and displacement time series (inset) inferred from Sentinel-1 data. The shaded rectangle in the inset indicates the overlap period between GRACE and Sentinel-1 data, shown in units (cm). Regions with the shades of purple and red are where higher levels of land subsidence are observed. **B** These subsidence locations coincide with areas that have pumping wells, shown on the right with red dots. Figure adopted from Massoud et al. (2021)

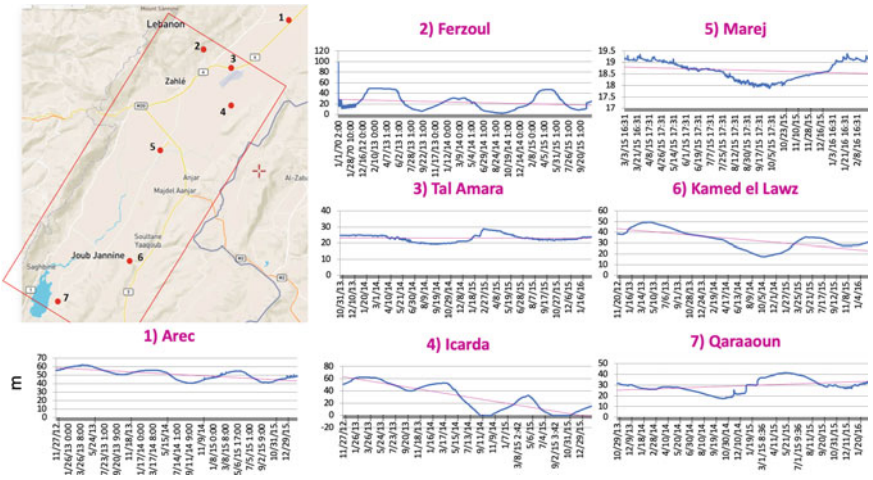

Fig. 5 Monitoring wells for 7 chosen locations, indicated on the map with red dots. These individual cases show the seasonal signals of groundwater depletion and recovery, but overall, there is a long-term trend of depletion in most of these wells and this is due to unsustainable groundwater pumping. Units for the timelines showing the groundwater well dynamics are in (m). Figure adopted from Massoud et al. (2021)

4.2 Monitoring Wells

Figure 4B shows the locations of groundwater pumping wells. As a visual comparison at first, the locations depicted in Fig. 4A that are experiencing land subsidence are the same locations shown in Fig. 4B to have pumping wells. To have a closer look at individual wells, we pinpoint seven different monitoring locations and highlight the results in Fig. 5.

These plots show that, for the individual wells included, there is a strong seasonal signal of groundwater depletion and recovery, and that there is an overall long-term trend of groundwater depletion in most of these wells. Note, the well measurements that are used for this study are processed from a larger data set containing well measurements for the region. There are limitations to using this data, such as continuity of data or the length of the data record. However, we extract data from different measurement wells that offer sufficient information at specific locations to gain insight on groundwater dynamics for the region.

5 Summary and Discussion

The Beqaa Plain, Lebanon, is one of the most agriculturally productive regions of the Middle East and has a heavy reliance on groundwater supplies to meet irrigation demand, especially after the severe pollution witnessed in the Litani River. In this

study, we investigated changes in water storage of various terms in the hydrologic cycle to ultimately estimate groundwater storage changes in the Beqaa Plain. To obtain our results, we utilized 15 years of Total Water Storage (TWS) data from the GRACE product for the Beqaa Plain and combined this information with other hydrologic data to estimate groundwater storage change. The remaining hydrologic variables included soil moisture storage, snow water equivalent, and canopy water storage, from the GLDAS model. For surface water storage, we used data from the Qaraaoun reservoir, the largest body of water in this region. The results reported in our study confirm recent findings that groundwater use in this region has been unsustainable and has caused depletion of the aquifer (c.f. Molle et al. 2017). Our analysis defines three separate domains within the study region, and our findings indicate that the Zahle District is where water is being lost at a much higher rate compared with the West Beqaa and Rashaya District, due to very slow recharge rates and unsustainable groundwater pumping. We show that the rate of groundwater storage change in the West Beqaa is nearly +0.08 cm/yr, in the Rashaya District is −0.01 cm/yr, and in the Zahle District the level of depletion is roughly −1.10 cm/yr. The results from the InSAR estimates from Sentinel-1 and the in-situ monitoring wells also show the groundwater depletion feature in this region.

The groundwater depletion that occurs in semi-arid regions around the world, like the Beqaa Plain, not only causes stress on the water resources of the area, but also creates other issues such as subsidence of the land surface. We laid out two hypotheses for this study to investigate whether satellite data and information from other sources can be useful to provide evidence of groundwater depletion in the Beqaa. Our first hypothesis was addressed by showing the ability of the GRACE data to successfully capture the changes in groundwater storage for the region. Our second hypothesis was answered by validating the results with other sources of information, one being satellite InSAR and the other being in-situ measurements (monitoring wells). Initial results from the InSAR analysis support the findings from GRACE and highlight the regions that are experiencing groundwater depletion and land subsidence due to unsustainable groundwater pumping (50–60 wells/km^2), namely in the Zahle District. Furthermore, the in-situ monitoring wells that provided sufficient data for this analysis show a depleting level of groundwater for most wells in the region.

Future efforts on this work can further focus on combining various sources of information, including satellite and in-situ measurements as well as model simulations, to obtain higher resolution estimates of groundwater storage change throughout the region. Efforts to combine GRACE with the newly launched GRACE Follow-On (GRACE-FO) data can be made to utilize longer time series of total water and groundwater storage changes. Also, gathering additional data from wells can be useful for inspecting the spatiotemporal variability of the ground response to water withdrawals, and to estimate elastic vs inelastic (i.e. seasonal versus long-term) properties of the groundwater system. This can provide information to identify specific regions that undergo irreversible compaction of the land surface and subsurface aquifers, which directly affects groundwater storage capacity of the area. These various questions can be investigated using the tools and methods presented in this study and will be essential for long-term sustainability and effective groundwater management. With

the availability of information from remote sensing and the wealth of data that is ready to be utilized for groundwater applications, it is becoming more possible to monitor the state of groundwater. Advancing this ability will be beneficial to local farmers, water managers, decision makers, and other entities or organizations that are stakeholders of groundwater resources.

References

Alley WM (2002) Flow and storage in groundwater systems. Science 296:1985–1990

El Hage M, Robinson CA, El-Baz F, Shaban A (2020) Fracture-controlled groundwater seeps into the Mediterranean Sea along the coast of Lebanon. Arabian J Geosci 13(13):1–14

Famiglietti JS, Lo M-H, Ho SL, Bethune J, Anderson KJ, Syed TH, Swenson SC, De Linage CR, Rodell M (2011) Satellites measure recent rates of groundwater depletion in California's Central valley. Geophys Res Lett 38

Famiglietti JS (2014) The global groundwater crisis. Nat Clim Chang 4:945–948

Faunt CC, Hanson R, Belitz K (2009) Groundwater availability of the central valley aquifer, California; Professional Paper 1766; U.S. Geological Survey: Reston, VA, USA

Feng W, Zhong M, Lemoine J-M, Biancale R, Hsu H-T, Xia J (2013) Evaluation of groundwater depletion in North China using the gravity recovery and climate experiment (GRACE) data and ground-based measurements. Water Resour Res 49:2110–2118

Forootan E, Rietbroek R, Kusche J, Sharifi M, Awange J, Schmidt M, Omondi P, Famiglietti J (2014) Separation of large scale water storage patterns over Iran using GRACE, altimetry and hydrological data. Remote Sens Environ 140:580–595

Harbaugh AW, Banta ER, Hill MC, McDonald MG (2000) MODFLOW-2000, The U.S. geological survey modular ground-water model-user guide to modularization concepts and the ground-water flow process; Open-File Report 00–92; U.S. Geological Survey: Reston, VA, USA

He X, Wada Y, Wanders N, Sheffield J (2017) Intensification of hydrological drought in California by human water management. Geophys Res Lett 44:1777–1785

Huang JP, Ji MX, Xie YK, Wang SS, He YL, Ran JJ (2016) Global semi-arid climate change over last 60 years. Clim Dyn 46:1131–1150

Khaki M, Ait-El-Fquih B, Hoteit I, Forootan E, Awange J, Kuhn M (2017) A two-update ensemble Kalman filter for land hydrological data assimilation with an uncertain constraint. J Hydrol 555:447–462

Khaki M, Ait-El-Fquih B, Hoteit I, Forootan E, Awange J, Kuhn M (2018) Unsupervised ensemble Kalman filtering with an uncertain constraint for land hydrological data assimilation. J Hydrol 564:175–190

Liu Z, Liu P-W, Massoud E, Farr TG, Lundgren P, Famiglietti JS (2019) Monitoring groundwater change in California's central valley using Sentinel-1 and GRACE observations. Geosciences 9:436

Lo M-H, Famiglietti JS (2013) Irrigation in California's central valley strengthens the southwestern us water cycle. Geophys Res Lett 40:301–306

Margulis SA, Cortés G, Girotto M, Durand M (2016) A Landsat-era Sierra Nevada snow reanalysis (1985–2015). J Hydrometeorol 17:1203–1221

Massoud EC, Purdy AJ, Miro ME, Famiglietti JS (2018) Projecting groundwater storage changes in California's Central valley. Sci Rep 8:12917

Massoud EC, Espinoza V, Guan B, Waliser DE (2019) Global climate model ensemble approaches for future projections of atmospheric rivers. Earth's Future 7(10):1136–1151
Massoud EC, Lee H, Gibson PB, Loikith P, Waliser DE (2020a) Bayesian model averaging of climate model projections constrained by precipitation observations over the contiguous United States. J Hydrometeorol 21(10):2401–2418
Massoud EC, Turmon M, Reager J, Hobbs J, Liu Z, David CH (2020b) Cascading dynamics of the hydrologic cycle in California explored through observations and model simulations. Geosciences 10(2):71
Massoud EC, Liu Z, Shaban A, El Hage M (2021) Groundwater depletion signals in the Beqaa plain, Lebanon: evidence from GRACE and Sentinel-1 data. Remote Sens 13(5):915
McCallum AM, Andersen MS, Giambastiani BM, Kelly BF, Ian Acworth R (2013) River–aquifer interactions in a semi-arid environment stressed by groundwater abstraction. Hydrol Process 27:1072–1085
Molle F, Nassif M-H, Jaber B, Closas A, Baydoun S (2017) Groundwater governance in Lebanon: the case of Central Beqaa. A Policy White Paper. No. 615-2018-4008
Moiwo J, Yang Y, Li H, Han S, Hu Y (2009) Comparison of GRACE with in situ hydrological measurement data shows storage depletion in Hai River basin Northern China. Water SA 35:663–670
Purdy AJ, David CH, Sikder S, Reager JT, Chandanpurkar HA, Jones NL, Matin MA (2019) An open-source tool to facilitate the processing of GRACE observations and GLDAS outputs: an evaluation in Bangladesh. Front Environ Sci 7:155
Reager JT, Thomas AC, Sproles EA, Rodell M, Beaudoing HK, Li B, Famiglietti JS (2015) Assimilation of GRACE terrestrial water storage observations into a land surface model for the assessment of regional flood potential. Remote Sens 7:14663–14679
Rodell Matthew, Houser PR, Jambor UEA, Gottschalck J, Mitchell K, Meng C-J, Arsenault K et al (2004) The global land data assimilation system. Bull Am Meteorol Soc 85(3):381–394
Rodell M, Velicogna I, Famiglietti JS (2009) Satellite-based estimates of groundwater depletion in India. Nature 460:999–1002
Scanlon BR, Longuevergne L, Long D (2012) Ground referencing GRACE satellite estimates of groundwater storage changes in the California central valley US. Wat Resour Res 48:W04520
Shaban A (2020) Water resources of Lebanon. Springer Science Publisher, 229 pp. ISBN 978-3-030-48716-4
Tapley BD, Bettadpur S, Ries JC, Thompson PF, Watkins MM (2004) GRACE measurements of mass variability in the earth system. Science 305:503–505
Tiwari VM, Wahr J, Swenson S (2009) Dwindling groundwater resources in northern India, from satellite gravity observations. Geophys Res Lett 36:18401
Voss KA, Famiglietti JS, Lo M-H, Linage C, Rodell M, Swenson SC (2013) Groundwater depletion in the Middle East from GRACE with implications for transboundary water management in the Tigris-Euphrates-Western Iran region. Water Resour Res 49:904–914
Watkins MM, Wiese DN, Yuan D-N, Boening C, Landerer FW (2015) Improved methods for observing earth's time variable mass distribution with GRACE using spherical cap mascons. J Geophys Res Solid Earth 120:2648–2671
Wiese DN, Yuan D-N, Boening C, Landerer FW, Watkins MM (2018) JPL GRACE Mascon ocean, ice, and hydrology equivalent water height RL05M.1 CRI filtered version 2, PO.DAAC, CA, USA. https://doi.org/10.5067/TEMSC-2LCR5. Accessed 01 Oct 2018
Woodhouse CA, Meko DM, Macdonald GM, Stahle DW, Cook ER (2010) A 1,200-year perspective of 21st century drought in southwestern North America. Proc Natl Acad Sci 107:21283–22128
Wootten AM, Massoud EC, Sengupta A, Waliser DE, Lee H (2020) the effect of statistical downscaling on the weighting of multi-model ensembles of precipitation. Climate 8(12):138
Xia Y, Mitchell K, Ek M, Cosgrove B, Sheffield J, Luo L, Alonge C, Wei H, Meng J, Livneh B, et al (2012) Continental-scale water and energy flux analysis and validation for North American land data assimilation system project phase 2 (NLDAS-2): 2. Validation of model-simulated streamflow. J Geophys Res 117, D03109. https://doi.org/10.1029/2011JD016048

Yang Z-L, Niu G-Y, Mitchell KE, Chen F, Ek MB, Barlage M, Longuevergne L, Manning K, Niyogi D, Tewari M et al (2011) The community Noah land surface model with multiparameterization options (Noah-MP): 2. Evaluation over global river basins. J Geophys Res Space Phys 116. D12110. https://doi.org/10.1029/2010JD015140

Zaitchik BF, Rodell M, Reichle RH (2008) Assimilation of GRACE terrestrial water storage data into a land surface model: results for the Mississippi river basin. J Hydrometeorol 9:535–548

Volcanic Terrains Reveal Bright Hydrogeological Prospects in Saudi Arabia: A GIS & RSA Linked Research on Harrat Rahat

Nayyer A. Zaigham, Omar S. Aburizaiza, Zeeshan A. Nayyar, and Gohar A. Mahar

1 Introduction

The basaltic lava-flows are the igneous rock formed by the solidification of the molten earth's material (magma) during the eruption of the volcanoes on the surface. The extent of spreading of the lavas depends on the effusion rates and their viscosity, which in turn depends on the mineral constituents of the lavas themselves (Walker 1993). The world largest igneous provinces are the Siberian basalt traps in Russia covering about 2000,000 km^2, Parana and Etendeka traps in Brazil covering about 1500,000 (1.5 × 106) km^2, the Daccan basalt province of India covering an area of about 500,000 km^2 in western and central India, Karoo basalt province of south Africa covering about 400,000 km^2, the Columbia basalt plateau of the north-western United States of America covering 160,000 km^2, Chilcotin basalt plateau in British Columbia, Canada, covering 50,000 km^2, and about 12 large basaltic provinces associated with the regional structural lines running 300–600 km distance in Australia (Stephenson et al. 1980; Rampino and Stothers 1988; Walker 1993; Peate 1997; Singhal 1997; Sen and Chandrasekharam 2011; Wikipedia 2013). Similarly in Saudi Arabia, the extensive continental-type eruptive lava-terrains of the Cenozoic

N. A. Zaigham (✉)
GeoEnvoTechServices (GETS), A-40, Bk-15, Jauhar, Karachi, Pakistan
e-mail: nazaigham@gmail.com

King Abdulaziz University, Jeddah, Saudi Arabia

O. S. Aburizaiza
Unit for Ain Zubaida Rehabilitation and Groundwater Research, King Abdulaziz University, Jeddah, Saudi Arabia

Z. A. Nayyar
Department of Applied Physics, University of Karachi, Karachi, Pakistan

G. A. Mahar
Department of Geography, Federal Urdu University, Karachi, Pakistan

A. Shaban (ed.), *Satellite Monitoring of Water Resources in the Middle East*,
Springer Water, https://doi.org/10.1007/978-3-031-15549-9_17

volcanism has produced 13 vast basaltic fields covering a total area of about 100,000 km^2 at the western rifted margin of Arabian Shield (Coleman et al. 1983).

It was observed on the basis of the documented literature reviews that the basalt-aquifer systems played the key role in providing indigenous and sustainable groundwater supplies worldwide. For examples, the Columbia River Basalt Group (CRBG), comprising the thick sequence of layered flood-basalt-flows, hosts the regional aquifer system, in portions of Washington, Oregon, and Idaho, which is the prime source of potable groundwater, and in many cases the only water supply for numerous communities, small water systems, individual homes, industry, and agriculture (Jefferson et al. 2006; Tolan et al. 2009). Likewise, the basalt accounted for 75% of all aquifer formations in Ngong area of Kenya, which provided the excellent yield of groundwater within weathered and/or fractured volcanic suits and contact zones (Mulwa et al. 2005). Similarly, four broad hydrogeological units were recognized for the entire volcanic province of Ethiopian plateau. Groundwater occurs in weathered zone above hard rock and in semi-confined to confined condition in the fissures, fractures, joints, cooling cracks, lava-flow junctions and also in the intertrappean beds between successive lava flows (Kebede 2013). Excellent yield of good quality groundwater (<2 mS/cm) was recorded from the Pliocene-Pleistocene basalts of the Hamilton area (Bennetts et al. 2003). Similarly, the Atherton Tablelands Tertiary to Quaternary age basaltic aquifer system played its role as a major source of groundwater supply for irrigation and other agricultural use in Australia (Locsey 2004). CGWB (2013) assessed 1000 L/minute yield from promising aquifer zones associated with the Deccan basaltic terrain in Khandwa, Khargone and Dhar districts of India. The presence of vesicles, amygdales and similar other structures, and the combination of weathering, jointing and fracture trends generally enhanced the potential of basaltic aquifers on a local scale, which were comprised nearly horizontal lava flows of late Cretaceous to early Eocene (Babar and Shah 2012).

On the basis of different literature reviews and the reconnaissance traversing, it was deduced that the basalt-terrains used to have significantly high percolating and recharging hydrogeological characteristics mainly because of the dual (i.e., primary and secondary) porosity and permeability. Thus, they have hosted the excellent basaltic-aquifers and also served as the potential sources for recharging the groundwater in the large areas of different parts of the world. Based on these observations, it seemed imperative to undertake exhaustive research activities for the assessment and exploration of groundwater potential(s) associated with the Saudi Arabian volcanic terrains on priority.

Coleman et al. (1983) presented detailed study of Cenozoic volcanic fields of Saudi Arabia and also highlighted for the need of groundwater exploration in the basaltic rocks. Though, the exploration activities on large scale have not been achieved so far as those should have been undertaken. However, some localized studies, were carried out in northern part of Harrat (volcanic terrain) Rahat in Madinah region, and indicated good groundwater prospects (Shaibani 2003; Shaibani et al. 2006).

Present paper describes (i) the general occurrences of the volcanic fields (Harrats) in Saudi Arabia with particular emphasis on Harrat Rahat, (ii) the hydrogeological

characteristics of volcanic terrains and the basaltic lava-flows, and (iii) several interactive GIS and satellite remote sensing linked hydrogeological models using different thematic layers, like the regional drainage maps, enhanced satellite images, map of eruptive centers and younger lava-flows, technical field photographs, the thickness map of basaltic thickness, etc.

2 Methodology

In view to accomplish the present research study, the following steps were adopted:

i. The archive literature and data, related to some volcanic fields and associated groundwater potentials of the world including Saudi Arabia, were acquired through internet and other sources, which were reviewed and the inferences drawn were incorporated.
ii. Field investigations were carried out to collect the geohydrological field data, technical field photos, on ground checking of the deductions made during the satellite remote sensing analyses and other observations in Harrat Rahat areas.
iii. The basalt fields (Harrats) were digitized, geo-referenced and a map of Saudi Arabian basalt fields was prepared, which was further used as a thematic layer for GIS modeling. The source of data was the preliminary drafted maps of Coleman et al. (1983).
iv. The drainage maps were extracted by digitizing from the published geological maps on scale 1:250,000 (maps source: Ministry of Petroleum and Mineral Resources, Kingdom of Saudi Arabia). The prepared drainage maps were integrated and used as the thematic layers in GIS modeling.
v. Two mosaics of satellite ETM images were prepared covering more than 100,000 km^2 area in the western part of Saudi Arabia parallel to Red Sea. The mosaics were enhanced for the thermal band classification (TCB) using single thermal band and natural colour function (NCF) using 4, 3, 2 bands.
vi. Based on the above thematic layers, different interactive overlays/models were generated by using ArcGIS and other software. Subsequently, the interpretations and inferences were deduced from these over-lays/models, which were discussed in this paper.

3 General Setup of Volcanic Terrains in Saudi Arabia

A large alkali basalt province, comprising 13 volcanic fields (Harrats) and spreading over an area of about 100,000 km^2, was located at the western rifted margin of the Arabian Plate in Saudi Arabia parallel to Red Sea. Southward, the trend of volcanic fields extended obliquely across the Red Sea into the East-African Rift region (Fig. 1A). This Cenozoic volcanism was related to the rifting of the Arabian and African plates and the consequent formation of Red Sea (Coleman et al. 1983;

Nyblade et al. 2006). The late-Cretaceous basaltic lava-flows in Yemen represented the earliest volcanic activity in the Arabia landmass (Shukri and Basra 1955), while the most recent eruption was recorded near Al-Madinah in 1256AD (Camp et al. 1987).

Modern reactivation of the volcanic eruptions was also observed around northern and southern ends of Red Sea. In northern section, vigorous seismicity occurred associated with the Lunayyir Volcano within the coastal belt, where nineteen earthquakes of magnitude ranging between 4 and 5.4 and a swamp of more than 30,000 micro-earthquakes occurred in 2009 (Choi 2010). There was no apparent eruption of the lava, except a long fissure observed on the ground with escaping of the gasses. On the other hand, a series of the eruptive volcanoes were reported within the axial trough in southern part of the Red Sea from latitude 16°N to 12°N. Most recently, a new surtseyan volcanic eruption occurred on December 19, 2011, at Az-Zubair archipelago, with exploding-lava material rising to a height of about 30 m (Vervaeck 2011). In addition, the active volcanism was also observed in southwestern on-land side at the southernmost end of the Sea. On 12th June 2011, the Anabro volcano re-erupted in the northern part of Eritrea within the tectonically active 'Afar-triangle' along the western coast of the Red Sea.

The Cenozoic Harrat Rahat is the second largest among the thirteen volcanic fields of the Saudi Arabia. The basalt lava-flows were extruded from the Oligocene time to the historical time onto the surface of the Precambrian shield of western rifted margin of Saudi Arabian continental plate.

3.1 Setup of Harrat Rahat

Geologically, Harrat Rahat was preserved a volcanic record that began in Oligocene time with intermittent activities continuing in the historical time and expected to continue in future too. The youngest historically recognized eruptive center was just east of Al-Madinah. In 1256 A.D., the 0.5 km^3 of alkali-olivine basalt was extruded during a period of 52-days through a 2.25-km long fissure at the north end of the Harrat Rahat (Camp et al. 1987). Harrat Rahat largely overlaid on the intensely faulted, fractured and jointed crystalline rocks of the mountainous Precambrian terrains. In the coastal plains, the basaltic lava-flows covered the younger Tertiary formations. Likewise, on the eastern side, the Harrat also covered the Precambrian terrains.

The customised thematic layer of Harrat Rahat (Fig. 1B), comprising the basaltic-flows and zone of eruptive centers, displayed that Harrat Rahat extended in a narrow-elevated terrain from latitude 21° 30′ N to 24° 30′ N and 30° E to 41° E in NNW-SSE orientation that has a length of more than 300 km between the area north of Makkah and south of Al-Madinah. There were linear clusters of cinder cones, craters and domes at the highest points of the crest, which represented four centers of eruptive activities, namely Harrat Al-Madinah, Harrat Bani Abdullah, Harrat Turrah and Harrat-ar-Rukhq from north to south.

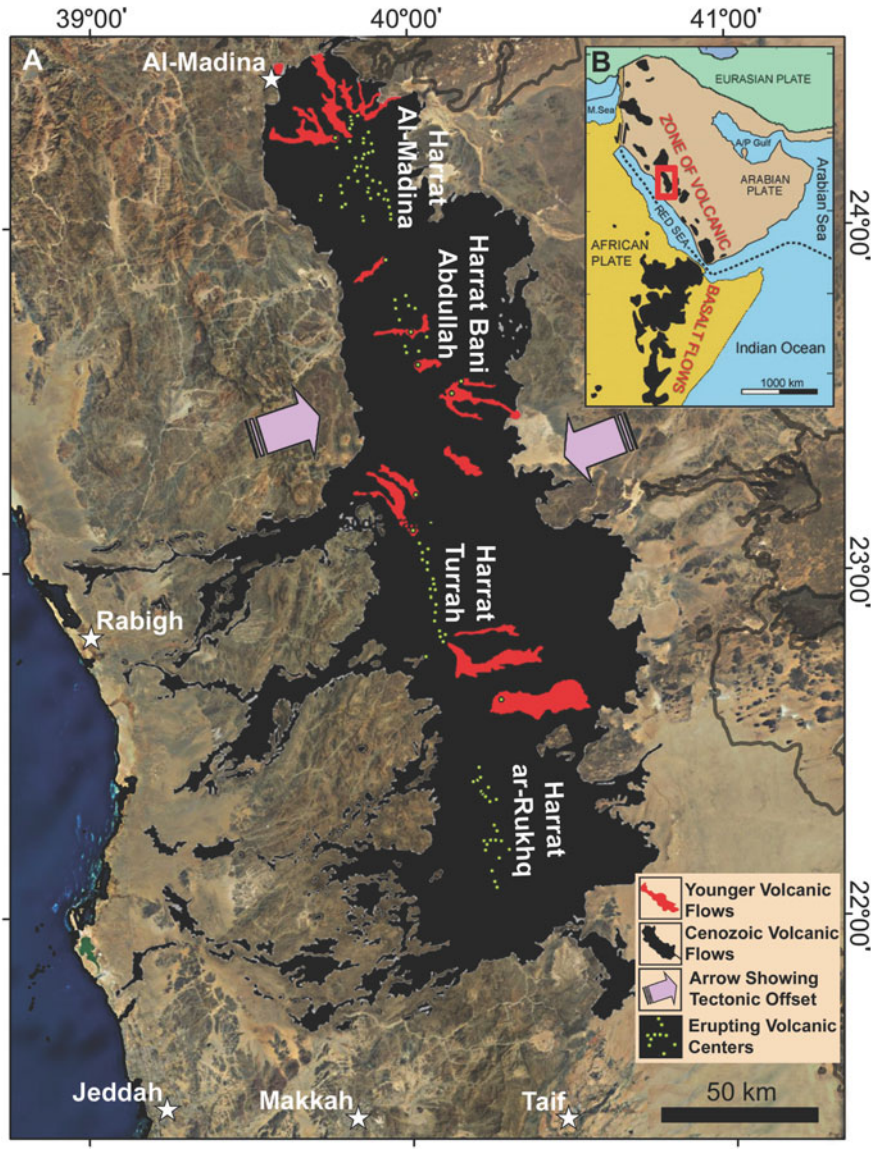

Fig. 1 The index map shows the distribution of the volcanic fields in Saudi Arabia with trans-continental volcanic continuation trends of volcanic fields between the Arabian and African (**A**). Customized map shows the distribution of older and younger basaltic lava-flows of Harrat Rahat, their linear trends of eruptive centers and segments of volcanic body (**B**). *Data Source* Coleman et al. (1983), Camp et al. (1987)

Each of the segments of volcanic activity was 50–75 km long and the offset of segments was about 10 km from each other. All the four segments were coalesced to form the Harrat Rahat as one body. Though, the alignment trends of the volcanic centers of the four segments apparently were the same, but a right-lateral east–west (RLEW) off-set was interpreted between the linear ridges of volcanic activity centers of the Harrat Bani Abdullah and the Harrat Turrah segments of Harrat Rahat as shown with large arrows (Fig. 1A). Based on basaltic lava-flow trends, the Harrat Rahat was longitudinally subdivided into northern (NHR: comprising Harrat Al-Madinah and Bani Abdullah) and southern (SHR: comprising Harrat Turrah and ar-Rukhq) Harrat Rahat zones parallel to the RLEW off-set. Another important observation was that the linear ridges of the volcanic activity centers indicated the symmetry with respect to the basaltic lava-flows in the NHR area, whereas such symmetry was not seen associated with the SHR basalt area. The NHR was a narrow relatively low elevated NNW-trending ridge almost without the western basaltic lava-flows. On the other hand, the SHR zone has four large, more than 100 km long, channels of basaltic lava-flows, with numerous branches, emerging from the crest of the volcanic eruption ridge and terminating near the coastline areas of the Red Sea. The westward trending lava-flows covered the major part of the highly deformed mountainous Precambrian rock terrains, the younger Tertiary sedimentary and also occasionally the Quaternary sediment deposits in the coastal plains of Red Sea.

On the basis of the field observations, it appeared that the westward moving tongues of the lava-flows followed (i) the preexisted or the paleochannels of the drainage systems, (ii) the semi-regional fault/fracture zones associated with the crystalline rock suits of Arabian Shield, and (iii) the low-lying tectonic depressions. In general, the crest-elevation of the volcanic ridge exhibited increasing trend from the north (Al-Madinah area) to the south (ar-Rukhq area). The average elevation of the volcanic field was about 650 m in Al-Madinah segment, 1,507 m at southern part and a maximum of 1,640 m in Harrat Turrah area at latitude 23°N.

4 Characteristics of Volcanic Rocks

The characteristics of the volcanic terrains were considered the key factors for the evaluation of the hydrogeological conditions, like (i) the volume, type, quality, liquidity, periodic frequency of lava-eruption, and (ii) the development of internal and external structures. Thus, the salient characteristic parameters of the Harrat Rahat volcanic terrains were evaluated in terms of their direct and/or indirect impacts on prevailing hydrogeology, so as to assess the groundwater potentiality.

4.1 Number of Eruptive Events

Stratigraphically, the northern (Al-Madinah and Bani Abdullah) volcanic segments of Harrat Rahat have four basaltic layers of eruptions occurred during Oligocene time to Historical time, but the southern (Turrah and Rukhq) segments have five basaltic layers of eruptions occurred during Oligocene to Pliocene time (Camp 1986; Ramsay 1986). The geological time difference coincided with the fact as discussed in the preceding section that the late-Cretaceous basaltic flows in Yemen (Shukri and Basra 1955) represented the earliest volcanic activity in the Arabia landmass, while the most recent eruption was recorded near Al-Madinah in 1256AD (Camp et al. 1987). On the basis of these studies, it was inferred that the volcanic activities became apparently dormant earlier in SHR segments as compared to NHR segments particularly the Al-Madinah segment where historical eruptions were continued. The setup of the hydrogeological conditions seems to be more mature in the SHR segments than the NHR segments as the Harrat Al-Madinah segment has substantial heat-flow at near surface due to its historical and modern volcanic activities. Such erupting events might have comparatively changed the hydrogeological environments.

4.2 Volcanic Eruption and Basaltic Lava-Flow Trends

The single most important factor controlling the form of a lava-flow is the effusion rate, i.e. the rate of lava (the magma and molten rocks) pouring out from the interior of the earth. On the basis of the field observations, it was deduced that the higher is the effusion rate, the greater will be the distance traveled by the hot basaltic lava before its cooling. In case of the SHR segments (i.e., Harrat Turrah and ar-Rukhq), the older erupted lava-flows (4th layer in descending order) travelled long distances, averaging about 150 km, from their erupting centers, situated on uplifted regional north–south trending faulted escarpment, towards the Red Sea (Fig. 1A). Eastward, the flow of the same lava units remained limited within less than 50 km. On the other hand, the basaltic lava-flows extruded northwards at relatively low effusion rates and produced a number of small lava-flow sequences, which overrun on each other in the vicinity of the erupting center(s) rather that flowing for the longer distances. Likewise, it was observed that the oldest 5th basaltic lava-flow and the other three basaltic lava flows (from top to 3rd order) were not travelled like the 4th layer of lava-flows, but remained restricted within the vicinities of their erupting centers. It was also observed that the oldest 5th basaltic lava-flow layer was only exposed on the eastern side of the SHR slopes overlain the older aeolian deposits. Similarly, all the NHR lava-flow layers remained restricted within the vicinities of their erupting centers. Upon cooling, such relatively short-distance travelled lava units produced the compound basaltic lava-flows.

In general, it was deduced that the fluid basalts associated with the eruptive centers of the Harrat Rahat more commonly moved down on the gently sloping

terrains, except the second oldest basaltic fluid magma associated with the SHR segments, which moved anomalously, under the influence of high effusion rate, for long distances by following the pre-existed stream/wadi channels as well as created their own ways too.

4.3 Coalesced Behaviour of Lava-Flows

The north-trending linear cluster zones of small eruptive centers, i.e., the cinder cones, periodically were erupted the magma that after each spell coalesced forming ultimately the large terrain of scoria, the suit of dark gray to reddish brown eruptive igneous rocks with abundant round bubble-like cavities or the vesicles indicating development of bulk porosity. It was inferred that the deposition of the alluvial sediments, windblown sands, development of weathered layers (like the lateritic horizons), and/or the overlapping of the basaltic lava-flows would have developed during the time-gap between older and younger spells of eruptions. Obviously, such overlaps would have caused the additional lateral porosity and permeability on regional scale providing the excellent hydrogeological conditions for the basaltic aquifers associated with different parts of the Harrat Rahat.

4.4 Thickness of Volcanic Terrain

The direct thickness determination of basaltic lava, all over the extent of Harrat Rahat, remained a complex problem. A few attempts were made during the hydrogeological borehole exploration in northern part of the Harrat Rahat. The localized thicknesses of the lava were estimated ranging from 300 to 400 m in the east of its axial divide (Daessle 1973; Torrent 1976; Campi 1969; Shaibani 2003). In this connection, the spectral analysis of low-level-flown aeromagnetic data (Blank and Sadek 1983) provided very useful information regarding the thickness estimates, which range from 26 to 380 m with the mean thickness of about 150 m in the Harrat Rahat region over the larger extent between latitude 24° N and 22° N. The areas further north of latitude 24° N covering the Harrat Al-Madinah were not surveyed and therefore the thicknesses were also not estimated. It was observed that the thicknesses of 200 m and/or more were associated with the main north-trending zone(s) of volcanic eruptive axial-ridge, otherwise the basalt thickness gradually decreased with the decrease of topographic elevation and the increase of the distances towards west and east with reference to the eruptive axial divide.

On the basis of the field investigations and the literature research study, it was interpreted that the general thickness variations might have been strongly influenced by the pre-Harrat NNW-trending topography resulting due to the regional Cenozoic faulting and uplifting during the Red Sea rifting processes. In the prevailing volcano-tectonic setup, the thick basaltic zones were expected to be the excellent targets

for the basalt-aquifers. On the other hand, the thin basaltic layers serve as rain-catcher 'buffer' for the direct recharge to the aquifers associated with the underlying highly faulted/fractured Precambrian crystalline terrains as observed during the field traverse.

4.5 Surface Nature of Basaltic Lava-Flow Terrains

During the field investigations and the remote sensing analyses, two surface types of basaltic lava-flows were observed. One type, comprising highly shattered loose basaltic lava debris at the surface lying on the intensely fractured and jointed upper layer of the lava-flows, extends over a vast region between Al-Madinah and Makkah areas (Fig. 2). The other type of the surface reflected the featureless flat-top surfaces of basaltic lava-flows with raised peripheral edges associated mostly with the westward trending basaltic lava-flows in the southern part of the Harrat Rahat (Fig. 3).

Practically, the in-situ fracturing and jointing of the basaltic lava were developed as the lava-flows started rapid cooling and solidifying into the coherent rock under the resulted onset of contraction phenomenal process. Such in-situ shattered lava-flow terrains provided highly porous surface and used to serve as the efficient sources to trap and retain the precipitation from the runoff and the fast evaporation; and subsequently allow quick percolation through highly fractured/jointed subsurface basalts for the recharge to the basalt-aquifers and/or the fractured zone aquifers of the underlain Precambrian crystalline basement rocks. Considering a vast area of such favorable terrain, it was anticipated that the large part of the precipitation was/is

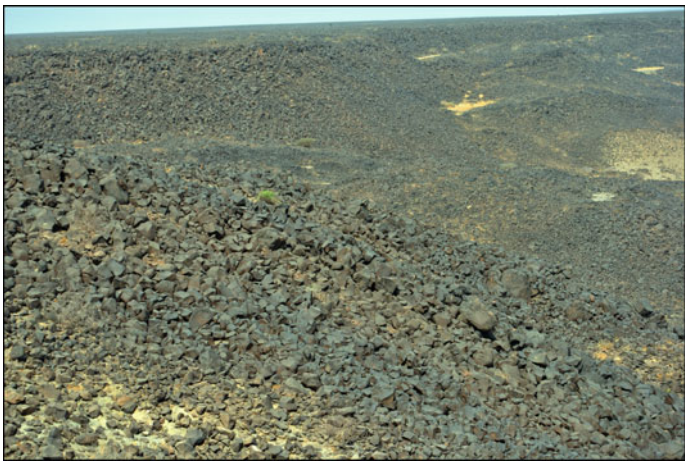

Fig. 2 Basaltic lava-flow terrain of Harrat Rahat, which shows a local escarpment of jointed, fractured and shattered basaltic lava debris in the foreground and its spreading trend in the background

Fig. 3 Satellite image of Rabigh drainage basin shows typical flat-topped basalt-flows with raised margins. The tributary wadis of catchment area display numerous small groundwater springs being oozed out within their courses from the basaltic lava-flows

being infiltrated into the subsurface to recharge the faulted/fractured zone(s) aquifers directly.

Similarly, the flat-top with elevated margins of the basaltic-flows provided the excellent environment to retain the rainwater from the faster runoff and to accumulate for efficient percolation into the underlain fractured basalts and/or Precambrian crystalline rock units. Figure 4 shows the scars of the rainwater accumulation on top of the basaltic lava-flow outcrops with the visible raised peripheral edges. At different locations numerous springs associated with such terrains were also observed mainly in the upstream areas of the tributaries (Fig. 3). Consequently, it was noted that all the wadis flowing towards Red Sea used to receive groundwater-flow in their tributaries emerging from the extensive basaltic terrain in the southern part of the Harrat Rahat.

4.6 Volcanic Rocks and Associated Structures

In general, the exposures of the basaltic lava-flows displayed strong development of joints, which were widely opened showing off-sets under the influence of desert-weathering conditions (Fig. 4A). The large deposits of scoria were found all along the length of the Harrat Rahat volcanic terrain. The dark gray to reddish brown exposures of the scoria rocks indicated the presence of the round bubble-like cavities and/or the vesicles in abundance. Varying sizes of scoria particles, between >2 mm and larger blocks randomly distributed, were observed in the field (Fig. 4B, C), which indicated

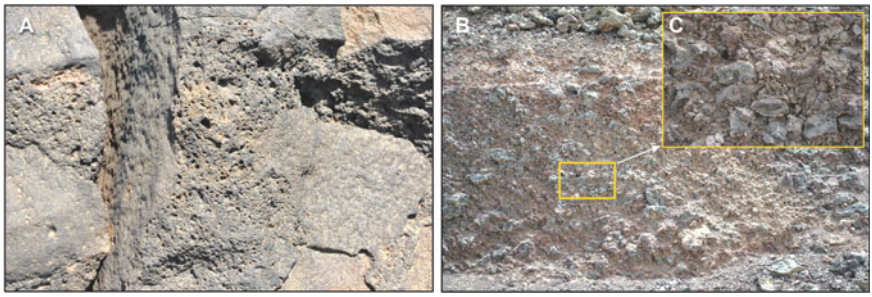

Fig. 4 The vesicles, the open cavities represent escaped gasses and dislocation along joint are seem in basaltic lava-flows within upstream areas of Wadi Qadiad drainage basin (**A**). The cross-section shows nature of scoria exposed in the northernmost part of Harrat Rahat in Al-Madinah area (**B**). Enlarge portion of (B) shows more details of the scoria (**C**)

significantly high porosity. The calculated values of the porosity range between 41 and 47% with an average of 43% (Sabtan and Shehata 2000).

As the basaltic lavas primarily tend to be the fluid with gases, they form thin flows that have considerable pore spaces, due to escaping of the gases at the tops and bottoms of the flows. Numerous basalt-flows commonly overlap and these flows were separated by soil zones or alluvial material, which form permeable zones. Columnar joints that develop in the central parts of the basalt sequence create passages that allow water to move vertically through the basalt (USGS 2012). Moreover, the volcanic rocks are characteristically fine-grained and often exhibit structures caused by their eruption and subsequent lava-flows, e.g., the flow banding formed by shearing of the lava as it flows, lava-tubes etc. Similar features were observed during the field investigations, which indicated the better possibilities to store the large reserves of the groundwater associated with the basaltic rocks of Harrat Rahat.

5 Enhanced Satellite Image Models of Harrat Rahat

The image models were prepared by using customized mosaics derived from the thematic ETM's enhanced image combination of 3, 5, 7 bands and the classification of the single thermal band-7. The study provided the useful understanding related to the interrelationship of the exposed complex setup of the Precambrian rocks and the Cenozoic volcanic terrains and their thermal anomalous trends associated with the Harrat Rahat and the surrounding areas. The study also helped in the cross-confirmation of the inferences drawn related to the hydrogeological setup of the study region.

5.1 Enhanced Image and Rahat Volcanic System

The GIS-linked interactive model was developed by integrating the mosaic of the enhanced images (customized for combination of 3, 5, 7 bands) and the Harrat Rahat basaltic lava-flows with other associated volcanic features (Fig. 5). The model indicated the probability that the SHR basaltic lava moved westward, while it was in the hot and molten form, under the strict control of the older geomorphology and the structural setup of the Precambrian Arabian Shield terrains. The lava over-filled the paleo-drainage channel and spread over the raised shoulders of the valleys, which caused development of several independent watersheds all along the Red Sea coastal belt at the western rifted margin of the Shield. The model also indicated the fact that the lava-flows generally formed the watershed-divides between the adjacent drainage basins as illustrated by the common boundary of two basins passing longitudinally through the lava-flow tongues. Thus, the thickness estimation of the lava-flow tongues was considered to play important role with reference to the prospective hydrogeological conditions. It was deduced that thicker the lava-tongues, the better prospects were expected to exist associated with the basaltic flows.

Coleman et al. (1983) also described that the westward-flowing streams (wadis) cut the gorges as much as 50 m deep through as many as 15 flows that had earlier filled the same wadis on the western edge of Harrat Rahat. Volcanic rocks about the flank of the Precambrian rock terrains and were found interbedded with conglomerate derived from the surrounding mountains. These sections of basalt and interbedded conglomerates indicated that there were several hundred meters of relief in the area at the time of the early eruptions. In contrast, on the eastern margin of Harrat Rahat, the wadis were not deeply incised and as many as 30 m of sections were rarely exposed. The low relief appeared to be the result of deflation of the sabkhah and sand surfaces that flanked the southeastern part of Harrat Rahat. During the present assessment, it was deduced that both the prevailing conditions suggest the better hydrogeological environments associated with the highly faulted/fractured Precambrian terrains buried at shallow depths.

Moreover, the groundwater enrichment of wadis or their tributaries was also observed by the development of the excellent agriculture activities within the wadis' courses during the field traversing as well as detailed RSA studies (Zaigham et al. 2015). For example, it was observed that one of the off-shoots bifurcated trending westward from the main lava-tongue striking NE-SW direction at the southeastern boundary of Rabigh basin. That offshoot of basaltic lava-flow was found terminated against the head of a tributary of the Rabigh drainage basin, which was being governed by the fault/fracture zone passing across the general NE-SW striking trend of the Precambrian rock terrain (Fig. 6).

The hydrological linkage of lava-flow's offshoot to fault/fracture controlled tributary is providing the substantial water recharging in its downstream part, which was reflected in the form of the noticeable agriculture activities. On the basis of the similar setups of the basaltic lava-flows, it was further interpreted that such basaltic lava-flows used to discharge the groundwater and recharge the aquifers through the

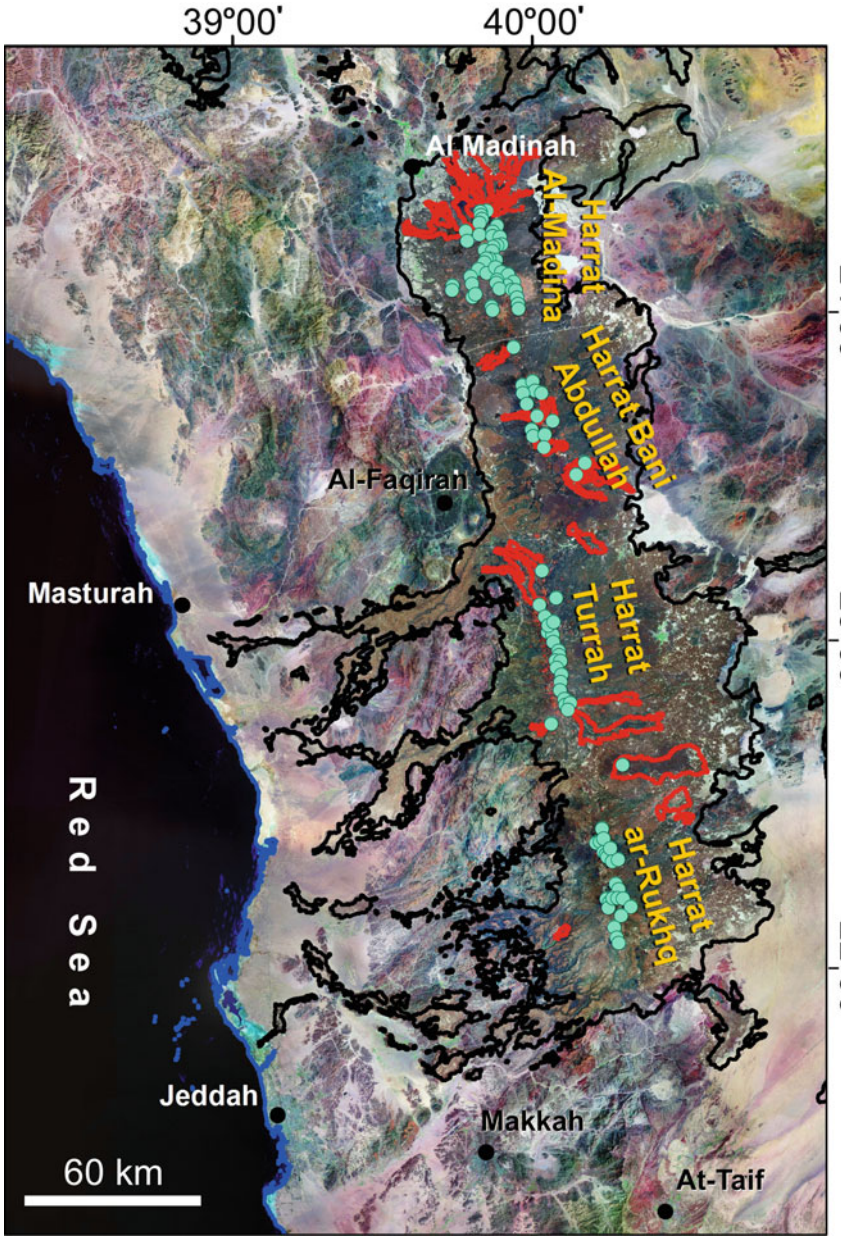

Fig. 5 Map shows an overlay of Harrat Rahat on the customized mosaic of the natural enhanced composite image using 3, 5, 7 bands

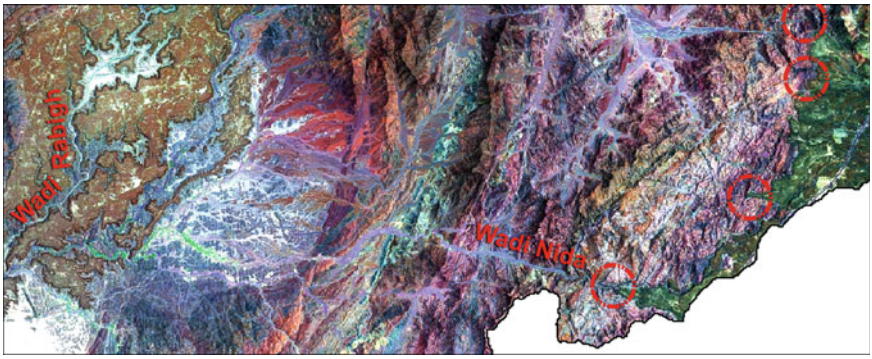

Fig. 6 Image shows west-trending intrusion of lava-flow fringes into the fault/fracture zones in the east, from where the tributary wadis emerged passing across the highly deformed terrain of the Precambrian shield rocks at yellow circle. At the western margin of the image, the agriculture development can be seen within the downstream course of the wadis

fault/fracture zone(s), which were buried beneath the thin soil layer of wadi(s) course at places.

5.2 Thermal Band Enhanced Image Model

The enhancement of ETM band-7 was performed and generated a customized mosaic of the enhanced images by using the thermal band classification (TBC) function. Subsequently, the GIS-linked interactive model was developed by integrating the TBC enhanced mosaic and the Harrat Rahat basaltic lava-flows with other associated volcanic features (Fig. 7). The TBC model displayed the behavior of the natural thermal variations associated with Harrat Rahat and different surrounding terrains of the Precambrian and Cenozoic exposed rocks. The patterns of the thermal anomalies clearly differentiated between the areas of lowest to the highest thermal characteristics associated with the lava-flow terrains, the igneous-metamorphic-sedimentary rocks, the moist and dry soils, the vegetation and the water bodies. It also differentiated the courses of the river/wadi beds with respect to the water moisture, leaky water pools or the vegetation. The anomalies of the thermal digital values shown interesting distribution pattern associated with different parts of Harrat Rahat between Makkah and Al-Madinah areas.

In the SHR areas, the eruptive axial zone and surrounding longitudinal areas of sub-Harrat Turrah and ar-Rukhq dominantly represent the anomalies of lowest values (green: 0–200 DN, i.e. digital number) and the low values (yellow: 200–215 DN) indicating the coolest to cooler nature of the scoria terrains. The eastern as well as the southern marginal areas and the western basaltic lava-flow tongues reflected by the moderate digital thermal values (violet: 215–230 DN). But on the western side of the SHR, the Precambrian rock terrains, exposed in between the basaltic lava-flows, also

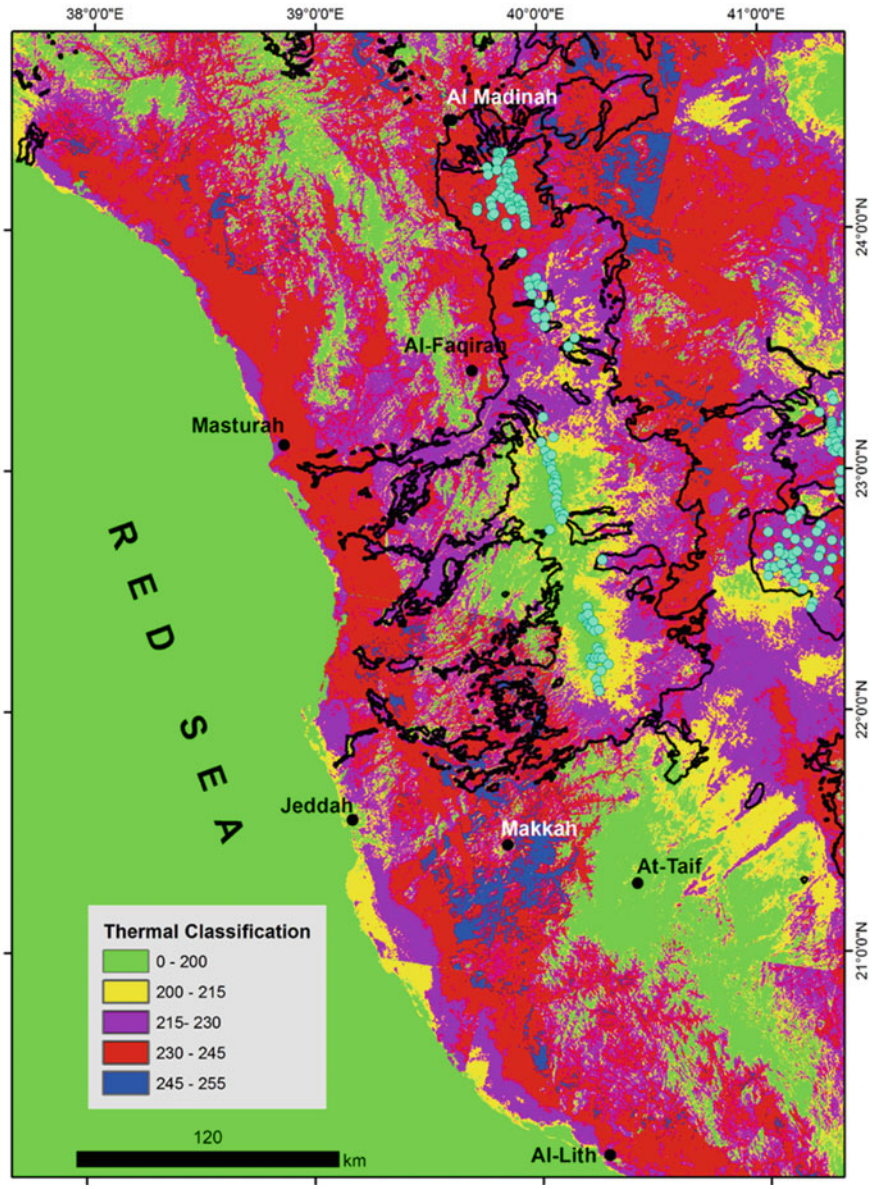

Fig. 7 Map shows an overlay of Harrat Rahat on the customized mosaic of the thermal band digital values

shown the dominant association of the lowest (coolest) thermal values. Those trends further southwestward continue in the form of narrow striation of lowest (coolest) to low (cooler) thermal values striking in NE-SW orientations associated with the fault/fracture zones representing the prospective aquifer targets on the regional scale. The western lava-flow tongues and the eastern and southern coalesced lava-flow terrains show moderate thermal values (violate: 215–230 DN) indicating the surface weathering of the lava-flows from fine to coarse grains with near surface moisture. At places, striations of cooler color (yellow: 200–215) were observed associated with the wadis' courses flowing within the basaltic lava-flows. Such conditions indicated the near-surface groundwater flow within those wadis.

On the other end, the sub-Harrats of NHR, Bani Abdullah and Al-Madinah, indicated totally different thermal characteristics from each other and also with respect to the sub-Harrats of SHR. On the contrary, no lowest thermal anomalous (green: 0–200 DN) zone was observed associated with the axial linear cluster of the eruptive centers within sub-Harrat Bani Abdullah. The moderate thermal values (violate: 215–230 DN) dominated in that part of NHR. However, the cooler thermal anomalies (yellow: 200–215 DN) were observed showing elongated radial distribution trends towards east, south and southwest from the linear cluster spreading of the eruptive centers. The wadis, flowing within the northern most basaltic lava-flow tongue of sub-Harrat Turrah, were found to have their catchment linked with southwestern part of the elongated radial distribution system of the low thermal anomalies (yellow: 200–215 DN) of the sub-Harrat Bani Abdullah in the southeast of Al-Faquirah locality.

On the other hand, the low (cooler) or the lowest (coolest) valued thermal anomalies were weakly developed within the sub-Harrat Al-Madinah segment particularly around the zone of the eruptive centers. In general, the eruptive rock material shown dominantly high (red: 230–245 DN) thermal anomalous character with smaller pockmarks of highest (blue: 245–255 DN) thermal values within the sub-Harrat terrain. However, all the younger lava-flows, erupted from the northern centers, reflected moderate (violate: 230–245 DN) thermal values. In addition, the small patches of moderate thermal values were also observed randomly distributed at some places.

One of the most important observations, from the hydrogeological point of view, was the linear narrow zone of lowest thermal anomalies prevailing parallel to the western boundary of sub-Harrats Bani Abdullah and Al-Madinah. This zone of the lowest thermal anomalies corresponds with the regional fault zone interpreted on the basis of the flow-trends of the drainage systems emerging from NHR segments (Fig. 8). Based on this observation, it was deduced that the western drainage networks emerging from NHR segments provide substantial recharge to more than 200 km long SE-NW trending regional fault/fracture zone(s) consisting of the bright prospects for the excellent fault/fracture zone aquifer(s), which is tentatively marked by red hollow arrows in Fig. 8. Likewise, a relatively wider zone comprising numerous small anomalies from the lowest (green) to moderate (violate) thermal values were also uniquely observed spreading from the eastern boundary of sub-Harrat Bani Abdullah to another big Harrat Al-Kishb eastward in NW–SE direction. Individually, these small thermal anomalies show strong NE-SW trends, which were also inferred to be the highly prospective groundwater region between the two major volcanic fields.

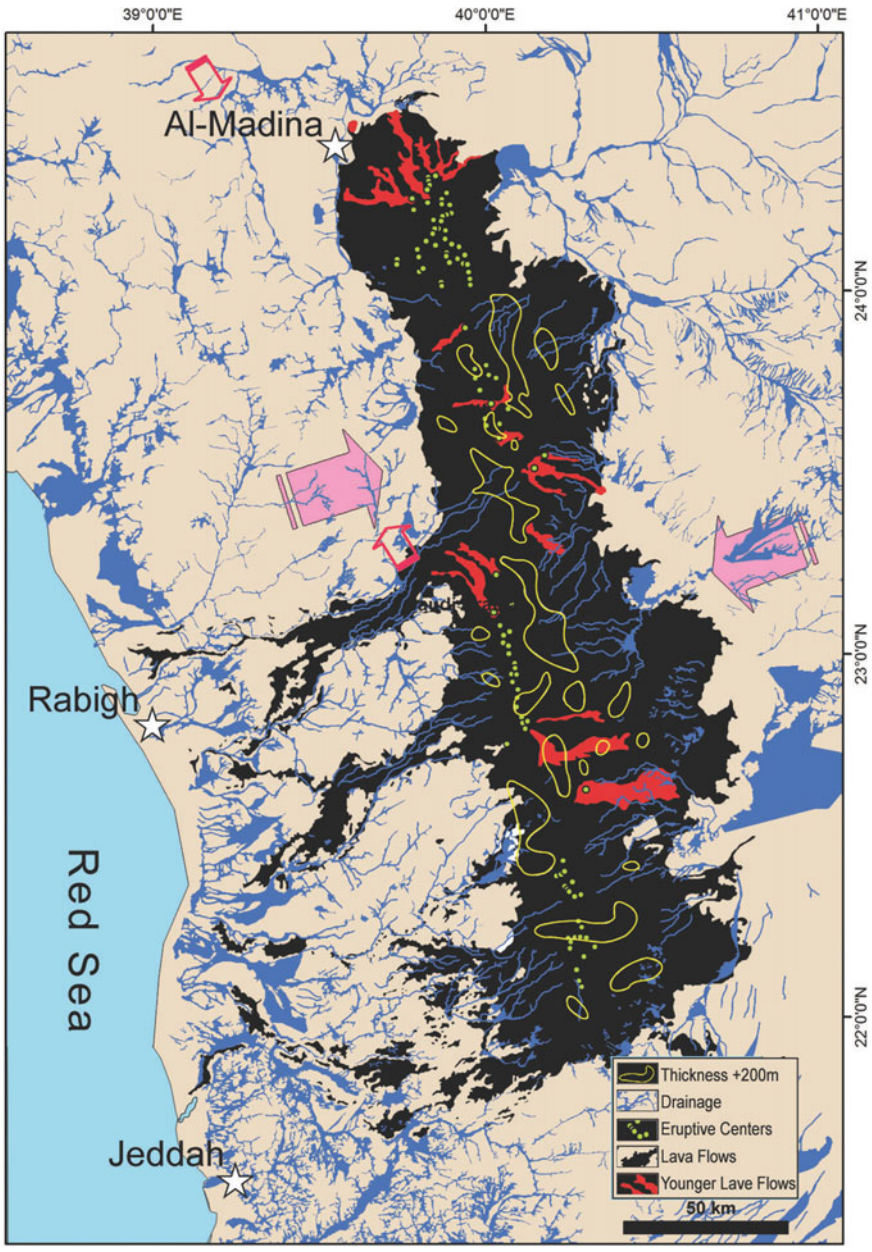

Fig. 8 Customized model shows interrelationship between the eruptive feature of Harrat Rahat, the estimated anomalies of basalt thicknesses greater than 200 m (as shown with white contour lines) and the drainage systems prevailing at the western rifted margin of Arabian Shield along the eastern coastal belt of Red Sea

On the basis of the results of the empirical analyses of the enhanced images subsequent correlation with the volcanic features, it has explicitly been identified that those terrains representing the lowest (coolest) to the low (cooler) thermal effects indicated the bright prospects for accumulation of the groundwater and the recharging of the basaltic as well as the fault/fracture zone aquifers. Such excellent hydrogeological conditions were manifested by the presence of the discharging of the groundwater in the form of the springs within the wadis' channels at places on the surface and/or the groundwater discharges along the Red Sea coastline as well as offshore areas.

6 GIS-Linked Hydrogeo-Model

Thematic Layers for GIS-linked Modeling: Several thematic layers were prepared for the present study, which included the geo-referenced boundary of Harrat Rahat basaltic bodies, the eruptive volcanic centers, the anomaly contours of the basaltic thickness, the semi-regional drainage networks, the salient city locations, eastern boundary of Red Sea, etc. The boundaries of the older and the younger basaltic bodies and the locations of the eruptive centers were digitized in the form of three separate thematic layers from the map of Coleman et al. (1983). The anomaly contours representing only 200 m basaltic thickness were digitized from the thickness contour map of the study on the spectral analysis of the 1976 aeromagnetic survey of the Harrat Rahat by Blank and Sadek (1983). The semi-regional drainage networks, the Red Sea coastline and the city locations were extracted and digitized, in the form of separate thematic layers from several geological maps published on 1:250,000 scale by the Deputy Ministry for Mineral Resources (1980's). The bit and pieces of all the thematic layers were domain-wise integrated and subsequently were georeferenced for further input during the hydrogeological modeling.

GIS-linked Model: All the prepared thematic layers were interactively superimposed to generate the rational model for the volcanic terrains of the Harrat Rahat that provided a good understanding regarding the associated hydrogeological features (Fig. 8). The model revealed the interesting interrelationship between the drainage systems, flowing westward and eastward with respect to the north-trending axial zones of eruptive centers and the maximum thick basalts, which represents the present elevated and steep topography of the Harrat Rahat. Thus, the cinder cones have steep relief and the scoria has an angle of repose of 30–40 degrees.

It was interpreted on the basis of the interactive analysis of the model that the NWW-trending axial zone of the eruptive volcanic centers and the associated thickest basaltic bodies commutatively plays important role as a regional 'water-divide'. It was observed that all the smaller tributaries used to emerge from the eruptive cones of the 'axial zone' in the upstream catchment areas, particularly the western drainage systems extending down to the Red Sea. On the other hand, the drainage networks, on the east side of the axial zone, displayed different nature of the wadis' flow trends as compared to the western ones. Most of the smaller wadis, emerged from the eastern

side of the zones of eruptive centers or the basalt thickness anomalies, and merged just after flowing short distances, particularly associated with Harrat Turrah and ar-Rukhq segments. Field investigations identified heavy deposition of windblown sand and silt at the eastern margins of these Harrat segments. From the eastern margins of these windblown deposits, the smaller wadis reappeared and flowed parallel to each other. In general, the drainage network is poorly development as compared to the drainage networks developed westward of the main volcanic eruptive axial uplifted north-trending regional water-divide.

In case of the NHR segments, the Bani Abdullah and Al-Madinah sub-Harrats, shown entirely different patterns of the drainage systems with each other and also as compared to SHR segments. The sub-Harrat Bani Abdullah shown no large drainage systems emerging from west or east sides of the well-defined zones of erupting centers and/or the thick-basalt, accept a few smaller sub-parallel flowing wadis terminating almost at the extent of the exposed lava-flows. Eastward, a few smaller tributaries emerge from sub-Harrat Bani Abdullah and merge into one contributory of very big drainage network of east Al-Madinah region flowing from north-central part of the Shield to northwest passing across the northernmost part of the sub-Harrat Al-Madinah.

On the other hand, apparently no major wadi or the wadi-system emerges from the zone of the axial erupting centers of sub-Harrat Al-Madinah. Uniquely, it was observed that the wadis emerged from the western marginal areas of this sub-Harrat. Moreover, weekly developed localized internal drainage trends were also noticed associated with the individual eruptive centers. The small tributaries did emerge in radial to sub-parallel patterns from the cinder crest, but they did not merge into any major wadi and/or made larger drainage network. It was observed that the flow of those tributaries was used to block at the short distances as soon as encountered with the overlying layer(s) of younger lava in the lower reaches. The seasonal drained rain-water got accumulated around the peripheries of the younger overlying lava-flows. The accumulated rainwater used to percolate and also expected to keep flowing through the buried contact-zone(s) between older and younger lavas and/or evaporates too. For an example, about 34 km distance in the southeast of Al-Madinah city, it was observed that the short-run drainage was developed from the crest of erupting centers at 1400 m elevation flowing northwestward (Fig. 9). The tributaries were intercepted at about 4–5 km down the slopes by the younger lava-flows, where the general ground elevation was about 1000 m. In this case, the periphery of the younger lava-flows was observed to serve as semi-regional dam(s) like structures. The water of periodic rains was seen accumulated around the periphery of the younger lava-flows in northwestern downstream area. White patches shown the clay development after percolation and subsequent evaporation of accumulated water. Such hydro-geological conditions were interpreted to be the most important factor for the excellent recharging of the lateral aquifer(s) in between the older and younger basaltic lava-flows.

On the basis of these inferences, it was deduced that such lateral aquifer zones seemed to be associated with the lateral unconformable alluvial/altered weathered sequences between the young, younger, youngest, old, older and/or oldest basaltic

Fig. 9 Panoramic scene shows emergence of tributaries from the crest of the eruptive centers, which have been blocked by the younger basaltic lava-flows. Moreover, the white pockmarks indicate the large-scale percolation of rainwater

lava-flows. The aquifer zones discharge groundwater and/or floodwater through fault/fracture zones in the form of wadis parallel to the western margin of sub-Harrat Al-Madinah. In the northwestern marginal part, the emerging wadi-system flowed along the margin of Harrat and merged into the other wadis' net-work of the Al-Madinah region. In southwest of sub-Harrat, two major drainage wadi systems emerged, which initially used to flow southward parallel to periphery of the basaltic periphery for short distances and then take almost 90° turning trend flowing north-westward again for relatively short distances. NW-flow directions of the main wadis' channels swings at cumulative 90°, but in opposite directions within the intensely deformed Precambrian hard rocks of Arabian Shield; the southern wadi-system turned in SSE direction and kept changing its directions further to westwards flowing significantly longer distance till it merged into the major Al-Abwa drainage network draining into the Red Sea; and the other northern one tooak 90° turn in NNW direction and ultimately merged into the downstream part of the regional Al-Madinah drainage network. From the general rectangular/trellis pattern of the wadi-courses, it was inferred that the regional, semi-regional and/or large fault/fracture zones control the flow directions of these drainage systems. It was also interpreted that the NNW-SSE flow directions of main wadis' course-segments were being controlled by a regional fault/fracture zone marked with arrows (Fig. 8), which seemed to be an excellent target for aquifer(s) within the faulted/fractured Precambrian rocks terrain.

Apparently, no major wadi emerged from the western or the northern margins of the sub-Harrat Al-Madinah. However, a large drainage network, in the regional hydrogeological setup, was used to flow from mid-northwest of Arabian Shield in southwest-northwest orientation passing across the northeastern part of the sub-Harrat. The main wadi course was intercepted by constructing a dam at the eastern margin of the lava-flows southeast of Al-Madinah city. The field investigations witnessed that such an interruption of the big drainage system provided enormous

water for its harvesting, particularly in flooding-periods after heavy rains in eastern region of Al-Madinah area.

In the case of the SHR segments, the Harrat Turrah and ar-Rukhq segments, it was assessed on the basis of the detailed field investigations and the intensive satellite remote sensing and the watershed analyses (Zaigham et al. 2015; Aburizaiza et al. 2012) that the majority of the tributaries of six drainage basins from Rabigh to Fatima emerged from the axial volcanic basaltic lava-flow terrains. An enormous amount of the accumulated rainwater used to recharge the fault/fracture zone aquifers of these basins from the elevated volcanic terrains of SHR segments through numerous tributaries covering the cumulative area of about 21,200 km^2 at the western rifted margin of Arabian Shield along the Red Sea coastal belt. In contrary, the SHR segments displayed the poor development of the drainage network emerging from the volcanic terrain on its eastern side.

7 Discussion

The dependence of the groundwater potential, particularly in the arid and semi-arid regions, was considered to be proportional to the available water sources to recharge the aquifer(s). In case of Saudi Arabia, PME (2005) analyzed that the seasonal and annual average precipitation in Saudi Arabia is generally low (±100 mm/year) except in the southwest region, where it is the highest (±500 mm/year) in the country. Rainfall varies from season to season and year to year and exhibits an interesting distribution trend extending from southwest of Makkah towards northeast across the country. On the other hand, the relative humidity exhibits a maximum seasonal variation in the inland and at the eastern coast areas, but the relative humidity is high all year round along the Red Sea coast. Thus, considering the prevailing climatic conditions, it is deduced that in case of the study area, the relatively low to moderate magnitude precipitation, except occasional thunderstorms, which create flash floods, is the only recharge source for the groundwater aquifer(s) against the high temperature conditions. Moreover, there is no glacier supported big river system in and around the study area or even in the country. On the basis of the general precipitation trends and the average values of precipitation, it has been assessed that the total area of 13-Harrats of Saudi Arabia, i.e., 100,000-km^2, may capture rainwater ranging between 20 and 30 km^3 annually.

However, it was observed that the main geomorphological terrains may have the average maximum precipitation in order of >100, 230 and 650 mm in low-lying coastal areas, foothill area and the mountainous areas respectively, which strongly reflects the orographic effects (PME 2005; Austin and Dirks 2006; Subyani et al. 2010; Almazroui et al. 2012). Thus, in case of Harrat Rahat elevated mountainous terrain, the average minimum precipitation of 200 mm/year and/or optimum 300 mm/year was into account for the estimation of an average range of the recharge conditions. Using the delineated total area of about 20,000 km^2 (Coleman et al. 1983) and the average precipitation, it has been determined that only the exposed Harrat

Rahat terrain captures about 4.0–6.0 km^3 rainwater annually that is about 20% of rainwater captured by the remaining 12-volcanic fields of Saudi Arabia. Moreover, considering the average thickness of 150 m and the total area of 20,000 km^2, the volume of the erupted basaltic lava-flows of Harrat Rahat was estimated to be about 3,000 km^3. Likewise, the calculated values of the primary porosity range between 41 and 47% with an average of 43% (Sabtan and Shehata 2000), and the secondary porosity and the permeability inferred on significantly higher side in the form of intense inherited jointing, fracturing and micro, mega or regional faulting as directly observed during the field traversing across the volcanic terrains.

Moreover, the field observations revealed that most the rainwater is trapped within the highly rough surface of the basaltic lava-flows in the form of the vast weathered and fractured blocky basalt terrains. Subsequently, the trapped rainwater percolates rapidly into the subsurface of the Harrat Rahat volcanic terrains. In turn, the runoff and the evaporation of the rainwater were weighed to be much lesser than subsurface infiltration. Under the prevailing hydrogeological conditions as discussed in preceding paragraphs/sections, it has been considered that the volcanic terrains of Harrat Rahat are the excellent sources for the recharge of basalt-aquifers as well as the fault/fracture-zone aquifers hosted within the Precambrian hard rock terrains exposed and/or buried beneath the basaltic lava-flows. The water-enrichment of these aquifers is reflected from the considerable discharges of groundwater along the coastline of Red Sea.

8 Conclusion

The results of the research have revealed the better understanding about the interrelationship among the prevailing hydrogeological setups, the nature of the basaltic lava-flows associated with the different segments of Harrat Rahat, and the bright prospective areas with respect to new groundwater findings. Moreover, it has also been identified that the basaltic lava and/or scoria serve dual roles in controlling the hydrogeological conditions in the study region. They were expected to host the basalt-aquifers as well as play excellent role as the recharge sources for the prospective fault/fracture-zone aquifers within the Precambrian rock terrains exposed and/or buried beneath the basaltic lava-flows of Harrat Rahat. Present study opens new areas for more detailed research studies for the exploration and the exploitation of groundwater resources within the identified region at the western rifted margin of Arabian Shield in Saudi Arabia.

Acknowledgements Authors are highly thankful to King Abdulaziz City for Science & Technology (KACST), Saudi Arabia to provide financial support vide Grant #: 8-WAT 140-3, and King Abdulaziz University, Jeddah, Saudi Arabia for providing technical support for the project work. Prof. K. A. Mallick, University of Karachi, Pakistan and Mr. Jamiluddin Ahmed, Ex-Director, Geological Survey of Pakistan, Pakistan, are highly acknowledged for their technical reviews of the manuscript.

References

Aburizaiza OS, Zaigham NA, Nayyar ZA, Mahar GA, Siddique A, Noor S (2012) Remote sensing analyses of offshore and land areas in Jeddah-Makkah-Taif & surrounding regions and appraisal of existing water resources: approved report of King Abdulaziz University, Jeddah by King Abdulaziz City for Science & Technology, Riyadh, 492p

Almazroui M, Islam N, Athar H, Jones PD, Rahman MA (2012) Recent climate change in the Arabian Peninsula: annual rainfall and temperature analysis of Saudi Arabia for 1978–2009. Int J Climatol 32(6):953–966. https://doi.org/10.1002/joc.3446

Austin GL, Dirks KN (2006) Topographic effects on precipitation. http://onlinelibrary.wiley.com/doi/10.1002/0470848944.hsa033/abstract

Babar, Shah II (2012) Influence of geological and geomorphological characteristics on groundwater occurrence in deccan basalt hard rock area of Tawarja river sub-basin Latur, Maharashtra, India. Res J Environ Earth Sci 4(4):440–447

Bennetts DA, Webb JA, Gray CM (2003) Distribution of Plio-Pleistocene basalts and regolith around Hamilton, western Victoria, and their relationship to groundwater re-charge and discharge. In: Advances in Regolith, pp 11–15

Blank RH, Sadek HS (1983) Spectral analysis of the 1976 aeromagnetic survey of Harrat Rahat, Kingdom of Saudi Arabia: USGS, Open-File Report 83–640, for Ministry of Petroleum and Mineral Resources, Deputy Ministry for Mineral Resources, Jiddah, Kingdom of Saudi Arabia, 29p

Camp VE (1986) Geological map of the Umm Al Birak Quadrangle, sheet 23D, Kingdom of Saudi Arabia: Ministry of Petroleum and Mineral Resources

Camp VE, Hooper PR, Roobol MJ, White DL (1987) The Madinah eruption, Saudi Arabia: magma mixing and simultaneous extrusion of three basaltic chemical types. Bull Volcanol 49(2):489–508

Campi R (1969) Ground water test holes in the Jabal Sayid area: Bureau de Recherches Geologiques et Minieres (Saudi Arabian Mission) Report 69-JED-29,42p

CGWB (2013) Systematic hydrogeological surveys: Central Groundwater Board (CGWB), Ministry of water resources, Govt of India, North central region, Bhopal. http://cgwb.gov.in/ncr/highlights.htm. Accessed 4 July 2013

Choi CQ (2010) Ancient volcanic field reawakens in Saudi Arabia: the Christian science monitor—CSMonitor.com. http://www.csmonitor.com/layout/set/print/Science/2010/0926/Ancient-volcanic-field-reawakens-in-Saudi-Arabia. Accessed 29 Oct 2013

Coleman RG, Gregory RT, Brown GF (1983) Cenozoic volcanic rocks of Saudi Arabia: USGS Open-file Rpt-83–788, 82p

Daessle M (1973) Jabal Sayid water-supply, Hydrogeological study of the Harrat Rahat basalt (Adh Dhumariyah district): Bureau de Recherches Geologiques et Minieres (Saudi Arabian Mission) Report 73-JED-9, 48 p

Jefferson A, Grant G, Rose T (2006) Influence of volcanic history on groundwater patterns on the west slope of the Oregon high cascades. Water Resour Res 42:W12411. https://doi.org/10.1029/2005WR004812

Kebede S (2013) Groundwater in Ethiopia. In: Springer hydrogeology. Springer-Verlag Berlin Heidelberg. https://doi.org/10.1007/978-3-642-30391-3_2

Locsey KL (2004) Hydro-geochemistry and hydrology of a basalt aquifer system, the Atherton Tablelands, North Queensland: PhD by Publication, Queensland University of Technology. http://eprints.qut.edu.au/16594/. Accessed 7 June 2012

Mulwa JK, Gaciri SJ, Barongo JO, Opiyo-Akech N, Kianji GK (2005) Geological and structural influence on groundwater distribution and flow in Ngong area, Kenya. Afr J Sci Technol 6(1):105–115

Nyblade A, Park Y, Rodgers A, Al-Amri A (2006) Seismic structure of the arabian shield lithosphere and red sea margin. MARGINS, Newslett 17:13–15

Peate DW (1997) The Parana-Etendeka province: in large igneous provinces: continental, oceanic, and planetary flood volcanism. Geophys Monogr 100 AGU:217–245

PME (2005). First National Communication on Kingdom of Saudi Arabia: Report by Presidency of Meteorology and Environment, Riyadh, KSA, submitted to the UNFCCC, 142p

Rampino MR, Stothers RB (1988) Flood basalt volcanism during the past 250 million years. Science 241: 663–668

Ramsay CR (1986) Geological map of the Rabigh Quadrangle, sheet 22D. Kingdom of Saudi Arabia: Ministry of Petroleum and Mineral Resources

Sabtan AA, Shehata WM (2000) Evaluation of engineering properties of scoria in central Harrat Rahat, Saudi Arabia. Bull Eng Geol Environ 59:219–225

Sen G, Chandrasekharam D (2011) Deccan traps flood basalt province: an evaluation of the thermochemical plume model: Springer. In: Ray J, Sen G, Ghosh (eds) Topics in igneous petrology, pp 29–53. https://doi.org/10.1007/978-90-481-9600-5_2

Shaibani MA (2003) Lava fields as potential groundwater sources in western Saudi Arabia. In: Sherif S, Al-Rashed (eds) Hydrology and water resources. Swets & Zeitlinger, Lisse. ISBN 90 5809 548 7

Shaibani A, Lloyd JW, Abokhodair AA, Al-Ahmari (2006) Hydrogeological and quantitative groundwater assessment of the basaltic aquifer, northern Harrat Rahat, Saudi Arabia. Arabian Gulf Univ, Arab Gulf J Sci Res 25:39–49

Shukri NM, Basra EZ (1955) Petrography of the alkaline volcanic rocks of Yemen. Inst Egypt Bull 36:129–164

Singhal BBS (1997) Hydrological characteristics of Deccan trap formations of India. In: Hard rock hydro-systems. IAHS Publication 241, pp 75–80

Stephenson PJ, Griffin TJ, Sutherland FL (1980) Cenozoic volcanism in northeastern Australia. In: Henderson RA, Stephenson PJ (eds) The geology and geophysics of northeastern, Australia, Geological Society of Australia, Queensland Division, Brisbane, pp 349–374

Subyani MA, Al-Modayan AA, Al-Ahmadi FS (2010) Topographic, seasonal and aridity influences on rainfall variability in western Saudi Arabia. J Environ Hydro 18 (2)

Tolan T, Lindsey K, Porcello J (2009) A summary of Columbia River Basalt Group geology and its influence on the hydrogeology of the Columbia River basalt aquifer system: Columbia basin ground water management area of Adams, Franklin, Grant, and Lincoln counties: Columbia Basin, Ground Water Management Area (GWMA), 32p. http://www.cbgwma.org/pdf/GWMA_Geology-Hydrogeology%20of%20CRBG_TEXT_June%202009.pdf

Torrent H (1976) Jabal Sayid water supply, part I, Hydrogeology of the Harrat Rabat basalt: Bureau de Recherches Geologiques et Minieres (Saudi Arabian Mission) Report 76-JED-8, 60 p

USGS (2012) Volcanic aquifers basic. http://water.usgs.gov/ogw/aquiferbasics/volcan.html. Accessed 28 June 2012

Vervaeck A (2011) Surtseyan eruption along the coast of Yemen forms a New Island-: Earthquake-report.com. http://earthquake-report.com/2011/12/29/surtseyan-eruption-along-the-coast-of-yemen-forms-a-new-island-today-eruption-cloud-stain/. Accessed 4 Jan 2012

Walker GPL (1993) Basaltic-volcano systems. In: Prichard HM, Alabaster T, Harris NBW, Neary CR (eds) Magmatic processes and plate tectonics. Geological Society Special Publication 76, pp 3–38

Wikipedia (2013) Siberian traps. http://en.wikipedia.org/wiki/Siberian_Traps. Accessed 29 Sept 2013

Zaigham NA, Aburizaiza OS, Mahar GA, Nayyar ZA, Siddique A (2015) Watershed analysis of Rabigh drainage basin, Saudi Arabia. Int J Water Resour Arid Environ 4(2):138–145. ISSN 2079-7079

Regional Mapping of Groundwater Potential Zones in the Saudi Arabia Using Remote Sensing and Machine Learning Algorithms

Samy Elmahdy and Mohamed Mohamed

1 Introduction

Groundwater plays a vital role in supplying fresh water for drinking and human activities such as industry and irrigation. However, excessive consumption of groundwater from groundwater aquifers and scarce rainfall make them susceptible to pollution-related activities (Elmahdy and Mohamed 2013; Dimock 1961).

Climate and rainfall pattern changes might affect groundwater recharge in the entire region and have led to sharp depletion in groundwater level and quality (Elmahdy and Mohamed 2013; Carmona et al. 2013). The hydrological setting of Saudi Arabia aquifers is explored only from oil wells and geophysical reports over a local scale due to its harsh weather, lack of rock outcrops, the complexity of hydrological systems, and limited data availability is very hard to investigate climate change the impacts on groundwater systems (Dimock 1961; Geert et al. 2001: De Graaf et al. 2017).

1.1 Geography and Hydrology of Saudi Arabia

Saudi Arabia lies between latitudes 15° 14′ 00″ N and 31° 1′ 52″ N and longitudes 36° 55′ 33″ and 52° 52′ 12″. It occupies an area of about 2.15 million km^2, and it represents the largest country in the region (Fig. 1). The rainwater flows from the mountainous area to the lowlands and depressions in the east, northwest, southeast

S. Elmahdy (✉) · M. Mohamed
Civil and Environmental Engineering Department, United Arab Emirates University, P.O. Box 15551, Al-Ain, UAE
e-mail: samy@uaeu.ac.ae

M. Mohamed
e-mail: m.mohamed@uaeu.ac.ae

A. Shaban (ed.), *Satellite Monitoring of Water Resources in the Middle East*,
Springer Water, https://doi.org/10.1007/978-3-031-15549-9_18

and the Red Sea in the west; recharging the aquifers in the region (Fig. 1). Saudi Arabia is located within inaccessible terrain due to its harsh climatic conditions. It is characterized by a dry hot climate, and temperature ranges from 41° to 55 °C during summer and from 15° to 27 °C during winter.

The rainfall during summer is low and ranges from 0 to 14 mm and could reach above 700 mm during October mm and is a function of groundwater recharge, which varies from 0 to 4% (Woods and Imes 1995) (Fig. 2a).

The aquifers are recharged at a rate of approximately 2200 MCM/year, most of which goes to recharging shallow aquifers (Edgell 1997). The rate at which aquifers are recharged partially depends on topographic slope, flow direction, faults density, and soil texture (Burdon 1982). Geographically, the region is divided into the continental shelf in the east and southeast and the Arabian Shield in the west.

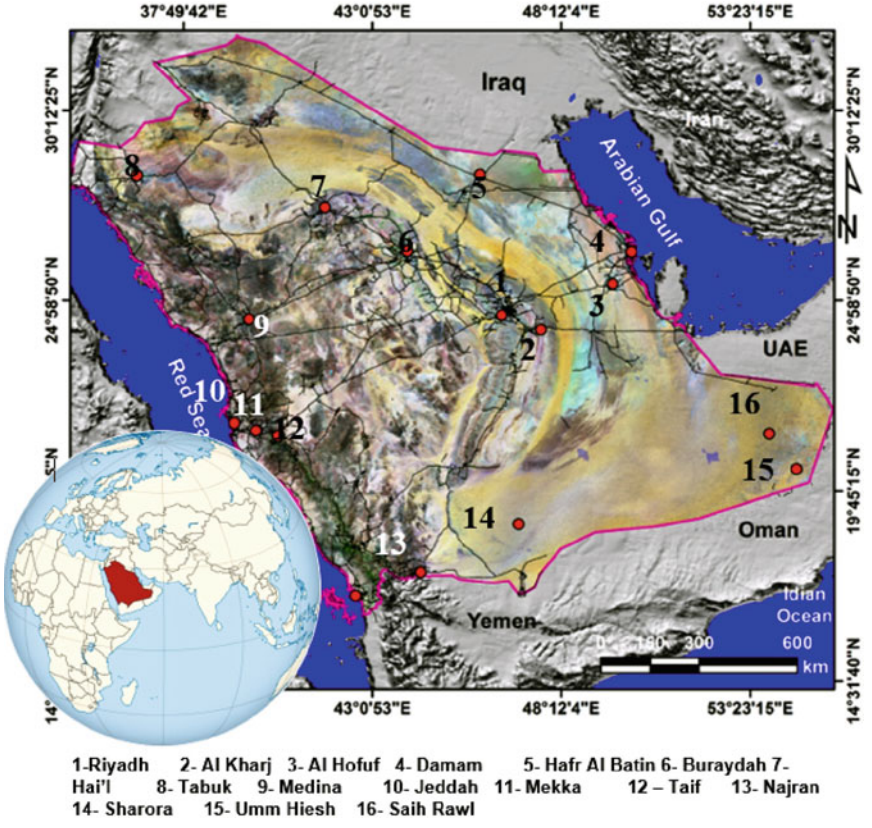

Fig. 1 RGB 652 band combination of 2021 Landsat-8 image of Saudi Arabia. Red points highlight city locations

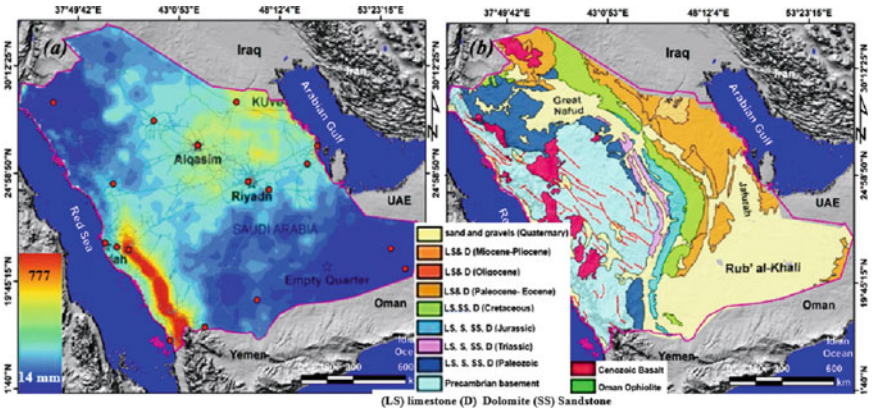

Fig. 2 Maps of rainfall (**a**), and geology (**b**) showing the spatial distribution of precipitation and lithological and structural unites across the Saudi Arabia (Dimock 1961; Geert et al. 2001)

1.2 Arabian Shield

The Arabian Shield is a rugged mountain range that consists of igneous and metamorphic rocks; it is identified as the Assir Mountains (elevation: 5000 m) and the Hejaz Mountain (elevation: 4500 m).

To the west, the shield consists of basalts of mid-tertiary and Quaternary periods and forms Harrat (Fig. 2b). This shield occupies the western side of the Arabian Peninsula and its rocks are relatively impermeable and are therefore not significant hydrologic aquifers (Brown 1960; Al-Sayari and Zoetl 1978; Al Tokhais and Rausch 2008; GASTAT 2016).

However, small yields of water could be found in the heavily fractured hard rocks. Hydrologically, the rocks forming the Arabian Shield are commonly impermeable and, thus, shed most of the rainwater falls on them, pushing a large amount of the rainwater to the adjoining sedimentary aquifers that can store some of the water (MAW 1984) (Fig. 2b).

1.3 The Continental Shelf

The continental shelf is a lowland and depression that consists largely of sedimentary rocks and includes the Nafud desert in the north and Al Rub Al Khali in the south (Fig. 2b). The major trends of the primary mountains in the region are mostly in the N34°W direction and parallel the Najd fault zone; the other system (N8°E) parallels the Hail Arc, and S89°W parallels the central Arabian Arch (Fig. 2b). The bedrock geology in the region consists mainly of Quaternary sandstone (porous aquifer)

underlain by carbonate rocks (karstifed fractured aquifer) (Clark 1989; Sharaf and Hussein 1996).

The continental shelf consists of six aquifers that are locally known as Wajid sandstone, Saq sandstone, Tabuk (Tawil), Minjur sandstones, Wasia/Biyadh/Sakah sandstones and Umm Er Radumalimestone (Fig. 3). These aquifers are consolidated sedimentary rocks (sandstone and limestone) located in the eastern and central parts of the region (Sharaf and Hussein 1996).

The Saq aquifer is the most valuable and occupies an area of approximately 300,000 km^2. It has the largest aerial extension and the most productive aquifer in the region (Edgell 1997). The Saq aquifer has a thickness ranging from 150 to 500 m and an effective porosity exceeding 15% (Sharaf and Hussein 1996; Edgell 1997). This shelf was formed and developed during the Cambrian and continued until the Pliocene Epoch. These layers exposed an intensive geologic event leading to folding and faulting followed by long periods of erosion by wind and water.

The hydrologic units in the Arabian Shelf consist of the Upper Mega Aquifer System and the Lower Mega Aquifer System. The Upper Mega Aquifer System is separated from the Lowe Mega Aquifer System by the Hith aquiclude. The Upper

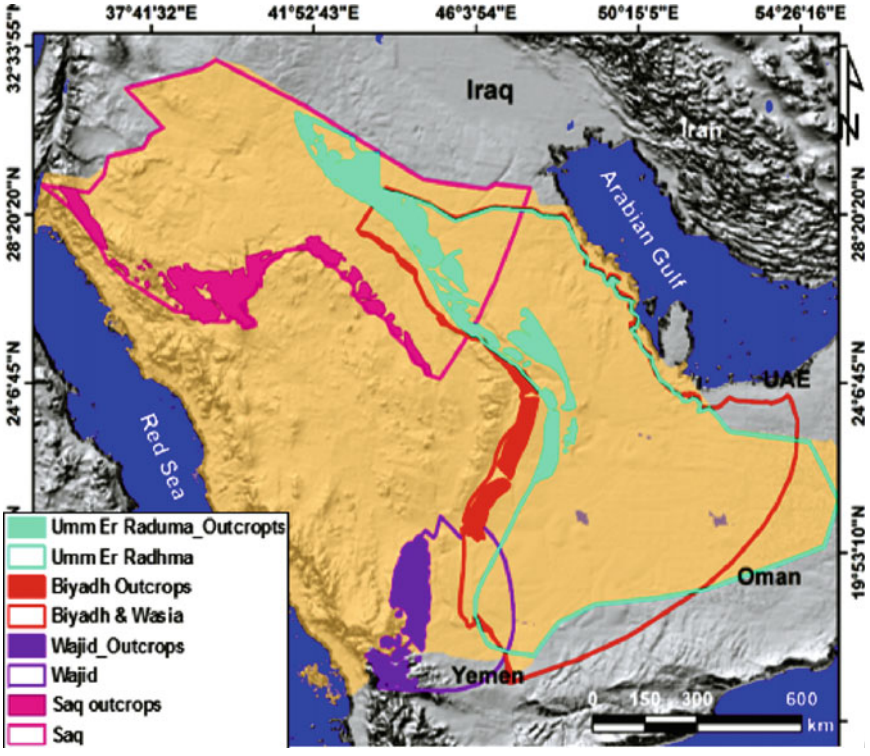

Fig. 3 Groundwater aquifers and their outcrops in the Saudi Arabia (Modified from Fanak 2012)

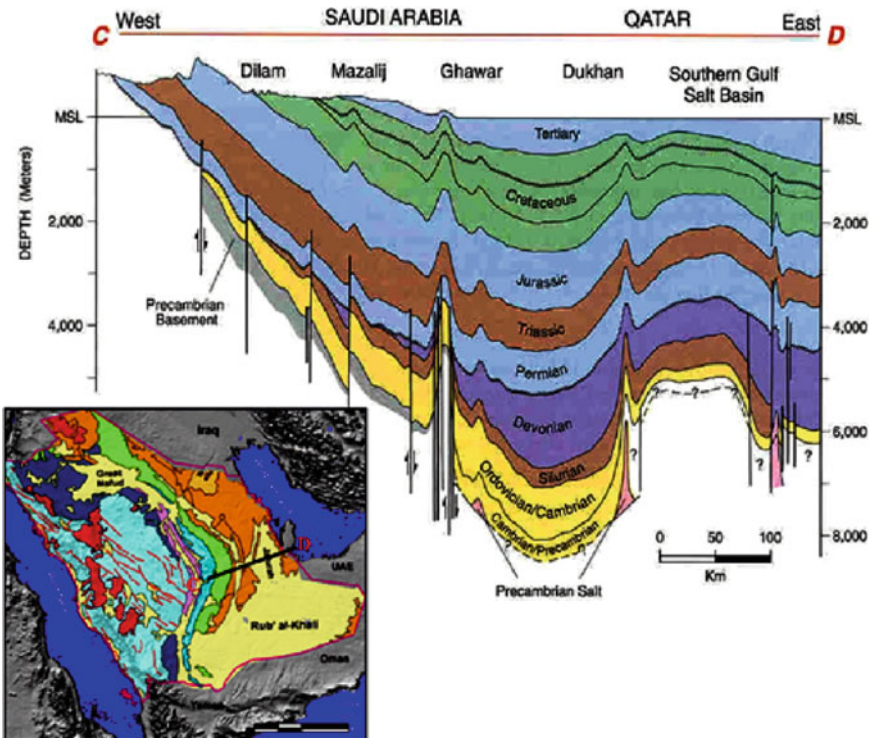

Fig. 4 Stratigraphic cross-section along the continental shelf and depth of groundwater aquifers. Source for this figure?

Mega Aquifer System comprises a sedimentary succession follow to the period from Jurassic to Tertiary (Figs. 3 and 4).

The sedimentary succession consists of limestone, dolomite, sandstone, gypsum and anhydrite. The primary aquifers of this system are from old to recent the Wasia-Biyadh (the oldest), Umm Er Radhuma, Dammam and Neogene (the recent). The secondary aquifers are the Aruma aquifer of the Cretaceous age. Both primary and secondary aquifers are partially separated by layers of aquitards, such as the Shu'aiba, the upper Wasia and the Rus aquitards. From the bottom to the top, the following water-bearing unites have been described: Hith Aquitard of Upper Jurassic consists of anhydrite that forms a cap and an effective seal over the aquifer of the Lower Cretaceous (a secondary aquifer).

1.4 The Lower Cretaceous Aquifer

The aquifer represents a number of waters bearing units in the middle of Saudi Arabia. The aquifer comprises argillaceous limestone and crops out over 80 km like a wide strip from Az Zulfi down to the southern border. The cretaceous formations are very important local aquifers due to their effective connected porosity with a rock conductivity value (K) of 3×10^{-5} m/s and storage coefficient (S) of 1×10^{-4}.

1.5 Wasia-Biyadh Aquifer

The aquifer represents the lowest member of the Cretaceous and comprises medium to coarse sandstone. Close to Arabian Shield, the Biydah and overlaying Wasia aquifers and indirect contact and create the Wasia-Biyadh aquifer and is known to be a principal aquifer in Saudi Arabia. The aquifer can be described as a porous aquifer and confined except the western part, which considered an un confined with a hydraulic conductivity (K) of 4×10^{-4} m/s and storage coefficient (S) of 5×10^{-4}.

1.6 Upper Wasia/Lower Aruma Aquitard

This aquitard separates the Wasia aquifer from the overlaying Aruma and Umm Er Radhuma aquifers and consists of shaly unit. The thickness of this unit ranges from 20 to 50 m. Moving to the east, the Upper Wasia shales are overlain by the Lower Arum shales and its thickness reaches about 500 m east Ghawar structure.

1.7 Aruma Aquifer

This aquifer represents a secondary aquifer and its importance is relative for the water supply of Saudi Arabia. Aruma formation is dominated by massive dolomitized limestones, marles and shales at the upper part of the formation. It can be described as a partly karstified bedrock aquifer and structured by several faults and joints. It is known as unconfined/confined aquifer and remains under leaky unconfined conditions in the east with an average hydraulic conductivity (K) value of 4×10^{-5} m/s and storage coefficient (S) of 1×10^{-4}.

1.8 Umm Er Radhuma Aquifer

The aquifer is dominated by limestone, dolomitic limestone and dolomites, where shale and marls form the upper part of the formation. This aquifer represents a principle hydrological aquifer and most of the water bearing is found to be in the eastern region. The aquifer thickness increases from the west to the east. It is a karstified fractured bedrock and identified as unconfined conditions exit near the state of Qatar.

1.9 The Dammam Aquifer

The aquifer remains under artesian confined aquifer conditions around Yabrin and leaky confined conditions toward the east of Saudi Arabia. The hydraulic conductivity (K) value ranges from 1×10^{-2} m/s and the storage coefficient (S) value of 1×10^{-4} m/s.

1.10 Neogene Aquifer

The aquifer is a principal aquifer and consists of a complex succession of marine and continental sedimentary rocks. The aquifer consists of three different lithological formations; (i) the Hadrukh Formation which consists of sandstone, marls, sandy marls and sandy limestones, (ii) the Dam Formation which comprises marls, clay and sandy limestones at the bottom, and (iii) Hofuf Formation which consists of sandstone and conglomerates with thin layers of limestone and marl. It is a mixture of fractured limestone bedrock and unconsolidated porous clastic aquifers with hydraulic conductivity (K) of 1×10^{-7} and storage coefficient (S) of 1×10^{-5}. In general, the Neogene is gently dipping and its maximum thickness of 500 m.

1.11 Rus Aquitard

The Rus Formation comprises limestones, dolomitic limestones, chalky limestones, shales and sulphates (gypsum and anhydrite). A complete Rus succession contains large portions of sulphates that constitute an efficient aquitard between the Umm Er Radhuma aquifer and the Dammam aquifer. In areas where no sulphates occur, the Rus Formation with its carbonate forms effectively an upward extension of the Umm Er Radhuma aquifer (Fig. 5).

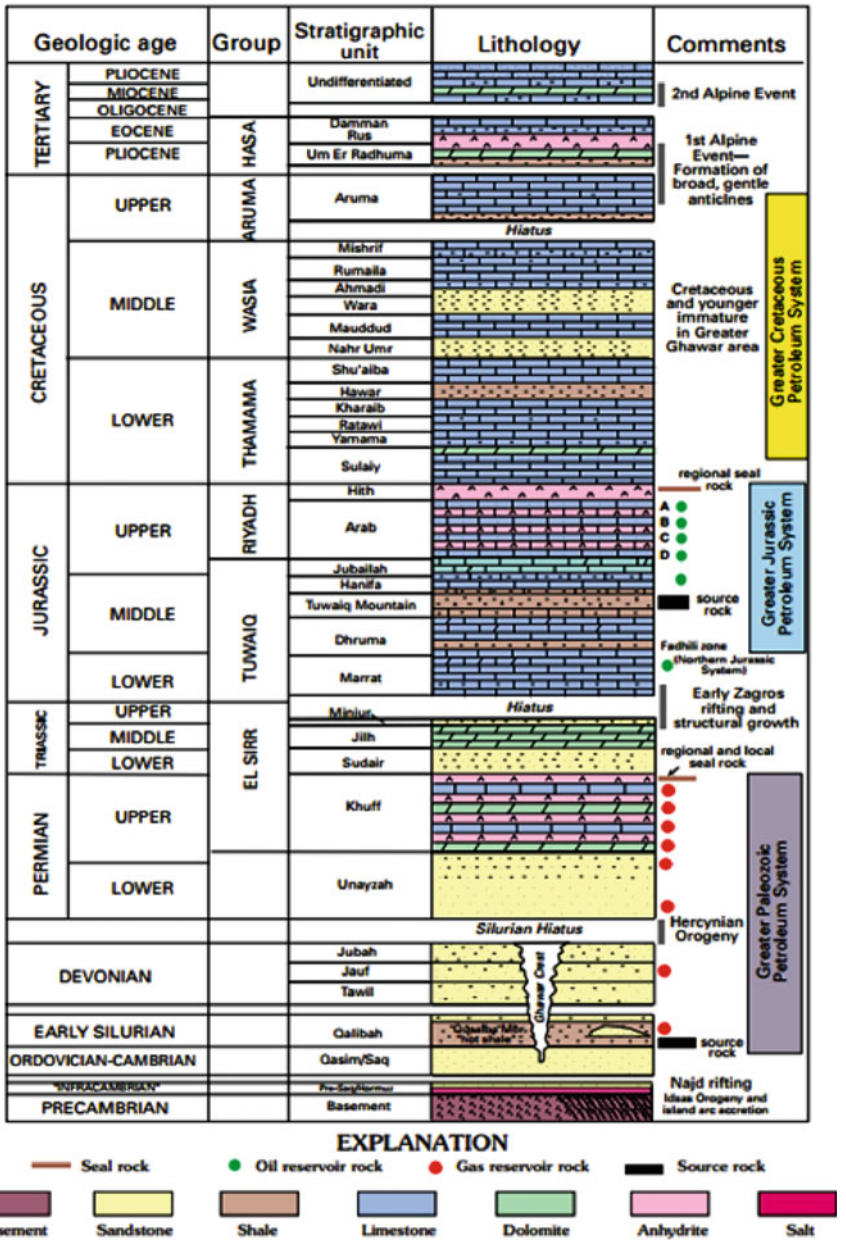

Fig. 5 Geological, lithological and hydrostratigraphical units of the Upper Mega Aquifer system in the Kingdom of Saudi Arabia. The corresponding hydraulic properties (hydraulic conductivity K, storage coefficient S, specific yield Sy), their averages, representative values and ranges are shown on the right side. Source for this figure?

These zones may serve as hydraulic windows between the Umm Er Radhuma and Dammam aquifers, where groundwater exchange is enabled across the confining units of the Lower Dammam.

1.12 Dammam Aquifer

It is a principal aquifer and composed of a succession of limestones, dolomitic limestones, marls and subordinate at the bottom (Midra shale, Saila shale and Alveolina) and carbonate rocks at the top. The maximum thickness of the formation reaches 450 m with an average of 120 m. The aquifer is composed of two sub-aquifers (Khobar and Alat aquifers), that are partly separated by the thin marl units of the Alat Marl.

2 Hydrological Applications of Remote Sensing and GIS in Saudi Arabia

Conventional approaches, such as drilling, hydrogeological, geological, field surveys, and geophysical methods, involve extensive labour in exploration activities that are costly in terms of money, time, and resources and also demand the participation of experts (Fetter 1994). However, remote sensing data have proved to be an excellent tool to map palaeochannels, drainage basins, susceptible map zones of groundwater potential and retrieve soil moisture (Pachur and Rottinger 1997; Hoelzmann et al. 2001; Elmahdy and Mohamed 2015; Elmahdy et al. 2020b, c).

Several researchers worldwide were used remote sensing data such as the Shuttle Radar Topographic Mission (SRTM) DEM with a spatial resolution of ~90 m, the Advanced Spaceborne Thermal Emission and Reflection Radiometer (ASTER) DEM with a spatial resolution of 30 m and the Advanced Land Observing Satellite (ALOS) DEM with a spatial resolution of 30 m, Landsat and the Advanced Spaceborne Thermal Emission and Reflection Radiometer (ASTER) images with a spatial resolution of 30 m and QuickBird images with a spatial resolution of 0.6 m. These various data can be downloaded via the webpage of the United States Geological Survey (USGS) (http://gdex.cr.usgs.gov/gdex/) and Japan Aerospace Exploration Agency, Earth Observation Research Center (https://www.eorc.jaxa.jp/ALOS/en/palsar_fnf/data/index.htm).

The SRTM and ALOS data were chosen due to their strong ability to penetrate extremely dry sand sheets and imagine near-surface features over a regional scale with low-cost manners (Roth and Elachi 1975). These various DEM were chosen because it is challenging to create a precise DEM over a regional scale from a topographic map (Elmahdy et al. 2020a; Jarvis et al. 2004). These DEMs and optical and SAR data were widely used to generate several hydrological, geological and metrological

factors such as lithological, lineaments, slope, altitude, lineaments density, stream networks and soil texture. These maps represent as good groundwater conditional factors (GWCFs) for groundwater potential mapping over a regional scale. It is important to note that the ALOS DEM has the lowest value of Root Mean Square Error (RMSE) than the SRTM DEM, the Advanced Spaceborne Thermal Emission and Reflection Radiometer (ASTER) DEM (Santillan and Makinano-Santillan 2016; Elmahdy et al. 2020d; Elmahdy et al. 2021a, b).

Mahmoud and Alazba (2014) mapped suitability maps to evaluate groundwater in the Jazan region, Saudi Arabia by applying a GIS-based decision support system (DSS). They fed the model by a set of input parameters (maps) such as rainfall, slope, land cover land use potential runoff coefficient and soil texture. Results include groundwater potential consists of five classes for suitability: excellent, good, moderate, poor and unsuitable. The spatial analysis exhibited that 50.5 and 31% of the region was classified as excellent and good for groundwater, respectively, while 16 and 2.5% of the region were classified as moderate and poor for groundwater, respectively.

Mumtaz et al. (2019) integrated remote sensing and geographic information system (GIS) based on geospatial-making techniques to delineate zones of groundwater potential in Al Assa Oasis, Saudi Arabia. Alshehri et al. (2020) developed a conceptual statistical model to map the spatial distribution of groundwater in a shallow aquifer in Al Qunfudah Province, Saudi Arabia.

The model starts by constructing an artificial neural network (ANN) and multivariate regression (MR) models. They used multi-sources datasets of remotes sensing such as the moderate resolution imaging spectroradiometer (MODIS) NDVI and land surface temperature (LST), radar backscatter coefficient (RBC) from Sentinel-1, soil moisture and ocean salinity (SMOS) measurements, global precipitation measurement (GPM), and tropical rainfall measuring mission (TRMM) in conjunction with hydrogeologic information (e.g., depth to water table (DTW). These various data were widely used to extract groundwater condition factors (GWCFs) such as lineaments, altitude, slope, aspect, topographic curvature and topographic wetness index.

Landsat and the Advanced Spaceborne Thermal Emission and Reflection Radiometer (ASTER) images with a spatial resolution of 30 m were used to extricate lineaments, stream networks and lithological units. Other data such as QuickBird images with a spatial resolution of 0.6 m were used for visual comparison of textural features (palaeodrainage networks and geological fractures) evident in SRTM and ASTER DEMs, and to determine whether any variation exists in patterns expressed by high-resolution optical data (Mohamed and Elmahdy 2016; Mohamed et al. 2021a).

3 Saudi Arabia's Hydrology from Radar Remote Sensing

The major topic of hydrological applications of the SAR data in the region, including Saudi Arabia and its adjoining countries, is the fossil water. The value of SAR

images for near-surface information was realized since 1982 when SAR information about the Jafurah sand field was captured from L-band SAR onboard the Spaceborne Imaging Radar (SIR-A) (Dabbagh et al. 1997). The use of SAR data in the region started with the hydromorphological applications in the late 1980s and then developed to include applications in hydrology and geology. Generally, SAR images have been widely used in the region nevertheless it is predictable to be on the growth since the ALOS data and image processing tools became available for free of charge.

Several studies have been achieved using the spatial geomorphology-related groundwater to identify zones of groundwater potential. The waves of SAR sensors have a strong ability to penetrate sand sheets and imagine near-surface palaeochannels, fault zones and alluvial fans (Roth and Elachi 1975; Schaber et al. 1997; Elmahdy and Mohamed 2013). These features have a bearing permeability and porosity of the rocks and thus water recharge conditions. Locally, limited numbers of studies have been applied to study the desert of Saudi Arabia using SAR data. Clark (1989) and Dabbagh et al. (1997) delineated palaeolake beds and the fluvial channels underneath sand sheets of Jafurah and Ar Rub Al Khali from the Shuttle Imaging Radar (SIR-C) imagery using manual screen digitizing (Fig. 6). Similar study has been achieved to automatically map the paleochannels underneath sand sheets of Ar Rub Al Khali (Sultan et al. 2008).

4 Saudi Arabia's Hydrology Monitoring Using *Gravity Recovery and Climate Experiment* (*GRACE*)

Gravity Recovery and Climate Experiment (*GRACE*) precisely tracked the spatial lateral variations in the gravitational potential in the earth, which is mostly caused by change in the terrestrial water storage on monthly to yearly time scales during the period from 2002 to 2017 (Rodell et al. 2004). This information allows researchers to analyse the spatiotemporal groundwater variation and for monitoring groundwater depletion and verify the GRACE result with the in-situ measurements (Rodell et al. 2004; Yeh et al. 2006; Syed et al. 2009; Wouters et al. 2014; Frappart and Ramillien 2018). Joodaki et al. (2014) estimated the monthly changes in the total water storage across the Middle East during February 2003 to December 2012 (Fig. 7).

The results show a large negative trend in the total water storage centered over western Iran and eastern Iraq, including the northern region of Saudi Arabia. They concluded that most of the long-term water losses are owing to a sharp depletion in groundwater storage (Fig. 8). Figure 8 shows that the highest groundwater depletion is correlated with areas with intensive agricultural activities and successive rate of groundwater extraction, mainly from the Saq aquifer.

As in-situ groundwater table measurements are commonly not sufficiently available for monitoring groundwater table changes over a regional-scale, the Gravity Recovery and Climate Experiment (GRACE) satellite mission, combined with external hydrological information, is extensively used to quantify the monthly and

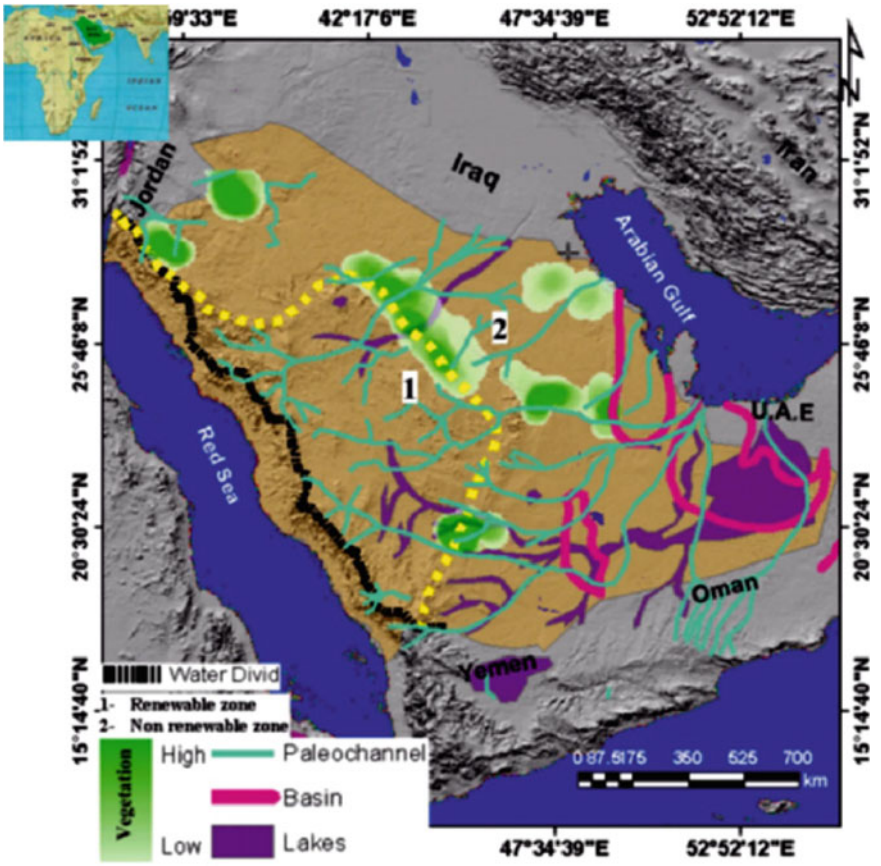

Fig. 6 Reference map showing the major fluvial channels palaeolakes mapped from SIR-C (e.g., Edgell 2006; Dabbagh et al. 1997), and aerial photographs (e.g., Clark 1989). Black line highlights water divides and green polygons highlight the circular farms densities in the region. The yellow line divides the region into renewable and non-renewable groundwater zones (Modified after Mohamed and Elmahdy 2016)

annual variations of groundwater storage in the major regional aquifers. This unique dataset revealed an important aquifer depletion in the region (Frappart and Ramillien 2018).

Fallatah (2018) concluded that there is a sharp depletion in groundwater quantity and quality as response to climate change and intensive agricultural activities (Fig. 8). A spatial relationship between intensive agricultural activities and land deformation has been investigated using an integration between remote sensing data and hydrological approach (Othman and Abotalib 2019). Such approach permitted a better understanding of the role of groundwater depletion in the formation of these deformation features (Fig. 9).

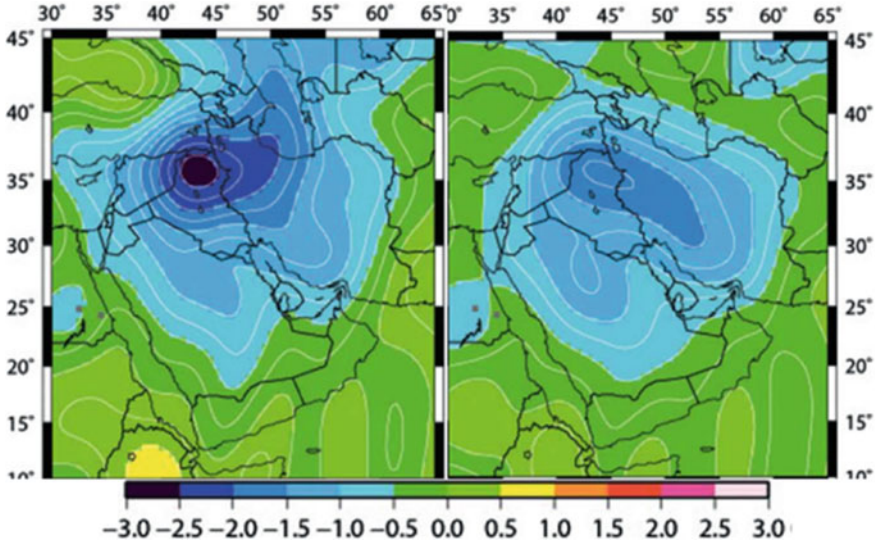

Fig. 7 Secular trend in groundwater (cm/yr) during 2003–2012, computed by subtracting CLM4.5 modeled soil moisture1snow1canopy1river storage (SSCR) from the GRACE total water storage results (CLM4.5 groundwater not subtracted)

5 Machine Learning Applications in Hydrological

Machine Learning (ML) can be described as the field of study gives machines or computers the ability to train without being explicitly programmed (Samuel 1959). It is a part of artificial intelligence that applies algorithms to synthesize the relationship among data and information (Turing and Haugeland 1950).

ML plays vital roles in the development of a host of user-centric innovation and owes its escalating adoption to its capability to describe the relationships within large layers of data in the ways that solve environmental problems in big data analysis, pattern recognition and information progress. It can be trained to:

(i) recognize objects, features and automatic speech.
(ii) convert acoustic information in a sequence of speech information into semantic structure in the form of a string of words.

ML is finding widespread uses in many geoscience applications such as big data analysis, mineral mapping and groundwater potential mapping. The main characteristics of ML is to generalize the training experience or training samples and produce a hypothesis that evaluates the target function. The attribute of this generalization permits the ML system to perform well on the hidden data examples in precisely predicting the upcoming data.

The main objective of using ML is to predict any future scenario or event that is unidentified by the machine (computer). In the Arabian Peninsula, limited numbers of automatic algorithms and machine learning approaches have been applied

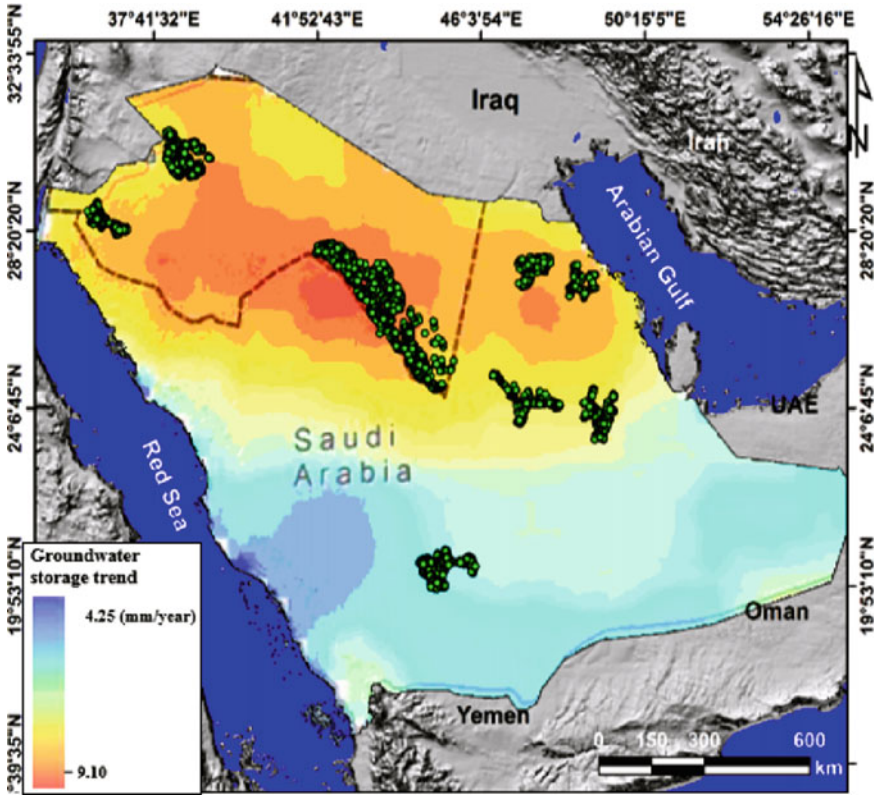

Fig. 8 Farmland locations (green points) are draped over a map of trend (mm/yr) in temporal (04/2002–01/2016) GRACE-derived terrestrial water storage (TWS) of the Arabian Peninsula showing the groundwater drawdown in the Northern Region of Saudi Arabia, particularly in the area underlain by the Saq, Kahfah, and Alluvium aquifers (Fallatah 2018)

for mapping hydrological features and predicting zones of groundwater potential. Machine learning and automatic algorithms have been widely used to reveal several palaleochannels, palaeolakes and mega-basins from SRTM DEM using the D8 algorithm (Fig. 10). Figure 10 exhibits that the area is characterized by nine tributaries mainly draining from the Assir, Hejaz and Oman mountains terminating at Err Rub Al Khali, Ad Dawasir, Sahba, Asulb, Arrimah, Nafud, Tabuk, Arran, and to the Red Sea in the west and the Arabian Gulf in the east southeast. These features were formed by a fluvial process during the late Quaternary (Clark 1989).

Mohamed and Elmahdy (2016) developed a hydrological approach based on Information Value (IV) model for mapping fluvial channels and topographic wetness in Saudi Arabia. To achieve this objective, they mapped regions of near-surface fluvial palaeochannels, mega-basins and topographic wetness from the new version of the Shuttle Radar Topographic Mission (SRTM) DEM with a spatial resolution of 30 m.

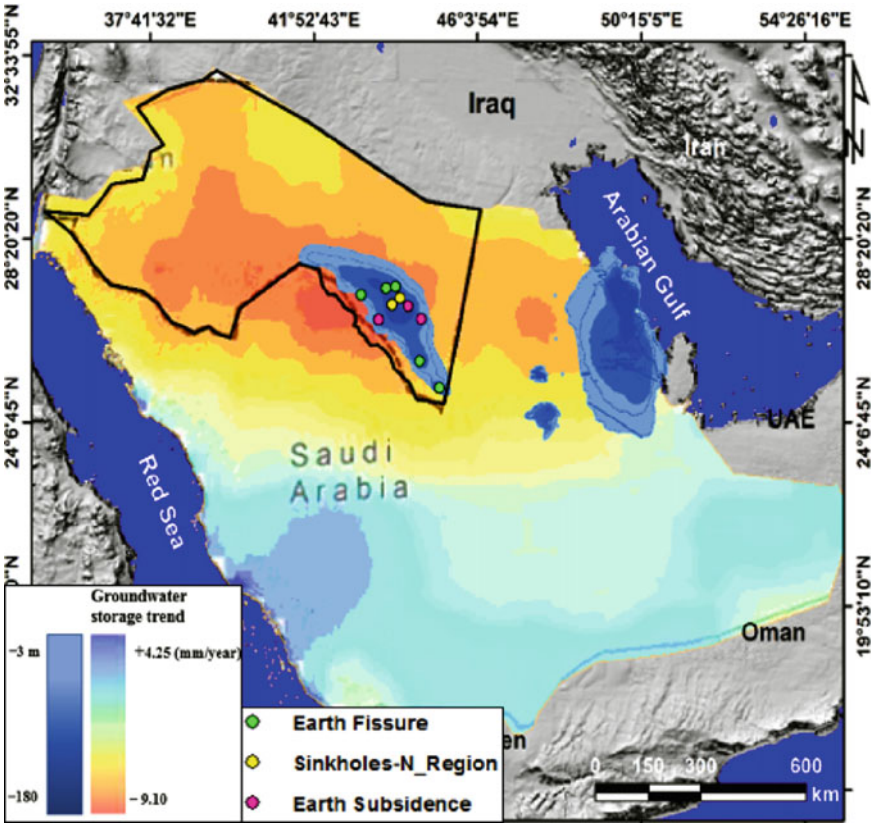

Fig. 9 Trend (mm/yr) in temporal (04/2002–01/2016) GRACE-derived terrestrial water storage (TWS) of the Arabian Peninsula (Modified after Fallatah 2018; Othman and Abotalib 2019)

These various features were utilized to calculate the topographic wetness (TW) of each mega-basin in Saudi Arabia based on the topographic slope of each mega-basin.

The new TW was employed to build a new model which can call information value (IV) in a geographic information system, which is a modified approach of the weight of evidence and validated using palaeochannels and palaeolakes mapped by Clark (1989), Dabbagh et al. (1997), and Edgell (2006) (Fig. 6).

The tributaries, which are 74–472 km in length, flow under the influence of slope and the NNW–SSE and NW–SE trending faults that are displaced 40-m depth and have a length of more than 9 km (Fig. 10). Figure 10 also exhibits that the mega-basins of Ar Rub Al Khali and Ad Dawasir, which occupy an area of 632.46 km^2, have the highest values for predictive power (>0.2). Figure 11 shows that the mega-basins of Ar Rub Al Khali and Sahba have the highest value of TWI (>3) and that the Arran and coastal mega-basins have the lowest value of TWI (<0.08) (Fig. 11a, b).

Figure 11 also exhibits that the basin of Dawasir has the lowest WoHE value of −4.8, while the basins of Al Juf and the Oman mountains have moderate WoHE

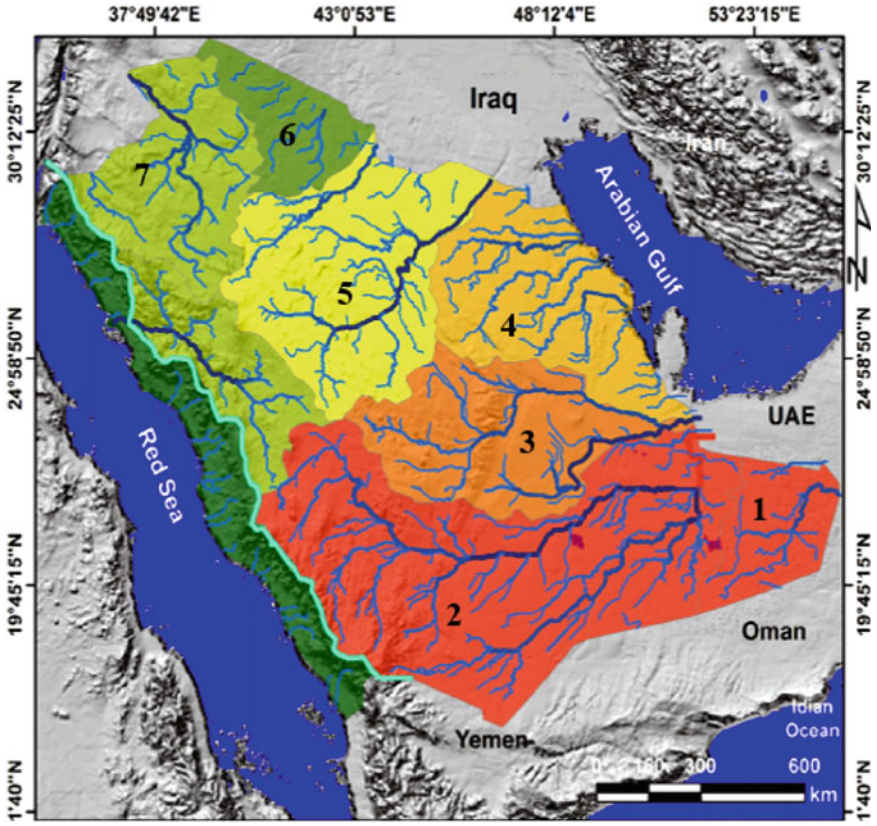

Fig. 10 Fluvial channel and mega-basin maps derived from SRTM DEM using D8 algorithm (**a**) showing flow direction, flow type and drainage basins in the region (after Mohamed and Elmahdy 2016)

values of 0.0185 and 0.016, respectively. The basins of Dhofar and Hadramout have the highest values for the WoHE of 0.0432 and 0.0258, respectively. The TWI reveals a strong agreement between IV and groundwater predictive power (Figs. 7d, 11c).

More recently, Elmahdy et al. (2021a) developed a remote sensing approach based on the weight of hydrological evidence (WoHE) for hydrological model of Ar Rub Al Khali. They used the Advanced Land Observing Satellite (ALOS) DEM and SAR images. The approach is based on calculating the logarithmic ratio of the total areas of distribution good (event) and distribution bad (non-event) of features such as faults, palaeochannels and zones of flow accumulation.

They found that the Ad Dawasir basin has the lowest rate of water seepage to the Ar Rub Al Khali aquifer, and thus the highest reserve of groundwater. The high values of the WoHE for Hadramout and Dhofar appear to be due to the absence of faults in each basin. They leak most of their water into Umm Al Hiesh area and Mutaridah Depression near Saudi Arabia and Oman borders, while Ad Dawasir basin seeps

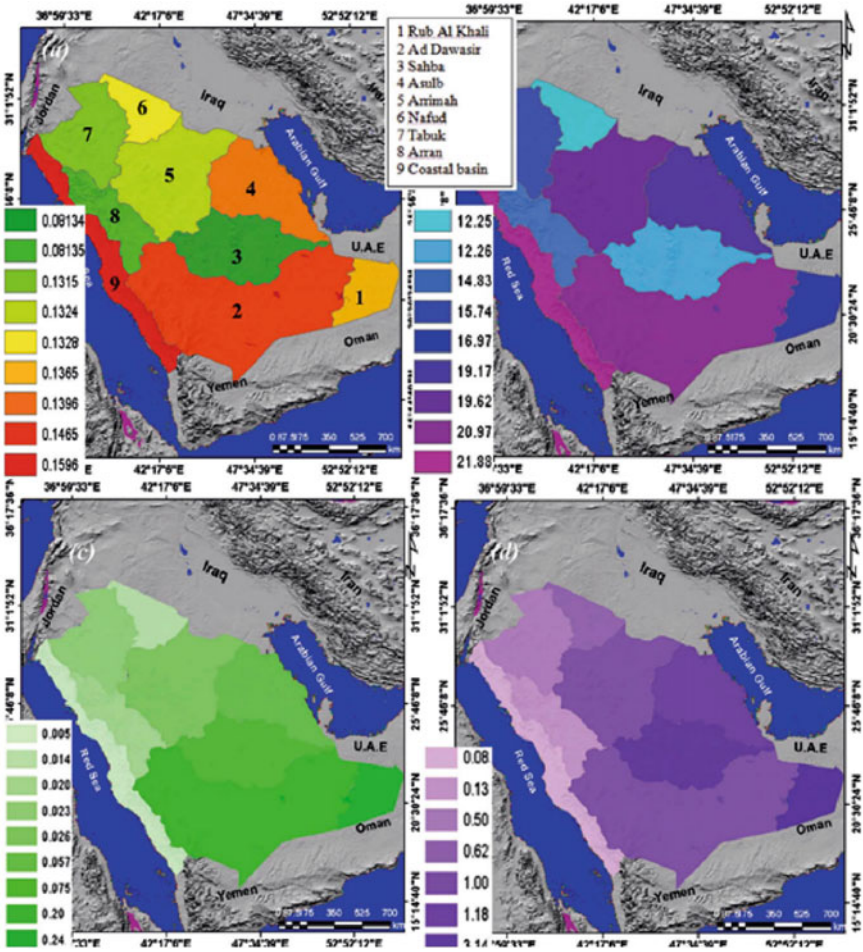

Fig. 11 Maps of fluvial channel distribution (**a**), fluvial channel density (**b**), IV (**c**), and topographic wetness index (TWI) (**d**), showing the influence of the spatial distribution of paleochannels and slope on the topographic wetness in the entire region sensors (after Mohamed and Elmahdy 2016)

most of its water directly to Mondafan and Wajid depressions near Saudi Arabia and Yemen borders. As the value for WoHE of each basin increases, the value for the groundwater potentiality decreases (Fig. 12).

More recently, groundwater potential mapping highlights sites of potential groundwater zones in the Ar Rub Al Khali (ARAK) (Elmahdy et al. 2021b). Elmahdy et al. (2021a) applied the Classification and Regression Trees (CART) model for regional mapping of groundwater potential in the Ar Rub Al Khali (Fig. 13). They found that factors such as faults and their associations palaeochannels and zones of flow accumulation have a positive impact on groundwater potential, especially in semi-arid remote regions.

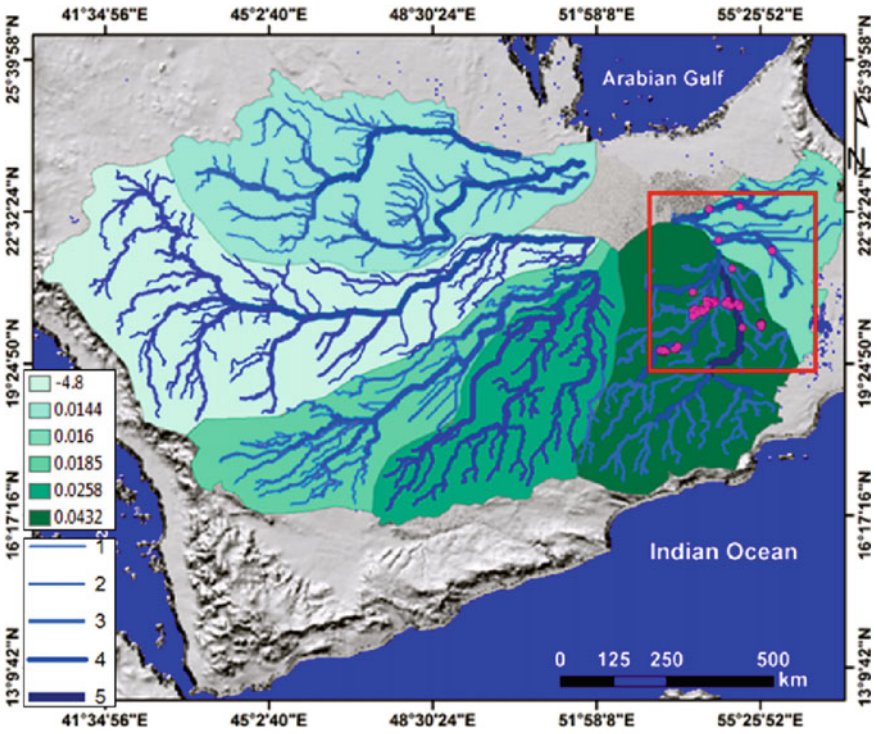

Fig. 12 Map of palaeochannels (in order) and drainage basins of the ARAK categorized based on the WoHE. Palaeochannels with a high order (dark blue) indicates flooded areas. Pink points in red square highlight lake locations observed on Google Earth (**b**) and suggesting groundwater potential (after Elmahdy et al. 2021b)

These fault zones improve the effective porosity of the groundwater aquifer and groundwater wells (Florinsky 2000; Sultan et al. 2008; Elmahdy and Mohamed 2014). These features also affect the landscape that controls water flow and accumulation (Florinsky 2000; Sultan et al. 2008; Elmahdy and Mohamed 2014). These features control the spatial distribution of palaeochannels, zones of flow accumulation (Ollier 1981; Florinsky 2000; Sultan et al. 2008; Elmahdy and Mohamed 2014).

There is no surprise since fault zones are often connected with palaeochannels and control altitude, slope zones of flow accumulation. Unfortunately, we cannot consider GWCFs such as LULC, lithology and plan curvature have not considered because the region is remote and inaccessible, and the terrain is characterized by a gentle slope covered by sand sheets. In such regions, the use of several GWCFs such as plan curvature, aspect, and LULC may not much affect the results and introduces errors (Mohamed and Elmahdy 2016; Elmahdy et al. 2020c). Thus, we assume that the GWPM obtained (Fig. 13) is rather realistic.

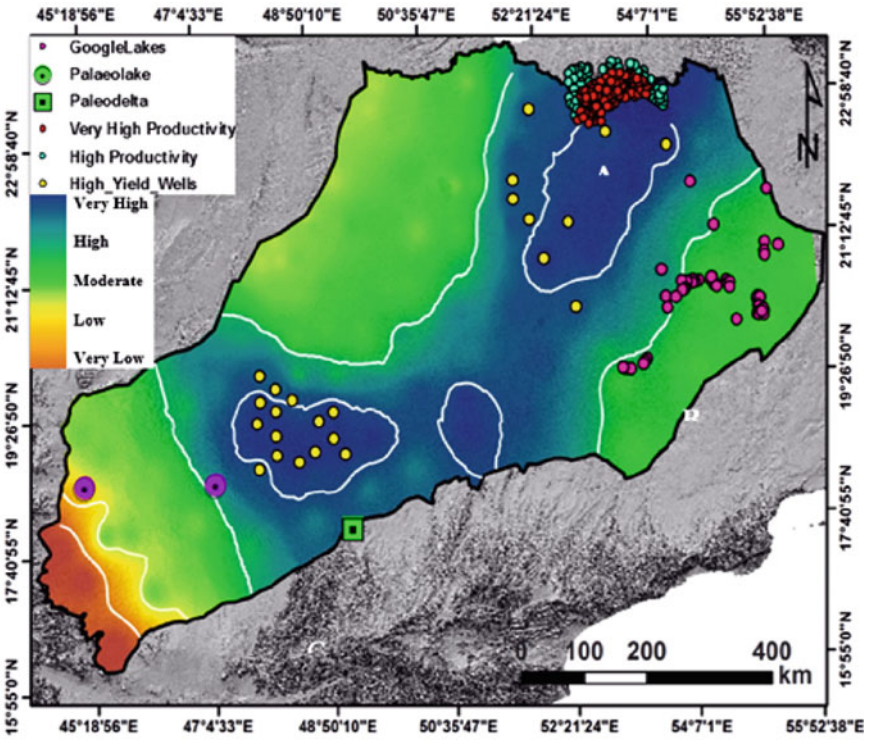

Fig. 13 Map of groundwater potentiality of the ARAK underneath sand sheets produced using the CART model. Pink points highlight recovered palaeolake locations and A, B and C point locations used for validation of the resulting GWPM (after Elmahdy et al. 2021b)

The lineaments and stream density-related factors had a strong relationship between these factors and groundwater potential, while the slope exhibits a negative relationship (Ozdemir 2011a, b). However, the result appeared to suggest that factors such as aspect and depth to the basement not have a significant level of contribution to groundwater potential. This result is in agreement with another study (Mohamed and Elmahdy 2016).

The map of groundwater potential produced using the CART model is shown in Fig. 14 (after Elmahdy et al. 2021a). The map shows that there are two zones of high and very high groundwater potentiality in the ARAK. The first zone is deep and located near the borders of Saudi Arabia and Yemen and Saudi Arabia and UAE borders like a U in shape (dark blue colour in Fig. 13), while the second zone is shallow and located near the borders of Saudi Arabia and Oman (green colour in Fig. 13).

The deep zone (sedimentary basin) extends from Ad Dawasir, Al Juf, Mondafan, Khujaymah and Sharourah near Saudi Arabia and Yemen borders to the SGSB, Shabita and Shieba near Saudi Arabia and UAE borders. This zone covers an area of

256,235 km^2 (45.2%) of the total area of the ARAK aquifer, which is estimated to be 566,838 km^2. Most of the high yield groundwater wells (yellow points in Fig. 8) and the discovered paleolakes were observed to be located within a higher density of paleochannels and fault zones, while the observed lakes were found to be located in the shallow depression of Mutaridah.

6 Conclusion

Remote sensing applications in Saudi Arabia started at the end of 1980s on an experimental basis, with manual screen digitizing and visual interpretation of fluvial channels by Clark (1989) and Dabbagh et al. (1997). Clark used SIR-C images to map ancient lake beds. Later, Dabbagh et al. (1997) used the same data to map fluvial channel pathways in the Jafurah sand sea and Al-Labbah Plateau, Saudi Arabia. These studies were based on visual interpretation and screen digitizing, which introduced a bias and timely and economic consumption. None of these studies attempted to automatically map fluvial channels from a DEM using algorithms. The use of remote sensing data has become a unique source of remarkably detailed hydrological and water resources management as well as geological information in Saudi Arabia. The integration of remote sensing and GIS paved the way for the expansion of this technology in the GCC region. The research community has expanded to include, the measurement of groundwater mass and monitoring groundwater level.

Thus far, a limited number of studies have been conducted to map fluvial channels, topographic wetness (TW) and zones of groundwater potential over regional scales in Saudi Arabia. With the aid of remote sensing data and machine learning algorithms in GIS, we have provided complete fluvial channel, TW and groundwater potential maps over regional scales in Saudi Arabia for the first time. These hydrological features, in conjunction with the geo-hydrological, were employed as groundwater conditioning factors (GWCFs) for developing techniques to map groundwater potential in remote arid regions over a regional scale. These factors are essential aspect in groundwater exploration and water resources studies. The obtained GWPMs are important aid to hydrologist in selecting sites of groundwater potential. Machine learning algorithms, which use remote sensing data, have permitted better understanding of the hydrologic setting of the Saudi Arabia.

Masses and level of groundwater changes in the northern region of Saudi Arabia have been observed, while zones of groundwater were reported in the northern region of the Saudi Arabia and Er Rub Al Khali near the border od Saudi Arabia with the UAE and Oman. In the northern region,

In Saudi Arabia, groundwater and surface flow from the Hejaz Mountains (sources of recharges) to the continental shelf and Arabian Gulf in the east and to the coastal aquifer to the Red Sea in the west. Additionally, the groundwater aquifer thicknesses increase from the west (Arabian shield) to the border of Saudi Arabi with UAE and Kuwait and Oman in the east and south. This chapter presents the hydrological application of remote sensing data and modified methods based on machine

learning to map zones of groundwater potential over a very regional scale with a moderate number of groundwater condition factors. This chapter is the prerequisite for bridging the gaps between research and operational techniques for hydrological remote sensing. The results presented in this chapter has permitted different sensors and machine learning algorithms to be compared across arid and semi-arid regions.

References

Alshehri F, Sultan M, Kark S, Alwagdani E, Alsefry S, Alharbi H, Sturchio N (2020) Mapping the distribution of shallow groundwater occurrences using remote sensing-based statistical modeling over southwest Saudi Arabia. Remote Sens 12(9):1361

Al-Sayari SS, Zoetl JG (1978) Quaternary period in Saudi Arabia. In: 1: Sedimentological, hydrogeological, hydrochemical, geomorphological, and climatological investigations in central and eastern Saudi Arabia, Springer, Wien

Al Tokhais AS, Rausch R (2008) The hydrogeology of Al Hassa springs. In: Proceedings of the 3rd international conference on water resources and arid environments 2008 and the 1st Arab water forum, 16: 10 fig. Riyadh

Brown GF (1960) Geomorphology of western and central Saudi Arabia. In: International geological congress, 21st. Copenhagen, proceedings, Section 9, pp 150–159

Burdon DJ (1982) Hydrogeological conditions in the middle east. Q J Eng Geol Hydrogeol 15(2):71–82

Carmona G, Varela-Ortega C, Bromley J (2013) Supporting decision making under uncertainty: Development of a participatory integrated model for water management in the middle Guadiana River basin. Environ Model Softw 50:144–157

Clark A (1989) Lakes of the Rub' Al-Khali. Aramco World 40(3):28–33

Dabbagh AE, Al-Hinai KG, Khan MA (1997) Detection of sand-covered geologic features in the Arabian Peninsula using SIR-C/X-SAR data. Remote Sens Environ 59(2):375–382

De Graaf IEM, van Beek RLPH, Gleeson T, Moosdorf N, Schmitz O, Sutanudjaja EH, Bierkens MFP (2017) A global-scale two-layer transient groundwater model: development and application to groundwater depletion. Adv Water Resour 102:53–67

Dimock WCA (1961) Study of the water resources of the Rub Al-Khali in Southern Saudi Arabia. Unpublished Groundwater Report 22, ARAMCO. p 183

Edgell HS (2006) Arabian deserts: nature, origin and evolution. Springer Science & Business Media

Edgell HS (1997) Karst and hydrogeology of Lebanon. Carbonates Evaporites 12(2):220–235

Elmahdy SI, Mohamed M (2013) Remote sensing and GIS applications of surface and near-surface hydromorphological features in Darfur region, Sudan. Int J Remote Sens 34(13):4715–4735

Elmahdy SI, Mohamed M (2014) Relationship between geological structures and groundwater flow and groundwater salinity in Al Jaaw Plain, United Arab Emirates; mapping and analysis by means of remote sensing and GIS. Arabian J Geosci 7(3):1249–1259

Elmahdy SI, Mohamed MM (2015) Automatic detection of near surface geological and hydrological features and investigating their influence on groundwater accumulation and salinity in southwest Egypt using remote sensing and GIS. Geocarto Int 30(2):132–144

Elmahdy SI, Ali TA, Mohamed MM, Yahia M (2020a) Topographically and hydrologically signatures express subsurface geological structures in an arid region: a modified integrated approach using remote sensing and GIS. Geocarto Int 1–21

Elmahdy SI, Mohamed MM, Ali TA, Abdalla JED, Abouleish M (2020b) Land subsidence and sinkholes susceptibility mapping and analysis using random forest and frequency ratio models in Al Ain, UAE. Geocarto Int 1–17

Elmahdy S, Mohamed M, Ali T (2020c) Land use/land cover changes impact on groundwater level and quality in the northern part of the United Arab Emirates. Remote Sens Jo 12(11):1715

Elmahdy SI, Ali TA, Mohamed MM, Howari FM, Abouleish M, Simonet D (2020d) Spatiotemporal mapping and monitoring of mangrove forests changes from 1990 to 2019 in the Northern Emirates, UAE using Random Forest, Kernel logistic regression and Naive Bayes tree models. Front Environ Sci 8:102

Elmahdy S, Ali T, Mohamed M (2021a) Hydrological modeling of Ar Rub Al Khali, Arabian Peninsula: a modified remote sensing approach based on the weight of hydrological evidence. Geocarto Int 1–21

Elmahdy S, Ali T, Mohamed M (2021b) Regional mapping of groundwater potential in ar rub al khali, arabian peninsula using the classification and regression trees model. Remote Sens 13(12):2300

Fallatah OA (2018) Assessing groundwater quantity and quality variations in arid regions due to climate changes and anthropogenic factors: case study Saudi Arabia

Fetter CW (1994) Applied hydrogeology, 4th ed. Englewood Cliffs, NJ, USA, Prentice Hall, pp 543–591

Florinsky (2000) IV Relationships between topographically expressed zones of flow accumulation and sites of fault intersection: analysis by means of digital terrain modelling. Environ Model Softw 15(1):87–100

Frappart F, Ramillien G (2018) Monitoring groundwater storage changes using the Gravity Recovery and Climate Experiment (GRACE) satellite mission: a review. Remote Sens 10(6):829

GASTAT (2016) General authority for statistics. http://www.stats.gov.sa/en Accessed 24 Dec

Geert K, Afifi AM, Al-Hajri SIA, Droste HJ (2001) Paleozoic stratigraphy and hydrocarbon habitat of the Arabian plate. GeoArabia 6:407–442

Hoelzmann P, Keding B, Berke H, Kröpelin S, Kruse HJ (2001) Environmental change and archaeology: Lake evolution and human occupation in the Eastern Sahara during the Holocene. Palaeogeogr Palaeoclimatol Palaeoecol 169:193–217

Jarvis A, Rubiano JE, Nelson A, Farrow A, Mulligan M (2004) Practical use of SRTM data in the tropics: comparisons with digital elevation models generated cartographic data

Joodaki G, Wahr J, Swenson S (2014) Estimating the human contribution to groundwater depletion in the Middle East, from GRACE data, land surface models, and well observations. Water Resour Res 50(3):2679–2692

Mahmoud SH, Alazba AA (2014) Identification of potential sites for groundwater recharge using a GIS-based decision support system in Jazan region-Saudi Arabia. Water Resour Manag 28(10):3319–3340

Ministry of Agriculture and Water (MAW) (1984) Water Atlas of Saudi Arabia. Riyadh, Saudi Arabia

Mohamed MM, Elmahdy SI (2016) Remote sensing and information value (IV) model for regional mapping of fluvial channels and topographic wetness in the Saudi Arabia. GIScience Remote Sens 53(4):520

Mumtaz R, Baig S, Kazmi SSA, Ahmad F, Fatima I, Ghauri B (2019) Delineation of groundwater prospective resources by exploiting geo-spatial decision-making techniques for the Kingdom of Saudi Arabia. Neural Comput Appl 31(9):5379–5399

Ollier C (1981) Tectonics and landforms. Longman, London, p 324

Othman A, Abotalib AZ (2019) Land subsidence triggered by groundwater withdrawal under hyper-arid conditions: case study from Central Saudi Arabia. Environ Earth Sci 78(7):243

Ozdemir A (2011a) GIS-based groundwater spring potential mapping in the Sultan Mountains (Konya, Turkey) using frequency ratio, weights of evidence and logistic regression methods and their comparison. J Hydrol 411:290–308

Ozdemir A (2011b) Using a binary logistic regression method and gis for evaluating and mapping the groundwater spring potential in the sultan mountains (aksehir, turkey). J Hydrol 405:123–136

Pachur HJ, Rottinger F (1997) Evidence for a large extended paleolake in the Eastern Sahara as revealed by spaceborne radar lab images. Remote Sens Environ 61:437–440

Razandi Y, Pourghasemi HR, Neisani NS, Rahmati O (2015) Application of analytical hierarchy process, frequency ratio, and certainty factor models for groundwater potential mapping using gis. Earth Sci Inf 8:867–883

Rodell M, Famiglietti JS, Chen J, Seneviratne SI, Viterbo P, Holl S, Wilson CR (2004) Basin scale estimates of evapotranspiration using GRACE and other observations. Geophys Res Lett 31(20)

Roth L, Elachi C (1975) Coherent electromagnetic losses by scattering from volume inhomogeneities. IEEE Trans Antennas Propagat 23(5):674–675

Samuel AL (1959) Some studies in machine learning using the game of checkers. IBM J Res Dev 3(3):210–229

Santillan JR, Makinano-Santillan M (2016) Vertical accuracy assessment of 30-m resolution alos, aster, and srtm global dems over Northeastern Mindanao, Philippines. Int Arch Photogramm Remote Sens Spatial Inf Sci 41

Schaber GG, McCauley JF, Breed CS (1997) The use of multifrequency and polarimetric SIR-C/X-SAR data in geologic studies of Bir Safsaf Egypt. Remote Sens Environ 59(2):337–363

Sharaf MA, Hussein MT (1996) Groundwater quality in the Saq aquifer. Saudi Arabia Hydrol Sci J 41(5):683–696

Sultan M, Sturchio N, Al Sefry S, Milewski A, Becker R, Nasr I, Sagintayev Z (2008) Geochemical, isotopic, and remote sensing constraints on the origin and evolution of the Rub Al Khali aquifer system, Arabian Peninsula. J Hydrol 356(1–2):70–83

Syed TH, Famiglietti JS, Chambers DP (2009) GRACE-based estimates of terrestrial freshwater discharge from basin to continental scales. J Hydrometeorol 10:22–40

Turing AM, Haugeland J (1950) Computing machinery and intelligence. In: The turing test: verbal behavior as the hallmark of intelligence, pp 29–56

Woods WW, Imes JL (1995) How wet is wet? Precipitation constraints on late quaternary climate in the southern Arabian Peninsula. J Hydrol 164:263–268

Wouters B, Bonin JA, Chambers DP, Riva REM, Sasgen I, Wahr J (2014) GRACE, time-varying gravity, earth system dynamics and climate change. Rep Prog Phys 77:116801

Yeh PJF, Swenson SC, Famiglietti JS, Rodell M (2006) Remote sensing of groundwater storage changes in Illinois using the gravity recovery and climate experiment (GRACE). Water Resour Res 42 (12)

https://water.fanack.com/publications/groundwater-of-the-mena-region/

A DRASTIC-Based Fuzzy C-means Clustering Technique for Evaluating Groundwater Vulnerability Under Uncertainty

Jahangir Abedi Koupai, Nastaran Zamani, and Farshad Rezaei

1 Introduction

Groundwater is a source of water which is globally important and valuable duo to the increasing population, industrial developments and agricultural activities especially in recent decades. The importance of this source of water is double in arid and semi-arid areas in which the access to surface water is restricted. On the other hand, once these resources get polluted, it would be extremely hard and even impossible to restore their original quality. Thus, it would be easier to protect groundwater from contamination than to remove pollutant from it. For management and exploitation of groundwater resources simulation models are applied comprehensively (Abedi Koupai and Golabchian 2015). Protection of groundwater needs a good knowledge of aquifer potential to pollution which is called by vulnerability. Vulnerability is the probability of groundwater pollution after emerging contaminant on the earth surface (Aller et al. 1987). There are two main category of vulnerability: Intrinsic Vulnerability and Specific Vulnerability. The first one is related to the aquifer's characteristics like: Hydraulic conductivity, hydraulic gradient, porosity, and etc. the second one is related to the vulnerability of aquifer to specific contaminant (Aller et al. 1987).

Vulnerability assessment methods are divided into four categories: 1- Subjective rating methods 2- Statistical analysis methods 3- Process based methods 4-

J. Abedi Koupai (✉) · N. Zamani
Department of Water Engineering, College of Agriculture, Isfahan University of Technology, 84156-83111 Isfahan, Iran
e-mail: koupai@iut.ac.ir

N. Zamani
e-mail: nastaran.zamani1@ag.iut.ac.ir

F. Rezaei
Department of Civil Engineering, Isfahan University of Technology, 84156-83111 Isfahan, Iran
e-mail: f.rezaei@alumni.iut.ac.ir

A. Shaban (ed.), *Satellite Monitoring of Water Resources in the Middle East*,
Springer Water, https://doi.org/10.1007/978-3-031-15549-9_19

Subjects hybrid methods. One of the most commonly used methods included in these categories are overlay and index methods, because of their ease to apply, applicability for large areas and reliability of their categorized results (Liggett and Talwar 2009). Among all methods in this category, DRASTIC method is widely used and is popular to evaluate groundwater vulnerability index even in regions with a range of hydrogeological settings (Pathak and Hiratsuka 2011). In this method the influencing factors of groundwater are divided into ranges and given ratings whether or not their value can be directly measured (Huicheng et al. 1999). The DRASTIC method was first introduced by Aller et al. (1987) to evaluate intrinsic vulnerability potential of groundwater containing seven parameters: **D**: Depth to groundwater, **R**: net Recharge, **A**: Aquifer media, **S**: Soil media, **T**: Topography, **I**: Impact of the vadose zone and **C**: hydraulic Conductivity. This method is based on 4 assumption: 1- pollution is speared on the ground surface 2- groundwater pollution is among water infiltration 3- pollution moves by water 4- the study area should be bigger than 4.5 km^2 (Aller et al. 1987). In this method the summation of all negative effects of these parameters contributes to the vulnerability index. The base of this method is Boolean logic but many researchers have modified this method through using fuzzy logic. For example, Pathak and Hiratsuka (2011) expressed that due to the linear nature of the DRASTIC formulation used to calculate vulnerability index, it is unable to show a continuous output of vulnerability index from the easiest to be contaminated to the most difficult to be contaminated. Hence, it is necessary to turn the linear traditional nature of DRASTIC to the fuzzy nature for assessing the groundwater vulnerability to contamination. Instead, integrated GIS-based fuzzy pattern recognition model can generate the continuous vulnerability function dissimilar stepwise DRASTIC index. This method has been used to demonstrate the groundwater vulnerability map to shallow groundwater of Kathmandu Valley as a case study. A comparison between the output of the fuzzy pattern recognition model and the DRASTIC was done. The results showed that 75% of the valley's shallow aquifer in fuzzy method and 58% of the aquifer in DRASTIC method is under coverage of high to very high vulnerability classes. In ordinary DRASTIC method any changes in one parameter value of a point may cause that point to move to another vulnerability class or points which have obviously different parameter values have its place to the same vulnerability class. While in fuzzy logic each point partly belongs to each class of vulnerability and does not necessarily belong to a specific class. Rezaei et al. (2013) expressed that a more spread and disorderly vulnerability map belongs to ordinary DRASTIC due to the nature of the Boolean logic applied in the structure of DRASTIC method, in contrast to the fuzzy-DRASTIC models.

Iqbal et al. (2015) used GIS-based fuzzy pattern recognition model to access groundwater vulnerability to contamination in Ranchi district, Jharkhand, India. In this study the performance of the developed model and standard DRASTIC were compared. Results revealed the better performance of GIS-based fuzzy pattern recognition model. It was shown that the difference between the parameter values within a pre-specified range was disregarded in DRASTIC method, because DRASTIC assigns a constant rating to the related parameters falling into a certain range. In other words, this method is incapable to configure the real effect of the variation in

the parameters on the vulnerability index (Iqhbal et al. 2015). Thus, it is necessary to apply the fuzzy methods to rate the DRASTIC parameters to let the rating mechanism more effectively reflect the real nature of the parameters generating the vulnerability index (Rezaei et al. 2013).

According to the nature of vulnerability classes, it seems to be suitable to use clustering techniques to directly classify vulnerability index, instead of calculating vulnerability index and then classifying the areas in terms of this index. Clustering algorithms are widely used for data categorization, data comparison and model construction. In clustering, a data set is partitioned into several groups in which the similarity within the data falling in a group is much more than that of the data belonging to different groups. This kind of dividing needs a similarity metric based on which two input vectors are taken and a value reflecting their similarity is returned. Because of sensitivity of some similarity metrics such as inner products to the range of elements, each of the input variable must be normalized to lie in the unit interval [0,1], when using this metric in the clustering process (Jang et al. 1997).

Data clustering versus data classification is an unsupervised learning process that doesn't need any labeled dataset as training data (Ghosh and Dubey 2013). One of the most useful methods in clustering is C-means method which can be used in the form of classic and fuzzy models under the name of K-means (hard C- means) and fuzzy C-means (FCM), respectively (Ghosh and Dubey 2013). K-means algorithm is a typical dynamic clustering algorithm in which the average of objects attributes only one cluster to each object, while fuzzy C-means is a clustering method that each data belongs to two or more clusters (Yang et al. 2013). Bezdek (1973) introduced Fuzzy C-Means clustering method, as an extended form of the hard C-Mean clustering method. FCM is applied to extensive range of problems related with feature analysis, clustering and classifier design, being used in agricultural engineering, chemistry, astronomy, geology, medical diagnosis, image analysis, shape analysis and target recognition (Ghosh and Dubey 2013). This method is approximately similar to multi-objective fuzzy pattern recognition model which was used by Huicheng et al. (1999). Their study showed that this method more effectively can use fuzziness in the process of assessing the vulnerability of groundwater. A case study of the Dalian Peninsula showed that the similar methodology for assessing the groundwater vulnerability is easy to apply and its results are practically useful (Shouyu and Guangtao 2003).

A summation of all different hydrological and hydrogeological parameters involving to vulnerability makes a DRASTIC index in its ordinary form. However, it is important to find the real relation between parameters involved in vulnerability and the vulnerability classes of an aquifer. The clustering techniques may be suitable tools to find unknown relation between parameters. These techniques could cluster the aquifer vulnerability based on the real similarities between the hydrogeological settings and their DRASTIC weighted ratings (Rezaei et al. 2016). Following this idea, this study aims to apply a new hybrid DRASTIC-based fuzzy C-means (FCM) clustering technique to facilitate groundwater vulnerability assessment in Damaneh-Daran aquifer in west central Iran. In Sect. 2, the methodology of the study is explained in three sub-sections, the first one describes the DRASTIC method in detail. In the second sub-section, the theory of FCM clustering method

is presented and the last sub-section introduces a method of sensitivity analysis for evaluating the degree of importance of the parameters involved in two vulnerability assessment methods. In Sect. 3 the study area is introduced. In Sect. 4 the results are presented and discusses, comparing the FCM method and the ordinary DRASTIC and the Sect. 5 concludes the paper.

2 Methodology

2.1 DRASTIC Method

The DRASTIC method is an overlay and index method including: Depth to water table, Net recharge, Aquifer media, Soil media, Topography, Impact of the vadose zone and Hydraulic conductivity. This method calculates the intrinsic vulnerability and is independent of the nature of the pollutants left at the land and land use. It is working under four key assumptions: (1) The contaminant is generated at the land surface; (2) The groundwater is recharged only by precipitation thereby the contamination is percolated to the groundwater table; (3) The contaminant has the mobility of water, thus flushing as easy as water; (4) The method can evaluate the vulnerability of the areas with at least 0.4 km^2 extensive (Aller et al. 1987). The DRASTIC index is calculated as Eq. 1 suggests (Aller et al. 1987):

$$V_{\text{Intrinsic}} = D_r D_w + R_r R_w + A_r A_w + S_r S_w + T_r T_w + I_r I_w + C_r C_w \quad (1)$$

where $V_{\text{Intrinsic}}$ is the DRASTIC index and the subscriptions of r and w stands for rating and weight of each parameter, respectively. The greater V, the more the probability for vulnerability to pollution will be. The greatest possible value of V is 226 and the smallest is 23, according to the ratings scope and weights given to the parameters. In Tables 1 and 2 the DRASTIC weighting and rating patterns for the quantitative and qualitative parameters of the method are shown, respectively.

Secunda et al. (1998) for estimating the specific vulnerability added landuse to the model as follow:

$$V_{\text{specific}} = V_{\text{Intrinsic}} + L_r L_w \quad (2)$$

where Vspecific is the specific vulnerability, and L_r is landuse rate and L_w is landuse weight. Many studies have done to evaluate specific and intrinsic vulnerability for example Akhavan et al. (2011) combined the intrinsic vulnerability by the potential contamination sources which were taken from landuse map to estimate the specific vulnerability. They revealed that using landuse map increased the area of moderately vulnerable region by about 9% but nitrate pollution in the region didn't have a good relation by vulnerable zones and vulnerability of groundwater to contamination had a strong correlation to natural conditions like soil, vadse zone, and aquifer media.

Table 1 Weighting and rating scheme for quantitative parameters in DRASTIC method (Aller et al. 1987)

Depth to water (m)	Rating	Recharge (mm/year)	Rating	Topography (%)	Rating	Conductivity (m/s)	Rating
0–1.5	10	>250	9	>18	9	>81.44	10
1.5–4.5	9	180–250	8	12–18	8	40.72–81.44	8
4.5–9	7	100–180	6	6–12	6	28.50–40.72	6
9–15	5	50–100	3	2–6	3	12.21–28.50	4
15–23	3	0–50	1	0–2	1	4.07–12.21	2
23–31	2					0.04–4.07	1
>31	1						
Weight:	**5**		**4**		**1**		**3**

Table 2 Weighting and rating scheme for qualitative parameters in DRASTIC method (Aller et al. 1987)

Aquifer media	Rating	Soil media	Rating	Impact of the vadose zone media	Rating
Karst limestone	10	Thin or absent, gravel	10	Karst limestone	10
Basalt	9	Sand	9	Basalt	9
Sand and gravel	8	Peat	8	Sand and gravel	8
Massive sandstone, Massive limestone	7	Shrinking and/or aggregate clay	7	Sandstone, limestone, sand and gravel	6
Bedded sandstone, limestone, shale	6	Sandy loam	6	Metamorphic/igneous	4
Glacial till	5	Loam	5	Shale, silt and clay	3
Weathered metamorphic/ igneous	4	Silty loam	4	Confining layer	1
Metamorphic/igneous	3	Clay loam	3		
Massive shale	2	Muck	2		
		Nonshrinking and nonaggregated clay	1		
Weight:	**3**		**2**		**5**

2.2 Fuzzy C-means (FCM) Clustering

As mentioned before, in ordinary DRASTIC a summation is held among all different negatively affecting hydrological and hydrogeological parameters contributing to vulnerability. As a result, it is a numerical ranking system to evaluate groundwater pollution potential. If assumed to find the real relation between parameters and

vulnerability classes of an aquifer, it would be useful to use fuzzy C-means clustering (FCM) technique. This technique can cluster the aquifer to different vulnerability zones based on the similarities between the corresponding hydrogeological parameters' weighted ratings defined in DRASTIC model. FCM, is a data clustering algorithm in which each data point belongs to a cluster with a fuzzy membership degree. This algorithm was proposed to improve the earlier hard C-means (HCM) clustering technique by Bezdek in 1973 (Jang et al. 1997).

A set of n input vectors of x_i, $i = 1, 2, \ldots, n$ is partitioned into c fuzzy groups in FCM to find each group's cluster center to minimize dissimilarity of the input vectors to these centers. FCM and HCM have a major difference which is hidden in the way to make data points belonging to several groups with a membership degree. This membership degree is 0 or 1 in HCM while falling in the interval [0,1] in FCM technique. To define a fuzzy partitioning, the membership matrix U have is defined whose elements are belonging to [0,1]. Thus, the summation of degrees of belongingness for a data set always should be equal to unity (Jang et al. 1997):

$$\sum_{i=1}^{c} u_{ij} = 1, \forall j = 1, \ldots, n. \tag{3}$$

The cost function (or objective function) for FCM which is aimed to be minimized is as follows (Bezdek 1981):

$$J(U, C_1, \ldots, C_c) = \sum_{i=1}^{c} J_i = \sum_{i=1}^{c} \sum_{j=1}^{n} u_{ij}^{m'} d_{ij}^2 \tag{4}$$

where u_{ij} is in [0,1], $d_{ij} = \|C_i - X_j\|$ is the Eculidean distance between ith cluster center and jth data point, c_i is the cluster center of the fuzzy group i, and $m' \epsilon [1, \infty)$ is a weighting power. Forming a new objective function J which is aimed to be minimized as follows in Eq. (5) is a necessary condition in Eq. (4) to reach a minimum (Jang et al. 1997):

$$\begin{aligned} &J(U, C_1, \ldots, C_c, \lambda_1, \ldots, \lambda_n) = J(U, C_1, \ldots, C_c) \\ &+ \sum_{j=1}^{n} \lambda_j \left(\sum_{i=1}^{c} u_{ij} - 1\right) = \sum_{i=1}^{c} \sum_{j=1}^{n} u_{ij}^{m'} d_{ij}^2 + \sum_{j=1}^{n} \lambda_j \left(\sum_{i=1}^{c} u_{ij} - 1\right) \end{aligned} \tag{5}$$

where λ_j, $j = 1, 2, \ldots, n$, are the Lagrangian multipliers for the n constraints in Eq. (3). By differentiating $J(U, C_1, \ldots, C_c, \lambda_1, \ldots, \lambda_n)$ with consideration of all its input arguments, the necessity for Eq. (4) to reach its minimum results in the Eqs. (6) and (7) (Jang et al. 1997):

$$c_{ik} = \frac{\sum_{j=1}^{n} u_{ij}^{m'} x_{jk}}{\sum_{j=1}^{n} u_{ij}^{m'}} \tag{6}$$

and

$$u_{ij} = \frac{1}{\sum_{k=1}^{c} \left(\frac{d_{ij}}{d_{kj}}\right)^{2/(m'-1)}} \tag{7}$$

where u_{ij} is the fuzzy membership degree of the jth input vector in the ith cluster, x_{jk} is the kth element of the jth input vector and c_{ik} is the kth element of the ith cluster, $i = 1, 2, \ldots, c$ and $k = 1, 2, \ldots, m$, where c is the number of clusters and m is the number of each data input's elements i. e. the DRASTIC parameters in this paper. The FCM algorithm is simply a trial and error procedure through successively implementing Eqs. (6) and (7). In a batch-mode operation, FCM determines the cluster centers c_i and the membership matrix U, consecutively using the following steps:

Step 1: initializing the membership matrix U with random values in [0,1] to satisfy the constraints in Eq. (3).
Step 2: calculating c fuzzy cluster centers c_i, $i = 1, 2, \ldots, c$, using Eq. (6).
Step 3: Stop, if the maximum difference between each element of U in the current iteration and the corresponding element in the previous iteration is below a certain threshold.
Step 4: computing a new U using Eq. (7). Go to step 2 (Jang et al. 1997).

It is also possible to first initialize the cluster centers and then implement the iterative procedure. There is no guarantee ensuring FCM technique to converge to an optimum solution (Jang et al. 1997). In the most researches implemented on FCM, the optimum value of *m'* is considered in the interval [1.25,2]. In this research this parameter was set to 1.25, 1.5, 1.75, and 2.

In the present study, FCM is employed for clustering and zoning the groundwater vulnerability to pollution. Thus, vulnerability map is calculated without directly calculating the DRASTIC index. In this method, the same ratings and weights of DRASTIC method are used to generate a matrix of seven rows and seven columns representing the seven clusters of vulnerability and the seven hydrogeological weighted ratings. Thus, the input vectors of the FCM algorithm are the 250 random points including seven DRASTIC hydrogeological data in the aquifer and the outputs are the membership degree of these points in the "most-vulnerable cluster" as explained in following. Maximum iteration and maximum tolerance was considered 100 and 10^{-6}, respectively. In the FCM algorithm, in addition to calculating the membership degree of each point in each cluster of vulnerability, the membership degree of each cluster in the most-vulnerable cluster was also calculated. Thus, all distances of the parameters from the minimum value of those parameters are calculated to generate the distance of each cluster from the "least-vulnerable cluster". The distances are then normalized over all clusters of vulnerability to be set in the interval [0,1] to receive the concept of fuzzy membership degree to itself. The more the distance to the "least-vulnerable cluster", the less the distance to its opposite cluster, i. e. the "most-vulnerable cluster" and thus, the more the vulnerability will be. The distance of each cluster to the "least-vulnerable cluster" was calculated by

compromise programming as follows:

$$dis(c) = \left\{ \sum_{j=1}^{7} w_j^p \left(\frac{r_{c,j} - r_{min_j}}{r_{max_j} - r_{min_j}} \right)^p \right\}^{1/p} \tag{8}$$

In which $dis(c)$ is the distance of cluster c from the least-vulnerable cluster, w_j is the weight of the jth parameter, $r_{c,j}$ is the rating of jth parameter in the cluster c, r_{min_j} and r_{max_j} are the minimum and maximum ratings assigned to the jth parameter, respectively and p is the distance parameter that in this study is set to 2 to represent Eculidian distance. Thus, the membership degree of each cluster in the "most-vulnerable cluster" can be calculated as follows:

$$md(i) = \frac{dis(i) - dis(min)}{dis(max) - dis(min)}; \; for i = 1, 2, \ldots, c \tag{9}$$

where $md(i)$ represents the membership degree of the cluster i in the "most-vulnerable cluster" where $i = 1, 2, \ldots, c$ and *dis(min)* and *dis(max)* are the minimum and maximum distances from the "least-vulnerable cluster", respectively. The lower the *md(i)*, the lower the membership degree in the "most-vulnerable cluster" and the lower the vulnerability of the cluster i relative to other clusters will be. Equation 10 illustrates how the membership degree of each point in the study area is calculated:

$$md(j) = \frac{\sum_{i=1}^{c} u_{ij}.md(i)}{\sum_{i=1}^{c} u_{ij}} \tag{10}$$

In which u_{ij} is the membership degree of the point j in the cluster i, and c is the number of clusters. $md(j)$ is the membership degree of the point j in the "most-vulnerable class",

For evaluating the goodness of the clustering procedure, diversity metric is needed. This metric can be calculated in the algorithm as follows:

$$div = \underset{j}{\text{mean}}(\underset{i}{\text{std}} x_{ij}) i = 1, 2, \ldots, n \;\; j = 1, 2, \ldots, m \tag{11}$$

In Eq. 11, n is the number of clusters and m is the number of the hydrogeological parameters (in this study is equal to 7, as is in the ordinary DRASTIC). The more the *div*, the better the outputs of the algorithm will be.

Then the final membership degrees assigned to the points in the study area (calculated in Eq. 10) are inserted to ArcGIS and interpolated to generate the final DRASTIC-based FCM vulnerability map for the study area.

2.3 Sensitivity Analysis

In any modeling project, sensitivity analysis is significant. In this study map removal sensitivity analysis is used to recognize the effect of each parameter in groundwater vulnerability of the region. Lodwick et al. (1990) introduced this method to measure the sensitivity of the model to removing each parameter from vulnerability calculations as follows:

$$s = \frac{\left|\frac{V}{N} - \frac{V'}{n}\right|}{V} \times 100 \tag{12}$$

In which s is the sensitivity of the model to the parameter removed, V and V' are vulnerability index resulting from participating all parameters in the vulnerability calculations and vulnerability index calculated when removing a parameter, respectively. N and n are the number of parameters involved in calculating V and V', respectively.

3 Case Study: Damanah-Daran Aquifer

Damaneh-Daran aquifer with an area of 220 km^2 is located between latitudes of 32°45′44″ and 33°4′9″ north and longitudes 50°22′6″ and 50°43′36″ east, in western part of Isfahan province, in the central plateau of Iran. In recent years, this region has encountered water quantity and quality crisis. The quantity problems are resulting from successive droughts, over-discharge from groundwater resources and lack of proper water resources management. The quality problems which leads to groundwater pollution is a consequence of using over-permissibly fertilizers in the agricultural sectors, such that in 2015 this plain was announced as prohibited aquifer. Figure 1 illustrates the place of the study area.

The most precipitation of this region falls during October till May. According to the precipitation data of synoptic and climatology stations, average annual precipitation of the plain and heights are 345 and 361 mm and the average temperature for these regions are reported 9.6 °C and 9.5 °C, respectively. The major direction of groundwater flow in this area is from east and north east to south west. The major aquifer compositions are related to the quaternary era.

4 Results and Discussion

In this study, based on the data gathered from study area, each layer of DRASTIC parameters was prepared. In the Figs. 2 and 3 groundwater contour map and its grading is illustrated, showing that from east of the study area to the west, the depth

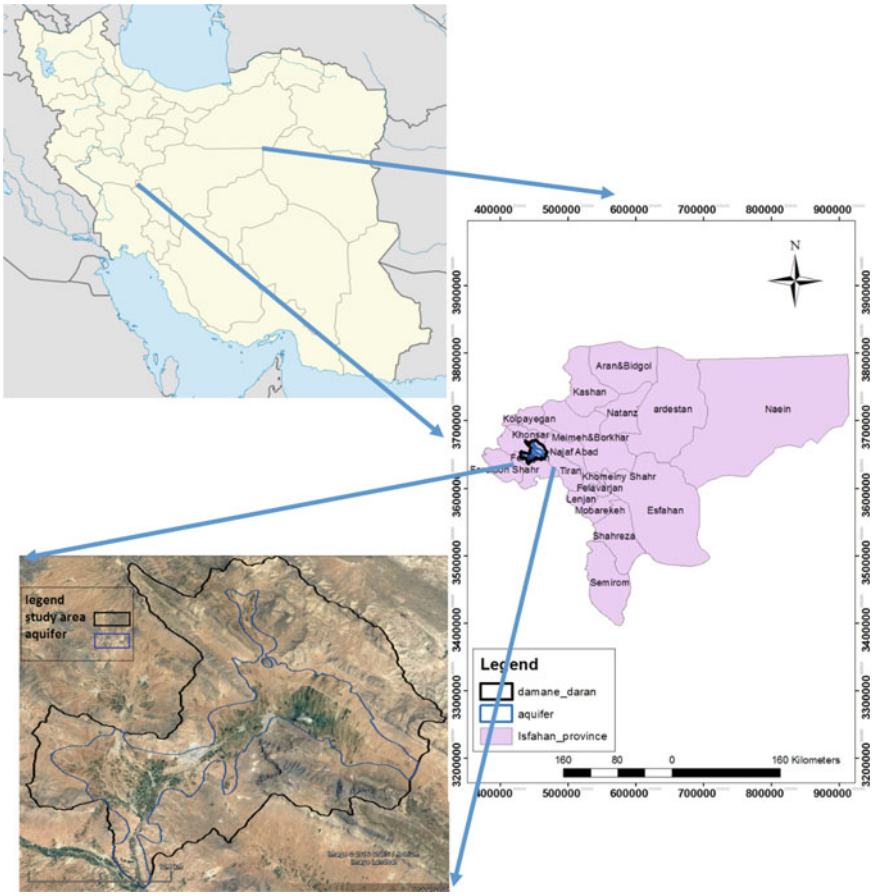

Fig. 1 Damaneh-Daran aquifer (ref: http://www.googleearth.com)

of water table is decreased and consequently its rating and the negative effect on the vulnerability is increased.

The most important parameters which affect recharge of groundwater are soil properties, unsaturated thickness, land cover, land slope, irrigation and precipitation that among these soil properties and precipitation are the most important. In a study by Goodarzi et al. (2015) it was revealed that small changes in precipitation and temperature have a significant effect on groundwater recharge where heavy soils are more sensitive to these changes. Net recharge of study area was estimated by Piscopo (2001) method in which three layers of slope, infiltration and precipitation in the region are integrated and create recharge map. (Awawdeh et al. 2015; Vaezihir and Tabarmayeh 2015; Javadi et al. 2011; Akbari and Rahimi-Shahrbabaki 2011). According to this method the recharge varies in this region from 0.000277 m/d in the west to 0.000348 in the east. The rating map of the recharge is shown in Fig. 4.

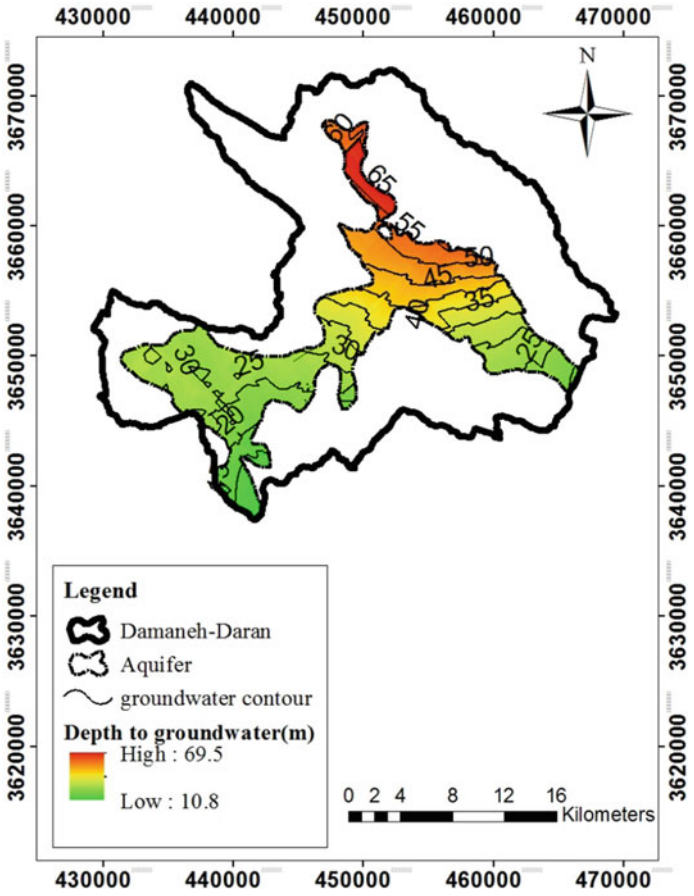

Fig. 2 Depth to groundwater and water table contour (2014)

In Figs. 5, 6, 7, 8 and 9 other parameters is presented. Aquifer media, soil media and impact of the vadose zone rating map were prepared from 22 existing well logs. Topography refers to the land slope of the ground and was taken from the DEM map of the region. Hydraulic conductivity was calculated based on the pumping tests of 8 wells in the study area.

After preparing all layers in the ArcGIS environment with a 100 by 100 m pixel size, the values assigned to the existing points were interpolated and reclassified to attribute each pixel a rating according to the rating mechanism presented in DRASTIC model, generating rating layers. Then, the map of groundwater vulnerability of the area was created by assigning weight to each rating layer and summation of all weighted ratings. In Fig. 10, the ordinary DRASTIC-based vulnerability map of the study area shows that western parts of the region are more vulnerable than eastern parts. In Table 3 area percentage covered by each class is indicated. Nearly

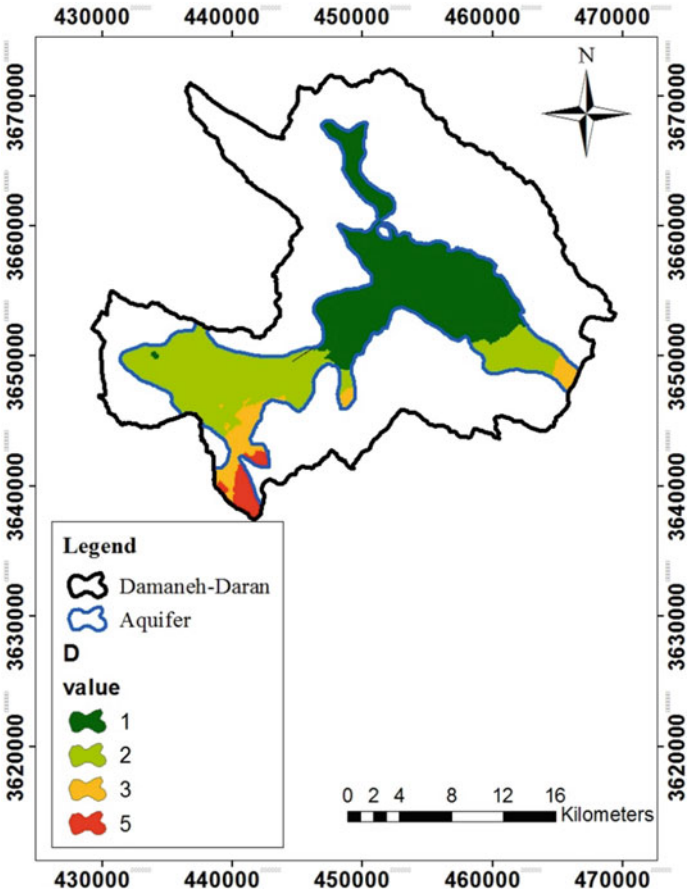

Fig. 3 The rating map of the depth to water table in DRASTIC model (2014)

33% and 28% of the study area are of low and high vulnerability potential, respectively. The mean value of DRASTIC index is equal to 94, meaning the study area has averagely medium vulnerability.

About 250 points from the study area were extracted and these points' corresponding weighted ratings in each layer including UTMx and UTMy[1] were inserted to an Excel file as an MATLAB program input data. These points are illustrated in Fig. 11. The outputs of the MATLAB program were the fuzzy membership degrees to the "most-vulnerable class" assigned to each point which were used again as an input to ArcGIS to generate final FCM-based vulnerability map. The interpolation was executed through membership degrees using the most suitable method of interpolation depending on different weighting powers used in the FCM algorithm. For

[1] Universal Transverse Mercator; UTMx and UTMy give the transversal and longitudinal (x,y) coordinates of each point.

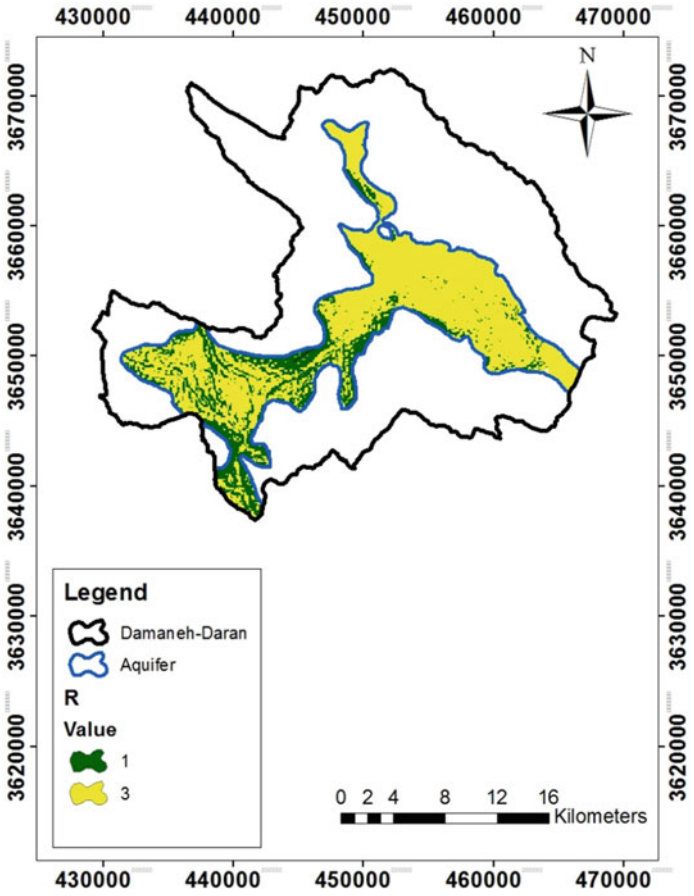

Fig. 4 The rating map of net recharge in DRASTIC model (2014)

interpolating membership degrees, $m' = 1.25$, 1.5 and 2, Spherical, Gaussian and Exponential model of Simple Kriging, respectively are found to be proper and for $m' = 1.75$, Exponential model of Ordinary Kriging is identified as the most suitable method for interpolation.

In Tables 4, 5, 6 and 7, the cluster centers of each weighting power is presented. These Tables show the elements of the center of each cluster, i.e. their weighted ratings of the DRASTIC seven hydrogeological parameters.

In Table 8 the cluster centers' membership degrees in the most-vulnerable class are presented. The classification of the vulnerability map was performed based on the Table 8, but because of very low area percentages covered by the "Extremely low" and "Extremely high" clusters, these two clusters were merged to the "Very low" and "Very high" clusters, respectively. Thus, the vulnerability map was presented in five clusters.

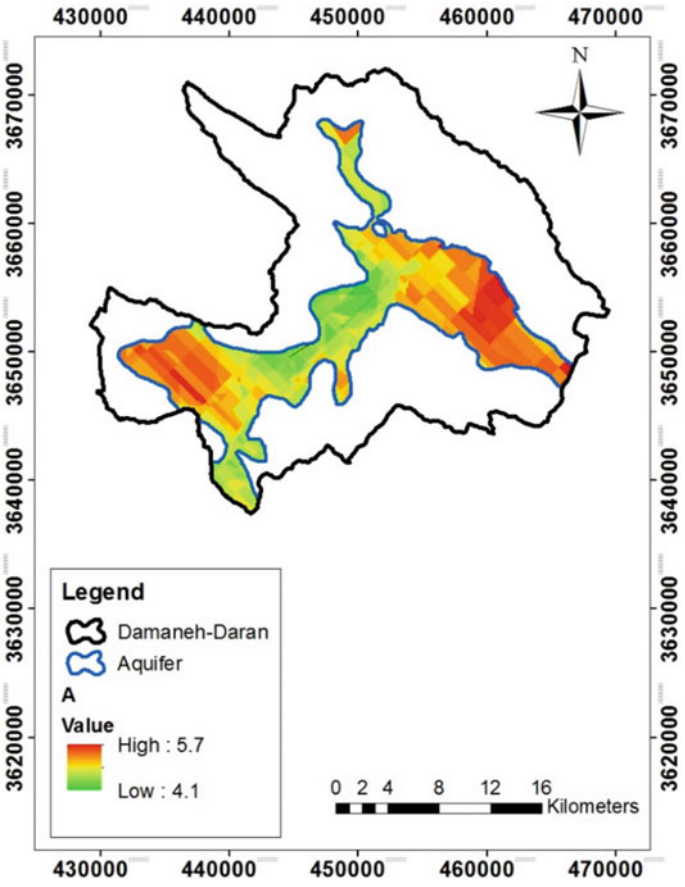

Fig. 5 The rating map of aquifer media in DRASTIC model (2014)

In Figs. 12, 13, 14 and 15, the vulnerability maps corresponding to the weighting power of 1.25, 1.5, 1.75 and 2 can be seen, respectively. As the Figures suggest, by increasing weighting power which results in increasing the fuzziness, the medium class of vulnerability is stressed and covers a higher amounts of area. Thus, the areas covered by another classes shrink to some extent such that the boundary of each class can be much obviously recognized. Consequently, for high values of the weighting powers, it will be easier to take protection measures for each region of the aquifer based on their potential to vulnerability.

In Table 9 the area percentage covered by each class shows that by increasing weighting power the percentage of the medium vulnerability cluster increases and the percentages of the extreme clusters like very low and very high decrease. In other word, by increasing fuzziness, points partly belong to all clusters and thus, the area of medium cluster which is the indicator of all clusters increase. In this study it seems that $m' = 1.75$ discriminates the classes of vulnerability better than other

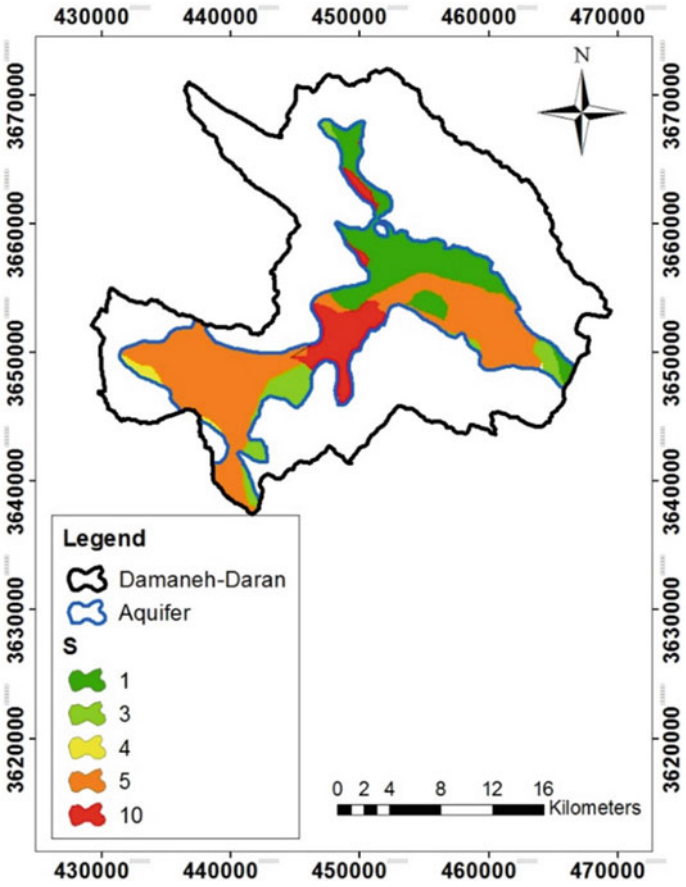

Fig. 6 The rating map of soil media in DRASTIC model (2014)

powers, whereas by $m' = 2$ fuzziness is very high and by $m' = 1.25$ and $m' = 1.5$, the discrimination of classes is not perfectly tangible.

It is shown that in m' = 1.75 the area percentages covered by low, medium and high vulnerability clusters decreases within 51%, 21% and 1% compared with ordinary DRASTIC, respectively, while the area percentages covered by very low and very high clusters increases 8 and 5 times than those of the ordinary DRASTIC, respectively, mainly due to partial membership of the hydrogeological settings in the fuzzy clusters, making the areas covered much more evenly distributed among different vulnerability classes. Although by increasing weighting power, the area percentages covered by very low and very high vulnerability clusters decreases, but even in m' = 2 the area percentages covered by these clusters are more than ordinary DRASTIC method. This is worth noting that although in some studies the K-means clustering technique is proposed as a more suitable, faster and easier method than FCM technique for clustering data points (Yang et al. 2013; Velmurugan 2012), in

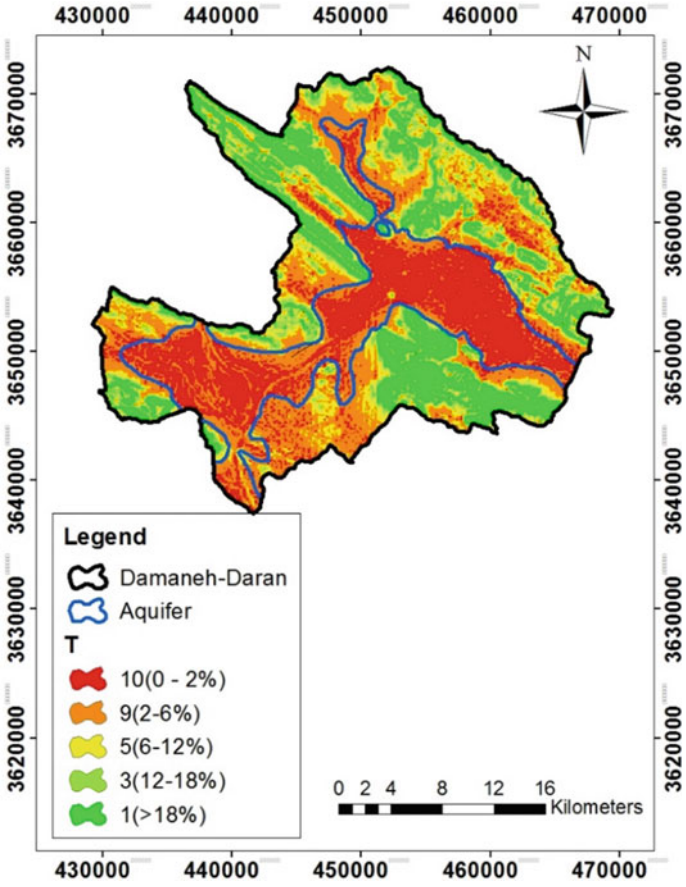

Fig.7 Topography and its rating in DRASTIC model in study area (2014)

this study, regarding the uncertain nature of vulnerability clustering affected by the hydrogeological variations, it is preferred to use fuzzy C-means clustering technique.

In This method ArcGIS helps to assess the vulnerability of not only particular points but also the points located in the total study area, compared to some other fuzzy methods that estimated the vulnerability in some sample points (Huicheng et al. 1999; Shouyu and Guangtao 2003).

In a study performed by Rezaei et al. (2016) in Zayandeh-Rud river basin aquifers in Iran to assess the vulnerability of groundwater, a hybrid method combining self-organizing maps and the ordinary DRASTIC method, named SOM-DRASTIC was used to deterministically do clustering the hydrogeological settings involving DRASTIC weighted ratings in the study area. Then, the distance of each cluster from the lowest-vulnerable cluster was evaluated using compromise programming technique. These distances were then converted to the fuzzy membership degrees assigned to the cluster centers and accordingly their covered settings in the area

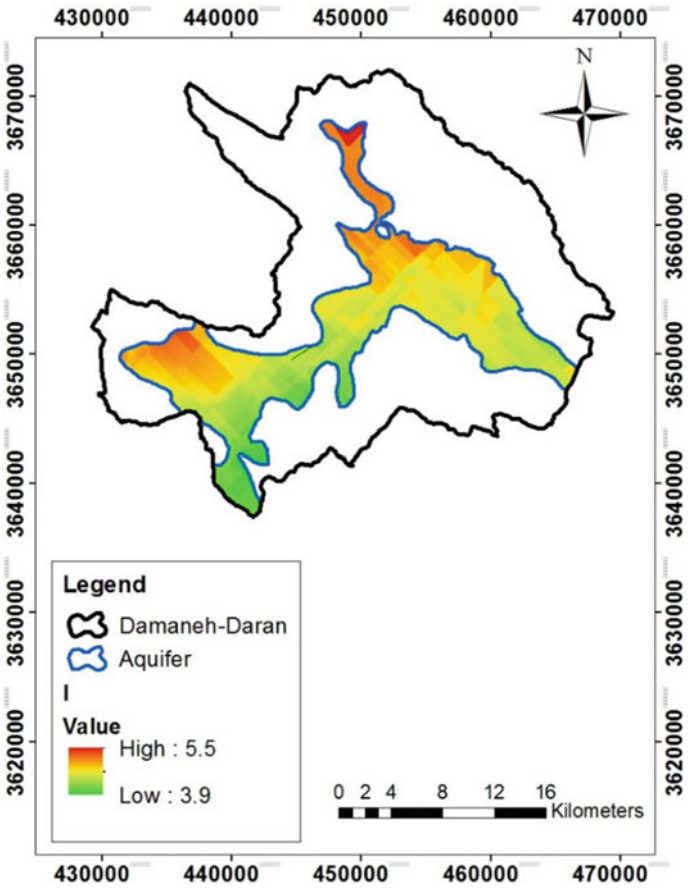

Fig. 8 The rating map of impact of the vadose zone in DRASTIC model (2014)

which resulted in forming the relative vulnerability map of the area by interpolation. In the FCM method similar process but in a faster and easier-to-use manner is conducted to estimate the vulnerability. In addition, the substantive uncertainty existing in any clustering process is addressed in the FCM method.

The results of the sensitivity analysis carried out for the ordinary DRASTIC are presented in Table 10. The results show that the vulnerability index is changed by removing impact of the vadose zone, hydraulic conductivity and soil media layers, respectively, much more than by removing other layers. Map removal sensitivity analysis is not only influenced by the parameters' theoretical weights but also depend on the value and the resulting rating of each parameter in the study area (Napolitano and Fabbri 1996).

For DRASTIC-based FCM sensitivity analysis, the DRASTIC vulnerability index (as illustrated in Eq. 12) is replaced by the membership degrees in the "most-vulnerable class". The results are shown in Table 11. The results indicate that the

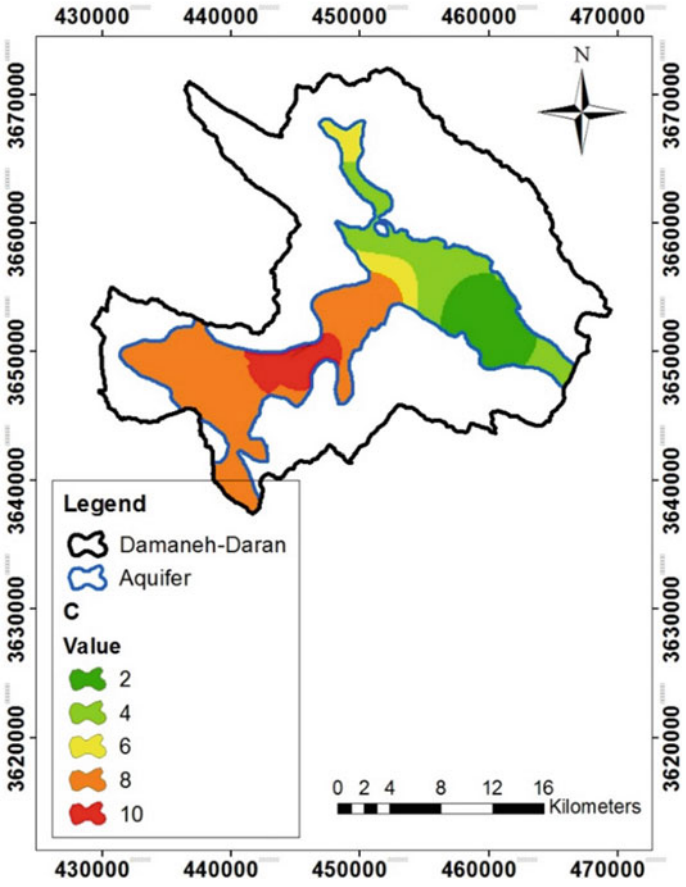

Fig. 9 The rating map of hydraulic conductivity in DRASTIC model (2014)

sensitivity values of all parameters are increased in FCM modeling compared to those presented by the ordinary DRASTIC. This is because of this fact that almost all vulnerability classes cover all hydrogeological settings in the study area as a result of fuzziness. Thus, all seven DRASTIC parameters that take part in forming these classes, contribute to form fuzzy membership degrees of vulnerability calculated for all hydrogeological settings in the study area and thus, receiving high sensitivities in sensitivity analysis carried out for FCM model. Some parameters like net recharge, aquifer media and topography which are more or less medium-effective on the vulnerability remain quite unchanged in the sensitivity when increasing the weighting power of *m*'. Because, these parameters somehow play role in forming almost all classes of vulnerability and thus, are indifferent in sensitivity when knowing the area covered by some of these classes increases and some ones decreases as the fuzziness is increasing. On the other hand, the parameters which much more moderately affect the vulnerability like hydraulic conductivity shows an increasing trend in sensitivity

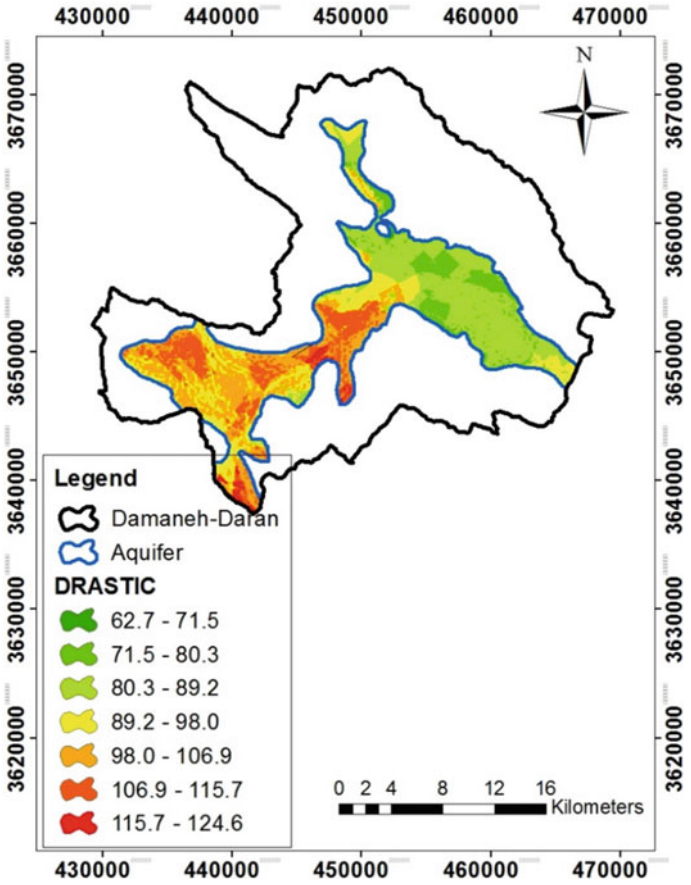

Fig. 10 DRASTIC index in the study area (2014)

Table 3 Classification of vulnerability index resulting from ordinary DRASTIC method

DRASTIC index	Vulnerability	Area covered (%)
62–75	Very low	2.10
75–87	Low	33.96
87–99	Medium	32.66
99–112	High	28.90
112–125	Very high	2.38

when increasing *m'*, mainly due to increase in the area covered by the medium class of vulnerability. The sensitivity analysis results also indicate a sudden jump in the amounts of sensitivity when the *m'* increases from 1.75 to 2. The main reason for this effect may be related to the amount of increase and decrease in the area covered by the medium and other classes of vulnerability, respectively. In fact, by assigning

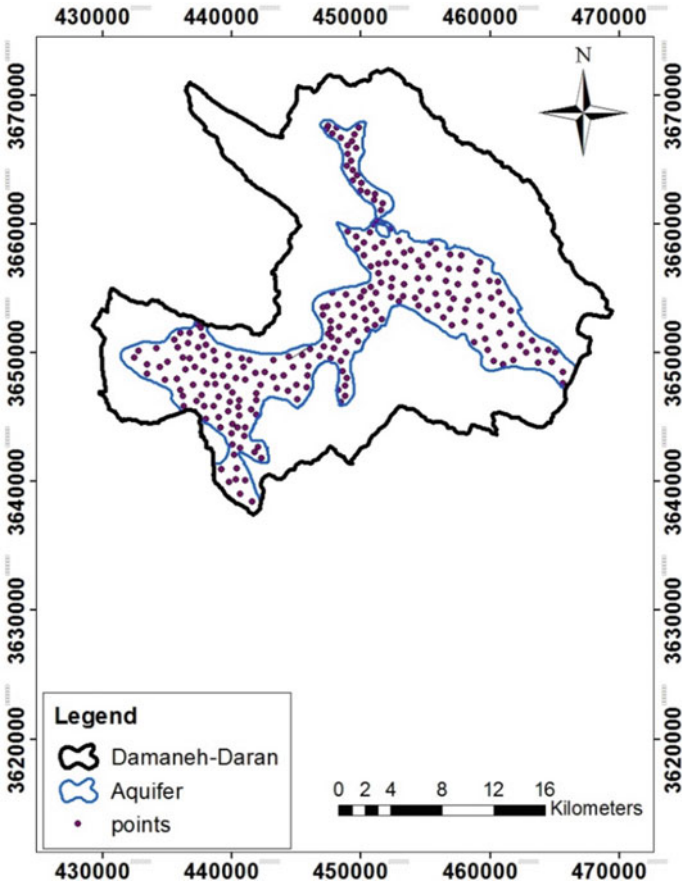

Fig. 11 Spatial distribution of 250 random points in the aquifer

Table 4 The cluster centers in $m' = 1.25$

Cluster number	D	R		A	S	T	I	C
1	6.79	10.97		15.71	10.54	9.86	23.72	7.72
2	11.00	4.04		14.65	9.33	8.78	22.98	24.92
3	24.97	7.00		14.04	7.51	8.88	20.54	23.99
4	10.31	11.98		15.12	9.75	9.85	23.75	24.91
5	5.03	11.95		14.39	2.74	9.65	25.11	19.52
6	6.29	8.75		14.06	19.99	9.61	22.97	24.68
7	5.59	11.70		15.16	2.35	9.35	24.72	11.35

Table 5 The cluster centers in $m' = 1.5$

Cluster number	D	R	A	S	T	I	C
1	6.87	11.46	15.81	9.96	9.88	23.62	7.20
2	10.95	4.28	14.68	9.49	8.91	23.03	24.74
3	5.10	11.89	14.42	2.72	9.63	25.13	19.34
4	5.33	11.79	15.13	2.36	9.48	24.80	11.52
5	5.98	8.92	14.01	19.90	9.63	23.02	24.58
6	10.25	11.91	15.21	9.87	9.84	23.87	24.69
7	24.61	6.95	14.06	7.59	8.88	20.59	23.95

Table 6 The cluster centers in $m' = 1.75$

Cluster number	D	R	A	S	T	I	C
1	24.05	6.62	14.09	7.61	8.88	20.64	23.95
2	10.68	4.45	14.75	9.67	9.00	23.18	24.56
3	5.22	11.86	15.09	2.32	9.56	24.85	11.75
4	6.80	11.68	15.88	9.83	9.91	23.60	6.79
5	5.16	11.86	14.51	2.73	9.62	25.18	18.91
6	10.12	11.86	15.32	9.95	9.83	24.04	24.42
7	5.81	9.47	13.96	19.77	9.70	23.08	24.50

Table 7 The cluster centers in $m' = 2$

Cluster number	D	R	A	S	T	I	C
1	10.06	4.53	14.87	9.90	9.05	23.59	24.31
2	15.58	5.50	14.36	9.63	9.02	21.56	24.18
3	5.21	11.86	14.57	2.63	9.64	25.21	18.50
4	6.59	11.78	15.92	9.82	9.93	23.60	6.59
5	5.17	11.91	15.07	2.26	9.62	24.88	11.89
6	10.05	11.87	15.42	9.98	9.84	24.20	24.20
7	5.65	10.61	13.86	19.69	9.82	23.19	24.33

Table 8 The cluster membership degrees in the most-vulnerable class

Clusters	$m' = 1.25$	$m' = 1.5$	$m' = 1.75$	$m' = 2$
Extremely low	0.00	0.00	0.00	0.00
Very low	0.27	0.28	0.31	0.21
Low	0.63	0.63	0.59	0.42
Medium	0.64	0.66	0.65	0.45
High	0.81	0.84	0.84	0.68
Very high	0.95	0.97	0.99	0.87
Extremely high	1.00	1.00	1.00	1.00

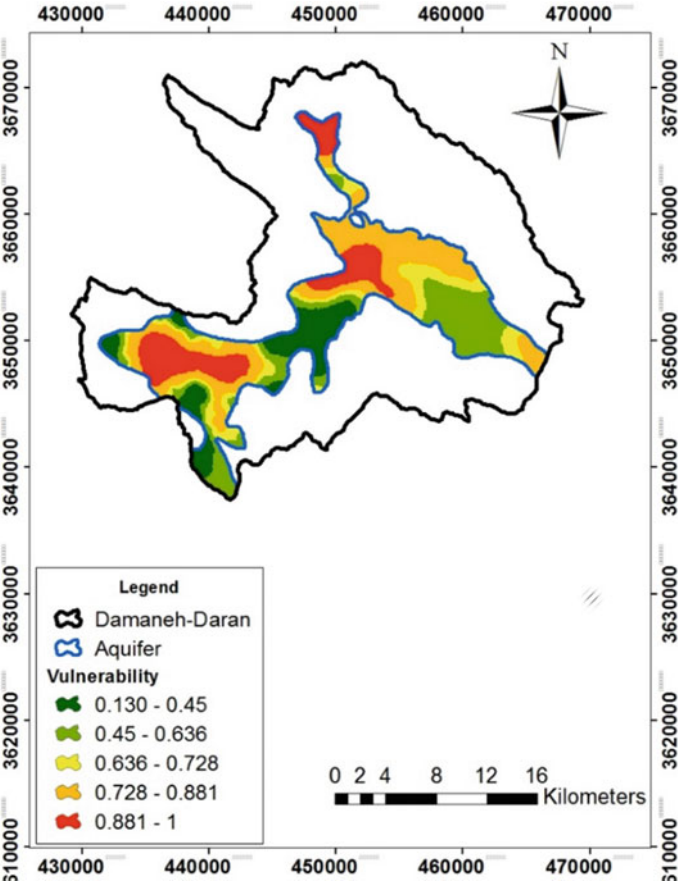

Fig. 12 Vulnerability map resulting from FCM method assuming $m' = 1.25$ (2014)

2 to m', a remarkable increase in the area covered by the medium classes is occurred which is much more than the amount of decrease in the area covered by other classes of vulnerability, leading all parameters to take part in forming all classes of vulnerability and thus, making all parameters have the highest sensitivities in this case. Based on the sensitivity analysis results on FCM, the soil media is found to be most-sensitive parameter when assuming $m' = 1.25$ and $m' = 2$, while the net recharge is of the highest sensitivity when assuming $m' = 1.5$ and $m' = 1.75$. Moreover, the topography is of the lowest sensitivity among other parameters in $m' = 1.25$, $m' = 1.5$ and $m' = 2$, while the aquifer media is the least-sensitive parameter in $m' = 1.75$, followed by depth to groundwater and topography.

To validate the FCM-DRASTIC methodology proposed in this paper, the fuzzy vulnerability indices are compared with the nitrate concentration as the main pollutant of the groundwater resources in the study area. First, the FCM-DRASTIC vulnerability map is reclassified into five classes from the lowest to the highest vulnerability.

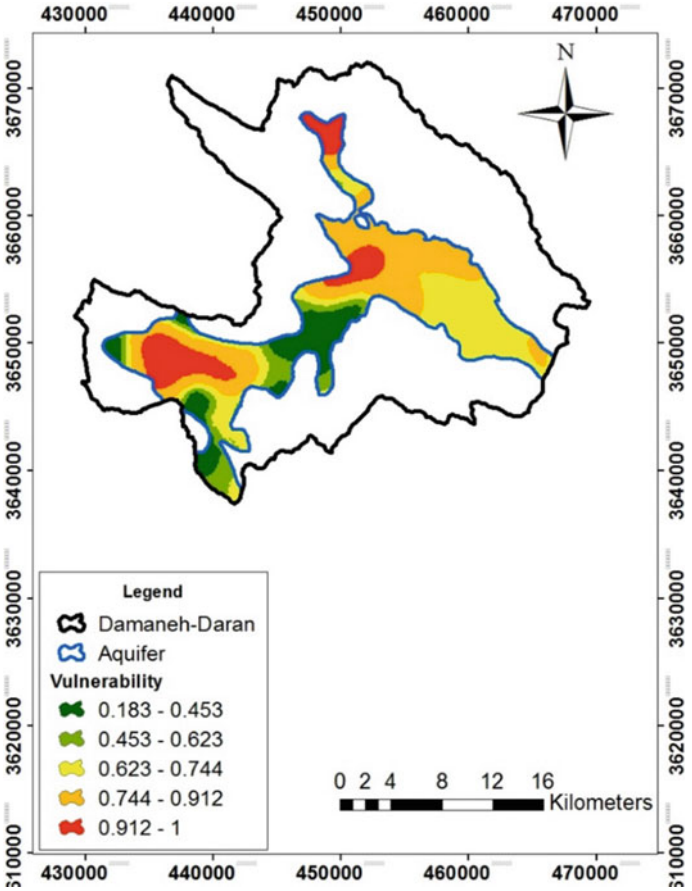

Fig. 13 Vulnerability map resulting from FCM method assuming $m' = 1.5$ (2014)

All classes are labeled a number including 1, 2, 3, 4 and 5, corresponding to the intensity of the values of each class. In addition, the nitrate concentration map is also reclassified into five classes representing the lowest concentration to the highest one. Then, 250 points are extracted from the maps each of which has a couple of the nitrate concentration and the vulnerability index. Afterwards, to the points whose two classes (nitrate and vulnerability) are similar in the label, the weight of 1 is assigned; for the points which are different in 1, 2, 3 and 4 labels, they are assigned the weights equal to 0.8, 0.6, 0.4 and 0.2 respectively. Then, the number of points gathered in each class is calculated as the size of each class after normalization, and finally, a weighed averaging procedure is performed over the size of all five classes, considering the corresponding weights and the normalized size of each of the classes. The result of the weighted average is assumed as the correlation coefficient between the nitrate concentration and the vulnerability index obtained for the whole study

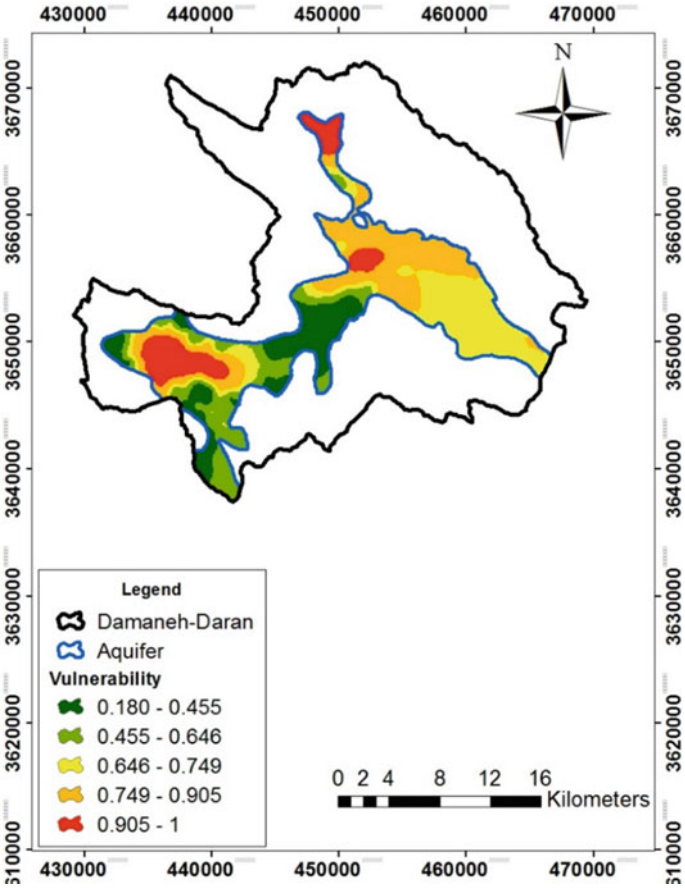

Fig. 14 Vulnerability map resulting from FCM method assuming $m' = 1.75$ (2014)

area. The nitrate concentration map is shown in Fig. 16. The correlation coefficient of the nitrate concentration and the vulnerability maps were calculated as 49%, 59%, 59% 60% and 40% for ordinary DRASTIC and FCM-DRASTIC with $m' = 1.25$, 1.5, 1.75 and 2, respectively. Accordingly, the FCM-DRASTIC method with $m' = 1.75$ is in much more accordance with the nitrate concentration and outperforms the ordinary DRASTIC and other variants of the FCM-DRASTIC in the study area (Fig. 16).

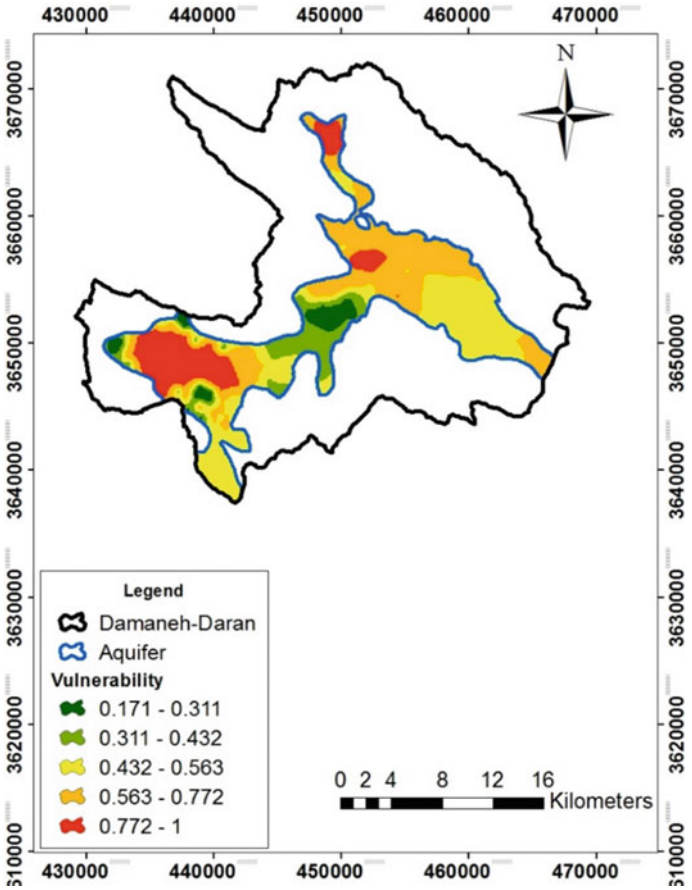

Fig. 15 Vulnerability map resulting from FCM method assuming $m' = 2$ (2014)

Table 9 Area percentages covered by each vulnerability cluster resulting from FCM method

Vulnerability	$m' = 1.25$	$m' = 1.5$	$m' = 1.75$	$m' = 2$
Very low	14.63	13.33	17.21	4.40
Low	23.09	9.71	16.49	10.76
Medium	12.31	27.90	25.72	33.88
High	32.00	34.40	28.53	35.61
Very high	17.97	14.67	12.04	15.35

Table 10 Statistical summary of map removal sensitivity analysis in ordinary DRASTIC

Parameter	Sensitivity range (%)	Mean sensitivity (%)	Standard Deviation	Coefficient of variation
Depth to groundwater	0–1.9	1.04	0.44	42.81
Net recharge	0–1.8	0.65	0.66	100.84
Aquifer media	0–1.7	0.39	0.33	82.53
Soil media	0.1–2.1	1.07	0.59	55.57
Topography	0.2–2.2	0.66	0.25	37.36
Impact of vadose zone	0.5–4.4	2	0.62	32.93
Hydraulic conductivity	0–3.1	1.23	0.70	57.39

Table 11 Mean sensitivity percentages resulting from map removal sensitivity analysis in FCM

Layer	$m' = 1.25$	$m' = 1.5$	$m' = 1.75$	$m' = 2$
Depth to groundwater	2.78	1.94	2.06	4.92
Net recharge	5.35	8.07	6.30	5.51
Aquifer media	4.16	3.29	1.90	3.53
Soil media	9.10	3.95	4.81	8.15
Topography	2.04	1.75	2.81	2.49
Impact of vadose zone	3.69	3.29	3.10	6.06
Hydraulic conductivity	3.40	3.76	4.38	4.47

5 Conclusion

Groundwater protection in arid and semi-arid regions like the central Iran where supplying drinking water from wells is of high importance causes authorities to have major concerns. Damaneh-Daran aquifer is one of the most important agricultural plains of Fereidan in Isfahan province, Iran. In this study, the intrinsic vulnerability map of aquifer was prepared using original DRASTIC model and also hybridizing DRASTIC and fuzzy C-means (FCM) clustering method. In DRASTIC-based FCM model, the ratings and weights considered for the effective parameters are the same as defined in DRASTIC, however, the FCM implements a new fuzzy approach to determine the vulnerability level of each hydrogeological setting in the study area. In this study, nearly all parameters receive higher vulnerability values in the western parts than eastern parts and thus, these regions are identified more vulnerable than the eastern parts. According to the ordinary DRASTIC map in this region, mean vulnerability index is equal to 94 and 34%, 32% and 29% of the region is of low, medium and high vulnerability, respectively.

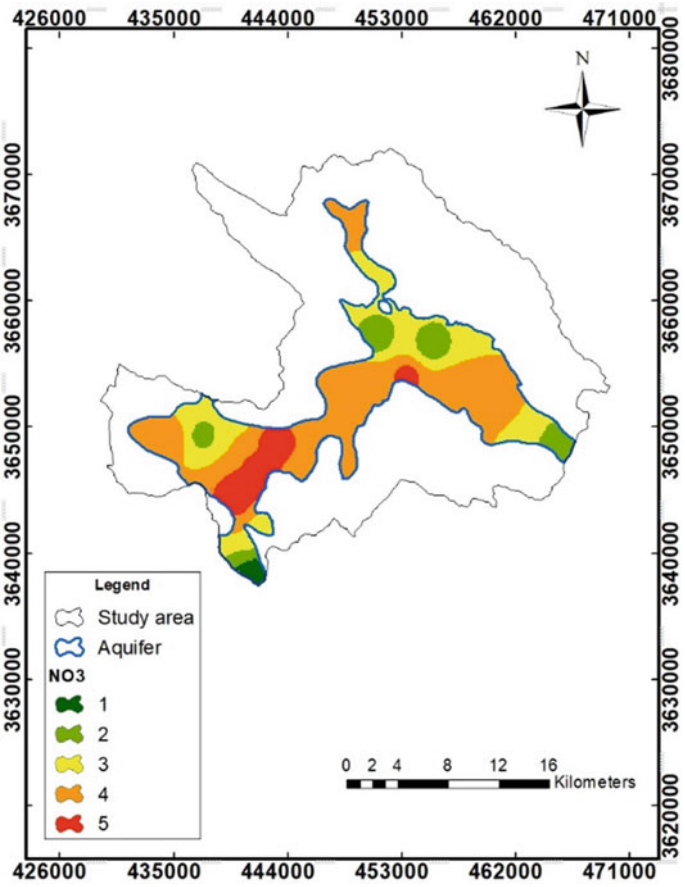

Fig. 16 Nitrate concentration map (2014)

In fuzzy C-means clustering method, by increasing fuzziness through increasing weighting power (*m'*), the boundaries of the clusters become more visible. It is also clear that by assuming an increasing trend for the weighting power, all points partly belong to all clusters and thus, the area of the medium cluster which is the indicator of all clusters increases. Also the FCM-DRASTIC method will not be comparable in different aquifers, since it can show the variations of the vulnerability point-by-point in a study area. The results indicate that by setting the weighting power of $m' = 1.75$, approximately 26% of the region has medium vulnerability. Hence, one of the benefits of setting $m' = 1.75$, compared to the other values tested in this study, is that considering this value neither makes vulnerability clusters so fuzzy that a large area is allocated to the medium clusters of vulnerability as the representative of all clusters nor so hard that makes clusters discrete and far different in the area covered by ignoring fuzziness of the clusters resulting from the spatial variations of hydrogeological parameters.

To validate the FCM-DRASTIC approach, the proposed model is compared to the nitrate concentration spatially distributed in the aquifer. The results suggest by setting $m' = 1.75$, the proposed method shows higher correlation with the nitrate concentration, as compared to the ordinary DRASTIC and the FCM-DRASTICs with other values of m'. Map removal sensitivity analysis also showed that removing impact of the vadose zone layer and the net recharge layer have the highest impact on the vulnerability index obtained by ordinary DRASTIC and the FCM-DRASTIC method assuming $m' = 1.75$, respectively.

Such a DRASTIC-based FCM-aided vulnerability mapping is not only suitable for land use planning, but can also clearly show the sensitive points to pollution, contributing the authorities to better decide for each place's application while protecting vital groundwater resources from contamination.

References

Abedi Koupai J, Golabchian M (2015) Estimation of hydrodynamic parameters of groundwater resources in Kouhpayeh-Segzi watershed using MODFLOW. J Water Soil Sci (JWSS) 19(72):281–293

Akbari GH, Rahimi-Shahrbabaki M (2011) Sensitivity analysis of water at higher risk subjected to soil contamination. Comp Meth Civil Eng 2(1):83–94

Akhavan S, Mousavi SF, Abedi-Koupai J, Abbaspour KC (2011) Conditioning DRASTIC model to simulate nitrate pollution case study: Hamadan-Bahar plain. Environ Earth Sci 63:1155–1167

Aller L, Bennett T, lehr J H, Petty R J and Hackett G (1987) DRASTIC: a standardized system for evaluating groundwater pollution potential using hydrogeologic setting. United States environmental protection agency. Region 5, Library (PL-12J)

Awawdeh M, Obeidat M, Zaiter, G (2015) Groundwater vulnerability assessment in the vicinity of Ramtha wastewater treatment plant, North Jordan. Appl Water Sci 5:321–334. https://doi.org/10.1080/01969727308546047

Bezdek JC† (1973) Cluster validity with fuzzy sets, J Cybernetics 3(3):58–73. https://doi.org/10.1080/01969727308546047

Bezdek JC (1981) Pattern recognition with fuzzy objective function algorithms. Plenum Press, New York

Ghosh S, Dubey SK (2013) Comparative analysis of K-means and fuzzy C- means algorithms. IJACSA 4(4):35–39

Goodarzi M, Abedi Koupai J, Heidarpour M, Safavi HR (2015) Analysis of the effects of various parameters on groundwater recharge using a hybrid method. J Water Soil Sci 19(73):287–299. https://earth.google.com/web/@33.01418097,50.49187116,2376.29510868a,17528.70589272d,35y,0h,0t,0r

Huicheng Z, Guoli W, Qing Y (1999) A multi- objective fuzzy pattern recognition model for assessing groundwater vulnerability based on the DRASTIC system. Hydrol Sci J 44(4):611–618

Iqbal J, Gorai AK, Katpatal YR (2015) Development of GIS-based fuzzy pattern recognition model (modified DRASTIC model) for groundwater vulnerability to pollution assessment. Int J Environ Sci Technol 12:3161–3174

Jang JR, Tsai Sun C, Mizutani E (1997) Neuro-Fuzzy and soft computing a computational approach to learning and machine intelligence. In: Jang JS (ed) Data clustering algoritm. Parentice Hall, Inc., Simon and Schuster/A Viacom Company, pp 451–453

Javadi S, Kavehkar N, Mousavizadeh MH, Mohamadi K (2011) Modification of DRASTIC model to map groundwater vulnerability to pollution using nitrate measurments in agricultural areas. J Agr Sci Technol 13:239–249

Liggett E, Talwar S (2009) Groundwater vulnerability assessments and integrated water resource anagement. Watershed Manag Bull 13(1):18–29

Lodwick W, Monson W, Svoboda L (1990) Attribute error and sensitivity analysis of map operations in geographical information system. Int J Geogr Inf Syst 4:13–28

Napolitano P, Fabbri AG (1996) Single- parameter sensitivity analysis for aquifer vulnerability assessment usin DRASTIC and SINTACS. Hydro GIS 96:559–566

Pathak DR, Hiratsuka A (2011) An integrated GIS based fuzzy pattern recognition model to compute groundwater vulnerability index for decision making. J Hydro-Environ Res 5:63–77

Piscopo G (2001) Groundwater vulnerability map explanatory notes. NSW department of land and water conservation. Land and water conservation. Australia, pp 1–18

Rezaei F, Ahmadzadeh MR, Safavi HR (2016) SOM-DRASTIC: using self-organizing map for evaluating groundwater potential to pollution. Stoch Environ Res Risk Assess. https://doi.org/10.1007/s00477-016-1334-3

Rezaei F, Safavi HR, Ahmadi A (2013) Groundwater vulnerability assessment using fuzzy logic: a case study in the Zayandehrood Aquifers. Iran. Environ Manag 51:267–277

Secunda S, Collin M, Melloul AJ (1998) Groundwater vulnerability assessment using a composite model combining DRASTIC with extensive land use in Israel's Sharon region. J Environ Manag 54:39–57

Shouyu C, Guangtao F (2003) A DRASTIC-based fuzzy pattern recognition methodology for groundwater vulnerability evaluation. Hydrol Sci J 48(2):211–220

Vaezihir A, Tabarmayeh M (2015) Total vulnerability estimation for Tabriz aquifer (Iran) by combining a new model with DRASTIC. Environ Earth Sci 74:2949–2965

Velmurugan T (2012) Performance comparison between k-means and fuzzy c-means algorithms using arbitrary data points. Wulfenia J 19(8):234–241

Yang H, Han D, Yu F (2013) Improved fuzzy c-means clustering algorithm based on sample density. J Theor Appl Inf Technol 48(1):210–214

Prospect of Retrieving Non-optical Water Quality Properties with Remote Sensing Techniques

Hala Abayazid

1 Introduction

With progressive developments and climate change concerns, water science studies are mostly dominated with sustainability as well as adaptive capacity issues. A comprehensive study for a hydro-system requires key informative inputs and series of procedure to follow historical trend, acquire updated spatially distributed data, apply analytical processes, model for alternative scenarios, and eventually recommend optimum effective policy. This multi-factorial task becomes easier with evolving Earth Observation (EO) technology and analytical techniques.

Advances in satellite imagery resolution and remote sensing techniques offer effective tools for dynamic, expanded and more frequent, monitoring processes with less laborious, time consuming field work. An enormous pool of information are deduced from radiative signals and energy detected. Absorbed, scattered, and emitted or reflected light carry informative characteristics to be revealed. Successful applications around the world, with acceptable accuracy and result reliability, encouraged wider usage in the environmental studies.

Retrieval of water quality properties from EO-based products proved promising, yet remotely estimated water quality parameters are mostly related to Inherent Optical Property (IOP). Visibility attribute, or optically active property, of surface water narrows down the parameters that can be assessed by remote sensing techniques. Consequently, early studies are mostly focused on water physical and biogeochemical components that are considered optically detectable (Giardino et al. 2014). Therefore, remotely deriving weak and/or non- optical water quality characteristics, that have no directly-detectable reflection, is challenging.

H. Abayazid (✉)
Coastal Research Institute, National Water Research Center, Ministry of Water Resources and Irrigation, Alexandria, Egypt
e-mail: halazid@yahoo.com

A. Shaban (ed.), *Satellite Monitoring of Water Resources in the Middle East*,
Springer Water, https://doi.org/10.1007/978-3-031-15549-9_20

This chapter is intended to cover aspects in space-based monitoring of water quality, with reference to the potentiality of retrieving non-optical properties. Successful results open the field to expand applications with EO products, and explore more water quality parameters that are interrelated with optically active properties.

2 Remote Sensing and Water Quality

Processed data of satellite imagery provide expanded information base, with extended spatial and temporal synoptic. Applications with remote sensing techniques have proved successful retrieval of water quality parameters that have directly-detectable spectral signals, which allow regular assessment and change mapping for sustainability studies.

Several researches in literature have addressed retrieval of water quality parameters using remote sensing techniques. Significant correlations have been found between specific water quality parameters and reflectance measured with satellite sensors. Retrieving properties such as water clarity; turbidity, and Total Suspended Solids (TSS) concentrations using earth observation imageries have been tackled in applied research studies worldwide (e.g. Sravanthi et al. 2013; Dona et al. 2014; Dorji and Fearns 2016; Abayazid and El-Gamal 2017). In 2008, He et al. presented water quality retrieval models with proven successful results for optical nitrogenous and phosphorous components (He et al. 2008). Other parameters such as vegetative content, chlorophyll-a (chl-a) and Colored Dissolved Organic Matter (CDOM)) have also been covered in various studies (e.g. Dona et al. 2014; Brezonik et al. 2005; Li et al. 2002).

Basic approach in most of the reviewed practices is to establish empirical/ semi-empirical relationship or develop algorithms, while relating alternate band combination with ground truth observations. Generally, the investigated correlation build statistical relationship between the remote sensing measurements (i.e., radiance, reflectance, energy) and in-situ water quality measurements, while using fine tuning empirical factors, in order to derive a water quality property with IOP (e.g., suspended sediment, turbidity…etc). The following section introduces applications with fairly new concept for retrieval of non-optically detectable variables in the surface water quality field.

3 Applications-Coastal Lakes in the Nile Delta

3.1 Sustainability: Development Processes and Climate Change Impact

Coastal lake is a place of interplay between sea, land and river system. Northern coastal lakes in Egypt have special ecosystem as well as socioeconomic importance. While internationally acknowledged as environmentally rich water bodies, these lakes are alleviating the non-favorable polluting effect of excessive land-based development activities, before reaching the Mediterranean Sea. Moreover, climate change challenge adds an important role for coastal lakes to act as natural adaptive measure that effectively buffer potential Sea Level Rise (SLR) and unprecedented extreme flood events. (Abayazid and El-Adawy 2019). Yet the compromised self-recovery mechanism in deltaic coastal lakes threats their beneficial capacity.

In Egypt, researches have addressed remote sensing-based inland water quality assessment, with respect to optical properties, especially with the growing concerns of the adverse effects of anthropogenic disturbance to the environmental conditions (e.g. Saad El-Din et al. 2013; Abayazid 2015; El-Kafrawy et al. 2015; Rostom et al. 2017).

This following section presents two case studies for remote sensing–based retrieval of a non-optically active property of water quality in shallow inland water body-deltaic lakes in Egypt (Fig. 1). First, results are demonstrated for an investigated approach to derive oxygen–related water quality parameter, namely Dissolved Oxygen (DO), in Lake Edku with reference to other optically retrievable properties that affect and be affected by DO concentrations. Then, an approach of deriving water salinity distribution in Lake Burullus is introduced in details.

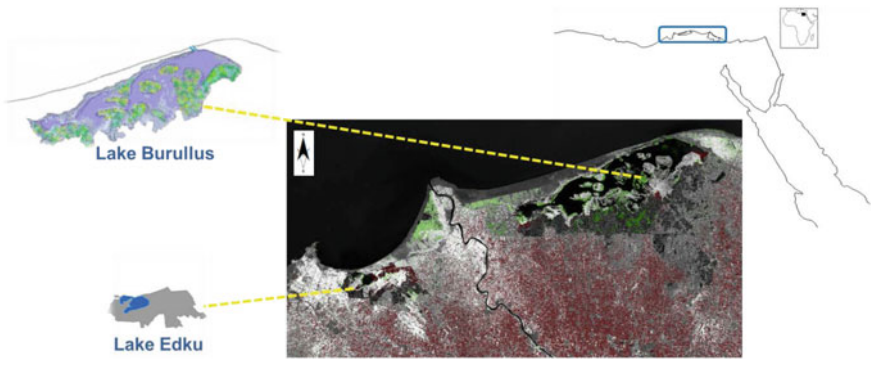

Fig. 1 Study Areas-Lake Edku and Lake Burullus in the Nile Delta of Egypt

4 Case Study1: Edku Coastal Lake-North of Egypt

The Dissolved Oxygen (DO) level is considered a decisive indicator of water system healthiness and governor of recovery capability. Yet, being a non-optical property, DO concentration cannot be directly detected using space-based imageries. The approach assumed was based on the potentiality of deriving DO levels from optically detectable water quality properties that interrelate with Oxygen presences in water.

Early theories by Streeter and Phelps modelling for Dissolved Oxygen in water bodies set principal grounds that dictate DO depletion and recovery (Chapra 1997). Hence, parameters that reflect Oxygen consumption and release, while considering regional conditions, have been investigated. Trophic and sediment-related properties were assumed key factors in selection. Also, temperature was added in the DO retrieval process as an important driver affecting Oxygen level in water, especially with the thermal anthropogenic releases and flow dynamic irregularity within Lake Edku.

The imageries used in the study are the freely available LandSat 8 Operational Land Imager (OLI) from the United States Geological Survey (USGS) Earth Explorer website. Corresponding seasonal ground truth DO data have been collected during spring, summer, fall and winter of year 2016. Images used in this study were acquired on nearest corresponding overpass dates to match the sampling data timing. The spectral range considered in the study is covering visible and Near-Infrared bands (2, 3, 4, and 5) as well as Thermal Infrared bands (10 and 11). Available field data were divided into two groups for, first, building algorithm models. Then performance has been tested with the reserved second group of data for validation process.

Comparative analysis of multiple regression algorithms were carried out using alternate combinations of parameters; namely, Turbidity, Total Suspended Solids (TSS), Chlorophyll-a, and Temperature.

Results show successful statistically significant correlation in a number of the combinations considered. Yet optimal DO retrieval algorithm model, with best fitting predictions as well as least data requirement and calculation efforts, has been concluded with Turbidity and natural logarithm of temperature, with about 80% accuracy degree.

Results proved promising success of predictions that relate optical to non-optical properties of water quality. Such application provides better distribution vision, using processed remote sensing products which, in turn, allow more analysis and cause–effect investigations. More details can be found in Abayazid and El-Adawy (2019) (Fig. 2).

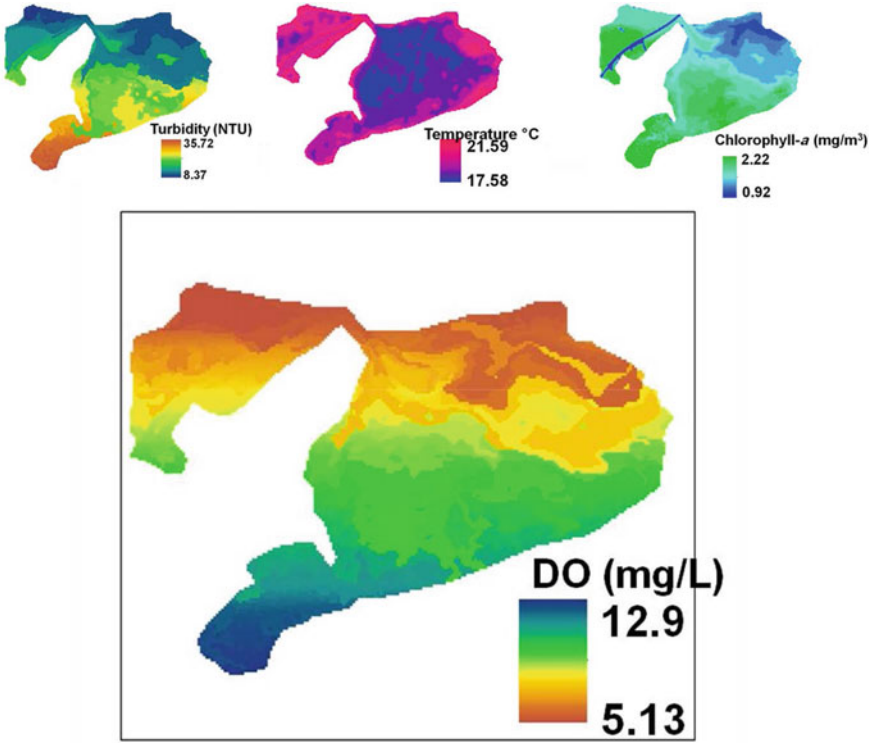

Fig. 2 Study results for Lake Edku

5 Case Study2: Salinity Distribution in Burullus Coastal Lake-North of Egypt

Progressive anthropogenic intrusion; population growth and development expansions, beside the alarming risks with climate change impact have caused concerns with sustainability and productive capacity of Lake Burullus. This deltaic Lake was considered representative selection; both for the growing concerns with declining ecological status, as well as the socio-economic importance as a key producer in fish farming industry in Egypt.

It has been established that the governing factors of changes in deltaic coastal lake water quality are strongly related to nutrient versus salinity levels within. Therefore, the current study presents an application of employing remote sensing to follow changes in water salinity distribution for Burullus coastal lake, as a principal factor for balanced bio-physical structure of coastal water as well as healthy aquatic ecosystem within. Salinity dictates many physical, chemical and biological processes in lake waters; aquatic plants density, biota structure, circulation behavior and sedimentation tendency, and hence flow dynamic pattern. In addition, salinity distribution is a

definitive indicator of the expected responses within the lake to the Sea Level Rise (SLR) phenomenon.

Mapping properties of water quality state within Lake Burullus using remote sensing have been addressed in earlier studies (such as; Hereher et al. 2010; Abayazid 2017…etc.). Typically, retrieval of the lake water quality from space-based products involves processing measured radiance/reflectance in combination with field measurements for certain detectable water quality parameters. With training then validations, acceptable results are found when highest correlation and lowest standard error are achieved.

Yet, satellite missions for salinity derivation, such as NASA's Aquarius mission, launched in June 2011 with 150 km spatial and 7-day temporal resolution, and the European Space Agency's global observations of Soil Moisture and Ocean Salinity (SMOS) mission, launched in November 2009 with about 200 km spatial and 10–30 day temporal resolution, are mainly intended to open oceans. These ranges of spatial and temporal resolutions are too coarse for an inland water body such as Lake Burullus. The Lake has relatively small area that requires satellite imageries at higher spatial resolution. Therefore, LandSat was considered appropriate in this study application.

While salinity has no spectral signature that can be directly detected with LandSat imagery, yet it can be inferred from certain strong inverse relationship that was earlier established. Previous studies reported the inherited decrease in Colored Dissolved Organic Matter (CDOM) coefficient with increasing water salinity (e.g. Moon et al. 2006; Guo et al. 2007; Sasaki et al. 2008; Bowers and Brett 2008).

Colored Dissolved Organic Matter (CDOM) is remotely detectable because of the bioactive optical property that influences light transmittance in the aquatic ecosystems (Williamson and Rose 2010). Early applications successfully developed algorithm for CDOM retrieval from satellite ocean color observations, based on the established relationship with the apparent optical properties (reflectance), particularly in the blue-green part of the spectrum (Kutser et al. 2005; Ahn et al. 2008). Then, based on the proved high inverse correlation, salinity can be estimated, with quantifiable interrelations between salinity and CDOM by empirical algorithms, or statistical models, using visible bands of the spectrum of space-based imagery.

Yet, successful derivation of salinity from CDOM levels and satellite images requires employing in-situ measurements in trainings and validations, so that a reliable relationship is established. Regrettably, field trips were not concluded for the time of this study due to health and safety restrictions.

With shortage in ground truth availability, the current research study applies a conceptual salinity distribution, based on the documented adverse effect of organic and nutrient contents in the lake. This compromised approach relates salinity levels to optically active nutrient-based indicators, represented by indexed Colored Dissolved Organic Matter (CDOM), and Chlorophyll-a concentrations. In addition, the Normalized Difference Vegetation Index (NDVI) has been included as an added factor in the developed logistic algorithm. Accordingly, generalized spatial distribution patterns of salinity in Lake Burullus, not the exact concentrations, have been concluded.

5.1 Lake Burullus Main Features

Lake Burullus is considered one of the most important lakes in Egypt. It is located between 30° 30’ to 31° 10′ E and 31° 21′ to 31° 35′ N (Fig. 3), in a dynamic region between Damietta and Rosetta branches of the River Nile (Abayazid and Al-Shinnawy 2012). The lake is about seventy (70) kilometers in length, with width ranges from six to fourteen (6–14) kilometers, and shallow water depth ranges from 0.42 to 2.07 m.

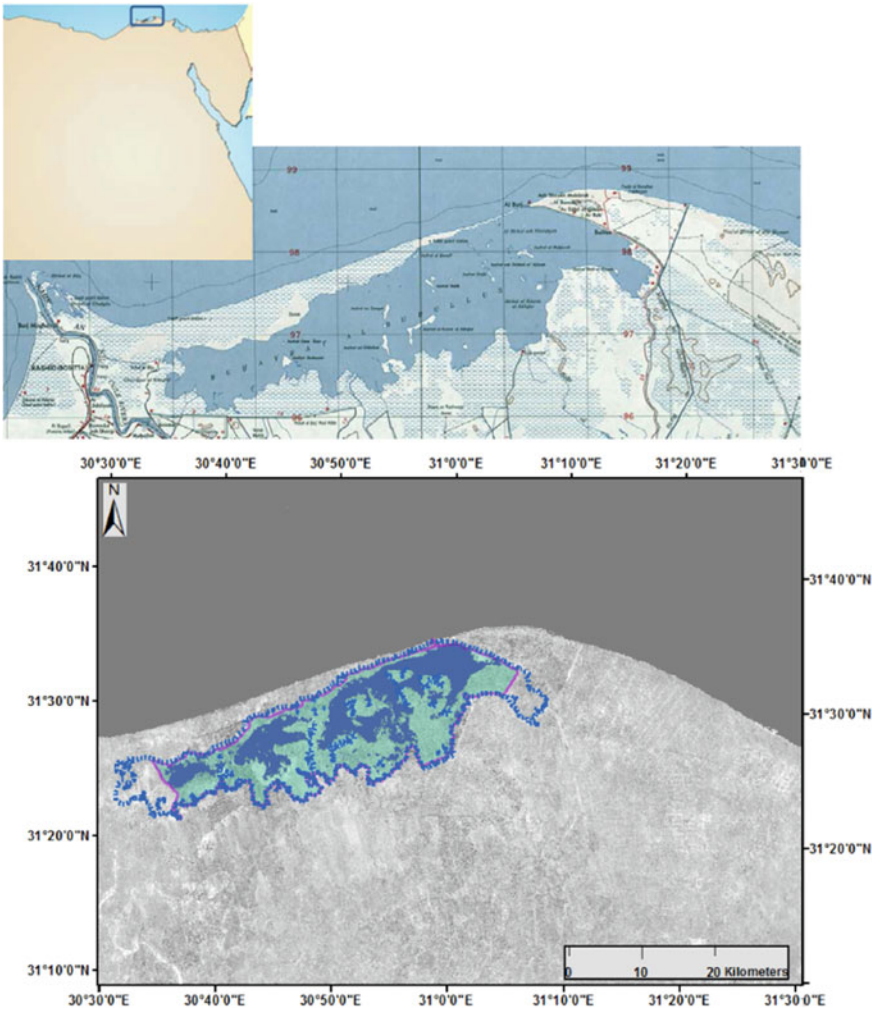

Fig. 3 Lake Burullus—Progressive anthropogenic intrusion & shrinking open water

The Burullus Lake has a historic reputation of having rich aquatic ecosystem and active socio-economic status. Its environmental importance comes from hosting rare plants and waterfowl. The lake is an important stop-over point for migrating birds. Therefore, Lake Burullus has been declared a nature reserve.

Yet, the lake is a receiving pool for considerable amounts of drainage waters with various characteristics, coming from development activities; e.g. urban sewage, industrial facilities, Waste Water Treatment Plants (WWTPs), fish farm practices, as well as drainage waters rich with chemicals fertilizers and pesticides from agricultural lands in western Delta region. Hence, the lake experiences deterioration in water quality state, with alarming ecosystem alteration.

5.2 Satellite Imageries

Imageries used in this case study application are from LandSat; the U.S. Geological Survey platform, with the following characteristics:

WRS_PATH = 177

WRS_ROW = 38

GRID_CELL_SIZE_REFLECTIVE = 30 m

SPACECRAFT_ID = "LANDSAT_5 MSS" and LANDSAT_8 OLI_TIRS".

Time steps in years 1984–2018.

5.3 Results

Results retrieved from the satellite imageries, in time steps from years 1984 to 2018, clearly demonstrate the dramatic changes experienced in the Burullus coastal lake. Expanded developments caused alteration in the lake structure and open water area. Figure 4 shows the increased intensity in NDVI levels by year 2018. That change in aquatic vegetative cover within the lake reflects the increasing nutrient-rich drainage waters from served watershed, with minor saline water inflows from the Mediterranean Sea.

Due to health safety restriction and economic constraints, the remote sensing-based retrieved salinity is established on deduced algorithm related to detectable spatial distribution of the selective organic –based indicators; namely NDVI, Chlorophyll-a (Fig. 5) and CDOM (Fig. 6). However, results are cross-checked with previous monitoring campaigns to the lake, and found correspond to the consulted historical observations in salinity trend within. Moreover, pronounced irregularity and disturbed distribution reported in certain locations (such as the high salinity level in the immediate spot to the connection point with the Mediterranean Sea, or the low

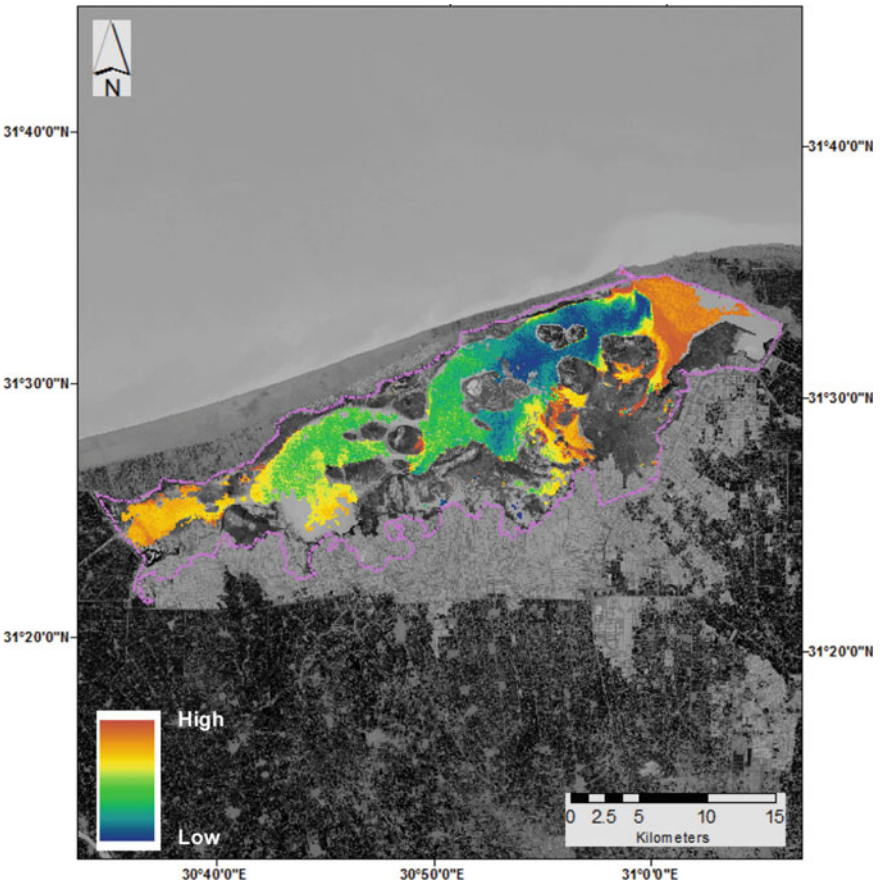

Fig. 4 Remotely derived spatial distribution of NDVI in Lake Burullus

saline content in trapped western zone of the lake) are clearly reflected in accordance with the reached results.

The concluded salinity distribution within the lake is based on cumulative indexing of representative nutrient organic presence impact, and documented adverse trend, proved by reviewed studies. Exemplar result of remotely derived salinity distribution in the lake is shown in Fig. 7. Results also show detectable flow disturbance and zonation within the lake (Fig. 8). Salinity distribution is, principally, related to flushing versus retention rate, as well as closeness to the opening with the Mediterranean Sea (Boghaz) versus inflow points of the agricultural drainage system. Figure 8 shows an example of the flow disturbance effect and slow water exchange in the far western zone of Lake Burullus and, accordingly, unbalanced water salinity degree.

Findings indicate acceptable representation achieved with combined optical factors. However, further investigation with complementary field measurements, will

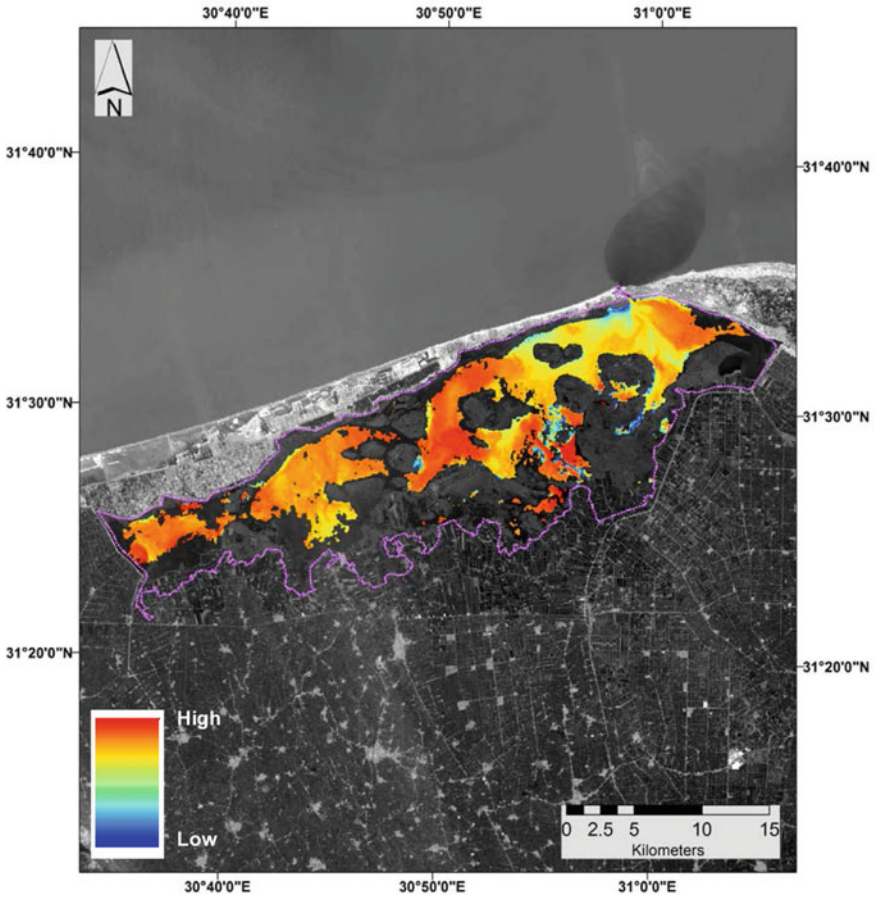

Fig. 5 Remotely derived spatial distribution of Chlorophyll-a in Lake Burullus

be needed to establish representative algorithm relating NDVI, Chlorophyll-a and CDOM to salinity levels in the coastal lakes.

6 Conclusions

Sustainable development, resources conservation and preparedness to climate change impact are issues that concern water science community. As data is a key requirement for thorough studies, regular monitoring and information collection become a necessity.

Field-based assessment of water quality state is usually challenged by limitations in spatial coverage, frequency of sampling as well as possible economic and

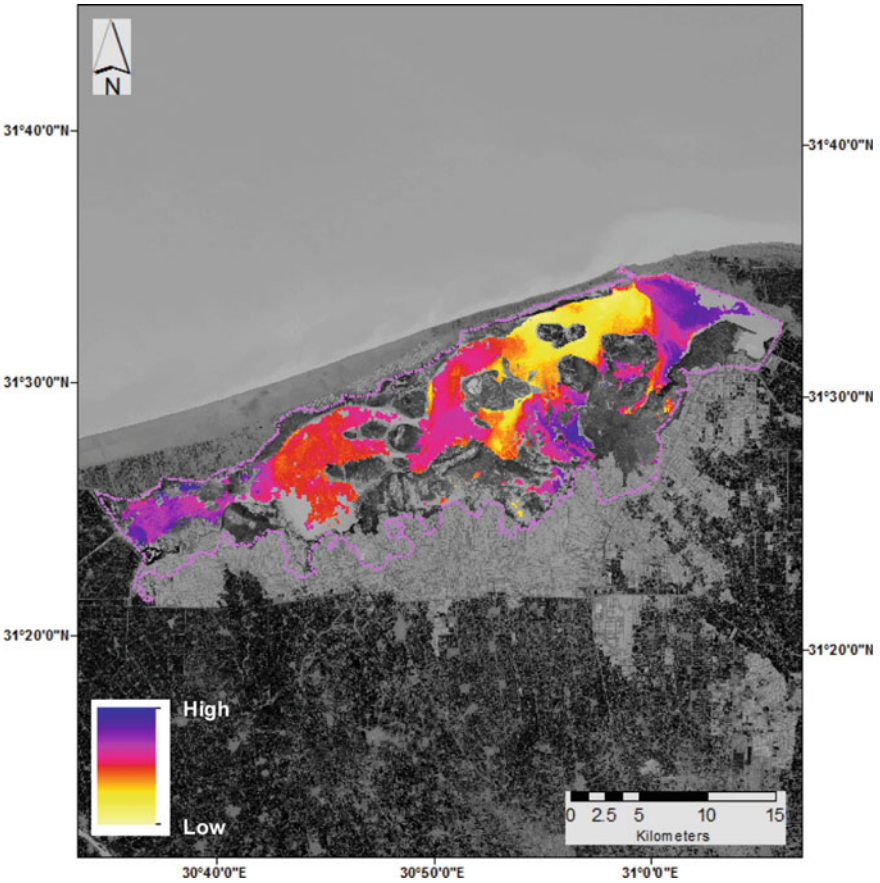

Fig. 6 Remotely derived spatial distribution of CDOM in Lake Burullus

accessibility obstacles. Meanwhile, applications with remote sensing techniques have proved successful retrieval of water quality parameters that have directly-detectable spectral signals, with acceptable accuracy and reliability of the results, which encouraged wider usage in the environmental studies.

The current research study presents a conceptual approach that demonstrates viability of deducing non-optical properties with reference to other decisive optical variables. Through applications in coastal Lakes of the Nile delta, namely Edku and Burullus, satellite-based data were employed for indirect retrieval of Dissolved Oxygen and salinity distribution, respectively.

Results proved acceptable representation for DO levels in Lake Edku, with provision of holistic trends that help understanding cause-effect patterns. Also, Earth Observation technique proved liable in reflecting spatial change of a key water quality feature, salinity distribution, within Lake Burullus. Besides, findings highlight problematic hotspots that require immediate management plan. Yet, derived salinity index

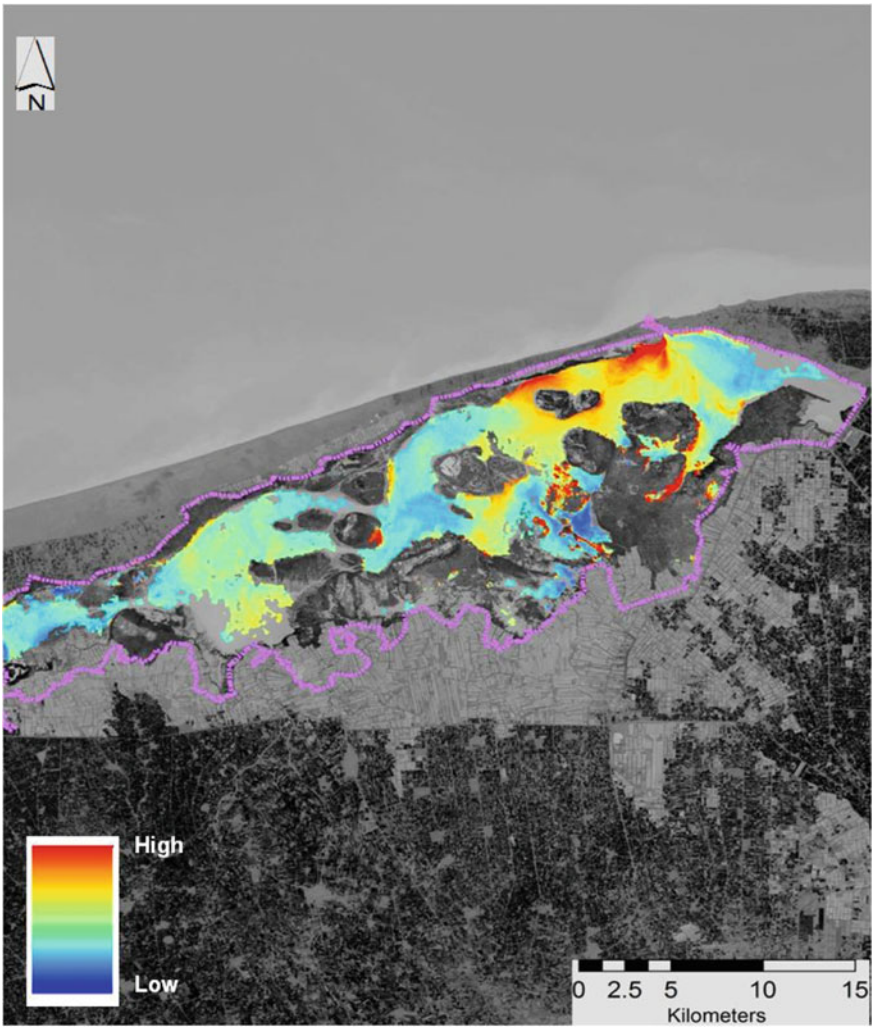

Fig. 7 Remotely derived Salinity distribution in Lake Burullus

is considered as indicative pattern, due to the shortage in spatially distributed in situ measurements for ground truthing. While the detected patchy salinity is verified with consulted historical trends, nonetheless, further analysis with field data are needed for more precise information on salinity levels within the lake.

This research introduces primary insight and lay a foundation for future studies covering inland water quality monitoring, and fill an essential gap in order to include non-optical properties with reference to detectable ones. The approach presented in this study encourages expanded applications with space-based Earth Observation

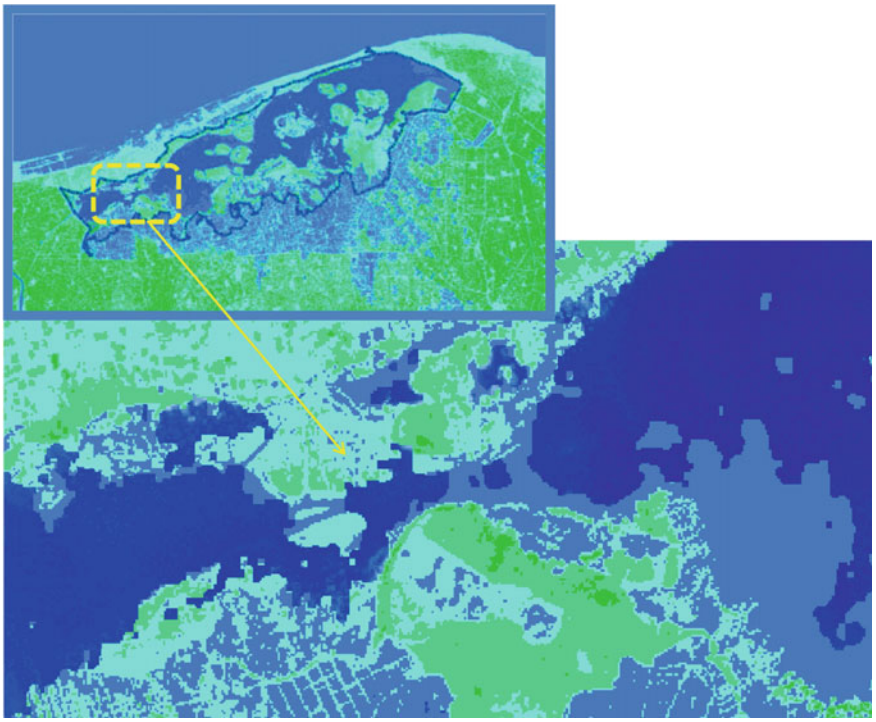

Fig. 8 Slow water exchange in far western zone of Lake Burullus

products for exploring non-detectable water quality parameters that are interlinked with optically active properties in surface water.

References

Abayazid H, El-Adawy A (2019) Assessment of a non-optical water quality property using space-based imagery in egyptian coastal lake. J Water Resour Protect 11:713–727. Scientific Research Publishing. ISSN Online: 1945-3108 ISSN Print: 1945-3094

Abayazid H (2017) Changes in coastal lake dynamic system and potential restoration. In: Egyptian coastal lakes and wetlands Part II, the handbook of environmental chemistry, multi-authored book. Springer International Publishing

Abayazid H, El-Gamal A (2017) Employing remote sensing for water clarity monitoring in the Nile Delta coast. Int Water Technol J IWTJ 7(4):265–277

Abayazid H (2015) Assessment of temporal and spatial alteration in coastal lakes—Egypt. In: The eighteenth international water technology conference IWTC, 12–14, Sharm El Sheikh–Egypt, pp 598–608

Abayazid H, Al-Shinnawy I (2012) Coastal lake sustainability: threats and opportunities with climate change. J Mech Civil Eng Int Organ Sci Res (JMCE/IOSR) 1(5): 33–41

Ahn Y, Shanmugam P, Moon J, Ryu J (2008) Satellite remote sensing of a low-salinity water plume in the East China sea. Ann Geophys 26:2019–2035
Bowers D, Brett H (2008) The relationship between CDOM and salinity in estuaries: sn analytical and graphical solution. J Mar Syst 73(1–2):1–7
Brezonik P, Menken KD, Bauer M (2005) Landsat-based remote sensing of lake water quality characteristics, including chlorophyll and colored dissolved organic matter (CDOM). Lake Reserv Manag 21:373–382
Chapra SC (1997) Surface water quality modeling. McGraw-Hill Co. Inc.
Dona C, Sánchez JM, Caselles V, Domínguez JA, Camacho A (2014) Empirical relationships for monitoring water quality of lakes and reservoirs through multispectral images. IEEE J Select Topics Appl Earth Observ Remote Sens 7(5):1632–1641
Dorji P, Fearns P (2016) A quantitative comparison of total suspended sediment algorithms: a case study of the last decade for MODIS and Landsat-based sensors. Remote Sens 8:810. https://doi.org/10.3390/rs8100810
El-Kafrawy S, Khalafallah A, Omar M, Khalil M, Yehia A, Allam M (2015) An integrated field and remote sensing approach for water quality mapping of Lake Burullus, Egypt. Int J Environ Sci Eng (IJESE) 6:15–20
Giardino C, Bresciani M, Stroppiana D, Oggioni A, Morabito G (2014) Optical remote sensing of lakes: an overview on Lake Maggiore. J Limnol 73(s1):201–214. https://doi.org/10.4081/jlimnol.2014.817
Guo W, Stedmon C, Han Y, Wu F, Yu X, Hu M (2007) The conservative and non-conservative behavior of chromophoric dissolved organic matter in Chinese estuarine waters. Mar Chem 107:357–366
He W, Chen S, Liu X, Chen J (2008) Water quality monitoring in slightly-polluted inland water body through remote sensing—A case study in Guanting reservoir, Beijing, China. Front Environ Sci Eng China 2(2):163–171. https://doi.org/10.1007/s11783-008-0027-7
Hereher M, Salem M, Darwish D (2010) Mapping water quality of Burullus lagoon using remote sensing and geographic information system. J Am Sci 7(1):138–143
Kutser T, Pierson D, Kallio K, Reinart A, Sobek S (2005) Mapping lake CDOM by satellite remote sensing. Remote Sens Environ 94:535–540
Li S, Wu Q, Wang X (2002) Correlations between reflectance spectra and contents of Chlorophyll-a in Chaohu Lake. J Lake Sci 9(14):228–234
Moon J, Yang C, Ahn Y (2006) Salinity estimation based on inherent optical property (IOP) in the southern Yellow sea and northern East China sea. In: Proceedings 4th JKWOC meeting, 18– 21 December 2006, Jeju National University, Jeju Island, Korea
Rostom N, Shalaby A, Issa Y, Afifi A (2017) Evaluation of Mariut Lake water quality using hyperspectral remote sensing and laboratory works, Egypt. J Remote Sens Space Sci 20, Supplement 1:S39–S48
Saad El-Din M, Gaber A, Koch M, Ahmed R, Bahgat I (2013) Remote sensing application for water quality assessment in Lake Timsah, Suez Canal, Egypt. J Remote Sens Technol 1(3): 61–74
Sasaki H, Siswanto S, Nishiuchi K, Tanaka K, Hasegawa T, Ishizaka J (2008) Mapping the low salinity changing diluted water using satellite-retrieved coloured dissolved organic matter (CDOM) in the East China sea during high river flow season. Geophys Res Lett 35:L04604. https://doi.org/10.1029/2007GL032637
Sravanthi N, Ramana IV, YunusAli P, Ashraf M, Ali MM, Narayana AC (2013) An algorithm for estimating Suspended Sediment concentrations in the coastal waters of India using remotely sensed reflectance and its application to coastal environments. Int J Environ Res 7(4):841–850
Williamson C, Rose K (2010) When UV meets fresh water. Science 329:637–639

A Combined Remote Sensing and Modelling Approach to Simulate the Impact of Climate Change on the River Discharge in a Lebanese Snow-Covered Basin

Ali Fadel, Ghaleb Faour, Mario Mhawej, Mahmoud Ghazal, and Lionel Jarlan

1 Introduction

Water stored as snowpack is an important component of the hydrological cycle in many regions throughout the world (Marchane et al. 2015; Tahir et al. 2019; Washington et al. 2019). In Mediterranean climate, it affects stream flow through snow meltdown during Summer season when there is no or little precipitation events. For instance, precipitation in Lebanon is limited to the winter season (December–March). However, snow provides water in the following months (May to August) as snowmelt influencing spring and river discharges (Mhawej et al. 2014); it corresponds up to 40% of stream flow in Lebanon (Shaban et al. 2004).

Monitoring the evolution of snow cover by in-situ measurements is almost impossible due to topographic and economic considerations. Satellite based remote sensing is usually used as synoptic and cost-effective method (Gul et al. 2017; Zhu et al. 2017). Landsat and MODIS are the most frequently used (Jabbar et al. 2020; Mhawej et al. 2014). However, one limitation of Landsat is its low temporal resolution of 16 days.

A. Fadel (✉) · G. Faour · M. Mhawej
National Center for Remote Sensing, National Council for Scientific Research (CNRS), Riad al Soloh, Beirut 1107-2260, Lebanon
e-mail: afadel@cnrs.edu.lb

G. Faour
e-mail: gfaour@cnrs.edu.lb

M. Ghazal
Faculty of Engineering, Lebanese University, P.O. Box 6573/14, Badaro, Museum, Hadath, Lebanon

L. Jarlan
CESBIO (UPS/CNRS/IRD/CNES/INRA), 18, Avenue Edouard Belin, 31401, Cedex 9 Toulouse, France
e-mail: lionel.jarlan@ird.fr

A. Shaban (ed.), *Satellite Monitoring of Water Resources in the Middle East*,
Springer Water, https://doi.org/10.1007/978-3-031-15549-9_21

MODIS (Terra/Aqua) is most widely used satellites which provides a coarse spatial resolution of 250/500 m and a high temporal resolution of one day. However, the main limitation while using MODIS corresponds to missing pixels' value related to bad weather conditions. Still, several gap-filling algorithms were already proposed. Temporal and spatial filters or imputations reduce cloud coverage by using information from neighboring non cloudy pixels in time or space. These filtering techniques are remarkably efficient in cloud reduction with overall accuracies ranging between 89% (Marchane et al. 2015) and 95% (Parajka and Blöschl 2008).

Snow covered areas (SCAs) are particularly vulnerable to increased temperatures of a future climate (Elias et al. 2016; Ma and Cheng 2003). The effect of global climate change on hydrologic systems, especially on mountain snow and glacier melt, can modify the timing and amount of runoff in mountainous watersheds. Any change in the flows of these river catchments due to climate variability may result in the form of catastrophic events like floods and droughts and hence will adversely affect the economy of the basin (Tahir et al. 2019; Fadel et al. 2020). Accurate stream flow simulation and forecast is of great importance to water resources management and planning (Abudu et al. 2010; Fadel et al. 2019, 2021; Shaban et al. 2021), and can provide a firm basis for forecasts of water resources availability while minimizing the risk and loss from floods caused by rapid snow and glacier melt (Abudu et al. 2012).

The Snowmelt Runoff Model (SRM) is simple deterministic hydrological model designed to simulate the impacts of temperature and precipitation change on snowpack, streamflow and water volume (Martinec and Rango 1986; Tayal Senzeba et al. 2015). It successfully underwent tests by the World Meteorological Organization with regard to snowmelt runoff simulations and can be an efficient tool to test the effect of different climate change scenarios on snow covered areas (Elias et al. 2016).

The Middle East region emerges as one of the hot spots for worsening extreme heat, drought and aridity conditions under climate change and possible temperature rise by up to 4 °C (Waha et al. 2017; Najem et al. 2020). A limited number of studies were achieved to simulate snow runoff, cloud gap correction and the impact of climate change on mountainous basins in the Middle East region. The objective of this study is to (1) produce improved estimates of snow cover area over the Ibrahim basin using daily MODIS product MOD10A1 (Terra) through cloud gap correction, (2) evaluate SRM's ability to simulate the daily stream flows of Ibrahim River, and (3) evaluate the effects of different climate change scenarios on river flow.

2 Materials and Methods

2.1 Study Site

Ibrahim Basin, located in Lebanon, cover an area of 326 km^2. Ibrahim River is 28 km long, 20 north of the capital Beirut (Fig. 1). Beginning at the crest of Mount Lebanon,

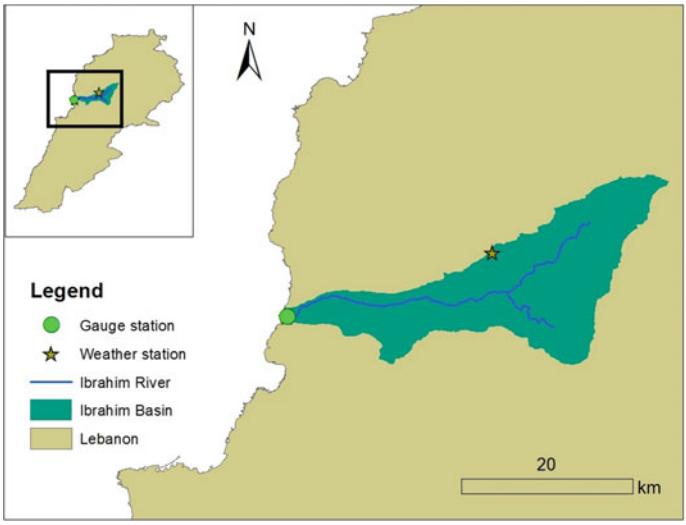

Fig. 1 Geographic location of Ibrahim River, the gauge station and weather station

the river flows westward, emptying into the Mediterranean Sea. Nahr Rouiess is the major tributary feeding Nahr Ibrahim, joining the main river in Kartaba. The Nahr Dibb and the Ouadi Ghabour are other major tributaries.

The basin is considered as a coastal watershed that supplies fresh water to major Lebanese cities. It has a Mediterranean climate with most of precipitation falls between November and April. Winter precipitation (December–March) accounts for 84% of the total annual precipitation (Fayad et al. 2017). The topography near Laqlouq (LAQ) is a relatively low plain (elevation between 1600 and 1800 m a.s.l.) and low-elevation mountains (1900–2100 m a.s.l.).

Geological formations outcropping in the Nahr Ibrahim range from the Jurassic to Cretaceous forming about 80% of the substrate of the Nahr Ibrahim watershed. The cretaceous formations outcrop near the coast and on the eastern part of the watershed heights where they are highly karstic (Hanna et al. 2018).

2.2 MODIS Snow Product

Moderate Resolution Imaging Spectroradiometer (MODIS) daily product was used to calculate the percentage of snow cover area in Ibrahim basin. MODIS is present on board of both Terra and Aqua. Terra was launched in December 1999, while Aqua was launched on May 2002. MODIS has 36 spectral bands between 0.405 and 14.385 μm, and acquires data at three spatial resolutions 250, 500 and 1000 m with a swath of 2330 km width. The MODIS snow products are created as a sequence of products beginning with and progressing, through spatial and temporal transformations. In this

study, the MODIS Terra snow cover daily L3 global gridded products MOD10A1 images were used. The tile corresponding to the region of the study is h20v5.

2.3 Cloud Correction

Cloud pixels represents a major challenge in the optical remote sensing of snow. Cloud free images are often rare in winter season preventing continuous snow monitoring and reducing the benefits of using these images in hydrological modeling. A diverse set of temporal, spatial and mixed algorithms can used to overcome this obstruction. Spatial algorithms are based upon majority filters and integrating DEM models. Temporal algorithms seek closest temporal neighbors to fill cloud gaps.

Cloud correction in this study was adapted from the methodology proposed by Parajka and Blöschl (2008) and by Marchane et al. (2015). It takes as input a daily image series of a catchment. It constitutes of three steps:

(1) If the surface of the mountainous areas (elevation higher than 1000 m) is covered with more than 60% of cloud, the tiles are simply discarded from the analysis.
(2) If a pixel is detected as a cloud or if no decision was made by the MODIS snow mapping algorithm, its elevation is compared to the average elevation of all snow-covered pixel of the image: if pixel elevation is above the average elevation of pixels marked as snow-covered, a 100% snow coverage is attributed; if elevation is below the average elevation, no change is applied. The average elevation of snowy pixels is computed individually for each catchment, in order to take into account specific conditions of snow occurrence.
(3) Finally, if the spatial filter described above fails to correct the potentially erroneous value, temporal neighbors are sought for. If there is snow between three days before and two days after the date of acquisition, the pixel value is simply replaced by its closest neighbor value. Priority is given to preceding neighbors because in case of a snow event during the two following days, correction could shift backward the event's timing.

To avoid errors emerging from wrong detection of a few numbers of pixels, spatial filter is done only in the case that snow extent exceeds 10%. In addition to that, each pixel with elevation less than 700 m is assigned Land.

2.4 Snowmelt Runoff Model (SRM)

SRM model is a degree-day model developed by Martinec and Rango (1986). It simulates daily stream flow by converting the degree days above the critical temperature into melt depths by degree-day factors. Each day, the water produced from snowmelt

and from rainfall is computed, superimposed on the calculated recession flow and transformed into daily discharge from the basin according to following equation:

$$Q_{n+1} = \left[c_{S_n} a_n (T_n + \Delta T_n) S_n + c_{R_n} P_n\right] \frac{A \cdot 10000}{86400} (1 - k_{n+1}) + Q_n k_{n+1}$$

where:

Q average daily discharge [$m^3 s^{-1}$],
c runoff coefficient expressing the losses as a ratio (runoff/precipitation), with c_S referring to snowmelt and c_R to rain,
a degree-day factor [cm °$C^{-1} d^{-1}$] indicating the snowmelt depth resulting from 1°-day,
T number of degree-days [°Cd],
ΔT the adjustment by temperature lapse rate when extrapolating the temperature from the station to the average hypsometric elevation of the basin or zone [°Cd],
S ratio of the snow-covered area to the total area,
P precipitation contributing to runoff [cm]. A preselected threshold temperature, T_{CRIT} determines whether this contribution is rainfall and immediate. If precipitation is determined by T_{CRIT} to be new snow, it is kept on storage over the hitherto snow free area until melting conditions occur.
A area of the basin or zone [km^2],
k recession coefficient indicating the decline of discharge in a period without snowmelt or rainfall,
n sequence of days during the discharge computation period.

2.5 Input Variables and Parameters

SRM User Manual recommends dividing the basin into elevation zones with a range of about 500 m each. The Ibrahim Basin was divided into 5 zones as shown in Fig. 2, and their elevation ranges and means are listed in Table 1.

Model variables including temperature and precipitation were calculated as the daily average and sum of half-hourly measures of the Laqlouq snow automated weather station (AWS), located at 1840 m in the north of the basin. More details about the sensors and the data of this station can be found in (Fayad et al. 2017). The snow extent was calculated daily for each zone after clipping. River discharge was obtained from Litani River Authority (LRA) gauge station located at the westward of the river where it empties into the Mediterranean Sea (Fig. 1).

Several parameters were used in the calibration procedure on the year 2015–2016. Trial and error calibration were used for adjusting model parameters manually and evaluating the goodness-of-fit. Calibrated SRM parameter values are shown in Table 2.

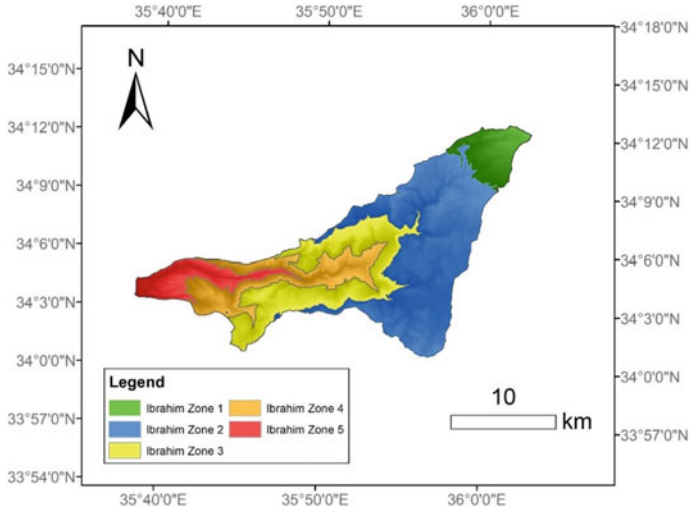

Fig. 2 Ibrahim Basin elevation zones used in SRM mode

Table 1 The five zones used in Ibrahim basin

Zone	Elevation range (m)	Hypsometric mean (m)	Zone area (km^2)
1	[0, 656]	397.13	25.90
2	[656, 1156]	929	46.33
3	[1156, 1656]	1388.4	72.56
4	[1656, 2156]	1917.31	140
5	[2156, 2656]	2328	25.10

Table 2 Parameters used for SRM model

Parameter (unit)	Value
Lapse rate (°C/100 m)	0.65
Lag time (hrs)	18
Critical Temperature (°C)	0
Degree day factor (cm $°C^{-1}$ d^{-1})	(Nov–Dec): 0.1 (Jan): 0.2 (Feb–July): 0.3
Runoff coeff. for rainfall (*Cr*)	(Nov–Jan): 0.25 (Feb–Apr): 0.6 (May–Jul): 0.35
Runoff coeff. for snowfall (*Cs*)	(Nov–Jan): 0.3 (Feb–Apr): 0.6 (May–Jul): 0.4
Xc	1
Yc	0.01

Table 3 Different possible climate change scenarios

Scenario code	Changed variables
S1 (T − 2P120%)	Subtract 2 °C of average temperature, increase precipitation by 20%
S2 (T + 2 P80%)	Add 2 °C to average temperature, reduce precipitation by 20%
S3 (T + 4 P70%)	Add 4 °C to average temperature, reduce precipitation by 30%

2.6 Model Evaluation Criteria

SRM model was evaluated using the Nash–Sutcliffe coefficient defined as:

$$\mathrm{NSCE} = 1 - \frac{\sum_{i=1}^{n}(Q_i - Q_i^{'})}{\sum_{i=1}^{n}(Q_i - Q)^2}$$

where Q_i is the measured daily discharge; Q_i' is simulated daily discharge; Q is average daily discharge for the simulation year or simulation season; n is number of daily discharge values.

2.7 Climate Change Scenarios

After calibration and validation, the SRM was used to study the impact of climate change scenarios on the Ibrahim River discharge. Table 3 presents 3 different possible future climate scenarios that may occur in Ibrahim Basin. It is predicted that temperatures in Lebanon will increase by around 1 °C on the coast to 2 °C in the mainland by the year 2040, and by 3.5 °C–5 °C respectively by 2090. Another effect of climate change is on the rainfall pattern, which is expected to decrease by 10–20% in the year 2040 and of 45% in the year 2090 (Ministry of Environment 2011).

3 Results and Discussion

3.1 MODIS Images Cloud Correction

Two images of the snow cover area before and after cloud gap filling are presented in Fig. 3. As shown from these images, huge correction was made between the original product (Fig. 3a) and the rectified one (Fig. 3b). As such, users intending to work on the original daily products might get biases and unreliable information concerning the actual snow extent. The importance of such correction also lies in identifying the date of each storm which is generally occurring in each new peak as shown in Fig. 4. The intensity of each snowstorm could be also quantified, mainly because the new

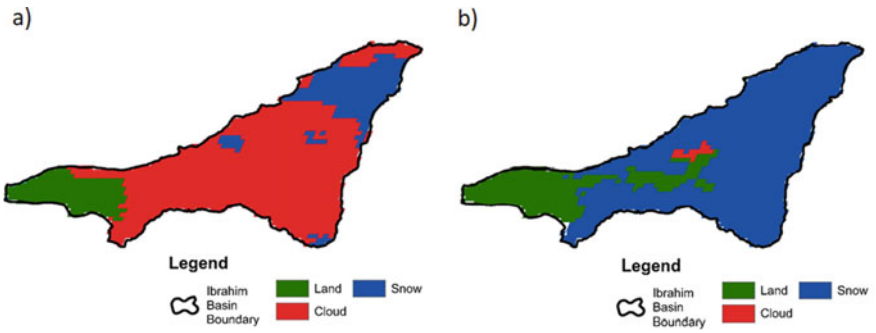

Fig. 3 Snow cover over Ibrahim basin on 8 February 2016, **a** before and **b** after cloud correction

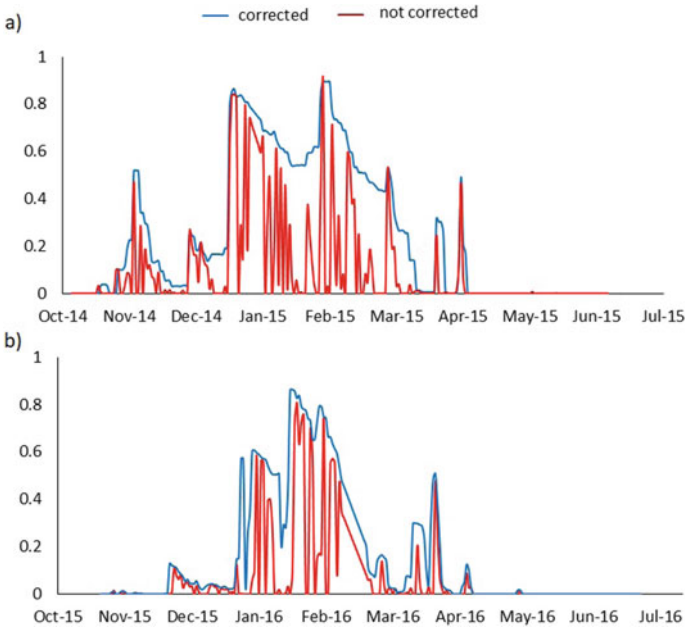

Fig. 4 Corrected versus not corrected snow extent in Ibrahim basin during the years **a** 2014–2015 and **b** 2015–2016

addition of snow cover extent is clearly produced. Such information is crucial for the basin water budget.

For application to hydrological models, in particular SRM, researchers can also use the 8 day-snow product MOD10A2 (Tekeli et al. 2005). Still, using the later product would prevent users from identifying the date of each storm and its respective intensity. Linear interpolation can be used for high cloud extents (Tahir et al. 2019) but could still generate many biases particularly because mountainous regions correspond generally to heterogeneous topography with steep slopes. Other studies

use dates where there is minimal uncertainty introduced by non-ideal sensor viewing or atmosphere conditions, particularly clouds (Decay curves of different types: exponential, sigmoidal or exponential are used as a fit for snow cover area (Steele et al. 2017).While the latter option could be the more adequate, it might as well overestimate low-depth snow cover as they tend to melt at a fast rate. Using a combination of the previously discussed approaches might be the best choice to tackle cloud removal and gap filling, which was already produced within this study. While further calibrations and thresholding should take place to better describe the Lebanese context, the proposed method in this work already generated very acceptable results with a much-reduced cloud extent.

3.2 SRM Snowmelt Runoff Simulations

Daily runoff simulation for the snow melting season of the years 2014–2015 was carried out after calibrating the SRM model for the year 2015–2016 (Fig. 5). Comparison between SRM simulations and field observation yielded an NSE of 0.73 in the year 2015–2016, and 0.55 in the year 2014–2015.

The Snowmelt-Runoff Model (SRM) is a temperature index model that was designed by Martinec to simulate and forecast daily streamflow in mountain basins where snowmelt is a major runoff factor. It has been applied globally on many basins with different areas and characteristics in a final objective to assess the effect of climate change scenarios on flow (Tahir et al. 2019) have applied SRM to Upper Indus Basin (UIB) of Pakistan. They found that SRM has efficiently simulated the

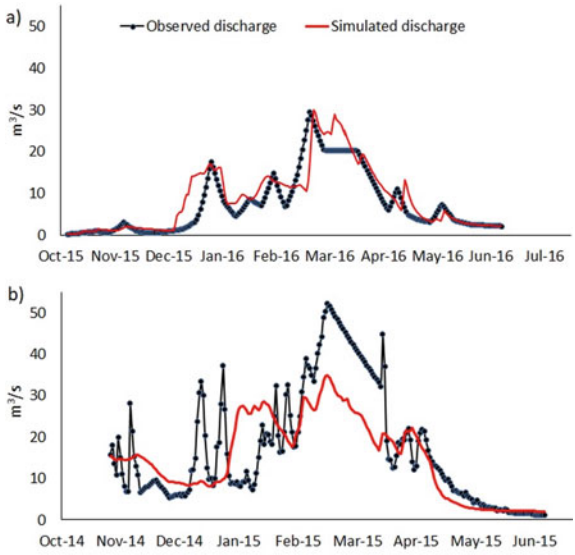

Fig. 5 Comparison of simulated discharge from SRM model and observed discharge during, **a** calibration and **b** validation periods

flow in Shyok River with average Nash–Sutcliff coefficient value (R2) of 0.8 (0.63–0.93) for all six years (2000–2006) of basin-wide and zone-wise simulations (Haq 2008) applied SRM using MODIs images to simulate runoff in Swat River. The model was calibrated for the melting season of 2004, with R2 = 0.74. When verified in 2005 and 2006, the precision was reduced to R2 = 0.54. SRM was successfully used to simulate streamflow from snowmelt in the Erdao-Songhua basin with Nash–Sutcliffe coefficient of determination 0.57, without further validation (Yang et al. 2016).

Although SCA precision was maximized in this study, SRM model yield lower NSE than in the some previously cited studies that applied SRM to basins characterized by large surface areas and lower variability in snow cover area. Ibrahim basin is relatively a small basin characterized by several time separated snowstorm events. This result in high fluctuations in the discharge of Ibrahim River making it more challenging for SRM.

The problem of the geological variation in the basin with continuous infiltration of rainfall during the winter season. The majority of the rainfall in the Ibrahim Basin penetrates into the rock, leaving little to land surface flow. All of the water that seeps into the limestone ultimately reappears as springs flowing from the rock, creating large caves, such as Afqa and Jeita. This may explain unsimulated peaks in the hydrological year 2014–2015, where the flow may be mainly due to groundwater subflow. Although high temperatures and snow cover yield high flow in the last 10 days of January 2015, the measured flow does not respond significantly. This delay of respond was manifested in a higher flow in February and March.

3.3 Impact of Different Climate Change Scenarios on River Flow

After the successful calibration and validation of the model, the SRM was applied to investigate the impact of climate variability on the Ibrahim River runoff by taking year 2016 as a baseline. The impact of the different tested climate change scenarios on the Ibrahim River discharge are presented in Fig. 6. First scenario (S1) characterized by a temperature decrease of 2 °C and a precipitation increase of 20% resulted in higher peaks of river discharge in March–April and continuous river flow in June and July with an increased runoff volume of 45% (Table 4). Such favorable scenario would ensure enough quantities of water for agriculture during dry season. Second scenario (S2) characterized by a 2 °Ctemperature increase, and a 20% precipitation decrease resulted in comparable discharges in January and February and lower discharges between March and June with a decreased runoff volume by 26%. Third scenario (S3) characterized by a 4 °Ctemperature increase, and a 30% precipitation decrease resulted in an early snow meltdown that have increased the discharge in January and decreased it between March and June with a decreased runoff volume by 29%.

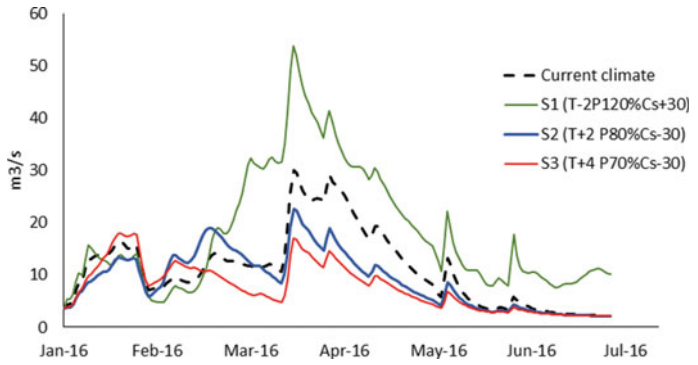

Fig. 6 Impact of different tested climate change scenarios on the Ibrahim River discharge

Table 4 Change in average discharge under different climate change scenarios

Climate change scenarios	Runoff volume (10^6 m^3)	Change in mean discharge (%)
S1 (T − 2P120%)	256	+45
S2 (T + 2 P80%)	130	−26
S3 (T + 4 P70%)	125	−29

Increased temperature and decreased precipitation will shift snow melting that is expected to start earlier. This will reduce significantly the water availability within this region and will have severe effects on water use and agriculture. Adding to these climatic drivers the factor of population growth and urbanization can lead to more intense water scarcity, making it increasingly challenging for managers to satisfy growing water demands from different water users (Phan et al. 2019; Xue et al. 2017). In such conditions, it is vital to identify and implement effective and efficient adaptive solutions to alleviate such situation.

4 Conclusion

Optical remote sensing can give an adequate estimations of snow cover. Such data, along with precipitation and temperature, can be used to simulate river flow in mountainous basins. The flow of Ibrahim River was simulated using SRM, a degree-day model. SRM showed good performance in simulating river discharge with acceptable NSCE values.

Climate change scenarios were applied to the model to assess their effect on flow, and they showed earlier peaks with lower water availability that may result in severe drought events. Basin managers are recommended to take actions that may include building up small dams that can ensure store water during high river discharge to be used later in dry season.

With a global trend to combat climate change, it is vital to acquire such information to draw better future water balance management plans. The proposed approach could be portable and applied in other regions, which would enable the estimation of the national water budget.

Acknowledgements This study was financed by the ERANET3-062 CHAAMS project.

References

Abudu S, Chunliang C, King J, Abudukadeer K (2010) Comparison of performance of statistical models in forecasting monthly streamflow of Kizil River China. Water Sci Eng 3:269–281. https://doi.org/10.3882/j.issn.1674-2370.2010.03.003

Abudu S, Cui C, Saydi M, King JP (2012) Application of snowmelt runoff model (SRM) in mountainous watersheds: a review. Water Sci Eng 5:123–136. https://doi.org/10.3882/j.issn.1674-2370.2012.02.001

Elias E, Rango A, Steele CM, Mejia JF, Baca R, James D, Schrader S, Gronemeyer P (2016) Simulated impact of climate change on hydrology of multiple watersheds using traditional and recommended snowmelt runoff model methodology. J Water Clim Chang 7:665–682. https://doi.org/10.2166/wcc.2016.097

Fadel A, Sharaf N, Siblini M, Slim K, Kobaissi A (2019) A simple modelling approach to simulate the effect of different climate scenarios on toxic cyanobacterial bloom in a eutrophic reservoir. Ecohydrol Hydrobiol 19(3):359–369

Fadel A, Mhawej M, Faour G, Slim K (2020) On the application of METRIC-GEE to estimate spatial and temporal evaporation rates in a mediterranean lake. Remote Sens Appl: Soc Environ 20:100431. https://doi.org/10.1016/j.rsase.2020.100431

Fadel A, Kanj M, Slim K (2021) Water quality index variations in a Mediterranean reservoir: a multivariate statistical analysis relating it to different variables over 8 years. Environ Earth Sci 80(2):1–13. https://doi.org/10.1007/s12665-020-09364-x

Fayad A, Gascoin S, Faour G, Fanise P, Drapeau L, Somma J, Fadel A, Al Bitar A, Escadafal R (2017) Snow observations in Mount Lebanon (2011–2016). Earth Syst Sci Data 9:573–587. https://doi.org/10.5194/essd-9-573-2017

Gul C, Kang S, Ghauri B, Haq M, Muhammad S, Ali S (2017) Using Landsat images to monitor changes in the snow-covered area of selected glaciers in northern Pakistan. J Mt Sci 14:2013–2027. https://doi.org/10.1007/s11629-016-4097-x

Hanna N, Lartiges B, Kazpard V, Maatouk E, Amacha N, Sassine S, El Samrani A (2018) Hydrogeochemical processes in a small Eastern Mediterranean Karst Watershed (Nahr Ibrahim, Lebanon). Aquat Geochem 24:325–344. https://doi.org/10.1007/s10498-018-9346-x

Haq M (2008) Snowmelt runoff investigation in River Swat upper basin using snowmelt runoff model, Remote Sens GIS Tech

Jabbar A, Othman AA, Merkel B, Hasan SE (2020) Change detection of glaciers and snow cover and temperature using remote sensing and GIS: a case study of the upper indus basin Pakistan. Remote Sens Appl Soc Environ 18:100308. https://doi.org/10.1016/j.rsase.2020.100308

Ma H, Cheng G (2003) A test of snowmelt runoff model (SRM) for the Gongnaisi River basin in the western Tianshan Mountains China. Chinese Sci Bull 48:2253–2259. https://doi.org/10.1007/BF03182862

Marchane A, Jarlan L, Hanich L, Boudhar A, Gascoin S, Tavernier A, Filali N, Le Page M, Hagolle O, Berjamy B (2015) Assessment of daily MODIS snow cover products to monitor snow cover dynamics over the Moroccan Atlas mountain range. Remote Sens Environ 160. https://doi.org/10.1016/j.rse.2015.01.002

Martinec J, Rango A (1986) Parameter values for snowmelt runoff modelling. J Hydrol 84:197–219. https://doi.org/10.1016/0022-1694(86)90123-X

Mhawej M, Faour G, Fayad A, Shaban A (2014) Towards an enhanced method to map snow cover areas and derive snow-water equivalent in Lebanon. J Hydrol 513:274–282. https://doi.org/10.1016/j.jhydrol.2014.03.058

Ministry of Environment (2011) Lebanon's Second National Communication to the United Nations Framework Convention on Climate Change

Najem S, Al Bitar A, Faour G, Jarlan L, Mhawej M, Fadel A, Zribi M (2020) Drought assessment using micro-wave timeseries of precipitation and soil moisture over the Mena Region. In: 2020 Mediterranean and middle-east geoscience and remote sensing symposium (M2GARSS). IEEE, pp 289–292

Parajka J, Blöschl G (2008) Spatio-temporal combination of MODIS images—Potential for snow cover mapping. Water Resour Res 44. https://doi.org/10.1029/2007WR006204

Phan DT, Smart CRJ, Stewart-Koster B, Sahin O, Hadwen LW, Dinh TL, Tahmasbian I, Capon JS (2019) Applications of Bayesian networks as decision support tools for water resource management under climate change and socio-economic stressors: a critical appraisal. Water. https://doi.org/10.3390/w11122642

Shaban A, Faour G, Khawlie M, Abdallah C (2004) Remote sensing application to estimate the volume of water in the form of snow on Mount Lebanon/Application de la télédétection à l'estimation du volume d'eau sous forme de neige sur le Mont Liban. Hydrol Sci J 49, null-653. https://doi.org/10.1623/hysj.49.4.643.54432

Shaban A, Drapeau L, Telesca L, Amacha N, Ghandour A (2021) Influence of snow cover on water capacity in the Qaraaoun Reservoir Lebanon. Arabian J Geosci 14(1):1–12

Steele C, Dialesandro J, James D, Elias E, Rango A, Bleiweiss M (2017) Evaluating MODIS snow products for modelling snowmelt runoff: case study of the Rio Grande headwaters. Int J Appl Earth Obs Geoinf 63:234–243. https://doi.org/10.1016/j.jag.2017.08.007

Tahir AA, Hakeem SA, Hu T, Hayat H, Yasir M (2019) Simulation of snowmelt-runoff under climate change scenarios in a data-scarce mountain environment. Int J Digit Earth 12:910–930. https://doi.org/10.1080/17538947.2017.1371254

Tayal Senzeba K, Bhadra A, Bandyopadhyay A (2015) Snowmelt runoff modelling in data scarce Nuranang catchment of eastern Himalayan region. Remote Sens Appl Soc Environ 1:20–35. https://doi.org/10.1016/j.rsase.2015.06.001

Tekeli AE, Akyu Z, Arda AS (2005) Using MODIS snow cover maps in modeling snowmelt runoff process in the eastern part of Turkey. Remote Sens Environ 97:216–230. https://doi.org/10.1016/j.rse.2005.03.013

Waha K, Krummenauer L, Adams S, Aich V, Baarsch F, Coumou D, Fader M, Hoff H, Jobbins G, Marcus R, Mengel M, Otto IM, Perrette M, Rocha M, Robinson A, Schleussner C-F (2017) Climate change impacts in the Middle East and Northern Africa (MENA) region and their implications for vulnerable population groups. Reg Environ Chang 17:1623–1638. https://doi.org/10.1007/s10113-017-1144-2

Washington B, Seymour L, Mote T, Robinson D, Estilow T (2019) Identifying and extracting a seasonal streamflow signal from remotely sensed snow cover in the Columbia River Basin. Remote Sens Appl Soc Environ 14:207–223. https://doi.org/10.1016/j.rsase.2018.03.003

Xue J, Gui D, Lei J, Zeng F, Mao D, Zhang Z (2017) Model development of a participatory Bayesian network for coupling ecosystem services into integrated water resources management. J Hydrol 554:50–65. https://doi.org/10.1016/j.jhydrol.2017.08.045

Yang Q, Chen S, Xie H, Hao X, Zhang W (2016) Application of snowmelt runoff model (SRM) in upper Songhuajiang Basin using MODIS remote sensing data. In: International geoscience and remote sensing symposium (IGARSS), pp 4905–4908. https://doi.org/10.1109/IGARSS.2016.7730280

Zhu L, Radeloff VC, Ives AR (2017) Characterizing global patterns of frozen ground with and without snow cover using microwave and MODIS satellite data products. Remote Sens Environ 191:168–178. https://doi.org/10.1016/j.rse.2017.01.020

Remote Sensing of Water Quality for Human Activity Use of Shat Al-Hilla"

Suhad M. Al-Hedny, Atheer Saieb Naji Al-Azawey, and Qassim A. Talib Alshujairy

1 Introduction

Water quality is such a broad concept in terms of physical, chemical, and biological characteristics to meet different uses and consumption. Water is facing excessive sources of pollutants, which mostly are human-made. The quality of water is affected by both point and non -point sources of pollution. Un-safety water sources cause the death of millions of people. The quality of water is just as important as its quantity (Ritchie et al. 2003). As a very complicated process with such broad impacts on human beings, it was supported as a core project and hot topic by international programs. This importance was the main reason why the specialists studied the indicators of the concept of water quality, which are still growing and have been developed so far in several countries (Mukherjee et al. 2009; Srivastava et al. 2010, 2011; Singh et al. 2010).

Water quality is a concept that includes all negative changes in the capacity of water to supply services for its beneficiaries. To a wider extent, water quality changes could be in such scope that the original use is no longer possible. Water quality index is the most generally used index to compare the capacity of physio-chemical and

S. M. Al-Hedny (✉)
Department of Environment, Faculty of Environmental Science, Al-Qasim Green University, Al-Hilla-Al-Diwaniyah Street, Babil 51013, Iraq
e-mail: suhad.khudair@environ.uoqasim.edu.iq

A. S. N. Al-Azawey
Department of Environmental Pollution, Faculty of Environmental Science, Al-Qasim Green University, Al-Hilla-Al-Diwaniyah Street, Babil 51013, Iraq
e-mail: atheersaieb@environ.uoqasim.edu.iq

Q. A. T. Alshujairy
Department of Soil and Water Science, College of Agriculture, University of Muthana, educational area, 3o, Samawah 66001, Iraq
e-mail: qassimtalib@mu.edu.iq

A. Shaban (ed.), *Satellite Monitoring of Water Resources in the Middle East*,
Springer Water, https://doi.org/10.1007/978-3-031-15549-9_22

biological parameters to the standard parameters to assess the appropriateness of the evaluated water for specific uses.

The orderly monitoring and management of water resources is the main key for sustainable development. Despite the in situ measurements of water parameters are accurate, they do not offer the spatial view needed for perfect monitoring of water resources. Evaluation of water parameters deviation, needs to the regular intervals information at a large scale, which is cost and time consuming (Kutser 2009). Over the last 10–20 years, many of developed nations provided historic water quality sampling open access data (Sheffield et al. 2018). Due to both the development of remotely sensed data production and the authors' efforts, the extracting of water quality parameters facilitating approaches of water resources monitoring (Srebotnjak et al. 2012).

Physio-chemical parameters (pH, Salinity, TDS, Tempriture, Turbidity etc.…) and biological parameters (Cholorophyll, total colloform TC) are the main remotely sensed parameters due to their direct relation to the reflection of water surface (Kirk 1983). The reflection from water surfaces depends on the measured parameter (substances concentration) and optimal wavelength that used to measure water quality. In general, remotely sensed water parameters determination have begun early from 1970s with slow progress toward universal algorithms (Clarke et al. 1970; Klemas et al. 1973; Holyer 1978). This shift created an effective tool for real time monitoring and managing water resources on different scales (Mishra et al. 2017).

Water—quality parameters for the possible use of water are characterized with wide variability in terms of the specific uses of water. Remote sensing method depends on the ability of measuring the spectral backscattered from water surface. Ritchie et al. (1974) developed an algorithmic approach to determine suspended sediments under empirical equation: $Y = A + BX$, where Y is the remotely sensed measurement and X is the interesting water quality parameter. A and B are empirical parameters derived according to statistical relationships between in situ and spectral measured parameters. Generally, reflectance at visible and near-infrared wavelengths is directly affected by sediments concentration in the surface water. The concentration of sediments increased the radiant reflectance from water surface. This radiance is affected by color, texture and type of sediment along with sun angle and sensor view (Loew et al. 2017). Torbick et al. (2013) concluded that wavelength between 700 and 800 nm are helpful for determining suspended sediments in surface water. Many studies considered that the suspended sediments can be spatially mapped in large scale water resources (Palmer et al. 2015; Gholizadeh et al. 2016; Stanley et al. 2019). Landsat bands used by Canziani et al. (2008) to determine Chl-a and the turbidity of shallow lakes, they integrated remotely sensed data with ANN algorithm to retrieve information at temporal and broad spatial scale. Integration the in situ measurements with satellite estimations could produce a better assessment of water quality (Wang et al. 2010). Empirical algorithms to determine algal blooms by measure Chl-a from space using information multispectral instrument of Sentinel-2 satellite was described by Nascimento Silva and Panella (2018). Chl-a, EC, pH, hardness and chloride were estimated from algorithms and several band ratio with high accuracy under different conditions and statistically methods of studying (Cao

et al. 2020; Jeihouni et al. 2020; Pahlevan et al. 2020). Different water quality parameters can be well evaluated by using the relationships between these parameters and the reflection (Guan et al. 2011; Khattab and Merkel 2014; Maier and Keller 2019; Wagle et al. 2020). The suitability of Euphrates river for irrigation was evaluated at any point along the river by using Landsat imagery for bands 1, 2 and 3. The same study found a strong negative correlation between water quality index and reflectance at band 2 (Bahrani et al. 2012).

Although there is a lot of discussion on water quality change, WQI studies in Iraq are still preliminary or nonexistent. Little efforts paid more attention to the impact of this change on the water for human consumption; to this end, this study aims to determine different physiochemical water parameters using remotely sensed and in situ determination of Shat-Al-Hilla. Water quality index (WQI) has been performed to map the suitability index of water for different human-consumption purposes in the study area.

2 Tools and Methods

2.1 Study Area

The Euphrates river intersects Babil governorate to splits it into two branches: Hindyah and Hilla. Babil is located in central Iraq between 32° and 33.25° North latitude and 44°–45° East longitude. The governorate is divided into four districts: Al-Musayab, Hilla, Al-Mahawil and Hashimiya. The governorate covers 5119 Km^2 of Iraq with a typical climate with temperature exceeding 40° in summer and the rainfall is restricted to the period between November and April with a very limited amount. The study collected five sites along Al-Hilla river as shown in Fig. 1. In situ measurements of water quality parameters were performed on samples that monthly collected from study sites for period from July, 2018 to March 2019.

2.2 Remotely Sensed Estimated Parameters

Landsat scenes were chosen due to their free availability, corrected before delivery for radiometric and distortions and it's medium to high spatial resolution.

The datasets covering the study area were freely acquired from USGS Earthexplorer website (http://earthexplorer.usgs.gov/). The image acquired to coincide with the period of water samples collecting from the study area. The Landsat 8 scene falls on path 168 and row 37 with scene cloud cover of 0.38%. The multispectral image Reflective band DN's were converted to reflectance according to LSDS-1574 (2019) by using Arc GIS 10.1.1, as follow:

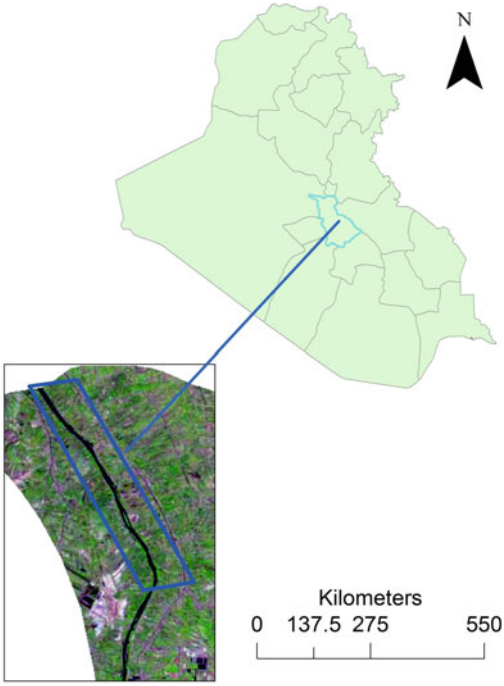

Fig. 1 Location and extent of the study area

$$\rho\lambda' = \frac{\left(M_\rho * Q_{cal} + A_\rho\right)}{\sin\theta_{SE}} \quad (1)$$

where:

ρλ'	TOA Planetary Spectral Reflectance, without correction for solar angle. (Unitless)
Mρ	Reflectance multiplicative scaling factor for the band (REFLECTANCE _MULT_BAND_n from the metadata)
Aρ	Reflectance additive scaling factor for the band (reflectance - add band_N from the metadata)
Qcal	Level 1 pixel value in DN
$\sin\theta_{SE}$	a correction for the solar elevation angle.

Different bands and band ratio were used to estimate the parameters under this study as shown in Table 1. ArcView 10.5 was used to derive water quality parameters in interest under this study conditions and MS Excel were used to compute WQI for the studied parameters.

Table 1 Bands, band combination and ratio used to estimate water parameters

Water quality parameters	Bands
Turbidity	(b5 * b4)/b3
TDS	Band 5
EC	(band 6/band 5) * band 7
Phosphorous	Band 7

2.3 Water Quality Index Calculation

This study used the standard formula to calculate water quality index for the studied parameters as follow:

$$\mathrm{WQI} = \frac{\sum_{i=1}^{n} \mathrm{wiqi}}{\sum_{i=1}^{n} \mathrm{wi}} \tag{2}$$

where:

n number of parameters
wi relative weight of the parameter *i*th
qi water quality rating of the *i*th parameter.

According to Brown et al. (1972), the calculation of qi is calculated as follow:

$$q_i = 100\left[\frac{V_i - V_{id}}{S_i - V_{id}}\right] \tag{3}$$

where Vi represents the observed value of *i*th parameter, Si is the standard permissible value of the *i*th and Vid is the ideal value of *i*th parameter in pure water. The ideal value for pH is 7.0 and the permissible value is 8.5 and 14.6 and 5 are the ideal and permissible values of the dissolved oxygen, respectively. While the ideal values of all other parameters is zero (Tripaty and Sahu 2005). Water quality was classified based on weight arithmetic WQI to Excellent with values of 0–25, good with values range from 26 to 50, poor with range of values from 51 to 75, very poor quality with values that ranged from 76 to 100 and unsuitable for drinking with values above 100 (Chatterjee and Raziuddin 2002). Water quality index was calculated for EC, pH, TH, NO_3, PO_4, Ca, Mg, DO and BOD parameters.

2.4 Analytical Method

Statistical relationships between in situ measured and spectral estimated parameters is the basis of the analytical method of this study. Spectral characteristics were used

in different ways to estimate water parameters, band combination, two band ratio and three band ratio to reduce the effects of water surface reflectance Table 1.

3 Results

3.1 Water Quality Index (WQI)

The results of the computed WQI for the studied physiochemical parameters: EC, pH, TH, NO_3, PO_4, Ca, Mg, DO and BOD shown in Table 2. Values of WQI fall within 51–75 of the classification of water quality. WQI was classified as a good water for drinking consumption with value of 26.4 for Autumn season at two stations of the studied regions.

The obtained values of WQI indicated that the unsuitability of Shatt Al-Hilla water for drinking use in all of the studied regions. Large amounts of data were summarized into simple terms of WQI classification (bad, poor, good and excellent) water for different use. As the most commonly used index, WQI with a single number can be used as a tool in comparing the quality of different water sources quality. WQI offers a very useful tool for water monitoring and management, but the in situ measurement of several water parameters is a cost and time-consuming task. According to the results shown in Table 2, almost closed values of WQI for the studied regions of Shatt AL-Hilla. The variation of the determined parameters between the studied region not observed by using this tool. The parameters with little variation or little values could be excluded. That means, more efforts are needed to evaluate water quality by considering the variation of the individual parameters and the simplicity of interpretation of water quality. According to several Iraqi studies of water quality suitability for different uses, some parameters were collected to be remotely determined (Ewaid et al. 2020; Abed et al. 2019; Ismail et al. 2014; Rabee et al. 2011).

Table 2 WQI for the sampled sites for period from Autumn 2018 to Summer 2019

Station	Autumn	Winter	spring	summer
S1	26.43	65.46	67.92	68.78
S2	26.56	66.71	68.45	68.79
S3	61.93	66.93	69.75	68.63
S4	63.37	67.36	68.39	68.74

3.2 Water Parameters Algorithm Development

The parameters of turbidity, Ec, TDS, and Phosphorous were extracted based on the spectral response of the water surface. Geo-referenced water parameters from the study regions and corresponding Landsat OLI 8 pixels were used to develop each parameter predictive model. The collected data were divided into two sets: the first set of 18 samples was used for calibration. While the second set of 15 samples were used for validation.

The performance of different measured water parameters and the used bands, band combination, and bands ratio showed a strong relationship. Figure 2 shows the statistical relation between bands reflectance and water parameters. The relations with high correction coefficient R2 were chosen as a fitting model to derive the water parameters.

The best predictor bands of turbidity was by using red, NIR and green bands with equation of "(b5 * b4)/b3" and value of R2 = 0.83. The reflectance at red and NIR regions were sensitive indicator for turbidity in other studies (Wang et al. 2006; Ferdi et al. 2007; Usali and Mohd 2010).

The selected band ratios [(b6/b5) * b7] was highly correlated with EC values. It was in the best fit curve of exponential model with value of R2 = 0.818 and RMSE = 0.082 as shown in Fig. 2. Water salinity is highly related with reflectance within visible and NIR regions of radiation. Clear water reflectance decreases in red and NIR regions, while it's reflectance increase in green region of radiation (Wua et al. 2008; Duong 2012).

This study paid more attention toward the water parameters that directly affect water quality for different uses. Total Dissolved Solids (TDS) represents a useful parameter for classifying drinking and irrigation water. Examination of the correlation coefficient of Landsat OLI8 bands with observed TDS values shows high values

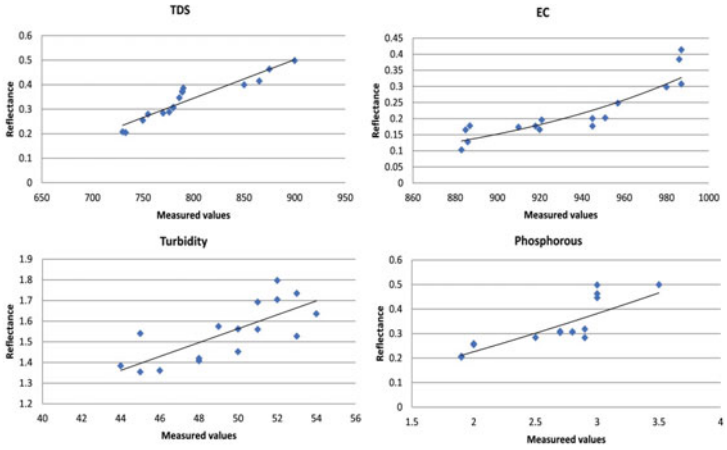

Fig. 2 Relational plots of the measured water parameters values versus reflectance

with bands 5, 6 and 7. Mostly the higher correlation was with band 5 (R2 = 0.88 and RMSE = 0.236). The mathematical combination of bands (4 and 5) gives low correlation with value of R2 = 0.51. The Phosphorous has strong correlation with bands 6 and 7 within SWIR regions of radiation. The highest correlation of phosphorous observed values was found to be with band 7 with R2 of 0.77 and RMSE = 0.257, which could be considered as a good fitting model for the estimating of missing data.

3.3 Algorithm Validation

To test the predictive capabilities of the fitting models, the performance of each water parameter equation was evaluated. The determination coefficient (R2) and root mean square error (RMSE) were used to evaluate the capability of each predictor model. Figure 3 illustrates the relation between predicted and measured values of different water parameters. The selected bands, combination and band ratio showed significantly successfully predicted of turbidity, TDS, EC, and phosphorous with values of R2 = 0.82, 0.89, 0.70, and 0.69 respectively. The RMSE values for all water parameters were ranged from 0.365 to 0.981. The results show the efficiency of using remote sensing for continuous measuring and monitoring of water parameters. Visible to short infra red regions of radiation data from nine spectral bands covered by Landsat OLI 8 collect images. This range of data can be successfully used to estimate various features of water parameters as successfully used in this study. This promised tool is based on the water surface reflectivity to propose the water reflectance model (Shang et al. 2021). The best fitting model absolutely depends on the optical properties of water parameter, wavelength, zenith angle, and conditions of region of interest. Therefore, empirical statistical methods are usually used to establish the best model for estimating water parameters (Abbas et al. 2021). The best model is developed based on the correlation coefficient between collected band and in situ water parameters.

3.4 Spatial Variation of Water Parameters

Iraq is facing seriously limitations along with the poor quality of water resources. An adequate supply of safe domestic water is the main challenge in many countries as well as in Iraq. GIS represents an effective tool for integration spatial and non spatial data to derive useful outputs and modeling. Figure 4 interpolates the spatial variation of TDS, EC, Turbidity, and phosphorous concentration along the study regions. Phosphorous is one of the most necessary water parameter to monitor. Increasing of it's concentration leads to oxygen deficiency with deadly consequences for aquatic organisms. Clearly variation of phosphorous concentration along the study region. As Fig. 4 shows, increasing of phosphorous concentration in the middle and the end

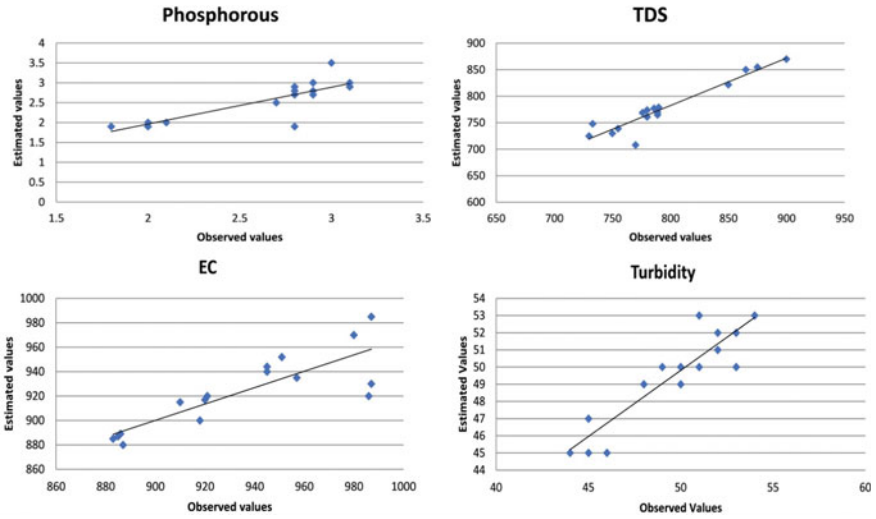

Fig. 3 Regression between estimated and observed water parameters values using different bands and bands combination

regions of the study area. These locations represent places for cattle and slaughterhouses, water treatment plant, and discharge of medical waste. The results of this study, observed high EC values that ranged from 883 to 987 μs/cm. These values are extremely high in comparing with value of 250 μs/cm according to Iraqi standards. The highest values of EC were concentrated in the end of the study region. Turbidity shows the same spatial distribution pattern of TDS (Fig. 4), as they show mainly higher values in the south region of the study area and minimum values at the northern region of the study area. In general both turbidity and TDS registered values ranged 44–53 NTU and 730–900 mg/l respectively. These values were higher than the standard values of drinking Iraqi limitation with value of 5 NTU for turbidity and 500 mg/l for TDS (Al-Saqqar et al. 2015). The distribution of EC, turbidity and TDS in the north were higher than those in the south of the study region. While the high concentrations of phosphorous distributed in the middle and south of the study region. This distribution clearly reflects the main activities along this region of Shatt Al-Hilla. The discharge of urban and different activities sewage/or wastewater on the both side of Shatt Al-Hilla have contributed in increasing of the studied water parameters concentrations. As consequence this leads to poor water quality for supplying the domestic water.

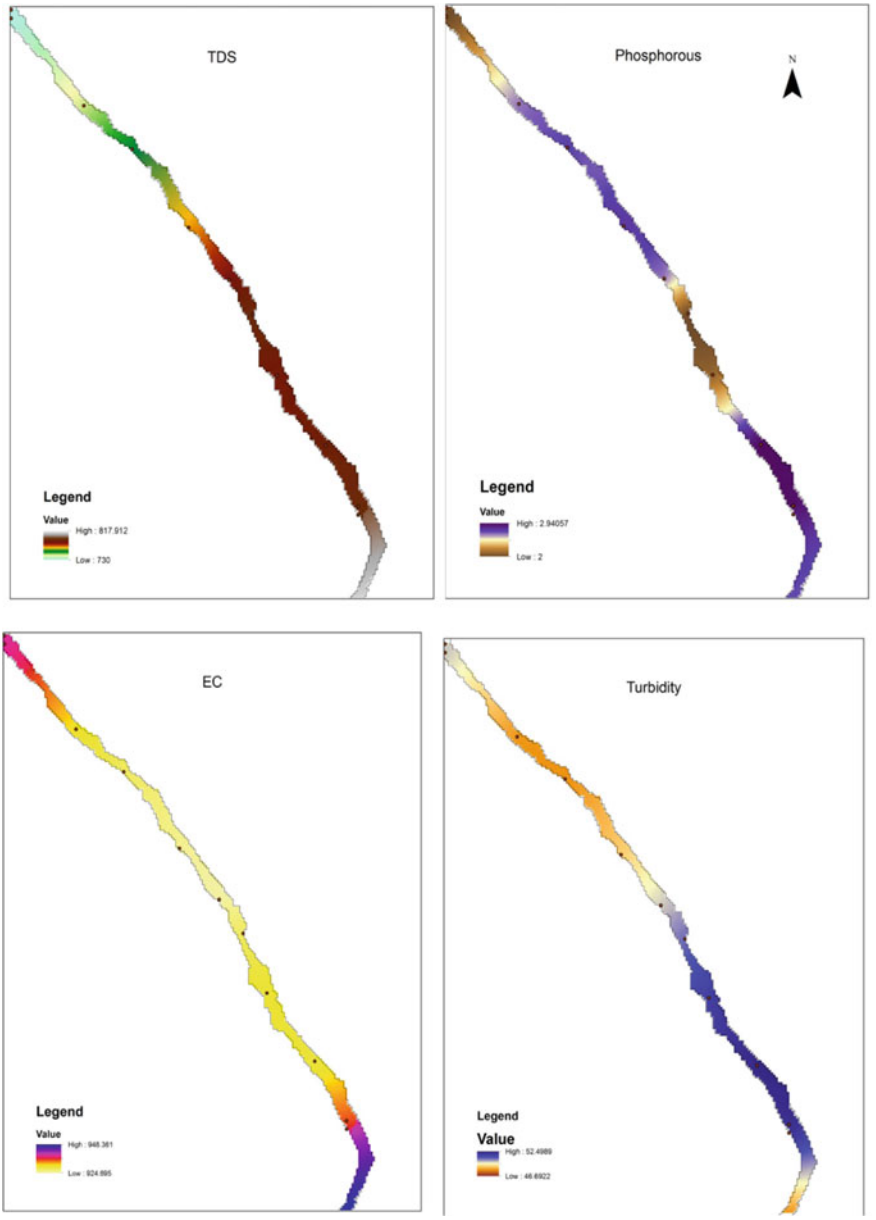

Fig. 4 Spatial variations of water parameters: Turbidity, TDS, EC and Phosphorous for 8th of September 2018

4 Conclusion

The main conclusions of this study are the following:

- The applying of WQI was encouraging since all of the studied water parameters successfully summarized into one classification tool. According to WQI, all studied locations for all seasons were classified as a poor water. Both location 1 and 2 were classified as a good water for autumn season.
- The main disadvantage of using WQI, is the difficulty of providing in -situ measures of each parameter, which considers as a very cost and time consuming task.
- Mostly, all of water parameters values were higher than the standard values of Iraqi drinking water limitations.
- Using bands, combination and bands ratio largely improved the efficiency of remote sensing technologies for water bodies monitoring. The visible through short infra red region of radiation were highly correlated with most of water parameters. This advantage of water optical properties offers different algorithms to derive water parameters.
- Clear variation in water characteristics was detected through using remote sensing and GIS technologies, where the studied parameters variation and distribution clearly mapped.
- Most of the studied parameters recorded high concentrations in the northern part comparison with the southern part of the study region.
- The decline in water quality to poor, clearly reflects the warless activities on the both side of Shatt Al-Hilla.
- Locally application of remote sensing methodology provided useful in-depth information that can be effectively used for water bodies monitoring and decision making.

References

Abbas MR, Rasib AW, Ahmed BB, Abbas TR (2021) Statistical remote sensing for prediction of inland water quality parameters for Shatt Al-Arab river in Iraq. IOP Conf Ser: Earth Environ Sci 722:012014

Abed SA, Ewaid SH, Al-Ansari N (2019) Evaluation of water quality in the Tigris river within Baghdad, Iraq using multivariate statistical techniques. J Phys Conf Ser 1294:072025

Al-Saqqar AS, Hashim A, Ali AM (2015) Water quality index assessment using GIS case study: Tigris River in Baghdad City. Int J Curr Eng Technol 5(4):2515–2520

Bahrani HS, Abdul Razzaq KA, Saleh SAH (2012) Remote sensing of water quality index for irrigation usability of the Euphrates river. WIT Trans Ecol Environ 164

Brown RM, McClelland NI, Deininger RN, O'Connor MF (1972) Water quality index-crashing, the Psychological Barrier. In: Proceedings of the 6th annual conference, advances in water pollution research, pp 787–794

Canziani G, Ferrati R, Marinelli C, Dukatz F (2008) Math Biosci Eng 5

Cao Z, Ma R, Duan H, Pahlevan N, Melack J, Shen M, Xue K (2020) Remote Sens Environ 248

Chatterjee C, Raziuddin M (2002) Determination of water quality index of a degraded river in Asanol Industrial area Raniganj, Burdwan, West Bengal. Nat Environ Pollut Technol 1(2):181–189
Clarke GL, Ewing GC, Lorenzen CJ (1970) Spectra of backscattered light from the sea obtained from aircraft as a measure of chlorophyll concentration. Science 167(3921):1119–1121
Duong ND (2012) Water body extraction from multi spectral image by spectral pattern analysis. Int Arch Photogramm Remote Sens Spatial Inf Sci XXXIX-B8
Ewaid SH, Abed SA, Al-Ansari N, Salih RM (2020) Developement and evaluation of water quality index for the Iraqi rivers. Hydrology 7:67
Ferdi L, Miller WO, Kehinde S (2007) Mapping turbidity in Charles River, Boston using a high resolution satellite. Environ Monitor Assess 132(1–3):311–320
Gholizadeh M, Melesse A, Reddi L (2016) A comprehensive review on water quality parameters estimation using remote sensing techniques. Sensors 16(8):1298
Guan X, Li J, Booty WG (2011) Water Resour Manag 25
Holyer RJ (1978) Toward universal multispectral suspended sediment algorithms. Remote Sens Environ 7(4):323–338
Ismail AH, Abed BS, Abdul-Qader S (2014) Application of multivariate statistical techniques in the surface water quality assessment of Tigris river at Baghdad stretch Iraq. J Univ Babylon 22:450–462
Jeihouni M, Toomanian A, Mansourian A (2020) Water Resour Manag 34:139
Khattab MF, Merkel BJ (2014) Application of landsat 5 and landsat 7 images data for water quality mapping in Mosul Dam Lake, Northern Iraq. Arab J Geosci 7:3557–3573
Kirk JTO (1983) Light and photosynthesis in aquatic ecosystems. Cambridge University Press, Cambridge, United Kingdom, 509 p
Klemas V, Borchardt JF, Treasure WM (1973) Suspended sediment observations from ERTS-1. Remote Sens Environ 2:205–221
Kutser T (2009) Passive optical remote sensing of cyanobacteria and other intense phytoplankton blooms in coastal and inland waters. Int J Remote Sens 30:4401–4425
Loew A, Bell W, Brocca L, Bulgin CE, Burdanowitz J, Calbet X et al (2017) Validation practices for satellite-based Earth observation data across communities. Rev Geophys 55:779–817
Maier PM, Keller S (2019) Work. Hyperspectral Image Signal Process. Evol Remote Sens
Mishra D, Ogashawara I, Gitelson A (2017) Bio-optical modeling and remote sensing of inland waters. Elsevier
Mukherjee S, Shashtri S, Singh C, Srivastava PK, Gupta M (2009) Effect of canal on land use/land cover using remote sensing and GIS. J Indian Soc Remote Sens 37(3):527–537
Nascimento Silva HA, Panella M (2018) Eutrophication analysis of water reservoirs by remote sensing and neural networks. Prog Electromagn Res Symp 458–463
Pahlevan N, Smith B, Schalles J, Binding C, Cao Z, Ma R, Alikas K, Kangro K, Gurlin D, Hà N, Matsushita B, Moses M, Greb S, Lehmann MK, Ondrusek M, Oppelt N, Stumpf R (2020) Remote Sens Environ 240:111604
Palmer SCJ, Kutser T, Hunter PD (2015) Remote sensing of inland waters: challenges, progress and future directions. Remote Sens Environ 157:1–8
Rabee AM, Abdul-Kareem BM, Al-Dhamin AS (2011) Seasonal variations of some ecological parameters in Tigris river water at Baghdad Region, Iraq. J Water Resour Prot 3:262
Ritchie JC, McHenry JR, Schiebe FR, Wilson RB (1974) The relationship of reflected solar radiation and the concentration of sediment in surface water of reservoirs. In: Shahrokhi F (ed) Remote sensing of earth resources, vol III. The University of Tennessee Space Institute, Tullahoma (TN), pp 52–72
Ritchie JC, Zimba PV, Everitt JH (2003) Remote sensing techniques to assess water quality. Photogramm Eng Remote Sens 69(6):695–704
Shang W, Jin S, He Y, Zhang Y, Li J (2021) Spatial-temporal variations of total Nitrogen and Phosphorus in Poyang, Dongting and Taihu Lakes from Landsat-8 data. Water 13:1704

Sheffield J, Wood EF, Pan M, Beck H, Coccia G, Serrat-Capdevila A, Verbist K (2018) Satellite remote sensing forwater resources management: Potential for supporting sustainable development in data-poor regions. Water Resour Res 54:9724–9758

Singh SK, Singh CK, Mukherjee S (2010) Impact of land-use and land cover change on groundwater quality in the Lower Shiwalik hills: a remote sensing and GIS based approach. Central Eur J Geosci 2(2):124–131

Srebotnjak T, Carr G, de Sherbinin A, Rickwood C (2012) A global water quality index and hot-deck imputation of missing data. Ecol Ind 17:108–119

Srivastava PK, Mukherjee S, Gupta M, Singh S (2010) Impact of urbanization on land use/land cover change using remote sensing and GIS: a case study. Int J Ecol Econ Stat 18(S10):106–117

Srivastava PK, Mukherjee S, Gupta M, Singh S (2011) Characterizing monsoonal variation on water quality index of river Mahi in India using Geographical Information System. Water Qual Expos Health 1–11

Stanley EH, Collins SM, Lottig NR, Oliver SK, Webster KE, Cheruvelil KS, Soranno PA (2019) Biases in lakewater quality sampling and implications for macroscale research. Limnol Oceanogr 64:1572–1585

Torbick N, Hession S, Hagen S, Wiangwang N, Becker B, Qi J (2013) Mapping inland lakewater quality across the lower Peninsula of Michigan using Landsat TM imagery. Int J Remote Sens 34(21):7607–7624

Tripathy JK, Sahu KC (2005) Seasonal hydrochemistry of groundwater in the barrier-spit system of Chilika lagoon. J Environ Hydrol 12(7):1–9

Usali N, Mohd HI (2010) Use of remote sensing and GIS in monitoring water quality. J Sustain Dev 3(3):228–238

Wagle N, Acharya TD, Lee DH (2020) Estimating Chlorophyll-a and dissolved oxygen based on landsat 8 bands using support vector machine and recursive partitioning tree regressions, p 6573

Wang F, Han L, Kung HT, Van Arsdale RB (2006) Applications of Landsat5 TM imagery in assessing and mapping water quality in Reelfoot Lalce. Tennessee Int J Remote Sens 27(23):5269–5283

Correction to: Atmospheric Rivers and Precipitation in the Middle East

Elias Massoud, Theresa Massoud, Duane Waliser, Bin Guan, and Agniv Sengupta

Correction to: Chapter "Atmospheric Rivers and Precipitation in the Middle East" in: A. Shaban (ed.), *Satellite Monitoring of Water Resources in the Middle East*, Springer Water, https://doi.org/10.1007/978-3-031-15549-9_4

In the original version of the book, the author name "Agniv Sengputa" has been changed to "Agniv Sengupta" in the Chapter "Atmospheric Rivers and Precipitation in the Middle East".

The chapter and book have been updated with the changes.

The updated original version of this chapter can be found at https://doi.org/10.1007/978-3-031-15549-9_4

A. Shaban (ed.), *Satellite Monitoring of Water Resources in the Middle East*, Springer Water, https://doi.org/10.1007/978-3-031-15549-9_23

Index

A
ACSAD, 89
Advanced Land Observing Satellite (ALOS) DEM, 319, 320, 326
Advanced Spaceborne Thermal Emission and Reflection Radiometer (ASTER), 6, 8, 34, 102, 108, 319, 320
Advanced Very High Resolution Radiometer (AVHRR), 8, 102, 103, 176
Aerial photographs, 1, 2, 7, 252, 322
Agricultural areas, 44, 106, 129, 143, 192, 195, 202, 203, 251
Algorithm, 51, 54, 56, 107, 130, 157, 177, 206, 207, 209, 210, 213, 215, 323, 324, 326, 330, 331, 337, 340–342, 346, 366, 368, 370, 372, 374, 380, 382, 394, 399, 400, 403
Analysis of variance, 137
Anti-Lebanon Mountain, 75
Aquiclude, 255, 257, 258, 314
Aquifer layers, 73
Aquifer systems, 25, 71–77, 79–85, 288, 314, 315, 318
Aquitard, 73, 77, 255, 257, 258, 315–317
Arabian Gulf, 29, 104, 171, 324, 330
Arabian Peninsula, 22, 23, 51, 60, 61, 65, 66, 73, 75, 76, 85, 95, 99, 313, 323–325
Arabian Shield, 79, 288, 292, 298, 303, 306–308, 312, 313, 316, 330
Arc-Catalog, 12
Arc-Map, 12
Arc-Toolbox, 12
Area of Interest (AOI), 9–11
Aridity, 22, 24, 380
Artificial recharge, 150
Atlas, 222
Atmospheric Rivers, 49–51, 56, 65

B
Bahrain, 17, 19, 20, 22, 71, 75, 76
Band combination, 11, 259, 312, 366, 397–399
Basalt aquifers, 254
Basalt-aquifer systems, 288
Basaltic lava-flows, 287, 289–298, 300, 302, 305–308
Bifurcation ratio, 235, 236, 244
Bitmap, 3
BOD, 397, 398
Boreholes, 40, 81, 84, 251, 252, 294
Brackish, 75

C
Canopy, 40, 276, 279, 280, 283
Carbonate rocks, 75, 76, 83, 254, 255, 314, 319
Catchment area, 43, 172, 174, 179, 184, 296, 304
Catchment boundaries, 42, 43
Cause–effect, 89
Cavities, 252, 294, 296, 297
Chlorophyll, 366, 368, 370, 372, 374
Circularity ratio, 235, 236, 244
Classifier, 11, 337
Climate change, 17, 22, 24, 31, 33, 43, 50, 54, 87–89, 94, 96, 97, 109, 137, 149, 150, 159, 162, 164, 166, 195, 198,

A. Shaban (ed.), *Satellite Monitoring of Water Resources in the Middle East*, Springer Water, https://doi.org/10.1007/978-3-031-15549-9

199, 201, 203, 275, 311, 322, 365, 367, 369, 374, 380, 385, 390
Climate change projections, 159
Climate change scenarios, 195, 198, 200–203, 380, 385, 387–389
Climate variability, 51, 380, 388
Cloud cover, 38, 41, 42, 45, 157, 395
Cloudy pixels, 380
Clustering techniques, 337, 340, 349, 350
CMIP5 models, 54, 55, 61
Coastal Lake, 367–369, 372, 374, 375
Coastal zones, 19, 89, 171, 174, 178, 179, 251
Conduits, 252
Contamination, 25, 41, 123, 335, 336, 338, 362
Cretaceous, 76, 81–84, 189, 190, 257, 288, 290, 293, 315, 316, 381
Cumulative deviation, 130, 131, 133, 137, 138, 140–142, 144

D
Dead Sea, 30, 32, 77, 79, 80, 219, 221, 224, 226, 228, 233, 237, 239–241, 243–247
Decision Support System (DSS), 320
Delineating, 42, 43
Dependability, 205–207, 210, 211, 215
Depletion, 41, 57, 106, 109, 251, 274, 275, 282, 283, 311, 321, 322, 368
Depression, 79–81, 83, 129, 253, 292, 311, 313, 326, 327, 330
Digital Elevation Model (DEM), 108, 228, 230, 231, 247, 319, 320, 324, 326, 330, 345, 382
Digital number, 177, 300
Domestic water, 41, 150–152, 164, 166, 400, 401
Downscaling, 51, 99, 100
Drainage density, 43, 172, 184, 230, 235–238, 244–246
Drainage network, 42, 43, 228, 230, 239, 302, 304–307
Drainage pattern, 42–44
DRASTIC-based fuzzy, 337
DRASTIC method, 336–339, 341, 349, 350, 353, 358, 361, 362
Drones, 2
Drought, 18, 21, 22, 24, 50, 57, 65, 121, 124, 129–131, 133–140, 143, 144, 189, 274, 275, 343, 380, 389

E
Earth Observation, 319, 365, 366, 375, 376
Economic and Social Commission for Western Asia (ESCWA), 72, 78, 79, 82, 83, 88–91, 94–96
Egypt, 17–20, 22, 23, 55, 75, 76, 102, 205, 207, 209, 222, 367–369, 371
Electromagnetic radiation, 2, 3
Embankments, 42
Environmental problems, 15, 323
Environmental studies, 365, 375
Environment for Visualization Images (ENVI), 9, 177
EO-based, 365
ERDAS Imagine, 9, 259
Er Rub Al Khali, 330
Eruptions, 287, 290, 292–294
Escarpement, 79, 293, 295
ETc, 206, 207, 210, 213, 366, 370
Euphrates, 18, 25, 29, 31–33, 42, 43, 96, 395
Eurasia, 59, 61
Evapotranspiration, 16, 29, 103, 106, 130, 134, 143, 189, 194, 196–199, 202, 203, 206, 209–211, 213–215
Evapotranspiration Index, 130, 133
Exploitability, 74, 75
Extreme flood, 367
Extreme precipitation, 50, 57
Extreme weather, 21

F
FAO, 16, 25, 91, 150, 155, 171, 172, 192, 209, 252
Fault-lineaments, 260, 262, 264, 265, 269
Fault zones, 302, 313, 321, 328, 330
Filtering, 11, 259, 380
Flat-top, 295, 296
Flight altitudes, 5, 7
Flood control, 38, 41, 42
Flood management, 41, 42
Flora, 132, 143
Flow-meters, 172
Flow/storage, 253
Fluvial, 81, 321, 322, 324, 326, 327, 330
Forecasting, 41, 44, 107, 162
Fossil, 71, 274, 320
Freshwater plumes, 173, 176, 177, 182
Fuzziness, 337, 348, 349, 352, 361
Fuzzy C-means (FCM), 337–342, 346, 349–352, 356–362

G
Gaza Strip, 219, 220, 222–224, 226–228, 231–233, 235, 239, 240, 247
Geo-Eye, 8
Geographic Information System (GIS), 11–13, 30, 33, 36–40, 45, 46, 72, 93, 177, 178, 227, 228, 263, 289, 298, 304, 319, 320, 325, 330, 395, 400, 403
Geological structures, 75, 239, 243
Geology, 40, 189, 203, 313, 321, 337
Geometric correction, 9, 136
Geo-political, 15, 18, 20, 21, 219
Geo-referencing, 10, 176, 177
Geo-spatial data, 1, 2, 5, 11, 12, 173, 263
GIS-based, 96, 320, 336
GIS layers, 12
GIS software, 12, 92
Global Land Data Assimilation System (GLDAS), 274, 276, 279, 280, 283
Global Positioning System (GPS), 4, 12, 116
Global warming, 23, 24
Goddard Earth Observing, 53
Graben, 74, 80
Gravimetry, 275
Gravity Recovery, 102, 106, 275, 321
Greater Beirut, 150, 164, 166
Groundwater aquifers, 150, 192, 226, 276, 307, 311, 314, 315, 328, 330
Groundwater depletion, 106, 274, 276, 281–283, 321, 322
Groundwater exploration, 252–254, 269, 288, 330
Groundwater level, 123, 124, 137, 143, 256, 275, 311, 330
Groundwater potentiality, 292, 327, 329
Groundwater potential zones, 319, 321, 324, 330, 331
Groundwater recharge, 207, 252, 253, 274, 311, 312, 344
Groundwater resources, 35, 43, 44, 72, 172, 227, 274, 284, 308, 335, 343, 356, 362
Groundwater seeps, 171, 172
Groundwater systems, 283, 311

H
Harrats, 288–308, 313
Hejaz, 313, 324, 330
Historical simulations, 51, 54, 55, 61–64
Hydraulic conductivity, 193, 316–318, 335, 336, 338, 345, 351, 352, 360
Hydrogeological models, 289
Hydrogeology, 73, 74, 189, 292
Hydrological characteristics, 227, 228
Hydropower, 41, 280
Hypsometric integrals, 237

I
IHE, 21
IKONOS, 7–9, 34
Image enhancement, 10
Inflows, 41, 42, 196, 199, 202, 203, 372, 373
Inherent Optical Property (IOP), 365, 366
In-situ measurements, 130, 157, 283, 321, 370, 379, 394, 395, 398
Interferometric Synthetic Aperture Radar (InSAR), 276, 281, 283
Intergovernmental Panel on Climate Change (IPCC), 22, 33, 54, 87, 96
Iran, 17–20, 22, 25, 51–59, 76, 77, 120–125, 127, 321, 337, 343, 350, 360
Iraq, 17–20, 22, 24, 29, 31–33, 43, 75–77, 120–122, 151, 321, 395, 400
Irrigation, 21, 31, 38, 40, 41, 44, 45, 71, 81, 130, 131, 139, 143, 144, 192, 196, 198–203, 205–207, 209–211, 213–215, 280, 282, 288, 311, 344, 395, 399
Irrigation Water Performance Assessment (IWPA), 205–208, 210, 213, 215

J
Jordan, 17, 19, 20, 22, 25, 30, 32, 75–77, 79–81, 220, 223, 224, 227
Jordan River, 30, 32, 172, 188, 191, 220, 224–226, 228, 233
Jurassic, 189, 191, 192, 258, 266, 268, 315, 381

K
Kuwait, 17, 19, 20, 22, 75, 76, 106, 330

L
Lag time, 174, 178–180, 182–184, 246, 384
Land cover/use, 44, 189, 243
Landforms, 42–44, 239, 246
Land observatory, 4, 8
Landsat 7 ETM+, 8, 135, 136, 259, 260, 269

Landsat 8, 8, 135, 136, 207, 209, 211–213, 215, 368, 395
Land Surface Temperature (LST), 157–159, 166, 209–212, 320
Lapse rate, 383, 384
Least Squares Mascon Fitting, 115, 117, 127
Lebanon, 6, 17–20, 22, 30, 73, 75, 76, 149, 150, 152, 153, 157, 162, 166, 171–176, 178, 179, 182, 184, 187, 188, 195, 197, 224, 251–253, 255–257, 259, 260, 269, 273, 275–277, 280, 282, 379, 380, 385
Limestone, 44, 77, 226, 254, 255, 257, 258, 314–317, 319, 339, 388
Lineaments, 35, 44, 252–256, 259–269, 320, 329
Lineaments map, 259–261
Linear features, 252, 253, 259–261
Linear regressions, 92, 108, 158, 160–162
Litani River, 155, 172, 280, 282, 383
Lithological crossing, 262
Lowlands, 311, 313

M
Machine learning, 100, 107, 323, 324, 330, 331
Marl, 257, 258, 317, 319
Matrix, 80, 92, 160, 265, 340, 341
Maximum temperature, 151, 152, 158, 159, 161, 162, 164
Meandering ratio, 172
Mediterranean climate, 131, 137, 152, 153, 159, 187, 189, 276, 379, 381
Mediterranean Sea, 23, 59, 60, 65, 172, 179, 220, 222, 224, 228, 233, 237, 239, 243–247, 367, 372, 373, 381, 383
Mega Aquifer, 314, 315, 318
Mesozoic, 81
Microwave, 3, 102, 106, 116
Middle East, 16–18, 20, 21, 25, 29–33, 35, 37–45, 49, 52, 57, 58, 65, 120, 127, 149, 171, 219, 275, 278, 282, 321
Middle East Region, 16–25, 29, 40, 380
Minimum water demand, 164
Model efficiency, 196
Model simulations, 51, 54, 55, 58, 66, 101, 274–276, 283
Moderate Resolution Imaging Spectroradiometer (MODIS), 8, 103, 157, 158, 176, 177, 182, 183, 207, 320, 379–382, 385
Moderate Resolution Imaging Spectroradiometer (MODIS-Terra), 173, 174, 176, 178–181, 184
Monitoring wells, 276, 282, 283
Mosaicking, 10
Mount Hermon, 30, 189
Multi-model, 52, 58, 63–65

N
National Aeronautics and Space Administration (NASA), 53, 115, 116, 175, 228, 275, 277, 370
Near-polar, 4, 116
Neogene, 76, 77, 255, 257, 277, 315, 317
Nile delta, 205–207, 212, 213, 215, 367, 375
Nile River, 18
Nile Valley, 95, 96
Nitrate, 80, 81, 338, 356–358, 361, 362
Non-optical, 366, 368, 375, 376
Normalized Difference Vegetation Index (NDVI), 211, 320, 370, 372–374
Normalized Difference Water Index (NDWI), 130, 131, 136, 137, 139–144
NTU, 401

O
Oceanography, 2
Oligocene, 290, 293
Oman, 17, 19, 20, 22, 23, 71, 75, 76, 104, 106, 123, 125, 126, 183, 324–326, 329, 330
Operational Land Imager (OLI), 8, 135, 136, 368, 399, 400
Optimization, 92, 194
Orates River, 172
Outcrops, 74, 77, 79, 81, 83, 84, 188, 189, 191, 311, 314, 381
Outflows, 35, 196, 197, 199, 202
Over-discharge, 343

P
Palaeochannels, 319, 321, 324–328
Palaeolakes, 321, 322, 324, 325, 329
Paleozoic, 81
Palestine, 17, 19, 22, 32, 75, 76, 219, 223, 224, 226–228
PCI, 9, 176
Penman-Monteith, 130, 194
Perennial rivers, 172

Permeability, 245, 254, 256, 277, 288, 294, 308, 321
Permeable zones, 297
Phosphorous, 366, 397, 399–402
Pliocene, 191, 257, 288, 293, 314
Pollution, 5, 17, 21, 38, 41, 46, 74, 282, 311, 335, 336, 338, 339, 341, 343, 362, 393
Porosity, 254–256, 288, 294, 297, 308, 314, 316, 321, 328, 335
Precambrian, 290, 292, 295, 297, 298, 300, 306, 308
Principal Component Analysis (PCA), 92
Productivity rate, 264
Protection measures, 42, 348
Pumping rate, 256, 274

Q
Qatar, 17, 19, 22, 75, 76, 317
Quaternary, 76, 81, 83, 191, 257, 258, 267, 268, 288, 292, 313, 324, 343
Quaternary rocks, 277

R
Radar, 3, 99, 108, 320, 321
Radiometric resolution, 5, 6, 34, 45
Radio waves, 2
Rainfall depth, 191, 198
Rainfall peaks, 174, 176, 178, 180, 183
Rainwater, 306–308, 311, 313
Raster data, 12, 90
Recharge map, 277, 344
Reflectance, 8, 9, 130, 136, 366, 370, 394–396, 398–400
Regression algorithms, 368
Relative humidity, 58, 155, 157, 158, 160, 161, 307
Relief gradient, 172
Remote sensing, 1–3, 5, 7, 30, 33–35, 38–40, 42, 44–46, 72, 85, 90, 100–103, 109, 130, 131, 134, 139, 140, 144, 152, 157, 173, 184, 206, 207, 215, 227, 228, 247, 252, 269, 274–276, 284, 289, 307, 319, 320, 322, 326, 330, 331, 365–370, 372, 375, 379, 382, 389, 394, 400, 403
Renewable water, 18, 20, 25, 29, 99, 102, 109, 187, 203
Reservoirs, 35, 38, 40–44, 102, 117, 144, 189, 191, 251, 275, 276, 279, 280, 283
Revisit time, 6
RICCAR, 88, 89, 91, 94
Riparian countries, 15, 18, 25, 71, 72, 76, 77
Rivers discharge, 179, 182
Root Mean Square Error (RMSE), 137, 139, 320, 399, 400
Rugged topography, 171, 172

S
Sahara, 52
Salinity, 31, 75, 80, 320, 367, 369, 370, 372–376, 394, 399
Saq aquifer, 314, 321
Satellite, 1–11, 30, 33–35, 37–39, 41–45, 53, 72, 99–101, 107, 108, 115–117, 127, 130, 131, 134–137, 139, 143, 157, 173, 174, 176–178, 180, 184, 209, 227, 228, 252–254, 259, 262, 269, 274–278, 283, 289, 296, 297, 307, 321, 365, 366, 370, 372, 375, 379, 380, 394
Saudi Arabia, 17, 19, 20, 22, 24, 32, 55, 71, 75, 77, 79–84, 102, 106, 120–122, 287–291, 307, 308, 311–314, 316–321, 324–327, 329, 330
Sedimentation, 41, 42, 369
Sensitivity analysis, 92, 96, 338, 343, 351–353, 356, 360, 362
Sensors, 1–3, 5–7, 9, 35, 102, 176, 321, 327, 331, 366, 383, 387, 394
Sentinel-1, 276, 281, 283, 320
Shared aquifers, 25, 72–74, 76, 77
Shuttle Radar Topography Mission (SRTM), 222, 228, 229, 232, 319, 320, 324, 326
Simplified Surface Energy Balance (SSEBop), 206, 207, 209, 210, 213
Sinai Peninsula, 75, 102
Snowmelt Runoff Model, 380, 382
Snowpacks, 274, 275, 280, 379, 380
Snowstorm, 385, 388
Socio-economic, 31, 88, 129, 144, 154, 164, 367, 369, 372
Soil moisture, 35, 43, 44, 100, 102–104, 106–110, 194–196, 198, 199, 202, 253, 274–276, 279, 280, 283, 319, 320, 370
Solar radiation, 3, 155, 158, 160–162, 166, 209
Spaceborne, 108, 157, 321
Space shuttle, 5
Spatial resolution, 1, 5–8, 39, 45, 90, 93, 134, 143, 153, 157, 176, 179, 182,

227, 228, 259, 276, 278, 319, 320, 324, 370, 380, 381, 395
Spectral resolution, 6, 45
Spectroradiometer, 157, 320, 381
Split-window, 157, 209
Standard Precipitation Index (SPI), 130, 131, 133–135, 137–140, 142–144
Statistical data, 90, 95
Stereoscopic photographs, 2
Stokes coefficients, 115–121, 123, 125
Storage coefficient, 79, 316–318
Strahler, 230, 231, 235–237
Stratigraphy, 73, 74, 79, 253
Streamflow, 43, 171, 172, 174, 194, 196, 198, 202, 380, 387, 388
Stream frequency, 43, 235, 236, 244
Structural features, 73, 74, 174
Subsidence, 281–283
Supervised classification, 11
Surface Energy Balance Algorithm for Land (SEBAL), 206, 207, 210
Surface mass, 117, 118
Sustainability, 2, 74, 283, 365–367, 369
Swath width, 7, 8
Syria, 17–19, 22, 29–32, 75–77, 120, 172, 224

T
Taurus-Zagros Mountain, 73
Temperature, 22–25, 35, 42, 45, 50, 51, 91, 96, 107, 108, 130, 132–134, 149, 151, 153–155, 157–162, 164, 166, 173, 176–178, 189, 191, 195, 196, 202, 206, 209, 210, 212, 213, 274, 275, 279, 307, 312, 343, 344, 368, 380, 382–385, 387–389, 395
Temperature-based Models, 162
Temporal gravity, 127
Temporal resolution, 6, 38, 45, 99, 100, 106, 176, 278, 370, 379, 380
Terrestrial environments, 4
Thematic maps, 11, 12
Thermal band, 176, 209, 211, 259, 289, 297, 300, 301
Thermal Infrared, 3, 368
Thiessen polygon, 124
Tiberias Lake, 224, 226
Tigris, 18, 25, 29, 31–33, 42, 43, 96
Topographic maps, 2, 7, 53, 178, 222, 319
Topography, 18, 40, 44, 100, 104, 107, 222, 228, 240, 243, 246, 253, 254, 294, 304, 336, 338, 339, 345, 350, 352, 356, 360, 381, 386
Torrential rain, 23, 180, 183
Total Dissolved Solids (TDS), 75, 80, 84, 394, 397, 399–402
Total Water Storage, 102–104, 106, 109, 116, 117, 121, 127, 275, 276, 278, 280, 283, 321, 323–325, 330
Training sites, 11
Turkey, 17–19, 22, 29, 31–33, 52, 53, 58, 59, 76, 77, 120–122, 131, 206

U
UNESCO, 18, 73
United Arab Emirates (UAE), 17, 19, 20, 22, 62, 66, 75, 76, 100, 103–105, 107–110, 329, 330
United States Geological Survey (USGS), 13, 91, 134, 228, 319, 368, 395

V
Validation, 109, 160, 194, 196, 197, 202, 329, 368, 370, 385, 387, 388, 399, 400
Vapor, 49, 50, 53, 55, 209
Visual interpretation, 34, 330
Volcanic fields, 288–292, 302, 308
Volcanic terrains, 288, 289, 292, 294, 296, 297, 304, 307, 308
Vulnerability, 87–96, 164, 246, 335–353, 356–362
Vulnerability index, 336, 337, 343, 351, 353, 356, 357, 360, 362

W
Waste Water Treatment Plants, 372, 401
Water availability, 16, 18–20, 41, 88, 89, 94, 95, 131, 150, 164, 187, 389
Water balance, 102, 130, 134, 150, 157, 188, 194, 196, 198, 199, 202, 276, 390
Water demand, 15, 16, 18, 20–22, 35, 43, 99, 106, 149–154, 158–166, 187, 188, 200–203, 206, 207, 209, 213, 215, 273, 389
Water Evaluation and Planning (WEAP), 192, 194, 196, 202
Water harvesting, 20, 184
Water quality, 31, 41, 42, 74, 75, 81, 84, 89, 227, 365–370, 372, 374–377, 393–399, 401, 403
Water Quality Index (WQI), 393, 395–398, 403

Watershed, 44, 102, 103, 152, 181, 184, 188, 194, 226–228, 232–247, 298, 307, 372, 380, 381
Water storage, 35, 41, 43, 102, 103, 106, 109, 116, 121, 124, 127, 150, 194, 276–280, 283, 321, 324, 325
Wavelength, 2, 3, 6, 11, 33, 35, 120, 136, 394, 400
Weather data, 155, 156
West Bank, 30, 32, 219, 220, 222–224, 226–228, 231–235, 239, 240, 247
Width/Length ratio, 172, 235, 236, 241, 244
Wind speed, 151, 155, 158–162, 191, 209, 212
World Meteorological Organization, 380

Y

Yemen, 17, 19, 20, 22, 23, 71, 75, 76, 81–83, 104, 106, 290, 293, 327, 329